SECURITY CLASSIFICATION OF THIS PAGE *(When Data Entered)*

REPORT DOCUMENTATION PAGE		READ INSTRUCTIONS BEFORE COMPLETING FORM
1. REPORT NUMBER AFFDL-TR-76-84	2. GOVT ACCESSION NO.	3. RECIPIENT'S CATALOG NUMBER
4. TITLE *(and Subtitle)* A Laboratory Investigation Into Flight Path Dispersions During Steep Descents of V/STOL Aircraft		5. TYPE OF REPORT & PERIOD COVERED Final, Sept.1972-June 1976
		6. PERFORMING ORG. REPORT NUMBER
7. AUTHOR(s) L. D. Reid, B. Etkin, H. W. Teunissen, P. C. Hughes		8. CONTRACT OR GRANT NUMBER(s) F33615-73-C-3013
9. PERFORMING ORGANIZATION NAME AND ADDRESS Institute for Aerospace Studies, University of Toronto, 4925 Dufferin St., Downsview, Ontario, Canada, M3H 5T6		10. PROGRAM ELEMENT, PROJECT, TASK AREA & WORK UNIT NUMBERS Project Number 8219 Task Number 0504
11. CONTROLLING OFFICE NAME AND ADDRESS Air Force Flight Dynamics Laboratory, Air Force Wright Aeronautical Laboratories, Air Force Systems Command, Wright-Patterson Air Force Base, Ohio 45433		12. REPORT DATE August 1976
		13. NUMBER OF PAGES
14. MONITORING AGENCY NAME & ADDRESS*(if different from Controlling Office)*		15. SECURITY CLASS. *(of this report)* Unclassified
		15a. DECLASSIFICATION/DOWNGRADING SCHEDULE
16. DISTRIBUTION STATEMENT *(of this Report)* Approved for public release; distribution unlimited.		
17. DISTRIBUTION STATEMENT *(of the abstract entered in Block 20, if different from Report)*		
18. SUPPLEMENTARY NOTES		
19. KEY WORDS *(Continue on reverse side if necessary and identify by block number)* Aircraft Response to Wind Shear and Turbulence Simulation of Planetary Boundary Layer Boundary Layer Wind Tunnel Turbulence Measurements		

20. ABSTRACT *(Continue on reverse side if necessary and identify by block number)*

A study into the prediction of V/STOL aircraft flight path perturbations during steep landing approaches has been completed in several phases. The study begins with a discussion of four possible approaches to the problem. The two most practical of these are developed in greater detail. The first of the latter is the fixed probe approach, where two point space/time correlations are measured in a boundary layer wind tunnel along the glide slope. The theory of this technique is derived in detail. The

DD FORM 1473 1 JAN 73   EDITION OF 1 NOV 65 IS OBSOLETE

SECURITY CLASSIFICATION OF THIS PAGE *(When Data Entered)*

second is the moving probe approach in which a suitable three component velocity probe is moved along the glide slope in a boundary layer wind tunnel and the time history of the resulting measurements used to determine the response of the aircraft. A candidate moving probe apparatus is analyzed and its feasibility evaluated.

Two similar boundary layer wind tunnels are used to generate simulations of the planetary shear layer. The properties of the 8" x 8" tunnel are described along with the associated instrumentation. This facility generates a boundary layer through a combination of a jet grid, a bluff barrier and floor roughness. The modification of the UTIAS subsonic wind tunnel into a 44" x 66" multiple-jet boundary layer facility and the development of associated instrumentation are described. The properties of the boundary layers generated in both tunnels are presented in detail.

A large number of fixed probe hot wire correlation measurements of the turbulent velocity components were completed with a scaled model of the planetary boundary layer. The majority of these measurements were confined to a mean velocity power law variation with an index of $n = 0.16$ and a glide slope angle of 15° with limited data also taken with glide slopes of 45° and 90° and some with $n = 0.35$.

Based on the correlation results from the 44" x 66" tunnel a preliminary attempt at fitting a von Kármán model to the results is carried out.

The linearized equations of motion for an aircraft following a glide slope in wind shear and turbulence are developed. The equations are formulated in such a manner as to allow the effects of wind shear and turbulence to be studied independently. Stability derivatives for a typical STOL aircraft are employed to simulate the flight of a realistic vehicle through the planetary boundary layer.

The response of the STOL aircraft to the turbulence simulated in the 44" x 66" tunnel is predicted using the longitudinal equations of motion. These results predict the scatter in the state vector elements during the landing approach due to the presence of turbulence along the glide slope.

FOREWORD

TABLE OF CONTENTS

TABLE OF CONTENTS

LIST OF TABLES

LIST OF FIGURES

LIST OF SYMBOLS

$\vec{A}$ nongravitational or aerodynamic force applied to the aircraft

$\bar{c}$ mean aerodynamic wing chord, ft.

C_D $\dfrac{\text{Drag}}{\frac{1}{2}\rho V^2 S}$ aircraft drag coefficient

C_{D_o} aircraft zero-lift, drag coefficient

C_{D_α} $\dfrac{\partial C_D}{\partial \alpha}\Big|_e$

C_L $\dfrac{\text{Lift}}{\frac{1}{2}\rho V^2 S}$ aircraft lift coefficient

C_{L^*} $\dfrac{L^*}{q_e S}$ coefficient based on lift and component of thrust in the lift direction

$C_{L_{C_T}}$ $\dfrac{\partial C_L}{\partial \bar{c}_T}\Big|_e$

C_{L_α} $\dfrac{\partial C_L}{\partial \alpha}\Big|_e$

C_m $\dfrac{\text{Pitching Moment}}{\frac{1}{2}\rho V^2 S \bar{c}}$ aircraft pitching moment coefficient about the centre of mass

$C_{m_{C_T}}$ $\dfrac{\partial C_m}{\partial \bar{c}_T}\Big|_e$

C_{mu} $\dfrac{\partial C_m}{\partial \tilde{u}}\Big|_e$

C_{mq} $\dfrac{\partial C_m}{\partial \tilde{q}}\Big|_e$

$C_{m\alpha}$ $\dfrac{\partial C_m}{\partial \alpha}\Big|_e$

$C_{m\dot\alpha}$ $\qquad \dfrac{\partial c_m}{\partial \alpha'}\bigg|_e$

$C_{m\eta}$ $\qquad \dfrac{\partial c_m}{\partial \eta}\bigg|_e$

C_T $\qquad \dfrac{\text{Thrust}}{\frac{1}{2}\rho V^2 S}$ thrust coefficient

$C_{T\pi}$ $\qquad \dfrac{\partial c_T}{\partial \pi}\bigg|_e$

C_{W_e} $\qquad \dfrac{mg}{q_e S}$

C_x $\qquad \dfrac{X}{\frac{1}{2}\rho V^2 S}$

$C_{x_{C_T}}$ $\qquad \dfrac{\partial c_x}{\partial c_T}\bigg|_e$

C_{xu} $\qquad \dfrac{\partial c_x}{\partial \tilde{u}}\bigg|_e$

$C_{x\alpha}$ $\qquad \dfrac{\partial c_x}{\partial \alpha}\bigg|_e$

C_z $\qquad \dfrac{Z}{\frac{1}{2}\rho V^2 S}$

C_{zu} $\qquad \dfrac{\partial c_z}{\partial \tilde{u}}\bigg|_e$

C_{zq} $\qquad \dfrac{\partial c_z}{\partial \tilde{q}}\bigg|_e$

$C_{z\alpha}$ $\qquad \dfrac{\partial c_z}{\partial \alpha}\bigg|_e$

$C_{z\dot{\alpha}}$ $\qquad \dfrac{\partial c_z}{\partial \alpha'}\bigg|_e$

$C_{z\eta}$ $\qquad \dfrac{\partial c_z}{\partial \eta}\bigg|_e$

$f(\zeta)$ $\qquad$ longitudinal correlation coefficient

f $\qquad$ frequency, Hz

$\mathcal{F}_B$ $\qquad$ body fixed reference frame

$\mathcal{F}_I$ $\qquad$ earth fixed reference frame

$\mathcal{F}_T$ $\qquad$ tunnel fixed reference frame

$\underrightarrow{F}$ $\qquad$ external force applied to the aircraft, lbs.

$g(\zeta)$ $\qquad$ lateral correlation coefficient

$\underrightarrow{g}$ $\qquad$ gravity vector or gust velocity vector (context will indicate correct usage)

$\underline{G}$ $\qquad \begin{pmatrix} \Delta\tilde{u}_t \\ \Delta\alpha_t \end{pmatrix}$ airspeed and angle of attack perturbations associated with turbulence field for the case of an aircraft unresponsive to turbulence

h $\qquad$ height above ground

$\underrightarrow{h}$ $\qquad$ vehicle angular momentum about centre of mass

h_G $\qquad$ thickness of the planetary boundary layer

H $\qquad$ wind tunnel height

$\underline{H}(t,t')$ $\qquad$ impulsive response matrix of the aircraft

$(\underrightarrow{i}_i, \underrightarrow{j}_i, \underrightarrow{k}_i)$ $\qquad$ unit vectors defining the reference frame $\mathcal{F}_i$

i_{yy} $\qquad 8I_{yy}/(\rho S\bar{c}^3)$

$\underline{I}_B$ $\qquad$ inertia matrix written with respect to $\mathcal{F}_B$

I_{xx} $\qquad \displaystyle\int (y^2 + z^2)dm$, etc.

I_{xz} $\qquad \displaystyle\int xz\, dm$, etc.

k $\qquad$ reduced frequency $\dfrac{f}{\bar{U}}$

k_{xpu}	location of the spectral peak in $\Phi_{uu}(k)$
k_{xpw}	location of the spectral peak in $\Phi_{ww}(k)$
L	aerodynamic rolling moment about the centre of mass in $\mathcal{F}_B$
$L*$	lift plus component of thrust in the lift direction
L_u^x	longitudinal turbulence scale
L_w^x	lateral turbulence scale
m	aircraft mass, slugs
M	aerodynamic pitching moment about the centre of mass in $\mathcal{F}_B$
$\overrightarrow{M}$	external moment about the aircraft centre of mass
n	velocity profile power law index
N	aerodynamic yawing moment about the centre of mass in $\mathcal{F}_B$
p	roll rate in $\mathcal{F}_B$ (right wing down positive) rad/sec
$\overrightarrow{p}$	aircraft momentum vector
q	pitch rate in $\mathcal{F}_B$ (nose up positive) rad/sec
q_e	dynamic pressure $\frac{1}{2}\rho V_e^2$
r	yaw rate in $\mathcal{F}_B$ (nose right positive) rad/sec
$\underline{R}_{BI}$	rotation matrix relating vector components in $\mathcal{F}_I$ to those in $\mathcal{F}_B$
R_{xy}	cross-correlation between $x(t)$ and $y(t)$
$\underline{\tilde{\mathbb{R}}}$	3 x 3 flight path correlation matrix containing elements $\tilde{\mathbb{R}}_{ij}$
$\mathbb{R}_{uv}(t_1,t_2)$	flight path correlation between $u(t)$ measured at z_1 and $v(t)$ measured at z_2, etc.
$\tilde{\mathbb{R}}_{uv}$	$\dfrac{\mathbb{R}_{uv}}{\hat{u}\,\hat{v}}$
S	distance downstream from jet grid or, wing planform area (context will indicate correct usage)
S_ℓ	length scale factor

xv

LIST OF SYMBOLS (CONT.)

S_v	velocity scale factor
S_t	time scale factor
t	time, sec.
t_1	time for aircraft to reach position of first probe, sec.
t_2	time for aircraft to reachposition of second probe, sec.
$t*$	$\bar{c}/(2V_e)$
t'_F	time to reach a specified height along modified glide slope assuming frozen flow in the wind tunnel, sec.
$\vec{T}$	thrust vector
T	time to reach decision height at end of landing approach, sec.
$(u\ v\ w)$	components of $\vec{V}$ in $\mathcal{F}_B$ or turbulence components in $\mathcal{F}_T$ (context will indicate correct usage and scale)
$(u_E v_E w_E)$	components of $\vec{V_E}$ in $\mathcal{F}_B$
$(u_g v_g w_g)$	turbulence components in $\mathcal{F}_I$
$\bar{U}$	mean wind tunnel velocity in the $\vec{i}_T$ direction
$\vec{V}$	airspeed vector
$\vec{V_E}$	velocity of aircraft centre of mass with respect to $\mathcal{F}_I$
$\vec{V_{EF}}$	velocity of moving probe with respect to $\mathcal{F}_I$ when moving down modified glide slope under frozen flow assumption
W	local mean wind speed or wind tunnel width (context will indicate correct usage)
W_G	wind speed at top of planetary boundary layer
$(x\ y\ z)$	spacial coordinates in $\mathcal{F}_T$
$(x_I y_I -h)$	coordinates of aircraft centre of mass in $\mathcal{F}_I$
$(x_N y_N z_N)$	spacial coordinates in $\mathcal{F}_N$
X	x component of aerodynamic force in $\mathcal{F}_B$, lb.
Y	y component of aerodynamic force in $\mathcal{F}_B$, lb.

z_1 height of first probe above ground level, corresponds to t_1

z_2 height of second probe above ground level, corresponds to t_2

Z z component of aerodynamic force in $\mathcal{F}_B$, lb.

Z_G thickness of the planetary boundary layer

α angle of attack of the aircraft's zero lift line, rad.

γ the angle $\overrightarrow{V}$ makes with the horizontal, positive downwards, rad.

γ_E glide slope angle with respect to the horizontal, rad.

δ_{ij} Kronecker delta $= 1$ for $i = j$; $= 0$ for $i \neq j$

$\delta(t)$ Dirac delta function

$\delta\alpha$ angle between $\overrightarrow{Te}$ and $\overrightarrow{Ve}$, rad. (see Fig. 165)

$\Delta\alpha$ $\dfrac{\Delta w}{V_e}$, angle of attack perturbation, rad.

$\Delta\tilde{\Gamma}$ $\dfrac{d(\Delta\tilde{w})}{d\,\tilde{t}}$

$\Delta\theta$ perturbation in the Euler elevation angle, rad.

$\Delta\phi$ perturbation in the Euler bank angle, rad.

$\Delta\psi$ perturbation in the Euler azimuth angle, rad.

$\Delta\underline{u}_c$ $\begin{pmatrix} \Delta\eta \\ \Delta\pi \end{pmatrix}$ control input

Δx perturbation in x

$\Delta\underline{x}$ $(\Delta\tilde{u}\ \Delta\alpha\ \Delta\tilde{q}\ \Delta\theta\ \Delta\tilde{x}_q\ \Delta\tilde{h})^T$ matrix of state variables

ϵ angle moving probe track makes with the horizontal, rad.

ζ $\dfrac{\xi}{1.339 L_u^x}$ variable in the von Kármán model

η elevator deflection, positive upwards, rad.

μ $2m/(\rho S\bar{c})$

ν kinematic viscosity of air, ft^2/sec

ξ	$\sqrt{\xi_1^2 + \xi_2^2 + \xi_3^2}$ spacial separation between velocity probes
$(\xi_1\ \xi_2\ \xi_3)$	the components of spacial separation between velocity probes
π	throttle setting (forward positive) measured in % of full throttle
ρ	density of air, slugs/ft^3
σ_x^2	the variance of the variable x
$\underline{\underline{\Sigma}}$	$<\underline{y}\,\underline{y}^T>$ dispersion matrix of state variables
τ	time delay, sec.
Φ_{xx}	power spectral density of the signal x(t)
$\underrightarrow{\omega}$	angular velocity of $\mathcal{F}_B$ with respect to $\mathcal{F}_I$, rad/sec
$(\ )_e$	denotes value on reference equilibrium
$(\ )_{ee}$	denotes value on reference equilibrium of Ref. 24
$(\ )'$	denotes value as measured in wind tunnel scale
$\dot{\underrightarrow{x}}$	$\dfrac{d\underrightarrow{x}}{dt}$ as seen from $\mathcal{F}_I$
$\overset{\circ}{\underrightarrow{x}}$	$\dfrac{d\underrightarrow{x}}{dt}$ as seen from $\mathcal{F}_B$
x'	$\dfrac{d\underset{\sim}{x}}{dt}$
$\underrightarrow{x}$	vector with components represented by the column matrix $\underline{x}$
$\underline{X}$	matrix
$\underline{x}_i$	column matrix representing the components of $\underrightarrow{x}$ in $\mathcal{F}_i$
$\underline{X}^T$	transpose of the matrix $\underline{X}$
$e^{\underline{A}t}$	$\underline{I} + \underline{A}t + \ldots + \dfrac{\underline{A}^k t^k}{k!} + \ldots$
x^*	complex conjugate of x
$\left.\begin{array}{c}\hat{x}\\ \overline{x^2}\end{array}\right\}$	root mean square value of x(t)
$\bar{x}$	mean value of x(t) or Laplace transform of x(t), depending on the context
$<x(t)>$	ensemble average of x(t)
$\tilde{x}$	nondimensionalized form of x (see Section 8.1.5)

Section I

INTRODUCTION

Safe and reliable landings of STOL and VTOL aircraft on steep descent paths in congested environments, low visibility and strong wind must be achieved if the all-weather air transport systems envisaged for the future are to become a reality. A central feature of the overall problem is the design of vehicle control and terminal guidance systems that will result in small enough dispersions of the flight path and vehicle attitude at some decision height. Figure 1 illustrates the nominal flight path with which we are concerned, i.e., the path that would be followed through the planetary boundary layer with an ideal guidance and control system. It consists of an approach that terminates at point A with airspeed V_A, a descent at angle γ_E to point B where airspeed is V_B, possibly different from V_A, and a subsequent flare and touchdown. The present investigation deals with the landing descent only and has not yet been extended to cover the flare and touchdown manoeuvres. Note that in Figure 1, the common case of γ_E = constant (that is, a straight line descent) has been shown, although a curved path descent could equally well have been chosen. Point B is at the decision height, where the choice is made whether to land or to abort. This decision depends, when the flight path perturbations are present, on whether or not the trajectory (more precisely the state vector) falls within a certain 'window'. The problem for the analyst and designer is to predict, for a given situation, the probabilities associated with this decision. It is not our purpose in this paper to deal with the required window size, nor with the probability levels needed, important as these questions may be. We are con-

1

cerned here rather with arriving at estimates of the dispersions of the vehicle's state vector at the decision height. In particular, the application of a boundary layer wind tunnel to this problem will be discussed and data presented in support of this approach. Accordingly, under the heading Approaches to Solution of the Problem, various approaches to this problem are outlined, with the description of a simplified approach using stationary probes being given under Theory of the Stationary-Probe Method. Under Experimental Facilities and Experimental Results, the development of facilities at UTIAS for laboratory simulation of the planetary boundary layer is described and the measurements which are required for application of the stationary-probe approach are presented.

Ideally, the state variables with which we would be concerned in discussing errors at A and B include the position vector, the velocity vector and the attitude, nine scalar variables in all. The angular velocity is probably unimportant. Also, in practice, it is probably good enough to define the window at B in terms of a severely restricted set of variables; for example, x, y, V and $\dot{z}$.

Of the factors that contribute to dispersion at the target plane (Figure 1) we can usefully separate out three (apart from guidance system errors):

     (i) the mean wind profile,

     (ii) errors in initial conditions at A,

     (iii) turbulence.

The way in which these three contribute to state errors at the target plane is illustrated in Figure 2 by the intercepts of an ensemble of tra-

2

jectories with the target plane - an ensemble related to a given wind field. R is the point at which the reference trajectory (see Figure 3) associated with correct initial conditions and zero turbulence pierces the target plane. The reference trajectory accounts for the mean wind profile, which may include cross wind, rotation of wind direction with height and local effects of buildings or terrain (the wind in Figure 1 is shown coplanar with the trajectory only for convenience). Curve (a) in Figure 2 represents the dispersion around R associated with initial errors at A that may occur with an assigned probability P_1. These may be the outcome of a stationary random process along the nearly horizontal path that precedes arrival at point A. A given initial error in position and/or velocity and/or attitude yields a single point in the target plane. The continuous curve (a) derives from a continuous set of initial errors. P_1 is the probability (e.g., .995) that the trajectory falls inside (a). Curve (b) on Figure 2 shows the additional dispersion at probability level P_2 associated with turbulence during the descent and a particular set of initial errors. We assume that the errors resulting from the initial conditions are independent of those produced by the turbulence, and hence that the joint probability is the product of the separate probabilities. If, furthermore, as will frequently be the case, the dispersions from the two sources can be linearly superposed, only one curve like (b) need be obtained - for zero initial error - and combined with every point of (a) to yield the envelope (c). The probability that the trajectory will lie inside (c) is then $P = P_1 P_2$.

In order to further clarify the different vehicle trajectories between A and B with which we will be concerned, the reader is referred

3

to Figure 3. The nominal path is equivalent to the glide slope and is that which the vehicle would follow if there were no dispersive factors at all or if it had an ideal guidance and control system. The reference trajectory is the path the aircraft would follow if there were no initial condition errors and no turbulence. It reflects the departure from the nominal path caused only by the mean velocity, and would be zero for an ideal control system (and thus R = B). Finally, the actual path flown by the aircraft includes the effect of all three of the factors listed above and its departure from the reference solution represents the effects of initial condition errors and turbulence.

The current generation of STOL airplanes - externally blown flaps, deflected slipstream, tilt wing, tilt duct, tilt rotor, augmentor wing - are limited to approach speeds of 50 knots or more and to descent angles of less than about 16° (Reference 1). Present developments are expected both to demand and to lead to even steeper glide slopes for STOL airplanes, perhaps by the use of reverse thrust combined with powered lift (Reference 2). Helicopters and other VTOL aircraft are of course capable of descents at all angles up to 90°. Many past studies of the response of vehicles to turbulence, during landing as well as in cruise, have determined the long term response by using a statistically stationary model of the input. This yields as outputs, among others, the mean-square values of the vehicle response variables. From these, with the common assumption of a Gaussian process, probabilities can be calculated (References 1, 3, 4). Although this may be a reasonable approach for CTOL airplanes with glide slopes of about 3° and high landing speeds, turbulence is of greater relative importance at low air speeds and the steeper angle of penetration

4

of the boundary layer makes the stationary model suspect for STOL and VTOL. Furthermore, an examination of data for a representative STOL landing indicates that ignoring the vehicle's transient response to the onset of turbulence as it penetrates the planetary boundary layer is also questionable. That is, from Reference 1 (CL 84, Case 12) in a typical landing at an airspeed of 60 knots and $\gamma_E = 13.3°$, the vehicle has the following characteristic oscillatory periods and wavelengths with the stability augmentation system on:

Mode	Period (sec)	Wavelength (ft)
Longitudinal, long	26	2640
Longitudinal, short	5.8	590
Lateral	8.5	860

The path length from an altitude of 500 ft. to a CAT IIB decision height of 100 ft., which would include most of the intense shear and turbulence, is only 1,740 ft. Thus we see that the characteristic distances are not small relative to the approach path length even though this is an essential condition for the transient response to be ignored*. It should be noted as well that the mean gradient itself has a strong effect on the characteristic modes of aircraft (Reference 5 , Sec. 9.9), an effect not included in the table above. Both the phugoid period and its time to half amplitude may be increased by as much as 100% in a strong wind shear.

The research reported herein was undertaken to answer some of the questions raised in the preceding discussion.

---

*The values in the above table are for the open-loop response of the vehicle and these would be modified when the loop is closed by a human pilot or an autopilot. A more exact assessment of the importance of the transient response could thus be made once a loop closure was selected.

Section II

APPROACHES TO SOLUTION OF THE PROBLEM

For purposes of design and operation, one wishes to know how any given landing system (vehicle + controls + terminal guidance) will perform in a statistical sense at any given airport in any given wind. It is clear that this entails a knowledge of the wind profile and turbulence, including local effects of terrain and nearby structures, that pertain to the airport in question. Presumably this information might be obtained in the field, but this is currently a costly and time consuming process that would be undertaken only rarely. The only feasible alternative, and one that can provide reasonably good results for the lower part of the atmosphere, say below 1,000 or 1,500 ft., is experimental measurement in a facility capable of simulating the atmospheric flow in this region - that is, in the planetary boundary layer. In a boundary layer wind tunnel, for example, one can model the geometry of the local airport and environs and collect data systematically and relatively inexpensively. One of the principal limitations of these facilities at present is their inability to include the Coriolis effects that result in the shift in wind direction with height, and hence to simulate faithfully the outer region of the boundary layer. However, the region of most intense shear and local effects of terrain and structures can be fairly well reproduced (see Experimental Facilities).

Assuming then that we have a laboratory facility available which can provide reasonable simulations of the atmospheric boundary layer, we now consider the possible alternatives for determining the effects of turbulence alone on the aircraft. We assume the aircraft is beginning its descent through the boundary layer from some known initial position A and

6

we wish to determine its dispersion from the reference trajectory as a
result of the turbulence it encounters - that is, we wish to determine
the value of P_2 associated with a given 'window'. The reference tra-
jectory itself may be determined from a knowledge of the mathematical
model of the aircraft/guidance system and the mean wind profile (see
Theory of the Stationary-Probe Method and also Reference 6).

There are basically four distinct approaches one may take toward
solving the above problem, each requiring different assumptions. These
solutions are described below in descending order of faithfulness.

(1) Obviously the most nearly 'exact' solution would be to build a faith-
ful, free-flying model of the aircraft and have it seek to follow
the prescribed nominal flight path from A to B (Figure 1) at corr-
ectly scaled speed with the correct guidance and control laws. By
making many descents under a given set of conditions, the ensemble
statistics of the state vector at the target plane could be coll-
ected. To get good statistics would take many 'flights' in the
tunnel in order to define the all-important tail of the probability
curve with adequate accuracy. This technique may not in principle
be beyond the state of the art, but it would appear to be inordinately
expensive, and would certainly require a very large wind tunnel in
order that the models of the aircraft not be too small. It does have
the advantage, however, of requiring no basic assumptions other than
that the laboratory simulation of the boundary layer is satisfactory,
and this of course is required for any wind tunnel solution.

(2) A considerably simpler approach would be to drive a rigid model
equipped with a force balance down the reference trajectory 'open

loop'. As noted above, this trajectory corresponds to zero initial errors and zero turbulence and can be calculated in advance. Using a six-component force balance and by making appropriate corrections for gravity and inertia forces, the transient aerodynamic inputs to the vehicle could be obtained. These time histories could then be used with a mathematical model of the vehicle to compute errors in the state vector at the target plane. In this approach, it must be assumed that the aerodynamic forces obtained on the reference trajectory are approximately the same as those that would have been found on the actual trajectory and hence large perturbations from the reference path would introduce significant errors. If desired, one could further assume that the aircraft guidance system has sufficiently high performance that the reference path is very close to the nominal glide slope. In this case, of course, the model could be driven along the latter path rather than the former. As with the previous solution, a large number of repetitions would be needed to obtain adequate statistics.

(3) The third approach would be somewhat like (2), but instead of measuring aerodynamic forces with a proper vehicle model, we would measure turbulence inputs from which these forces could in principle be calculated by linear aerodynamics. That is,

$$\underline{f}(t) = L\{\underline{g}(t)\}$$

where $\underline{f}(t)$ is the six component force vector, L is a linear operator and $\underline{g}(t)$ is the m component 'gust vector'. When L is not state-dependent, the simple transfer function form results; that is,

$$\underline{f}(s) = \underline{T}(s)\underline{g}(s)$$

8

in which $\underline{T}(s)$ is a 6 x m matrix containing constant gust derivatives (Reference 5, Sec. 13.3). The use of this approach requires that this matrix be determined either from theory or experiment and that the vector $\underline{g}(t)$ be defined and measured. This measurement could be performed with hot-wire or other turbulence-measuring devices, and various levels of approximation are possible by making different assumptions concerning the makeup of $\underline{g}(t)$ (Reference 5, Sec. 13.3). The advantage of this solution, of course, is that only probes rather than actual vehicle models are required. When $\underline{f}(t)$ has been generated in this fashion for any one trial, it can be used in the same way as $\underline{f}(t)$ measured by method (2) to compute the vehicle response. As with methods (1) and (2), this approach would require a large number of trials to obtain adequate statistical reliability of the results. A brief study of this technique is presented under Feasibility of the Moving Probe Technique.

(4) Finally, the approach that uses the simplest equipment is one which employs neither moving models nor moving probes but instead collects the flow statistics at fixed points. This method is the one presently being used in an experimental investigation at UTIAS and is described in detail under Theory of the Stationary-Probe Method. It has the principal advantages of using fixed probes and not requiring a large number of replicates, but it does require many individual measurements to be taken and more assumptions than the previous methods. Unlike (3), for which nonlinearities (other than those excluded by the $\underline{f}$ - $\underline{g}$ relation hypothesized above) can be included, method (4) requires a completely linear system. From the standpoint of validity

9

for linear systems, of course, it is equivalent to (3) insofar as it yields approximate mean-squares and mean products of the deviations of the state variables at the target plane. However, it is less faithful than (3) in that one can only take the next step and proceed to statements about probabilities with the aid of an assumption about the form of the probability distribution function - for example, that it is Gaussian. In addition, ergodicity of the turbulence signals is a necessary (but weak) assumption.

Section III

THEORY OF THE STATIONARY-PROBE METHOD

We postulate that we have an adequate mathematical model of the beam-following system comprising the vehicle, its controls (human or automatic) and the guidance loop. This model may be denoted symbolically in state vector form by

$$\underline{\dot{y}}(t) = \underline{f}(y,t) + \underline{B}(y)\ \underline{g}(t) \tag{3.1}$$

where $\underline{y}(t)$ is the n x 1 state vector (including all closed-loop control variables), $\underline{g}(t)$ is the m x 1 "gust" or turbulence input vector, and $\underline{B}$ is an n x m matrix of coefficients that in general are state dependent. The time variable is included in $\underline{f}$ to allow for the possibility that the descent might have some programmed variables - for example, flap angle or propeller pitch or wing tilt - as functions of time.

Consider now the reference solution, for which the initial conditions are the nominal or ideal ones and for which the wind is laminar and steady with respect to its mean profile. Let the reference solution be denoted $\underline{y}_o(t)$ so that from (3.1), with $\underline{g}(t) = 0$ for a laminar wind,

$$\underline{\dot{y}}_o(t) = \underline{f}(\underline{y}_o,t). \tag{3.2}$$

This reference solution provides the constant position error at the target plane associated with wind shear. It of course also provides errors in airspeed, bank angle, etc., at the target plane, which may be important factors in the decision to be taken as to whether to land or abort.

Now consider a set of perturbation solutions (i.e., small departures from the reference solution) associated either with small deviations in the initial conditions or with turbulence. The constraint of 'smallness' is imposed to yield a linear system for analysis, and the usual confidence in linear flight-dynamic solutions leads to the expectation that they will be of practical

11

utility for realistic levels of disturbance. The perturbation is denoted by $\Delta \underline{y}(t)$, so that from (3.1)

$$\underline{\dot{y}}_o(t) + \Delta \underline{\dot{y}}(t) = \underline{f}(\underline{y}_o + \Delta \underline{y}, t) + \underline{B}(\underline{y}_o + \Delta \underline{y}) \, \underline{g}(t). \qquad (3.3)$$

Now to first order in $\Delta \underline{y}(t)$, we have

$$\underline{f}(\underline{y}_o + \Delta \underline{y}, t) = \underline{f}(\underline{y}_o, t) + \underline{A}(t) \, \Delta \underline{y}(t) \qquad (3.4)$$

where

$$\underline{A}(t) = \begin{pmatrix} \dfrac{\partial f_1}{\partial y_1} & \cdots & \dfrac{\partial f_1}{\partial y_n} \\ \vdots & & \vdots \\ \dfrac{\partial f_m}{\partial y_1} & \cdots & \dfrac{\partial f_m}{\partial y_n} \end{pmatrix}$$

(where y_i and f_i are the ith elements of $\underline{y}$ and $\underline{f}$) which, on substitution into (3.3), serves to eliminate the reference solution. Also, since $\underline{g}(t)$ is taken as small, the second term of (3.3) to first order is $\underline{B}(\underline{y}_o) \, \underline{g}(t)$. Finally, the perturbation equation can be written as

$$\Delta \underline{\dot{y}} = \underline{A}(t) \, \Delta \underline{y}(t) + \underline{B}(t) \, \underline{g}(t) \qquad (3.5)$$

since $\underline{y}_o(t)$ is a known function of time.

Equation (3.5) can now provide the second and third contributions to errors at the target plane referred to in the <u>Introduction</u>. The initial condition errors are found by solving (3.5) with $\underline{g}(t) = 0$ and $\underline{y}(0) \neq 0$; the gust response is treated with $\underline{y}(0) = 0$ and $\underline{g}(t) \neq 0$.

3.1 Response to Turbulence

Since we are primarily concerned here with the perturbations $\Delta \underline{y}(t)$ in response to gusts $\underline{g}(t)$, we shall simply write $\underline{y}$ for $\Delta \underline{y}$ in the subsequent development. The differential equations for the perturbations, (3.5), are linear and have a solution which may be written as follows (Reference 7):

$$\underline{y}(t) = \underline{H}(t, 0) \, \underline{B}^{-1}(0) \, \underline{y}(0) + \int_o^t \underline{H}(t, t') \, \underline{g}(t') dt' \qquad (3.6)$$

where the initial time $t = 0$ has been selected at point A in Figure 1.

12

$\underline{H}(t,t')$ is often referred to as the impulsive response matrix. It is the solution to the system

$$\dot{\underline{H}}(t,t') = \underline{A}(t)\,\underline{H}(t,t') + \underline{B}(t)\,\delta(t-t')$$

$$\underline{H}(t',t') = 0 \tag{3.7}$$

where $\delta(t-t')$ is the Dirac delta function. This system can be written in a more convenient form for computation by integrating with respect to the variable t over a range t_o to t where $t_o < t' < t$. This results in the system

$$\dot{\underline{H}}(t,t') = \underline{A}(t)\,\underline{H}(t,t')$$

$$\underline{H}(t',t') = \underline{B}(t') \tag{3.8}$$

for $t > t'$. This set of equations is then solved by direct integration on a digital computer.

In the present context (dynamics), the ith column of $\underline{H}$, say $\underline{h}_i$, may be viewed as the response of the system (3.5) to a unit impulse in the ith input: $g_i(t) = \delta(t-t')$. If $\underline{A}(t)$ were not time-dependent, an explicit analytical expression for $\underline{H}$ would be available: $\underline{H}(t,t') = \exp\{(t-t')\underline{A}\}\,\underline{B}(t')$, (see Reference 7).

For the remainder of this section, we shall focus attention exclusively on the contributions of turbulence to $\underline{y}(t)$, and shall set $\underline{y}(0) = 0$. We proceed to find the mean products $\overline{y_i y_j}$ by considering the elements of the dyadic (i.e., outer) product $\underline{y}\underline{y}^T$. From (3.6), with $\underline{y}(0) = 0$, the ensemble mean of $\underline{y}\underline{y}^T$ at time t is

$$< \underline{y}(t)\underline{y}^T(t) > \,=\, < \int_o^t \underline{H}(t,t_1)\underline{g}[\vec{r}(t_1),t_1]dt_1 \int_o^t \{\underline{H}(t,t_2)\underline{g}[\vec{r}(t_2),t_2]\}^T \, dt_2 >$$

$$= \int_o^t \int_o^t \underline{H}(t,t_1) < \underline{g}[\vec{r}(t_1),t_1]\underline{g}^T[\vec{r}(t_2),t_2] > \underline{H}^T(t,t_2)\, dt_1\, dt_2 \tag{3.9}$$

An explicit dependence of $\underline{g}$ on position $\vec{r}$ has been shown in (3.9); that is $\underline{g}(\vec{r},t)$ is the random gust input at time t at the position $\vec{r}$ in the trajectory.

13

Thus it is seen that the gust input to the aircraft varies with time for two reasons: (i) the explicit time dependence, and (ii) the dependence on $\vec{r}$ which, in turn, varies with time.

In general, for two arbitrary positions $\vec{r}_1$ and $\vec{r}_2$, we can define the correlation matrix by

$$\underline{R}(\vec{r}_1,\vec{r}_2,t_2-t_1) = \,< \underline{g}(\vec{r}_1,t_1)\underline{g}^T(\vec{r}_2,t_2) > \tag{3.10}$$

The dependence is shown to be on the difference (t_2-t_1), and not on t_1 and t_2 individually, because the turbulence is assumed to be stationary. If it were also homogeneous (which it is not) $\underline{R}$ would similarly depend only on the difference $(\vec{r}_2-\vec{r}_1)$.

Returning now to (3.9), the crucial point to note is that $\vec{r}_1$ and $\vec{r}_2$ are not arbitrary but are in fact the position of the aircraft at times t_1 and t_2, respectively. Thus, the correlation $< \underline{g}[\vec{r}(t_1),t_1]\,\underline{g}^T[\vec{r}(t_2),t_2] >$ called for by (3.9) is a 'constrained' version of the $\underline{R}$ defined in (3.10). This special type of correlation matrix will be denoted by $\underline{\mathcal{R}}$ the flight path correlation matrix, that is,

$$\underline{\mathcal{R}}(t_1,t_2) = \underline{R}[\vec{r}(t_1),\vec{r}(t_2),t_2-t_1]. \tag{3.11}$$

Note that $\underline{\mathcal{R}}$ depends only on the two variables t_1 and t_2. Moreover, it is symmetric with respect to these two variables in the sense that

$$\underline{\mathcal{R}}^T(t_2,t_1) = \underline{\mathcal{R}}(t_1,t_2) \tag{3.12}$$

This follows from the fact that, from (3.10),

$$\underline{R}^T(\vec{r}_2,\vec{r}_1,t_1-t_2) = \,< \{\underline{g}(\vec{r}_1,t_1)\underline{g}^T(\vec{r}_2,t_2)\}^T >$$
$$= \,< \underline{g}(\vec{r}_2,t_2)\underline{g}^T(\vec{r}_1,t_1) >$$
$$= \underline{R}(\vec{r}_1,\vec{r}_2,t_2-t_1) \tag{3.13}$$

and it has important implications for the number of measurements needed for $\underline{\mathcal{R}}$.

14

For example, if $\underline{R}(t_1, t_2)$ is known for all $t_2 \geqslant t_1$, then (3.12) provides $\underline{R}$

for all $t_2 < t_1$. In any case, (3.9) is now written

$$< \underline{y}(t)\, \underline{y}^T(t) > = \int_0^t \int_0^t \underline{H}(t,t_1)\, \underline{R}\,(t_1,t_2)\underline{H}^T(t,t_2)\, dt_1 dt_2 \qquad (3.14)$$

and this is the main result of this section.

In utilizing (3.14), two assumptions may be made that are consistent with linear analysis. In the first place, when $\underline{R}$ is calculated using (3.11), the reference trajectory $\underline{r}(t)$ may be used in place of the actual (perturbed) trajectory. In effect, one neglects a 'perturbation on a perturbation' - a second-order effect. The second assumption is similar; to obtain results in the target plane, the upper limit of the integration in (3.14) may be taken as the time of arrival for motion along the reference trajectory rather than the time associated with an actual trajectory.

Note that the integrand in (3.14) contains one ingredient, $\underline{R}$, that depends only on the turbulence field and on the kinematics of the flight trajectory and another, $\underline{H}$, that is basically a system property. Normally, $\underline{H}$ is calculated from a dynamics and control analysis (see (3.8)) while $\underline{R}$ can be measured in the atmosphere or, as in the present case, in a suitable laboratory simulation of the flow. Although there is no fundamental impediment to measuring $\underline{R}$ for the reference trajectory, it is experimentally much more convenient to measure it for the nominal (straight-line) trajectory. The difference between the two is due to the mean wind profile, as explained in the introduction; however, with an acceptable autopilot, this difference should be small and thus the assumption $\underline{R}$ (reference trajectory) $\approx \underline{R}$ (nominal trajectory) should be a reasonable one.

To assist in understanding what (3.14) means, consider the simple

15

case in which there is only one input, say vertical gust w, and one output, say normal displacement error z_n. Thus $\underline{g}(t)$ is w and $\underline{y}(t)$ is z_n. Then (3.14) gives the mean-square of z_n directly as

$$< z_n^2(t) > = \int_o^t \int_o^t h_{zw}(t,t_1) \mathcal{R}_{ww}(t_1,t_2) h_{zw}(t,t_2) dt_1 dt_2 \qquad (3.15)$$

Here $h_{zw}(t,t_1)$ is the error z_n at time t that results from a unit impulse in w at time t_1. The cross-correlation

$$\mathcal{R}_{ww}(t_1,t_2) = < w(r_1,t_1)w(r_2,t_2) > \qquad (3.16)$$

is the ensemble mean of the products of w at the two (fixed) locations $\underline{r}_1$ and $\underline{r}_2$ on the nominal trajectory that correspond to the two (fixed) times t_1 and t_2 (Figure 3). Finally, the assumption of ergodicity of the turbulence permits us to replace the ensemble mean of (3.16) with the time average

$$\mathcal{R}_{ww}(t_1,t_2) = \overline{w(r_1,t)w(r_2,t+\tau)}, \ \tau = t_2 - t_1 \qquad (3.17)$$

Notice that the time delay in this relation is such that the signal from the upper probe is always delayed with respect to that from the lower probe. (Reversal of this delay would correspond to a take-off manoeuvre.)

The important point in the above derivation is that it leads to a measurement made with stationary probes instead of moving ones. The result (3.17) is simply the cross-correlation of w measured at the points $\underline{r}_1$ and $\underline{r}_2$ with time delay $(t_2 - t_1)$. This kind of turbulence measurement is the sort commonly and routinely made in many aerodynamics laboratories using conventional hot wire anemometry techniques. The general result, referring back to (3.10) and (3.11), is

$$\underline{\mathcal{R}}(t_1,t_2) = \overline{\underline{g}(\underline{r}_1,t)\underline{g}^T(\underline{r}_2,t+\tau)}, \tau = t_2 - t_1 \qquad (3.18)$$

16

To recapitulate, (3.14) is the basic equation from which the mean squares and products of the state variables of interest can be computed at the decision window. To carry out the computation, one needs three things:

(i)   the computed reference solution,

(ii) the computed matrix of impulse response functions, $\underline{H}$, and

(iii) the turbulence input matrix $\underline{\mathcal{R}}$, either measured or otherwise approximated.

The elements of (3.14) must then be evaluated numerically to produce mean squares and mean products of y_n, z_n, etc., at the target plane. Finally, these mean values can be used with the assumption of a Gaussian process to compute the probabilities P_2 (Figure 2) associated with a given dispersion. That is, in computing the probability that the state variables at point B lie within a specified decision window in state space, one uses the normal multivariate probability function (Reference 5 , Eq. 2.6,31) which makes use of the mean products (the off-diagonal components of (3.14) as well as the mean squares).

3.2   The Input Vector

The degree of approximation in the final computed results of dispersion at the decision window, and the difficulty of measurement, both depend very much on the choice of gust input vector $\underline{g}(t)$ (see Reference 5, Sec. 13.3). The simplest case occurs when the variation of the turbulence over the vehicle is neglected, and the three turbulent velocities at the C.G. are taken as the inputs. In this case the components of $\underline{g}(t)$ in $\mathcal{F}_I$ are given by

$$\underline{g}_I(t) = \begin{bmatrix} u_g(t) \\ v_g(t) \\ w_g(t) \end{bmatrix} \quad \text{and in } \mathcal{F}_T \text{ by} \quad \underline{g}_T(t) = \begin{bmatrix} u(t) \\ v(t) \\ w(t) \end{bmatrix} \qquad (3.19)$$

See Fig. 1 for the orientation of these frames.

For a more faithful representation of the turbulence, one may add gradients in the velocites, such as $\partial w/\partial y$, which produces rolling moments, and $\partial w/\partial x$,

17

which produces pitching moments. Which additional terms will be needed in any particular application depends on the vehicle, the turbulence and the accuracy desired. Although adding gradient terms to g(t) generally complicates the measurements, there is an exception with respect to streamwise gradients. Assuming that the turbulence components are being measured in the $\mathcal{F}_T$ coordinate system, which is most convenient, the correlations of derivatives with respect to x can be derived from Taylor's hypothesis of frozen turbulence (which is usually a reasonable approximation for the flows considered). That assumption relates spatial and temporal gradients by

$$W \frac{\partial}{\partial x} = - \frac{\partial}{\partial t}$$

where W is the local mean wind speed (in the x direction). Thus, for example,

$$w_x \triangleq \frac{\partial w}{\partial x} = - \frac{1}{W} \frac{\partial w}{\partial t} \tag{3.20}$$

and the cross-correlation of this derivative at t_1 and t_2 is

$$R_{w_x w_x}(t_1, t_2) = \frac{1}{W_1 W_2} R_{w_t w_t}(t_1, t_2) \tag{3.21}$$

where W_1, W_2 are the wind values at the two reference points. But the correlation of the time derivative of a variable is related to that of the variable itself; that is,

$$R_{w_t w_t}(t_1, t_2) = \frac{\partial^2}{\partial t_1 \partial t_2} R_{ww}(t_1, t_2) \tag{3.22}$$

so that the correlation of w_x can be derived from that of w by

$$R_{w_x w_x}(t_1, t_2) = \frac{1}{W_1 W_2} \frac{\partial^2}{\partial t_1 \partial t_2} R_{ww}(t_1, t_2) \tag{3.23}$$

and similarly for other x gradients. The double differentiation required by (3.23) can in principle be performed with sufficient accuracy if the R_{ww} data

18

are good enough. With respect to y gradients, no comparable general method is available, and recourse would be needed to measurements with special probes (for example a small airfoil that could measure rolling moment) or to theory (for example Reference 8).

3.3 Time History of Aircraft Position

As indicated in the previous section it is necessary to determine $\mathbb{R}(t_1,t_2)$ for $t_2 > t_1$ for pairs of points along the glide slope. Before this can be carried out it is necessary to find the relationship between time and position for an aircraft flying down the glide slope. Thus when the two hot-wire probes are positioned at specific points on the glide slope the particular value of (t_2-t_1) required for the evaluation of $\mathbb{R}(t_1,t_2)$ can be determined. If we assume that a good first order estimate of these times can be based on airspeed undisturbed by turbulence and perfect tracking of the glide slope then the following analysis will produce the required results.

Consider the motion of the aircraft along the glide slope as shown in Figure 4. It flies at airspeed V at some angle γ relative to the mean wind W so that its motion relative to the ground is at speed V_E and angle γ_E. Thus at any particular height z, we may obtain the velocity vector diagram shown. If we let W, V and V_E represent magnitudes of the respective velocity vectors, then the vector sum $\underset{\rightarrow}{V}_E = \underset{\rightarrow}{W} + \underset{\rightarrow}{V}$ yields

$$V_E \cos \gamma_E = -W + V \cos\gamma \qquad (3.24)$$

and

$$V_E \sin \gamma_E = V \sin\gamma \qquad (3.25)$$

where V_E, W, V, γ and γ_E are functions of z in general. Solving, we get

$$V_E = -W\cos\gamma_E + [W^2(\cos^2\gamma_E-1) + V^2]^{1/2} \qquad (3.26)$$

and

19

$$\gamma = \sin^{-1}[V_E \sin\gamma_E/V] \tag{3.27}$$

where Eq. (3.26) corresponds to the case of $\gamma_E \leq 90^\circ$ ($V/W > 1$). Thus if γ_E, W and V are specified, the above equations may be solved for V_E and γ.

The time t to reach any point on the glide path defined by height z is found as

$$t(z) = -\int_{z_A}^{z} \frac{dz}{V_E(z)\sin\gamma_E(z)} \tag{3.28}$$

In the present analysis V and γ_E will be taken to be constants corresponding to a constant airspeed landing approach along a conventional straight ILS beam. $t(z)$ has been evaluated on a digital computer to cover all cases run in the wind tunnels. A typical listing of $t(z)$ is found in Table I and illustrated in Fig. 5. These data were generated for tests in the small (8" x 8") tunnel. Note that in the illustrated case $t = 0$ is referenced to $z = 858$ ft. in full scale while the top of the boundary layer is taken to be 1000 ft. Thus, for this example, if the upper probe is located at $z' = 5.5$ in. and the lower at $z' = 4.0$ in. then the correlation functions are determined with the signals from the upper probe time delayed by $(t_2'-t_1') = (.02128-.00576) = .01552$ sec.

3.4 Scaling and Parameter Selection

Before the fixed probe technique of this section can be applied and before an analysis of the moving probe technique can be performed (see Section IV) it is necessary to determine the proper scaling to employ in the wind tunnel and to select a representative range of velocity parameters.

When measurements of turbulence properties in a boundary layer wind tunnel are to be made with hot wire probes the basic scaling problem is assumed to be one involving length and time. (See Section 5.1 for a further

20

discussion of boundary layer simulation.) The length scale is used to obtain proper turbulence scales and distances relative to the glide slope. The time scale is used to obtain proper velocities and frequencies of events taking place in the turbulent field.

Let unprimed symbols represent full scale parameters and primed symbols represent wind tunnel parameters.[†] Length scaling is obtained by representing the full scale boundary layer thickness Z_G by the wind tunnel boundary layer thickness Z_G'. Thus, in general, length scaling becomes

$$\ell' = S_\ell \, \ell$$

where

$$S_\ell = Z_G'/Z_G \tag{3.29}$$

Time scaling is arrived at through velocity scaling and length scaling. The full scale gradient velocity W_G (the wind speed at Z_G) is represented in the tunnel by W_G' (the wind speed at Z_G').

Thus in general, velocity scaling becomes

$$V' = S_V \, V$$

where

$$S_V = W_G'/W_G \tag{3.30}$$

Combining length and velocity scaling one obtains time scaling

$$t' = \frac{\ell'}{V'} = \frac{S_\ell}{S_V} \, \frac{\ell}{V} = S_t \cdot t$$

where

$$S_t = S_\ell/S_V \tag{3.31}$$

---

† This convention is not applied in the case of the turbulence components (u v w) in order to simplify the notation required. The context will indicate whether full scale or wind tunnel scale applies when these symbols are used.

The following table summarizes the scales established for the present wind tunnels for n = 0.16.

	Z_G or Z_G' ft.	W_G or W_G' fps	S_ℓ	S_V	S_t
Actual Atmosphere	1000	68*			
8" x 8" tunnel	7/12	34	5.83×10^{-4}	0.50	1.17×10^{-3}
44" x 66" tunnel	3	90	3.00×10^{-3}	1.36	2.20×10^{-3}

* In the case of the 44" x 66" tunnel simulation the actual atmosphere W_G was assumed to be 66 fps.

The tunnel velocity scales have been selected to ensure ease of measurement of flow properties. In the case of the 44" x 66" tunnel the scale of turbulence generated by the flow was an additional consideration. As pointed out in Ref. 11, Reynolds number simulation is not necessary in generating an acceptable boundary layer provided that the floor of the tunnel is aerodynamically rough, as was the case with the present tunnels.

In Fig. 1 the velocity $W(z)$ represents the time-averaged mean velocity of the wind in the frame $\mathcal{F}_I$. If we restrict ourselves to the case of a neutrally stable atmosphere and further neglect Coriolis effects, then the variation of this velocity with height can be reasonably well represented by the so-called power-law profile, that is,

$$W(z)/W_G = (z/Z_G)^n \qquad (3\ 32)$$

Both Z_G and n depend on the roughness of the earth's surface, with typical values as suggested by Davenport (Ref. 9) given in the table below. While these values are by no means exact, they do give a reasonable estimate of the mean wind speed if this speed is not too low. Further characteristics of the planetary flow are described in detail in Refs. 10 and 11.

SURFACE TYPE	n	Z_G, FT
Flat, open country	0.16	1000
Woodland forest	0.28	1300
Urban	0.35	1600

As discussed in Sec. I, present maximum values of γ_E for STOL vehicles are $\sim 16^{\circ}$. Since in the present case we are concerned with both STOL and VTOL vehicles, we select values of γ_E of 15°, 45° and 90°. As for $W(z)$, its value is adequately specified by the value chosen for the gradient wind W_G. This wind may range from zero to values of 120-140 fps. Higher values are not of interest for the present investigation since this represents an upper limit on STOL landing airspeeds and we require that $V/W > 1$ for all W. Also, the lower range of W is not pertinent since shear-generated turbulence will be very small in this range and only thermal instability effects will be of prime concern. Finally, we will assume constant values of the airspeed V for any given flight and straight glide slopes. Typical values are determined by vehicle landing and stall speeds and by maximum allowable descent rates. Thus if we use the parameter V/W_G to represent airspeed values, the considerations outlined above lead to the following criteria:

(i) $\sim$ 10-20 fps $< W_G < \sim$ 120 fps

(ii) $V_{max} \sim$ 120 fps $\rightarrow (V/W_G)_{max} \sim 120/W_G$

(iii) $V/W_G > 1$

These criteria are displayed graphically in Fig. 6.

23

Section IV

FEASIBILITY OF THE MOVING PROBE TECHNIQUE

Four approaches to solving the problem of the statistics of the aircraft position after its flight through the planetary layer have been described. In the present section, we shall consider in detail the third approach - that is, the use of a probe moving through the flow at properly scaled velocities and measuring the relevant transient turbulence inputs on each of many repeated runs.

With reference to Figure 3, we are concerned with the flight of the vehicle from A to B through the simulated planetary boundary layer. We will assume that the reference trajectory is approximately the same as the glide slope and that this is a straight line. Thus the moving probe will travel the linear path between A and B.

If we consider the case of the simplest possible input vector, i.e.,

$$\underline{g}_T(t) = \begin{bmatrix} u(t) \\ v(t) \\ w(t) \end{bmatrix}$$

then the moving probe must be able to simultaneously measure three turbulence components. If we extend our range of interest to include gradients of these velocities, however, then specially designed probes will be required, and it is emphasized that these probes must be such as to allow these gradients to be obtained simultaneously with the turbulent velocities. Then for any given run of the probe down the glide path, a set of time functions will be measured which can be used as numerical inputs to the aerodynamic mathematical model to determine the vehicle force inputs and ultimately its location in the target plane at B. An ensemble of the runs will then provide the desired statistics.

24

There are two main advantages of the moving probe approach over the stationary probe solution. First, and probably most important, is the fact that no assumption is required about the statistics of the dispersion of the vehicle location in the target plane; that is, P_2 (Figure 2) can be determined regardless of whether it is Gaussian or not. Second, we can apply the measured inputs to any system, linear or non-linear, so long as its mathematical model is known. In order to capitalize on these advantages, however, we require a probe that is capable of simultaneous measurements of all the desired input signals and which can be moved through the simulated flow at a precisely controlled speed.

For the present analysis it will be assumed that our large (44" x 66") wind tunnel is to be employed. The parameters selected for study can be found in Table 2. In addition the following values were used:

$$W_G' = 34 \text{ fps}$$

$$W_G = 68 \text{ fps}$$

$$Z_G' = 3 \text{ ft}$$

$$S_V = W_G'/W_G = 1/2$$

Consider a moving probe arrangement such as that shown in Figure 7 for $\gamma_E = 45°$. The probe is guided by some form of rigid track and is driven by a chain (or belt) which is mounted on a pair of sprockets. To achieve minimum flow interference effects, the sprockets should be located outside the tunnel, with openings provided to allow the chain to pass through. A typical run consists of the probe initially at rest at the top of the tunnel and accelerated to its appropriate velocity V_E' at A, the height of which we choose to be $z_A' = 31$". It then moves at the velocities dictated by the computations of Section 3.3 until it reaches some point B, say at $z_B' = 3$", which corresponds to the full

25

scale decision height. At this stage it is decelerated and brought to rest
by the time it reaches the floor. For the cases of $\gamma_E = 15^{\circ}$ and 90°, different
tracks would be used and the actual distances of probe travel would of course
be different if the same values of z' were retained for A and B. For this type
of arrangement, then, Table 2 shows the velocities and times at the start (A)
and end (B) of the probe runs along the glide path for the complete range of the
parameters concerned. It is seen that even with the half-speed scaling used here,
quite large probe velocities may in some cases be required. Thus large accelerations
will of course also be required. The case for $n = 0.35$, $V/W_G = 1.9$ and $\gamma_E = 45^{\circ}$
is seen to be the worst, although it would seem reasonable not to be too concerned
with this particular one since it is probably beyond our range of interest. We
will consider the same case for $V/W_G = 1.5$, however, and in Figure 8 the
complete probe speed profile for this particular run is shown together with
another less extreme case. The very large accelerations that will be required
in some of these runs are clearly seen, with the most extreme values occurring
just before B is reached and during the probe deceleration. Obviously the
reduction of the larger of these accelerations would alleviate the mechanical
design and control problems involved, and the possible methods for doing this
are discussed in the following section.

4.1 Frozen Flow Assumption

It is clearly seen in Fig. 8 that the largest accelerations during
a given run could be significantly reduced if larger values for z_B' were chosen -
say 6" instead of 3". The disadvantage of this approach, of course, lies in
the loss of the data for the lower altitudes. That is, if z_B' were 6", the
minimum full scale height for which data could be obtained would be
267' for the $n = 0.35$ flows (with $Z_G = 1600'$) and 167' for the
$n = 0.16$ flows (with $Z_G = 1000'$) and these are larger than we would

26

like. Another possibility for reducing accelerations is the reduction of
the simulated flow velocity scale factor below the 1/2 value used here.
However, this results in reduced signals and difficulty in obtaining
satisfactory mean velocity profiles in some cases, and is best avoided if
possible. A superior method is provided by making the assumption of horizontally
frozen flow - that is, the turbulence measured at any level in the flow behaves as
though it were the result of a field of turbulence frozen in time which is
carried along by the mean flow W.

In Fig. 9 , the probe leaves point A in a typical run along A B at the
correctly scaled velocity V_E'. It reaches point D after t' seconds and
if we assume horizontally frozen flow, the turbulence it measures is that which was at
point C at t' = 0 and has been carried to D by the mean flow. Thus the
length CD is $W'(z')t'$. Similarly, the turbulence measured at any point on
the correctly scaled run down the true glide path comes from a specific
known location (path ACG) upstream where it was located at t' = 0. Thus if
we have the probe travel along some new path such as AEK which is further from
ACG than the original path, it must be moved at a slower speed V_{EF}' to allow
the turbulence sufficient time to travel the added distances such as DE.
Consequently the horizontally frozen flow hypothesis allows us to move the probe at a
slower speed along a different path to measure the identical signal we
would get at the correctly scaled speed along the original path.

Consider now the problem of determining the optimum path for
minimizing V_{EF}'. There are two approaches that could be taken. First, we could
specify the velocity V_{EF}' at which we wish the probe to travel and solve for
the required new path by finding the angle ϵ . The logical choice would be
V_{EF}' = constant for all z'; however, due to the variation of W' and V_E' with
z', this would lead to a curved path. This path would of course be different
for each run, depending on the values of V_E', and in addition, curved paths

27

would likely be mechanically more of a problem than straight paths. Thus we use the reverse procedure. That is, the new path is chosen by selecting a constant value for ϵ and then solving for the required value of V'_{EF} at each height. By choosing ϵ to be a constant for all z', V'_{EF} becomes a function of z' and can be determined for any desired run. It is smaller than V'_E, the amount depending on the value selected for ϵ. Consequently some solutions have been obtained as outlined below for a range of ϵ such that an optimum value for minimum V'_{EF} can be estimated.

In Figure 9, the time required for the probe to reach point D along AB is

$$t' = - \int_{z'_A}^{z'} \frac{dz'}{V'_E \sin\gamma_E} \qquad (4.1)$$

Along the path AK, the probe moves at the lower velocity V'_{EF} and reaches point E at a time

$$t'_F = - \int_{z'_A}^{z'} \frac{dz'}{V'_{EF} \sin\epsilon} \qquad (4.2)$$

V'_{EF} must be chosen such that the time difference $t'_F - t'$ is the time required for the turbulence to move from D to E at the velocity $W'(z')$; that is,

$$t'_F - t' = DE/W'(z') \qquad (4.3)$$

From Figure 9 it can be shown that

$$DE = (z'_A - z')(\cot\gamma_E + \cot\epsilon) \qquad (4.4)$$

Thus the above equation may be written

$$\int_{z'}^{z'_A} \left[\frac{1}{V'_{EF} \sin\epsilon} - \frac{1}{V'_E \sin\gamma_E} \right] dz' = \frac{z'_A - z'}{W'} \left[\cot\gamma_E + \cot\epsilon \right] \qquad (4.5)$$

28

and by differentiating with respect to z' we get

$$\frac{1}{V'_{EF}\sin\epsilon} - \frac{1}{V'_E\sin\gamma_E} = (\cot\gamma_E + \cot\epsilon)\left[\frac{1}{W'} + \frac{z'_A - z'}{(W')^2}\frac{dW'}{dz'}\right] \qquad (4.6)$$

Rearranging, this may be written as

$$\frac{V'_{EF}}{V'_E} = \frac{\sin\gamma_E}{\sin\epsilon + V'_E\sin(\gamma_E + \epsilon)[1/W' + (z'_A - z')/(W')^2\,dW'/dz']} \qquad (4.7)$$

and we thus have an expression for the reduced probe velocity at any point along the new path through the flow. It is seen that this velocity is a function not only of the new path itself (i.e., ϵ) but also of the original velocity V'_E and the wind profile $W'(z')$, both of which are known. It is through these latter parameters that the z'-dependence is felt. Once V'_{EF} is known at any z', the traverse time t'_F along the new path can be determined from (4.2).

Consider now the question of the optimum value of ϵ for producing the maximum possible reduction in probe velocity along the new path. As an indication of the effect of varying ϵ on this velocity, we make the simplifying assumption of constant W'. In this case, (4.7) becomes

$$\frac{V'_{EF}}{V'_E} = \frac{\sin\gamma_E}{\sin\epsilon + V'_E/W'\,\sin(\gamma_E + \epsilon)} \qquad (4.8)$$

Values of V'_E/W' ranging from nearly zero to 1 or 2 could be encountered in our range of interest. Consequently (4.8) has been plotted as a function of ϵ for each γ_E with V'_E/W' as parameter, with the results shown in Fig. 10. These curves indicate clearly that for $\gamma_E = 15°$ or $45°$, the optimum ϵ will be fairly close to $90°$ while for $\gamma_E = 90°$, the optimum ϵ lies in the $60-45°$ range. Consequently we select for the present purposes the values $\epsilon = 90°$

for $\gamma_E = 15°$ and $45°$ and $\epsilon = 45°$ for $\gamma_E = 90°$

Having chosen values for ϵ, we may now use (4.3) and (4.7) along with the known values of $V_E'(z')$ and $W'(z')$ for each run to determine the required velocities and times at all points in the new probe trajectories. The new speed profiles for the runs originally given in Figure 8 are shown in Figure 11. It is clearly seen that the large accelerations required in the original runs have been greatly reduced as a result of the frozen flow assumption and the use of the new trajectories. Similar results are observed in Figure 12 for the case of a run with $\gamma_E = 90°$ and $\epsilon = 45°$. From these and other similar results, the values shown in Table 3 have been obtained for the general range of velocities and accelerations at which we must be capable of moving the probe for our range of interest, both with and without the frozen flow assumptions. The advantages of this assumption are obvious.

The foregoing discussion shows clearly how the assumption of frozen flow may be used to reduce the performance requirements of the probe-moving apparatus designed for this approach. Even in the case where ϵ is chosen to be $90°$ for all values of γ_E some reduction has been achieved. In this particular case, of course, we have the added advantage that only one track assembly need be used so that the mechanical complexity of the system is considerably reduced. Unfortunately, however, we must view these results with some degree of skepticism in that the validity of the frozen flow hypothesis is by no means a foregone conclusion. In particular, the case of $\gamma_E = 15°$ requires that the turbulence pattern remain frozen over a distance as large as 3 or 4 boundary layer thicknesses in the lower regions of the flow. As an indication of whether or not this could reasonably be expected, the data obtained by Favre (Reference 12) in a laboratory boundary layer on a flat plate are useful. His results for two point, space-time correlations of the longitudinal (u) component of turbulence

30

suggest that the maximum distances over which the turbulence remains 'frozen' are of the order of one boundary layer thickness or less, depending on the degree of 'thawing' one is willing to accept. This translates into a minimum value of γ_E of roughly 45° which could reasonably be represented by a run down a 'frozen flow' track at $\epsilon = 90^{\circ}$. For the case of $\gamma_E = 15^{\circ}$, this track would be unacceptable and another track at ϵ no less than 160° would have to be used. It is to be noted, however, that even though the amount of reduction in probe velocity is much less for $\epsilon = 160^{\circ}$ than for $\epsilon = 90^{\circ}$, as indicated by Figure 10, there is still a significant reduction in the accelerations required along the 'frozen flow' track as compared to those along the original track. This is clearly seen in Figure 13 and suggests that even though an assumption of frozen flow will require two or possibly three different tracks, it is still useful for reducing the performance requirements of the probe-moving system.

The above conclusions are based on a fairly crude estimate of the validity of the frozen flow hypothesis using results for only the longitudinal components of turbulence. It would therefore seem useful to specifically test its validity in the present application. This could be done indirectly using two stationary probes at the same height on the original and the 'frozen flow' trajectories. A comparison of the time delayed signal from the front probe with the signal from the rear probe could be used to indicate the degree to which the frozen flow hypothesis is valid at each height.

4.2 Probe Requirements

As discussed in the previous section, the moving probe approach requires simultaneous measurement of all the input signals of interest in

31

any particular run, unless a particular input is derivable from some other

signal that is measured. Consequently even for the case of the simplest input

$$\underline{g}_T(t) = \begin{bmatrix} u(t) \\ v(t) \\ w(t) \end{bmatrix}$$

the probe must be capable of monitoring the three velocities simultaneously.

This can be done using a commercially available triple-wire hot wire

anemometer probe together with three channels of anemometry with linearizers

and the appropriate data handling equipment. The DISA Model 55F81 probe

uses three independent wires of platinum plated tungsten aligned at 90° to

each other and appears to be the most advantageous probe of this type.

The individual signals from the three wires are functions of W', $\underline{V'_E}$,

u, v, w. Since W' and $\underline{V'_E}$ are known then it is possible to determine the

three turbulence components by using suitable signal processing. The

most significant limitation of this probe is the requirement that the

instantaneous velocity vector must always lie inside a cone of half-angle

35° with respect to the probe axis to avoid probe support interference and

thermal cross-talk among the wires. If we assume Gaussian turbulence with

an intensity of 20% for the component $(w_{\perp})$ perpendicular to the vehicle

airspeed vector $\underline{V}$ (see Fig. 4) i.e., RMS $\{w_{\perp}\}$ = 0.2W, then the magnitude

of $w_{\perp}$ is less than 0.49W for 99% of the time. Thus a rough estimate of the

maximum angle δ that the instantaneous air velocity vector makes with respect

to $\underline{V}$ is given by:

$$\delta = \tan^{-1} \frac{0.49W}{|\underline{V}|} < \tan^{-1} \frac{0.49W}{W} \qquad (4.9)$$

or $\delta < 26^{\circ}$ since $|\underline{V}| > W$ for all cases of interest.

This means that the probe axis should be kept within 9° of the $\underline{V}$ direction.

32

Table 4 indicates the range in γ, the angle that $\underset{\rightarrow}{V}$ makes with the x axis

for specific run conditions. If the probe axis alignment for a given run is

set at the mid-point in γ experienced on that run then the requirement is

that the perturbations in γ about that value not exceed 9°. It is seen that

this condition is met for all cases except those for $\gamma_E = 90^{\circ}$ and three

cases for $\gamma_E = 45^{\circ}$. In addition, if the frozen flow assumption is made and

a new probe path with slower velocities is used, the range of γ will be still

less. Thus for most runs there should be no velocity angle limitation problem

provided that an appropriate orientation is selected for the probe at the start

of the run. A simple coordinate rotation may then be used to obtain the signals

in the desired reference frame.

The frequency response requirements of the sensing probe are

determined from the range of interest of the nondimensional frequency in the

full scale flow. This range is roughly $0.02 < fz/V < 10$ (Reference 10) where f

is the frequency and z is a characteristic length, say height. Typical values

of these variables for the full scale and model flows are given in the table

below and indicate that the probe in the larger simulation tunnel should have

a usable (i.e., flat) frequency range of about 0.2 to 300 Hz. This requirement

presents no problem for the triple wire probe. As for other characteristics of

this instrument, they are virtually the same as those of standard X-type hot

wire probes and a discussion of these properties is given in Reference 11 among

others. Cable lengths of up to 150 ft. can be used if necessary, thus

simplifying the problem of monitoring the signal from the moving probe. In

addition, the probes should easily be capable of withstanding accelerations even

as large as 100 g since typical drag forces on the wires due to the mean flow

are up to eight times as large as these inertial forces.

	V(typ.),fps.	z(typ.),ft.	f(Range)Hz
Full Scale	80	500	.0032-1.6
8" x 8" tunnel	40	0.3	2.6-1300
44" x 66" tunnel	40	1.5	0.5-266

As for the measurement of other input quantities such as y-gradients of the turbulent velocities, special probes must be designed if these data are required. An estimate of these gradients of the velocities can be obtained from the outputs of two probes at different lateral positions. That is, if two triple-wire probes separated in the lateral (y) direction by a typical aircraft wingspan (~1.5" in the 44" x 66" wind tunnel) are used in a given run, the signal for each like component obtained at the same time from the two probes can be used to estimate the gradient in that component over the wing span. The accuracy of this approach is obviously dependent on the characteristic wavelength in the lateral direction, being better as this wavelength increases. Extension of the input to include gradients found in this way would, however, require only an extra triple-wire probe and the associated anemometry equipment.

To obtain x-gradients (such as $\partial w/\partial x$) would require either the analytic approach suggested in Section 3.2 or still further refinement, such as a novel probe design, or alternatively, the addition of a third probe displaced in the x-direction. If three probes, each capable of measuring (u,v,w) are used, the input data can be treated in the form of Skelton's method (Reference 13), which requires that the aerodynamic coefficients describing the gust forces then be expressed in a compatible form.

4.3 Probe-Moving Apparatus

We consider in this section the mechanism whereby the probe or probes are to be moved through the tunnel with the precisely controlled speed. As mentioned previously, some form of guide track would appear to be a necessity. A trolley-like device would carry the probe down this track under the control of a chain attached to its front and back coupled to a driven sprocket. A cross-sectional view of a typical track configuration is shown in Figure 14 assuming a sprocket diameter of 4". The trolley sketched here allows variation of the probe's initial angle and should be built of a lightweight material so as to minimize the torque requirements of the drive motor. The location of the drive motor is shown typically in Figure 15, where an arrangement for $\gamma_E = 90^\circ$ is displayed. This motor must be capable of accelerating the appropriate masses at the values given in Table 3, with the exact range of values depending on the assumptions made. The relevant masses include the probe, the trolley, two pulleys, the chain and possibly some additional mass to account for the signal cables. This last effect would likely be eliminated and in fact some reduction of the effective mass of the system could be achieved for parts of a run if the cables were taken up during the run on a spring loaded drum such as that shown in Figure 15. The spring would have to keep the bundle of cables taut and should thus assist in accelerating the probe to the correct values. Deceleration, however, would of course be made more difficult and some optimum situation would have to be chosen. It might in fact be advantageous to place this drum at the top of the track, instead of the bottom, to obtain maximum benefits in the deceleration. In any case, for an arrangement such as this, it is suggested that the total effective mass of the system that must be accelerated by the drive motor could be limited to a value of $M \sim 1/32$ slugs.

The power and speed requirements of the drive motor can be determined from the data of Table 3. For a sprocket with a radius $R = 1/6$ ft, the probe and motor speed are related by

$$\omega = V_E'/2\pi R = 0.955 \ V_E' \qquad (4.10)$$

where ω is the motor speed in rev/sec and V_E' has dimensions of fps. Similarly, the linear and rotational accelerations are related by $\dot{\omega} = 0.955 \ \dot{V}_E'$. The motor torque is given by

$$T = M R \ \dot{V}_E' = 0.00518 \ \dot{V}_E' \ \text{ft-lb} \qquad (4.11)$$

and its power consumption can be found from

$$P = 2\pi T \omega = 0.0325 \ \dot{V}_E' \ \omega = 0.0311 \ \dot{V}_E' \ V_E' \ \text{ft-lb/sec} \qquad (4.12)$$

In addition, the largest torques are generally encountered at maximum speed. Thus using the above relations and the data of Table 3, the results for the maximum torque and power requirements of the motor are obtained (see Table 5).

These results and those of Table 3 indicate the specifications that must be met by the drive motor in the moving probe system. The motor itself should likely be a DC type which is controlled using a servo-feedback loop from the output of a motor tachometer as shown in Fig. 16. The input voltage V_i would be proportional to $V_E'(t')$ or $V_{EF}'(t')$ as shown typically in Figures 11 to 13, such that the motor speed ω could produce the correct values of probe speed according to (4.10). The voltage signal could be obtained quite simply by using a digital computer to produce the desired function and digital-to-analog conversion to obtain the analog signal on tape for use as the system input. The basic question to be answered for a system of this type is the difficulty in having it meet the specifications given above and its resulting complexity and cost. Indications from manufacturers of motor and control systems are that the requirements for the case of the frozen flow assumption

36

in which two values of ϵ (90° and 45°) are used can be satisfied using a fairly

standard system. For the other cases, however, only the accelerations required

during the acceleration and the actual run between A and B (Figure 7) can be

reasonably straightforwardly achieved. The large power required for the

deceleration lies beyond standard ranges and several thousand dollars would

likely be required to develop a motor and control system to meet this requirement.

It would seem, however, that any probe-moving system ultimately built should in fact

be capable of allowing the non-frozen case to be studied as well as the frozen

case. This is because there is always some degree of approximation associated

with the frozen hypothesis and tests of its validity with stationary probes might well

indicate unacceptably large 'thawing' of the flow in this application. In addition,

this capability would allow more direct testing of the frozen flow hypothesis by

comparison of the data from the two appropriate moving probe runs. We therefore

require a method for overcoming the deceleration problem for the non-frozen case

at a reasonable cost.

One possible solution to the deceleration problem would be the use of

a clutch between the motor and driven sprocket and a disc brake at the other

sprocket. These could be magnetically activated so that a photocell located

at point B in Figure 7 could trigger both a declutching and braking response

as the probe passed this point, thereby stopping the probe itself but allowing

the motor to run freely. It is likely, however, that a system of this type

would be not much cheaper than a custom designed servo-system. It is therefore

suggested that the best, or at least the most economical approach to follow

would be to place an opening in the tunnel floor through which the probe and

trolley could both pass. In this way the probe braking distance would be

increased and the required deceleration magnitude could be reduced to an

acceptable value. A sealed enclosure could be placed around the lower pulley

37

and take-up drum in Figure 15 to prevent air exchanges with the outside of the tunnel; the hole in the floor would not be expected to cause significant interference with the flow.

In the preceding discussion, we have considered the cost of building a system based on only one track. As discussed in Sec. 4.1, this would be sufficient if the frozen flow hypothesis were valid regardless of the distance travelled by the flow from a given point. In reality, however, at least two and probably three tracks would be required if three angles of glide path ($\gamma_E = 15^{\circ}$, 45° and 90°) are to be investigated, even when the frozen hypothesis is valid over reasonable distances. Consequently the sprocket arrangement at least at one end of the track must be moveable and the track itself must be extendable or replaceable. In addition, we must consider the question of glide paths which are not directly upwind but are yawed horizontally with respect to the mean flow. This would require the capability of yawing the guide track in both the frozen and non-frozen cases and could only be done if the sprockets, etc., at both ends of the track are moveable. Obviously the complexity and cost of the entire moving probe apparatus increases greatly when both variable γ_E and variable yaw are to be provided, and an increase by a factor of at least 2 in the overall cost of the system would not appear to be an overestimate. For the stationary probe approach to the problem, of course, no extra difficulty is encountered either in varying γ_E or providing measurements along yawed glide paths, and this is therefore another significant advantage of that technique.

4.4 Instrumentation

The amount of instrumentation and data handling equipment required for the moving probe solution in addition to that already available at UTIAS would depend on the number of input characteristics to be obtained. In the simple case of the turbulent velocities u, v and w alone, only one triple-wire

38

probe and one spare would be needed, since the required hot wire anemometry is available. If gradients were also to be obtained, at least three triple-wire probes (including at least one spare) would be required in addition to at least two more channels of anemometry. As for signal handling, the input voltage V_i could be easily produced with existing equipment. The output signals from either one or two moving triple-wire probes could be digitized for further handling. This would require sampling at a minimum rate of 600 per second for the frequencies of interest here and again should present no unusual difficulties for existing facilities at UTIAS.

Finally, we consider the number of independent runs that must be performed in order to obtain reliable statistics for the distribution of the vehicle location in the target plane. For χ^2-testing at the 5% significance level, Reference 14 indicates that we must have at least 5 readings in each class interval in order that the appropriate test statistic have the χ^2 distribution. In addition, we must have a minimum number of class intervals depending on the number of observations that are taken. If we assume the dispersion of the target point is Gaussian then it is found that reliable χ^2-testing can be done out to two standard deviations from the mean if at least 300 observations are used, since this would yield 5.2 readings in the last class interval. If 200 runs were used, there would be 4.0 readings in this interval. Thus we see that 200-300 runs would be required for any glide angle in order to supply sufficient data for reliable χ^2-testing at the 5% significance level.

Section V

EXPERIMENTAL FACILITIES

As discussed in Theory of the Stationary-Probe Method , one of the main prerequisites for applying the stationary-probe solution to the problem under consideration is the input matrix of turbulence cross-correlations, $\underline{R}$. While this information can (and ultimately should) be obtained from atmospheric measurements, it is desirable from the standpoint of both cost and expediency to obtain at least initial measurements from a suitable wind tunnel simulation of the atmospheric flow. There are at present two facilities at UTIAS capable of producing such a simulation, and measurement of $\underline{R}$ in these facilities is currently in progress.

5.1 The UTIAS 8" x 8" Multiple-Jet Wind Tunnel

A small, eight-inch-square multiple-jet wind tunnel (Figs. 17 and 18) has been used at UTIAS to produce boundary layer flows up to 7" thick with gradient velocities up to about 35 fps. It is an open-circuit tunnel and is driven on the ejector principle by an array of 64 jets located across a section near its upstream end. The velocities of these jets may be individually controlled, thereby allowing flows with virtually any desired mean velocity profile to be produced in the test section. A barrier plate located across the tunnel floor is used to trip the flow and produce the desired levels of turbulence in the test section. Varying the height of this barrier allows different values of turbulence intensity to be obtained, while particular velocity profiles may be virtually independently retained by simple jet velocity adjustment. The turbulence produced by the barrier is maintained in the downstream direction by surface roughness elements placed on the tunnel floor. Further details of this tunnel and its operation can be found in Reference 15.

40

In simulating the atmospheric boundary layer in the multiple-jet tunnel, some fundamental assumptions must be made about the nature of the prototype flow. First, the atmosphere is assumed to be neutrally stable with the turbulence being generated primarily due to the interaction of a strong wind with surface roughness. In addition, Coriolis effects must be assumed to be negligible in the atmospheric flow because it is not possible to simulate them in the wind tunnel. In general, these assumptions tend to limit the flows which can properly be simulated to those which do not extend too far above the earth's surface and in which the mean wind speed is fairly high. However, the important effects of terrain in producing local shears can be simulated reasonably well, while the high wind speed case is often the critical one for aeronautical applications. As for the increase in the mean speed with height above the surface, power-law relationships are assumed to represent adequately the actual variation. Should any modification to such profiles be desired, however, the technique of jet velocity adjustment allows such modifications to be produced quite easily.

5.1.1 8" x 8" Wind Tunnel Flow Characteristics

The characteristics of the laboratory simulation of the flow over flat, open country (n = 0.16) are shown in Figs. 19 to 23. (Note that y' = 0 corresponds to the tunnel center line and S represents the distance downstream of the jet grid.) The mean velocity profiles produced at the test section entrance are seen in Fig. 19 to follow the desired curve very well. Good lateral uniformity (i.e., two-dimensionality) has been achieved and little change in this profile was found throughout the test section. The parameters of the desired curve are $W_G' = 34$ fps and $Z_G' = 7"$. Thus with respect to the full scale planetary flow ($W_G = 68$ fps, $Z_G = 1000$ ft), the velocity scale factor is 1/2 and the length scale factor is 1/1715 for the present simulation.

41

Turbulence intensity profiles for the three fluctuating components are shown in Fig. 20 and agree well with corresponding atmospheric data. Typical power spectral density curves are presented in Fig. 21 and Reynolds stress results in Fig. 22. In Fig. 23, the longitudinal component integral scale is seen to agree reasonably well with suggested atmospheric results and also with the results obtained in another boundary layer wind tunnel simulation of this flow. The vertical scale, however, agrees with suggested atmospheric data only in the lower regions of the flow and is considerably smaller than desired in the upper half of the tunnel. Since representing the vertical eddies in the simulated flow on too small a scale may be a disadvantage, particularly for aircraft applications such as the present investigation, some effort was made to increase these scale values.

5.1.2 Roof Tests

In the planetary boundary layer, large scale velocity fluctuations in the vertical direction tend to be suppressed at lower heights due to the presence of the earth's surface. For this reason vertical component scales in this region are smaller than at higher altitudes and we find a distinct increase in L_w^x with height, as indicated by the suggested atmospheric results in Fig. 23. The same effect should of course apply in the simulated flow and this accounts for the observed increase of L_w^x with height in the lower half of the tunnel. In this flow, however, we also have a solid boundary at the top of the boundary layer and it is suggested that this is the probable cause of the low values of L_w^x found in the upper region of the flow. That is, unlike the full scale planetary flow, we have in this simulation no free stream region above the boundary layer, with the result that the presence of the roof suppresses large scale vertical fluctuations and thus prevents L_w^x from increasing with height as it should. One possible method of overcoming this difficulty would be to raise the roof to allow for a

42

free stream region. This would, however, considerably increase the tunnel power requirements and in the present facility it would necessitate major reconstruction. Another approach would be simply to simulate the planetary flow on a smaller scale (i.e., $Z_G' < 7"$), but in the present case the boundary layer thickness would be unusably small and in addition we would be left with too few jets in the boundary layer region of the tunnel to provide adequate control of the mean velocity profile. It was therefore decided in the present case, due to time limitations, to perform some fairly crude experiments involving variation of the tunnel roof configuration in an attempt to remove its suppressive effect on L_w^x.

In order to carry out the desired tests, the last three tunnel sections shown in Fig. 17 (S = 36" to 76") were removed and replaced by a new 40" section with a removable roof. In this way the roof boundary condition could be easily altered by simply exchanging various roof sections. The configurations investigated are shown and identified in Fig. 24.

The effect of the different roof types on the vertical component scale was determined by measuring $L_w^{x'}$ for each case in the test section entrance plane (S/H = 6.75). For the case of the slotted roof (No. 2) several heights were considered while for the remaining cases, the value at z' = 6.5" ($z'/Z_G' = 0.93$) was used to typify the roof effects. Scales were found using the spectral-fit approach in which it is assumed that the vertical component power spectrum can be reasonably fitted by a von Kármán model spectrum. Then from the location of the peak of the spectrum (k_{xpw}') along the frequency axis, $L_w^{x'}$ is determined using the model spectrum result (see Appendix A).

$$L_w^{x'} = \frac{0.106}{k_{xpw}'} \tag{5.1}$$

This approach yields true integral scales only insofar as the measured spectra actually follow the model spectrum shape, but in the case of the original solid roof the agreement is seen to be fairly good (Fig. 25). This is in fact

43

the only reasonable method for estimating scale in the present case, particularly
when correlation curves have a significant negative region. Further discussion
of the various approaches for scale determination can be found in Ref. 11.

The scale results obtained for the case of a slotted roof (No. 2, Fig.
24) are shown in Fig. 23 where it is evident that no significant change
has resulted in the lower region of the flow. In the upper section, good data
could not be obtained. The reason for this stems from the fact that the use
of the slots in the roof resulted in a serious 'beating' phenomenon in this
region of the flow. This phenomenon could be felt by an observer by placing a
hand above the slots, and its presence is clearly seen in the spectral measure-
ments as displayed in Fig. 25 . It is obvious that the spectrum no longer
resembles the von Kármán model, and comparison of the scales obtained by the
above technique from these two spectra is virtually meaningless. The possible
alternative of using correlations rather than spectra to determine scales is
precluded in practise by the large negative region of the appropriate auto-
correlation curve as shown in Fig. 26 . In addition to the measurement problem,
of course, is the fact that a spectral shape including this low frequency peak
is entirely unacceptable as a simulation of atmospheric turbulence.

Initial attempts at removing the beating phenomenon from the flow involved
the use of screens placed over the slots in an attempt to break up the organized
pattern which was producing it. This procedure in fact had no major effect on
the spectral peak save for shifting it slightly along the frequency axis (Fig.
25). That is, for the slotted roof with no screens (Case No. 2), the frequency
of the peak was roughly 16 Hz, while with the coarse screen (Case No. 3) it was
about 22 Hz and with the fine screen (Case No. 4) about 31 Hz. Its magnitude
however, was relatively unaffected by the screens. Suspecting that the beating
might somehow be associated with the size or shape of the slots, we tested a

44

roof with holes rather than slots (Case No. 5). This resulted in removal of the beating but only at the expense of returning the flow, including $L_w^{x'}$, to virtually the same condition it was in with the original solid roof. When the roof was removed altogether (Case No. 6) the spectral peak reappeared at $\sim$ 19 Hz, and when a fine screen was added (Case No. 7) it was merely shifted again to about 30 Hz. Finally, slots normal to the flow direction were tried (Case No. 8) by placing 2" wide slats across the open roof at spacings ranging from 1/2" to 3". In this case, no peak was observed when the probe was located at $z' = 6.5$" directly below a slat, but it reappeared at about 38 Hz if the probe was below the open space when d was 3". In the former case, however, the scale was again no larger than that obtained with a solid roof.

The exact cause of the beating phenomenon described above remains unknown, although we may speculate on its origin. The fact that it appears to be associated with those configurations for which no solid boundary exists between the flow inside the tunnel and the laboratory air outside leads one to consider the intermittency found at the edge of shear layers, and in particular in the outer regions of a turbulent boundary layer. This intermittency has been discussed by Klebanoff (Ref. 16) and stems from the fact that the boundary between the turbulent and non-turbulent flow is quite sharp and has an irregular, constantly changing shape such as that shown in Fig. 27. Thus a probe located at a point such as x alternately sees a turbulent and non-turbulent flow. Klebanoff's results suggest an average wavelength for this irregular outline to be about twice the boundary layer thickness, which in the present case would be about 1.3 ft. If the outline were then assumed to be frozen and carried past the probe with the free stream velocity ($\sim$ 32 fps), the resulting intermittency would have a frequency of roughly 25 Hz, and this is in the general region of the frequencies observed for the spectral peak. As a further investigation of this intermittency, oscilloscope traces of the turbulent signal just above the level of the tunnel

45

roof with no roof present were studied. Intermittent bursts of turbulence were indeed observed here with a frequency of ~ 15-20 per second, suggesting that there might in fact be a correlation between this phenomenon and the beating that was observed. However, it seems extremely unlikely that this effect could remain significant when screens are located between the tunnel flow and the laboratory air as for Case No. 7.

In the present experiment, although a start was made on the use of a plastic membrane roof, there was unfortunately little time available to pursue further investigations into either the beating phenomenon or the problem of the low values of $L_w^{x'}$ near the roof. These investigations are strongly recommended for future research. For the present, the solid roof configuration was accepted as the most reasonable and was used for all the measurements presented in this report.

5.1.3 Instrumentation

The basic instrumentation used in the present experiment is identical to that used and described in Ref. 11. Complete details can be found in the appendices of that report and thus only a brief resumé of this equipment is included here.

All turbulent flow velocity measurements made in the 8" x 8" tunnel were obtained with four channels of DISA type 55D01 constant temperature hot wire anemometers and type 55D10 linearizers. The hot wire probes used were DISA type 55E30 single wire probes for the longitudinal component and type 55A38 miniature cross-wire probes for both the longitudinal and lateral components.

Autocorrelations and cross-correlations of the velocity components in this experiment were obtained using a Princeton Applied Research (PAR) Model 100 Signal Correlator. This instrument produces time-delay correlation curves on-line for any two input signals for a maximum delay time τ_{max} which may be selected between 0.1 msec and 1.0 seconds. One hundred points on the correlation curve are

available in the form of analog voltages stored at the output of simple RC filter networks.

Power spectral densities of the velocity components were obtained by Fourier transformation of correlation curves using the digital computer, which subsequently was also used to plot the results. A block diagram of the complete system, including the hot-wire instrumentation, is shown in Fig. 28a and photographs in Fig. 28b.

5.2 The UTIAS (44" x 66") Boundary Layer Simulation Tunnel

The new boundary layer simulation tunnel at UTIAS is a modified version of an older, closed-circuit, low-speed tunnel in which the multiple-jet concept has been incorporated to produce the desired boundary layer flows. An 8 x 12 array of 96 jets (Figure 29) is used to drive the tunnel in the boundary layer simulation mode, with additional energy being supplied as desired by the original, 60 horsepower axial fan located in the tunnel return section. This fan may also be used to operate the tunnel in a uniform flow mode. That is, with the jets turned off, it is capable of producing a uniform, relatively low-turbulence (2-3% intensity) flow in the test section with a mean speed of up to 100 fps.

The velocities of the jets in the array can be adjusted in groups of three by a set of 32 servo-controlled butterfly valves located in the air supply lines. The positions of these valves may be adjusted from a central control panel, thus simplifying the creation of particular velocity profiles in the test section. Air is supplied to the jets from a 75 horsepower centrifugal blower and leaves the tunnel via a set of exhaust doors at the downstream end of the test section. As in the small jet tunnel, barrier-plates are used to generate turbulence and surface roughness is used to maintain it in the downstream direction.

47

The test section of the new tunnel is 44" high, 66" wide and has a usable length of 12 feet. A variable-angle roof has been provided to allow some control over longitudinal static pressure gradients through the test section. This section describes the design, construction and calibration of this facility (Reference 16).

5.2.1 Basic Design Considerations

The basic design for modifying the original UTIAS subsonic wind tunnel is a scaled-up closed-circuit version of the small, 8" square prototype tunnel described in the previous section. The latter tunnel (Fig. 18) is an open circuit model which is driven on the ejector principle by an array of 64 jets located across its cross-section. The jets are circular and form an 8 x 8 grid (Fig. 30) with a separation of 1" between adjacent jets (i.e., a 'meshlength' of 1"). Primary air is supplied to the jets through the sides of the tunnel via individual lines from a centrifugal blower.

The basic parameters of the prototype tunnel that could be varied in a new facility were the number of jets, their shape, their geometrical arrangement, and the total jet area as defined by the ratio $\alpha = A_2/A_j$ where A_j is the total jet area and A_2 is the tunnel open area at the jet grid. The simple ejector analysis of References 11 and 17 was used to predict tunnel performance. For the prototype tunnel a value of 20 was chosen for α and this was again used in the new facility. If friction losses are included in the analysis it is found that

$$U_2/U_j = 0.17 \tag{5.2}$$

$$U_3/U_j = 0.21 \tag{5.3}$$

Where all velocities are assumed to be average values; U_2 is the

velocity of the air outside the jets at the exit plane of the jets, U_j is
the jet velocity, and U_3 is the flow velocity in the mixed flow region
(see Fig. 31).

The experimental results of Reference 11 were found to agree quite
well with these values and consequently they were used for predicting design
velocities in the new tunnel.

As for the number and arrangement of jets in the new tunnel, the
basic pattern used in the prototype was retained. The eight rows of jets
in the small tunnel allowed a good degree of control over the velocity
profile and still permitted the production of reasonable turbulence scale
values when barriers were used. Equal lateral and vertical jet spacing
provided reasonable lateral homogeneity of the flow and was thus also
retained. The shape of the individual jets, however, was changed from
round to square in the new tunnel in order to simplify their construction.
The results of Reference 11 suggest that such a change should have no
significant effect on the flows produced in the mixed-flow region of the
tunnel.

5.2.2 Details of 44" x 66" Tunnel

The original closed-circuit UTIAS subsonic wind tunnel is shown
in Fig.32 in schematic form. The most convenient and economical way to modify
this facility to the multiple-jet configuration was to replace the contraction cone,
test section and diffuser between A and B in the drawing with a new contraction,
a jet grid section, and a boundary-layer-growth and test section. Thus a total
length of 449" was available for the new section, and it was this dimension that
determined its height. That is, we wished to produce boundary layer flows having
the maximum possible thickness in the available space. From Ref.11, it was

49

found that for the multiple-jet type of tunnel, a usable test section was available between 5-1/2 and 8-1/2 tunnel heights from the jet exit plane. Thus allowing roughly 6-1/2 feet for the contraction cone and jet grid sections, a total length of about 371" was available in which to place about 8-1/2 tunnel heights. This yielded the design tunnel height of 44" and should allow boundary layer flows up to 36" thick to be obtained. As for the tunnel width, the results of Ref. 11 showed that in some cases fairly large boundary layers could be encountered on tunnel walls when a barrier was used to produce turbulence in the test section. For this reason, and because increased tunnel width is advantageous for large terrain models, a width of 66" was selected. A layout of the modified tunnel is given in Fig. 33 and a general view is seen in Fig. 34.

Jet Grid Section

With a tunnel cross-section 44" x 66" and an area ratio $\alpha = 20$, the total jet area is fixed at 138 sq. in. In addition, the use of eight jet rows results in a jet spacing of 5.5" vertically and consequently twelve columns of jets for equal vertical and lateral spacing. The complete array therefore consists of 96 jets each having an area of 1.44 in^2. Square jets were designed (1.2" x 1.2") with each row being covered by an airfoil to reduce friction losses just as in the prototype. An upstream view of the entire grid is given in Fig. 35 together with the notation system chosen for jet identification. Fig. 36 is a photo of the completed grid.

As seen in Fig. 35, the columns of jets have been identified in groups of three. The reason for this is that each group of three in any row is controlled by a single external butterfly valve as far as the jet velocity is concerned. That is, the velocity of each of these jets cannot be individually controlled and all three in any group must be altered together. This was done to reduce the number of valves and valve control devices from 96 to 32 and thus mini-

mize the system cost.

Blower Requirements

Computations indicated that a total static pressure rise of about 20" H_2O must be supplied by the blower. This figure and a volume flow requirement of 15,240 cfm were used to select a Canadian Blower and Force Model 55 MW industrial exhauster with a 75 HP General Electric motor. No speed control was required for this blower since a reduction in its delivery will be required only infrequently and can be achieved by throttling its inlet.

Tunnel Return Section

We see in Fig.33 that the modified wind tunnel is still a closed circuit tunnel, in the return section of which an axial fan and drive motor (60 HP) are located. There are two basic consequences of this feature of the facility. First, we must provide exhaust ports somewhere in the circuit so that the primary air supplied by the jet supply blower is allowed to leave the tunnel. Three doors have been provided for this purpose in the region downstream of the test section, as shown in Fig. 33. The area of each of these doors is about 4-1/2 ft^2 so that the velocity of the exhausting air is less than 20 fps at maximum operating conditions. The second consequence involves the axial fan itself. It will of course 'windmill' if left off during operation of the tunnel in the ejector-driven mode. In this case, it can be represented in the tunnel performance equations by a small pressure loss term to predict its effect. If, however, it is turned on during a run, the sign of this term can be reversed and the fan can supply a pressure boost to the ejector system. This permits a higher test section velocity to be achieved for a fixed jet velocity or, conversely, it reduces the jet velocity required for a desired test section velocity (i.e.,

U_3/U_j would be increased). Since the degree and nature of the improvement to the ejector system that might be obtained from this fan was not exactly known, it was decided to ignore its possible benefits in determining the tunnel blower requirements and assume only that it could reduce its own contribution to friction losses to zero.

One additional feature of the presence of the axial fan in the tunnel return section is the capability for operation of the tunnel in a reduced-turbulence mode. That is, with the jet supply blower off, operation of the axial fan permits flows of up to 100 fps with 2-3% turbulence intensity to be obtained in the tunnel test section.

Tunnel Test Section

The new tunnel 'growth' and test sections are shown in some detail in Fig. 39. The growth section consists of the region between the jet exit plane and the test section entrance and contains any barriers used in producing turbulence as well as roughness on the floor. The test section itself is about 12 ft in length and has an access door in the side wall as well as a roof which may be opened along the last 8 ft of its length. In addition, the entire test section roof is hinged at the test section entrance so as to permit some control of the static pressure gradients in the test section. The degree of control was chosen so as to allow removal of the gradients resulting from boundary layer growth on all walls through the test section.

Valves and Servo-Control System

The velocity of the jets in the small prototype tunnel is controlled by a simple gate valve and a rotameter in each supply line is used to measure its value. In the new facility this velocity, when required, is measured using a Pitot probe at the jet exit and the static pressure on the tunnel walls at the jet exit plane. The jet velocities are controlled, as mentioned above, in groups of three by simple butterfly

52

valves. These valves (Figs. 34 and 37) consist of a rotating flat plate located in a short length of 4" diameter pipe. An 8:1 gear reduction is used to increase position sensitivity and to reduce torques. Sixteen valves are located on each side of the jet grid section of the tunnel.

In order to obtain a particular velocity profile in the tunnel test section, an iterative procedure is used in the new tunnel just as it was in the prototype. That is, a probe is placed at some location in the desired plane of the test section and the flow leaving the appropriate jets in the grid is adjusted until the desired velocity is achieved at the probe location. This procedure is repeated iteratively until the desired flow is obtained throughout the plane. To simplify this procedure, it was decided to mechanize the valve adjustment system by using a servo-motor-and-feedback system for each valve. The complete system of 32 channels allows setting of the position of any valve from a central control panel by the simple adjustment of a command potentiometer. Valve position is indicated by a potentiometer connected to the valve itself and its output is fed back to the control circuit ('manual' mode). The complete control circuit for one channel (i.e., one valve) is shown in Fig. 40 and includes automatic stops and warning lights at the two extreme valve positions (open and closed).

Instrumentation

The running temperature of each fan motor and the tunnel test section can be monitored by the operator at the tunnel control panel. This is achieved through the use of thermistors which can be linked through a switch to a simple bridge measurement circuit on the panel.

A system for traversing the tunnel has been constructed utilizing

a standard lead screw drive. It is shown in Fig. 41. The probe holder may be driven both horizontally and vertically. The apparatus has been made easily removable and may be moved to different measurement planes manually with a minimum of effort.

In order to position the probe accurately, electronic switches, consisting of a photodiode, a light source, and a blade to interrupt the light, have been placed on the lead screws. Pulses from these switches are counted by two electronic counters. This allows positioning to within one revolution of the lead screw. This, combined with the probe holder play, allows setting accuracy of approximately 0.1 in. With proper gating, the counters may also be used in conjunction with a pulse generator as a frequency counter. Inputs must be in the form of pulses.

A schematic of the data acquisition system is shown in Fig. 42a and photographs in Fig. 42b. It consists of four channels of DISA 55D01 anemometers accompanied by four DISA 55D10 linearizers. These instruments provide flow measurement capabilities of approximately 3-300 fps with a flat frequency response up to 100 KHz. Outputs from these units are conditioned by a PACE TR48 analog computer. This is a solid state 10 volt machine with 40 amplifiers, 10 integrators, and 2 multipliers presently available.

Signal filtering can be provided both by the TR48 and a Multimetrix Model AF420 active filter. The latter is a two-channel system which provides 2 channels of high or low pass filter or a single channel band pass filter. It features digital cutoff frequency selection and a 24 db/octave roll-off.

Cross- and auto-correlation may be obtained with the PAR model 100 correlator. This instrument provides 100 analogue estimates of correlation with values of τ (time delay) ranging from $\tau_{max}/100$ to τ_{max} where τ_{max} is the maximum value which may be selected in the range 1 - .0001 sec.

Each estimate of the correlation is an average of the correlation over the $\Delta\tau = \tau_{max}/100$ interval. In addition, correlations can also be obtained using an HP 2100A digital computer.

RMS voltages are measured on the Bruel and Kjaer model 2417 random noise meter with a 30 sec. time constant setting.

Data can be fed via the Hewlett Packard Model 5610A A/D converter into the HP 2100A digital computer. The A/D converter is capable of 100,000 samples per sec. The computer has 24K core storage, supplemented by a magnetic tape system. The computer cycling time is 980 nsec. Algol, Basic, Fortran, and Assembler are the languages used on this system. Other equipment in this system includes a digital plotter, high speed paper tape reader, teletype and tape punch, D/A converter, and Fast Fourier Transform hardware.

The use of this system for the spectral analysis performed during the present calibration has reduced our data acquisition and computation times by a factor of two over the system described in Sec. 5.1.3.

5.2.3 <u>44" x 66" Tunnel Calibration</u>

In general the approach used in this calibration of the 44" x 66" tunnel has been based on a comparison of typical flow properties with those found in the 8" x 8" tunnel, along with some direct comparisons with atmospheric data where possible. The 8" x 8" tunnel calibration used as a basis is outlined in Ref. 11 in considerable detail. Given the current general lack of full scale data for comparison and the limited faithfulness of the simulation provided by wind tunnels (e.g., lack of thermal effects, wind direction changes with height, etc.) it was felt that this approach was justified. Within these limitations it was found that an acceptable planetary boundary layer simulation could be achieved in a useful test section of 3 ft height, 3 ft width, and 12 ft length.

Planetary Boundary Layer Characteristics

The purpose of the new boundary layer tunnel is to simulate the earth's planetary boundary layer. The simulation is based on the following information taken from Ref. 10.

(a) Velocity Profile

The height of the boundary layer as well as its velocity profile varies with the roughness of the terrain over which it travels. This velocity profile is approximately a power law profile governed by the relation (see Sec. 3.4)

$$\frac{W(z)}{W_G} = \left(\frac{z}{Z_G} \right)^n \tag{5.4}$$

(b) Atmospheric Turbulence

The power spectral densities of the turbulent wind velocities of the earth's planetary boundary layer have been found to be well represented by the von Kármán model for isotropic, homogeneous turbulence (Ref.10). This model is contained in Appendix A and illustrated in Fig. 55. This allows the use of the spectral peak method in calculating turbulence scale lengths. The two integral scale length relations which were used as atmospheric models for comparison with the scale lengths found in the tunnel are (Ref. 10)

$$L_u^x \simeq 20 \sqrt{z} \tag{5.5}$$

and

$$L_w^x \simeq .4z \tag{5.6}$$

These are plotted in Fig. 64.

Test Section Velocity Profile (Clean Tunnel Configuration)

The tunnel layout is illustrated in Fig. 43. All measurements were made at the upstream and downstream ends of the test section. These are at $s = 5.5H$ and $S = 8.5H$, respectively.

A velocity profile at the S = 5.5H plane is shown in Fig. 44. The profile has been nondimensionalized by the maximum profile velocity ($\bar{U}_{max}$ = 100 fps) and the tunnel width (W) and tunnel height (H). This is the profile when the clean tunnel is powered by the upper fan only. In this configuration the barrier strip and the floor roughness are absent. A similar profile is obtained when the jets power the tunnel, and the jet exit speeds are equal. The wall boundary layers are fairly small in this configuration as would be expected.

The dished shape of the profile is caused by the abrupt contraction cone. The main consideration in the design of the contraction cone was length. Since the tunnel was designed for high turbulence and fairly low velocities, it was thought that little benefit would be gained from a classic contraction cone design with its excessive length requirements. Consequently, a fairly simple design was used. The abruptness in the contraction causes higher local velocities in the outer flow, resulting in the dish-shaped profile. For further discussion of this effect, the reader is referred to Ref. 18.

This profile is important because if the upper fan is to be used with the jets, then the superposition of this flow on that of the jets must be considered. At very high speed settings of the upper fan, this could limit the degree of profile adjustment available from the jets.

Velocity Range

The jet drive system was designed for a 55 fps uniform profile with the upper fan overcoming only its own losses. It was found that this 55 fps velocity could be attained without the aid of the upper fan. Utilizing the upper fan plus the jet drive system, a maximum velocity of 120 fps can be reached. With the tunnel powered by the upper fan only, a velocity of 100 fps is attained. In this configuration, however, the profile has the dished shape, mentioned earlier, which would allow use of only the central portion of the test section.

It was mentioned that the tunnel could be operated in a low
turbulence mode. This is best achieved by utilizing the jets to fill out the profile
produced by the upper fan. It was found that in this configuration, turbulence
intensity levels ($\hat{u}/W$) were in the range from .02 to .03.

In the clean tunnel configuration the wall and floor boundary layers were
limited to approximately 4 in. at the upstream end of the test section. This in
no way approaches laminar flow, but could be used for such things as calibration of
cup anemometers or pitot-static tubes used for industrial purposes. It could
also be used for studies of wind loading on structures where aeroelastic effects
are not being studied.

Temperature

A time history of the tunnel temperature is shown in Fig. 45 . From
this it can be concluded that a half hour warm-up time eliminates much of
the temperature drift. The tunnel, being a modified closed circuit type, runs
well above the ambient temperature. However, with the jets turned on there is an
air exchange of approximately 15,000 cfm. This makes the tunnel more sensitive to
ambient temperature than a closed return tunnel, but also limits the operating
temperature to approximately 25°F above ambient. For this reason, the tunnel
never reaches a temperature where it must be shut down to cool. This provides a
virtually unlimited operation cycle.

Turbulence Producing Devices

(a) Floor Roughness

Roughness on the floor is provided by a vinyl carpet. It is very
durable and clean. Dust particles that accumulate in the mat are easily picked
up with a vacuum cleaner. The bristles protrude about one-half inch into the
airstream and are formed in clumps in a regular array. Figure 46 shows this
material.

With the carpet in place, turbulence intensity measurements were again

taken. (The upper fan alone was used in this test, the barrier was absent.) It was found that the turbulence intensity increased only slightly and only in the bottom 6 in. of the tunnel. The floor boundary layer with uniform flow increased somewhat, but wall boundary layers were negligibly affected.

(b) Barrier

Based on the results from the prototype tunnel (Ref.11), a 5-in barrier was placed at a point 1-1/2 tunnel heights downstream of the jets (see Fig. 43). The results achieved are discussed in the next sub-section.

Profile Setting (Roughness and Barrier Present)

At present, the only profile to be set, other than the uniform profile is the power law profile discussed in Sec. 3.4 with n = 0.16. This was done using the grid of measurement positions at S = 5.5H shown in Fig. 47.

As mentioned earlier, the jet grid is controlled in sets of three jet horizontally. This allows three jets to be set by one valve. In order to set the profile, lateral spacing corresponding to the (b) measurement position for each set of three jets (see Fig. 47) was used. After setting the profile, velocity measurements were taken at each of the entire set of measurement positions. Some results of this profile measurement are shown in Fig. 48. The non-uniformity of the lateral profile is caused by two things. The first factor is the dished profile discussed earlier. This causes the centre of the tunnel to be slow. The second reason for the non-uniformity is the presence of the wall boundary layers. It was found that these boundary layers were increased considerably when the barrier was installed. At the beginning of the test section their thickness was about 14 in.

With the roughness and barrier in place, the wall boundary layers have grown to include the first column of measurement points (see Fig.49). This causes the velocity measurements at those (b) points to be lower than the free

59

stream velocity by about 10%. This, combined with the velocity defect at the tunnel's centre produces a 10% variation in the lateral velocity profile. This variation cannot be removed with the trimming valves which were designed strictly to equalize jet exit velocities. They cannot overcome large influences such as wall boundary layers.

In order to achieve better uniformity, the 1c and 4a positions (see Fig. 47) are used for measurements at the walls. This allows the boundary conditions of the flow to be set to a known value. The flow velocities between these measurement positions and the near walls are of no interest. This change in measurement position allows the setting of a lateral profile varying less than ± 3% between columns 1c and 4a as shown in Fig. 50.

Since each valve controls a horizontal group of 3 jets, and only one measurement position is used for each valve, the measurement positions are further apart in the horizontal than in the vertical direction. This causes the setting of one valve to affect the flow controlled by the valves immediately above and below it more than those to either side. The influence region of each jet is shown roughly in Fig. 51. Since the velocity at each measurement point is greatly affected by the valves controlling the velocity at points immediately above and below it, a simple iterative technique in setting the profile requires a large number of iterations. The procedure used is as follows.

The flow velocity is measured for an entire column of measurement positions. Using these, the profile is set at that column by considering the interaction of the jets and adjusting each accordingly. When this process has been completed, the remaining columns are set in the same manner. The entire setting procedure is repeated three times on the average. Using the motorized traversing gear described earlier, about 1-1/2 days are needed to set a new velocity profile.

The two lower rows of jets cannot be used to control the velocity

60

profile near the tunnel floor due to the barrier (see Fig. 43). This, however, is not a serious problem since the natural velocity defect near the floor causes the velocity to fall off in accordance with the power law profile that has been set. These two lower rows of jets are set at near maximum settings. This tends to increase the turbulence in the tunnel by hitting the barrier with high speed air.

The velocity profile was originally set with $W_G' = 55$ fps. It was found, however, that the $L_u^{x'}$ were much too low. In order to rectify the situation an 8 in. barrier was installed. This increased the scales somewhat, but caused severe distortion of the power spectral density plots. This invalidated any scale measurements since the spectral shape varied a great deal from the von Kármán model.

The original 5-in barrier was then replaced and W_G' increased by also turning on the upper fan. This increased the scale lengths without distorting the spectral shape. A study of the variation of scale length with velocity was then performed. It was concluded from this study that a gradient velocity of 90 fps was needed. For this reason the tunnel profile was set with $W_G' = 90$ fps. Figure 52 shows the results of this study. In scaling the prototype tunnel, it was initially felt that scale length would be proportional to barrier height. The scale length was assumed to be governed by the size of the detached boundary layer region immediately behind the barrier. However the size of this region with respect to the size of the barrier seems to vary a great deal with experiment (Ref. 19). This would lead one to suspect that local conditions at the edge of the barrier, and upstream, must have a large effect on the size of the detached region. This perhaps explains why the scale did not increase exactly linearly with barrier height.

The turbulence intensity profiles that resulted from the 5-in barrier and $W_G' = 90$ fps are plotted in Fig. 53. These data were obtained along a 15° glide slope down the tunnel centre line and thus span most of the test section. As

61

in the case of the 8" x 8" tunnel (see Fig. 20), these plots appear to be in reasonable general agreement with corresponding atmospheric data.

Since the tunnel exchanges air with the atmosphere at a rate of 15000 cfm, the gradient velocity tends to vary slightly with atmospheric conditions. This is caused by changes in loading of the blower motor due to changes in air density, as well as changes in loading due to temperature changes in the belt drive system. These variations cause the gradient velocity to fluctuate from day to day with the maximum fluctuation being approximately $\pm 5\%$. This, however, does not affect the nondimensionalized profile which stays within 3% of the desired profile (see Fig. 54 for typical vertical profiles).

Measurement of Reynolds stress in the simulated flow has been carried out at a few locations along the tunnel centre line. Values of $\overline{uw}/\hat{u}\hat{w}$ are similar to those found in the 8" x 8" tunnel (see Fig. 22). Some difficulty was encountered when measuring $\overline{uv}/\hat{u}\hat{v}$ due to the small values generated. The data tended to be scattered about a value of $\overline{uv}/\hat{u}\hat{v} = 0.1$. Thus it was concluded that these results were acceptable.

Spectral Data

Appendix B describes the techniques of power spectral density analysis used for this calibration. Figures 55 to 58 show plots of $\frac{k}{\overline{u^2}}\Phi_{uu}(k)$ vs kz at different points in the test section. The von Kármán spectrum is also shown for comparison. From these plots it may be seen that the measurement of scale lengths using the spectral peak method, described in Appendix A, is reasonable. A typical plot of $\frac{\Phi}{\overline{u^2}}_{uu}(f)$ vs f' is shown in Fig. 59.

Figures 60 to 62 show some $\frac{k}{\overline{w^2}}\Phi_{ww}(k)$ plots. Here it was found that above jet row D in the tunnel (i.e., the $.7Z_G$ point of the boundary layer) the spectra were sufficiently different from the von Kármán that they could not be used to get a precise estimate of L_w^x (see Fig. 60). Figure 63 gives a typical $\frac{\Phi}{\overline{w^2}}_{ww}(f')$

plot.

Figure 64 shows the results of scale measurement at various points in the test section using the spectral peak method   and   compares these with the values calculated from   (5.5)   and (5.6).

One of the deficiencies found in the small 8" x 8" tunnel is illustrated in Fig. 21.   At high values of kz it is seen that the power spectrum ϕ_{uu} drops off at a faster rate than that found in the atmosphere. This is thought to be due to viscous dissipation which is the phenomenon whereby turbulent energy is lost from the flow. This occurs in turbulent eddies of small physical dimensions. Since the same fluid is used in the tunnel as exists in the full scale atmosphere it would be expected that this effect would be noticed at a smaller value of kz in the tunnel. When similar measurements were made in the large 44" x 66" tunnel (see Fig. 55, for example) this effect was generally found to be absent within our measurement range. Thus it is concluded that the viscous dissipation region has been shifted to a sufficiently high frequency to allow us to neglect its effect.

A similar drop in the power spectral density below the von Kármán model is also observed at low frequencies (see Figs. 21 and 55). This is thought to be due to the finite dimensions of the wind tunnel test section suppressing the generation of large wavelength phenomena. Even in the actual atmosphere this region of the power spectrum is not well defined and thus this effect is not felt to be a limiting factor in the present simulation.

Flow Properties Along the Test Section

Due to the nature of the flow in a wind tunnel, the wall boundary layers continue to grow and turbulence energy is dissipated along the length of the test section. This leads to some modification of the flow properties. As shown in Fig. 54 the velocity profile remains unchanged. Figures 55 to 58 and 60 to 62 indicate that the changes in the shape of the power spectral

density curves are minor with some distortion occurring at the top of the boundary layer. This is reflected in the integral scale profiles of Fig. 64 where it is seen that a small increase in L_u^x occurs in going downstream in the test section while no change in L_w^x is apparent. It is felt that the observed trends are sufficiently small that they should not interfere with the generation of representative cross-correlation data in the tunnel.

64

Section VI

EXPERIMENTAL RESULTS - FIXED PROBE APPROACH

6.1 Distribution of Probe Locations

Due to the time consuming nature of the fixed probe measurement technique it is important to minimize the number of locations at which correlations are computed. Because our cross-wire probes can only measure either u and v or u and w simultaneously at a single point, four separate runs are required to obtain the entire R matrix associated with a given pair of points. The orientation of the probes must be changed between these runs in order to measure the necessary velocity components. The required combinations are given in Table 6.

When the double integral leading to the system response matrix is examined (3.14)

$$< \underline{y}(t)\underline{y}^T(t) > = \int_0^t\int_0^t \underline{H}(t,t_1) \ \underline{R}(t_1,t_2)\underline{H}^T(t,t_2)dt_1 dt_2$$

it is seen that the greatest contributions come from regions in the (t_1,t_2) plane where $\underline{H}(t,t_i)$ and $\underline{R}(t_1,t_2)$ are large. These regions are shown schematically in Fig. 65 by cross hatching. In general, $\underline{R}(t_1,t_2)$ will be greatest for $t_1 \approx t_2$, $\underline{H}(t,t_1)$ for $t_1 \approx t$, and $\underline{H}(t,t_2)$ for $t_2 \approx t$. Thus the area of greatest interest may be the upper right hand corner of Fig. 65a where $t_1 \approx t_2 \approx t$. Since $t_1 = t_2$ corresponds to $z_1 = z_2$ and we are interested in conditions at the end of the landing approach descent where t corresponds to z_B (see Fig. 1) then the desired probe locations in the (z_1, z_2) plane are as shown in Fig. 65b. These facts should be reflected in the choice of probe locations, with more attention placed on measurements towards the bottom of the approach path and on measurements with small probe separations. The actual sets of probe locations employed in the present work are indicated in Figs. 66 and 67. Note that the

65

symmetry implied by (3.12) results in the values measured for $\mathbb{R}_{uv}(t_1,t_2)$ for $t_2 > t_1$ also being used for $\mathbb{R}_{vu}(t_2,t_1)$ for $t_2 > t_1$, etc.

6.2 Measurements in the 8" x 8" Tunnel

A preliminary set of correlation measurements were made in the 8" x 8" tunnel before the 44" x 66" tunnel was completed. $\mathbb{R}_{uu}$, $\mathbb{R}_{vv}$, and $\mathbb{R}_{ww}$ were determined for a range of experimental conditions. These data are presented in nondimensional form as $\widetilde{\mathbb{R}}$ where typically $\widetilde{\mathbb{R}}_{uv} \equiv \dfrac{\mathbb{R}_{uv}}{\hat{u}\,\hat{v}}$ and $\hat{u}$ is measured at the probe location corresponding to u and $\hat{v}$ at the location corresponding to v. The distribution of probe locations is shown in Figure 66. Note that the u measurements were made with single wire probes and their more compact design allowed extra measurements to be made at small probe separations as indicated. The $\gamma_E = 15^{\circ}$ data were all taken below $z' = 4"$ due to test section length limitations. Due to various reasons, measurements were not always taken at the lowest positions for the lower probe nor at the lowest position for the upper probe. The simple probe holder employed is shown in Figure 68. This system was based on 1/4" pipe and required that each probe's location be established by two position measurements to place it on the required glide slope.

6.2.1 Measurement Technique (8" x 8") Tunnel)

Values of the correlation matrix $\widetilde{\underline{Q}}\,(t_1',t_2')$ for various values of t_1' and t_2' were obtained as follows. For $\widetilde{\mathcal{R}}_{uu}(t_1',t_2')$, for example, a single wire probe was placed at some fixed point P_o on the glide path corresponding to height z_P' from the floor of the tunnel. Another probe was placed at a point Q_o below it on the glide path, at height z_Q'. The fluctuating velocity signals from these probes were then cross-correlated using the PAR correlation system (see Sec. 5.2.2), yielding the correlation between the signals for 100 values of delay time τ of $u(P_o)$ with respect to $u(Q_o)$, $0 < \tau < \tau_{max}$ (see, for example,

66

Fig. 69). Knowing z_P' and z_Q', the appropriate t_1' and t_2' for this pair of points P_o and Q_o for any particular airspeed V could then be found from the time tables described in Sec. 3.3 with the necessary scale factors for the simulated flow taken into account. Consequently the time difference $\Delta t' = t_2' - t_1'$ could be determined and by selecting the value of the cross-correlation at $\tau = \Delta t'$, $\widetilde{\mathcal{R}}_{uu}(t_1', t_2')$ was obtained. For the same pair of points P_o and Q_o but different airspeed, the time tables yield different values of t_1', t_2' and $\Delta t'$ such that the value of $\widetilde{\mathcal{R}}_{uu}(t_1', t_2')$ was obtained from the same cross-correlation curve but at a different value of τ. By moving only the lower probe to a different value of z_Q' and obtaining a new cross-correlation, $\widetilde{\mathcal{R}}_{uu}(t_1', t_2')$ could be found for the same t_1' but differing t_2'. Obviously then, by selecting appropriate values of P_o and Q_o along the glide path, $\widetilde{\mathcal{R}}_{uu}(t_1', t_2')$ could be determined for the entire range of interest of t_1' and t_2'.

The rms values of the turbulent components used to normalize $\underline{\mathcal{R}}$ were obtained from the Bruel and Kjaer random noise voltmeters.

Based on the above procedure for finding the values of $\underline{\widetilde{\mathcal{R}}}(t_1', t_2')$, it is estimated that the maximum experimental error in each point should be no greater than about 12-14%. The statistical variability of any value depends on its magnitude and on the shape of the signal spectrum but should in general be considerably less than the above figure. (See also Section 6.3.1).

6.2.2 Some Features of Two-Point Cross-Correlation Data

In Fig. 69 we see a typical two-point time-delay cross-correlation curve for the longitudinal velocity component for $\gamma_E = 90^o$. It is clearly seen here that the maximum correlation between the two points occurs at a value of time delay other than zero, which is where it would occur if the flow were homogeneous. Rather, the peak is found at a positive lag time τ_m, which

represents a delay of the signal from P_o with respect to that from Q_o (see Fig. 70). If we assume frozen flow then we may translate this time lag into the spatial separation

$$\Delta x'_m = W'(z'_Q) \cdot \tau_m \qquad (6.1)$$

Thus the line $P_o \, Q_m$ in the sketch may be considered the line of maximum correlation at this location in the flow, and its slope is given by $\Delta z'$ and $\Delta x'_m$. In a homogeneous flow, this line would be normal to the floor of the tunnel but in a boundary layer flow it has a slope which may be a function of z'.

If we consider values of γ_E less than 90°, we ultimately will reach a situation in which the line $P'_o \, Q_o$ (see Fig. 70) will have a slope smaller than that of the line of maximum correlation, $P_o \, Q_m$. In this case, we would expect the peak of the time-delay cross-correlation curve to appear at a negative value of τ_m. This of course corresponds to a delay of the signal at Q_o with respect to that at P'_o rather than vice-versa. This is in fact the case, as indicated by the results shown in Fig. 71 for the case of $\gamma_E = 45^o$. In the present experiment, we are interested only in delays of the signal from P_o with respect to that from Q_o (i.e., $\tau \geq 0$) and thus in most cases other than $\gamma_E = 90^o$ we do not observe a peak at all in our range of interest. For more results and discussion of optimum time-delays for maximum two-point correlations in a boundary layer flow, the reader is referred to Ref. 12.

The curves of Figs. 69 and 71 are typical of all the raw correlation data obtained for the three velocity components and the three values of γ_E used in this experiment. Curves of this type have been used to obtain the final flight path correlation data, $\underset{\sim}{\tilde{R}}(t'_1, t'_2)$, as discussed below.

6.2.3 Flight Path Cross-Correlation Results (8" x 8" Tunnel)

As described above the experimental work in the 8" x 8" wind tunnel facility involved a large number of two-point space-time turbulent velocity

component correlations (approximately 1000) within the simulated planetary boundary layer. Spatial separations of the probes were determined by the desired glide path geometry with fixed aircraft descent angles of $\gamma_E = 15°$, $45°$, and $90°$ being selected for the present study. Cross-correlations covering a range of time delays (positive time delays of upper measurement with respect to the lower measurement) were obtained with the correct time delay for each point pair being selected later to develop the final flight path correlations, $\widetilde{\underline{R}}(t_1', t_2')$. Of the basic correlation information, two typical plots only (for $\widetilde{\underline{R}}_{u\dot{u}}$) are shown, Fig. 69 and Fig. 71, in nondimensional form.

The derived flight path correlations, obtained with a mean wind variation corresponding to a power law index of 0.16, are plotted beginning at Fig. 73 and continuing through to Fig. 102. The following cases have been covered for this mean wind speed variation:

(i) $\widetilde{\underline{R}}_{uu}$, $\widetilde{\underline{R}}_{vv}$ and $\widetilde{\underline{R}}_{ww}$ turbulent cross-correlations.

(ii) Flight path approach angles, $\gamma_E = 15°$, $45°$, $90°$.

(iii) Aircraft velocity ratios, $V/W_G = 1.0, 1.2, 1.5, 1.9$ (except for the case $\gamma_E = 90°$ for which only $V/W_G = 1.0$ and 1.2 were used due to excessive rates of vertical descent for the aircraft at the higher speed ratios.)

(iv) $W_G = 68$ fps, $W_G' = 34$ fps, $Z_G = 1000$ ft, $Z_G' = 7$ in.

In addition, initial measurements, with a mean wind speed variation corresponding to a power law index of 0.35, are also included, in Figs. 103 through 106. For this wind profile the following data have been obtained:

(i) $\widetilde{\underline{R}}_{uu}$ turbulent cross-correlations

(ii) Flight path approach angle $\gamma_E = 45°$

(iii) Aircraft velocity ratios $V/Wg = 1.0, 1.2, 1.5, 1.9$

(iv) $W_G = 68$ fps, $W_G' = 34$ fps, $Z_G = 1600$ ft, $Z_G' = 7$ in.

In all cases the derived flight correlations correspond to simulated aircraft landing approaches flown at constant air speed along straight-in approach paths. These particular flight constraints result in a continuously increasing aircraft ground speed as the target plane is approached (see Fig. 5). The turbulence characteristics of the shear layer, as simulated and measured in this facility, are presented in Figs. 20 through 23.

The data are presented as a function of t_1' and $(t_2'-t_1')$, i.e., in terms of time as measured in the wind tunnel frame. In order to convert these values back to full scale time they must be multiplied by $1/S_t = 857$.

The desired flight path correlations, $\tilde{\underline{Q}}(t_1,t_2)$, form, in general, a warped surface over the t_1,t_2 plane with the final aircraft flight dispersions being obtained by a double (area) integration in this plane (see (3.14)) over the range $0 \leq t_1 \leq T$; $0 \leq t_2 \leq T$. In a homogeneous turbulent field (with a uniform velocity profile), the $\tilde{\underline{Q}}(t_1,t_2)$ surface could be described in terms of a single curve if plotted as $\tilde{\underline{Q}}(t_2-t_1)$ with the single independent variable (t_2-t_1). A rough schematic drawing of one half of the general $\tilde{\underline{Q}}(t_1,t_2)$ surface, which is to be described by the present shear layer measurements, is indicated in Fig. 72. Note that the other half of this surface is found to be the **mirror** image of that presented, reflected about the line $t_1 = t_2$. To simplify the description of this surface and to show the important deviations from flow homogeneity, as experienced by the descending aircraft, the $\tilde{\underline{\mathcal{R}}}(t_1',t_2')$ correlations are presented as a series of curves utilizing the parameter t_1', with independent variable $(t_2'-t_1')$. The parameter t_1' is given numerically by the time in seconds taken by the aircraft to descend from a fixed starting point ($z' = 6$ in.) to the upper turbulence measurement point z_1' (in the wind tunnel frame). See Table 7.

70

Plotting the flight path correlation results in terms of the time delay $t_2'-t_1'$ for a given approach condition (i.e., fixed values of γ_E, V/Wg and n) collapses the data to a very considerable degree. However, for a given flight condition, important inhomogeneity effects due to the shear layer are evident through the progressive shifting of the individual curves as the initial turbulence measurement position is altered in the layer. In general, with one important exception, the effect of the shear layer has been to produce an increase in the measured turbulence correlations for a given value of $t_2'-t_1'$ (time delay) in the lower regions of the boundary layer relative to the same correlations measured in the upper portions of the layer. Thus the flight path correlations, with the exception of the u-u correlations at $\gamma_E = 90^o$, tend to fall off noticeably more quickly in the upper boundary layer regions. In attempting to interpret this trend physically it must be emphasized that equal delay increments along the flight path do not correspond to equal displacements in the boundary layer, since the absolute aircraft velocity is not constant along the flight path. In fact, for the constant air speed flight cases simulated herein, equal time delays correspond to smaller displacements along the flight path in the upper portions of the boundary layer (where the measured correlations are relatively smaller) than they do in the lower portions of the boundary layer. This would imply that for equal spacial separations a somewhat more pronounced change in correlation magnitudes would be experienced in traversing the shear layer.

In the special case of the $\widetilde{\mathcal{R}}_{uu}$ correlations at $\gamma_E = 90^o$, this general finding was reversed. At all speed ratios, a significantly higher u-u correlation is obtained in the outer portion of the boundary layer, relative to correlations at the same time delay measured closer to the ground plane.

The influence of flight path angle γ_E on the measured correlations appears to be modest. At equal values of time delay and aircraft velocity ratio and at similar positions within the boundary layer, all correlations appear to be

similar. The effect of flight path angle may be seen in the cross plots drawn in Figs. 107 to 109.

The $\tilde{R}_{uu}$ correlations are generally larger than the comparable $\tilde{R}_{vv}$ and $\tilde{R}_{ww}$ data, especially at the shallower flight path angles of $\gamma_E = 15^\circ$ and 45°. At $\gamma_E = 90^\circ$, $\tilde{R}_{uu}$ and $\tilde{R}_{vv}$ are quite comparable and significantly larger than $\tilde{R}_{ww}$.

The effect of aircraft speed, at all flight angles and for all three velocity correlations, has been to progressively shrink the correlation surface towards the t_1, t_2 plane as the simulated aircraft velocity is increased. Because of the higher flight dynamic pressures involved, this reduction in correlation at the higher aircraft velocities may not result in reduced aircraft response to the turbulence. The progressive collapse of the correlations with increasing aircraft velocity is presently interpreted as resulting from the increased spacing of the measurement points at fixed values of time delay. The effect of the aircraft velocity is summarized in the cross plots presented in Figs. 110 through 115.

An additional feature indicated by the flight path correlations, as plotted, is the progressive increase in inhomogeneity of the measured correlation data across the boundary layer as the flight path angle increases to $\gamma_E = 90^\circ$. This is most evident for the v-v and w-w correlations, and is seen by the larger displacements of the correlation curves for a given change in t_1' in the boundary layer as the flight path angle is increased.

The effects of the mean velocity power law in the shear layer at one approach path angle ($\gamma_E = 45^\circ$), and for the u-u correlations only, may be seen by comparing data in Figs. 77 to 80 for n = 0.16 with data in Figs. 103 to 106 for n = 0.35. This limited comparison indicates that a somewhat increased $\tilde{R}_{uu}$ correlation is achieved with n = 0.35 at all velocity ratios. This increased

correlation has removed, to a large extent, the areas of negative correlation measured at large time delays with n = 0.16. There is indication from the data for n = 0.35 that higher correlations are achieved for a given time delay at the outer edges of the boundary layer relative to the same correlation obtained with the initial measurement point located closer to the ground. This trend is the reverse of that obtained generally for n = 0.16, except for the special case of $\widetilde{\widehat{R}}_{uu}$ at $\gamma_E = 90^\circ$ where the same reversed trend is again noted. It appears probable that a similar changeover in the $\widetilde{\widehat{R}}_{uu}$ characteristics is occurring with the n = 0.35 power law data as with the n = 0.16 data but at a lower value of γ_E. More detailed measurements are obviously required to confirm this indication.

6.3 Measurements in the 44" x 66" Tunnel

A complete set of flight path correlation measurements was obtained in the 44" x 66" tunnel. These data are presented in nondimensional form as $\widetilde{\widehat{R}}$.

The distribution of probe locations employed is shown in Figure 67. A complete set of $\widetilde{\widehat{R}}$ data was taken at each probe pair location indicated except for some cases with $V/W_G = 1$ where time delays greater than the 0.16 sec. limit of the analysis program were required. In these cases the value of R_{ij} had already dropped to zero and thus no significant data were lost. The upper location limit resulted from the test section length and the lower limit from probe holder size effects. In this instance the probes were positioned along a rail set at $\gamma_E = 15^\circ$ for ease of adjustment. The system is illustrated in Figure 116. The rail is isolated from the tunnel as much as possible by securing it to the cement floor of the laboratory in order to avoid vibrational problems. Figure 117 gives a more detailed picture of the probe holder and rail. Tests were made to determine whether the presence of the rail influenced the flow field at the probe sensing stations. Figures 118 and 119 show correlation and power spectral density measurements made with the rail present and absent (with the probe held on the post illustrated in

73

Figure 120). No rail effect was found. Similar measurements were made for small probe separations to investigate interference effects due to the close proximity of the probe holders. Again no detectable effect was found.

6.3.1 Measurement Technique (44" x 66" Tunnel)

Values of the correlation matrix $\underline{\tilde{R}}(t_1', t_2')$ were determined using the fixed probe technique outlined in Section 6.2.1. However in this study the HP2100A minicomputer was used to compute the results. In general four velocity signals were available from the two cross-wire probes in the flow field. The software was designed to compute the rms values of each of these signals and the cross correlations between the upper probe and lower probe signals at specified values of time delay τ. For example, if the upper probe is measuring u_P and v_P while the lower probe is measuring u_Q and w_Q then the program produces $\hat{u}_P$, $\hat{v}_P$, $\hat{u}_Q$, $\hat{w}_Q$, $\tilde{R}_{u_P u_Q}$, $\tilde{R}_{v_P u_Q}$, $\tilde{R}_{u_P w_Q}$ and $\tilde{R}_{v_P w_Q}$. The values of $\underline{\tilde{R}}$ are determined at 3 values of τ specified by the operator. The values of τ are selected before each run using the time tables described in Section 3.3 in order to produce flight path correlations for 3 selected speed ratios V/W_G.

The following specifications describe the correlation program performance as set up in the present study:

Data sampling time	20 sec.
Data sampling rate	2,500 sps/channel
Program running time (after data is loaded)	100 sec.
Precision in setting τ	± 10 μs.
Allowable τ range	10 μs - 0.16 sec.
Number of τ's selected per run	3

The output from the above computation is stored on magnetic tape and printed by the teletype.

The form of the analysis program resulted in multiple measurements of several correlations. This comes about because at any probe location it is necessary to perform runs with the cross-wire probes in two **orientations** (90° apart) in order to generate all three turbulent velocity components. A single orientation produces u along with either v or w. Thus in order to obtain all elements in the matrix $\widetilde{R}$ for a particular pair of probe locations it is necessary to perform 4 tunnel runs, each with different probe pair orientations. Table 6 summarizes this effect. It is seen that 4 estimates of $\widetilde{R}_{uu}$, 2 of $\widetilde{R}_{uv}$, $\widetilde{R}_{vu}$, $\widetilde{R}_{wu}$, $\widetilde{R}_{uw}$ and single estimates of the remaining elements are obtained. The multiple estimates were averaged to produce the results reported herein.

Estimates of the statistical variability of the data were obtained empirically by analyzing the results produced by the above mentioned multiple measurements. In addition, $\widetilde{R}_{uu}$ was measured for $z_P' = 25$ in. and $z_Q' = 24.5$ in. many times (26) during the course of the experiment. Typical results of this analysis are shown in Figs. 121 and 122. Here it is seen that the variance in the data remains fairly constant, independent of time delay as τ becomes large. Note that the variance of normalized data is forced to zero as time delay approaches zero as a result of this process. Appendix C discusses the underlying variance due to the finite record lengths employed and it is seen that the observed trend is consistent with theory. Of course, systematic error due to probe effects may also be present. The data of Fig. 121 were obtained from a number of different probes and recalibrated probes. The surprising low values of variance indicate that the normalizing process is quite successful

in reducing the variability of $\tilde{\underline{R}}$ estimates at small τ. The influence of probe errors is then shifted into the estimates of signal rms values. As indicated in Section 5.1.3 it is felt that the hot wire anemometer system employing cross-wire probes should produce errors in raw velocity measurements of less than 5%.

6.3.2 Flight Path Cross-Correlation Results (44" x 66" Tunnel)

The experimental measurements in the 44" x 66" tunnel were taken at 58 probe pair locations (see Fig. 67) along a $\gamma_E = 15°$ glide slope. Cross-correlations were obtained for time delays corresponding to three flight speeds by selecting the proper $(t_2' - t_1')$ values before each run.

The measured flight path correlations, obtained for a mean wind with a 0.16 power law profile, are plotted in Figs. 132 to 158 in nondimensional form. The following cases have been studied:

(i)   The complete $\tilde{\underline{R}}$ matrix.

(ii)   Flight path approach angle $\gamma_E = 15°$.

(iii)   Aircraft velocity ratios, $V/W_G = 1.0, 1.5, 2.0$.

(iv) $W_G = 66$ fps, $W_G' = 90$ fps, $Z_G = 1000$ ft, $Z_G' = 36$ in.

In all cases the landing approaches were assumed to be at constant air speed along a straight approach path. The simulated turbulence characteristics are summarized in Figs. 53 and 64.

The data are presented as a function of t_1' and $(t_2' - t_1')$. In order to convert these values to full scale time they must be multiplied by $1/S_t = 455$.

As in the case of the results presented in Section 6.2.3, the $\tilde{\underline{R}}(t_1', t_2')$ are presented as a series of curves utilizing the parameter t_1', with $(t_2' - t_1')$ as the independent variable. The parameter t_1' is given as the time in seconds taken by the aircraft to descend from a fixed starting point ($z' = 35.82"$) to the upper turbulence measurement point z_1' (in the wind tunnel frame). See Table 8.

The $\tilde{\underline{R}}$ results obtained in the 44" x 66" tunnel have been compared with corresponding 8" x 8" tunnel data by using the appropriate S_t and plotting

76

both sets against full scale time delays $(t_2 - t_1)$. Typical results are shown in Figs. 124 to 126. Here results obtained for the same speed ratios V/W_G and approximately the same upper probe location in the shear layer are plotted. Overall, both tunnels appear to be producing similar results. When several sets of comparisons are studied however it appears that on the average the 8" x 8" tunnel correlations lie slightly above those found for the 44" x 66" tunnel. Three possible causes for this slight shift have been considered:

1. Turbulence scale (L_i^X) differences between the two tunnels.

2. The influence of the low-pass filters used for dc removal.

3. The influence of viscous dissipation effects that cannot be scaled properly.

As shown in Appendix A, if the frozen flow hypothesis is assumed, then the scales L_i^X and T_i can be related by the equation:

$$L_i^X = \bar{U} \, T_i \tag{6.2}$$

If one assumes that the first zero crossing of the $R_{ii}(\tau)$ plot is related to T_i, and hence L_i^X, then a difference in L_i^X and/or $\bar{U}$ between the two tunnels could cause the observed trend in the data. From the velocity profile plots of Figs. 19 and 54 and the scale comparison plot of Fig. 64 it is seen that it is unlikely that the observed differences could be due to this effect.

The influence of the low-pass filters on correlation estimates can be shown to be represented by the convolution of a window function with the true underlying correlation. This is developed in Appendix D where it is demonstrated that the filters used in the present study should not influence our correlation estimates in the time delay ranges employed.

Finally, the difference between the viscous dissipation processes in the two tunnels has already been mentioned in Section 5.2.3. This effect is

77

seen in the shape of power spectral density plots at high frequencies. Overly small simulation tunnels tend to have the large energy losses due to this effect occur at too low a frequency. A useful parameter for assessing the importance of this effect is the ratio k_v/k_p where k_v represents the reduced frequency at which the viscous cut-off of the energy spectrum of the turbulence becomes noticeable and k_p is the reduced frequency at which the spectrum $k\Phi(k)$ peaks. In Reference 20 it is suggested that this ratio can be represented for $\Phi_{uu}(k)$ by,

$$k_v/k_p = C(\hat{u}/\nu k_p)^{0.75} \tag{6.3}$$

where C is a constant equal to $0.015 \pm .0075$ as determined empirically from flows with a wide range in scale.

In order to indicate the order of magnitude that this viscous dissipation effect might have on $R_{uu}(\tau)$ measurements a simple analysis will be carried out for conditions corresponding to the data of Figure 124. For $z/Z_G \simeq 0.5$ and for n = 0.16 the following data apply (the tunnel k_p data were taken from Figs. 21 and 56, the full scale data from Reference 11). Note that the tunnel data are as measured in the model frame and have not yet been scaled up to full scale.

Flow	k_p ft^{-1}	C	$\hat{u}$ fps	ν ft^2/sec	k_p/k_v	k_v computed ft^{-1}
Actual Atmosphere	4×10^{-4}	0.015	5.0	1.57×10^{-4}	1.26×10^4	5.06
8" x 8" Tunnel	0.617	0.015	2.4	1.57×10^{-4}	30	18.28
44" x 66" Tunnel	0.131	0.015	6.0	1.57×10^{-4}	188	24.67

When the k_v data are scaled up to full scale for the tunnel cases and converted to viscous cutoff frequency ω_{vco} one obtains the following values:

Actual Atmosphere ω_{vco} = 1889 rad/sec (for W_G = 66 fps)

8" x 8" Tunnel ω_{vco} = 4.10 rad/sec

78

44" x 66" Tunnel ω_{vco} = 27.59 rad/sec.

Now if it is assumed that the power spectra are effectively truncated at ω_{vco} by viscous dissipation (a simplifying assumption made to check the worst possible case) then by using the approach developed in Appendix D the influence of viscous dissipation on correlation estimates can be seen by looking at the convolution of the appropriate window function

$$G(\tau) = \frac{\omega_{vco}}{\pi} \frac{\sin \omega_{vco} \tau}{\omega_{vco} \tau} \tag{6.4}$$

with the true correlation (where $G(\tau)$ is found (in this case) by transforming the box car function with limits $\pm \omega_{vco}$). The shape of $G(\tau)$ is illustrated in Fig. 127. Note that it is dominated by a central lobe of width $\tau_W = 2\pi/\omega_{vco}$. For the three cases being considered above the full scale values of τ_W are:

$\cdot$ Actual Atmosphere τ_W = 0.0033 sec

   8" x 8" Tunnel τ_W = 1.530 sec

   44" x 66" Tunnel τ_W = 0.228 sec

Assuming that the shape of the $R_{uu}(\tau)$ plot of Fig. 123 is typical of actual atmospheric results, it is seen that the initial zero crossing occurs at τ of about 20 sec (full scale). When the window of (6.4) is convoluted with this type of plot (for the central lobe widths τ_W listed above) it is found that the only significant effect occurs near the first zero crossing where the curve is distorted slightly in the region of $\tau = 20 \pm \tau_W$ sec. so as to increase slightly in magnitude and thus shift the zero crossing to a value of time delay approximately τ_W sec greater. Thus when the flight path correlations such as those of Fig. 124 are computed from the raw correlation results one would expect the results from the 8" x 8" tunnel to lie slightly above those from the 44" x 66" tunnel due to this effect. The difference between the 44" x 66" tunnel data and the actual atmosphere would appear to be negligible in the present example.

79

Thus it is seen that of three possible sources for the observed
trend in the comparison data only viscous dissipation effects appear to be sig-
nificant. Of course, other effects could be taking place due to slight diff-
erences in the details of how the data were gathered and analyzed. At the pre-
sent time, however, their source is not obvious.

In discussing the details of the $\widetilde{R}$ data obtained in the 44" x 66"
tunnel, comparisons will be made with those obtained in the 8" x 8" tunnel and
those predicted by the von Kármán model for homogeneous isotropic turbulence.
The generation of the latter comparison data is described in detail in Appen-
dix E. Basically these latter comparison data represent the measurements
that would have been obtained with the probe spacings and time delays employed
in this study if the tunnel flow had the characteristics of high altitude
turbulence. Such a comparison highlights the effects of the boundary layer
on correlation measurements. The values of integral scale and mean velocity
were taken to be those at $z' = 25"$ ($L_u^{x'} = 14.8"$, $\overline{U}' = 84.9$ fps) in evalua-
ting the von Kármán model.

The $\widetilde{R}_{uu}$ data are contained in Figs. 132-134. Generally speaking
most of the data for a given speed ratio tend to collapse onto a common curve
except for the results at the two largest values of t_1'. In the latter cases
a slight trend towards increased correlation at larger separations $(t_2'-t_1')$
is indicated. When these results are compared with the corresponding ones from
the 8" x 8" tunnel (Figs. 73-76) it is seen that the smaller tunnel data show
a slightly more pronounced separation of the correlation curves for increasing
t_1' values. A sample comparison is given in Fig. 124 for $V/W_G = 1.5$. Note
that these results are plotted against full scale (t_2-t_1). When the $\widetilde{R}_{uu}$ data
are compared with that generated by the von Kármán model the result is as shown
in the sample plot of Fig. 129. Due to the larger spacial separation between
the hot wire probes for a given value of $(t_2'-t_1')$ as t_1' becomes larger (i.e.,

closer to the floor of the tunnel where V_E is increasing, see Fig. 5) the

values of $\tilde{R}_{uu}$ determined from the von Kármán model actually decrease slightly

as t_1' increases. All the tunnel data lie below the model results with the

least difference between the two occurring for small values of $(t_2'-t_1')$

(as is expected since both sets of normalized data must approach unity as

$(t_2'-t_1')$ approaches zero). The other obvious effect of the boundary layer

on the correlation measurements has been the previously mentioned increase in

correlation for a given $(t_2'-t_1')$ as t_1' increases for measurements near the

bottom of the layer (large t_1' values).

The $\tilde{R}_{uv}$ data are contained in Figs. 135-137. All the data for a

given speed ratio tend to collapse onto a common curve. The results all have

a modest positive peak near $(t_2'-t_1') = 0$ and drop to zero for $(t_2'-t_1') > 0.3$,

.016, or .012 sec. in the case of $V/W_G = 1.0$, 1.5, or 2.0 respectively. No

8" x 8" tunnel results were taken for $\tilde{R}_{uv}$ and the von Kármán model predicts

$\tilde{R}_{uv} = 0$.

The $\tilde{R}_{uw}$ data are contained in Figs. 138-140. The data for a given

speed ratio tend to collapse onto a common curve except for the results for

the smallest value of t_1' in the cases of V/W_G equal to 1.5 and 2.0 which appear

to be less negative than the rest. The data are characterized by a negative

peak near $(t_2'-t_1') = 0$ and increase to zero for $(t_2'-t_1') > .03$, .03, or .02

sec. in the case of $V/W_G = 1.0$, 1.5, or 2.0 respectively. No 8" x 8" tunnel

results were taken for $\tilde{R}_{uw}$. A comparison with the von Kármán model is presented

in Fig. 130 for the case $V/W_G = 1.5$. It is seen that the model predicts a

fairly constant small positive value for $\tilde{R}_{uw}$, quite unlike that measured in the

boundary layer.

The $\tilde{R}_{vu}$ data are contained in Figs. 141-143. The results are almost

identical to those described under $\tilde{R}_{uv}$.

The $\widetilde{R}_{vv}$ data are contained in Figs. 144-146. Most of the data for a given speed ratio tend to collapse onto a common curve characterized by a positive peak at $(t_2'-t_1') = 0$ and a region of negative correlation following the first zero crossing. For speed ratios $V/W_G = 1.5$ and 2 the data for the largest value of t_1' ($t_1' = .182$ sec.) appear to show a more positive correlation than the rest. When these results are compared with the corresponding ones from the 8" x 8" tunnel (Figs. 83-86) it is seen that the results are quite similar. A sample comparison is given in Fig. 125 for $V/W_G = 1.5$. The greatest difference between these data sets appears to be the need to go lower in the boundary layer in the 44" x 66" tunnel to detect the increased correlation exhibited by the largest t_1' data. A sample comparison with the von Kármán model results is presented in Fig. 131. It is seen that the model results also exhibit a negative correlation region. As in the case of $\widetilde{R}_{uu}$, the $\widetilde{R}_{vv}$ experimental data generally lie below the model results and show an increased correlation trend with increasing t_1' opposite to that for the model.

The $\widetilde{R}_{vw}$ data are contained in Figs. 147-149. The data for a given speed ratio tend to collapse onto a common curve except for the results at the largest value of t_1' in the cases of V/W_G equal to 1.5 and 2.0. In these instances the correlations seem to be more negative near $(t_2'-t_1') = 0$ than for the rest of the data. In general the correlations are nearly zero except for a slight negative trend near $(t_2'-t_1') = 0$. No 8" x 8" tunnel results were taken for $\widetilde{R}_{vw}$ and the von Kármán model predicts $\widetilde{R}_{vw} = 0$.

The $\widetilde{R}_{wu}$ data are contained in Figs. 150-152. The data for V/W_G equal to 1.0 tend to collapse onto a common curve. All the data indicate a negative peak at $(t_2'-t_1') = 0$ and exhibit a region of positive correlation following the first zero crossing. In the cases of speed ratios $V/W_G = 1.5$ and 2.0 it

82

Approved for Public Release

is seen that there is a trend towards more positive correlation as t_1' increases (towards the bottom of the boundary layer). These results are different from those obtained for $\tilde{\mathbb{R}}_{uw}$ where the region of positive correlation was absent and some data indicated a more positive correlation towards the top of the boundary layer. The $\tilde{\mathbb{R}}_{wu}$ data also cross the horizontal axis at lower values of $(t_2'-t_1')$ than do the $\tilde{\mathbb{R}}_{uw}$ results. No 8" x 8" tunnel results were taken for $\tilde{\mathbb{R}}_{wu}$. The von Kármán model results for $\tilde{\mathbb{R}}_{wu}$ are as shown in Fig. 130 (since this model predicts that $\tilde{\mathbb{R}}_{uw} = \tilde{\mathbb{R}}_{wu}$). The boundary layer results are completely different from those produced by the model.

The $\tilde{\mathbb{R}}_{wv}$ data are contained in Figs. 153-155. The results for $V/W_G = 1.0$ appear quite similar to those for $\tilde{\mathbb{R}}_{vw}$. However, those for $V/W_G = 1.5$ and 2.0 are characterized by a slight positive peak at $(t_2'-t_1') = 0$ and a negative region following the first zero crossing. This effect becomes more pronounced as V/W_G and t_1' increase. No 8" x 8" tunnel results were taken for $\tilde{\mathbb{R}}_{wv}$ and the von Kármán model predicts $\tilde{\mathbb{R}}_{wv} = 0$.

The $\tilde{\mathbb{R}}_{ww}$ data are contained in Figs. 156-158. The data for a given speed ratio tend to collapse onto a common curve except for the results at the two largest values of t_1'. For these cases a slight trend towards a more positive correlation at large values of $(t_2'-t_1')$ is indicated. The results are similar to those for $\tilde{\mathbb{R}}_{vv}$ except that the $\tilde{\mathbb{R}}_{ww}$ data tend to have their first zero crossing at lower values of $(t_2'-t_1')$ unlike the corresponding ones from the 8" x 8" tunnel (Figs. 93-96) where the zero crossing is seen to be similar to that of the $\tilde{\mathbb{R}}_{vv}$ data. The sample comparison plot given in Fig. 126 indicates that the 8" x 8" tunnel results show a more positive correlation overall than those from the 44" x 66" tunnel. The computed $\tilde{\mathbb{R}}_{ww}$ values for the von Kármán model turned out to be extremely close to those for $\tilde{\mathbb{R}}_{vv}$ (due to the shallow glide slope angle of only 15°) and thus Fig. 131 depicting the $\tilde{\mathbb{R}}_{vv}$ results is

83

applicable here. Again the comments made concerning this figure apply to $\tilde{\mathbb{A}}_{ww}$ as well.

In summary the following general statements can be made about the $\tilde{\underline{\mathbb{A}}}$ data from the 44" x 66" tunnel for $\gamma_E = 15°$ and n = 0.16.

(1) The measured $\tilde{\underline{\mathbb{A}}}$ data showed significant departures from homogenous, isotropic model results.

(2) Much of the data for a particular element of $\tilde{\underline{\mathbb{A}}}$ can be represented by a single curve. The greatest departures from this single curve occur in the lowest portion of the boundary layer

(3) The $\tilde{\mathbb{A}}_{ij}$ data for $i \neq j$ have peak values much smaller than those for $i = j$. In some instances the correlation could be reasonably taken to be zero.

(4) The 44" x 66" tunnel data tend to be slightly less positive than the 8" x 8" tunnel results.

(5) The influence of t_1' on $\tilde{\underline{\mathbb{A}}}$ becomes apparent at positions lower in the boundary layer in the case of the 44" x 66" tunnel when compared with the 8" x 8" tunnel.

Section VII

PRELIMINARY MODEL FITS TO EXPERIMENTAL $\tilde{R}$ DATA

The objective of the model fitting outlined in this section is rather limited in scope. The aim is to take an established theoretical model and empirically select its parameters to achieve a reasonable description of the measured $\tilde{R}$ data from the 44" x 66" tunnel. This fitting is for the purpose of minimizing the number of wind tunnel measurements required in the application of the fixed-probe technique. Of course the close scrutiny of the experimental results in the course of model fitting will also improve our understanding of the trends exhibited by the $\tilde{R}$ data.

Based on the comparisons of the wind tunnel $\tilde{R}$ data with the predictions of the von Kármán model (e.g., Figs. 129 and 131) it was decided that this model might form a reasonable basis for fitting empirical curves to the test results. As outlined in Appendix E, the von Kármán model assumes isotropic, homogeneous, Gaussian, and frozen flow. Probably none of these conditions apply exactly in the case of the earth's boundary layer, but as the curves of Figs. 129 and 131 demonstrate the general features of $\tilde{R}$ are represented by such a model (at least when the same velocity component is being measured at the two locations).

One approach to this model fitting problem is to first establish the physical location of the two measurement points and the corresponding values of $L_u^{x'}$ and W'. Then by a suitable choice of representative values for $L_u^{x'}$ and W' deduced from the above, $\tilde{R}$ could be predicted from equation (E.1). That is:

$$\tilde{R}_{ij}(\xi_1, \xi_2, \xi_3) = [f(\zeta) - g(\zeta)] \frac{\xi_i \xi_j}{\xi^2} + g(\zeta)\delta_{ij} \qquad (7.1)$$

In order to carry out this last step it is first necessary to transform the time delay employed in the wind tunnel measurement of $\tilde{R}$ (namely

85

$(t_2' - t_1'))$ into an equivalent spatial separation. In the case of isotropic,
homogeneous, frozen flow one proceeds as follows. Assuming that the mean
flow is in the positive x-direction and that the mean flow velocity is W'
then a time delay of τ seconds introduced into the signal from the upper probe
is equivalent to an additional spatial separation in the x-direction of
$-W'\tau$. (See Taylor's hypothesis in Appendix A.) And thus a typical flight
path correlation as measured in this study would be given by

$$\widetilde{R}_{uu}(t_1', t_2') = \widetilde{R}_{ij}(\xi_1, \xi_2, \xi_3) \qquad (7.2)$$

$$i = j = 1$$
$$\xi_1 = (z_2' - z_1')/\tan\gamma_E - W'(t_2' - t_1')$$
$$\xi_2 = 0$$
$$\xi_3 = z_2' - z_1'$$

Now if one wishes to carry over the hypothesis of frozen flow to
the present case involving wind shear in order to apply (7.2) a problem
arises. If it is assumed that the flow is frozen in horizontal layers and
that each layer is travelling at the local mean wind speed then the spacial
organization among the turbulence components becomes a function of time.
This loss of spacial organization results from the various layers slipping
over one another such that a fixed time delay between the signals from two
hot wire probes at different levels in the flow no longer corresponds to a
single fixed spacial separation in the flow field. Once this was realized
it was found that no a priori best choice for the variation of W' and $L_u^{x'}$
with probe location was obvious.

In effect the above approach represents an attempt to model the
results found for a limited spacial separation in a shear flow by the best
fit equivalent isotropic, homogeneous, Gaussian, frozen flow results. To
the extent that the physical probe separations employed spanned only a portion

86

of the shear layer before $\tilde{\mathbb{R}}$ became negligibly small (and only modest changes in W' and $L_u^{x'}$ occurred, see Table 9) it does not seem unreasonable to assume that the gross features of the flow field in a particular measurement region could be fitted by such a model. In order to further refine this fitting process the parameters W' and $L_u^{x'}$ have been allowed to vary depending on the exact location of the two measurement points in the flow field. The corresponding value of mean square turbulence used to nondimensionalize the correlation function will be taken to be the product of the rms values of the appropriate turbulence components existing at the two spacial locations. The resulting theoretical formulation has been called the Modified Von Kármán Model to identify it separately from the previous model plots of Section 6.3.2. (Note that no attempt has been made to fit $\tilde{\mathbb{R}}_{ij}$ data for $i \neq j$ due to the poor fitting results indicated in Section 6.3.2 for these cases.)

The approach taken in this preliminary model fitting study has been to examine a particular set of $\tilde{\mathbb{R}}_{uu}$ measurements (for $V/W_G = 1.5$) and to fit a reasonable curve to these data. Then using the W' and $L_u^{x'}$ values applied in this case, see how well the model fits the $\tilde{\mathbb{R}}_{vv}$ and $\tilde{\mathbb{R}}_{ww}$ data. In particular, model fits to the data of Figs. 133a, 145a and 157a were attempted. The corresponding values of W' and $L_u^{x'}$ for the upper probe and the lowest position of the lower probe are given in Table 9. The ranges of W' and $L_u^{x'}$ have been kept within these limits in the present study.

In order to gain some experience into how W' and $L_u^{x'}$ separately influence the model's prediction of $\tilde{\mathbb{R}}_{uu}$ the effect of varying W' for a fixed value of $L_u^{x'}$ is shown in Fig. 159 and the effect of varying $L_u^{x'}$ for a fixed value of W' is shown in Fig. 160. In the case of $\tilde{\mathbb{R}}_{uu}$ it is seen from (7.2) that the curve must start at $\tilde{\mathbb{R}}_{uu} = 1$ for $(t_2' - t_1') = 0$ and approach $\tilde{\mathbb{R}}_{uu} = 0$ for $(t_2' - t_1') \rightarrow \infty$ and always remain positive since $[f(\zeta) - g(\zeta)]$ is always positive. Thus, as is seen in Figs. 159 and 160, varying W' and $L_u^{x'}$ affects the shape of the curve to the greatest extent in the middle

portion. Increasing $L_u^{x'}$ and decreasing W' results in an increased $\tilde{\mathfrak{R}}_{uu}$ in this region.

As indicated in Section 6.3.2, for a given speed ratio V/W_G, most of the measured $\tilde{\mathfrak{R}}_{uu}$ data tend to collapse onto a common curve except for the results at the two largest values of t_1' which tend to lie above the rest. As a first attempt at fitting the modified model to these results the following algorithm for selecting W' and $L_u^{x'}$ was tried based on values measured at $S = 5.5H$ and using linear extrapolation between the values given in Table 9:

W' taken as value at z_2

$L_u^{x'}$ taken as the average of values at z_1' and z_2'.

The results of this approach are shown in Fig. 161 for three values of t_1' along with the measured data for $t_1' = .1528$ sec., which proved to be the best fit for this case. When the trend for increasing t_1' in the modified model data is compared with that for the corresponding measured data (see for example Fig. 162) it is found that the modified model does not predict the higher overall values for the $t_1' = .1822$ sec. case and in fact it is seen in Fig. 161 that the modified model results for $t_1' = .0717$ sec. lie above the rest. Several other simple algorithms for selecting W' and $L_u^{x'}$ within the allowed range were attempted without much more success. This was due to the fairly small range in W' and $L_u^{x'}$ for any given t_1' (see Table 9).

As a compromise solution it was decided to find a single modified model curve that would represent the complete set of measured $\tilde{\mathfrak{R}}_{uu}$ data, and ignore the spread in the data at the largest t_1' values for the time being. The results based on $t_1' = .1228$ sec. ($z_1' = 16.5$ in.) were found to be most suitable and since they originated from the middle of the boundary layer they seemed to be an acceptable representative choice. After several simple algorithms for selecting W' and $L_u^{x'}$ were tested for this case it was found that the best fit (marginally) was achieved by using the values of these parameters at z_2'. The results of this procedure are shown in Fig. 162.

88

As noted above there is no straightforward way of achieving a negative value of $\tilde{\mathfrak{R}}_{uu}$ with this model. This resulted in the relatively poorer fit to the measured data at the higher values of $(t_2' - t_1')$. It was deemed that this fit was a reasonable average representation of the experimental data.

The same model parameters were then used to generate $\tilde{\mathfrak{R}}_{vv}$ and $\tilde{\mathfrak{R}}_{ww}$. The $\tilde{\mathfrak{R}}_{vv}$ results are shown in Fig. 163. In this case the modified model results can become negative because $\xi_2 = 0$ and thus $\tilde{\mathfrak{R}}_{ij} = g(\zeta)$ which becomes negative for ζ large (see Fig. 128). Once again the fit to the average experimental data is reasonable but the modified model results lie above the experimental ones for higher values of $(t_2' - t_1')$. Due to the small values for ξ_3 generated for $\gamma_E = 15^\circ$ it turns out that the modified model predicts $\tilde{\mathfrak{R}}_{vv} \approx \tilde{\mathfrak{R}}_{ww}$ for the present case. Since the measured $\tilde{\mathfrak{R}}_{ww}$ data have their zero crossing at smaller values of $(t_2' - t_1')$ than the measured $\tilde{\mathfrak{R}}_{vv}$ data, it was decided that some underlying reason for this had to be determined if the current modified model was to be of any use. A partial answer was found when the lateral scale $L_w^{x'}$ was examined in the region where these measurements were taken for the case $t_1' = .1228$ sec. Whereas the theory behind the von Kármán model predicts that $L_u^x = 2L_w^x$ it is found that this is not true in general in our flow field (see Fig. 64). For the case $t_1' = .1228$ sec., at z_1' $2L_w^{x'} = 9.8$ in and at z_{2min}' $2L_w^{x'} = 10.0$ in. When these values were used instead of the higher $L_u^{x'}$ values of Table 9 then a slightly better modified model fit to the experimental results was achieved (see Fig. 164). A further reduction in scale magnitude would be required to improve this fit. Since this step is outside the general guidelines adopted it was not pursued further here.

Whether the above curve fits are acceptable or not for use in the fixed probe analysis technique must be determined by runs through the computer simulation described in Section IX. It appears at this stage that the modified

89

von Kármán model as used in this study is useful in predicting the

general features of the $\mathbb{R}$ matrix. Further investigation is required to

verify the best approach in applying this technique.

Section VIII

AIRCRAFT DYNAMICS

In this section are considered the motion equations for a STOL aircraft on a landing glide path. These equations form the basis for a computer code designed to predict a landing aircraft's response to turbulence when combined with the flight path correlation measurements of Section VI. A typical STOL transport aircraft is used to exercise the algorithm and to generate sample results.

8.1 Aircraft Response to Wind Shear

The aircraft is assumed to be encountering a headwind W(h), as described in earlier sections. To conform to conventional notation, z in this section will be 'down' in whichever reference frame is under consideration; height above the ground, which was denoted z in earlier sections, will herein be denoted by h. Standard sign conventions are used for all variables (e.g., see Ref. 5).

If the aircraft velocity with respect to the ground be $\vec{V}_E$ and the aircraft velocity with respect to the air be $\vec{V}$, and the wind velocity (i.e., the air velocity with respect to the ground) be $\vec{W}$, then by the law of vector velocity addition,

$$\vec{V}_E = \vec{V} + \vec{W} \tag{8.1}$$

We shall regard as basic the following motion equations from vectorial mechanics:

$$\dot{\vec{p}} = \vec{F} \tag{8.2}$$

$$\dot{\vec{h}} = \vec{M} \tag{8.3}$$

where $\vec{p}$ and $\vec{h}$ are, respectively the momentum and

91

angular momentum (about the mass centre) of the aircraft. $\underset{\rightarrow}{F}$ and $\underset{\rightarrow}{M}$ are respectively the external force and external moment (about the mass centre) on the vehicle. The overdot denotes differentiation with respect to an inertial reference frame; this frame may reasonably taken to be the earth for this investigation. This means that the rotation of the earth on its axis is neglected; the earth will also be regarded as flat.

We shall further use

$$\underline{p} = m \underset{\sim E}{V} \tag{8.4}$$

$$\underline{h} = \underline{I} \; \underline{\omega} \tag{8.5}$$

where m and $\underline{I}$ are the mass and inertia matrix of the system, and $\underset{\rightarrow}{V_E}$ and $\underset{\rightarrow}{\omega}$ are the velocity and angular velocity of the aircraft with respect to an inertial frame (ie., the ground). Relations (8.4) and (8.5) imply that the aircraft is modelled as a single rigid body. In particular contributions to $\underline{p}$ and $\underline{h}$ from the following sources are neglected: elastic deformations, rotating propellers and engine components, and deflecting control surfaces.

8.1.1 Reference Frames

As mentioned above, we already have in mind an inertial reference frame, $\mathscr{F}_I$, in order to write the motion equations (8.2) and (8.3) and with negligible error it may be assumed for the present development that this frame is fixed to the earth. The orthonormal dextral triad $(\underset{\rightarrow}{i}_I \; \underset{\rightarrow}{j}_I \; \underset{\rightarrow}{k}_I)$ associated with $\mathscr{F}_I$ are defined as follows: $\underset{\rightarrow}{i}_I$ is parallel to the level runway; $\underset{\rightarrow}{k}_I$ is down, and $\underset{\rightarrow}{j}_I = \underset{\rightarrow}{k}_I \times \underset{\rightarrow}{i}_I$, i.e., to the right (see Fig. 1).

The second reference frame we shall need is $\mathscr{F}_B$, a body-fixed frame. There are, of course, an infinity of body-fixed frames, and we intend to select the one which is most convenient. One possibility (since

we are taking the aircraft to be a rigid body) is the so called principal-inertia-axis frame, in which the cross-products of inertia vanish. A better choice exists, however, as will be explained subsequently. For the present, we need only note that the orthonormal dextral triad $(\vec{i}_B \quad \vec{j}_B \quad \vec{k}_B)$ associated with $\mathcal{F}_B$ has $\vec{i}_B$ and $\vec{k}_B$ in the plane of symmetry of the aircraft with $\vec{i}_B$ nominally 'forward', $\vec{k}_B$ nominally 'down' and $\vec{j}_B$ nominally to the right.

The unit vectors for $\mathcal{F}_I$ and $\mathcal{F}_B$ are related by a rotation matrix* $\underline{R}_{BI}$ viz., for a general vector $\vec{u}$:

$$\underline{u}_2 = \underline{R}_{21} \, \underline{u}_1 \tag{8.6}$$

where the column matrix $\underline{u}_i$ represents the components of $\vec{u}$ in $\mathcal{F}_i$. The nine elements of $\underline{R}_{BI}$ will be denoted r_{ij} for convenience:

$$\underline{R}_{BI} = \left\{ \; r_{ij} \; \right\} \tag{8.7}$$

An alternative reference frame is the so-called 'wind frame' (Ref. 5).

We now express the important vectors in terms of their components in these reference frames.

The wind velocity expressed in $\mathcal{F}_I$:

$$\underline{W}_I = \begin{pmatrix} -W \\ 0 \\ 0 \end{pmatrix} \tag{8.8}$$

and the gravity vector:

$$\underline{g}_I = \begin{pmatrix} 0 \\ 0 \\ g \end{pmatrix} \tag{8.9}$$

At this point in the development the assumption that the mean wind is

---

*A rotation matrix is a 3 x 3 orthogonal matrix whose determinant is +1.

aligned with the runway has been made. If it is desired to include a crosswind component in the analysis then a new form for $\underline{W}_I$ including this is required and the reference equilibrium of Section 8.3 must be suitably modified.

As seen by the aircraft, the aircraft velocity with respect to the air, $\underset{\rightarrow}{V}$ is expressed in $\mathcal{F}_B$:

$$\underline{V}_B = \begin{pmatrix} u \\ v \\ w \end{pmatrix} \tag{8.10}$$

Therefore, from (8.1) and (8.6), the components of $\underset{\rightarrow}{V}_E$ expressed in $\mathcal{F}_B$ are

$$\begin{pmatrix} u - W\,r_{11} \\ v - W\,r_{21} \\ w - W\,r_{31} \end{pmatrix} = \underline{V}_{E_B} \tag{8.11}$$

Similarly we express the angular velocity components in $\mathcal{F}_B$ using conventional notation:

$$\underline{\omega}_B = \begin{pmatrix} p \\ q \\ r \end{pmatrix} \tag{8.12}$$

Under our current assumptions, the inertia matrix, if expressed in $\mathcal{F}_B$, corresponds to a constant matrix:

$$\begin{pmatrix} I_{xx} & 0 & -I_{xz} \\ 0 & I_{yy} & 0 \\ -I_{zx} & 0 & I_{zz} \end{pmatrix} = \underline{I}_B \tag{8.13}$$

Because the xz plane of the frame $\mathcal{F}_B$ lies in the plane of symmetry of the aircraft it follows that $I_{xy} = I_{yx} = I_{yz} = I_{zy} = 0$. The definition of $\underline{I}$ implies that $I_{zx} = I_{xz}$.

To complete the specification of the important vectors in terms of their components in appropriate reference frames, we mention that the torque components are

$$\underline{M}_B = \begin{pmatrix} L \\ M \\ N \end{pmatrix} \tag{8.14}$$

and the nongravitational forces are

$$\underline{A}_B = \begin{pmatrix} X \\ Y \\ Z \end{pmatrix} \tag{8.15}$$

where

$$\vec{A} = \vec{F} - m\vec{g} \tag{8.16}$$

The torque and nongravitational forces are due to thrust and all other influences of the surrounding air on the aircraft.

The position of the aircraft may be found by integrating the differential equations inferred from (8.11) and (8.6), namely

$$\begin{pmatrix} \dot{x}_I \\ \dot{y}_I \\ -\dot{h} \end{pmatrix} = \underline{R}_{BI}^T \begin{pmatrix} u \\ v \\ w \end{pmatrix} - \begin{pmatrix} W \\ 0 \\ 0 \end{pmatrix} \tag{8.17}$$

where $(x_I \ y_I \ -h)$ are the components of aircraft position in $\mathscr{F}_I$.

8.1.2 Scalar Motion Equations in Body Axes

As is customary with this class of problem, we require two types of time derivative for vectors: rate of change as seen by $\mathscr{F}_I$, and rate of change as seen by $\mathscr{F}_B$. We have already agreed to denote the former by an overdot (e.g., equations (8.2), (8.31)); we shall denote the latter by an overcircle. For any vector $\vec{u}$, these two are related by

$$\dot{\vec{u}} = \overset{\circ}{\vec{u}} + \vec{\omega} \times \vec{u} \tag{8.20}$$

(see for example Ref. 5, equation 4.6,9) where it will be recalled that $\underset{\rightarrow}{\omega}$ is the angular velocity of $\mathcal{F}_B$ with respect to $\mathcal{F}_I$. Note that $\overset{\circ}{\underset{\rightarrow}{\omega}} = \overset{\cdot}{\underset{\rightarrow}{\omega}}$.

In particular, we have

$$\overset{\cdot}{\underset{\rightarrow}{V}} = \overset{\circ}{\underset{\rightarrow}{V}} + \underset{\rightarrow}{\omega} \times \underset{\rightarrow}{V} \qquad (8.21)$$

$$\overset{\cdot}{\underset{\rightarrow}{h}} = \overset{\circ}{\underset{\rightarrow}{h}} + \underset{\rightarrow}{\omega} \times \underset{\rightarrow}{h} \qquad (8.22)$$

Consider the motion equations (8.2) and (8.3). When these are combined with equations (8.4), (8.5) and (8.11) it is seen that the moment equations do not involve the wind W. Thus the applicable moment equations are identical to those developed in Ref. 5 for a stationary atmosphere. The force equations are derived as follows.

Substituting (8.16), (8.4) and (8.1) into (8.2) obtain

$$m(\overset{\cdot}{\underset{\rightarrow}{V}} + \overset{\cdot}{\underset{\rightarrow}{W}}) = m \underset{\rightarrow}{g} + \underset{\rightarrow}{A} \qquad (8.23)$$

substituting for $\overset{\cdot}{\underset{\rightarrow}{V}}$ from (8.21) into (8.23) and writing the components in $\mathcal{F}_B$ obtain

$$m(\overset{\cdot}{\underline{V}}_B + \tilde{\underline{\omega}}_B \underline{V}_B + \underline{R}_{BI} \overset{\cdot}{\underline{W}}_I) = m \underline{g}_B + \underline{A}_B \qquad (8.24)$$

$$\tilde{\underline{\omega}}_B = \begin{pmatrix} 0 & -r & q \\ r & 0 & -p \\ -q & p & 0 \end{pmatrix}$$

Thus when all vectors are expressed in terms of the components agreed upon in the last section the scalar motion equations, expressed in body axes, are

$$\left.\begin{array}{l} m\,(\dot{u} + qw - rv - r_{11}\,\dot{W}) = X + mg\,r_{13} \\ m\,(\dot{v} + ru - pw - r_{21}\,\dot{W}) = Y + mg\,r_{23} \\ m\,(\dot{w} + pv - qu - r_{31}\,\dot{W}) = Z + mg\,r_{33} \end{array}\right\} \qquad (8.25)$$

$$I_{xx}\dot{p} - I_{xz}(\dot{r} + pq) + (I_{zz} - I_{yy})\,qr = L$$

$$\left.\begin{array}{l} I_{yy}\dot{q} - I_{xz}(r^2 - p^2) + (I_{xx} - I_{zz})\,rp = M \\[6pt] I_{zz}\dot{r} - I_{zx}(\dot{p} - rq) + (I_{yy} - I_{xx})\,pq = N \end{array}\right\} \qquad (8.26)$$

To complete the system equations, we note the kinematical relations. From (8.17),

$$\left.\begin{array}{l} \dot{x}_I = r_{11}u + r_{21}v + r_{31}w - W \\[6pt] \dot{y}_I = r_{12}u + r_{22}v + r_{32}w \\[6pt] -\dot{h} = r_{13}u + r_{23}v + r_{33}w \end{array}\right\} \qquad (8.27)$$

and since (from Ref. 5, equation 4.6,7),

$$\dot{\underline{R}}_{BI} = -\tilde{\underline{\omega}}_B\,\underline{R}_{BI} \qquad (8.28)$$

we have the nine first-order equations

$$\left.\begin{array}{l} \dot{r}_{1i} = r\,r_{2i} - q\,r_{3i} \\[6pt] \dot{r}_{2i} = p\,r_{3i} - r\,r_{1i} \\[6pt] \dot{r}_{3i} = q\,r_{1i} - p\,r_{2i} \end{array}\right\} \qquad (8.29)$$

for $i = 1, 2, 3$. The r_{ij} are not independent variables, and any of the relations implied by the fact that $\underline{R}_{BI}^T\underline{R}_{BI}$ is the unit matrix may be used as checks. Note the computational simplicity of the right sides of (8.29).

8.1.3 Selection of Reference Equilibrium

Because of the wind gradient, neither the nominal flight trajectory nor the reference flight trajectory (as described in Section I) are equilibrium trajectories (i.e., the state variables are not constant along the trajectory). This is of importance because the dependence of the aerodynamic force $\underline{A}$ on

97

the history of $\underset{\rightarrow}{V}(t)$ and $\underset{\rightarrow}{\omega}(t)$ is not known except in an approximate fashion. More specifically, the aerodynamic forces are customarily linearized about some reference equilibrium flight condition, $\underset{\rightarrow}{V}(t) \equiv \underset{\rightarrow e}{V}$, $\underset{\rightarrow}{\omega}(t) \equiv \underset{\rightarrow e}{\omega}$; as a consequence, this 'linear' analysis is actually an 'infinitesimal' analysis (asymptotically exact as $\Delta\underset{\rightarrow}{V} \rightarrow \underset{\rightarrow}{0}$ and $\Delta\underset{\rightarrow}{\omega} \rightarrow \underset{\rightarrow}{0}$) and will suffer increasing errors (the magnitude of which cannot be ascertained from the linear analysis itself) as $\|\Delta\underset{\rightarrow}{V}\|$ and $\|\Delta\underset{\rightarrow}{\omega}\|$ increase.

In addition, a further class of approximations is made in the linear analysis: the Bryan expansion with its associated 'stability derivatives'. A discussion of this latter approximation is given in Section 5.11 of Ref. 5. The Bryan expansion should not be expected to yield reliable results in situations where $\Delta\underset{\rightarrow}{V}$ or $\Delta\underset{\rightarrow}{\omega}$ are changing rapidly. Of course neither of these approximations (linearization; Bryan expansion) are made alacritously. They are made of necessity. One simply

does not know the forces and moments on one's aircraft, at time t, that arise from arbitrary histories: $\underset{\rightarrow}{V}(t')$, $\underset{\rightarrow}{\omega}(t')$, $t' \leq t$. This does not alter the fact, however, that the results of analysis should be viewed with increasing suspicion as the deviations from equilibrium become larger (on account of linearization) and as the rate of these deviations becomes larger (on account of Bryanization). The latter is particularly noteworthy in the context of calculating the response to turbulence.

One candidate reference equilibrium corresponds to a rectilinear glide slope, at constant airspeed, with no wind ($W \equiv 0$). This trajectory is characterized by the following kinematics when $\mathcal{F}_B$ is selected with $\underset{\rightarrow B}{i}$ aligned into the relative wind:

$$p, q, r \equiv 0 \tag{8.30}$$

$$u \equiv V_e; \quad v, w \equiv 0 \tag{8.31}$$

where V_e is the airspeed. It follows that

$$x_I = x_{Io} + (V_e \cos\gamma_e)t$$
$$y_I \equiv 0 \qquad\qquad\qquad \Big\} \qquad (8.32)$$
$$h = h_o - (V_e \sin\gamma_e)t$$

where γ_e is the flight path angle (defined as positive below the horizontal in this report). The non-zero elements of the $\underline{R}_{BI}$ matrix are (see (8.44)),

$$r_{11} = \cos\gamma_e = r_{33}$$
$$r_{13} = \sin\gamma_e = -r_{31} \qquad \Big\} \qquad (8.33)$$
$$r_{22} = 1$$

This solution is feasible dynamically provided it is possible to find aerodynamic/thrust forces and moments such that, for (8.30) and (8.31),

$$L, M, N, Y = 0$$
$$X \equiv -mg \sin\gamma_e \overset{\Delta}{=} X_e \qquad \Big\} \qquad (8.34)$$
$$Z \equiv -mg \cos\gamma_e \overset{\Delta}{=} Z_e$$

This is clearly a requirement of any normal airplane, for some range of V_e and γ_e.

The trouble with the reference equilibrium characterized by (8.30) - (8.34) is that when headwinds are added of the same order of magnitude as V_e, one is taken so far from the reference equilibrium that the linear analysis is likely to be unreliable. To circumvent this difficulty, a less obvious but more serviceable reference equilibrium is selected, namely one that has the desired rectilinear glide slope (at angle γ_E) and the desired constant airspeed, V_e, but that has a constant headwind W_e. The headwind chosen is the headwind at some point along the glide slope h_C

$$W_e \equiv W(h_C)$$

where the function $W(h)$ is intended to refer to the power-law profile

described earlier in Section 3.4.

$$W(h) = W_G \, (h/h_G)^n \tag{8.35}$$

This is a reasonable choice because over the range in h for which $\tilde{\mathbb{C}}$
measurements are available from the 44" x 66" tunnel (694' < h < 69') the
range in W is given by 62 fps < W < 43 fps, a spread of only 19 fps.
It will also be assumed that the following two requirements are made of
the flight path from h_A down to h_B:

      (i) the airspeed is constant $\equiv V_e$;

      (ii) the flight path is rectilinear at an angle γ_E below

           the horizon.

Thus this reference equilibrium trajectory is still characterized by
the following kinematics (again with $\mathcal{F}_B$ selected so that $\underset{\rightarrow}{i}_B$ is aligned with $\underset{\rightarrow}{V}$):

$$p, \, q, \, r \, = \, 0 \tag{8.36}$$

$$u \equiv V_e; \quad v, \, w \equiv 0 \tag{8.37}$$

but this does not uniquely specify the trajectory since all the
quantities in (8.36, 37) are expressed in $\mathcal{F}_B$, and two important
given quantities, $\underset{\rightarrow}{g}$ and γ_E, are related to $\mathcal{F}_I$. The $\underline{R}_{BI}$ matrix is still
given by (8.33) but now γ_e is not independently given and follows
instead from (3.26) and (3.27):

$$V_{Ee} \, = \, \sqrt{V_e^2 - W_e^2 \, \sin^2\gamma_E} \, - \, W_e \cos\gamma_E \tag{8.38}$$

$$\gamma_e \, = \, \sin^{-1} \, (V_{Ee}\sin\gamma_E/V_e) \tag{8.39}$$

where, recall, $\{ V_e, W_e, \gamma_E \}$ were given constants. This relationship is illustrated
in Fig. 4.

    In place of (8.32) then, we have

$$\left.\begin{aligned}
x_{Ie} &= x_{IA} + (V_{Ee}\cos\gamma_E)t \\
y_{Ie} &\equiv 0 \\
h_e &= h_A - (V_{Ee}\sin\gamma_E)t
\end{aligned}\right\} \tag{8.40}$$

and (8.34) still apply. All quantities with the subscript $(.)_e$ are constants except $x_{Ie}(t)$ and $h_e(t)$.

8.1.4 Perturbations About the Reference Equilibrium

In general the aircraft will not actually fly along the reference equilibrium flight path due to (i) initial conditions at point A, (ii) the fact that the wind is not constant at W_e, (iii) turbulence, and (iv) actuation of controls to combat the effects of the first three. An analysis is now undertaken to produce a set of linear differential equations that govern the deviations from equilibrium in response to the four factors mentioned above. Representing the perturbations about the reference equilibrium values as Δu etc. we set

$$u = V_e + \Delta u \; ; \; v = \Delta v \; ; \; w = \Delta w \tag{8.41}$$

$$p = \Delta p \; ; \; q = \Delta q \; ; \; r = \Delta r; \; W = W_e + \Delta W \tag{8.42}$$

and the kinematical perturbations may be written

$$x = x_e + \Delta x \; ; \; y = \Delta y \; ; \; h = h_e + \Delta h \tag{8.43}$$

$$\underline{R}_{BI} = \begin{pmatrix} \cos\gamma_e + \sin\gamma_e\Delta\theta & \cos\gamma_e\Delta\psi & \sin\gamma_e - \cos\gamma_e\Delta\theta \\ -\Delta\psi - \sin\gamma_e\Delta\phi & 1 & \cos\gamma_e\Delta\phi \\ -\sin\gamma_e + \cos\gamma_e\Delta\theta & -\Delta\phi - \sin\gamma_e\Delta\psi & \cos\gamma_e + \sin\gamma_e\Delta\theta \end{pmatrix} \tag{8.44}$$

(8.44) is the transformation matrix based on Euler angles relating $\mathcal{F}_B$ to $\mathcal{F}_I$ given as equation (4.5,4) in Ref. 5. Here the three Euler angles are given as azimuth angle $= \Delta\psi$, elevation angle $= -\gamma_e + \Delta\theta$, and bank angle $= \Delta\phi$. The external (nongravitational) forces and moments for the perturbed motion are

$$X = X_e + \Delta X \; ; \; Y = \Delta Y \; ; \; Z = Z_e + \Delta Z \tag{8.45}$$

$$L = \Delta L \; ; \; M = \Delta M \; ; \; N = \Delta N \tag{8.46}$$

With these substituted into (8.25) - (8.27) and (8.29), and keep-

ing only first-order terms, after eliminating the reference equilibrium solution we obtain:

$$m(\Delta\dot{u} - \cos\gamma_e\Delta\dot{W}) = \Delta X - mg\cos\gamma_e\Delta\theta$$

$$m(\Delta\dot{w} - V_e\Delta q + \sin\gamma_e\Delta\dot{W}) = \Delta Z + mg\sin\gamma_e\Delta\theta$$

$$I_{yy}\Delta\dot{q} = \Delta M$$

$$\Delta\dot{\theta} = \Delta q$$

$$\Delta\dot{x}_I = \cos\gamma_e\Delta u + V_e\sin\gamma_e\Delta\theta - \sin\gamma_e\Delta w - \Delta W$$

$$\Delta\dot{h} = -\sin\gamma_e\Delta u + V_e\cos\gamma_e\Delta\theta - \cos\gamma_e\Delta w$$

For the 'longitudinal' equations, and

$$m(\Delta\dot{v} + V_e\Delta r) = \Delta Y + mg\cos\gamma_e\Delta\phi$$

$$I_{xx}\Delta\dot{p} - I_{xz}\Delta\dot{r} = \Delta L$$

$$-I_{zx}\Delta\dot{p} + I_{zz}\Delta\dot{r} = \Delta N$$

$$\Delta\dot{\phi} = \Delta p - \tan\gamma_e\Delta r \qquad (8.48)$$

$$\Delta\dot{\psi} = \sec\gamma_e\Delta r$$

$$\Delta\dot{y}_I = \Delta v + V_e\cos\gamma_e\Delta\psi$$

for the 'lateral equations'. Note that the $\Delta\dot{\theta}$, $\Delta\dot{\phi}$ and $\Delta\dot{\psi}$ equations follow from Ref. 5 equations 5.2,9.

8.1.5 Longitudinal Aerodynamics

A specification is now given of the aerodynamic forces ΔX, ΔZ, ΔM that appear in (8.47);

$$\Delta X = X_u\Delta u + X_w\Delta w + X_\pi\Delta\pi \qquad (8.49)$$

$$\Delta Z = Z_u\Delta u + Z_w\Delta w + Z_{\dot{w}}\Delta\dot{w} + Z_q\Delta q + Z_\eta\Delta\eta + Z_\pi\Delta\pi \qquad (8.50)$$

$$\Delta M = M_u\Delta u + M_w\Delta w + M_{\dot{w}}\Delta\dot{w} + M_q\Delta q + M_\eta\Delta_\eta + M_\pi\Delta\pi \qquad (8.51)$$

Here $\Delta\eta$ is a change in elevator angle and $\Delta\pi$ is a change in throttle

102

setting. These two quantities will be regarded as the control variables for the longitudinal equations.

The force and moment derivatives in (8.49) and (8.50) are now reconstituted in terms of the conventional 'stability derivatives' as follows (Ref. 23):

$$X_u = -\rho V_e S C_{L*} \tan \gamma_e + \tfrac{1}{2} \rho V_e S C_{xu}$$

$$X_w = \tfrac{1}{2} \rho V_e S C_{x\alpha}$$

$$X_\pi = q_e S C_{x_{CT}} C_{T_\pi}$$

$$Z_u = -\rho V_e S C_{L*} + \tfrac{1}{2} \rho V_e S C_{zu}$$

$$Z_w = \tfrac{1}{2} \rho V_e S C_{z\alpha}$$

$$Z_{\dot{w}} = \tfrac{1}{2} t* \rho V_e S C_{z\dot{\alpha}}$$

$$Z_q = t* q_e S C_{zq}$$

$$Z_\eta = q_e S C_{z\eta}$$

$$Z_\pi = -q_e S C_{L_{CT}} C_{T_\pi} - q_e S \delta\alpha C_{T_\pi}$$

$$M_u = \tfrac{1}{2} \rho V_e S \bar{c} C_{mu}$$

$$M_w = \tfrac{1}{2} \rho V_e S \bar{c} C_{m\alpha}$$

$$M_{\dot{w}} = \tfrac{1}{2} t* \rho V_e S \bar{c} C_{m\dot{\alpha}}$$

$$M_q = t* q_e S \bar{c} C_{mq}$$

$$M_\eta = q_e S \bar{c} C_{m\eta}$$

$$M_\pi = q_e S \bar{c} C_{m_{CT}} C_{T_\pi}$$

where α = angle of attack of the aircraft zero lift line

$\Delta\alpha = \Delta w/V_e$

$q_e = \tfrac{1}{2} \rho V_e^2$

$\bar{c}$ = mean wing chord

$t* = \bar{c}/(2 V_e)$

$C_{L*} = L_*/(q_e S)$

L_* = lift plus component of thrust in the lift direction.

103

To make the results more meaningful and interesting, the values of the stability derivatives should be reasonable for an actual aircraft. The data used are largely from Ref. 24 and represent a twin engined STOL aircraft with flaps. We find that the derivatives that are not sensitive to reference equilibrium conditions have the following numerical values,

$$C_{zu} = 0$$

$$C_{z\dot{\alpha}} = -2.150/\text{rad} \qquad C_{m\eta} = 2.068/\text{rad}$$

$$C_{zq} = -7.144/\text{rad} \qquad C_{L_{CT}} = 0.55$$

$$C_{z\eta} = 0.5236/\text{rad} \qquad C_{x_{CT}} = 0.75$$

$$C_{m\alpha} = -2.026/\text{rad} \qquad C_{m_{CT}} = -0.1698$$

$$C_{m\dot{\alpha}} = -8.663/\text{rad} \qquad C_{m_u} = 0$$

$$C_{mq} = -28.76/\text{rad} \qquad (\partial T/\partial u)_e = 0$$

where

$$C_{T\pi} = 6.5617 \ \frac{P_m}{q_e S} \left(\frac{0.1311}{V_e} + 0.0021 \right) \qquad (8.52)$$

and the other constant are

$$m = 341.9 \ \text{slugs} \qquad \bar{c} = 6.5 \ \text{ft.}$$

$$I_{yy} = 23,472 \ \text{slug-ft}^2 \qquad S = 420 \ \text{ft}^2$$

$$P_m = 357,500 \ \text{ft.lb/sec.} \qquad \rho = .00238 \ \text{slugs/ft}^3$$

For the other stability derivatives, we must take into account the fact that the reference equilibrium of Ref. 24 was level flight at $V_e = 118.2$ ft/sec whereas the present reference equilibrium is descending flight at a specified W_e, V_e and γ_E. The stability axes of Ref. 24 will need to be rotated slightly, about $\vec{j}_B$, in order to coincide with our own stability axes. Let this rotation be $\delta\alpha$.

104

Now, from Ref. 23,

$$C_{z\alpha} = -C_{L\alpha} - C_{De} \qquad (8.53)$$

Since Ref. 24 gives

$$C_{z\alpha} = -6.109/\text{rad}; \quad C_{De} = 0.320$$

we conclude that

$$C_{L\alpha} = 5.789/\text{rad}$$

which is independent of flight condition. Also, if we assume that

$$C_D = C_{Do} + K\, C_L^2 \qquad (8.54)$$

then

$$C_{D_\alpha} = 2K\, C_{Le} C_{L\alpha} \qquad (8.55)$$

Now Ref. 24 gives

$$C_{x\alpha} = 0.9832/\text{rad}; \quad C_{Le} = 1.576$$

so we conclude that, since (Ref. 23)

$$C_{x\alpha} = C_{Le} - C_{D_\alpha} \qquad (8.56)$$

we must have

$$C_{D_\alpha} = 0.593/\text{rad}.$$

We now may regard (8.54) and (8.55) as two equations in two unknowns for C_{Do} and K, since we now know C_{De}, C_{Le}, C_{D_α}, $C_{L\alpha}$. The result is

$$C_{Do} = 0.242; \qquad K = 0.0314 \qquad (8.57)$$

From now on in this section the subscript $(.)_e$ refers to our own equilibrium, not that of Ref. 24.

The force balance on the aircraft for our reference equilibrium leads to (taking $\delta\alpha$ to be a small angle, see Fig. 165b),

$$\left.\begin{aligned}
C_{Le} + C_{Te}\, \delta\alpha &= C_{We}\cos\gamma_e \\
C_{Te} + C_{We}\, \sin\gamma_e &= C_{De}
\end{aligned}\right\} \qquad (8.58)$$

105

where $C_{We} = mg/(q_e S)$. Now, in Ref. 24 the reference equilibrium is characterized by the thrust vector $\underrightarrow{T}_{ee}$ (where $(\cdot)_{ee}$ is a temporary notation for the reference equilibrium of Ref. 24) being aligned with $\underrightarrow{V}_{ee}$ (see Fig. 165a) and making an angle α_{ee} with respect to the vehicle zero lift line ($z\ell\ell$). We will assume that the thrust line is fixed at α_{ee}. Also it is assumed here that

$$C_{L_{ee}} = C_{L_\alpha} \cdot \alpha_{ee} \tag{8.59a}$$

In the case of the present reference equilibrium $\underrightarrow{T}_e$ makes an angle $\delta\alpha$ with respect to $\underrightarrow{V}_e$ (since in general $\alpha_e \neq \alpha_{ee}$) as seen in Fig. 165b. Also it is assumed here that

$$C_{L_e} = C_{L_\alpha} \cdot \alpha_e \tag{8.59b}$$

From the geometry of Fig. 165 it is seen that

$$\alpha_{ee} = \alpha_e - \delta\alpha \tag{8.59c}$$

Thus

$$\delta\alpha = (C_{L_e} - C_{L_{ee}})/C_{L_\alpha} \tag{8.59d}$$

Combining (8.59d) with

$$C_{De} = C_{Do} + K\,C_{L_e}^2 \tag{8.60}$$

a cubic for C_{L_e} may be extracted from (8.58):

$$a_1\,C_{L_e}^3 + a_2\,C_{L_e}^2 + a_3\,C_{L_e} + a_4 = 0 \tag{8.61}$$

where

$$\left. \begin{aligned}
a_1 &= K \\
a_2 &= -K\,C_{L_{ee}} \\
a_3 &= C_{L_\alpha} + C_{Do} - C_{We}\sin\gamma_e \\
a_4 &= -C_{L_{ee}}(C_{Do} - C_{We}\sin\gamma_e) - C_{L_\alpha}C_{We}\cos\gamma_e
\end{aligned} \right\} \tag{8.62}$$

106

By neglecting the $\delta\alpha$ term in the first of (8.58), we have the approximate solution

$$\approx C_{Le} \approx C_{We} \cos\gamma_e \qquad (8.63)$$

when (8.58) to (8.61) are solved along with (8.38) and (8.39) the results are as follows for $W_G = 66$ fps, $W_e = 57$ fps, $\gamma_E = 15°$.

V/W_G	1.0	1.5	2.0
C_{Le}	4.663	2.219	1.257
$\approx C_{Le}$	5.060	2.234	1.253
C_{De}	0.925	0.397	0.292
C_{Te}	0.741	0.145	0.103
$\delta\alpha$ (rad)	0.533	0.111	-0.055

The values for $V/W_G = 1$ show that this case is unrealistic for normal aircraft. The second line in the table is from (8.63).

Now that these values are available, we have C_{Le}, C_{De}, C_{Te}, and in addition (from Ref. 23 and Fig. 165),

$$
\begin{aligned}
C_{L*} &= C_{Le} + C_{Te}\,\delta\alpha \\
C_{xu} &= \frac{(\partial T/\partial u)e}{\tfrac{1}{2}\rho V_e S} - 2(C_{De} - C_{Le}\tan\gamma_e) \\
C_{x\alpha} &= C_{Le} - C_{D\alpha} \\
C_{z\alpha} &= -C_{L\alpha} - C_{De}
\end{aligned}
\qquad (8.64)
$$

and this completes a specification of the stability derivatives.

We may now return to (8.47) and substitute the subsequent developments to obtain a set of first-order linear differential equations for the motion. To nondimensionalize, proceed as follows (Ref. 23):

107

$$\Delta\tilde{u} = \Delta u/V_e \quad ; \quad \Delta\alpha = \Delta w/V_e$$

$$\tilde{t} = t/t* \quad ; \quad \mu = 2m/(\rho S \, \bar{c})$$

$$i_{yy} = 8I_{yy}/(\rho S \, \bar{c}^3) \quad ; \quad \tilde{q} = \bar{c}q/(2V_e)$$

$$\tilde{W} = W/V_e \quad ; \quad \Delta\tilde{x}_I = 2\Delta x_I/\bar{c} \quad ; \quad \Delta\tilde{h} = 2\Delta h/\bar{c}$$

$$\left.\rule{0pt}{40pt}\right\} \qquad (8.65)$$

where

$$t* = \bar{c}/(2V_e)$$

Then the system of equations may be written (with a prime denoting differentiation with respect to $\tilde{t}$):

$$\underline{A}_L \, \Delta\underline{x}' = \underline{A}_R\Delta\underline{x} + \underline{B}_R\Delta\underline{u}_c + \underline{a}_\Gamma\Delta\tilde{\Gamma} + \underline{a}_W\Delta\tilde{W} \qquad (8.66)$$

where

$$\Delta\underline{x}^T = (\Delta\tilde{u} \quad \Delta\alpha \quad \Delta\tilde{q} \quad \Delta\theta \quad \Delta\tilde{x}_I \quad \Delta\tilde{h}) \qquad (8.67)$$

$$\Delta\underline{u}_c^T = (\Delta\eta \quad \Delta\pi) \qquad (8.68)$$

$$\underline{a}_\Gamma^T = (2\mu\cos\gamma_e \quad -2\mu\sin\gamma_e \quad 0 \quad 0 \quad 0 \quad 0) \qquad (8.69)$$

$$\underline{a}_W^T = (0 \quad 0 \quad 0 \quad 0 \quad -1 \quad 0) \qquad (8.70)$$

$$\underline{A}_L = \begin{pmatrix} 2\mu & 0 & 0 & 0 & 0 & 0 \\ 0 & 2\mu - C_{z\dot\alpha} & 0 & 0 & 0 & 0 \\ 0 & -C_{m\dot\alpha} & i_{yy} & 0 & 0 & 0 \\ 0 & 0 & 0 & 1 & 0 & 0 \\ 0 & 0 & 0 & 0 & 1 & 0 \\ 0 & 0 & 0 & 0 & 0 & 1 \end{pmatrix} \qquad (8.71)$$

$$\underline{A}_R = \begin{pmatrix} -2C_{L*}\tan\gamma_e + C_{xu} & C_{x\alpha} & 0 & -C_{L*} & 0 & 0 \\ -2C_{L*} & C_{z\alpha} & 2\mu + C_{zq} & C_{L*}\tan\gamma_e & 0 & 0 \\ 0 & C_{m\alpha} & C_{mq} & 0 & 0 & 0 \\ 0 & 0 & 1 & 0 & 0 & 0 \\ \cos\gamma_e & -\sin\gamma_e & 0 & \sin\gamma_e & 0 & 0 \\ -\sin\gamma_e & -\cos\gamma_e & 0 & \cos\gamma_e & 0 & 0 \end{pmatrix} \qquad (8.72)$$

$$\underline{B}_R = \begin{pmatrix} 0 & C_{x_{CT}} C_{T_{\pi}} \\ C_{z\eta} & -(C_{L_{CT}}+\delta\alpha)C_{T_{\pi}} \\ C_{m\eta} & C_{m_{CT}} C_{T_{\pi}} \\ 0 & 0 \\ 0 & 0 \\ 0 & 0 \end{pmatrix}$$

(8.73)

$$\Delta\widetilde{W} = [W(h) - W(h_e)] / V_e$$

$$\Delta\widetilde{\Gamma} = \frac{d(\Delta\widetilde{W})}{d\widetilde{t}} = -\sin\gamma_e \frac{d\widetilde{W}}{d\widetilde{h}}$$

The last equation follows from:

$$\frac{dW}{dt} = \frac{dW}{dh} \cdot \frac{dh}{dt}$$

where

$$W = W_e + \Delta W \quad (W_e \text{ is a constant})$$

$$h = h_e + \Delta h$$

thus

$$\frac{dW}{dt} = \frac{d\Delta W}{dh} \left(\frac{dh_e}{dt} + \frac{d\Delta h}{dt} \right)$$

$$\approx \frac{d\Delta W}{dh} \frac{dh_e}{dt} \text{ (to first order)}$$

but from Fig. 4

$$\frac{dh_e}{dt} = -V_e \sin\gamma_e$$

also

$$\frac{dW}{dh} = \frac{d\Delta W}{dh} \quad \text{and} \quad \frac{dW}{dt} = \frac{d\Delta W}{dt}$$

thus

$$\frac{d\Delta W}{dt} \approx -V_e \frac{dW}{dh} \sin\gamma_e$$

or

$$\frac{d\Delta\widetilde{W}}{d\widetilde{t}} \approx -\sin\gamma_e \frac{d\widetilde{W}}{d\widetilde{h}}$$

8.2 Aircraft Response to Turbulence

To account for the influence of turbulence on the aircraft, we now make the so-called 'point approximation', in which the distribution of turbulence over the vehicle is neglected, and the turbulence components are taken as being approximately uniform over the vehicle. More faithful models are possible with a substantial increase in work (Chapter 13 of Ref. 5). In addition, from a longitudinal dynamic standpoint, we will assume that the turbulence components parallel to the plane of aircraft symmetry are equivalent to the combined effects of slight changes in airspeed and angle of attack ($\Delta \tilde{u}_t$ and $\Delta \alpha_t$). These effects then produce aerodynamic forces on the vehicle in a manner similar to $\Delta \tilde{u}$ and $\Delta \alpha$. Now:

$$\Delta \tilde{u}_t = -(\cos \gamma_e \, u_g + \sin \gamma_e \, w_g)/V_e \tag{8.74}$$

$$\Delta \alpha_t = (\sin \gamma_e \, u_g - \cos \gamma_e \, w_g)/V_e \tag{8.75}$$

Note that $u_g(t)$, $w_g(t)$ are components of the gust vector in $\mathcal{F}_I$.

As a first approximation modify (8.66) to include turbulence as follows:

$$\underline{A}_L \Delta \underline{x}' = \underline{A}_R \Delta \underline{x} + \underline{B}_R \Delta \underline{u}_c + \underline{a}_T \Delta \tilde{\Gamma} + \underline{a}_W \Delta \tilde{W} + \underline{A}_g \, \underline{G} \tag{8.76}$$

where

$$\underline{G}^T = (\Delta \tilde{u}_t \;\; \Delta \alpha_t) \tag{8.77}$$

$$\underline{A}_g = \begin{pmatrix} -2C_{L*}\tan\gamma_e + C_{xu} & C_{x\alpha} \\ -2C_{L*} & C_{z\alpha} \\ 0 & C_{m\alpha} \\ 0 & 0 \\ 0 & 0 \\ 0 & 0 \end{pmatrix} \tag{8.78}$$

Note that the effects of $(\Delta \tilde{u}_t' \;\; \Delta \alpha_t')$ have been omitted from this preliminary analysis.

To isolate the individual derivatives $\Delta \tilde{u}'$, $\Delta \alpha'$, etc., on the left side, we premultiply (8.76) by $\underline{A}_L^{-1}$, obtaining

$$\Delta \underline{x}' = \underline{A}\, \Delta \underline{x} + \underline{B}_c\, \Delta \underline{u}_c + \underline{a}\, \Delta \tilde{\Gamma} + \underline{b}\, \Delta \tilde{W} + \underline{B}_g \underline{G} \qquad (8.79)$$

where

$$(\underline{A}\ \underline{B}_c\ \underline{a}\ \underline{b}\ \underline{B}_g) = \underline{A}_L^{-1}\ (\underline{A}_R\ \underline{B}_R\ \underline{a}_\Gamma\ \underline{a}_W\ \underline{A}_g) \qquad (8.80)$$

To complete the specification of (8.79), it is necessary to say something about the control $\Delta \underline{u}_c$. For an actual aircraft, this control would be exercised by a pilot or an autopilot. Both of these are beyond the scope of this report, and we shall instead assume a preprogrammed set of control deflections that, in the absence of turbulence, maintains a specified reference trajectory. Note that with this approach to the problem $\Delta \underline{u}_c$ acts as an independent external input to the system of equations (as do $\Delta \tilde{\Gamma}$, $\Delta \tilde{W}$, and $\underline{G}$) unlike the case where an autopilot or pilot is acting in a continuous closed-loop manner. As a result, the dynamical properties of the system are represented by $\underline{A}$ (a function of the reference equilibrium only) and the response to turbulence can be found as perturbations about the reference equilibrium (rather than the more general case requiring perturbations about the reference trajectory). This effect is the result of representing the reference trajectory as a perturbation about the reference equilibrium trajectory. The response of the linear system of (8.79) to the prescribed forcing functions $(\Delta \underline{u}_c,\ \Delta \tilde{\Gamma},\ \Delta \tilde{W}$ and $\underline{G})$ can be represented by the sum of the response to turbulence alone (all other inputs set to zero) and the response to the remaining inputs with the turbulence input set to zero. The deviations $\Delta \underline{x}$ in (8.79) are accordingly broken into two contributions, viz.,

$$\Delta \underline{x} = \Delta_r \underline{x} + \underline{y} \qquad (8.81)$$

111

Here $\Delta_r\underline{x}$ represents the deviations of the reference trajectory from the reference equilibrium:

$$\underline{x}_r = \underline{x}_e + \Delta_r\underline{x} \qquad (8.82)$$

and $\underline{y}$ represents the additional deviations about the reference equilibrium due to turbulence. With these definitions, (8.79) is also split into two parts as follows:

$$\Delta_r\underline{x}' = \underline{A}\,\Delta_r\underline{x} + \underline{B}_c\,\Delta\underline{u}_c + \underline{a}\,\Delta\widetilde{\Gamma} + \underline{b}\,\Delta\widetilde{W} \qquad (8.83)$$

$$\underline{y}' = \underline{A}\,\underline{y} + \underline{B}_g\underline{G} \qquad (8.84)$$

and the effects of wind shear and turbulence can be studied independently.

It is interesting to note that it can be shown that the approximate response computed from (8.84) represents exactly (under the present assumptions) the state vector $(\Delta\widetilde{u}_E\;\;\Delta\alpha_E\;\;\Delta\widetilde{q}\;\;\Delta\theta\;\;\Delta\widetilde{x}_I\;\;\Delta\widetilde{h})$ for the case where the vehicle stability derivatives are as given in Section 8.1.5 for $W_e \neq 0$ but with W_e taken to be zero in the linearized equations of motion, where

$$\Delta\underline{V}_{E_B}^{\,T} = (\Delta u_E\;\;\Delta v_E\;\;\Delta w_E)$$

$$\Delta\widetilde{u}_E = \Delta u_E/V_e$$

$$\Delta\alpha_E = \Delta w_E/V_e \quad .$$

112

Section IX

AIRCRAFT LANDING APPROACH RESULTS (LONGITUDINAL)

As mentioned above, an investigation of the landing control system (e.g., pilot or autopilot) is beyond the scope of this report. Nevertheless, this subject is addressed below in a preliminary manner, after which this Section is concluded with some typical numerical results on the dispersion matrix, $< \underline{y} \, \underline{y}^T >$, for the aircraft characterized in Section 8.1.5 based on the 44" x 66" tunnel measurements of $\mathcal{R}$. Since the tunnel data do not exist above a full scale height of 694.4' it is convenient to assume that the aircraft does not encounter wind shear or turbulence above this altitude.

9.1 Characteristic Modes

In Ref. 24, the reference equilibrium was level flight at 118.2 ft/sec, and the short-period (SP) and phugoid (Ph) modal characteristics (natural frequency and damping ratio) were given as:

$$\omega_{SP} = 1.757 \text{ rad/sec}; \quad \zeta_{SP} = 0.654$$

$$\omega_{Ph} = 0.319 \text{ rad/sec}; \quad \zeta_{Ph} = 0.219$$

As a mutual check, our own program (see Appendix G) gave the following values for the same conditions:

$$\omega_{SP} = 1.757 \text{ rad/sec}; \quad \zeta_{SP} = 0.654$$

$$\omega_{Ph} = 0.323 \text{ rad/sec}; \quad \zeta_{Ph} = 0.135$$

Since the purpose in using the data of Ref. 24 was to define a representative STOL aircraft, and not to reproduce their results per se, the slight anomaly in the phugoid damping ratio was not considered important.

For the landing path reference equilibrium described earlier

113

in Section 8.1.5 (with W_e = 57 fps and W_G = 66 fps) the same program gave the following results:

V_e/W_G	ω_{SP}	ζ_{SP}	ω_{Ph}	ζ_{Ph}
2.0	1.954	0.651	0.290	0.204
1.5	1.470	0.655	0.388	0.132
1.0	1.021	0.669	0.552	0.073

Thus it is seen that the phugoid damping is significantly reduced and that the separation between the periods of the two modes is reduced as V_e/W_G becomes smaller.

9.2 Control During Landing

Referring to the discussion following (8.80), it is recalled that the reference flight path from h_A down to h_B is considered to be controlled in some specified manner. The first attempt at this assumed that:

(i)   the airspeed is constant $\equiv V_e$

(ii)   the flight path is rectilinear at an angle γ_E below the horizon.

It can be shown that the consequence of these assumptions for the perturbations $\Delta_r \underline{x}$ is that

$$\Delta_r \tilde{u} = 0 \qquad\qquad (9.1)$$

$$\Delta_r \gamma \equiv \Delta_r \alpha - \Delta_r \theta = - k_e \Delta \tilde{W} \qquad\qquad (9.2)$$

where

$$k_e = \frac{\sin\gamma_E}{\cos(\gamma_E - \gamma_e)} \qquad\qquad (9.3)$$

The conditions (9.1) and (9.2) can conceptually be realized by suitably choosing $\Delta\eta$ and $\Delta\pi$ along the trajectory. Unfortunately, this specification leads to an unstable system. Even a less ambitious specification namely, choosing $\Delta\eta$ to keep the aircraft precisely on the glide slope is unstable.

It is felt that these problems represent a limiting effect similar to setting the gain too high in a feedback control loop. Based on this, the approach outlined below was followed.

More practical control strategies could be selected that would lead both to a stable system, and to a satisfaction of the conditions (9.1) and (9.2) to within a reasonable tolerance. To place the effects of such control in perspective, it should be noted that, for our example aircraft, if no control were exercised at all the perturbations at a decision height of 69 ft (with $V_e = 2W_G$, $W_e = 57$ fps $W_G = 66$ fps, a wind power law index of 0.16 and zero initial conditions) are:

$$\Delta u = -2 \text{ ft/sec}; \qquad \Delta q = -5.2 \times 10^{-3} \text{ rad/sec};$$

$$\Delta \alpha = 2 \times 10^{-3} \text{ rad}; \qquad \Delta \theta = -3.5 \times 10^{-2} \text{ rad};$$

$$\Delta x_I = 19 \text{ ft} \qquad \Delta h = -55 \text{ ft}.$$

The reference path results were obtained with the aid of a variable-step-size predictor/corrector numerical integration algorithm (see Appendix G). The resulting deviations from the reference equilibrium glide slope are shown in Fig. 166. It is seen that for the case $\Delta\eta = \Delta\pi = 0$ the aircraft diverges below the desired glide path as the landing approach continues.

In an attempt to improve on this glide slope performance a simple control algorithm was implemented whereby

$$\Delta\eta = -.05 \left(\Delta\tilde{h} + 10 \, \Delta\tilde{h}' \right)$$

$$\Delta\pi = 2\Delta\tilde{W}$$

The results for this case are also shown in Fig. 166 where it is seen that quite precise glide slope tracking is achieved down to h = 200'. Below this height its performance degrades somewhat. No attempt was made to optimize this control law. It will be assumed that the resulting time histories for $\Delta\eta$ and $\Delta\pi$ are implemented in an open-loop fashion once they are determined.

9.3 Dispersions Caused by Turbulence

At any time t during the landing, perturbations in the various state variables have a zero ensemble average. Their ensemble mean squares and ensemble mean products are nonzero, however, and are given by (3.14) repeated here for convenience:

$$\underline{\Sigma}(t) \equiv \; < \underline{y}(t) \; \underline{y}^T(t) > \; = \int_0^t \int_0^t \underline{H}(t,t_1) \underline{R}(t_1,t_2) \; \underline{H}^T(t,t_2) dt_1 dt_2 \qquad (9.4)$$

where $\underline{\Sigma}(t)$ is called the dispersion matrix. In this section, $\underline{y}$ will consist of dimensional variables:

$$\underline{y}^T(t) = (\Delta u \quad \Delta\alpha \quad \Delta q \quad \Delta\theta \quad \Delta x_I \quad \Delta h) \qquad (9.5a)$$

where
$$\underline{\dot{y}} = \underline{\mathbb{A}} \; \underline{y} + \underline{\mathbb{B}} \; \underline{G}_T \qquad (9.5b)$$

and the turbulence is represented by

$$\underline{G}_T^T = (u \; w) \qquad (9.5c)$$

and thus the $\underline{H}$ matrix is expressed as (from Section 3.1 and (8.84))

$$\underline{H}(t,\tau) = \exp[(t-\tau) \; \underline{\mathbb{A}}] \; \underline{\mathbb{B}} \qquad (9.6)$$

where $\underline{\mathbb{A}}$ and $\underline{\mathbb{B}}$ are the dimensionalized counterparts of $\underline{A}$ and $\underline{B}_g$ defined by (8.80). In fact,

$$\underline{\mathbb{A}} = \left(\frac{2V_e}{\bar{c}} \right) \underline{S} \; \underline{A} \; \underline{S}^{-1} \qquad (9.7)$$

116

Approved for Public Release

$$\mathbb{B} = \left(\frac{2V_e}{\bar{c}} \right) \underline{S}\ \underline{B}\ \underline{S}_g^{-1} \tag{9.8}$$

where

$$\underline{S} = \text{diag}\left\{ V_e,\ 1,\ (2V_e/\bar{c}),\ 1,\ (\bar{c}/2),\ (\bar{c}/2) \right\} \tag{9.9}$$

$$\underline{S}_g^{-1} = \begin{pmatrix} -\cos\gamma_e/V_e & -\sin\gamma_e/V_e \\ \\ \sin\gamma_e/V_e & -\cos\gamma_e/V_e \end{pmatrix} \underline{T} \tag{9.10}$$

$$\underline{T} = \begin{pmatrix} -1 & 0 \\ \\ 0 & -1 \end{pmatrix} \tag{9.11}$$

The matrix $\underline{S}$ contains the scale factors that convert from dimensionless to dimensional variables; $\underline{S}_g$ does likewise and, additionally, converts the dimensional turbulence inputs from wind tunnel frame ($\mathcal{F}_T$) components into the nondimensional airspeed and angle of attack perturbations $(\Delta \tilde{u}_t, \Delta \alpha_t)$. $\underline{Q}$ (dimensional) comes from the 44" x 66" tunnel measurements of Section 6.3.2 and thus has its turbulence components expressed in $\mathcal{F}_T$.

There can be several approaches to the evaluation of the right side of (9.4). One possibility is described in Appendix F and G, and the numerical results below were calculated in that manner. The results were also checked using a somewhat cruder approximation in which the integrand in the double integration was approximated by a piece-wise constant surface. This gave an order-of-magnitude corroboration of the results.

For $V_e = 2W_G$ and $W_e = 57$ fps, the value of the dispersion matrix $\underline{\Sigma}(t)$ is shown in Table 10 at ten equal time intervals along the landing approach path from $h_A = 694$ ft down to $h_B = 69$ ft. The final

117

root-mean-square values of Δu_E $\Delta \alpha_E$ Δq, $\Delta \theta$, Δx_I and Δh are, respectively 9.8 fps, 0.07 radians, 0.11 radians/sec., 0.08 radians, 80 ft., and 47 ft. Since the aircraft is stable with respect to the first four variables, one would expect a steady-state variance to be reached, if the input were at a constant level. In the present instance, however, the r.m.s. of the turbulence increases along the flight path and so the mean-square response to it likewise continues to grow. With respect to the variables Δx_I and Δh, for which no stabilizing feedback has been provided (see 8.84), one would expect their variances to continue to grow with time even if the turbulence intensity were uniform. An analogy to the 'random walk problem' may be helpful here for which it is known that the variance in position grows with time. This time dependence is illustrated in Fig. 167.

Table 11 shows the final value of $\underline{\Sigma}$ (i.e., the value at 69 ft) when $V_e = 1.5 \ W_G$. The variances are generally larger than for $V_e = 2W_G$. One factor in this increase for the cases of Δx_I and Δh is simply that the aircraft has been influenced by turbulence for a longer duration (namely 56 seconds as compared to 32 seconds). Also this trend is consistent with the substantial reduction in the phugoid damping ratio noted earlier (Section 9.1).

The total longitudinal response of the aircraft is thus made up of the reference trajectory of Section 9.2 and the response to turbulence found above. A similar analysis could be carried out for the lateral response.

Section X

CONCLUSIONS AND RECOMMENDATIONS

10.1 Conclusions

1. The fixed probe theory allows the determination of the dispersion of
an aircraft's state variables by using two-point time/space cross-
correlations among the turbulence velocity components. The moving
probe technique requires many replicates to produce such data, but
also gives additional information concerning the distribution function
of the dispersions and individual response time histories. Due to
the mechanical complexity of the moving probe technique the fixed
probe approach seems to be the more practical one.

2. The UTIAS boundary layer tunnels can successfully simulate planetary
boundary layer flow through the use of a jet grid, bluff barrier, and
floor roughness.

3. When flight path correlations were measured in the two tunnels the
following conclusions were drawn:

(3.1) The effects of inhomogeneity was most noticeable towards the
bottom of the boundary layer. These effects were most apparent in the
8" x 8" tunnel results.

(3.2) Much of the nondimensional correlation data produced in the
44"x 66" tunnel could be reasonably represented by a single curve.

(3.3) Attempts at fitting a modified von Kármán model to the results
from the 44" x 66" tunnel met with reasonable success. The use of
such models could greatly reduce the number of measurements required
when applying the fixed probe technique.

10.2 Recommendations

1. Further work is required in order to assess the implications involved
in representing the effects of turbulence as a perturbation about the

119

perturbed path due to wind shear.

2. The modified von Kármán turbulence model should be tested in the analysis program in order to assess its utility in this application.

3. Results from the fixed probe theory should be compared with other more approximate approaches for predicting aircraft response in order to determine their relative merits.

4. The work reported in this report should be repeated for a range of wind profiles and including the effects of man-made structures near the airport.

APPENDIX A

TURBULENCE DEFINITIONS

A detailed discussion of turbulence theory and definitions is given in Ref. 25. The brief descriptions and definitions given below are taken from Ref. 10.

(a) Correlations

A one-dimensional correlation of two functions of three variables is defined as

$$R_{f_1 f_2}^{z}(x_1, y_1, z_1) = \lim_{B \to \infty} \frac{1}{2B} \int_{-B}^{B} f_1(0,0,z) f_2(x_1, y_1, z_1 + z) \, dz$$

where x_1, y_1, z_1 are constants which separate the arguments of the two functions, and z is the variable with respect to which the product is being averaged. The operation

$$\lim_{B \to \infty} \frac{1}{2B} \int_{-B}^{B} dz$$

is the averaging operation. In this report the averaging process will be done with respect to time only. Therefore the superscripts on the correlation may be dropped as it will be understood that these are one-dimensional correlations with respect to time. For convenience we can define

$$\overline{f_1(t) f_2(t)} = \lim_{T \to \infty} \frac{1}{2T} \int_{-T}^{T} f_1(t) f_2(t) \, dt$$

In this report, the functions of interest are the velocities u, v, w. These are functions of the four variables, x, y, z, t.

The argument of the correlation function defines the separation in space and time of the two velocity functions. Therefore

$$R_{uv}(x_1, y_1, z_1, \tau_1) = \overline{u(0,0,0,t) v(x_1, y_1, z_1, t+\tau_1)}$$

$$R_{vu}(x_1, y_1, z_1, \tau_1) = \overline{v(0,0,0,t) u(x_1, y_1, z_1, t+\tau_1)}$$

x_1, y_1, z_1, τ_1 are constants.

For convenience, any zeroes in the correlation argument are dropped thus:

$$R_{uv}(\tau) = R_{uv}(0,0,0,\tau)$$

etc.

The correlation $R_{uv}(\tau_1)$ is a single value while $R_{uv}(\tau)$ is a function of the variable τ. Likewise, $R_{uv}(x)$ is a function of the variable x where x is the separation in the x-direction.

One property of the correlation function that is useful is .

$$R_{uv}(0) = \overline{u(t)\ v(t)}$$

or

$$R_{uu}(0) = \overline{u(t)\ u(t)} = \overline{u(t)}^2 = \text{the mean square value.}$$

The correlations $R_{ii}(\tau)$ are known as autocorrelations. The correlations $R_{ij}(\tau)$ are known as cross-correlations.

(b) <u>Scales</u>

$$L_i^x \equiv \int_0^\infty \tilde{R}_{ii}(x)\ dx$$

$$L_i^y \equiv \int_0^\infty \tilde{R}_{ii}(y)\ dy$$

$$L_i^z \equiv \int_0^\infty \tilde{R}_{ii}(z)\ dz$$

$$T_i \equiv \int_0^\infty \tilde{R}_{ii}(\tau)\ d\tau$$

The first three scales have the dimensions of length. These scales are the area under the appropriate correlation functions. If there is a high correlation at large separations, then the scale will be large, indicating that

the size of the turbulent eddies in the flow must be fairly large since there is very slight correlation between eddies. In this manner the length scales are a measure of the size of the turbulence.

The last scale has the dimension of time and represents a characteristic time inherent in the flow.

(c) Power Spectral Densities

Another use of the correlation function is to obtain spectral information. The one-dimensional power spectral density is defined as the Fourier transform of the one-dimensional correlation function. Multidimensional spectral densities are Fourier transforms of multidimensional correlation functions. The one-dimensional spectral density is the only one of interest here.

$$\Phi_{ij}(k_x) \equiv 2 \int_{-\infty}^{\infty} R_{ij}(x) \, e^{-j2\pi k_x x} \, dx$$

$$\Phi_{ij}(k_y) \equiv 2 \int_{-\infty}^{\infty} R_{ij}(y) \, e^{-j2\pi k_y y} \, dy$$

$$\Phi_{ij}(k_z) \equiv 2 \int_{-\infty}^{\infty} R_{ij}(z) \, e^{-j2\pi k_z z} \, dz$$

$$\Phi_{ij}(f) \equiv 2 \int_{-\infty}^{\infty} R_{ij}(\tau) \, e^{-j2\pi f \tau} \, d\tau$$

$$\Phi_{ij}(k) \equiv 2 \int_{-\infty}^{\infty} R_{ij}(\tau) \, e^{-j2\pi k \bar{U} \tau} \, d\tau$$

where k is the reduced frequency $f/\bar{U}$ and k_x, k_y, k_z are wave numbers corresponding to the x,y,z directions.

(d) Taylor's Hypothesis

This is the assumption that the flow's turbulent velocity structure is fixed in time when viewed from a reference frame moving at the mean flow speed

123

$\bar{U}$ while the changes in velocity at a fixed measurement point are caused by the convection of this "frozen" flow past the measurement point at the mean velocity. This assumption is a good one if $\bar{U} \gg u,v,w$. It allows us to substitute time separation in correlations for spatial separation in the x direction. Thus we have

$$R_{ij}(x_1) = R_{ji}(\tau_1)$$

where

$$x_1 = \bar{U}\,\tau_1$$

and

$$L_i^x = \bar{U} \int_0^\infty \tilde{R}_{ii}(\tau)\,d\tau$$

and

$$\Phi_{ij}(k_x) = 2\bar{U} \int_{-\infty}^\infty R_{ji}(\tau)\,e^{-j2\pi k_x \bar{U}\tau}\,d\tau$$

and from the equation for $\Phi_{ij}(k)$

$$\Phi_{ij}(k_x) = \bar{U}\,\Phi_{ji}(k)\,\Big|_{k=k_x}$$

(e) <u>Spectral Peak Method of Estimating L</u>

If we assume that the von Kármán model for power spectral density holds then (Ref.10)

$$\frac{k_x \Phi_{uu}(k_x)}{\overline{u^2}} = \frac{4L_u^x k_x}{[1 + 70.7(L_u^x k_x)^2]^{5/6}}$$

$$\frac{k_x \Phi_{ww}(k_x)}{\overline{w^2}} = \frac{4k_x L_w^x \{1 + 188.4(2L_w^x k_x)^2\}}{[1 + 70.7(2L_w^x k_x)^2]^{11/16}}$$

By differentiating the right hand sides with respect to k_x and equating it to zero to find the location of the peak value, we get

124

$$k_{xpu} = \frac{.146}{L_u^x} \quad \text{for } u$$

$$k_{xpw} = \frac{.106}{L_w^x} \quad \text{for } w$$

This gives $L_u^x = \frac{.146}{k_{xpu}}$ and $L_w^x = \frac{.106}{k_{xpw}}$

Since frozen flow is an underlying assumption in the von Kármán model then

$$\Phi_{ii}(k_x) = \bar{U} \, \Phi_{ii}(k)\Big|_{k=k_x} \quad \text{(see item (d) above)}. \quad \text{Thus the scale } L_u^x \text{ can be determined}$$

from the peak position of the $k\Phi_{uu}(k)/\overline{u^2}$ vs kz plot, etc.

125

APPENDIX B

POWER SPECTRAL DENSITY ESTIMATION

The power spectral density measurements presented in this report were found by Fourier transforming correlation estimates produced by a PAR Model 100 correlator. In the case of the 8" x 8" tunnel data the transformation was carried out on an off-line IBM 1130 computer. In the case of the 44" x 66" tunnel data an on-line HP 2100A computer was employed. Both machines implemented the same algorithms. The details of the theory behind these estimates is contained in Appendix B of Ref. 16.

In general terms the signals representing the fluctuating turbulence velocities were produced by DISA hot wire equipment. The d.c. levels were removed by passing the signals through first order high pass filters patched on a general purpose analog computer. These were then processed on a PAR Model 100 correlator (in some cases after passing through a low pass filter) and these correlation estimates used as input to the digital computer. Fourier transformation of the data then resulted in power spectral density estimates. This digital program included a Hanning window subroutine to improve side lobe performance.

To avoid aliasing problems the time delay increment $\Delta\tau$ selected for the PAR correlator on any one run was chosen small enough to ensure that

$$\frac{2\pi}{\Delta\tau} > \omega_H + \omega_B \tag{B.1}$$

where ω_B is the frequency (rad/sec) above which no significant power exists in the signal being examined, and ω_H is the highest frequency at which a power estimate is desired. In our work ω_H was taken to be $\pi/2\Delta\tau$, or one half the Nyquist frequency.

126

The frequency resolution of this process is approximately $2\pi/\tau_{max}$, where for the PAR correlator $\tau_{max} = 100 \, \Delta\tau$. Thus the lowest frequency estimate was typically at π/τ_{max} rad/sec. Thus some aliasing problems can arise if very low frequency estimates are required since this requires a large $\Delta\tau$. In such cases a fourth-order Butterworth filter was used as a low-pass filter upstream of the PAR correlator with its cutoff frequency set to $\pi/\Delta\tau$ rad/sec. This effectively reduces ω_B to $\pi/\Delta\tau$ and thus inequality (B-1) is satisfied. The filter characteristics are such that a negligible influence is felt at frequencies below ω_H.

The only other filter in the circuit (the dc removal high pass filter) has its break frequency located well below the lowest frequency of interest in the velocity signals and thus has no influence on the measured power spectrum.

The spectral data presented in this report for the 8" x 8" tunnel runs were obtained from single 100 sec records processed by the PAR correlator. In the case of the 44" x 66" tunnel runs, 5 estimates were obtained in the above manner. Their mean and standard deviations are plotted on the graphs of power spectral density. All these data are presented as one-sided spectra.

127

APPENDIX C

STATISTICAL VARIABILITY OF R_{xx} MEASUREMENTS

In the idealized case of white noise passed through a perfect low pass filter of bandwidth B (i.e., no output signal power beyond B and a flat power spectrum below B) Reference 14 indicates that for finite time records:

$$\sigma^2_{R_{xx}} = \frac{1}{2BT}(R^2_{xx}(\tau) + R^2_{xx}(0))$$

where T is the record length of the signal x(t). Thus as $\tau \to 0$

$$\sigma^2_{R_{xx}} \to \frac{R_{xx}^2(0)}{BT}$$

For our data R_{xx} generally decreases in magnitude as $\tau \to$ large values. Thus for τ large $R_{xx}(0) \gg R_{xx}(\tau)$ and

$$\sigma^2_{R_{xx}} \to \frac{R^2_{xx}(0)}{2BT} \quad \text{, independent of } \tau.$$

This effect is illustrated in Fig. 123 where the results obtained from five measurements of raw $R_{uu}(\tau)$ data were used to estimate the standard deviation. These data were obtained from the PAR correlator with τ_{max} set at 0.20 sec. The increase in σ is clearly seen for $\tau \to 0$ as is the fairly constant value of σ for τ large. Now when normalized data are used (e.g., $\tilde{R}_{xx} = \frac{R_{xx}(\tau)}{\hat{\hat{xx}}} = \frac{R_{xx}(\tau)}{R_{xx}(0)}$) this forces the variance at $\tau = 0$ to become zero and modifies the variance at other values of τ as well. However one would expect the influence of this modification to die out as τ became large. This effect can be seen in the data of Figs. 121 and 122 to some extent.

APPENDIX D

THE INFLUENCE OF FILTERS ON CORRELATION ESTIMATES

In general, if a signal $x(t)$ is filtered by a linear network $F(j\omega)$ prior to processing by a correlation algorithm such that

$$\bar{y} = F(s)\,\bar{x} \qquad (D.1)$$

represents the output signal $y(t)$ (where here $\bar{x}$ represents the Laplace Transform of $x(t)$ and s is the Laplace Transform variable) then from linear theory

$$\phi_{yy}(\omega) = |F(j\omega)|^2\,\phi_{xx}(\omega) \qquad (D.2)$$

Thus the estimate $R_{yy}(\tau)$ of the desired underlying correlation $R_{xx}(\tau)$ is given by

$$R_{yy}(\tau) = \int_{-\infty}^{\infty} \phi_{yy}(\omega) e^{j\omega\tau}\,d\omega = \int_{-\infty}^{\infty} \phi_{xx}(\omega)|F(j\omega)|^2\,e^{j\omega\tau}\,d\omega \qquad (D.3)$$

But

$$\phi_{xx}(\omega) = \frac{1}{2\pi}\int_{-\infty}^{\infty} R_{xx}(\tau) e^{-j\omega\tau}\,d\tau \qquad (D.4)$$

thus

$$R_{yy}(\tau) = \frac{1}{2\pi}\int_{-\infty}^{\infty}\int_{-\infty}^{\infty} |F(j\omega)|^2\,R_{xx}(v) e^{-j\omega v}e^{j\omega\tau}\,dv\,d\omega \qquad (D.5)$$

changing the order of integration

$$R_{yy}(\tau) = \frac{1}{2\pi}\int_{-\infty}^{\infty}\int_{-\infty}^{\infty} |F(j\omega)|^2 e^{j(\tau-v)\omega} R_{xx}(v)\,d\omega\,dv$$

$$= \int_{-\infty}^{\infty} G(\tau-v)\,R_{xx}(v)\,dv$$

$$= G(\tau)* R_{xx}(\tau) \qquad (D.6)$$

where

$$G(\tau) = \frac{1}{2\pi}\int_{-\infty}^{\infty} |F(j\omega)|^2\,e^{j\omega\tau}\,d\omega \qquad (D.7)$$

129

And in general, if

$$\phi_{yy}(\omega) = H(j\omega)\phi_{xx}(\omega) \tag{D.8}$$

then

$$R_{yy}(\tau) = G(\tau)* R_{xx}(\tau) \tag{D.9}$$

where

$$G(\tau) = \frac{1}{2\pi}\int_{-\infty}^{\infty} H(j\omega)e^{j\omega\tau}d\omega \tag{D.10}$$

Now consider the case of our dc removal circuits. The output of a first order low pass filter is subtracted from its input signal to remove the dc component. Let the low pass filter be represented by $LP(j\omega)$. Thus the processed signal $o(t)$ is related to the original signal $i(t)$ by

$$\bar{o} = \bar{i} - LP(s)\ \bar{i} \tag{D.11}$$

where

$$LP(s) = \frac{1}{1 + sT} \tag{D.12}$$

from the theory of power spectral densities it follows that

$$\phi_{oo}(\omega) = \phi_{ii}(\omega) + |LP(j\omega)|^2\phi_{ii}(\omega) - LP(j\omega)\phi_{ii}(\omega) - LP^*(j\omega)\phi_{ii}(\omega)$$

$$= \phi_{ii}(\omega) + |LP(j\omega)|^2\phi_{ii}(\omega) - 2R_e\{LP(j\omega)\}\phi_{ii}(\omega) \tag{D.13}$$

thus

$$R_{oo}(\tau) = R_{ii}(\tau) + G(\tau)* R_{ii}(\tau) \tag{D.14}$$

where

$$G(\tau) = \frac{1}{2\pi}\int_{-\infty}^{\infty}\left[|LP(j\omega)|^2 - 2R_e\{LP(j\omega)\}\right]e^{j\omega\tau}d\omega \tag{D.15}$$

Now from (D.12)

$$LP(j\omega) = \frac{1}{1 + j\omega T} = \frac{1 - j\omega T}{1 + \omega^2 T^2} \tag{D.16}$$

and

$$|LP(j\omega)|^2 = \frac{1}{1 + \omega^2 T^2} \tag{D.17}$$

130

$$2R_e\{LP(j\omega)\} = \frac{2}{1 + \omega^2 T^2} \tag{D.18}$$

thus

$$|LP(j\omega)|^2 - 2R_e\{LP(j\omega)\} = \frac{-1}{1 + \omega^2 T^2} \tag{D.19}$$

and

$$G(\tau) = \frac{-1}{2\pi} \int_{-\infty}^{\infty} \frac{e^{j\omega\tau}}{1 + \omega^2 T^2} \, d\omega$$

$$= -\frac{1}{2T} e^{-|\tau|/T} \tag{D.20}$$

Thus

$$R_{oo}(\tau) = R_{ii}(\tau) - \left[\frac{e^{-|\tau|/T}}{2T} \right] * R_{ii}(\tau) \tag{D.21}$$

Based on full scale filter time constant values of $T = 4285$ sec. for the 8" x 8" tunnel and $T = 6052$ sec. for the 44" x 66" tunnel and $R_{oo}(\tau)$ with a first zero crossing at roughly 20 sec. (see Fig. 122) it can be seen that the contribution from the convolution of (D.21) is negligible, that is, typically less than $1/T$ times the area under $R_{ii}(\tau)$ between $\tau = 0$ and $\tau = 20$ sec.

APPENDIX E

VON KÁRMÁN MODEL FOR TURBULENCE CORRELATIONS

A reasonable model for describing turbulence in clear air at altitudes from below 5000 to 40,000 ft. is one assuming isotropic, homogeneous, Gaussian, and frozen flow. If the von Kármán model is used to describe the power spectral densities of the flow then the following function can be shown to represent the correlation among the various turbulence components (see, for example, Ref. 5).

$$\tilde{R}_{ij}(\xi_1, \xi_2, \xi_3) = [f(\zeta) - g(\zeta)] \frac{\xi_i \xi_j}{\xi^2} + g(\zeta) \delta_{ij} \tag{E.1}$$

where: i or $j = 1$ represents the x direction

        i or $j = 2$ represents the y direction

        i or $j = 3$ represents the z direction

$R_{ij}(\xi_1, \xi_2, \xi_3)$ represents the correlation between the ith turbulent component at (x,y,z) and the jth turbulent component at $(x + \xi_1, y + \xi_2, z + \xi_3)$, e.g., $R_{12} \equiv R_{uv}$. Note that no time delay is present due to the assumption of frozen flow.

δ_{ij} is the Kronecker delta

ξ $= \sqrt{\xi_1^2 + \xi_2^2 + \xi_3^2}$

$f(\zeta)$ and $g(\zeta)$ are, respectively, the longitudinal and lateral correlation coefficients; for the von Kármán model these are given by

$$f(\zeta) = \frac{2^{2/3}}{\Gamma(1/3)} \zeta^{1/3} K_{1/3}(\zeta) \tag{E.2}$$

$$g(\zeta) = \frac{2^{2/3}}{\Gamma(1/3)} \zeta^{1/3}[K_{1/3}(\zeta) - \frac{1}{2} \zeta K_{2/3}(\zeta)] \tag{E.3}$$

with $\qquad$ $\zeta \qquad = \dfrac{\xi}{1.339 \, L_u^x}$

$$\Gamma(1/3) = 2.6789$$

$K \qquad$ = modified Bessel function of the

second kind.

In order to apply this model to situations where time domain measurements are taken and time delays included, use is made of the frozen flow assumption. If the axes are so oriented that the mean flow is in the positive x direction $(\bar{U})$ then ξ_1 must be replaced by $(\Delta x - \bar{U} \cdot \tau)$ where τ is the time delay applied to the measurement at (x,y,z). Here Δx represents the probe separation in the x direction and it follows the same sign convention as ξ_1.

The model of (E.1) was programmed on a digital computer and use made of the frozen flow assumption in generating $\tilde{\underline{R}}$ data corresponding to the probe separations and time delays incorporated in the present study. Figure 128 is a plot of $f(\zeta)$ and $g(\zeta)$ as generated by this program. It is seen from (E.1) that the following hold:

$$\tilde{R}_{ij} = \tilde{R}_{ji}$$
$$\tilde{R}_{ij} = 0 \qquad \text{for } i \neq j \text{ and one of } \xi_i, \xi_j = 0$$
$$\tilde{R}_{ij} = g(\zeta) \text{ for } i = j \text{ and } \xi_i = 0$$
$$\tilde{R}_{ij} = f(\zeta) \text{ for } i = j \text{ and } \xi^2 = \xi_i^2$$

In the present case of measurements made along a glide slope aligned with the mean wind, $\xi_2 = 0$ and hence this theory predicts

$$\tilde{R}_{uv} = \tilde{R}_{vu} = \tilde{R}_{wv} = \tilde{R}_{vw} = 0$$

and $\qquad \tilde{R}_{vv} = g(\zeta).$

133

APPENDIX F

EVALUATION OF STATE DISPERSION MATRIX

We begin with the notation

$$\underline{\underline{\Sigma}}(t) \; \underline{\underline{\Delta}} < \underline{y}(t)\underline{y}^T(t) > \qquad (F.1)$$

where $\underline{y}(t)$ is the state response to turbulence, as governed by Eq. (8.84). From Eq. (3.14) we have

$$\underline{\underline{\Sigma}}(t) = \int_0^t \int_0^t \underline{\underline{H}}(t,t_1) \; \underline{\underline{R}}(t_1,t_2)\underline{\underline{H}}^T(t,t_2)dt_1dt_2 \qquad (F.2)$$

Our first task is to take advantage of the fact that the symmetry condition (3.12)

$$\underline{\underline{R}}(t_1,t_2) = \underline{\underline{R}}^T(t_2,t_1) \qquad (F.3)$$

exists; in fact, only $\underline{\underline{R}}$ values for $t_2 > t_1$ were measured in the wind-tunnel. Thus, for Eq. (F.2), we can write

$$\underline{\underline{\Sigma}}(t) = \int_{t_1=0}^{t} \int_{t_2=0}^{t_1} (\cdot)dt_1dt_2 + \int_{t_1=0}^{t} \int_{t_2=t_1}^{t} (\cdot)dt_1dt_2 \qquad (F.4)$$

and we use (F.3) in the first term. After reversing the roles of t_1 and t_2 and changing the order of integration in the first term, and defining

$$\tau = t_1$$
$$\sigma = t_2 - t_1 \qquad (F.5)$$

Eq. (F.4) becomes

$$\underline{\underline{\Sigma}}(t) = \int_0^t \int_0^{t-\tau} \underline{\underline{J}}(t,\tau,\sigma)d\sigma \; d\tau \qquad (F.6)$$

where

$$\underline{J}(t,\tau,\sigma) = \underline{H}(t,\tau) \; \underline{\mathfrak{R}}(\tau,\tau+\sigma)\underline{H}^{T}(t,\tau+\sigma)$$

$$+ \underline{H}(t,\tau+\sigma) \; \underline{\mathfrak{R}}^{T}(\tau,\tau+\sigma)\underline{H}^{T}(t,\tau) \qquad (F.7)$$

Note that since $\underline{J}^{T} = \underline{J}$, then $\underline{\Sigma}^{T} = \underline{\Sigma}$ as should be.

There are many possible approaches to the double integration in (F.6). A complicating factor is that the integrand depends explicitly on t. A second source of complexity is that the experimental data for $\underline{\mathfrak{R}}$ are not available in a uniform grid. In an attempt to circumvent these difficulties to some extent, the following procedure was employed, in which a differential equation for $\underline{\Sigma}$ was formulated. Denoting,

$$\underline{\mathbf{g}}(t,\tau) = \int_{0}^{t-\tau} \underline{J}(t,\tau,\sigma)d\sigma \qquad (F.8)$$

we can differentiate

$$\underline{\Sigma}(t) = \int_{0}^{t} \underline{\mathbf{g}}(t,\tau)d\tau \qquad (F.9)$$

by Leibnitz's Rule to obtain

$$\underline{\dot{\Sigma}}(t) = \int_{0}^{t} \underline{\dot{\mathbf{g}}}(t,\tau)d\tau + \underline{\mathbf{g}}(t,t) \qquad (F.10)$$

where the overdot indicates a partial differentiation with respect to t. However, from (F.8),

$$\underline{\mathbf{g}}(t,t) = \underline{0} \qquad (F.11)$$

and

$$\underline{\dot{\mathbf{g}}}(t,\tau) = \int_{0}^{t-\tau} \underline{\dot{J}}(t,\tau,\sigma)d\sigma + \underline{J}(t,\tau,t-\tau) \qquad (F.12)$$

135

Since

$$\underline{H}(t,\tau) = \exp[\underline{A}(t-\tau)] \; \underline{B} \qquad (F.13)$$

we have

$$\underline{J}(t,\tau,t-\tau) = \exp[\underline{A}(t-\tau)] \; \underline{B} \; \underline{R}(\tau,t) \; \underline{B}^T$$
$$+ \; \underline{B} \; \underline{R}^T(\tau,t) \; \underline{B}^T \; \exp[\underline{A}^T(t-\tau)] \qquad (F.14)$$

and it may similarly be shown that

$$\underline{\dot{J}}(t,\tau,\sigma) = \underline{A} \; \underline{J}(t,\tau,\sigma) + \underline{J}(t,\tau,\sigma) \; \underline{A}^T \qquad (F.15)$$

Thus (F.12) becomes

$$\underline{\dot{\mathscr{E}}}(t,\tau) = \underline{A} \; \underline{\mathscr{E}}(t,\tau) + \underline{\mathscr{E}}(t,\tau) \; \underline{A}^T + \underline{J}(t,\tau,t-\tau) \qquad (F.16)$$

where $\underline{J}$ may be regarded as the "source" term, and is given by (F.14). Substituting (F.16) into (F.10) yields

$$\underline{\dot{\Sigma}}(t) = \underline{A} \; \underline{\Sigma}(t) + \underline{\Sigma}(t) \; \underline{A}^T + \int_0^t \underline{J}(t,\tau,t-\tau)d\tau \qquad (F.17)$$

Alternatively, replacing $t-\tau$ by σ, we may rewrite (F.17) as

$$\underline{\dot{\Sigma}}(t) = \underline{A} \; \underline{\Sigma}(t) + \underline{\Sigma}(t) \; \underline{A}^T + \int_0^t \underline{J}(t,t-\sigma,\sigma)d\sigma \qquad (F.18)$$

where

$$\underline{J}(t,t-\sigma,\sigma) = \exp[\underline{A} \; \sigma] \; \underline{B} \; \underline{R}(t-\sigma,t) \; \underline{B}^T + \underline{B} \; \underline{R}^T(t-\sigma,t) \; \underline{B}^T \exp[\underline{A}^T\sigma] \quad (F.19)$$

The experimental (wind-tunnel) data are in the form of a table of values of

$$\underline{R}(t_i,t_i+\sigma_j); \quad i = 1, \; \ldots \; , \; N; \quad j = 1, \; \ldots \; , \; N_i \qquad (F.20)$$

136

At a given t_i, the value of $\underline{\mathbb{Q}}$ at other than σ_j is obtained by linear interpolation of the form

$$\underline{\mathbb{Q}}(t_i, t_i + \sigma) \cong \underline{\mathbb{Q}}(t_i, t_i + \sigma_j) + \left[\frac{\underline{\mathbb{Q}}(t_i, t_i + \sigma_{j+1}) - \underline{\mathbb{Q}}(t_i, t_i + \sigma_j)}{\sigma_{j+1} - \sigma_j} \right] (\sigma - \sigma_j) \quad \text{(F.21)}$$

With the aid of this interpolation formula, (F.19) then gives $\underline{J}(t_i, t_i - \sigma, \sigma)$ for all σ in the range $0 \leq \sigma \leq t$. A trapezoidal integration scheme is then indicated for the integral in (F.18), permitting finally the numerical solution for the differential equation for $\underline{\Sigma}(t)$. The initial condition on $\underline{\Sigma}$ is, from (F.2),

$$\underline{\Sigma}(0) = \underline{0} \quad \text{(F.22)}$$

In this manner, the dispersion matrix for the state variables may be computed for any point on the trajectory.

APPENDIX G

COMPUTER CODES

```
      IMPLICIT REAL*8(A-H,O-Z)
      REAL*8  MU,MASS,IYY,IIYY,KK,NDEX,KE
      COMPLEX *16 ZSIG(6),CEXPAS(6,6)
      COMPLEX Z(3)
      LOGICAL LAM
      LOGICAL*4 UU,UW,WU,WW,WANT,WANTV,WANTC
      REAL*4 A(4)
      COMPLEX*16 LAMAAD(6),UUAAD(6,6),DET,UUAADI(6,6)
      DIMENSION WWK(6,6)
      DIMENSION SOURCE(6,6)
      DIMENSION IIR(6),IIC(6)
      DIMENSION OO(6,6),OP(6)
      DIMENSION PROD(6,6)
      DIMENSION TADD(6,6)
      DIMENSION WR(6),WI(6),ZZ(6,6) ,FV1(6),IV1(6)
      DIMENSION AL(6,6),AR(6,6),ALINV(6,6),WK(66),XI(3),XR(3)
      DIMENSION BR(6,2),AGGAM(6,1),AWW(6,1),AG(6,2),AA(6,6),BBC(6,2),
     1A1(6,1),B(6,1),BB(6,2),
     1EE(2,6),BGGAM(2,1),EEAA(2,6),EEBBC(2,2),EEA(2,1),EEB(2,1),
     2EEBBCI(2,2),WK1(20),TEMP26(2,6),TEMP66(6,6),AAS(6,6),TEMP21(2,1),
     3TEMP61(6,1),AS(6,1),BS(6,1),TTMP21(2,1)
      DIMENSION Y(6),YP(6),WK2(30)
      DIMENSION EEBCE(2,6),EEBCB(2,1)
      DIMENSION SSGI(2,2),SSS(6,6),SSSI(6,6),AAD(6,6),BBD(6,2),
     1TEMP62(6,2),WK3(150),TS(7),NSIG(7),SIGSS(12,7),RRDATA(2,2,12,7),
     1YY(36),SIGSIG(6,6),YYP(36)
      DIMENSION TRR(11,7),DHGT(11,7),HGT(7)
      COMMON AA,B,A1,EEBCE,EEBCB,BBC,WWGGH,HGGH,NDEX,WWEH,DETA,DPI,SINGE
     1,HEHO,KE,CCZN,MU,CCZAD
      COMMON/PASS/LAMAAD,UUAAD,UUAADI
      COMMON/PASS/BBD,SIGSS,TS,RRDATA,NN,NSIG
      COMMON/SINGLE/AAD
      EXTERNAL LAND
      EXTERNAL CORREL
      LAM = .FALSE.
      RHO=0.002378
      SS=420.0
      C=6.5
      MASS=341.9D0
      MU=2.0D0*MASS/(RHO*SS*C)
      IIYY=23472.0
      IYY=8.0*IIYY/(RHO*SS*C**3)
C   CALCULATION OF REFERENCE EQUILIBRIUM VALUES
      NDEG=3
      PI=3.14159
      KK=0.0314
      CCDDO=0.242
      CCLLOO=1.576
      CCLLA=5.789
      CCDDCT=-0.75
      CCLLCT=0.55
      CCMCT=-0.1698
      CCZN=0.5236
      CCMN=2.068
      G=32.2
      WWGG=66.0
      RATIO=2.0
      VVE=RATIO*WWGG
```

139

```
        QE=RHO*VVE*VVE/2.0
        CCWWE=MASS*G/(QE*SS)
        PPMAX=3.575E5
        CCTTPI=6.5617*PPMAX/(QE*SS)*(0.1311/VVE+0.0021)
        HO=694.44
        H1=69.0
        HGG=1000.0
        HGGH=HGG/(C/2.0)
        NDEX=0.16D0
        GAMEE=15.0*PI/180.0
        WWE = 57.0D0
        WWEH=WWE/VVE
        WWGGH=WWGG/VVE
        VVEEE=DSQRT(VVE*VVE-WWE*WWE*DSIN(GAMEE)**2)-WWE*DCOS(GAMEE)
        GAME=DARSIN(VVEEE*DSIN(GAMEE)/VVE)
        COSGE=DCOS(GAME)
        SINGE=DSIN(GAME)
        TANGE=SINGE/COSGE
        TT=(HO-H1)/VVE/SINGE
        A(1)=KK
        A(2)=-KK*CCLLOO
        A(3)=CCLLA+CCDDO-CCWWE*SINGE
        A(4)=-CCLLOO*(CCDDO-CCWWE*SINGE)-CCLLA*CCWWE*COSGE
C   USE IMSL SUBROUTINE ZPOLYR TO FIND THE ROOTS OF THE POLYNOMIAL
C   A(1)*X**NDEG+A(2)*X**(NDEG-1)+..................
C   Z IS A COMPLEX ARRAY
        CALL ZPOLYR(A,NDEG,Z,Z,IER)
        WRITE(6,10) IER
10      FORMAT(1H1,'ERROR CODE = ',I6)
        DO 11 I=1,3
         XR(I)=REAL(Z(I))
11      XI(I)=AIMAG(Z(I))
        DO 12 K=1,3
        IF(XI(K) .NE. 0.0) GO TO 13
12      CONTINUE
        WRITE(6,100)
100     FORMAT(1H1,'THREE REAL ROOTS ARE')
        WRITE(6,101) XR
101     FORMAT(1H0,1P3E20.6)
        GO TO 14
13      DO 21 K=1,3
        IF (XI(K) .EQ. 0.0) GO TO 22
21      CONTINUE
22      CCLLE=XR(K)
14      CCDDE=CCDDO+KK*CCLLE**2
        CCTTE=CCDDE-CCWWE*SINGE
        DALF=(CCLLE-CCLLOO)/CCLLA
        WRITE(6,105) CCLLE,CCDDE,CCTTE,DALF
105     FORMAT(1H0'CCLLE = ',1PE14.6,5X,'CCDDE = ',1PE14.6,5X,'CCTTE = ',
       11PE14.6,5X,'DALF = ',1PE14.5)
        CCLLEA=CCWWE*COSGE
        CCDDEA=CCDDO+KK*CCLLEA**2
        CCTTEA=CCDDEA-CCWWE*SINGE
        WRITE(6,106) CCLLEA,CCDDEA,CCTTEA,RATIO
106     FORMAT(1H0,'CCLLEA = ',1PE14.6,5X,'CCDDEA = ',1PE14.6,5X,
       1'CCTTEA = ',1PE14.6,2X,'RATIO = ',1PE9.2)
C   THIS COMPLETES A CALCULATION OF THE REFERENCE EQUILIBRIUM CONDITIONS
        CCLLS=CCWWE*COSGE
```

```
                CCXU=-2.0*(CCDDE-CCLLS*TANGE)
                CCDDA=2.0*KK*CCLLE*CCLLA
                CCXA=CCLLS-CCDDA
                CCZA=-(CCLLA+CCDDE)
                CCZAD=-2.150
                CCZQ=-7.144
                CCMA=-2.026
                CCMAD=-8.663
                CCMQ=-28.76
                DO 31 I=1,6
                DO 31 J=1,6
                AL(I,J)=0.0
       31       AR(I,J)=0.0
                AL(1,1)=2.0*MU
                AL(2,2)=2.0*MU-CCZAD
                AL(3,2)=-CCMAD
                AL(3,3)=IYY
                AL(4,4)= 1.0
                AL(5,5)=1.0
                AL(6,6)=1.0
                AR(1,1)=-2.0*CCLLS*TANGE+CCXU
                AR(1,2)=CCXA
                AR(1,4)=-CCLLS
                AR(2,1)=-2.0*CCLLS
                AR(2,2)=CCZA
                AR(2,3)=2.0*MU+CCZQ
                AR(2,4)= CCLLS*TANGE
                AR(3,2)=CCMA
                AR(3,3)=CCMQ
                AR(4,3)=1.0
                AR(5,1)=COSGE
                AR(5,2)=-SINGE
                AR(5,4)=SINGE
                AR(6,1)=-SINGE
                AR(6,2)=-COSGE
                AR(6,4)=COSGE
                IDGT=0
                CALL LINV2F(AL,6,6,ALINV,IDGT,WK,IER)
                WRITE(6, 88) IER
       88       FORMAT(1H0,'ERROR CODE = ',I6)
                DO 44 I=1,6
                DO 44 J=1,2
       44       AG(I,J)=AR(I,J)
                AG(5,1) = 0.
                AG(5,2) = 0.
                AG(6,1) = 0.
                 AG(6,2) = 0.
                CALL MATML(6,6,6,ALINV,AR,AA)
                CALL MATML(6,6,2,ALINV,AG,BB)
       C ......
                IF(LAM) GO TO 1000
                SSGI(1,1)=-COSGE/VVE
                SSGI(2,2)=SSGI(1,1)
                SSGI(2,1)=SINGE/VVE
                SSGI(1,2)=-SSGI(2,1)
                DO 300 I=1,6
                DO 300 J=1,6
                SSS(I,J)=0.0D0
```

141

```
300      SSSI(I,J)=0.0D0
         SSS(1,1)=VVE
         SSS(2,2)=1.0D0
         SSS(3,3)=2.0D0*VVE/C
         SSS(4,4)=1.0D0
         SSS(5,5)=C/2.0D0
         SSS(6,6)=C/2.0D0
         DO 301 I=1,6
301       SSSI(I,I)=1.0D0/SSS(I,I)
         CALL MATML(6,6,2,SSS,BB,TEMP62)
         CALL MATML(6,2,2,TEMP62,SSGI,BBD)
         DO 302 I=1,6
         DO 302 J=1,2
302      BBD(I,J)=BBD(I,J)*2.0D0*VVE/C
         CALL MATML(6,6,6,SSS,AA,TEMP66)
         CALL MATML(6,6,6,TEMP66,SSSI,AAD)
         DO 303 I=1,6
         DO 303 J=1,6
303      AAD(I,J)=AAD(I,J)*2.0D0*VVE/C
         DO 777 I=1,6
         DO 777 J=1,6
777      TADD(I,J)=AAD(I,J)
         MATZ=1
          CALL RG(6,6,TADD,WR,WI,MATZ,ZZ,IV1,FV1,IER)
         DO 781 I=1,6
781      LAMAAD(I)=DCMPLX(WR(I),WI(I))
         KK=1
84       IF(WI(KK) .NE. 0.0D0) GO TO 81
         DO 82 I=1,6
82       UUAAD(I,KK)=ZZ(I,KK)
         KK=KK+1
         IF(KK .GT. 6) GO TO 83
         GO TO 84
81       CONTINUE
         DO 85 I=1,6
         UUAAD(I,KK)=DCMPLX(ZZ(I,KK),ZZ(I,KK+1))
85       UUAAD(I,KK+1)=DCONJG(UUAAD(I,KK))
         KK=KK+2
         IF(KK .LE. 6) GO TO 84
83       CONTINUE
         DO 780 I=1,6
         DO 780 J=1,6
780      UUAADI(I,J)=UUAAD(I,J)
C   INVERT THE COMPLEX MATRIX UUAADI
         CALL MINVCD(UUAADI,6,6,DET,IIR,IIC)
CC   THIS IS THE WIND TUNNEL DATA
         IVELW = 3
         NN = 7
         DO 700 N=1,5
700      NSIG(N) = 10
         NSIG(6) = 11
         NSIG(7) = 11
         NTABLE=27
         DO 704 K=1,NTABLE
         DO 701 N=1,NN
         READ(5,702) IVEL,IR,IC
702      FORMAT(3I2)
         WANTV = IVEL .EQ. IVELW
```

142

```
        UU = IR .EQ. 1 .AND. IC .EQ. 1
        UW = IR .EQ. 1 .AND. IC .EQ. 3
        WU = IR .EQ. 3 .AND. IC .EQ. 1
        WW = IR .EQ. 3 .AND. IC .EQ. 3
        WANTC = UU .OR. UW .OR. WU .OR. WW
        WANT = WANTV .AND. WANTC
        READ(5,703) HGT(N),(DHGT(M,N),TRR(M,N),M=1,11)
703     FORMAT(8E10.3)
        IF(.NOT. WANT) GO TO 701
        TS(N) = (HO - HGT(N))/VVE/SINGE
        MM = NSIG(N)
        MMM1 = MM - 1
        DO 708 M=1,MMM1
        SIGSS(M,N) = DHGT(M,N)/VVE/SINGE
        IF(UU)      RRDATA(1,1,M,N) = TRR(M,N)
        IF(UW)      RRDATA(1,2,M,N) = TRR(M,N)
        IF(WU)      RRDATA(2,1,M,N) = TRR(M,N)
708     IF(WW)      RRDATA(2,2,M,N) = TRR(M,N)
        SIGSS(MM,N) = TT-TS(N)
        DO 709 I=1,2
        DO 709 J=1,2
709     RRDATA(I,J,MM,N) = 0.0
701     CONTINUE
704     CONTINUE
C******* END OF TUNNEL DATA INPUT
        TTINT = TT/10.0D0
        DO 308 I=1,36
308     YY(I)=0.0D0
        IN=1
        SA=0.0D0
        FIN = TTINT
555     H=TTINT/15.0D0
        CALL RKGIL(YY,36,SA,FIN,H,CORREL)
        DO 309 I=1,6
        DO 309 J=1,6
        INDEX=6*(J-1)+I
309     SIGSIG(I,J)=YY(INDEX)
        WRITE(6,536) FIN
536     FORMAT(1H0,'FIN = ',1PE20.6)
        WRITE(6,534)
534     FORMAT(1H0,'SIGSIG VALUES')
        WRITE(6,533) ((SIGSIG(I,J),J=1,6),I=1,6)
533     FORMAT(1H ,1P6D18.8)
        IN=IN+1
        IF(IN .GT. 10) STOP
        SA = SA + TTINT
        FIN = FIN + TTINT
        GO TO 555
C ......
1000    KE=DSIN(GAMEE)/DCOS(GAMEE-GAME)
        DO 41 I=1,6
        DO 41 J=1,2
41      BR(I,J)=0.0
        BR(1,2)=-CCDDCT*CCTTPI
        BR(2,1)=CCZN
        BR(2,2)=-(CCLLCT+DALF)*CCTTPI
        BR(3,1)=CCMN
        BR(3,2)=CCMCT*CCTTPI
```

```
        DO 42 I=1,6
 42     AGGAM(I,1)=0.0
        AGGAM(1,1)=2.0*MU*COSGE
        AGGAM(2,1)=-2.0*MU*SINGE
        DO 43 I=1,6
 43     AWW(I,1)=0.0
        AWW(5,1)=-1.0
        CALL MATML(6,6,2,ALINV,BR,BBC)
        CALL MATML(6,6,1,ALINV,AGGAM,A1)
        CALL MATML(6,6,1,ALINV,AWW,B)
        DO 45 I=1,2
        DO 45 J=1,6
 45     EE(I,J)=0.0
        EE(1,1)=1.0
        EE(2,2)=-1.0
        EE(2,4)=1.0
        BGGAM(1,1)=0.0
        BGGAM(2,1)=KE
        CALL MATML(2,6,6,EE,AA,EEAA)
        CALL MATML(2,6,2,EE,BBC,EEBBC)
        CALL MATML(2,6,1,EE,A1,EEA)
        CALL MATML(2,6,1,EE,B,EEB)
C    INVERT EEBBC AND CALL IT EEBBCI
        IDGT=0
        CALL LINV2F(EEBBC,2,2,EEBBCI,IDGT,WK1,IER)
        WRITE(6,88)IER
        CALL MATML(2,2,6,EEBBCI,EE,EEBCE)
        CALL MATML(2,2,1,EEBBCI,BGGAM,EEBCB)
        HEHO=HO/(C/2.0)
        HEH1=H1/(C/2.0)
        DELT=(HEHO-HEH1)/100.0/SINGE
        HEH=HEHO
C    SET INITIAL VALUES
        DO 333 L=1,6
333     Y(L)=0.0
C    USE IMSL SUBROUTINE TO SOLVE THE THE SYSTEM OF DIFFERENTIAL EQUATIONS
C    SA IS STARTING POINT AND FIN IS FINAL POINT OF INTEGRATION
C    H IS INITIAL GUESS OF THE INTEGRATION STEP SIZE WHICH WILL BE ADJUSTED
        SA=0.0
 46     FIN=SA+DELT
        H=DELT
        CALL DASCRU(LAND,SA,FIN,H,6,Y,WK2,IER)
        WRITE(6,88) IER
        WRITE(6,89) H
 89     FORMAT(1H0,'ADJUSTED STEP SIZE = ',E13.3)
        WRITE(6,95) DETA,DPI
 95     FORMAT(1H ,'DETA = ',E20.5,10X,'DPI = ',E20.5)
        WRITE(6,90) FIN
 90     FORMAT(1H0,'SOLUTIONS AT POINT',2X,1PE20.5)
        WRITE(6,91) Y
 91     FORMAT(1H0,1P6E20.5)
        SA=FIN
        IF((HEHO-SINGE*SA+Y(6)) .LE. HEH1) GO TO 47
        GO TO 46
 47     STOP
        END
```

144

```
        SUBROUTINE RKGIL(Y,NORD,A,B,H,DER)
        IMPLICIT REAL*8(A-H,O-Z)
        DIMENSION Y(36),Z1(36),YY1(36),P(10),Q1(36),YPRIM(36)
        R2=SQRT(2.)                                              RKGIL002
C       A1=1.-0.5*R2                                             RKGIL003
        A1=0.2928933                                             RKGIL004
C       A2=-2.+3./R2                                             RKGIL005
        A2=0.1213205                                             RKGIL006
C       A3=2.-R2                                                 RKGIL007
        A3=0.5857867                                             RKGIL008
C       A4=1.+1./R2                                              RKGIL009
        A4=1.7071070                                             RKGIL010
C       A5=-2.-3./R2                                             RKGIL011
        A5=-4.1213207                                            RKGIL012
C       A6=2.+R2                                                 RKGIL013
        A6=3.4142136                                             RKGIL014
C       A7=1./6.                                                 RKGIL015
        A7=0.1666666                                             RKGIL016
C       A8=-1./3.
        A8=-0.3333333                                            RKGIL018
        NSTEP=0.5+(B-A)/H
        L=0                                                      RKGIL020
        X=A                                                      RKGIL021
100     CALL DER(NORD,X,Y,YPRIM)                                 RKGIL022
        DO 1  I=1,NORD                                           RKGIL023
        Z1(I)=YPRIM(I)*H                                         RKGIL024
        YY1(I)=Y(I) + 0.5*Z1(I)                                  RKGIL025
1       Q1(I)=Z1(I)                                              RKGIL026
        CALL DER(NORD,X+0.5*H,YY1,YPRIM)
        DO 2  I=1,NORD                                           RKGIL028
        Z1(I)=YPRIM(I)*H                                         RKGIL029
        YY1(I)=YY1(I) +  A1*(Z1(I)-Q1(I))                        RKGIL030
2       Q1(I)=A2*Q1(I)+A3*Z1(I)                                  RKGIL031
        CALL DER(NORD,X+0.5*H,YY1,YPRIM)
        DO 3  I=1,NORD                                           RKGIL033
        Z1(I)=  YPRIM(I)*H                                       RKGIL034
        YY1(I)=YY1(I) + A4*(Z1(I) -Q1(I))                        RKGIL035
3       Q1(I)=A5*Q1(I) +A6*Z1(I)                                 RKGIL036
        CALL DER(NORD,X+H,YY1,YPRIM)
        DO 4  I=1,NORD                                           RKGIL038
        Z1(I)=YPRIM(I)*H                                         RKGIL039
4       Y(I)= YY1(I) + A7*Z1(I) + A8*Q1(I)                       RKGIL040
        X=X+H                                                    RKGIL041
        L=L+1                                                    RKGIL042
        IF(L-NSTEP)100,5,5                                       RKGIL043
5       B=X
        RETURN
        END                                                      RKGIL045
```

```
      SUBROUTINE CORREL(NORD,T,YY,YYP)
      IMPLICIT REAL*8(A-H,O-Z)
      DIMENSION SOURCE(6,6),AAD(6,6),BBD(6,2),SIGSS(12,7),TS(7),NSIG(7),
     1RRDATA(2,2,12,7),SIGSIG(6,6),SIGP(6,6),YY(36),YYP(36)
      COMPLEX*16 LAMAAD(6),UUAAD(6,6),UUAADI(6,6)
      COMMON/PASS/LAMAAD,UUAAD,UUAADI
      COMMON/PASS/BBD,SIGSS,TS,RRDATA,NN,NSIG
      COMMON/SINGLE/AAD
      DO 1 I=1,6
      DO 1 J=1,6
      INDEX=6*(J-1)+I
    1 SIGSIG(I,J)=YY(INDEX)
      CALL VALINT(T,SOURCE,BBD,SIGSS,NN,TS,NSIG,RRDATA)
      DO 2 I=1,6
      DO 2 J=1,6
      SIGP(I,J)=SOURCE(I,J)
      DO 2 K=1,6
    2 SIGP(I,J)=SIGP(I,J)+SIGSIG(I,K)*AAD(J,K)
      DO 3 I=1,6
      DO 3 J=1,6
      DO 3 K=1,6
    3 SIGP(I,J)=SIGP(I,J)+AAD(I,K)*SIGSIG(K,J)
      DO 4 I=1,6
      DO 4 J=1,6
      INDEX=6*(J-1)+I
    4 YYP(INDEX)=SIGP(I,J)
      RETURN
      END
```

```
       SUBROUTINE VALINT(T,SOURCE,BBD,SIGSS,NN,TS,NSIG,RRDATA)
       IMPLICIT REAL*8(A-H,O-Z)
       DIMENSION X(21),SOURCE(6,6),AAD(6,6),BBD(6,2),SIGSS(12,7),TS(7),
      1NSIG(7),RRDATA(2,2,12,7)
       REAL*8  IINT(6,6)
       NX=20
       NXM1 = NX - 1
       DEL = T/DFLOAT(NXM1)
       X(1)=0.0D0
       DO 1 M = 2,NX
    1  X(M) = DFLOAT(M-1)*DEL
       CALL FIND(T,0.0D0,IINT,BBD,SIGSS,NN,TS,NSIG,RRDATA)
       DO 2 I=1,6
       DO 2 J=1,6
    2  SOURCE(I,J)=IINT(I,J)
       DO 3 M = 2,NXM1
       SIG=X(M)
       TMS=T-SIG
       CALL FIND(TMS,SIG,IINT,BBD,SIGSS,NN,TS,NSIG,RRDATA)
       DO 4 I=1,6
       DO 4 J=1,6
    4  SOURCE(I,J)=SOURCE(I,J)+2.0D0*IINT(I,J)
    3  CONTINUE
       SIG = X(NX)
       TMS=T-SIG
       CALL FIND(TMS,SIG,IINT,BBD,SIGSS,NN,TS,NSIG,RRDATA)
       DO 5 I=1,6
       DO 5 J=1,6
    5  SOURCE(I,J)=SOURCE(I,J)+IINT(I,J)
       DO 6 I=1,6
       DO 6 J=1,6
    6  SOURCE(I,J)=DEL/2.0D0*SOURCE(I,J)
       RETURN
       END
```

147

```
      SUBROUTINE FIND(T,SIG,IINT,BBD,SIGSS,NN,TS,NSIG,RRDATA)
      IMPLICIT REAL*8(A-H,O-Z)
      DIMENSION RRDATA(2,2,12,7),TS(7),NSIG(7),SIGSS(12,7),AAD(6,6),
     1BBD(6,2),TEMP66(6,6),SIGS(12)
      REAL*8 IINT1D(6,6,7),IINT(6,6)
      NNM1=NN-1
      DO 1 N=1,NNM1
      IF(T .LE. TS(N+1)+SIG) GO TO 2
1     CONTINUE
2      NP1=N+1
      MM=NSIG(N)
      DO 3 M=1,MM
3     SIGS(M)=SIGSS(M,N)
      CALL FIND2(N,SIG,TEMP66,BBD,SIGS,MM,RRDATA)
      DO 4 I=1,6
      DO 4 J=1,6
4     IINT1D(I,J,N)=TEMP66(I,J)
      MM=NSIG(NP1)
      DO 5 M=1,MM
5     SIGS(M)=SIGSS(M,NP1)
      CALL FIND2(NP1,SIG,TEMP66,BBD,SIGS,MM,RRDATA)
      DO 6 I=1,6
      DO 6 J=1,6
6     IINT1D(I,J,NP1)=TEMP66(I,J)
      DO 7 I=1,6
      DO 7 J=1,6
7     IINT(I,J)=IINT1D(I,J,N)+(IINT1D(I,J,NP1)-IINT1D(I,J,N))/(TS(NP1)
     1-TS(N))*(T-(TS(N)+SIG))
      RETURN
      END
```

```
      SUBROUTINE FIND2(N,SIG,IINT1D,BBD,SIGS,MM,RRDATA)
      IMPLICIT REAL*8(A-H,O-Z)
      COMPLEX*16 LAMAAD(6),UUAAD(6,6),UUAADI(6,6) ,CDEXP
      COMPLEX*16 ZSIG(6),CEXPAS(6,6)
      DIMENSION RRDATA(2,2,12,7),AAD(6,6),EXPAS(6,6),BBD(6,2),PRODT(2,6)
     1,SIGS(12),TEMP62(6,2),WK(6,6),W(6),TEMP22(2,2),TEMP66(6,6)
      REAL*8 IINT1D(6,6)
      COMMON/PASS/LAMAAD,UUAAD,UUAADI
      COMMON/SINGLE/AAD
      MMM1=MM-1
      DO 11 I=1,6
      ZSIG(I)=LAMAAD(I)*SIG
11    ZSIG(I)=CDEXP(ZSIG(I))
      DO 12 I=1,6
      DO 12 J=1,6
      CEXPAS(I,J)= (0.0D0,0.0D0)
      DO 12 K=1,6
12    CEXPAS(I,J)=CEXPAS(I,J)+UUAAD(I,K)*ZSIG(K)*UUAADI(K,J)
      DO 15 I=1,6
      DO 15 J=1,6
15    EXPAS(I,J)=CEXPAS(I,J)
      CALL MATML(6,6,2,EXPAS,BBD,TEMP62)
      DO 1 I=1,2
      DO 1 J=1,6
1     PRODT(I,J)=TEMP62(J,I)
      DO 2 M=1,MMM1
      IF(SIG .LE. SIGS(M+1)) GO TO 3
2     CONTINUE
3     DO 4 I=1,2
      DO 4 J=1,2
4     TEMP22(J,I)=RRDATA(I,J,M,N)+(RRDATA(I,J,M+1,N)-RRDATA(I,J,M,N))
     1/(SIGS(M+1)-SIGS(M))*(SIG-SIGS(M))
      CALL MATML(6,2,2,BBD,TEMP22,TEMP62)
      CALL MATML(6,2,6,TEMP62,PRODT,TEMP66)
      DO 5 I=1,6
      DO 5 J=1,6
5     IINT1D(I,J)=TEMP66(I,J)+TEMP66(J,I)
      RETURN
      END
```

```
      SUBROUTINE LAND(Y,THAT,L,YP)
      IMPLICIT REAL*8(A-H,O-Z)
      REAL*8 N ,KE,MU
      DIMENSION Y(6),YP(6),AA(6,6),B(6,1),A1(6,1),EEBCE(2,6),EEBCB(2,1),
     1BBC(6,2),TEMP61(6),DU(2)
      COMMON AA,B,A1,EEBCE,EEBCB,BBC,WWGGH,HGGH,N,WWEH,DETA,DPI,SINGE,
     1HEHO,KE,CCZN,MU,CCZAD
      HH=HEHO-SINGE*THAT+Y(6)
      RATIO=WWGGH/HGGH*(HH/HGGH)**(N-1.0)
      GGAMH=N*RATIO*(-SINGE)
      DELWWH=HH*RATIO-WWEH
      DO 1 I=1,6
      TEMP61(I)=A1(I,1)*GGAMH+B(I,1)*DELWWH
      DO 1 J=1,6
    1 TEMP61(I)=TEMP61(I)+AA(I,J)*Y(J)
      DO 2 I=1,2
      DU(I)=EEBCB(I,1)*GGAMH
      DO 2 J=1,6
    2 DU(I)=DU(I)-EEBCE(I,J)*TEMP61(J)
      DU(1)=-0.05*(Y(6)+ 10*TEMP61(6))
      IF(DABS(DU(1)).LT.0.35) GO TO 10
      DU(1)=DU(1)/DABS(DU(1))*0.35
   10 CONTINUE
      DU(2) = 2.D0*DELWWH
      DO 3 I=1,6
      YP(I)=TEMP61(I)
      DO 3 J=1,2
    3 YP(I)=YP(I)+BBC(I,J)*DU(J)
      DETA=DU(1)
      DPI=DU(2)
      RETURN
      END
```

150

```
      SUBROUTINEMINVCD(A,IA,MA,DETA,IR,IC)                 00000000
      IMPLICITREAL*8(A-H,O-Z)                              00001000
      COMPLEX*16A(IA,IA),PIV,DETA,TEMP,PIV1                00002000
      DIMENSIONIR(MA),IC(MA)                               00003000
      DO1I=1,MA                                            00004000
      IR(I)=0                                              00005000
   1  IC(I)=0                                              00006000
      DETA=(1.0D0,0.0D0)                                   00007000
      S=0.0D0                                              00008000
      R=MA                                                 00009000
   2  CALLSUBMCD(A,IA,IA,MA,MA,IR,IC,I,J)                  00010000
      PIV=A(I,J)                                           00011000
      DETA=PIV*DETA                                        00012000
      Y=CDABS(PIV)                                         00013000
      IF(Y.EQ.0.)GOTO17                                    00014000
      IR(I)=J                                              00015000
      IC(J)=I                                              00016000
      PIV=(1.0D0,0.0D0)/PIV                                00017000
      A(I,J)=PIV                                           00018000
      DO5K=1,MA                                            00019000
   5  IF(K.NE.J)A(I,K)=A(I,K)*PIV                          00020000
      DO9K=1,MA                                            00021000
      IF(K.EQ.I)GOTO9                                      00022000
      PIV1=A(K,J)                                          00023000
   6  DO8L=1,MA                                            00024000
   8  IF(L.NE.J)A(K,L)=A(K,L)-PIV1*A(I,L)                  00025000
   9  CONTINUE                                             00026000
      DO11K=1,MA                                           00027000
  11  IF(K.NE.I)A(K,J)=-PIV*A(K,J)                         00028000
      S=S+1.0D0                                            00029000
      IF(S.LT.R)GOTO2                                      00030000
  12  DO16I=1,MA                                           00031000
      K=IC(I)                                              00032000
      M=IR(I)                                              00033000
      IF(K.EQ.I)GOTO16                                     00034000
      DETA=-DETA                                           00035000
      DO14L=1,MA                                           00036000
      TEMP=A(K,L)                                          00037000
      A(K,L)=A(I,L)                                        00038000
  14  A(I,L)=TEMP                                          00039000
      DO15L=1,MA                                           00040000
      TEMP=A(L,M)                                          00041000
      A(L,M)=A(L,I)                                        00042000
  15  A(L,I)=TEMP                                          00043000
      IC(M)=K                                              00044000
      IR(K)=M                                              00045000
  16  CONTINUE                                             00046000
      RETURN                                               00047000
  17  WRITE(6,18)                                          00048000
  18  FORMAT(' MATRIX IS SINGULAR')                        00049000
      RETURN                                               00050000
      END                                                  00051000
```

```
        SUBROUTINESUBMCD(A,IA,JA,MA,NA,IR,IC,I,J)        00000000
        IMPLICITREAL*8(A-H,O-Z)                          00001000
        COMPLEX*16A(IA,JA)                               00002000
        DIMENSIONIR(MA),IC(NA)                           00003000
        I=0                                              00004000
        J=0                                              00005000
        TEST=0.0D0                                       00006000
        DO5K=1,MA                                        00007000
        IF(IR(K).NE.0)GOTO5                              00008000
        DO4L=1,NA                                        00009000
        IF(IC(L).NE.0)GOTO4                              00010000
        X=CDABS(A(K,L))                                  00011000
        IF(X.LT.TEST)GOTO4                               00012000
        I=K                                              00013000
        J=L                                              00014000
        TEST=X                                           00015000
    4   CONTINUE                                         00016000
    5   CONTINUE                                         00017000
        RETURN                                           00018000
        END                                              00019000
```

```
      SUBROUTINE MATML(L,M,N,A,B,C)
      IMPLICIT REAL*8(A-H,O-Z)
      DIMENSION A(L,M),B(M,N),C(L,N)
      DO 1 I=1,L
      DO 1 J=1,N
      C(I,J)=0.0
      DO 2 K=1,M
    2 C(I,J)=C(I,J)+A(I,K)*B(K,J)
    1 CONTINUE
      RETURN
      END
```

```
        SUBROUTINE MATSUB(L,M,A,B,C)
        IMPLICIT REAL*8(A-H,O-Z)
        DIMENSION A(L,M),B(L,M),C(L,M)
        DO 1 I=1,L
         DO 1 J=1,M
  1     C(I,J)=A(I,J)-B(I,J)
        RETURN
        END
```

TABLE 1

FLIGHT PATH TIME HISTORY

γ_E = 45 DEGREES, V/W$_G$ = 1.20, V = 81.5 FPS

FULL SCALE – W/68 = (Z/1000)** 0.16
MODEL– – W/34 = (Z'/7)** 0.16

FULL SCALE								MODEL		
z ft.	W fps	V_E fps	$V_E \cos\gamma_E$	$V_E \sin\gamma_E$	t sec	γ deg	V/W	V'_E fps	z' in.	t' sec.
858.0	66.3	19.8	14.0	14.0	0.0	9.9	1.22	9.9	6.006	0.00000
850.8	66.2	19.9	14.1	14.1	0.5	9.9	1.23	9.9	5.955	0.00059
843.7	66.1	20.0	14.1	14.1	1.0	10.0	1.23	10.0	5.905	0.00117
836.5	66.0	20.1	14.2	14.2	1.5	10.0	1.23	10.0	5.855	0.00176
829.4	65.9	20.2	14.3	14.3	2.0	10.1	1.23	10.1	5.805	0.00234
822.2	65.9	20.3	14.4	14.4	2.5	10.1	1.23	10.1	5.755	0.00292
815.1	65.8	20.4	14.4	14.4	2.9	10.2	1.23	10.2	5.705	0.00349
807.9	65.7	20.6	14.5	14.5	3.4	10.2	1.24	10.3	5.655	0.00407
800.8	65.6	20.7	14.6	14.6	3.9	10.3	1.24	10.3	5.605	0.00463
793.7	65.5	20.8	14.7	14.7	4.4	10.3	1.24	10.4	5.555	0.00520
786.5	65.4	20.9	14.8	14.8	4.9	10.4	1.24	10.4	5.505	0.00575
779.4	65.3	21.0	14.8	14.8	5.4	10.5	1.24	10.5	5.455	0.00632
772.2	65.2	21.1	14.9	14.9	5.9	10.5	1.25	10.5	5.405	0.00688
765.1	65.1	21.2	15.0	15.0	6.3	10.6	1.25	10.6	5.355	0.00743
757.9	65.0	21.4	15.1	15.1	6.8	10.6	1.25	10.7	5.305	0.00799
750.8	64.9	21.5	15.2	15.2	7.3	10.7	1.25	10.7	5.255	0.00853
743.7	64.8	21.6	15.2	15.2	7.7	10.8	1.25	10.8	5.205	0.00908
736.5	64.7	21.7	15.3	15.3	8.2	10.8	1.26	10.8	5.155	0.00962
729.4	64.6	21.8	15.4	15.4	8.7	10.9	1.26	10.9	5.105	0.01016
722.2	64.5	21.9	15.5	15.5	9.1	10.9	1.26	10.9	5.055	0.01069
715.1	64.4	22.1	15.6	15.6	9.6	11.0	1.26	11.0	5.005	0.01123
707.9	64.3	22.2	15.7	15.7	10.0	11.1	1.26	11.1	4.955	0.01176
700.8	64.2	22.3	15.8	15.8	10.5	11.1	1.27	11.1	4.905	0.01228
693.7	64.1	22.4	15.9	15.8	10.9	11.2	1.27	11.2	4.855	0.01281
686.5	64.0	22.6	15.9	15.9	11.4	11.2	1.27	11.3	4.805	0.01333
679.4	63.9	22.7	16.0	16.0	11.8	11.3	1.27	11.3	4.755	0.01385
672.2	63.8	22.8	16.1	16.1	12.3	11.4	1.27	11.4	4.705	0.01436
665.1	63.7	22.9	16.2	16.2	12.7	11.4	1.28	11.4	4.655	0.01488
657.9	63.5	23.1	16.3	16.3	13.1	11.5	1.28	11.5	4.605	0.01539
650.8	63.4	23.2	16.4	16.4	13.6	11.6	1.28	11.6	4.555	0.01589
643.7	63.3	23.3	16.5	16.5	14.0	11.6	1.28	11.6	4.505	0.01640
636.5	63.2	23.5	16.6	16.6	14.4	11.7	1.28	11.7	4.455	0.01690
629.4	63.1	23.6	16.7	16.7	14.9	11.8	1.29	11.8	4.405	0.01740
622.2	63.0	23.7	16.8	16.8	15.3	11.8	1.29	11.8	4.355	0.01789
615.1	62.9	23.9	16.9	16.9	15.7	11.9	1.29	11.9	4.305	0.01839
607.9	62.7	24.0	17.0	17.0	16.1	12.0	1.29	12.0	4.255	0.01888
600.8	62.6	24.1	17.1	17.1	16.5	12.1	1.30	12.0	4.205	0.01936
593.6	62.5	24.3	17.2	17.2	17.0	12.1	1.30	12.1	4.155	0.01985
586.5	62.4	24.4	17.3	17.3	17.4	12.2	1.30	12.2	4.105	0.02033
579.4	62.3	24.6	17.4	17.4	17.8	12.3	1.30	12.3	4.055	0.02081
572.2	62.1	24.7	17.5	17.5	18.2	12.3	1.31	12.3	4.005	0.02128
565.1	62.0	24.9	17.6	17.6	18.6	12.4	1.31	12.4	3.955	0.02176
557.9	61.9	25.0	17.7	17.7	19.0	12.5	1.31	12.5	3.905	0.02223
550.8	61.8	25.1	17.8	17.8	19.4	12.6	1.32	12.5	3.855	0.02270
543.6	61.6	25.3	17.9	17.9	19.8	12.6	1.32	12.6	3.805	0.02316
536.5	61.5	25.4	18.0	18.0	20.2	12.7	1.32	12.7	3.755	0.02362

TABLE 2

VALUES OF PROBE VELOCITIES AT POINTS A & B

FOR $W_G = 68$ fps, $W_G' = 34$ fps, $Z_G' = 3$ ft.

Y_E	V/W_G	v fps (full scale)	V' fps (model)	n = 0.16, Z_G = 1000 Ft. A: z'=31'', z=860' t sec.	A: z'=31'', z=860' V_E' fps	B: z'=3'', z=83' t sec.	B: z'=3'', z=83' V_E' fps	n = 0.35, Z_G = 1600 Ft. A: z'=31'', z=1370' t sec.	A: z'=31'', z=1370' V_E' fps	B: z'=3'', z=133' t sec.	B: z'=3'', z=133' V_E' fps
15°	1.0	68.0	34.0	0	0.85	3.03	11.3	0	1.8	1.46	19.9
	1.2	81.5	40.7	0	7.8	.817	18.1	0	8.8	.621	26.8
	1.5	102	51.0	0	18.2	.416	28.5	0	19.2	.354	37.1
	1.9	129	64.5	0	31.9	.254	42.2	0	32.9	.228	50.7
45°	1.0	68.0	34.0	0	1.1	.841	13.7	0	2.4	.419	22.3
	1.2	81.5	40.7	0	9.9	.243	21.2	0	11.0	.190	29.4
	1.5	102	51.0	0	21.8	.130	32.1	0	22.8	.113	39.9
	1.9	129	64.5	0	36.7	.0818	46.3	0	37.6	.0750	53.7
90°	1.0	68	34	0	7.4	.161	25.2	0	10.8	.232	30.8
	1.2	81.5	40.7	0	23.7	.084	33.6	0	25.0	.150	38.0

TABLE 3

PROBE VELOCITIES AND MAXIMUM ACCELERATIONS
FOR ALL CASES STUDIED

	Velocity Range, fps	Max.Starting Accel. fps^2	Max.Stopping Accel. fps^2	Largest Accel. During Run fps^2
Non-frozen flow	0 – ~40	~300	~ -2900	~500
Frozen flow, $\epsilon = 90^\circ$ for $\gamma_E = 15^\circ, 45^\circ$ and $\epsilon = 45^\circ$ for $\gamma_E = 90^\circ$	0 – ~20	~130	~ -65	~-40
Frozen flow $\epsilon = 90^\circ$ for all γ_E	0 – ~40	~300	~-2900	~220

157

TABLE 4

RANGE OF γ FOR RUNS ALONG
ORIGINAL GLIDE PATH (IN DEGREES)

n $\rightarrow$	0.16				0.35			
γ_E \ V/W_G	1.0	1.2	1.5	1.9	1.0	1.2	1.5	1.9
$15°$	1-6	2-7	5-9	7-11	1-10	3-10	5-11	7-12
$45°$	2-21	9-25	17-29	23-32	3-29	11-32	18-35	24-38
$90°$	12-50	35-60			18-70	37-72		

TABLE 5

MOTOR TORQUE AND POWER REQUIREMENTS

	Starting		Stopping		During Run	
	Torque Ft-Lb.	Power Watts	Torque Ft-Lb.	Power Watts	Torque Ft-Lb.	Power Watts
Non-frozen flow	1.55	320	15	4650	2.6	840
Frozen flow $\epsilon = 90°$ & $45°$	.67	108	.34	17	.21	29
Frozen flow $\epsilon = 90°$ for all γ_E	1.55	320	15	4650	1.14	350

TABLE 6

PROBE PAIR VELOCITY MEASUREMENTS

UPPER PROBE VELOCITY COMPONENTS	LOWER PROBE VELOCITY COMPONENTS	$\mathcal{R}$ ELEMENTS MEASURED
u,v	u,v	uu,uv,vu,vv
u,w	u,v	uu,uv,wu,wv
u,w	u,w	uu,uw,wu,ww
u,v	u,w	uu,uw,vu,vw

TABLE 7

8" x 8" TUNNEL

TIMES FOR AIRCRAFT TO REACH UPPER PROBE POSITION FROM z' = 6"

z'_1 (in.)	z_1/z_G	$\gamma_E = 15°$, n = 0.16				$\gamma_E = 45°$, n = 0.16				$\gamma_E = 90°$, n=0.16		$\gamma_E = 45°$, n = 0.35			
		t'_1 (V/W=1.0) sec.	t'_1 (V/W=1.2) sec.	t'_1 (V/W=1.5) sec.	t'_1 (V/W=1.9) sec.	t'_1 (V/W=1.0) sec.	t'_1 (V/W=1.2) sec.	t'_1 (V/W=1.5) sec.	t'_1 (V/W=1.9) sec.	t'_1 (V/W=1.0) sec.	t'_1 (V/W=1.2) sec.	t'_1 (V/W=1.0) sec.	t'_1 (V/W=1.2) sec.	t'_1 (V/W=1.5) sec.	t'_1 (V/W=1.9) sec.
6.0	.86	–	–	–	–	.0000	.0000	.0000	.0000	.0000	.0000	.0000	.0000	.0000	.0000
5.5	.79	–	–	–	–	.0401	.0058	.0027	.0016	.0099	.0035	–	–	–	–
5.0	.71	–	–	–	–	.0678	.0112	.0053	.0032	.0181	.0068	.0321	.0097	.0049	.0030
4.5	.64	–	–	–	–	.0887	.0164	.0078	.0047	.0253	.0101	–	–	–	–
4.0	.57	.3841	.0730	.0335	.0195	.1051	.0213	.0103	.0063	.0317	.0133	.0504	.0177	.0094	.0059
3.5	.50	.4322	.0886	.0413	.0242	.1186	.0259	.0127	.0078	.0374	.0164	–	–	–	–
3.0	.43	.4717	.1032	.0488	.0288	.1297	.0302	.0151	.0092	.0426	.0194	.0629	.0245	.0136	.0087
2.5	.36	.5047	.1168	.0561	.0333	.1391	.0343	.0173	.0107	.0475	.0224	–	–	–	–
2.0	.29	.5322	.1294	.0630	.0377	.1470	.0381	.0195	.0121	.0519	.0252	.0721	.0302	.0173	.0113
1.5	.21	.5553	.1409	.0697	.0419	.1537	.0416	.0216	.0135	.0560	.0279	.0758	.0327	.0190	.0125

161

TABLE 8

44" x 66" TUNNEL

TIMES FOR AIRCRAFT TO REACH UPPER PROBE POSITION FROM $z' = 35.82"$

z_1'	z_1/Z_G	$\gamma_E = 15^{\circ}$, $n = 0.16$		
		t_1'	t_1'	t_1'
		$(V/W_G = 1.0)$	$(V/W_G = 1.5)$	$(V/W_G = 2.0)$
in.		sec.	sec.	sec.
25.0	.69	3.097	.0717	.0371
19.0	.53	3.377	.1083	.0567
16.5	.46	3.458	.1228	.0647
14.0	.39	3.526	.1367	.0725
11.0	.31	3.593	.1528	.0816
8.0	.22	3.648	.1680	.0905
5.0	.14	3.691	.1822	.0990

TABLE 9

44" x 66" TUNNEL

Range of W' and $L_u^{x'}$ Parameters for $V/W_G = 1.5$

at S = 5.5H

t_1' sec.	z_1' in.	z_{2min}' * in.	W' at z_1' fps	W' at z_{2min}' fps	$L_u^{x'}$ at z_1' in.	$L_u^{x'}$ at z_{2min}' in.
.0717	25.0	18.5	84.9	80.9	14.8	13.0
.1228	16.5	10.0	79.4	73.3	12.8	10.8
.1528	11.0	4.5	74.4	64.5	11.2	11.2
.1822	5.0	2.5	65.6	58.7	11.2	11.3

*z_{2min}' is smallest value of z_2' used for a given z_1'.

TABLE 10

DISPERSION MATRIX $\underline{\Sigma}(t)$ for $V/W_G = 2.0$

$$\underline{\Sigma}(t) = <\underline{y}(t)\ \underline{y}^T(t)>$$

$$\underline{y}^T = (\Delta u_\varepsilon\quad \Delta\alpha_\varepsilon\quad \Delta q\quad \Delta\theta\quad \Delta x_I\quad \Delta h)$$

---

t (sec) = 3.174813D+00   h(ft) REF EQUIL = 632

4.0401405D+00	-2.0764754D-02	1.8113791D-03	-3.9649354D-02	5.3436811D+00	-4.1152492D+00
-2.0764754D-02	5.2738632D-04	1.1219632D-04	3.9185040D-04	-2.3449229D-02	-1.5147981D-02
1.8113791D-03	1.1219632D-04	4.7106868D-04	5.3207420D-04	1.2609281D-02	1.0528876D-02
-3.9849354D-02	3.9185040D-04	5.3207420D-04	5.2084353D-04	-4.4843207D-02	3.6021537D-02
5.3436811D+00	-2.3449229D-02	1.2609281D-02	-4.4843207D-02	8.1079152D+00	-4.1060148D+00
-4.1152292D+00	-1.5147981D-02	1.0528876D-02	3.6021537D-02	-4.1060148D+00	1.5508292D+01

---

t (sec) = 6.349626D+00   h(ft) REF EQUIL = 569

1.2481866D+01	-3.7497623D-02	1.8134025D-02	-6.6311736D-02	3.2323550D+01	-2.5153268D+01
-3.7497623D-02	6.9872609D-04	1.2699567D-04	5.5123694D-04	-5.5621038D-02	1.0878546D-02
1.8134025D-02	1.2699567D-04	7.3039799D-04	3.6965192D-04	7.2877514D-02	-2.2964475D-02
-6.6311736D-02	5.5123694D-04	3.6965192D-04	7.7246463D-04	-8.3453395D-02	1.1494439D-01
3.2323550D+01	-5.5621038D-02	7.2877514D-02	-8.3453395D-02	1.1032567D+02	-6.5614487D+01
-2.5153268D+01	1.0878546D-02	-2.2964475D-02	1.1494439D-01	-6.5614487D+01	1.0052391D+02

---

t (sec) = 9.524439D+00   h(ft) REF EQUIL = 507

1.8945828D+01	-5.6475500D-02	2.8542463D-02	-7.2120670D-02	6.7237764D+01	-4.4953856D+01
-5.6475500D-02	9.2998204D-04	1.9047777D-04	6.8906036D-04	-1.2793630D-01	4.4475591D-01
2.8542463D-02	1.9047777D-04	1.1906675D-03	8.6156295D-05	1.5194622D-01	-6.1267103D-01
-7.2120870D-02	6.8906036D-04	8.6156295D-05	1.1519262D-03	8.5024980D-02	-1.2762811D-01
6.7237764D+01	-1.2793043D-01	1.5194622D-01	8.5024980D-02	4.3571254D+02	-1.6736370D+02
-4.4953856D+01	4.4475691D-01	-6.1267103D-01	1.2722811D-01	-1.6736370D+02	2.1154806D+02

164

TABLE 10   (CONTINUED)

t (sec) = 1.269925D+01   h(ft) REF EQUIL = 444

```
 2.5263227 6D+01   -7.1266362 8D-02    3.6656174 7D-02   -1.0177369 1D-01    8.4389560 9D+01   -6.4524065 5D+01
-7.7266362 8D-02    1.3343990 4D-03    3.6304907 5D-04    9.4711999 6D-04   -2.1445268 4D-01    7.3140995 2D-02
 3.6656174 7D-02    3.6304907 5D-04    2.1081758 3D-03    1.2969096 2D-04    1.7825382 2D-01   -9.2341310 0D-02
-1.0177369 1D-01    9.4711999 6D-04    1.2969096 2D-04    1.8844829 9D-03    4.3112542 0D-01    2.0957621 9D-01
 8.4689500 9D+01   -2.1445268 4D-01    1.9825382 3D-01    4.3112542 0D-01    9.7718186 0D+02   -1.9119823 9D+02
-6.4524065 5D+01    7.3140995 2D-02   -9.5341310 0D-02    2.0957621 9D-01   -1.9119823 9D+02    2.4533412 0D+02
```

t (sec) = 1.587406D+01   h(ft) REF EQUIL = 382

```
 3.4944937 0D+01   -1.0073275 7D-01    5.4920317 0D-02   -1.4741715 0D-01    8.8141957 8D+01   -7.9084321 7D+01
-1.0073275 7D-01    1.8156417 6D-03    5.8190554 8D-04    1.2909968 9D-03   -2.6418300 8D-01    1.0460617 2D-01
 5.4920317 0D-02    5.8190554 8D-04    3.3522894 2D-03    1.1825772 5D-04    2.1238647 0D-01   -1.6781014 1D-01
-1.4741715 0D-01    1.2909968 9D-03    1.1825772 5D-04    2.6670466 6D-03    7.6586970 0D-01    3.4505698 0D-01
 8.8141957 8D+01   -2.6418300 8D-01    2.1238647 0D-01    7.6586970 0D-01    1.6280982 5D+03   -1.2231049 0D+02
-9.0843217 0D+01    1.0460617 2D-01   -1.6781014 1D-01    3.4505698 0D-01   -1.2231049 0D+02    5.7866607 0D+02
```

t (sec) = 1.904888D+01   h(ft) REF EQUIL = 319

```
 4.5872385 4D+01   -1.2631110 0D-01    7.2776356 2D-02   -1.8323061 4D-01    9.2674488 1D+01   -1.4165927 4D+02
-1.2631110 0D-01    2.1275223 5D-03    7.3824241 5D-04    1.5611295 8D-03   -2.9465792 5D-01    1.6279799 0D-01
 7.2776356 2D-02    7.3824241 5D-04    4.5207511 5D-03    1.2719816 0D-04    2.2917066 7D-01   -2.6299518 0D-01
-1.8323061 4D-01    1.5611295 8D-03    1.2719816 0D-04    3.4260591 7D-03    1.0474062 0D+00    4.0045862 8D-01
 9.2674488 1D+01   -2.9465792 5D-01    2.2917066 7D-01    1.0474062 0D+00    2.3420701 6D+03   -3.4361733 7D+01
-1.4165927 4D+02    1.6279799 0D-01   -2.6299518 0D-01    4.0045862 8D-01   -3.4361733 7D+01    8.9653807 8D+02
```

t (sec) = 2.222369D+01   h(ft) REF EQUIL = 257

```
 5.7143634 6D+01   -1.5399411 6D-01    8.6880004 3D-02   -2.2079524 9D-01    1.0251566 0D+02   -1.8243571 3D+02
-1.5399411 6D-01    2.5549325 2D-03    9.5692013 2D-04    1.8602713 1D-03   -3.2184622 5D-01    2.4084252 8D-01
 8.6880004 3D-02    9.5692013 2D-04    5.9139588 7D-03    1.4357743 3D-04    2.5378616 1D-01   -3.4538052 6D-01
-2.2079524 9D-01    1.8602713 1D-03    1.4357743 3D-04    4.2876500 0D-03    1.3126601 8D+00    4.1448974 5D-01
 1.0251566 0D+02   -3.2184622 5D-01    2.5378616 1D-01    1.3126601 8D+00    3.1379394 6D+03    4.0171035 5D+01
-1.8243571 8D+02    2.4084252 8D-01   -3.4538052 6D-01    4.1448974 5D-01    4.0171035 5D+01    1.2212879 1D+03
```

165

TABLE 10 (CONCLUDED)

t (sec) = 2.539850D+01 h(ft) REF EQUIL = 194

6.99690645D+01	-1.83418634D-01	1.05067306D-01	-2.67091028D-01	1.19083309D+02	-2.25157047D+02
-1.83418634D-01	3.06994575D-03	1.20524940D-03	2.18027314D-03	-3.54286272D-01	3.18634478D-01
1.05067306D-01	1.20524948D-03	7.54151886D-03	1.53056585D-04	2.90999511D-01	-4.17598763D-01
-7.67091028D-01	2.18027314D-03	1.53056585D-04	5.23045705D-05	1.50090325D+00	4.03277645D-01
1.19083309D+02	-3.54286272D-01	2.90999511D-01	1.58090325D+00	4.03245604D+03	9.76073805D+01
-2.25157047D+02	3.18634478D-01	-4.17598763D-01	4.58276460D-01	9.76073805D+01	1.54026322D+03

t (sec) = 2.857332D+01 h(ft) REF EQUIL = 132

8.39285250D+01	-2.12006161D-01	1.27562821D-01	-3.07352363D-01	1.41811534D+02	-2.73091970D+02
-2.12006161D-01	3.63429377D-03	1.52452375D-03	2.53130513D-03	-3.83564016D-01	4.04481192D-01
1.27562821D-01	1.52452375D-03	9.49090738D-03	1.52518590D-04	3.54916820D-01	-5.05140728D-01
-3.07352363D-01	2.53130513D-03	1.52518590D-04	6.18291041D-05	1.90703266D+00	5.18525330D-01
1.41811534D+02	-3.83564016D-01	3.54916820D-01	1.90703266D+00	5.15382370D+03	1.35422791D+02
-2.73091970D+02	4.04481192D-01	-5.05140728D-01	5.18525330D-01	1.35422791D+02	1.60167472D+03

t (sec) = 3.174813D+01 h(ft) REF EQUIL = 69

9.55547463D+01	-2.31360653D-01	1.45136889D-01	-3.37265876D-01	1.59099869D+02	-3.22316561D+02
-2.31360653D-01	4.26361380D-03	1.90454111D-03	2.90691144D-03	-3.71971290D-01	4.70159940D-01
1.45136889D-01	1.90454111D-03	1.16007512D-02	1.53216537D-04	3.89738424D-01	-5.52338226D-01
-3.37265876D-01	2.90691144D-03	1.53216537D-04	7.17694811D-05	2.34444056D+00	5.00233899D-01
1.59099869D+02	-3.71971290D-01	3.89738424D-01	2.34444056D+00	6.39707257D+03	1.47511528D+02
-3.22316561D+02	4.70159940D-01	-5.52338226D-01	5.66657680D-01	1.72517326D+02	2.24273360D+03

166

TABLE 11

DISPERSION MATRIX $\underline{\Sigma}(t)$ for $V/W_G = 1.5$

$$\underline{\Sigma}(t) = <\underline{y}(t)\ \underline{y}^T(t)>$$

$$\underline{y}^T = (\Delta u_\varepsilon\ \ \Delta \alpha_\varepsilon\ \ \Delta q\ \ \Delta \theta\ \ \Delta x_I\ \ \Delta h)$$

t(sec) = 5.641208D+01   h(ft.)   REF EQUIL = 69

1.88448349D+02	-6.58217064D-01	5.33959852D-01	-7.95018185D-01	1.71760812D+02	-5.38040597D+02
-6.58217064D-01	1.19232878D-02	4.04489720D-04	6.97539498D-03	-7.20058929D-01	1.32627283D+00
5.33959852D-01	4.04489720D-04	2.06279159D-02	2.31438166D-04	6.21139860D-01	-1.86694220D+00
-7.95018185D-01	6.97539498D-03	2.31438166D-04	2.47241147D-02	5.39944925D+00	4.19914600D+00
1.77560812D+02	-7.20058929D-01	6.21139860D-01	5.39944925D+00	1.46679118D+04	1.55281039D+03
-5.38040597D+02	1.32627283D+00	-1.86694220D+00	4.19914600D+00	1.55281039D+03	4.29729317D+03
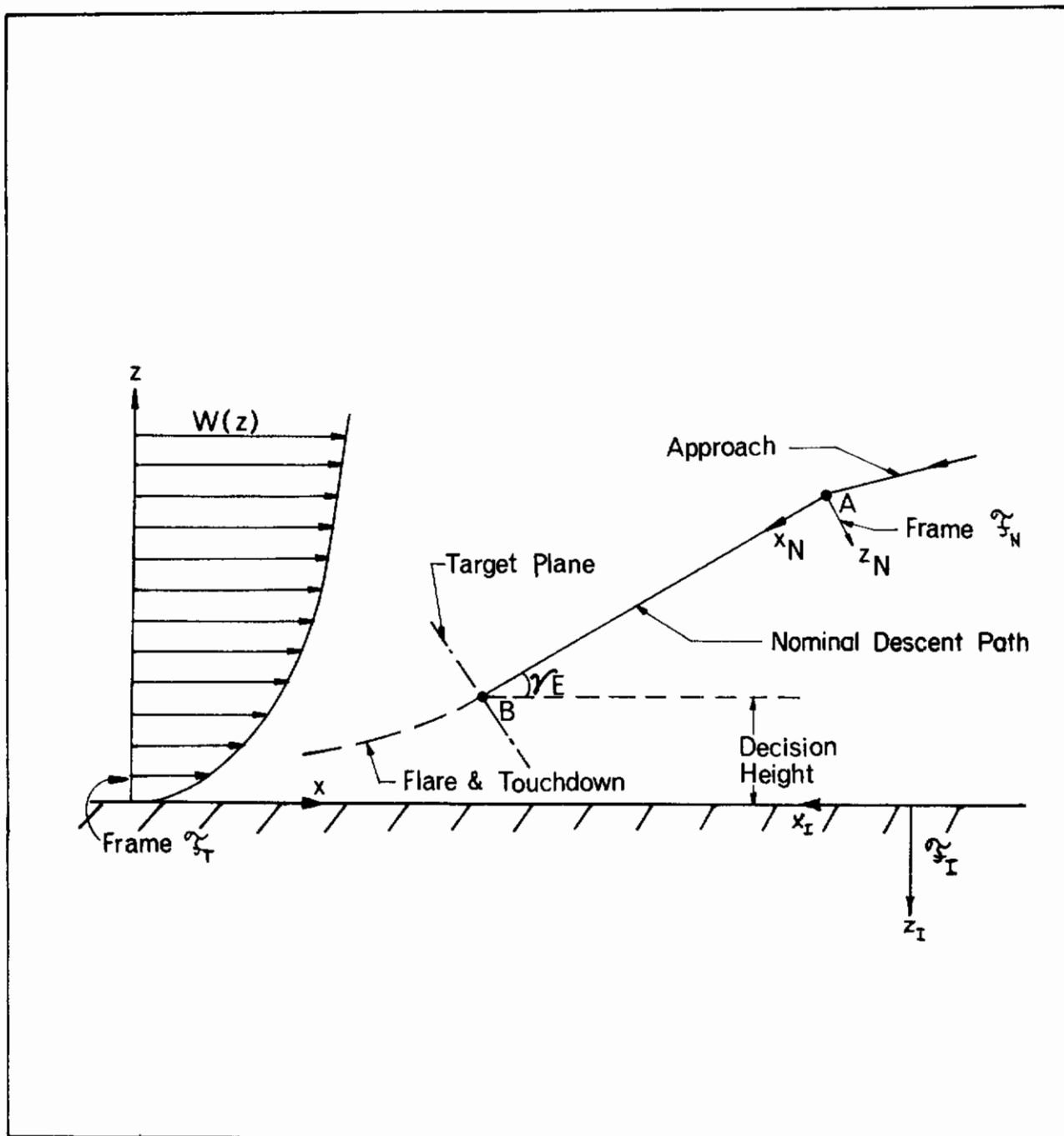
FIGURE 1. TYPICAL AIRCRAFT DESCENT THROUGH THE PLANETARY BOUNDARY LAYER
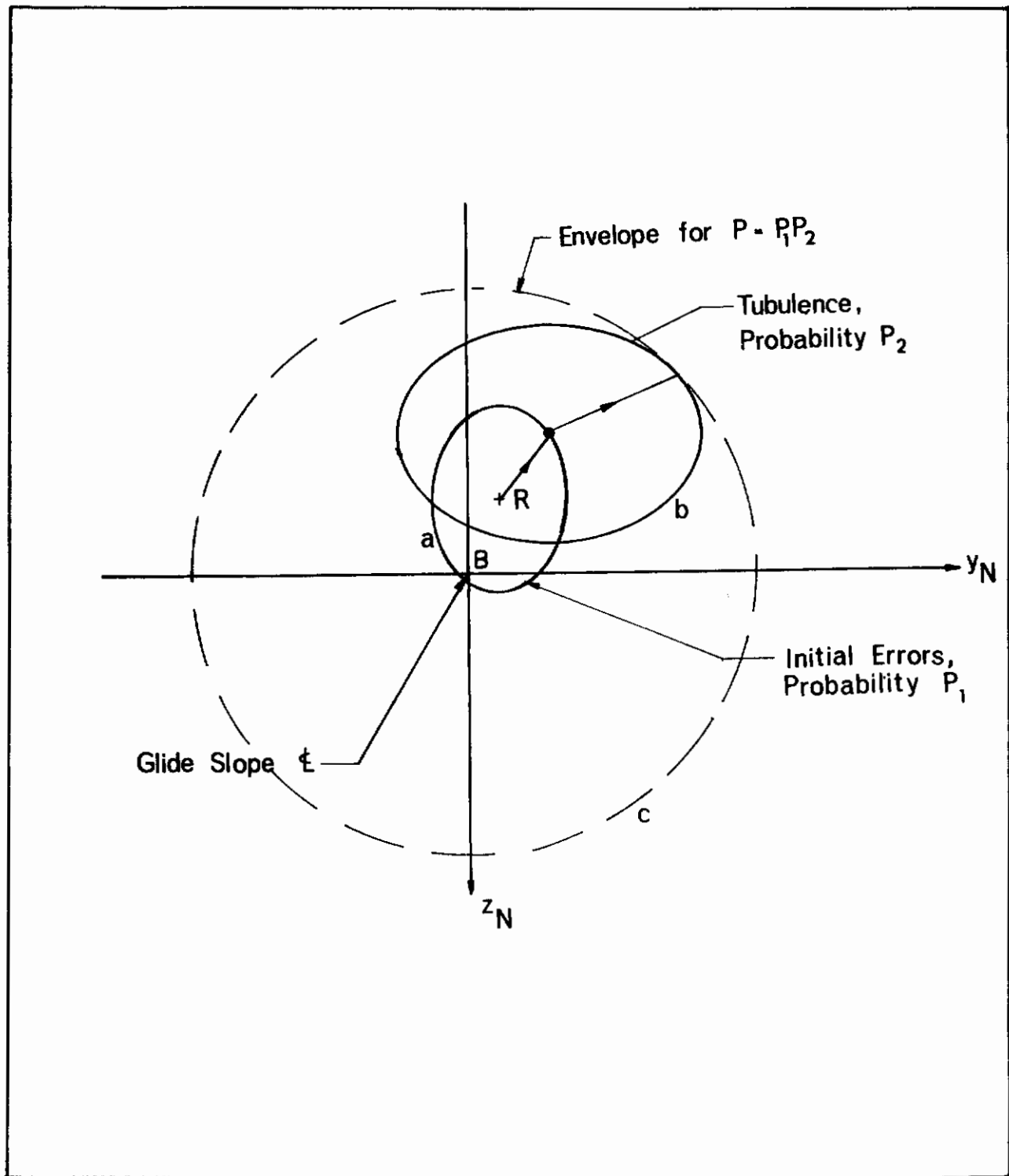
FIGURE 2.   PROBABILITY CONTOURS OF FLIGHT PATH INTERCEPTS ON TARGET PLANE
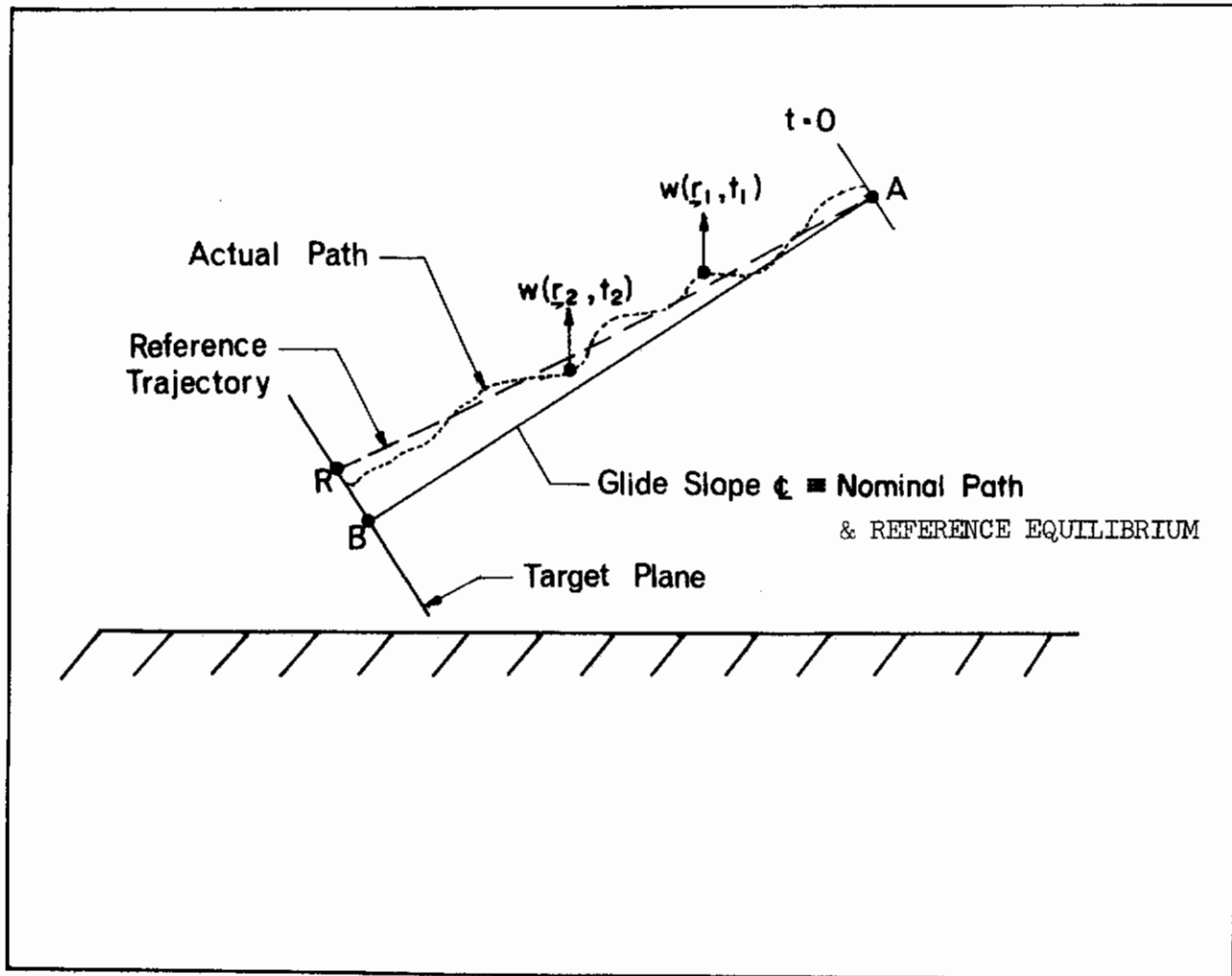
FIGURE 3.   AIRCRAFT TRAJECTORIES AND REFERENCE PARAMETERS
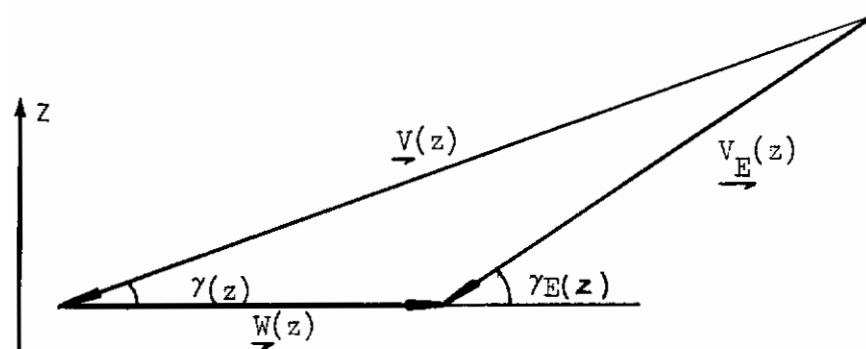
FIGURE 4.   FLIGHT PATH GEOMETRY
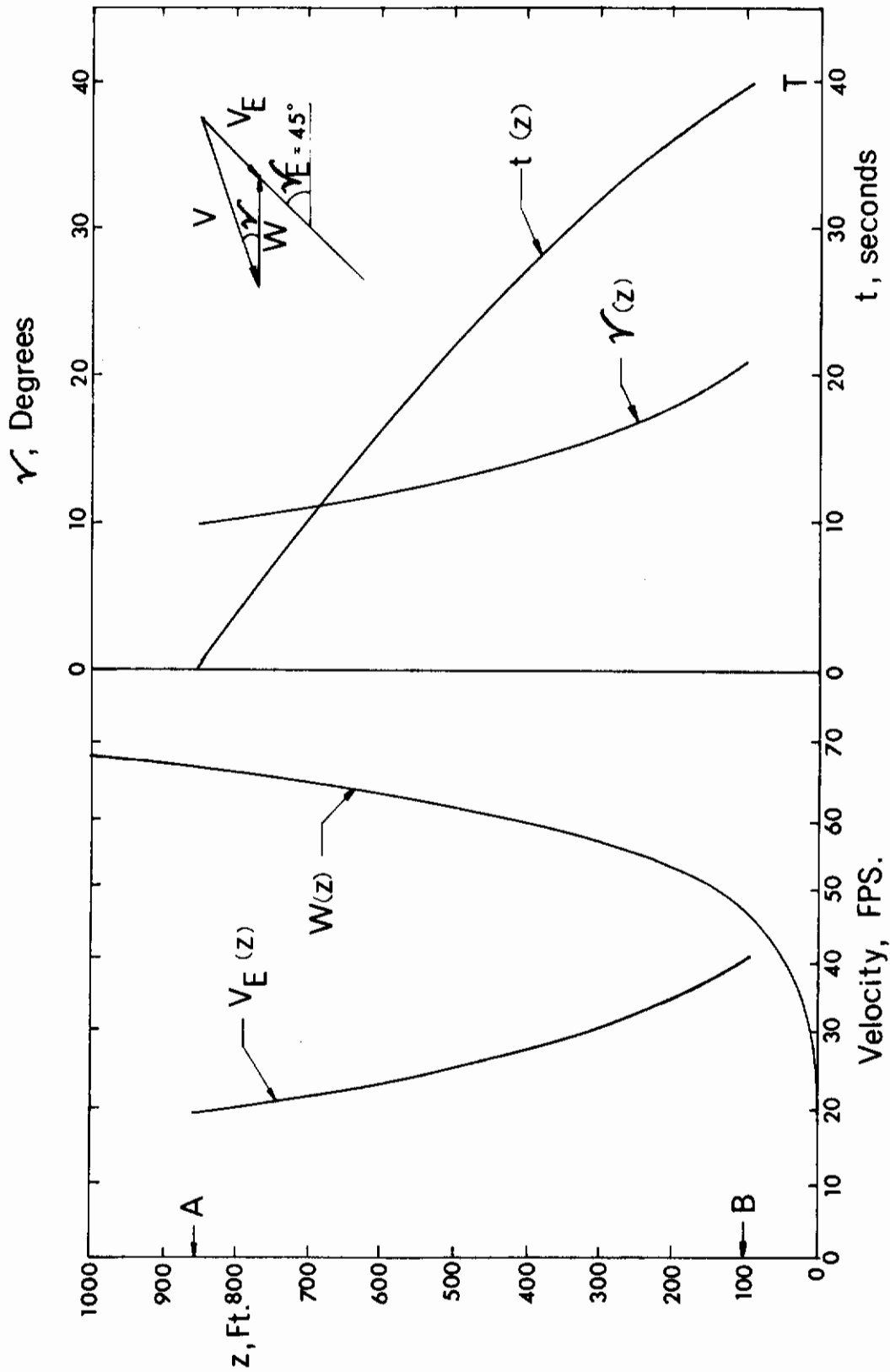
FIGURE 5. TYPICAL FLIGHT PATH CHARACTERISTICS
$\gamma_E = 45°$, $V' = 81.6$ fps, $V/W_G = 1.2$, $n = 0.16$

172
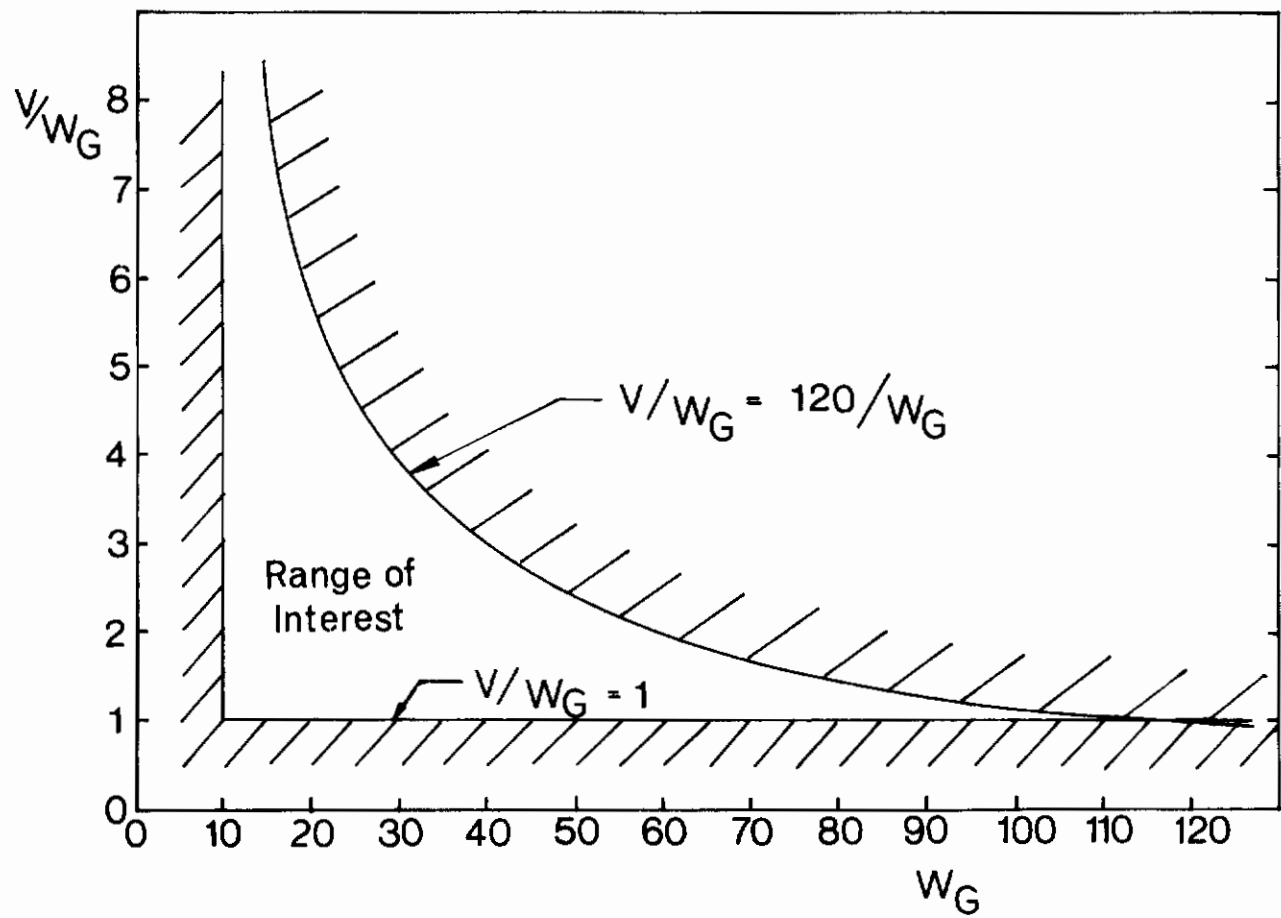
FIGURE 6.   RANGE OF INTEREST FOR FLIGHT PARAMETERS

The figure shows a plot with V/W_G on the vertical axis (ranging from 0 to 8) and W_G on the horizontal axis (ranging from 0 to 120). Two curves are labeled: $V/W_G = 120/W_G$ and $V/W_G = 1$. The enclosed region is labeled "Range of Interest".

173
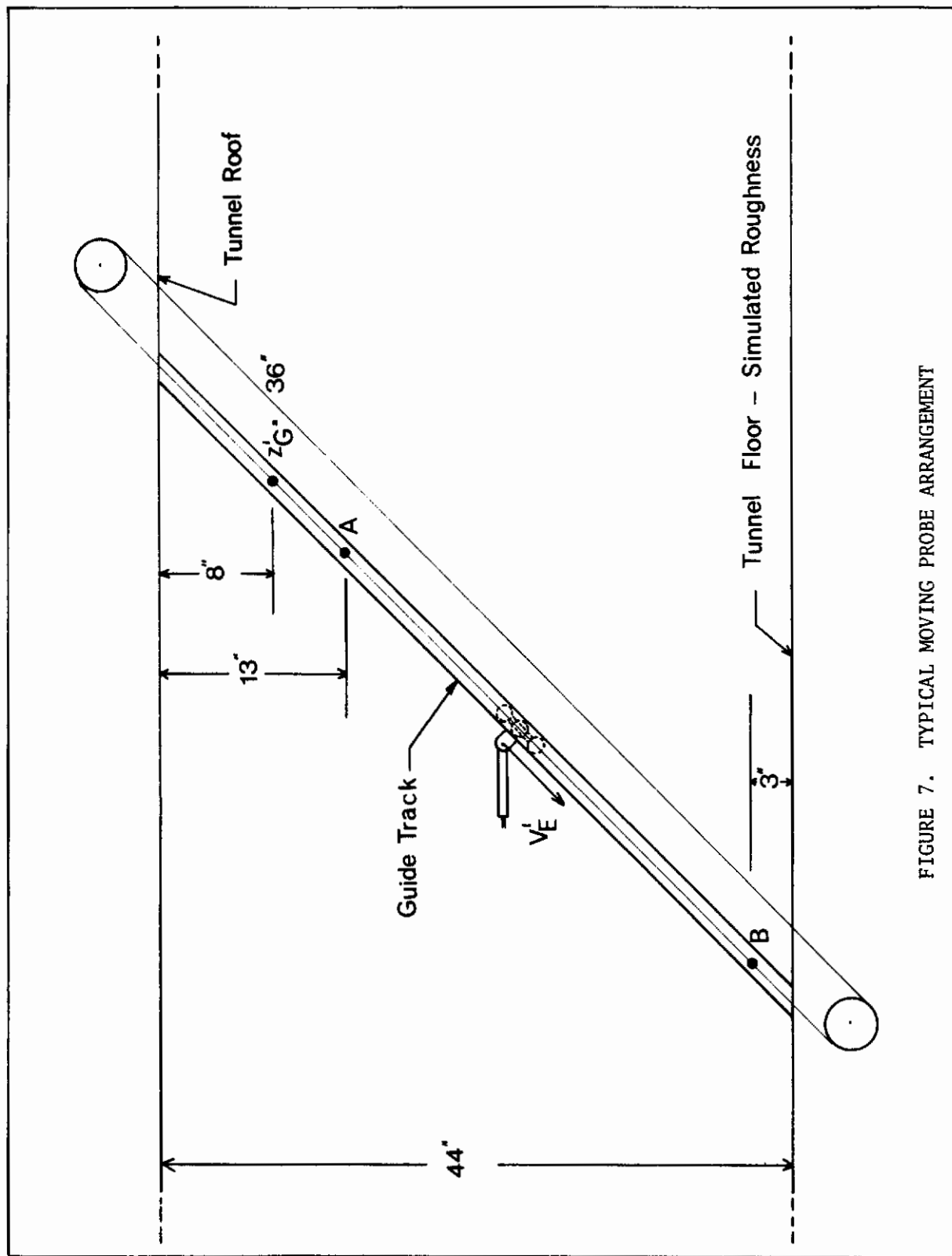
FIGURE 7. TYPICAL MOVING PROBE ARRANGEMENT

174
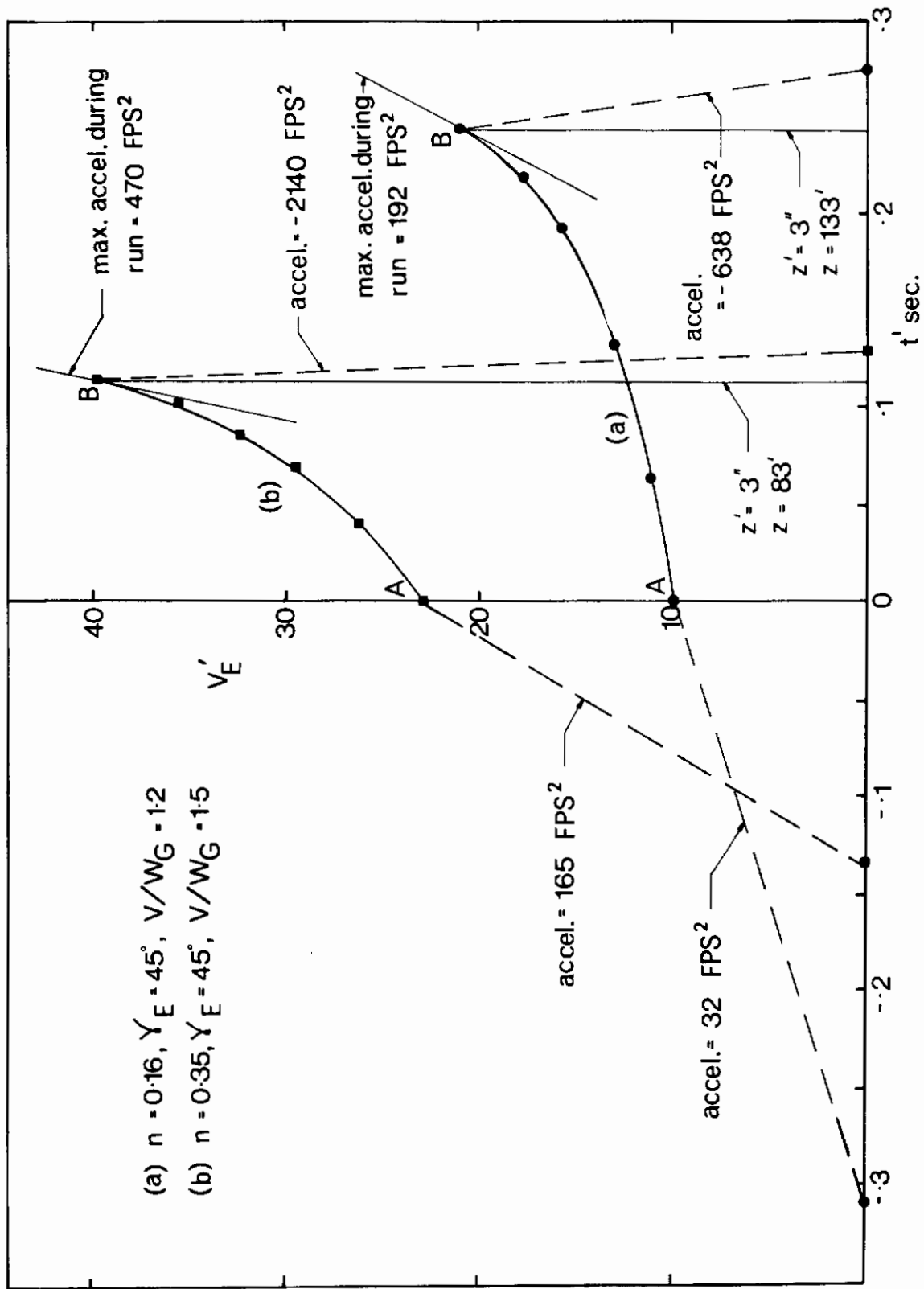
FIGURE 8. TYPICAL MOVING PROBE SPEED PROFILES
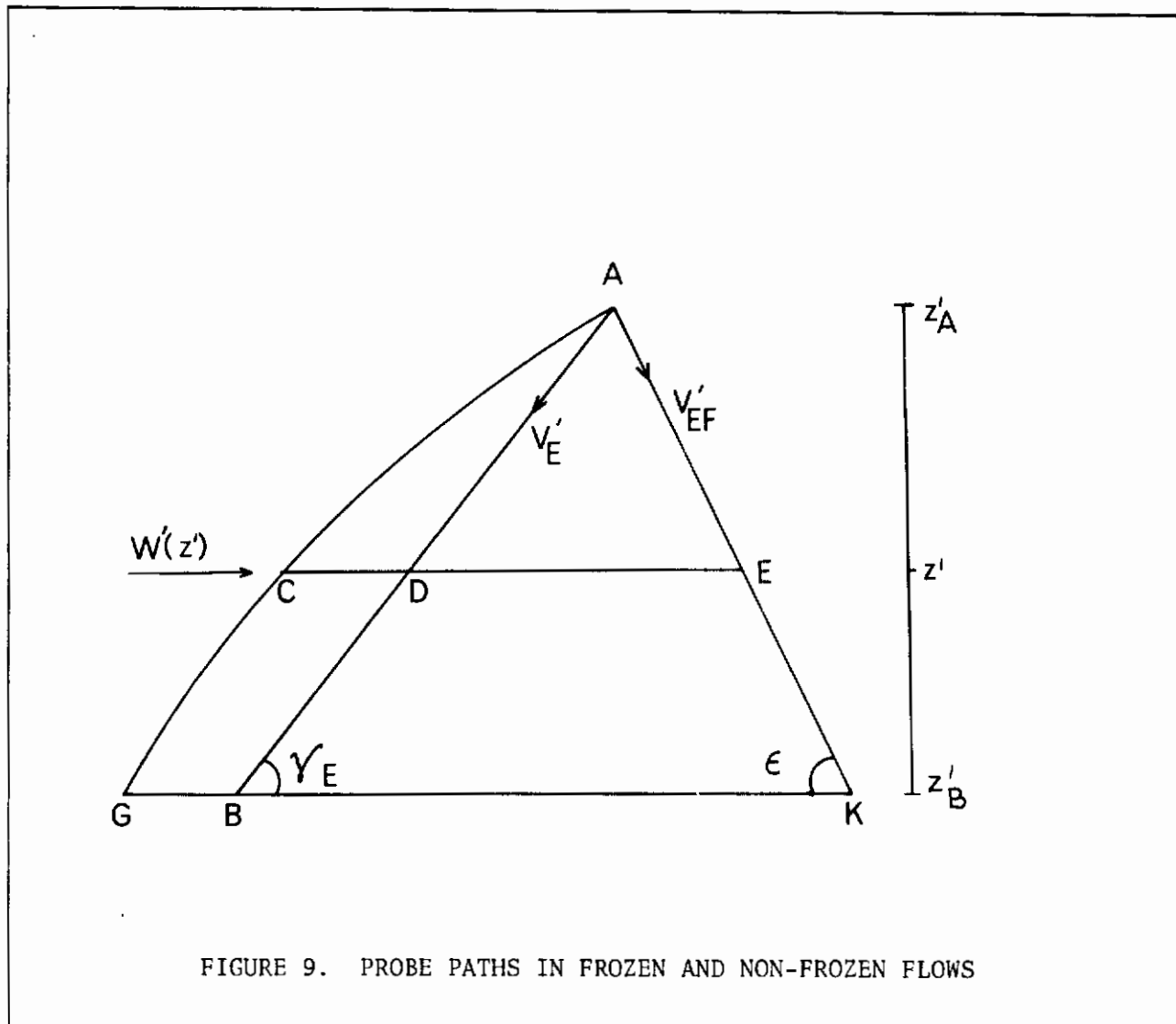
FIGURE 9. PROBE PATHS IN FROZEN AND NON-FROZEN FLOWS
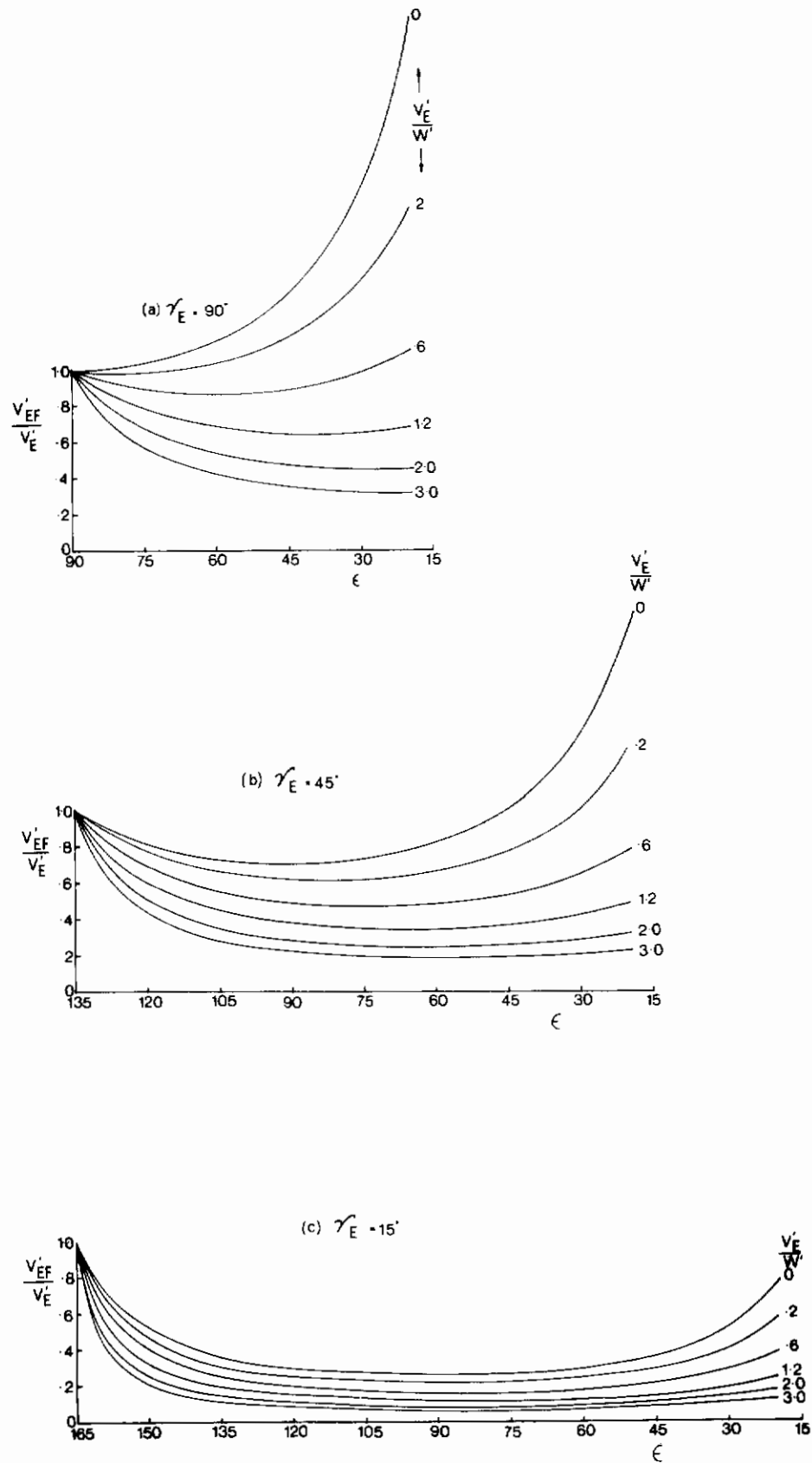
FIGURE 10. VARIATION OF V_{EF}'/V_E' WITH ϵ AND V_E'/W'

177
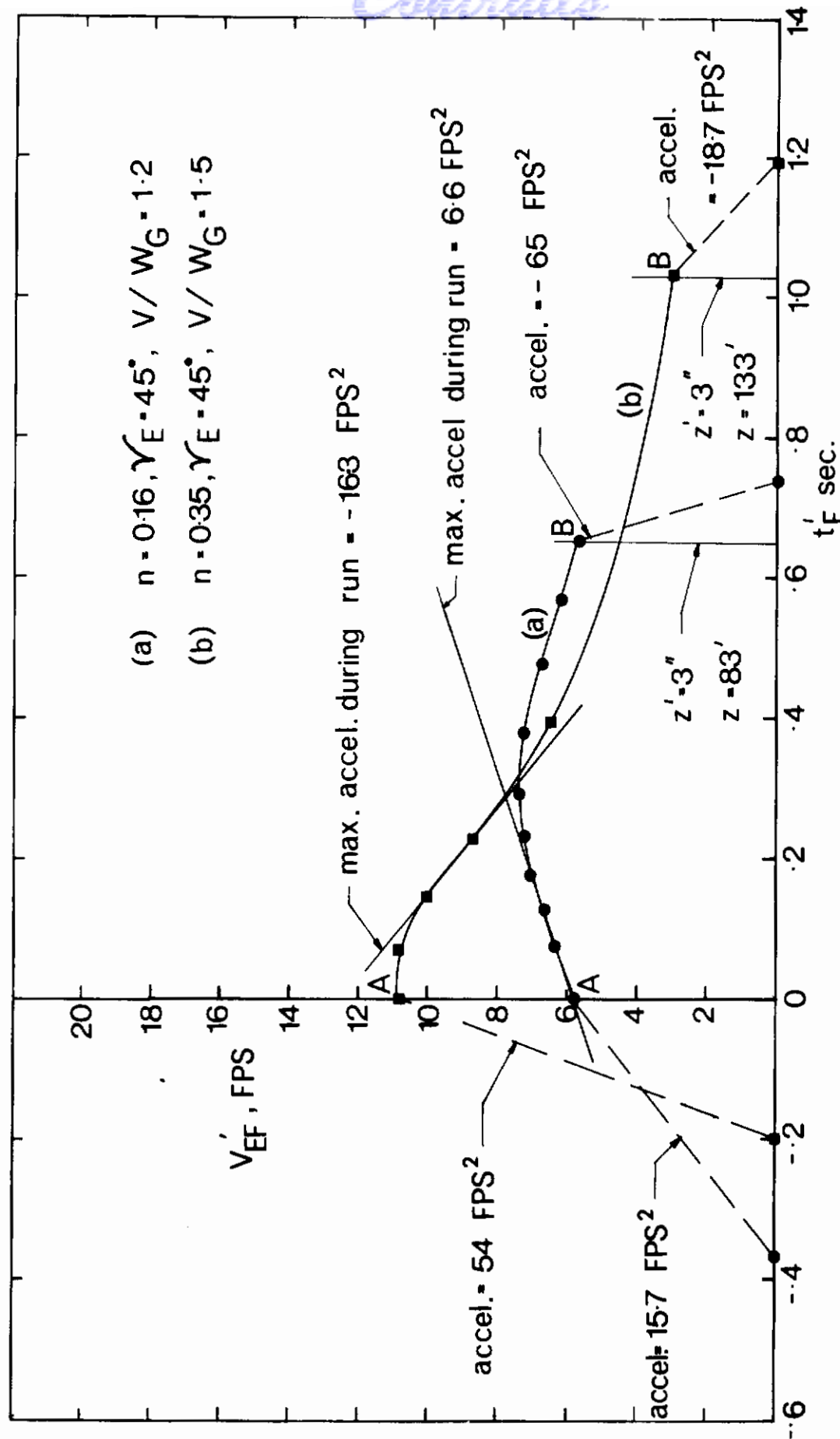
FIGURE 11.   MOVING PROBE SPEED PROFILES ASSUMING FROZEN FLOW FOR $\epsilon = 90°$
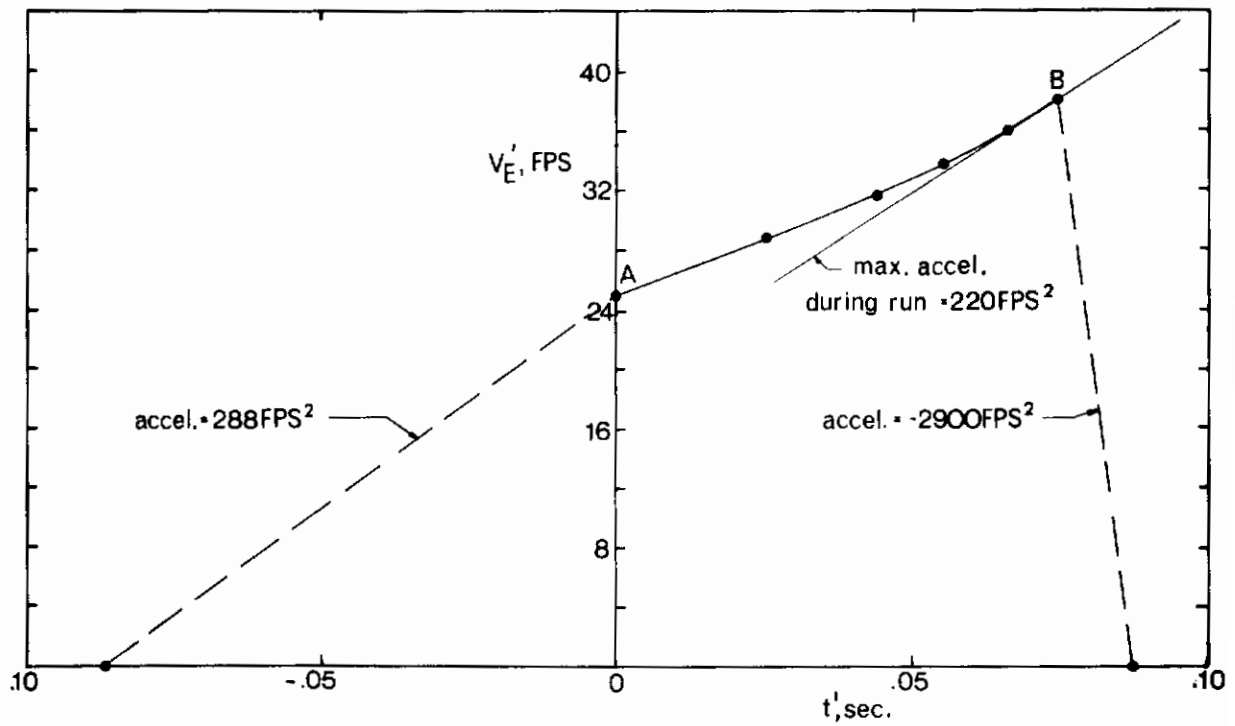
(a) WITHOUT FROZEN HYPOTHESIS

(b) FROZEN FLOW CASE , $\epsilon = 45°$

FIGURE 12.   SPEED PROFILES FOR $\gamma_E = 90°$, n = 0.35, $V/W_G = 1.2$

179
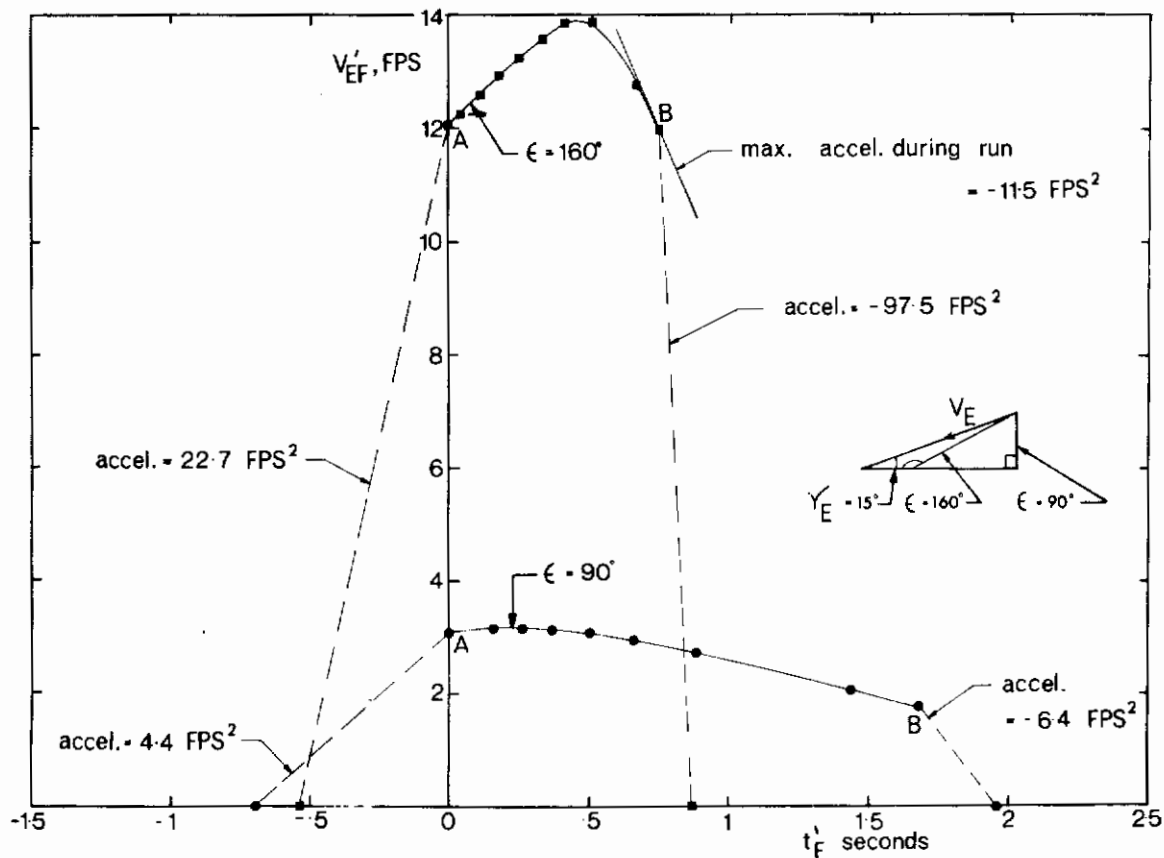
FIGURE 13. SPEED PROFILES FOR $\gamma_E = 15°$, $n = 0.16$, $V/W_G = 1.5$

180
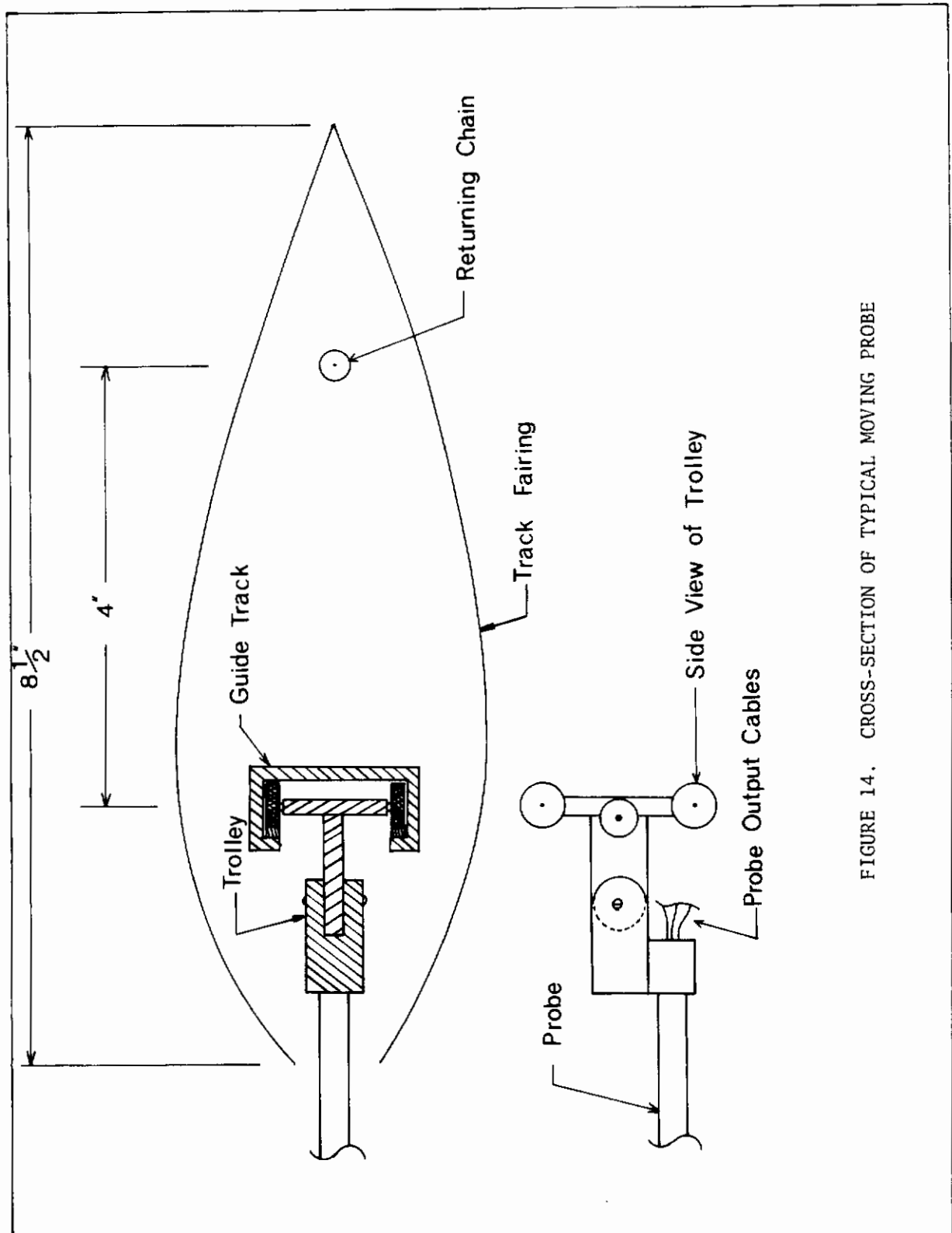
FIGURE 14.   CROSS-SECTION OF TYPICAL MOVING PROBE

Returning Chain

Track Fairing

Guide Track

Trolley

Side View of Trolley

Probe Output Cables

Probe

8½"

4"
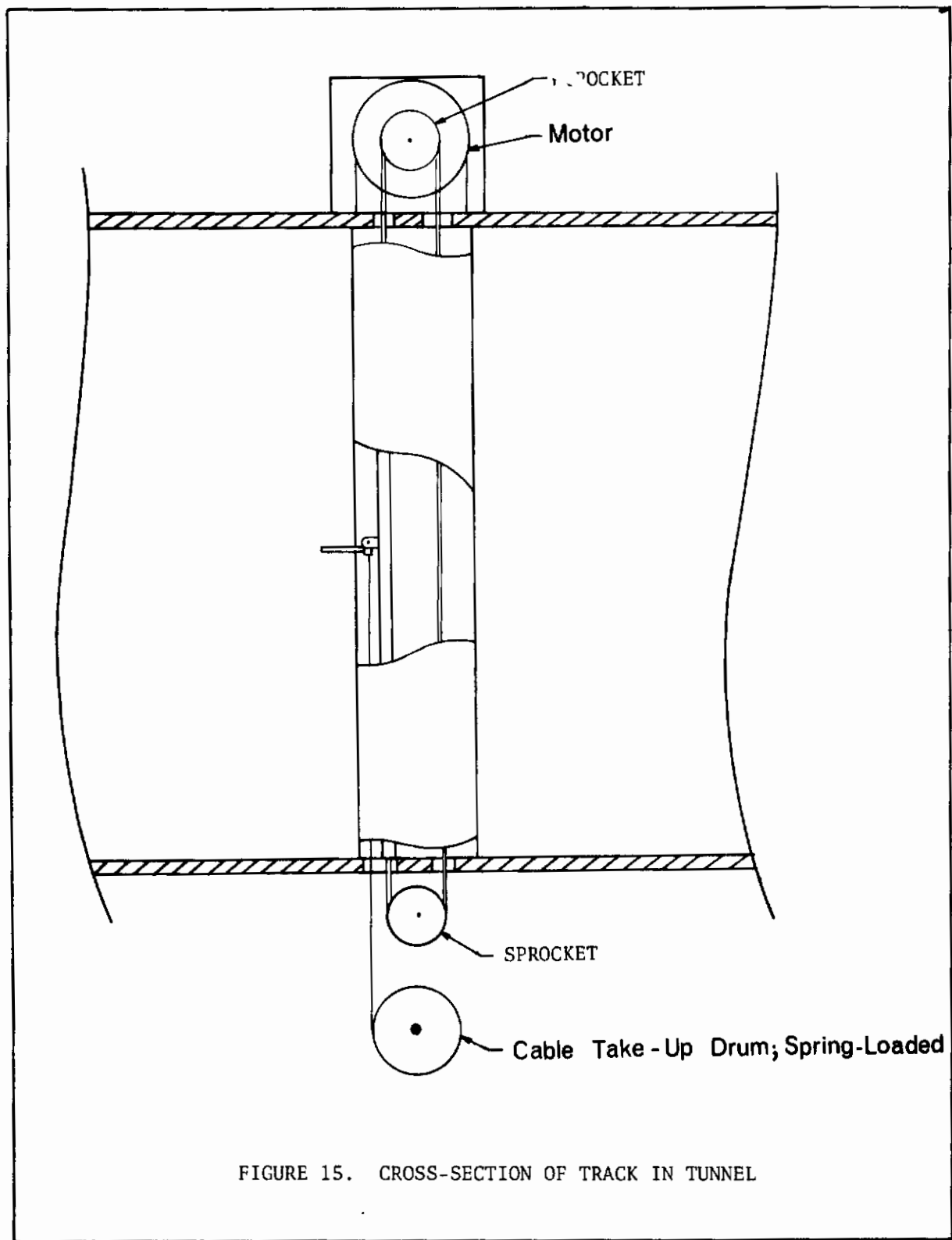
FIGURE 15.   CROSS-SECTION OF TRACK IN TUNNEL

182
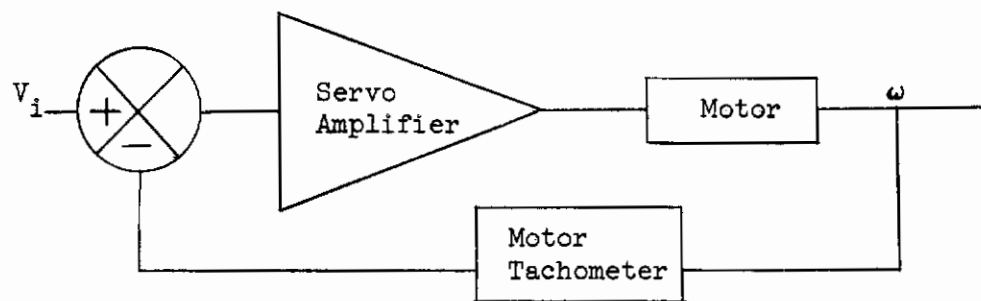
FIGURE 16. MOTOR DRIVE CIRCUIT
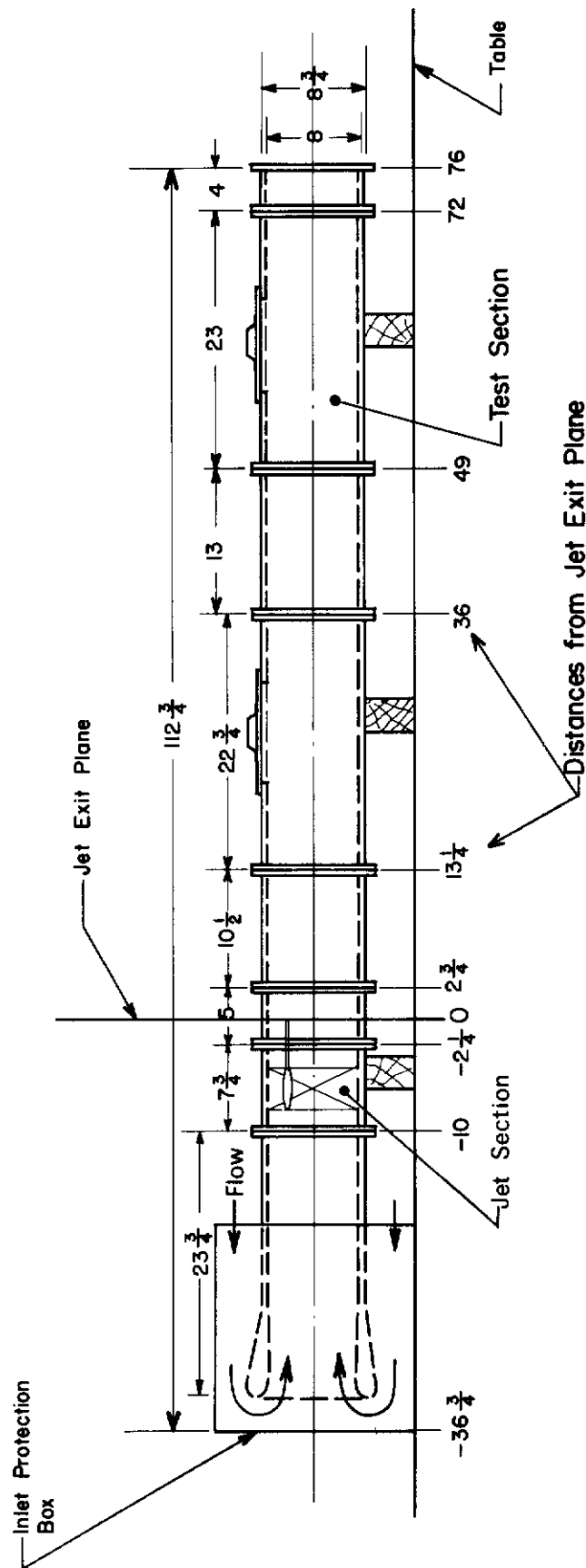
FIGURE 17. AERODYNAMIC OUTLINE OF THE UTIAS 8" x 8" MULTIPLE JET WIND TUNNEL
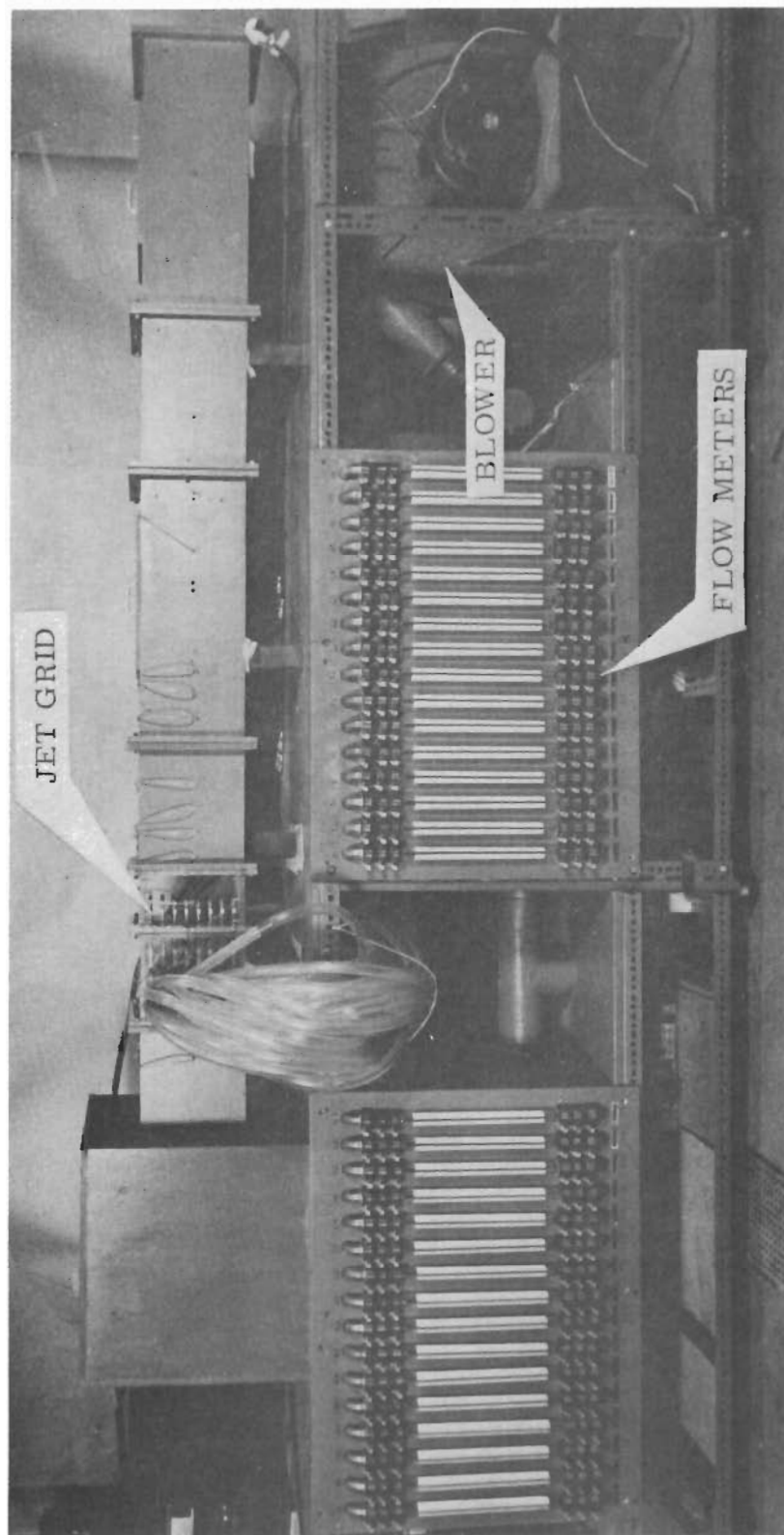
FIGURE 18. UTIAS 8" x 8" MULTIPLE JET WIND TUNNEL

185

$$\frac{W'}{W'_G} = \left(\frac{z'}{z'_G}\right)^{0.16}$$
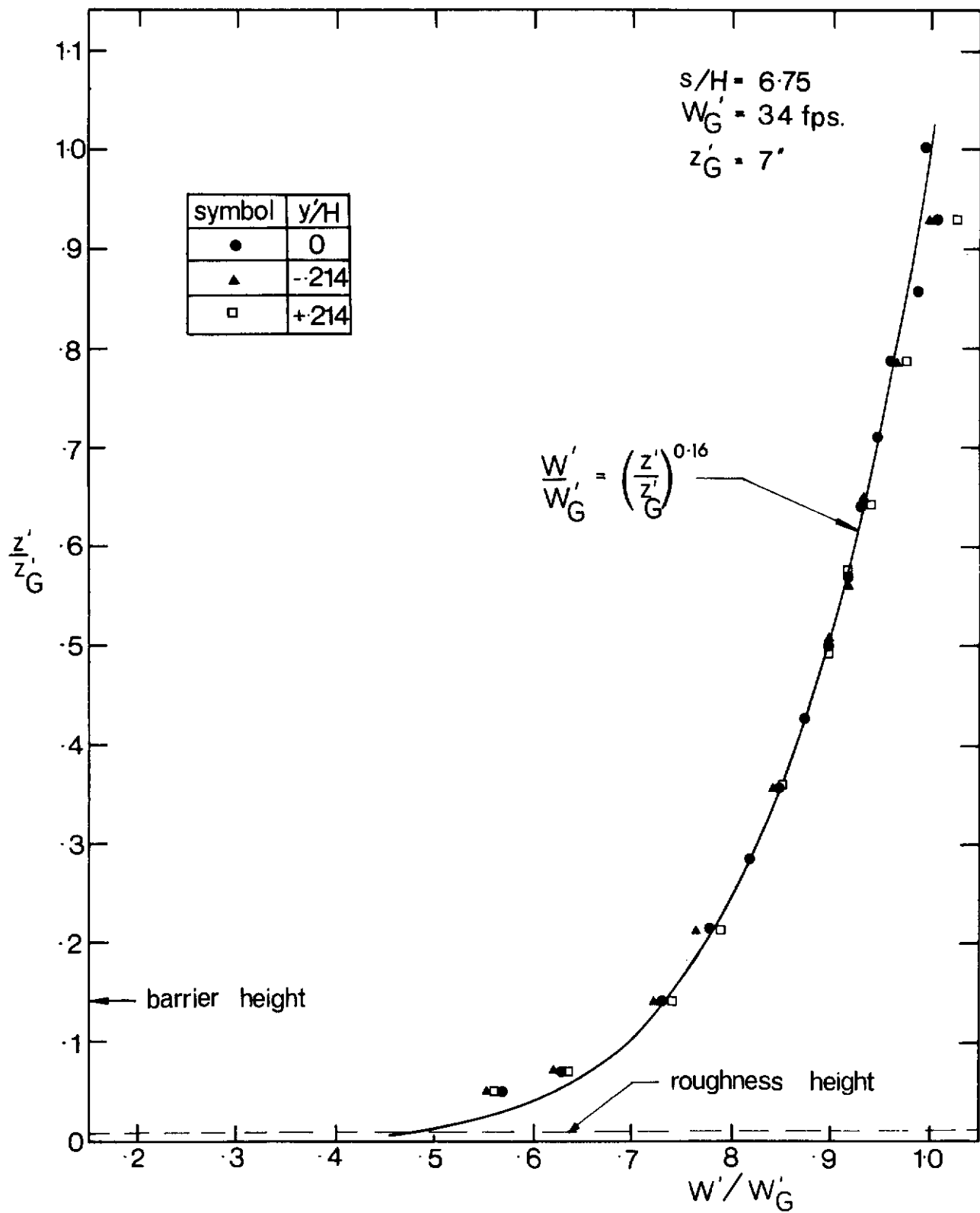
FIGURE 19.   MEAN VELOCITY PROFILES IN SIMULATED FLOW, 8" x 8" TUNNEL
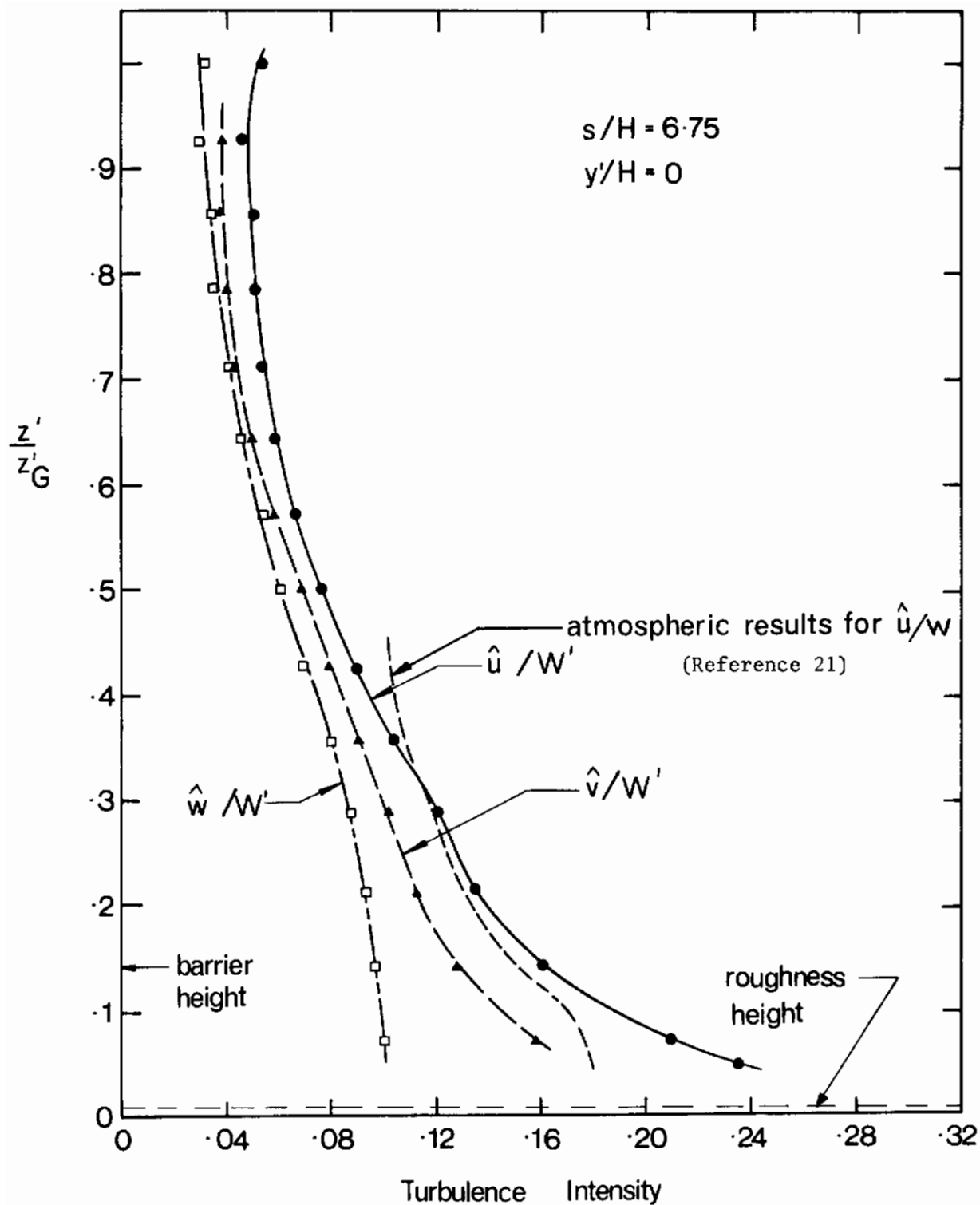
FIGURE 20. TURBULENCE INTENSITY PROFILES IN SIMULATED FLOW,
8" x 8" TUNNEL

187
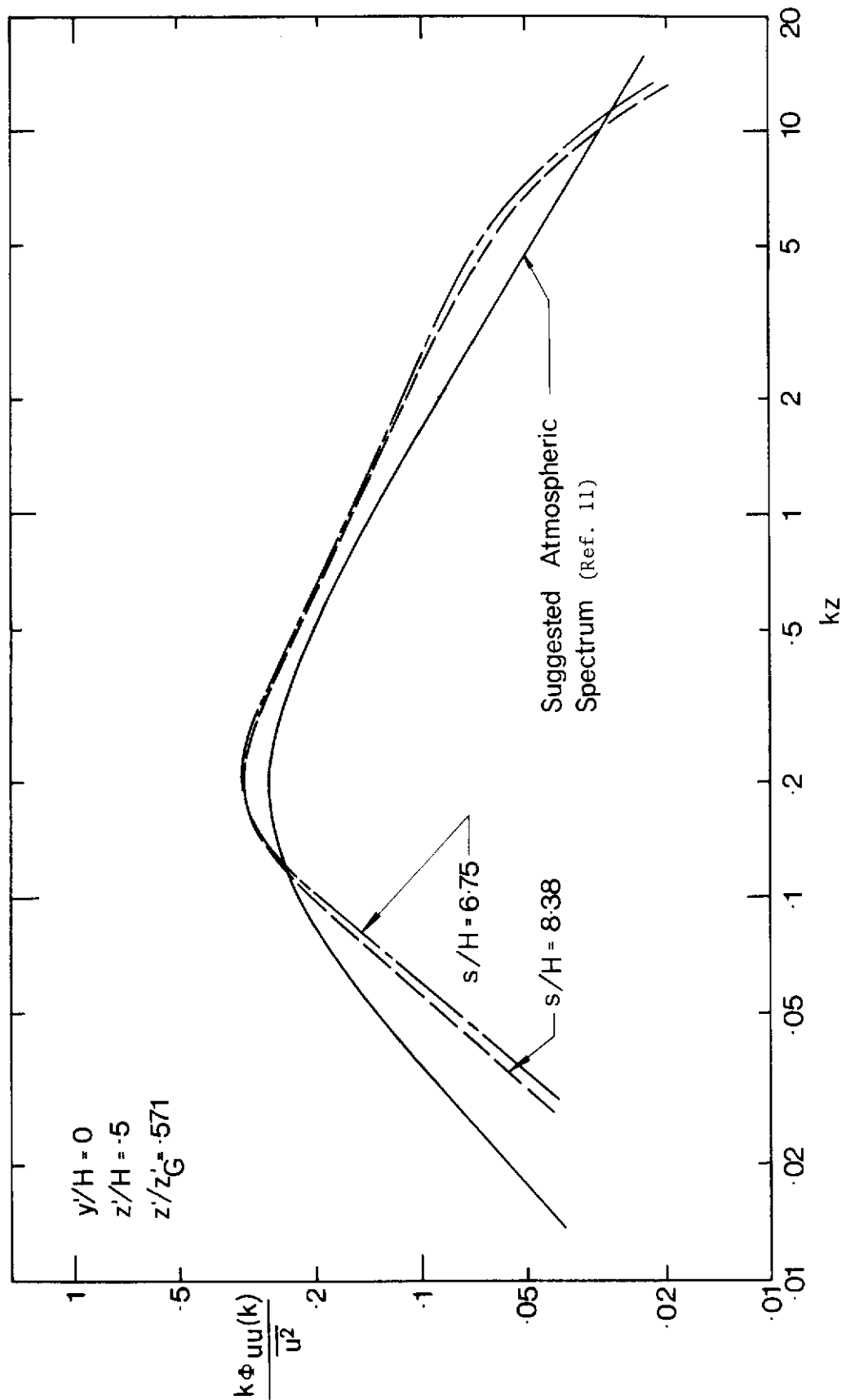
FIGURE 21.   LONGITUDINAL COMPONENT POWER SPECTRA   ON TUNNEL CENTRE LINE,
8'' x 8'' TUNNEL
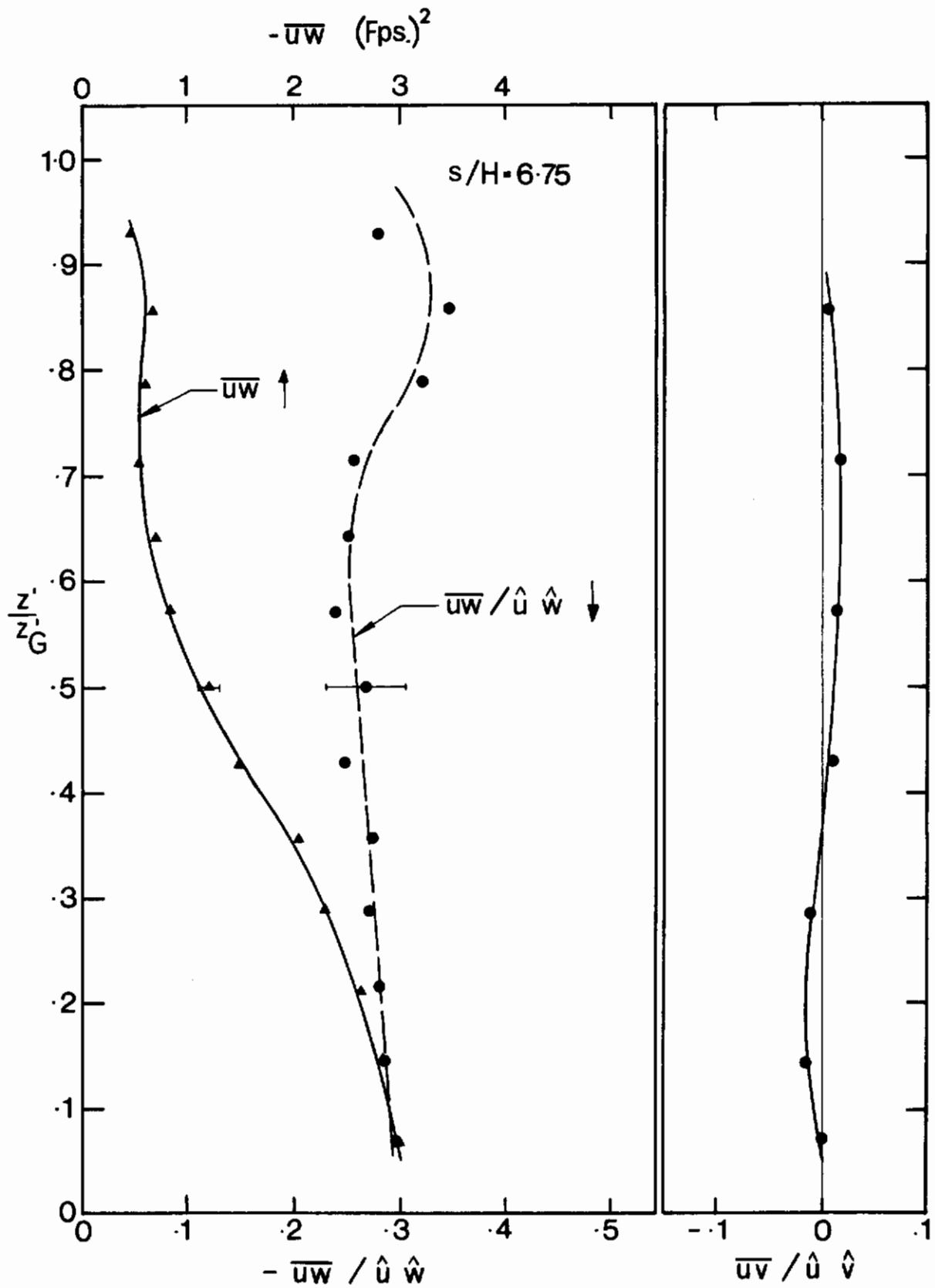
FIGURE 22.   REYNOLDS STRESS PROFILES IN SIMULATED FLOW,
8" x 8" TUNNEL

189
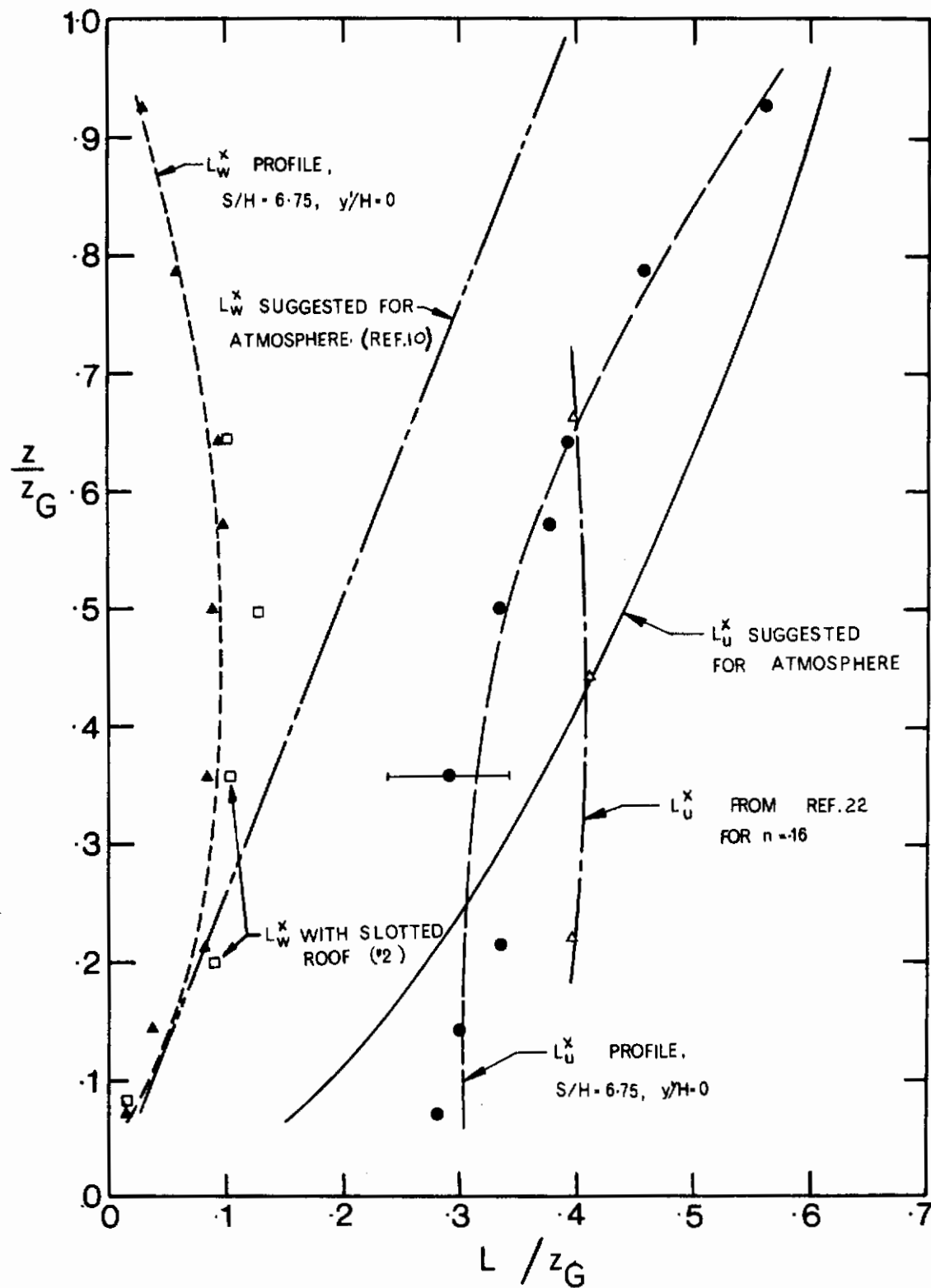
FIGURE 23.   INTEGRAL SCALE PROFILES IN SIMULATED FLOW,
8" x 8" TUNNEL

190
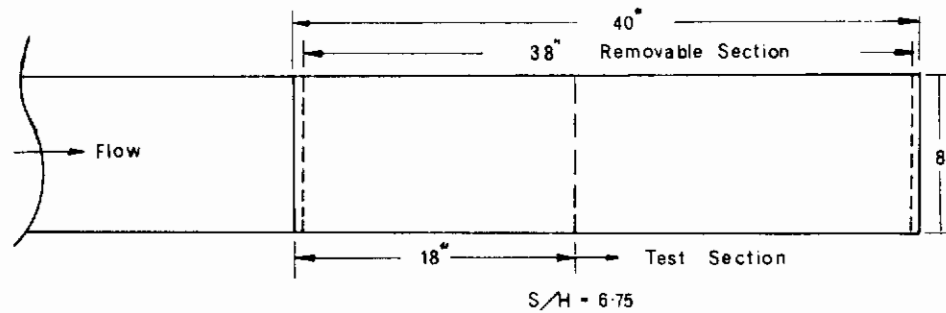
(a) LOCATION OF REMOVABLE ROOF SECTION

1. SOLID ROOF

2. SLOTS:

$\frac{1}{2}$" TYP

$\frac{1}{2}$" TYP
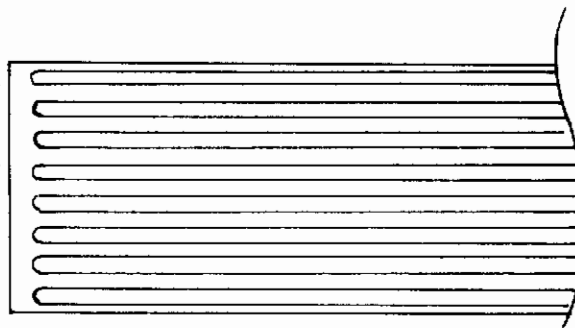
3. SLOTS AS ABOVE WITH COARSE SCREEN (MESH $\sim \frac{1}{2}$") ON TOP

4. SLOTS AS ABOVE WITH FINE SCREEN (MESH $\sim \frac{1}{16}$") ON TOP

5. HOLES:

1" TYP

$\frac{1}{2}$" TYP
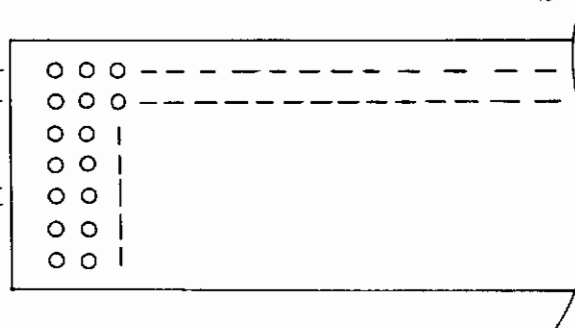
6. OPEN ROOF

7. OPEN ROOF WITH FINE SCREEN

8. BLOCKS:
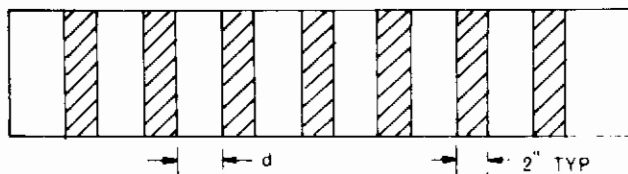
FIGURE 24.   TEST ROOF CONFIGURATIONS
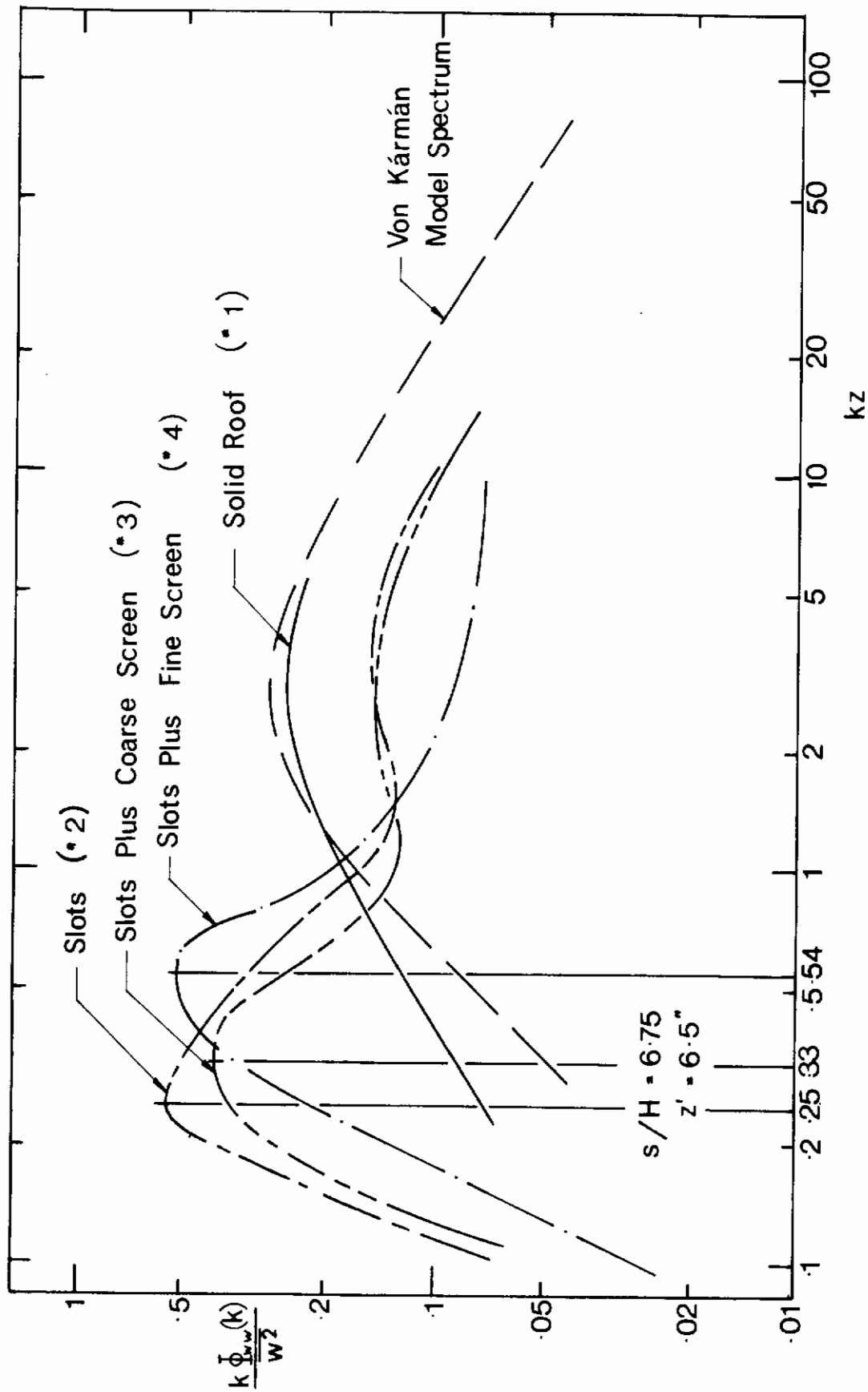
FIGURE 25.   EFFECT OF DIFFERING ROOF CONFIGURATIONS ON THE VERTICAL
COMPONENT POWER SPECTRUM
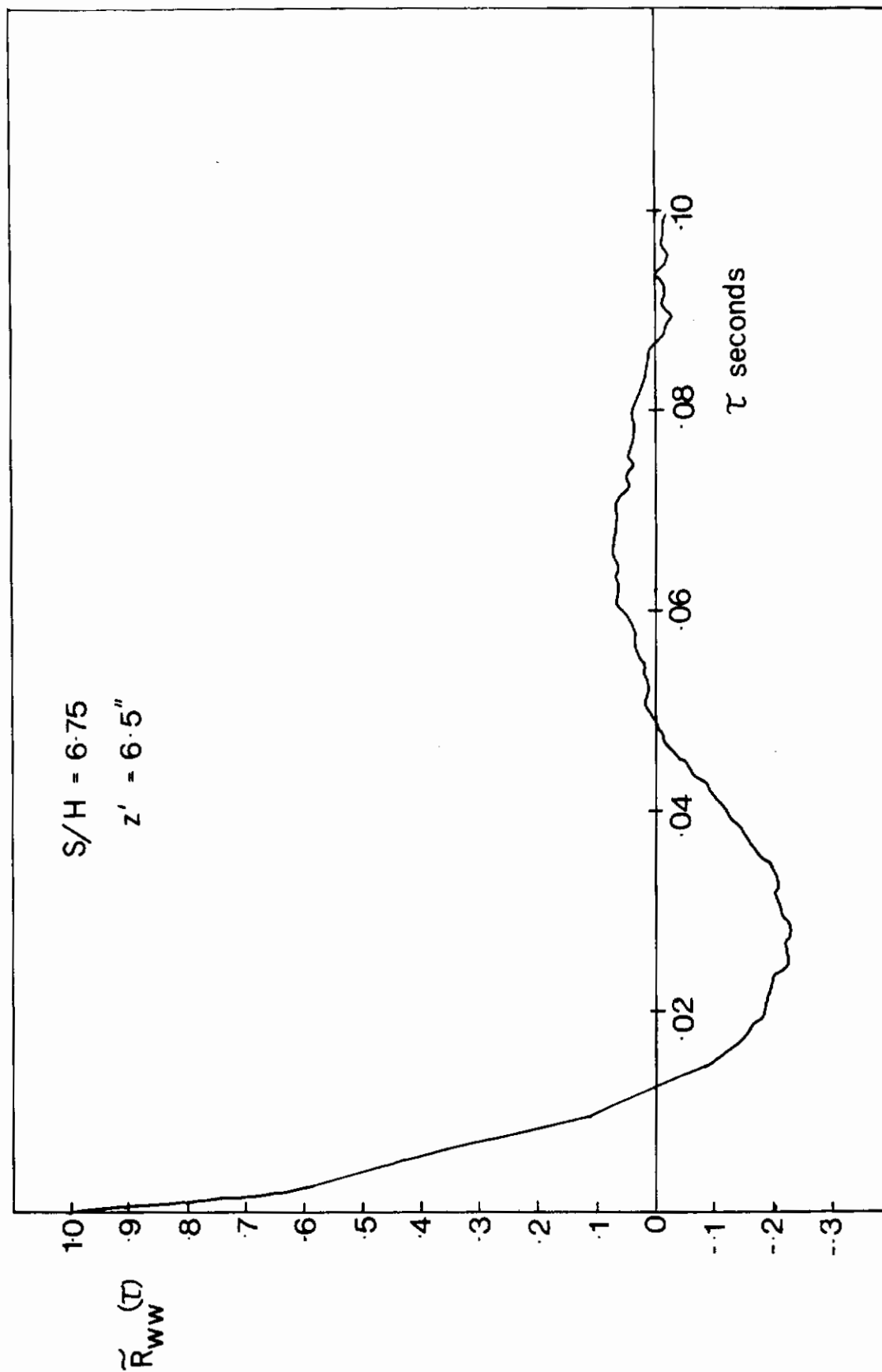
FIGURE 26. AUTOCORRELATION OF VERTICAL COMPONENT WITH SLOTTED ROOF #2

193

Free Stream

• x

Nominal
Boundary
Layer
Thickness
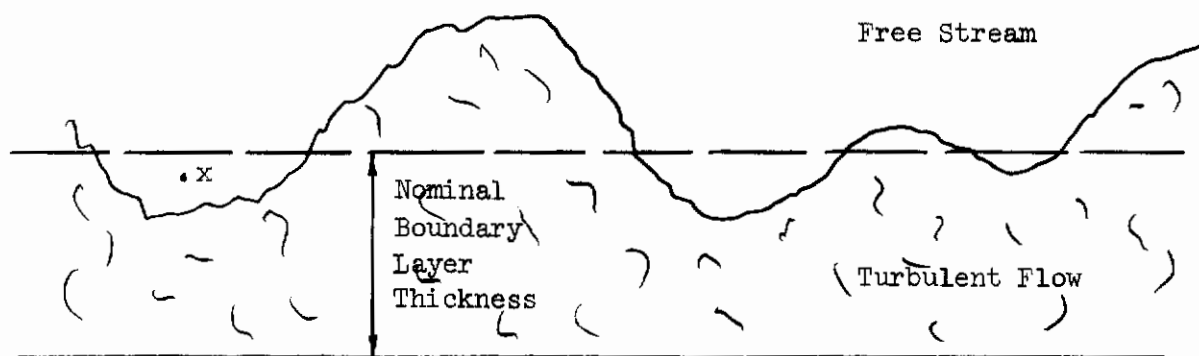
Turbulent Flow

FIGURE 27.   INTERACTION OF A TURBULENT FLOW WITH AN ADJACENT FREE STREAM

194
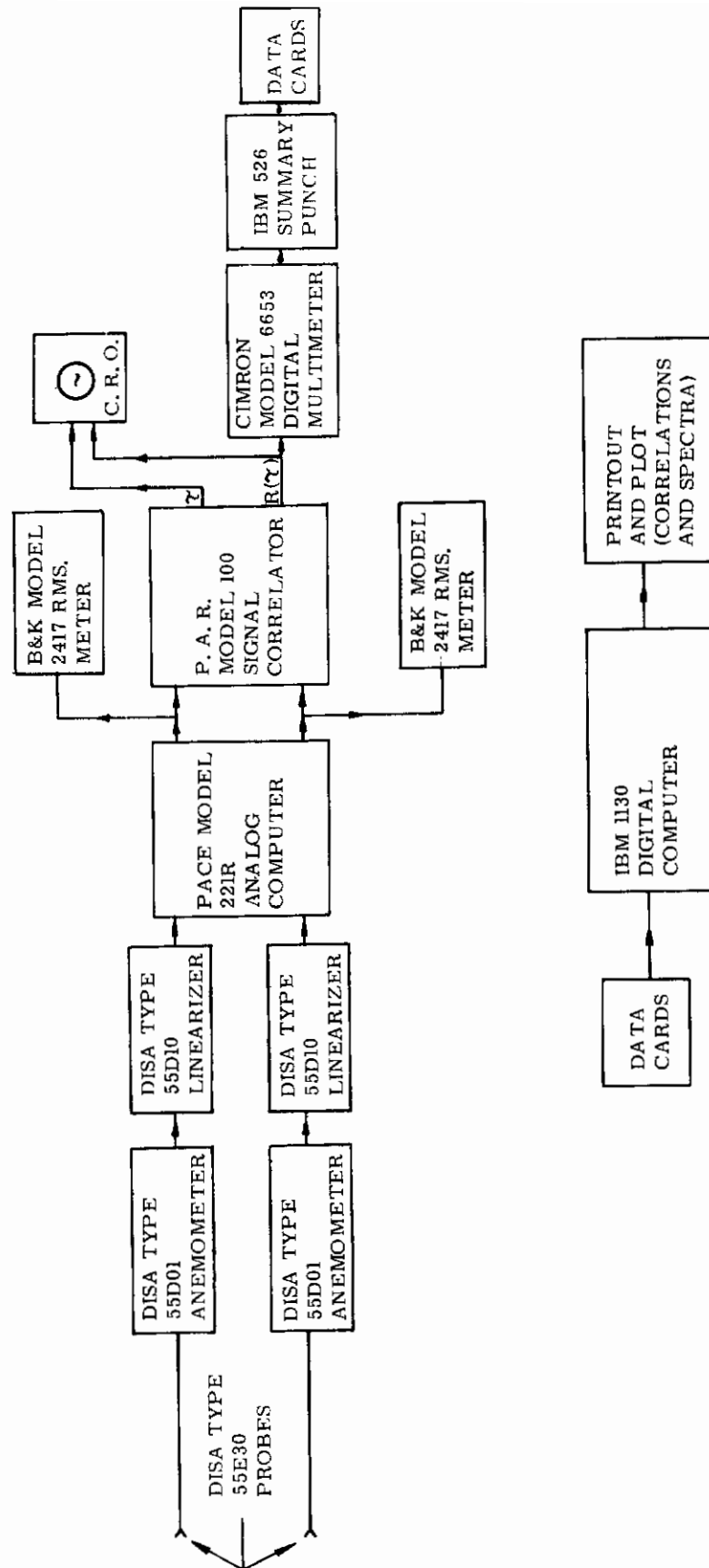
FIGURE 28a. DATA HANDLING SYSTEM, 8" x 8" TUNNEL
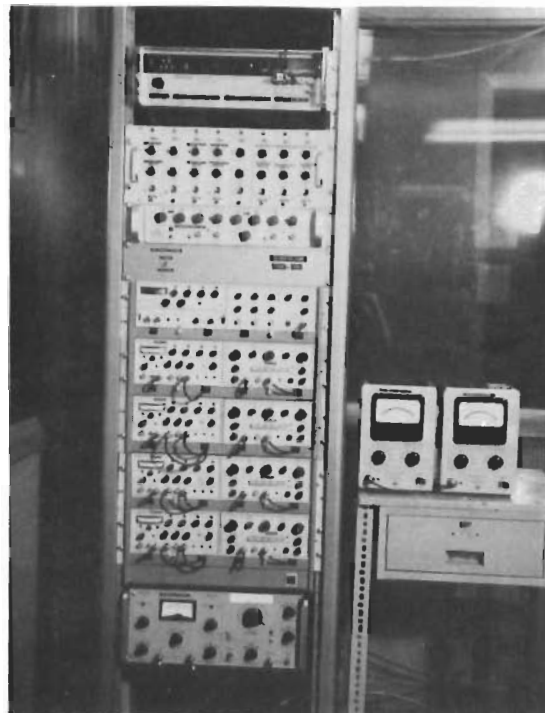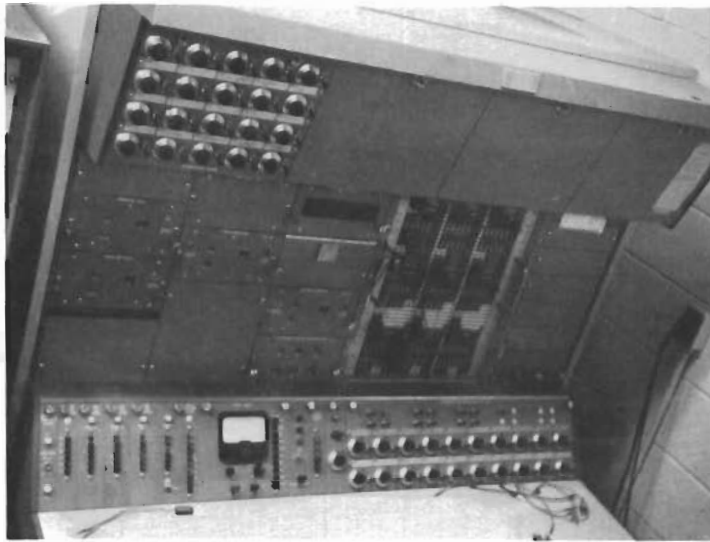
FIGURE 28b. DATA HANDLING SYSTEM, 8" x 8" TUNNEL

196
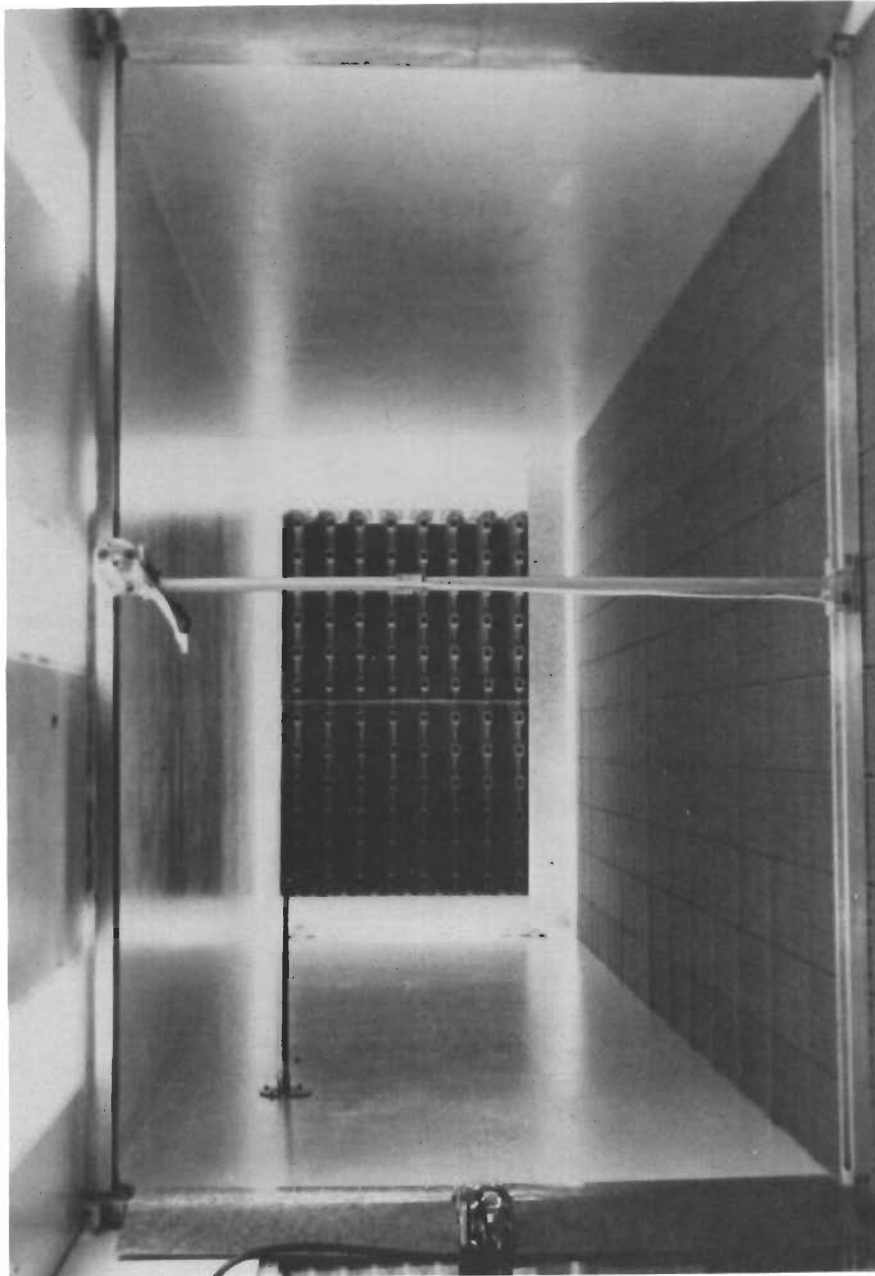
FIGURE 29. 44" x 66" BOUNDARY LAYER SIMULATION TUNNEL JET ARRAY
VIEWED UPSTREAM FROM THE TEST SECTION
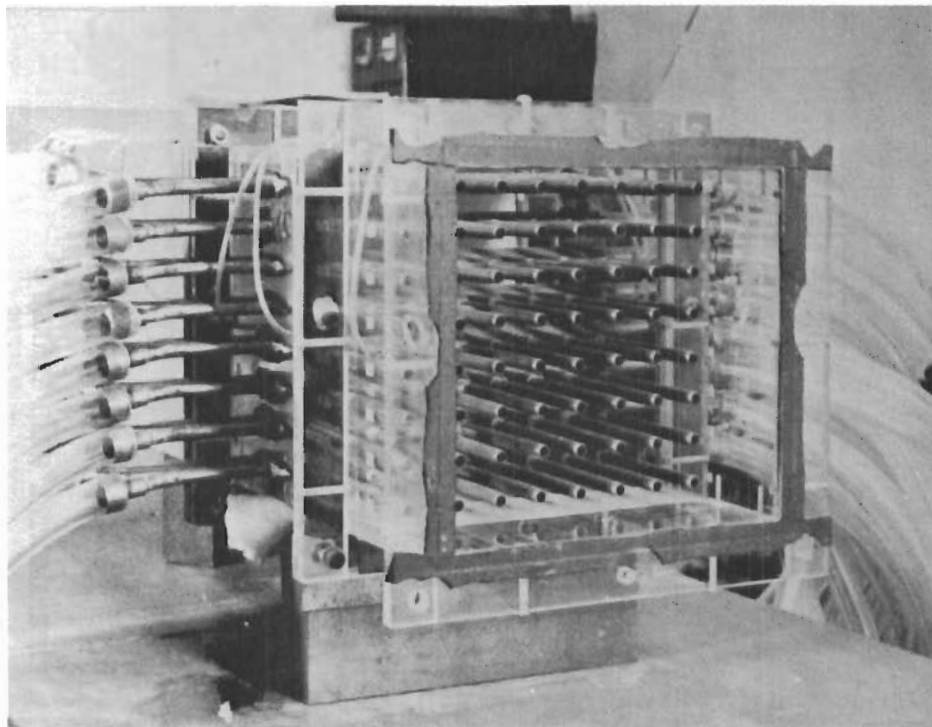
FIGURE 30. 8" x 8" TUNNEL JET SECTION
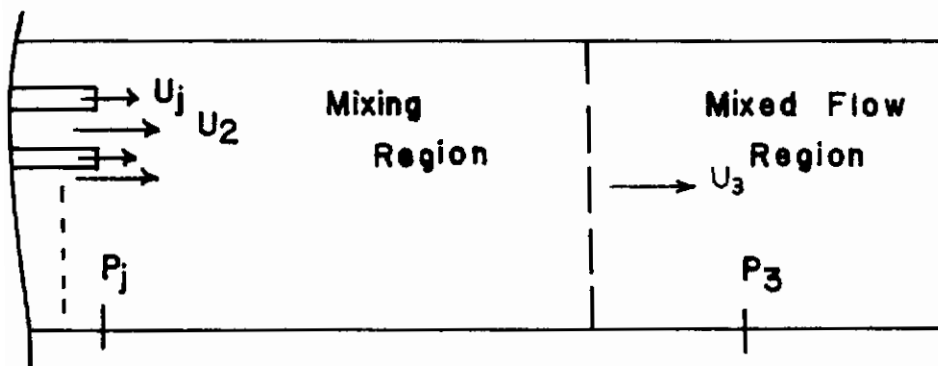
FIGURE 31. MIXING REGION
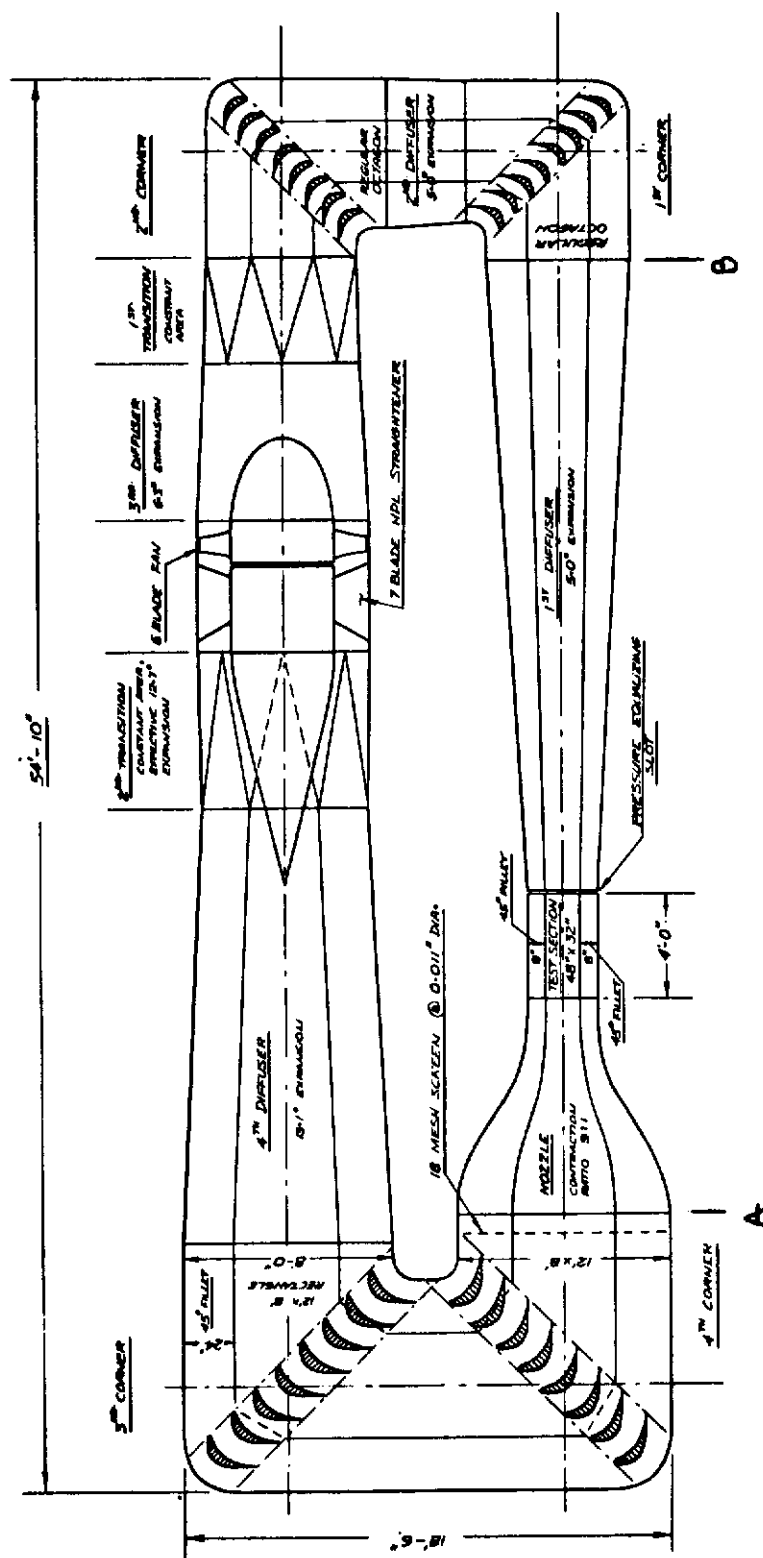
FIGURE 32. ORIGINAL LARGE WIND TUNNEL AERODYNAMIC OUTLINE

FIGURE 33. 44" x 66" TUNNEL AERODYNAMIC OUTLINE

201
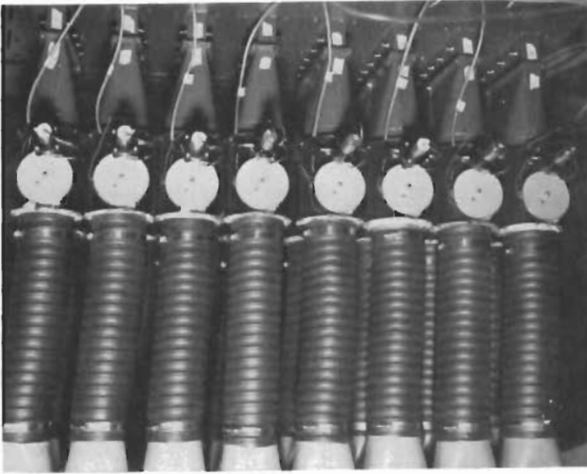
(c) BUTTERFLY VALVES AND SERVOS

(b) TEST SECTION

(a) GENERAL

FIGURE 34. GENERAL VIEWS OF 44" x 66" TUNNEL

202
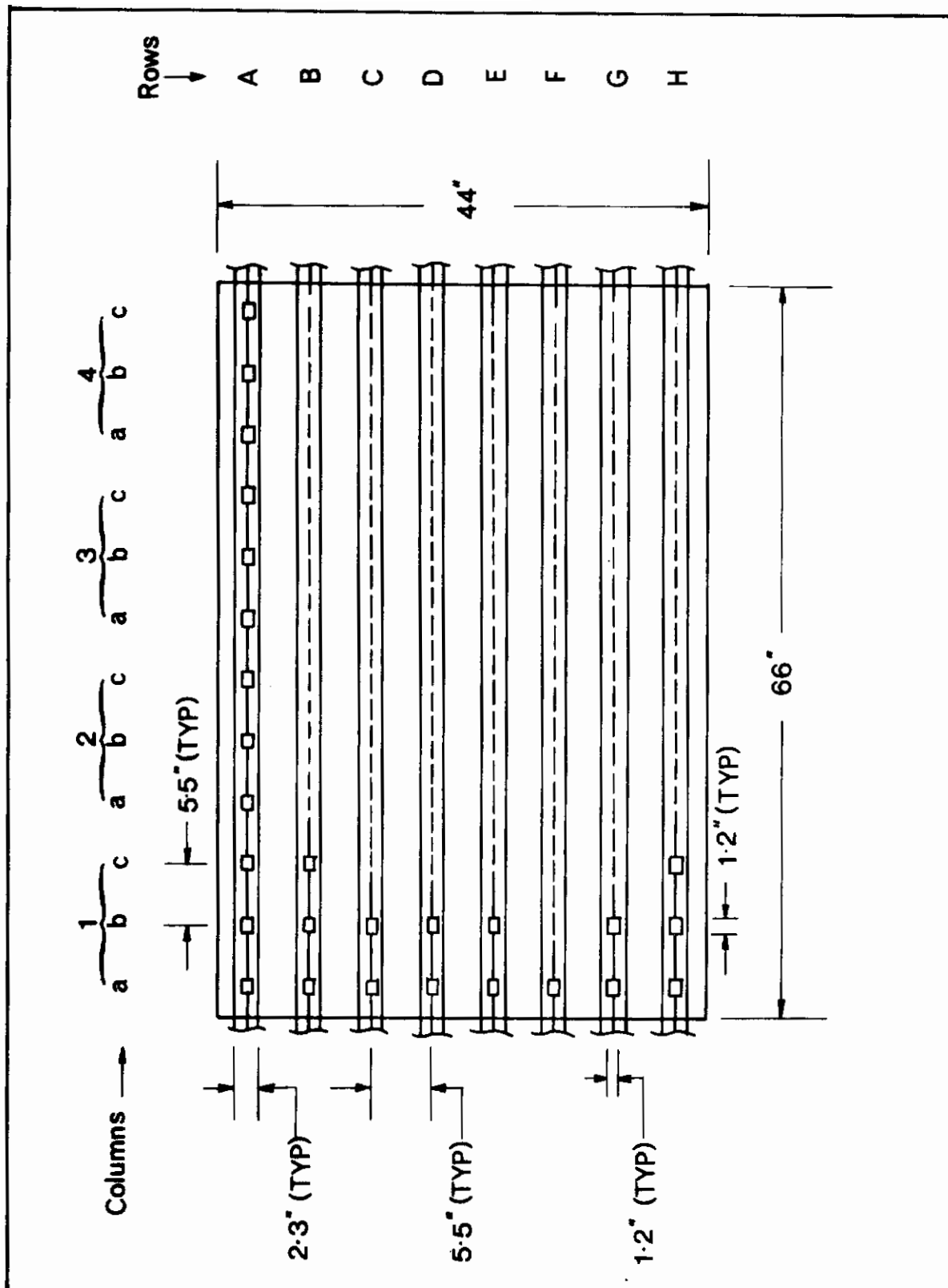
FIGURE 35. LAYOUT OF JET GRID SECTION, 44" x 66" TUNNEL
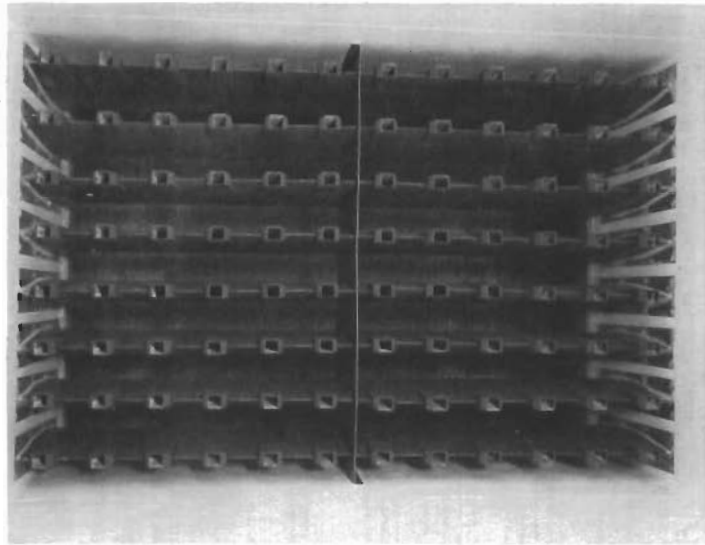
FIGURE 36.   UPSTREAM VIEW OF JET GRID, 44" x 66" TUNNEL
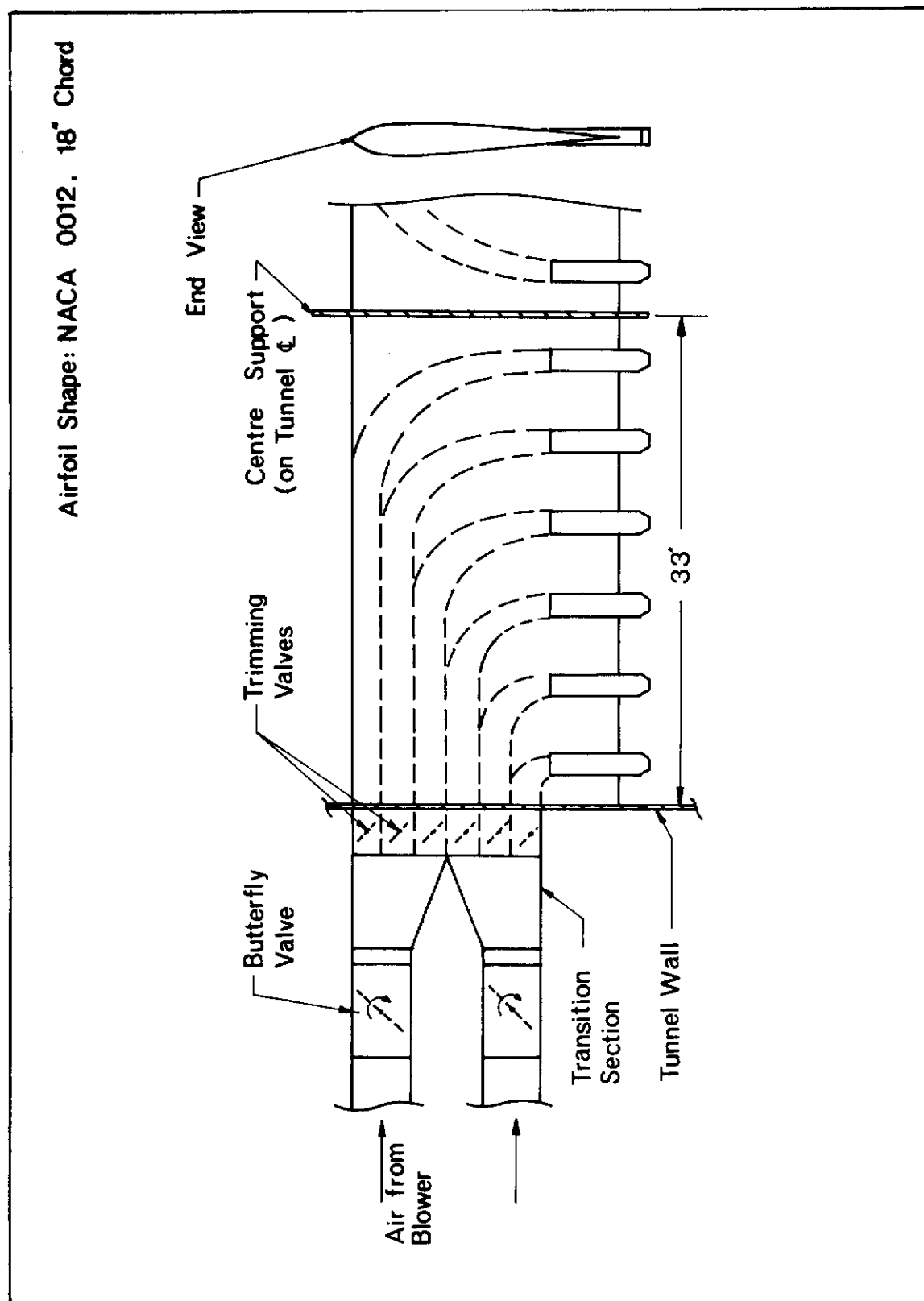
FIGURE 37. LAYOUT OF A TYPICAL ROW OF JETS AND SUPPLY LINES, 44" x 66" TUNNEL

205
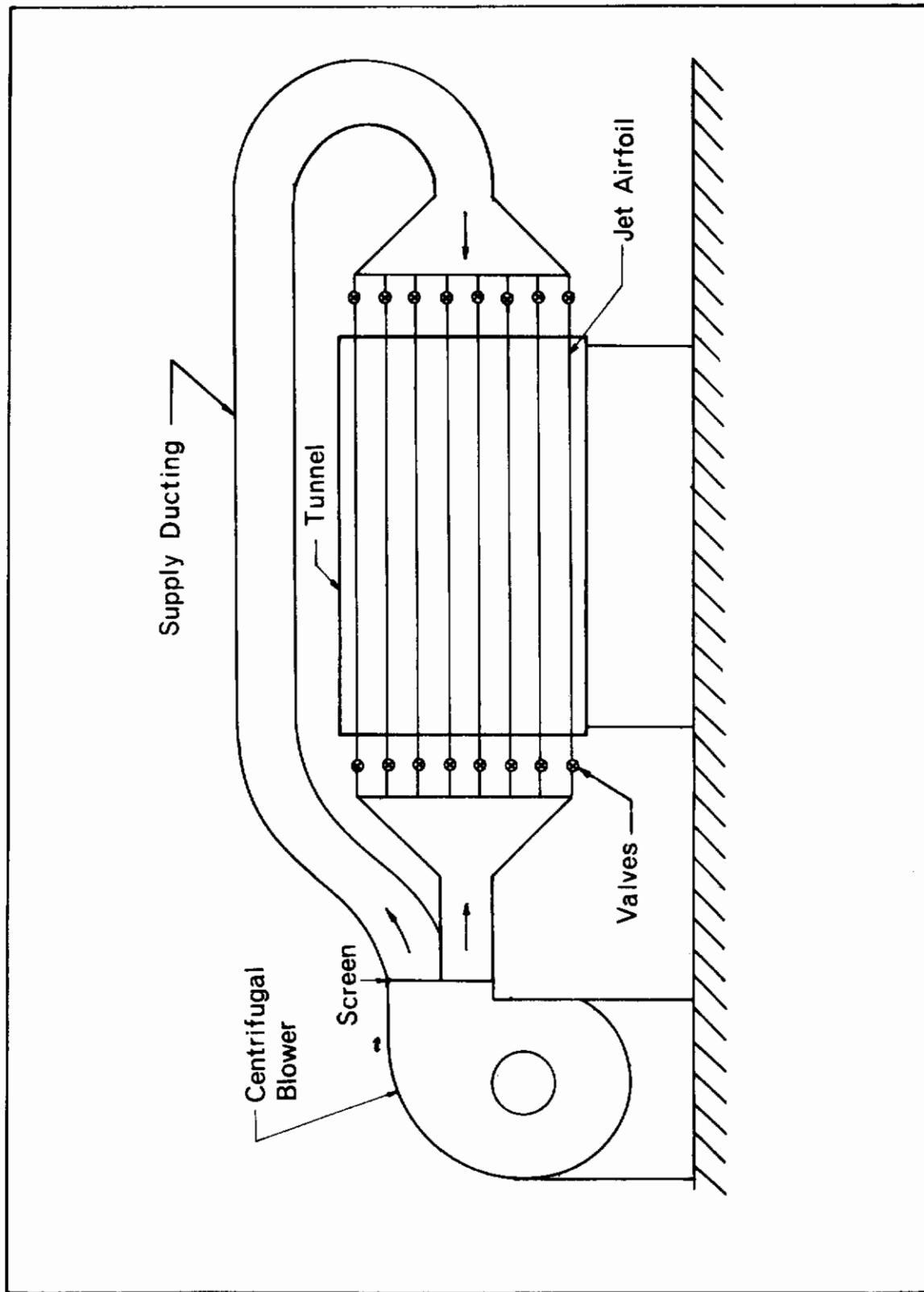
FIGURE 38. LAYOUT OF JET SUPPLY SYSTEM, 44" x 66" TUNNEL
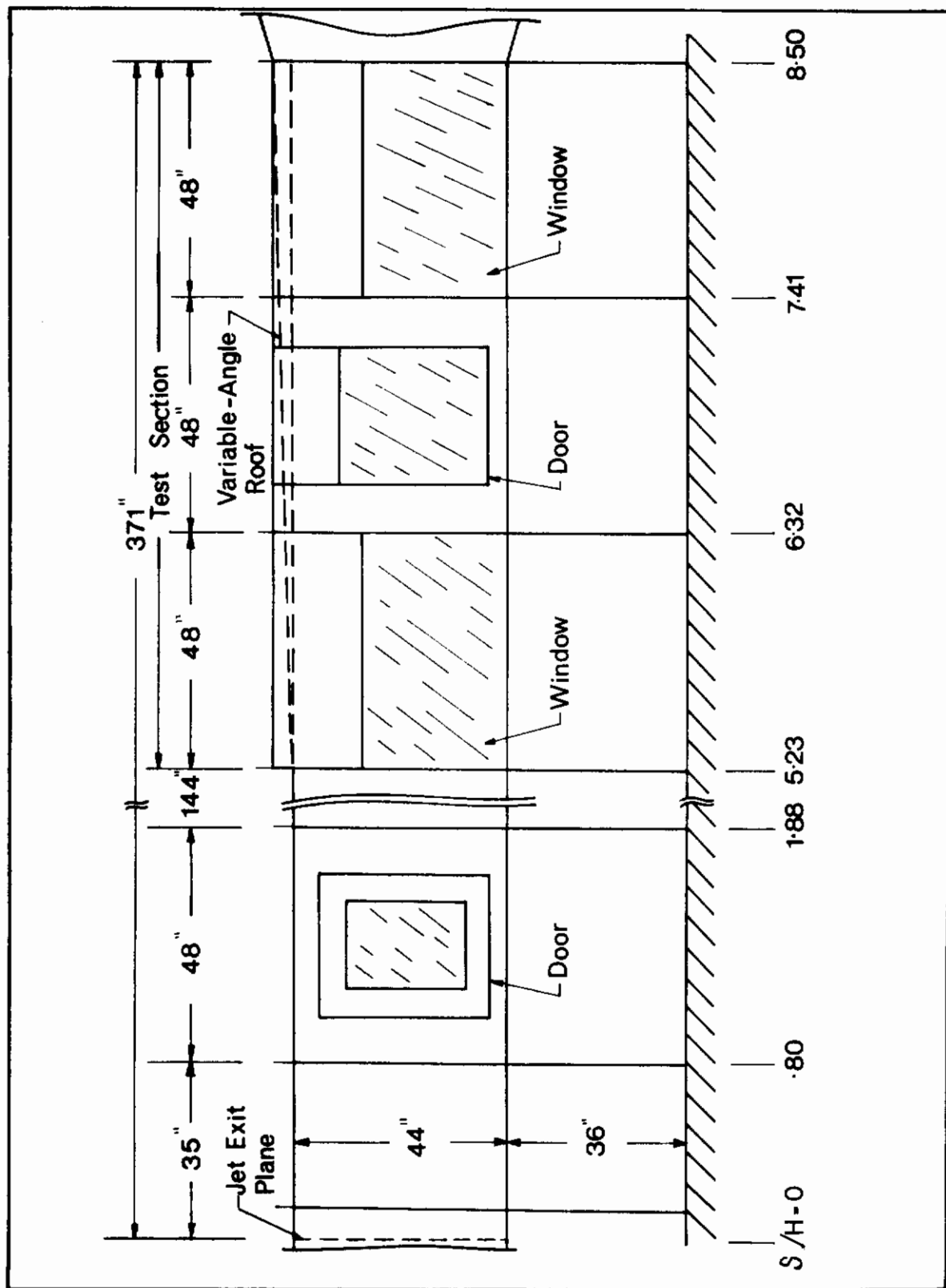
FIGURE 39. 44" x 66" TUNNEL GROWTH AND TEST SECTIONS

207
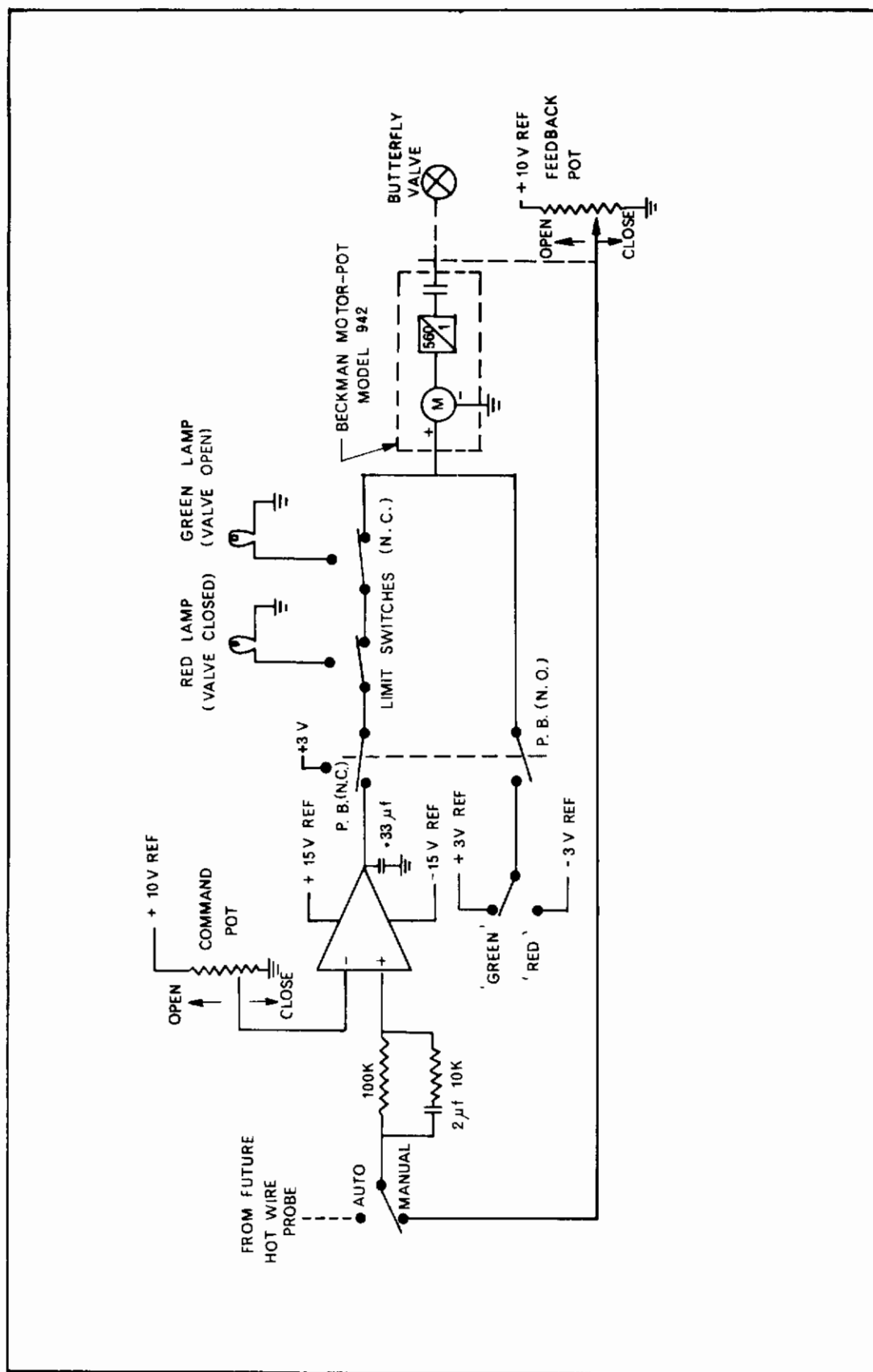
FIGURE 40. BUTTERFLY VALVE CONTROL CIRCUIT 44" x 66" TUNNEL
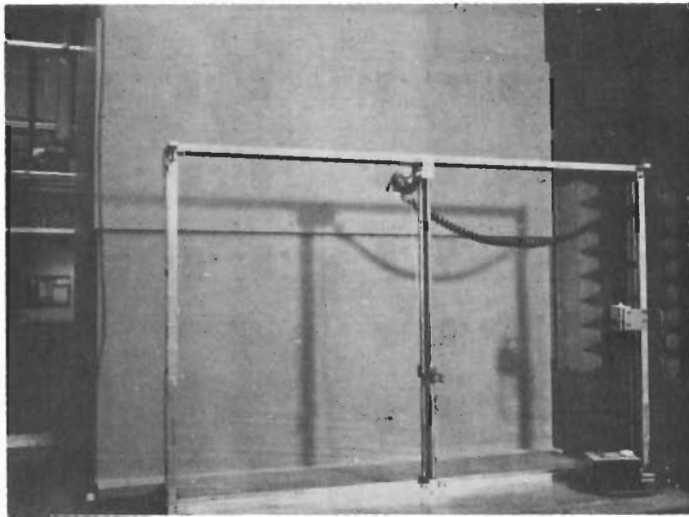
FIGURE 41.   TRAVERSING RIG 44" x 66" TUNNEL
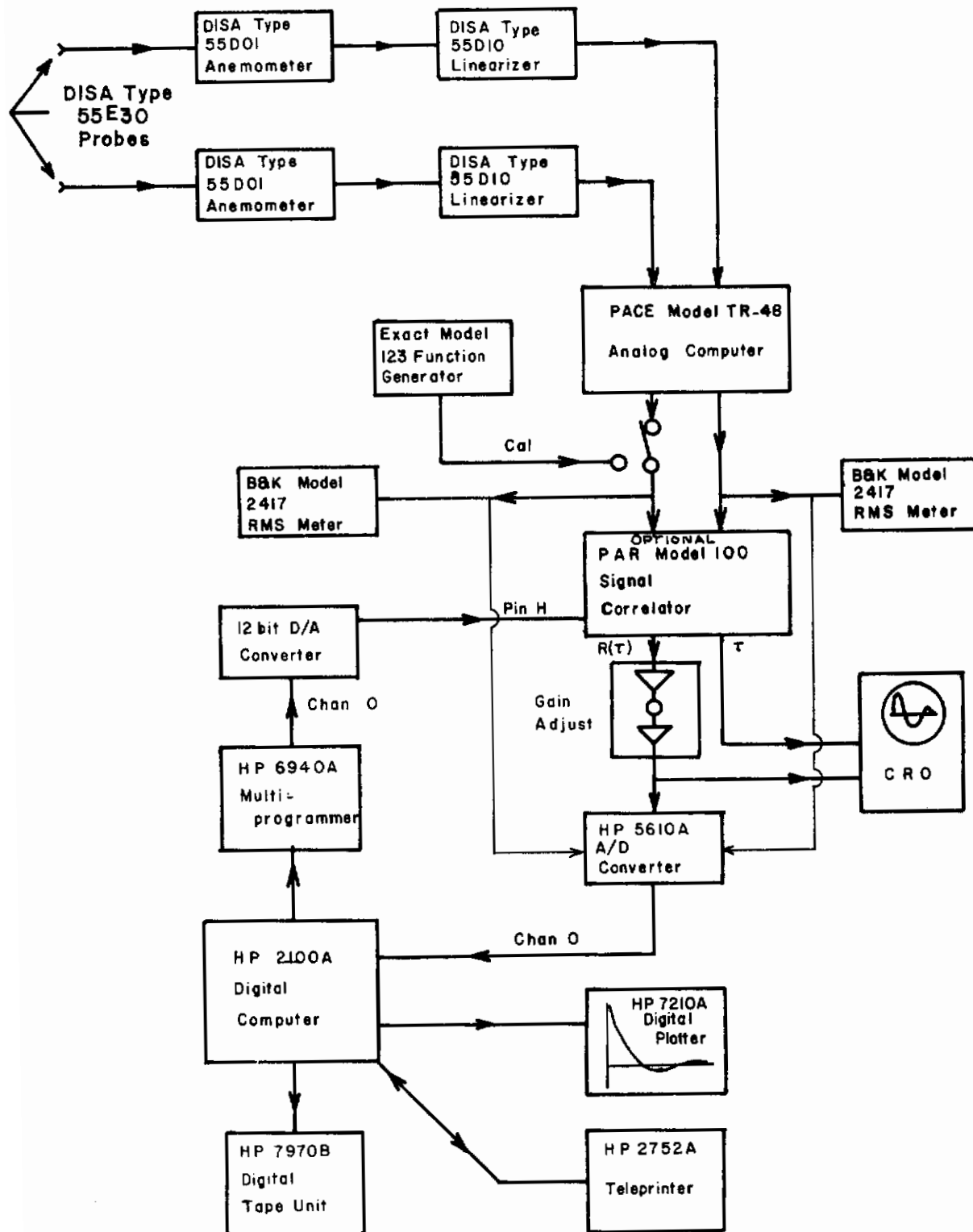
FIGURE 42a. DATA HANDLING SYSTEM, 44" x 66" TUNNEL
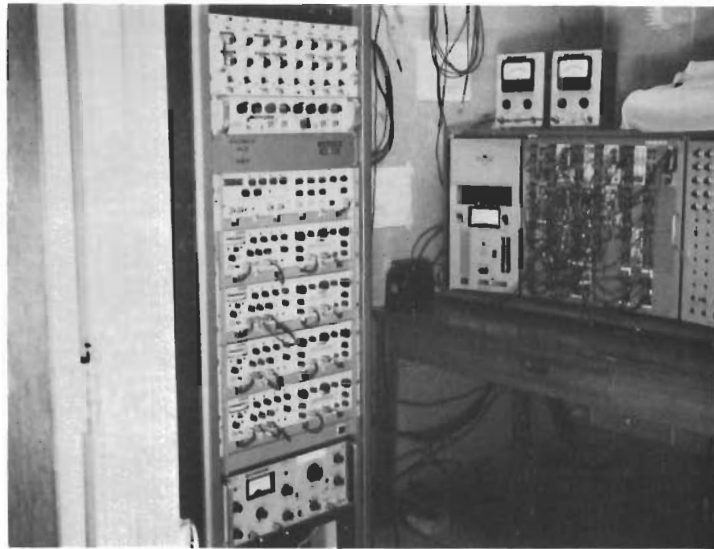
FIGURE 42b.   DATA HANDLING SYSTEM, 44" x 66" TUNNEL

211
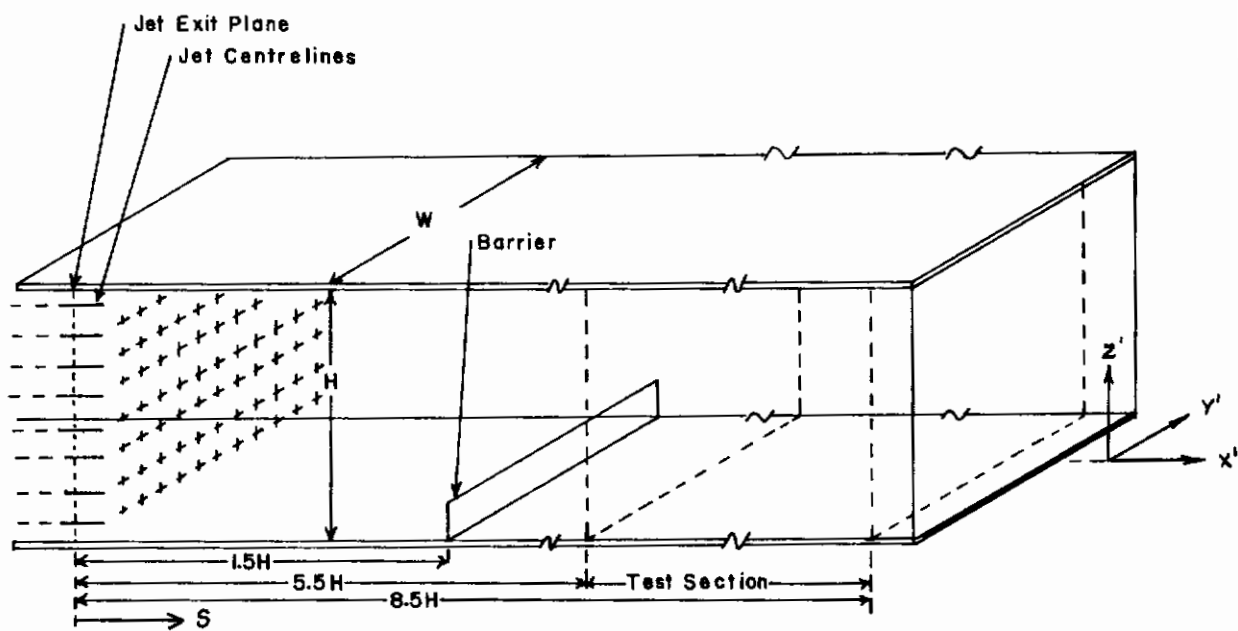
FIGURE 43.   44" x 66" TUNNEL LAYOUT

S = 5.5 H
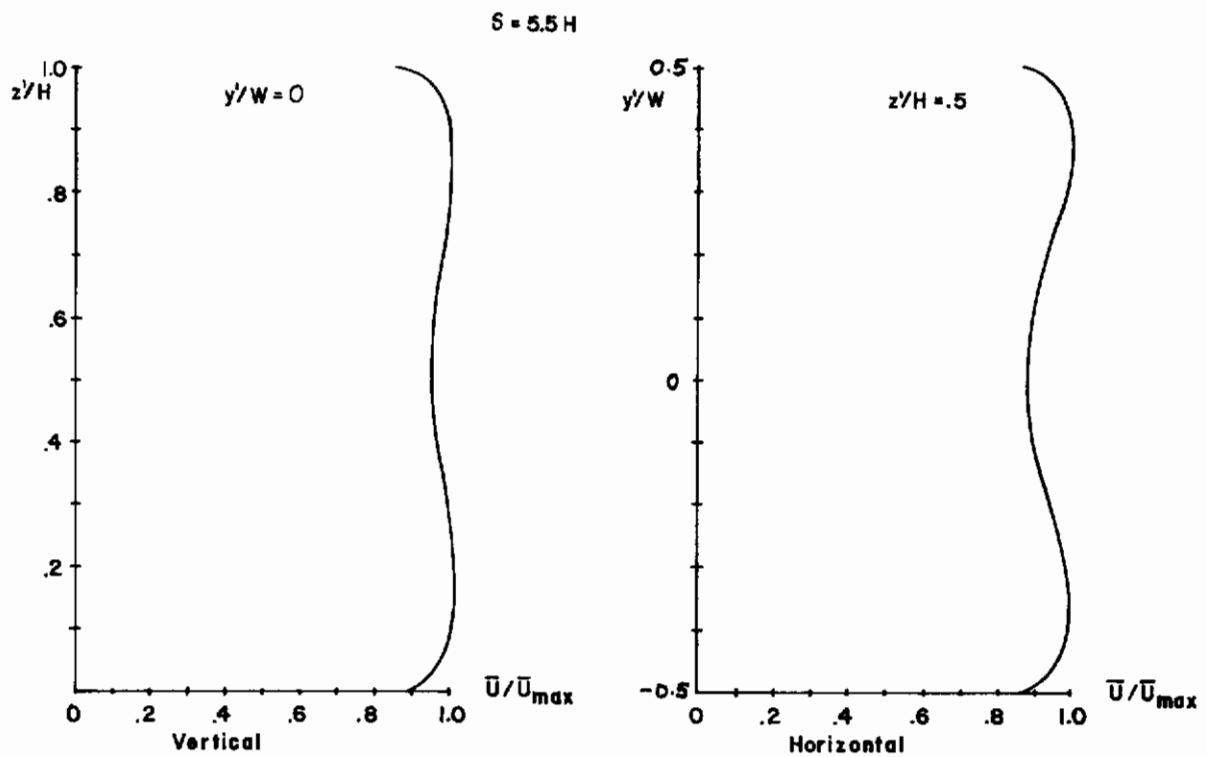
FIGURE 44.   MEAN VELOCITY PROFILES IN 44" x 66" TUNNEL
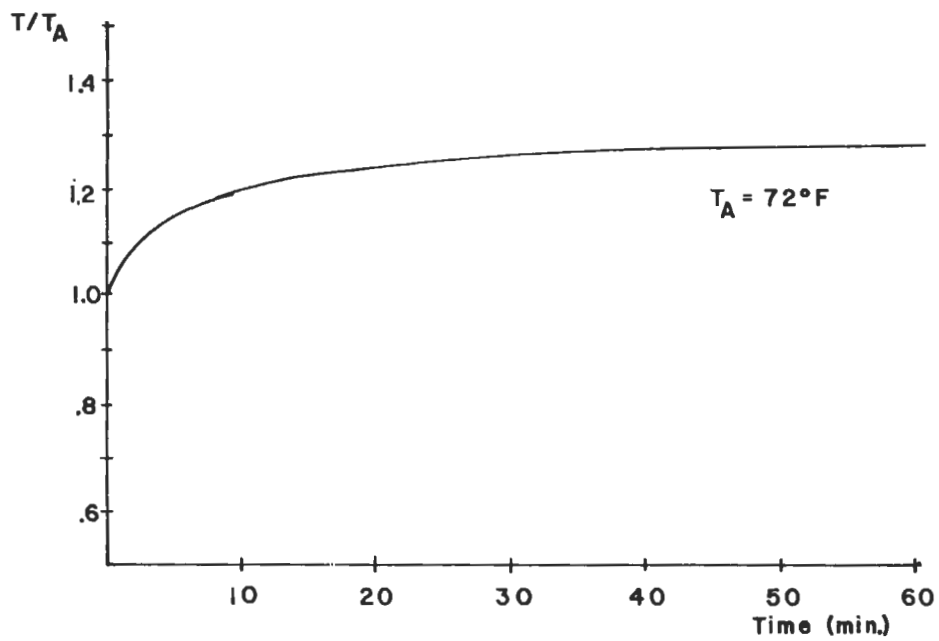
FIGURE 45.   44" x 66" TUNNEL TEMPERATURE HISTORY

FIGURE 46.   FLOOR ROUGHNESS FOR n = 0.16, 44" x 66" TUNNEL

Note: Positions Coincide
With Jet Exit Locations
At S = 0

(.5 +Y'/W)			.042	.123	.208	.292	.375	.458	.542	.625	.708	.792	.875	.960	

z'/Z'$_G$	z'/H		1			2			3			4			H = 44"
			a	b	c	a	b	c	a	b	c	a	b	c	W = 66"
1.145	.938	A	+	+	+	+	+	+	+	+	+	+	+	+	Z'$_G$ = 36"
.994	.813	B	+	+	+	+	+	+	+	+	+	+	+	+	
.840	.688	C	+	+	+	+	+	+	+	+	+	+	+	+	
.688	.513	D	+	+	+	+	+	+	+	+	+	+	+	+	
.534	.438	E	+	+	+	+	+	+	+	+	+	+	+	+	
.383	.312	F	+	+	+	+	+	+	+	+	+	+	+	+	
.229	.187	G	+	+	+	+	+	+	+	+	+	+	+	+	
.077	.063	H	+	+	+	+	+	+	+	+	+	+	+	+	
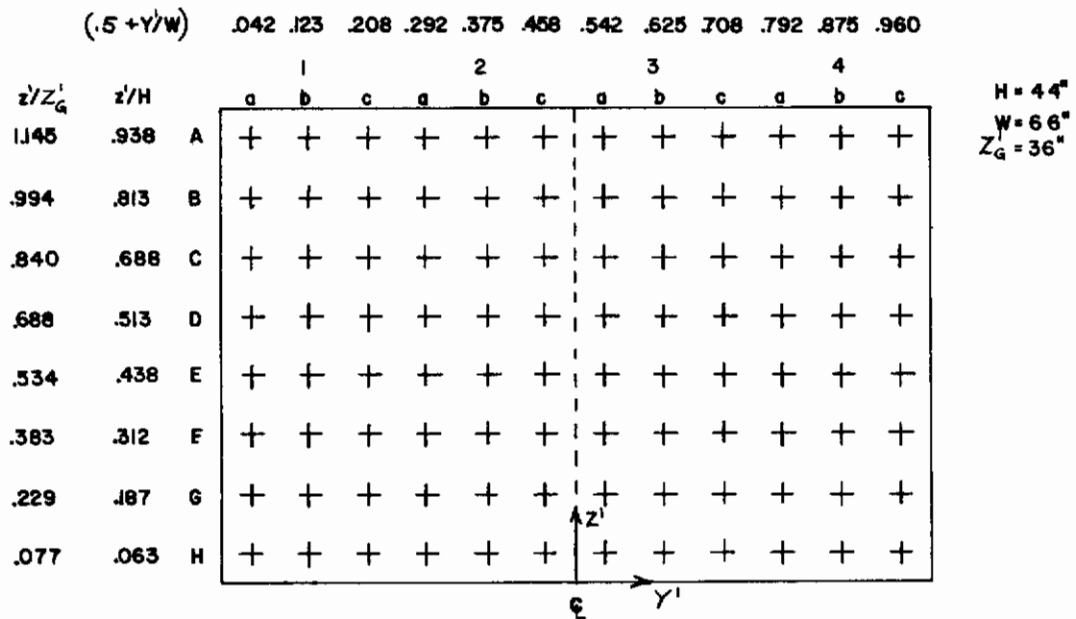
FIGURE 47.   GRID OF MEASUREMENT POSITIONS LOOKING UPSTREAM,
44" x 66" TUNNEL
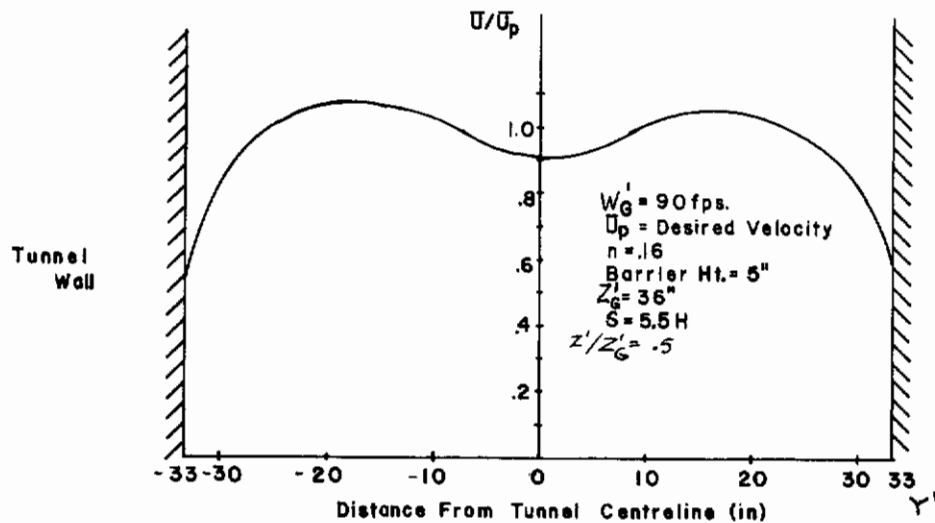
FIGURE 48.   MEAN LATERAL VELOCITY PROFILE IN SIMULATED FLOW,
44" x 66" TUNNEL WITH FLOOR ROUGHNESS AND BARRIER PRESENT

215
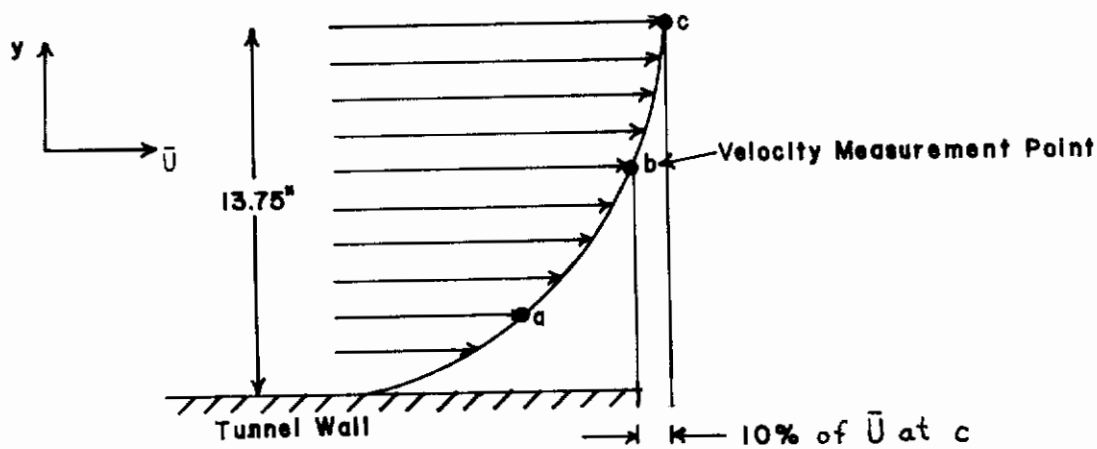
FIGURE 49. WALL BOUNDARY LAYER PROPERTIES, 44" x 66" TUNNEL
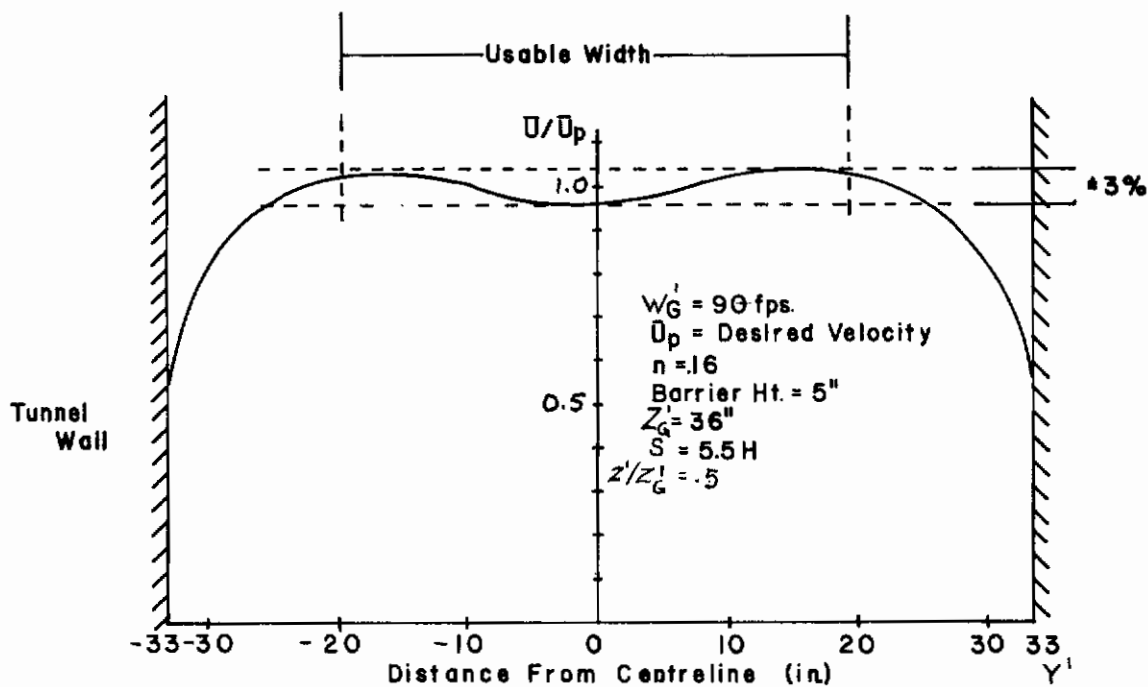
FIGURE 50. IMPROVED MEAN LATERAL VELOCITY PROFILE IN 44" x 66" TUNNEL

216
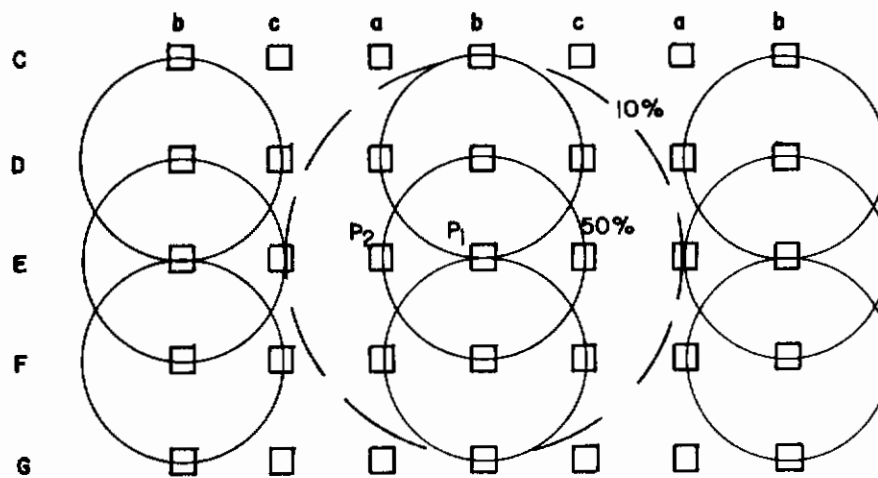
FIGURE 51. QUALITATIVE DESCRIPTION OF JET INFLUENCE REGIONS,
44" x 66" TUNNEL

Percentages represent $(\Delta U_{p_2}/\Delta U_{p_1})$ x 100, the change in velocity at P_2 resulting from a change in velocity at P_1, normalized by the velocity change at P_1.
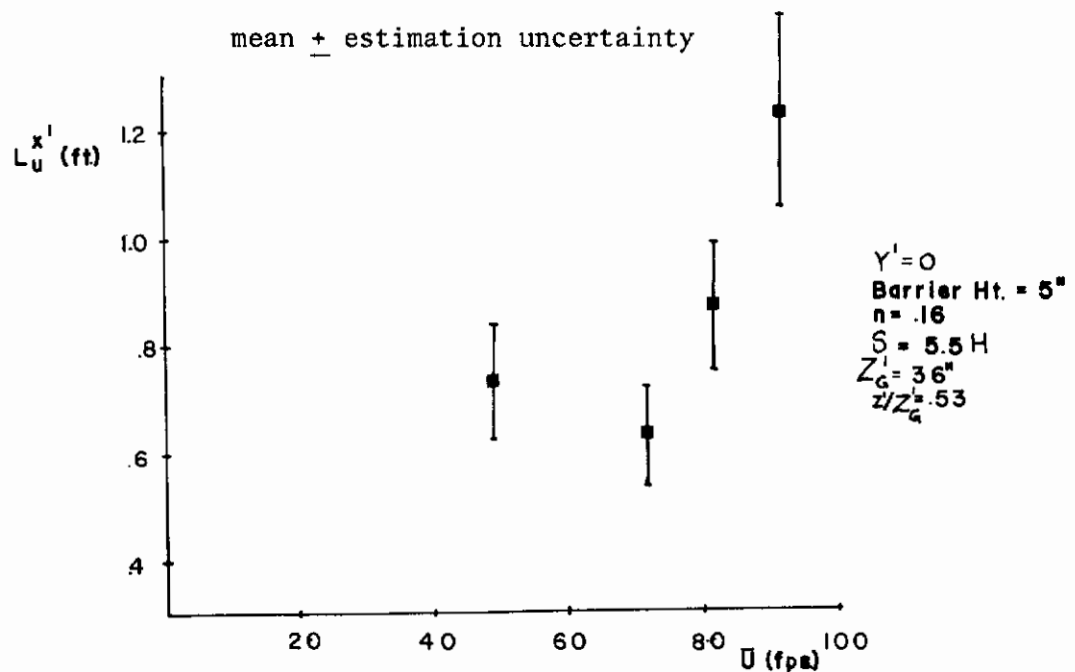
FIGURE 52. THE INFLUENCE OF MEAN VELOCITY ON INTEGRAL SCALE
IN THE 44" x 66" TUNNEL

217
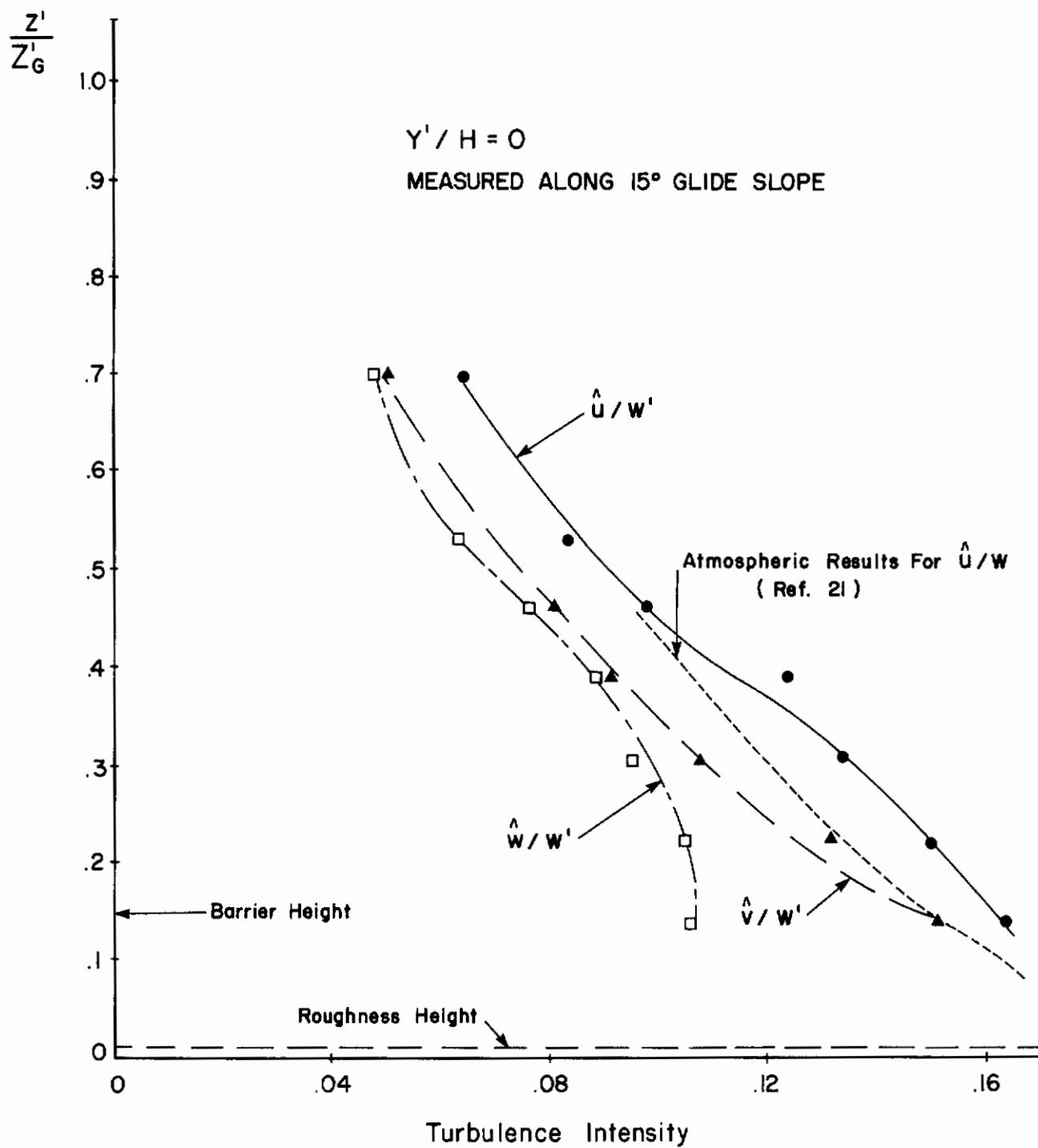
FIGURE 53. TURBULENCE INTENSITY PROFILES IN SIMULATED FLOW, 44" x 66" TUNNEL

218

$W'_G = 90$ fps
$Z'_G = 36$ "

Symbol	Y'/W	S/H
x	−.21	5.5
⊙	−.04	5.5
●	.04	5.5
⊡	.21	5.5
△	.21	8.5

$$\frac{W'}{W'_G} = \left(\frac{Z'}{Z'_G}\right)^{0.16}$$

Z'/Z'_G

←—Barrier Height

Roughness Height

W'/W'_G
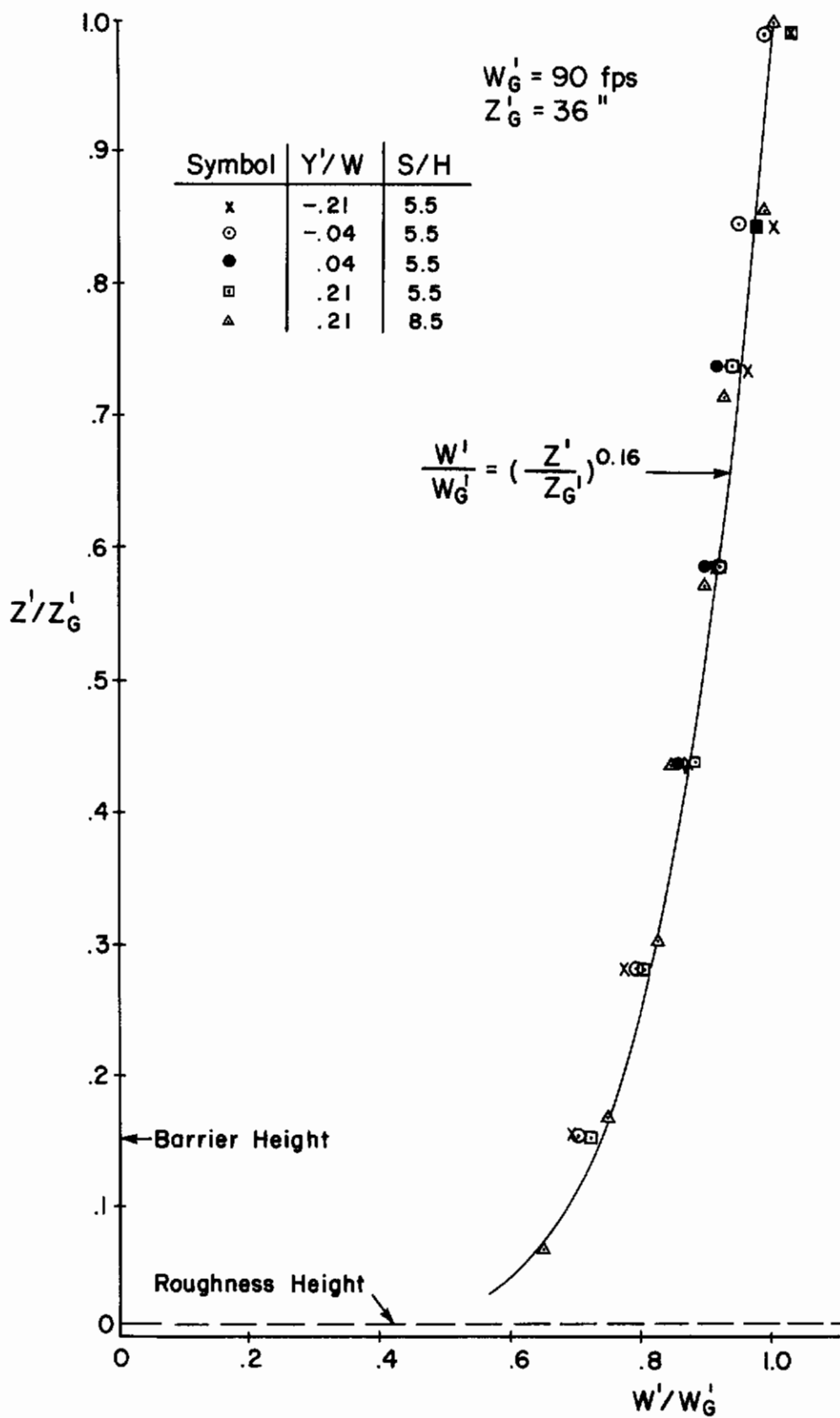
FIGURE 54. MEAN VELOCITY PROFILES IN SIMULATED FLOW, 44" x 66" TUNNEL

219
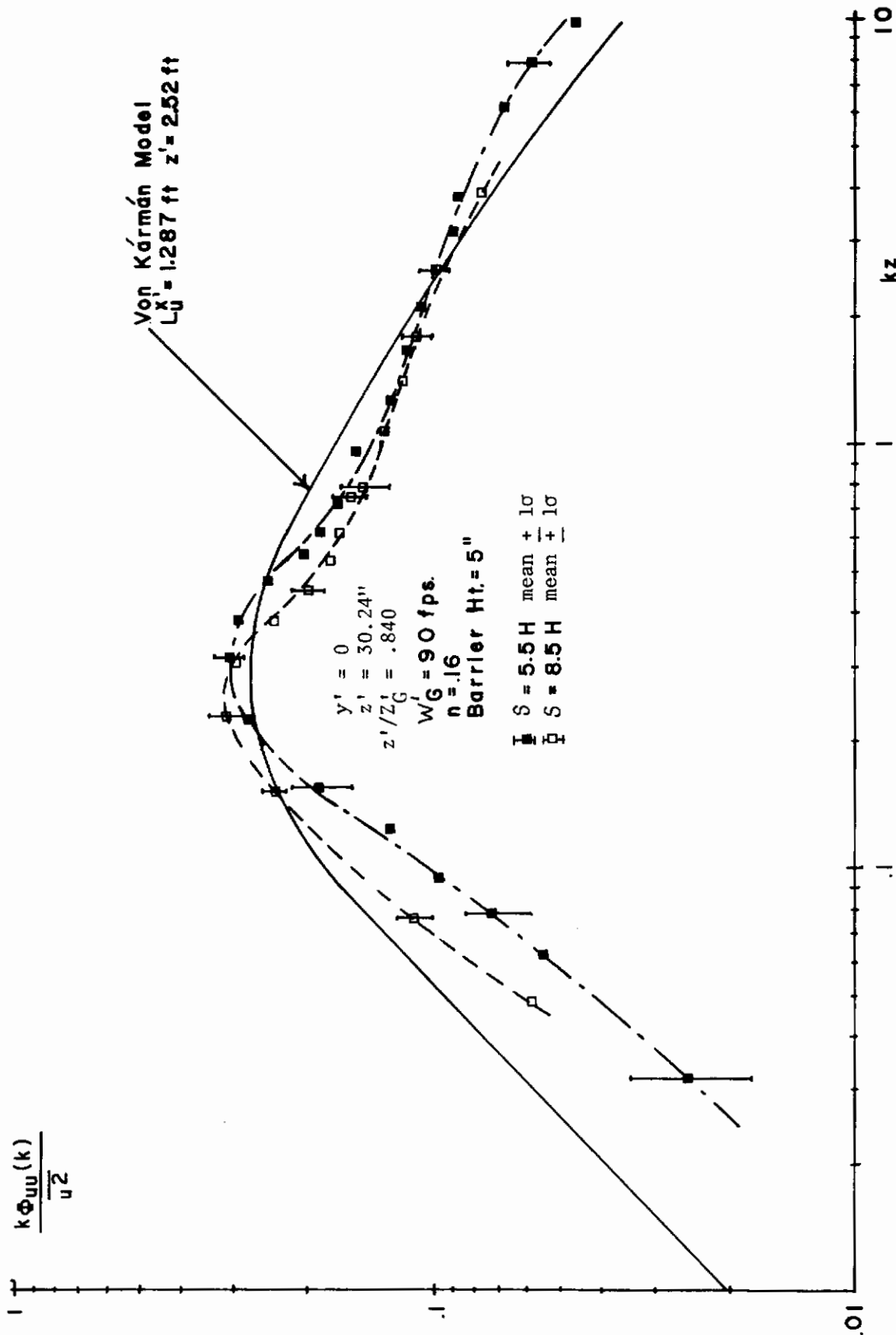
FIGURE 55. LONGITUDINAL COMPONENT POWER SPECTRA ON TUNNEL CENTRE LINE, 44" x 66" TUNNEL
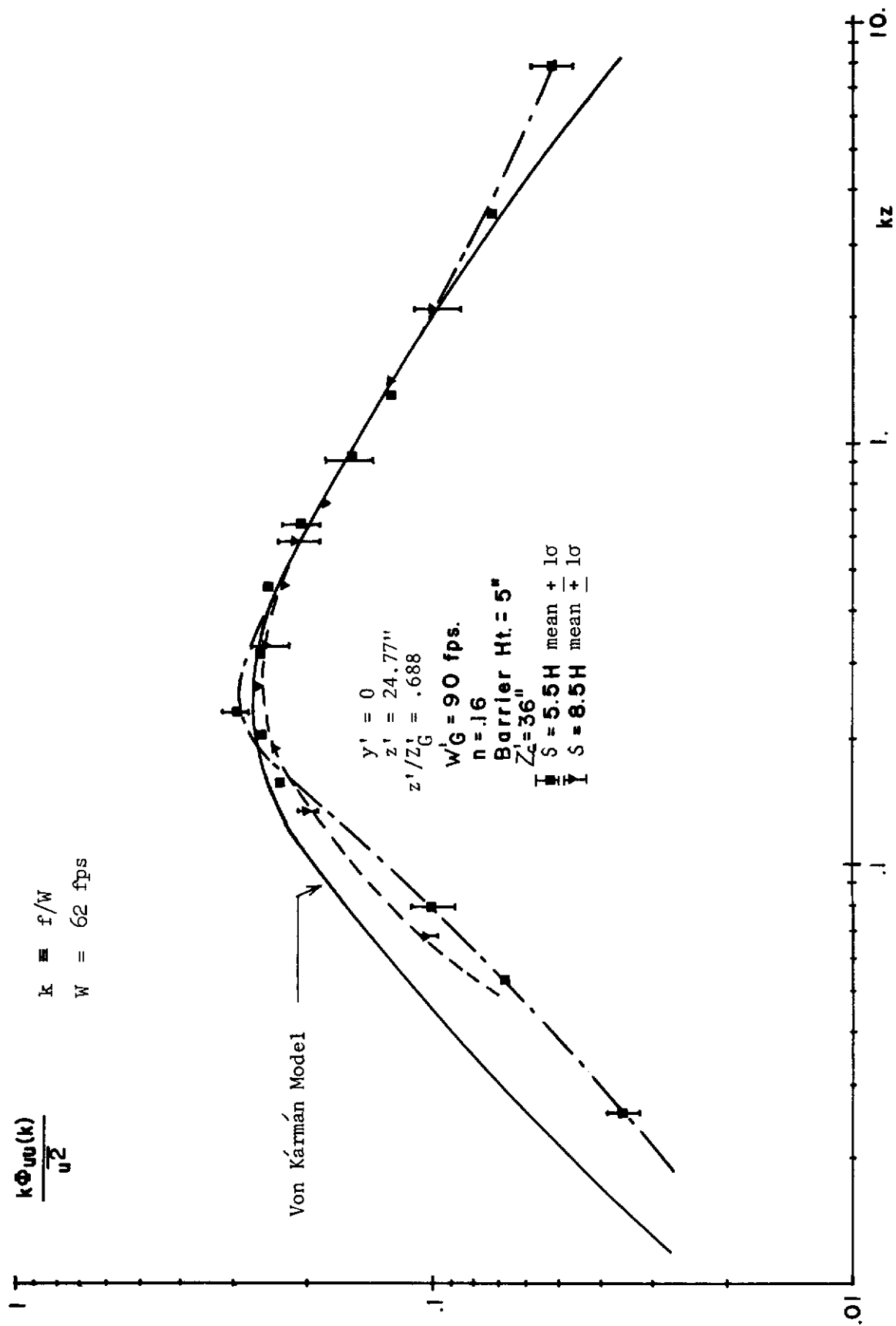
FIGURE 56. LONGITUDINAL COMPONENT POWER SPECTRA ON TUNNEL CENTRE LINE,
44" x 66" TUNNEL

221
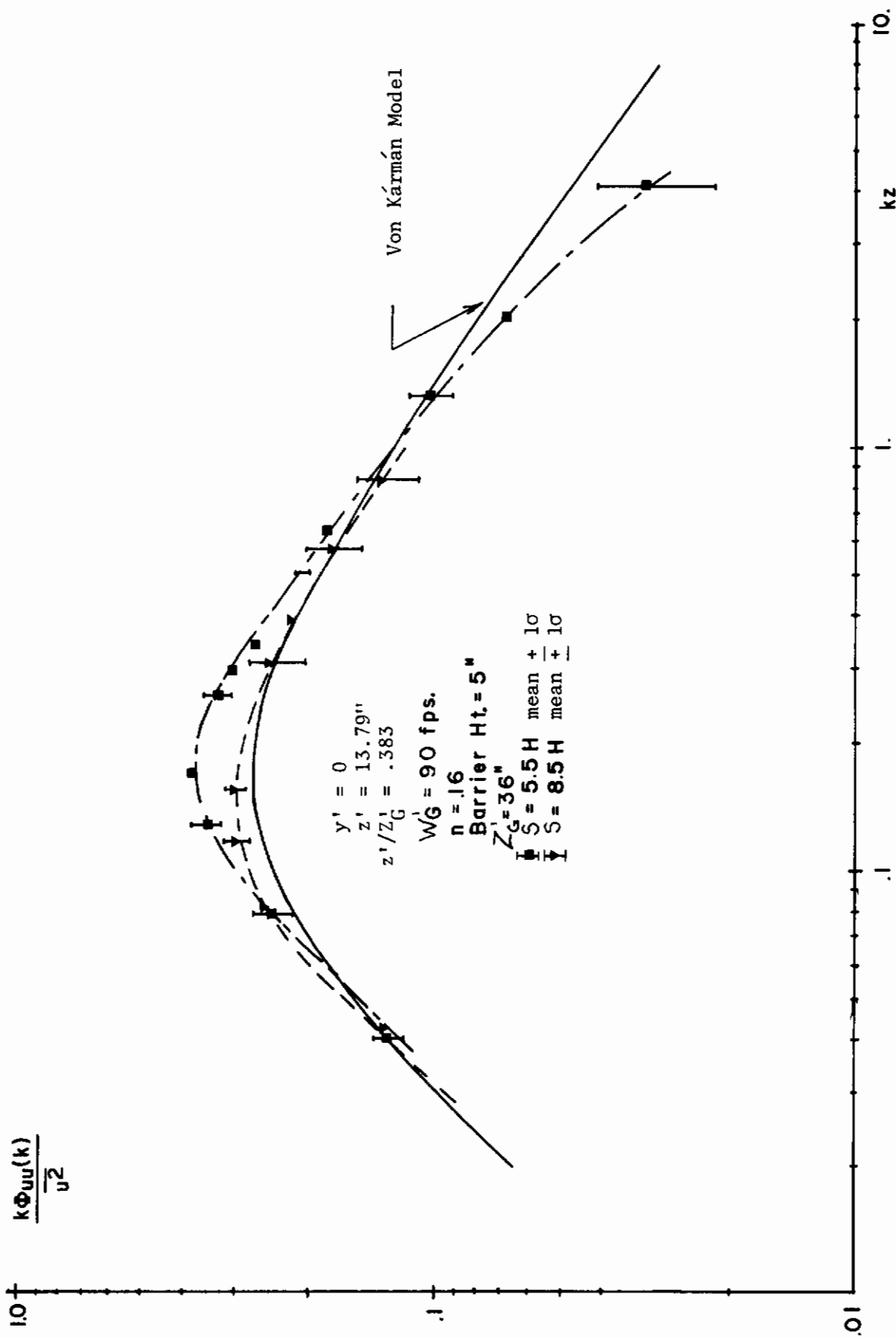
FIGURE 57. LONGITUDINAL COMPONENT POWER SPECTRA ON TUNNEL CENTRE LINE,
44" x 66" TUNNEL

$$\frac{k\Phi_{uu}(k)}{u^2}$$

y' = 0
z' = 2.77"
z'/Z'_G = .077
W/G = 90 fps.
n = .16
Barrier Ht. = 5"
Z'_G = 36"
S = 5.5 H   mean + 1σ
S = 8.5 H   mean + 1σ

Von Kármán Model

kz
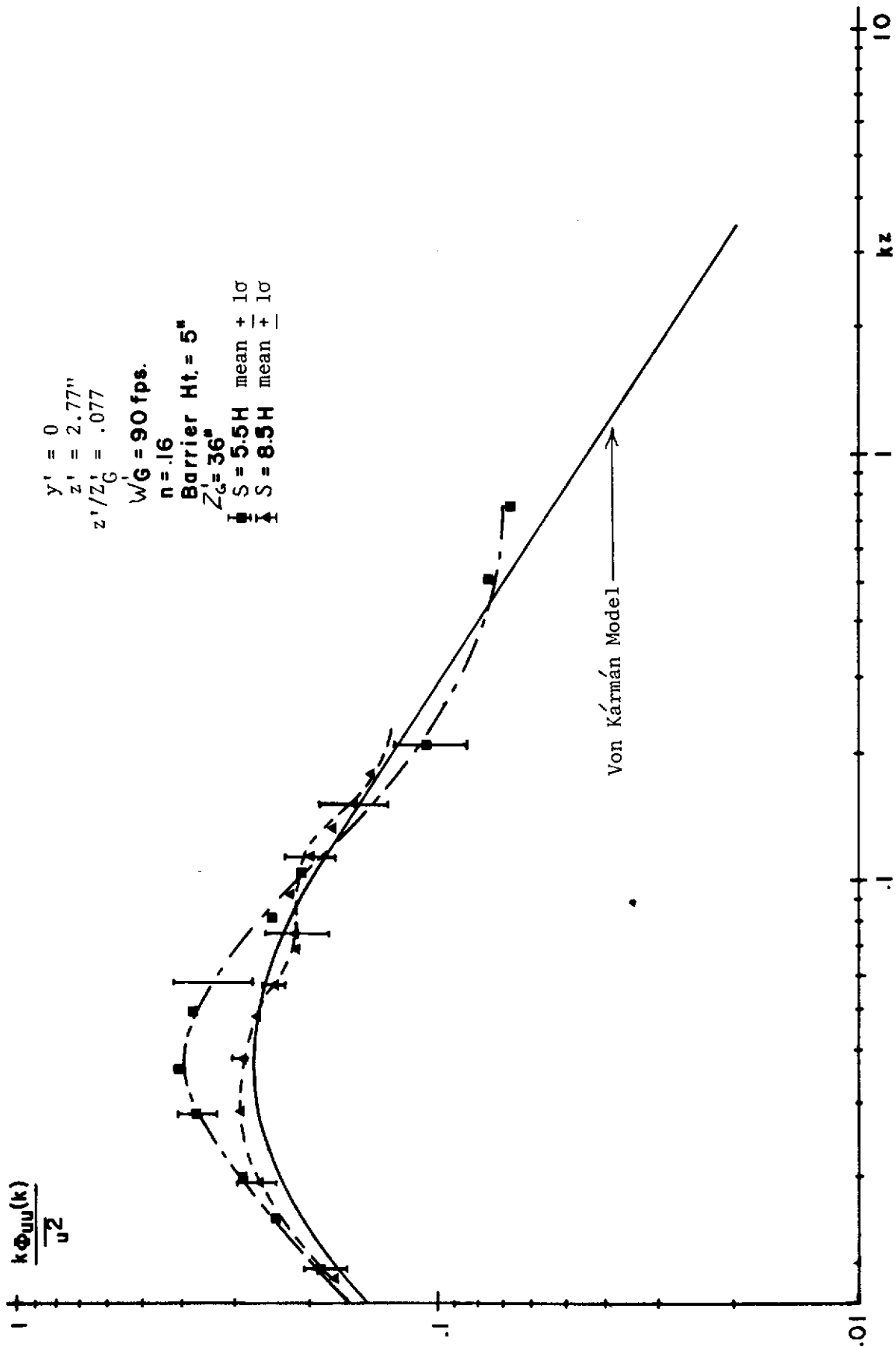
FIGURE 58.   LONGITUDINAL COMPONENT POWER SPECTRA ON TUNNEL CENTRE LINE,
44" x 66" TUNNEL

223
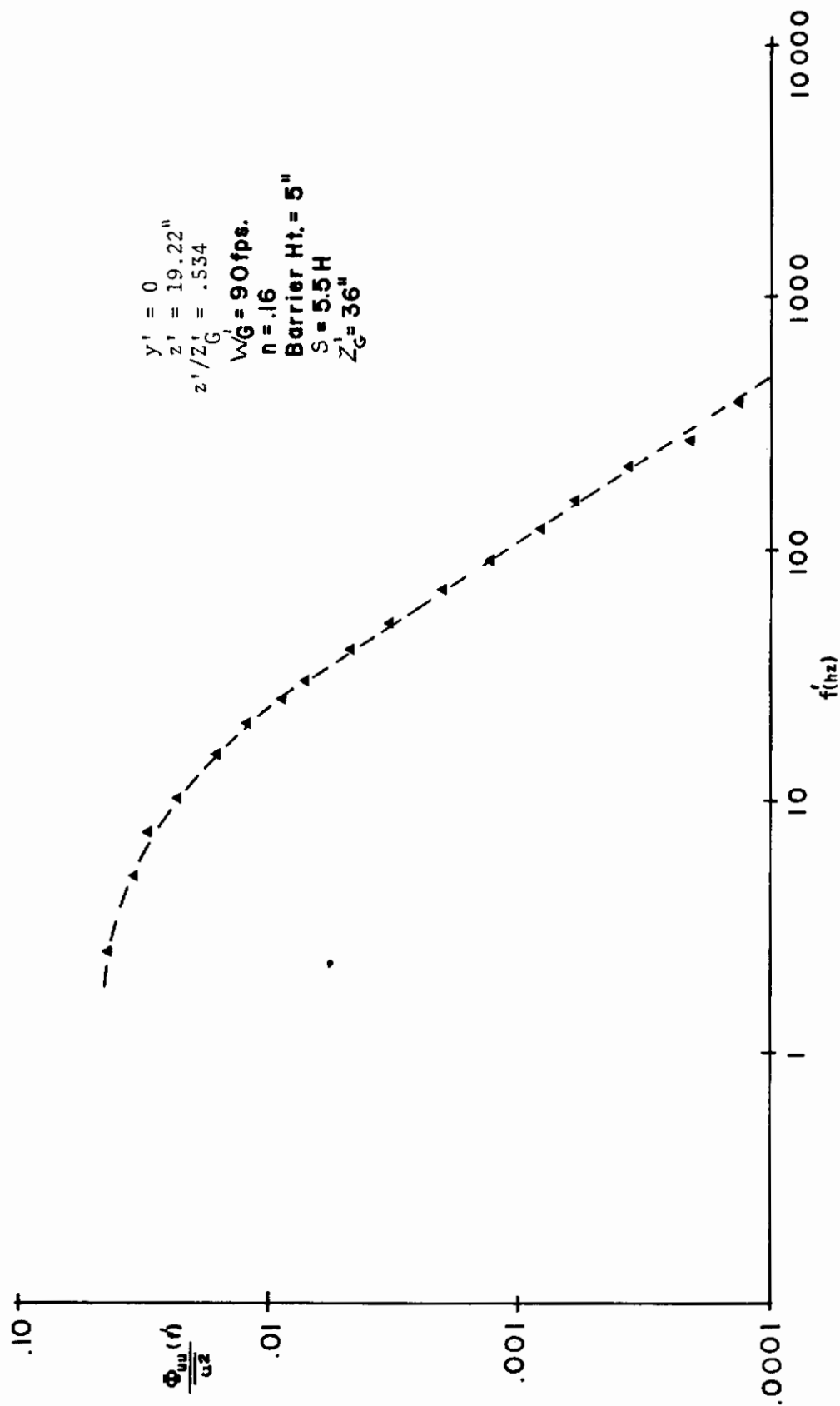
FIGURE 59. LONGITUDINAL COMPONENT POWER SPECTRA ON TUNNEL CENTRE LINE, 44" x 66" TUNNEL
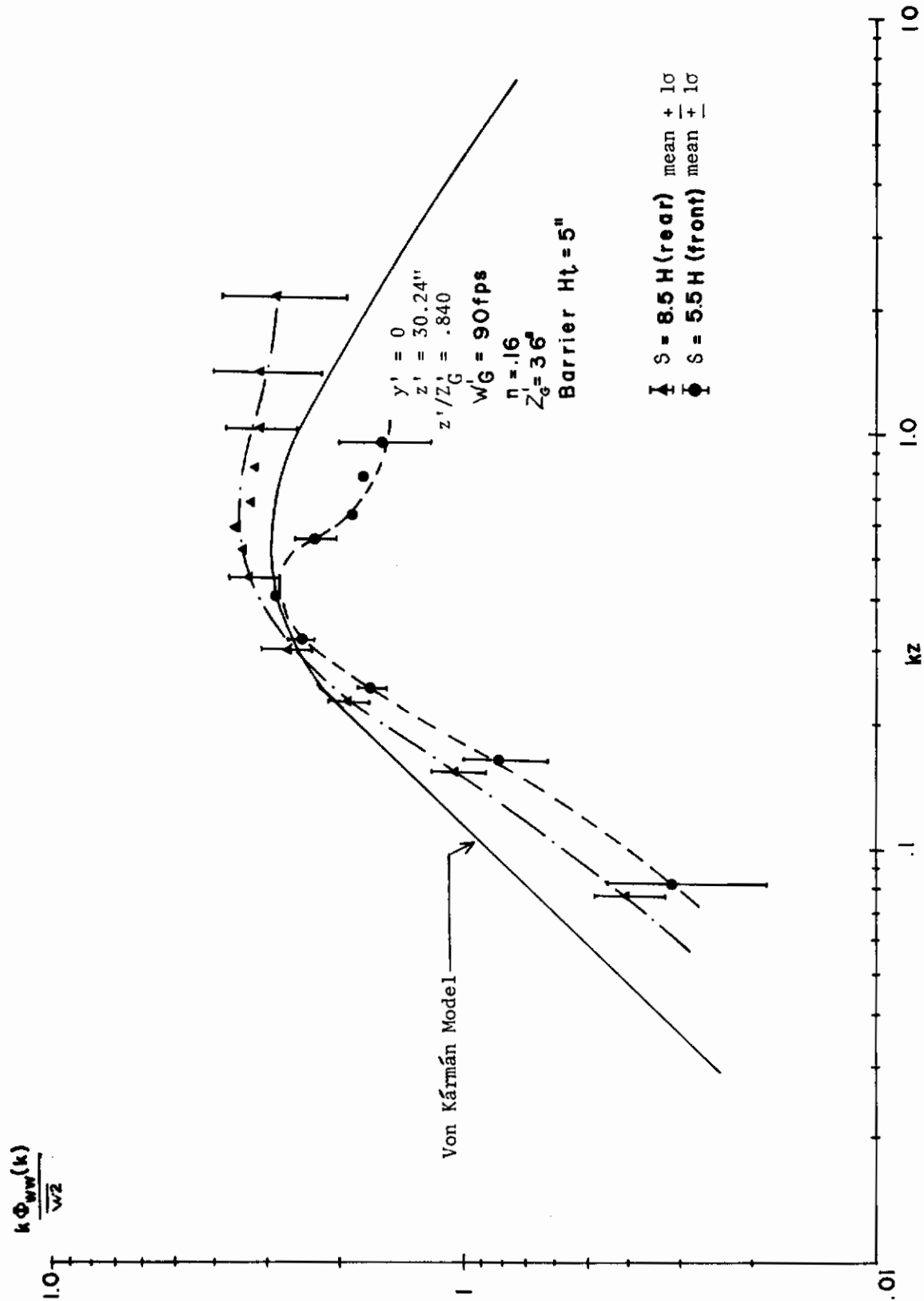
FIGURE 60. VERTICAL COMPONENT POWER SPECTRA ON TUNNEL CENTRE LINE,
44" x 66" TUNNEL
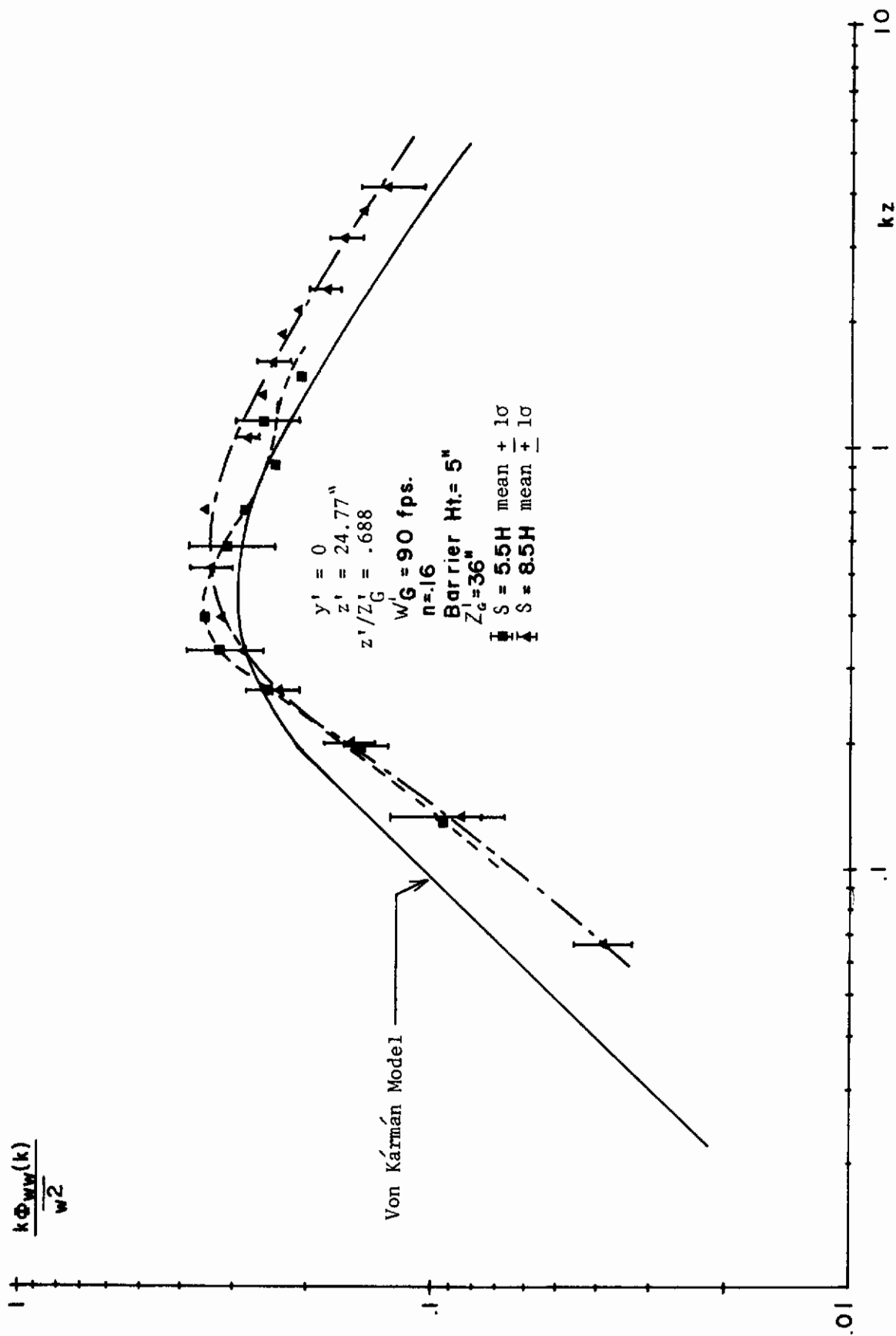
FIGURE 61. VERTICAL COMPONENT POWER SPECTRA ON TUNNEL CENTRE LINE,
44" x 66" TUNNEL

Plot axes and labels:

$\dfrac{k\Phi_{ww}(k)}{w^2}$ (vertical axis)

kz (horizontal axis)

Von Kármán Model

$y' = 0$
$z' = 24.77"$
$z'/Z_G' = .688$

$W_G' = 90$ fps.
$n = .16$
Barrier Ht. = 5"
$Z_G' = 36"$

$\blacksquare$ S = 5.5H mean $+$ 1σ
$\blacktriangle$ S = 8.5H mean $\pm$ 1σ
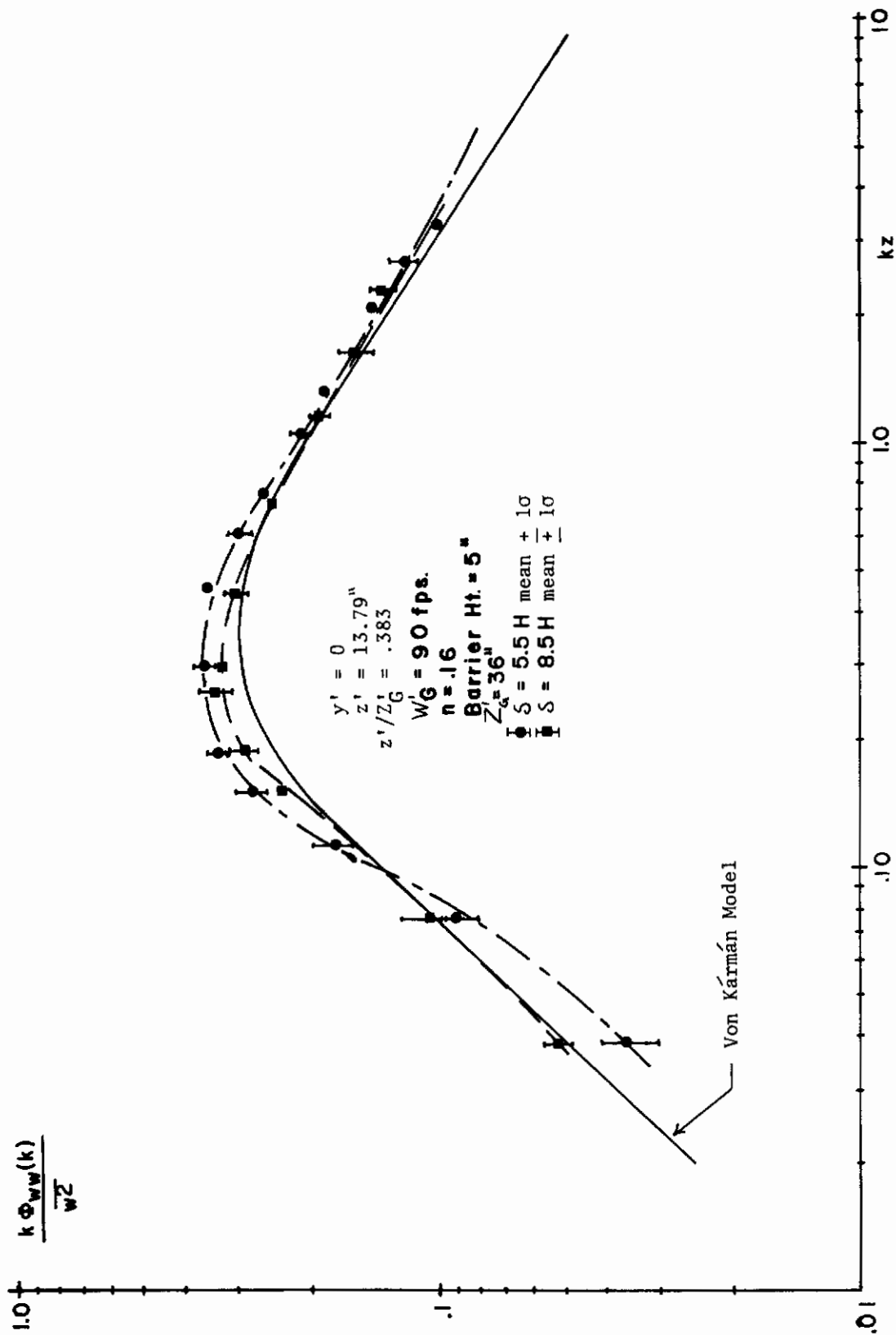
FIGURE 62. VERTICAL COMPONENT POWER SPECTRA ON TUNNEL CENTRE LINE,
44" x 66" TUNNEL
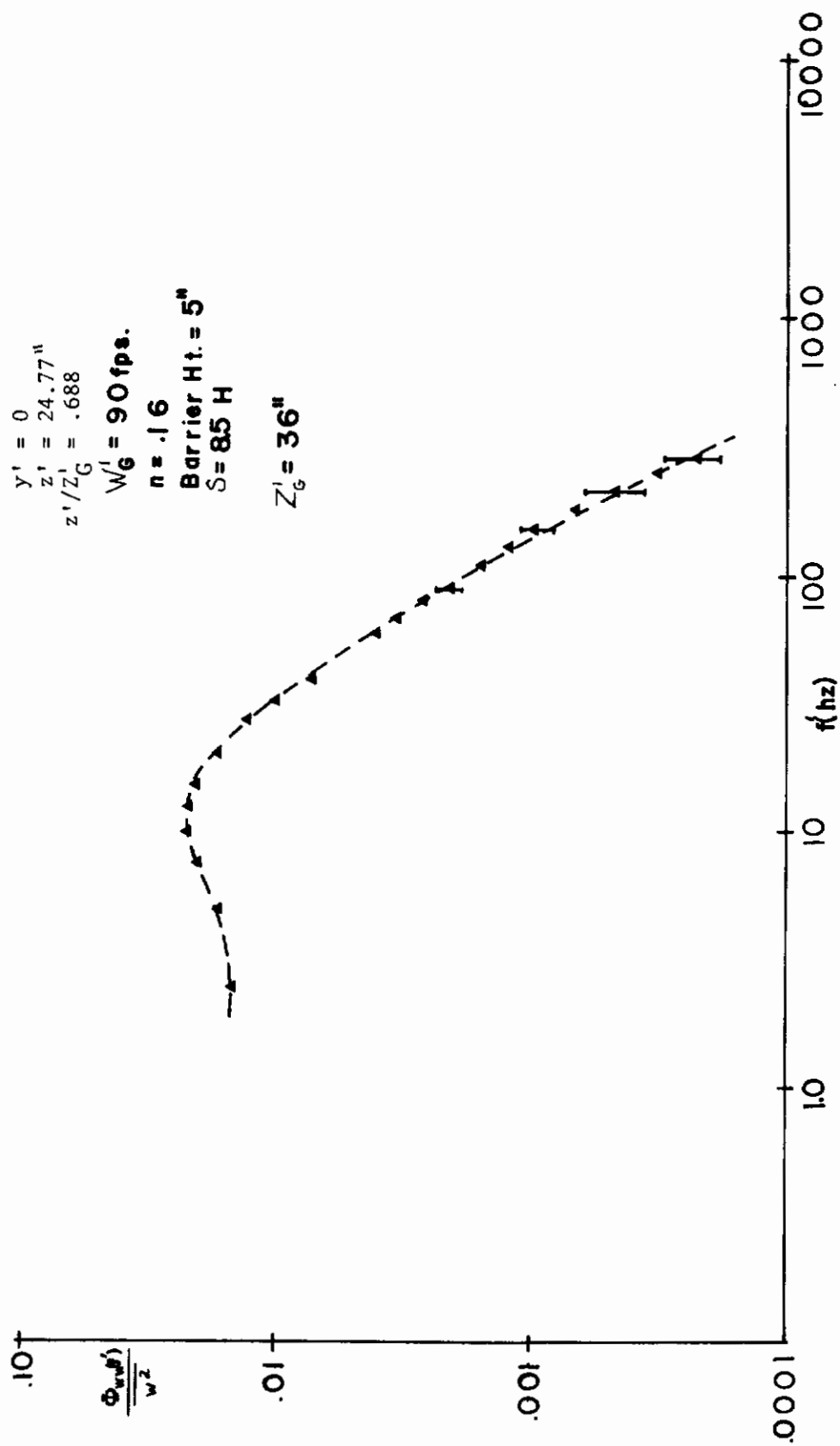
FIGURE 63. VERTICAL COMPONENT POWER SPECTRA ON TUNNEL CENTRE LINE, 44" x 66" TUNNEL
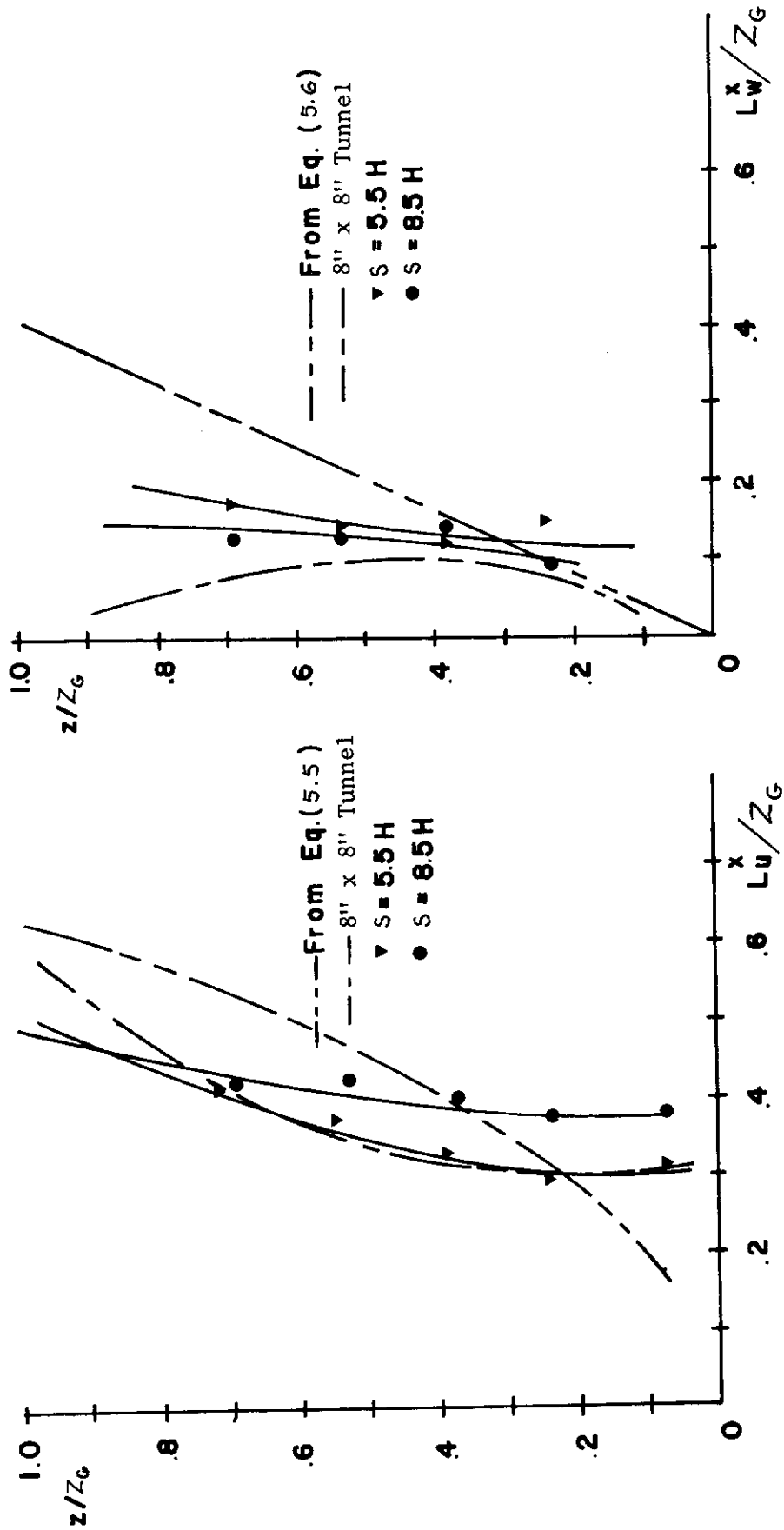
FIGURE 64. INTEGRAL SCALE PROFILES IN SIMULATED FLOW,
44" x 66" TUNNEL

229
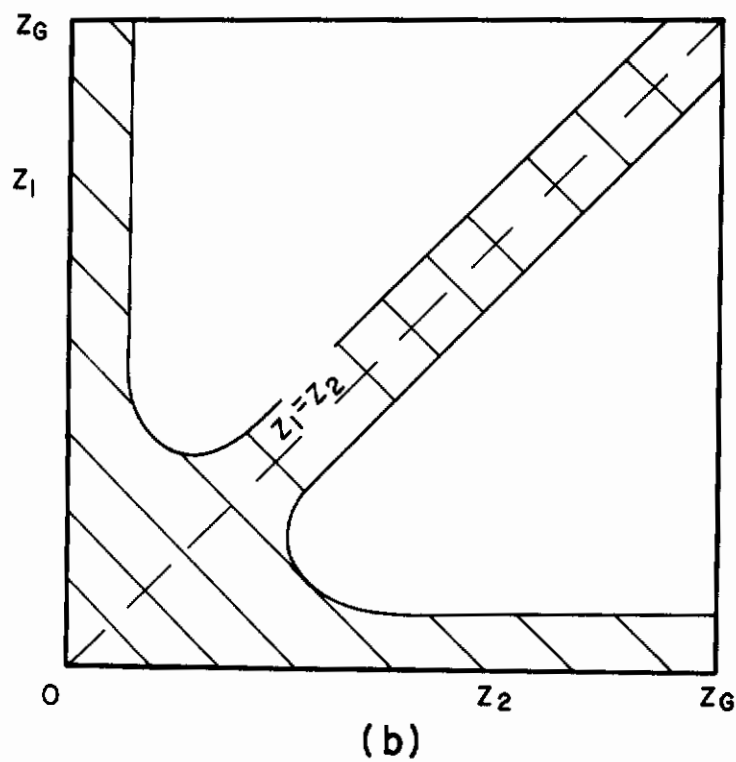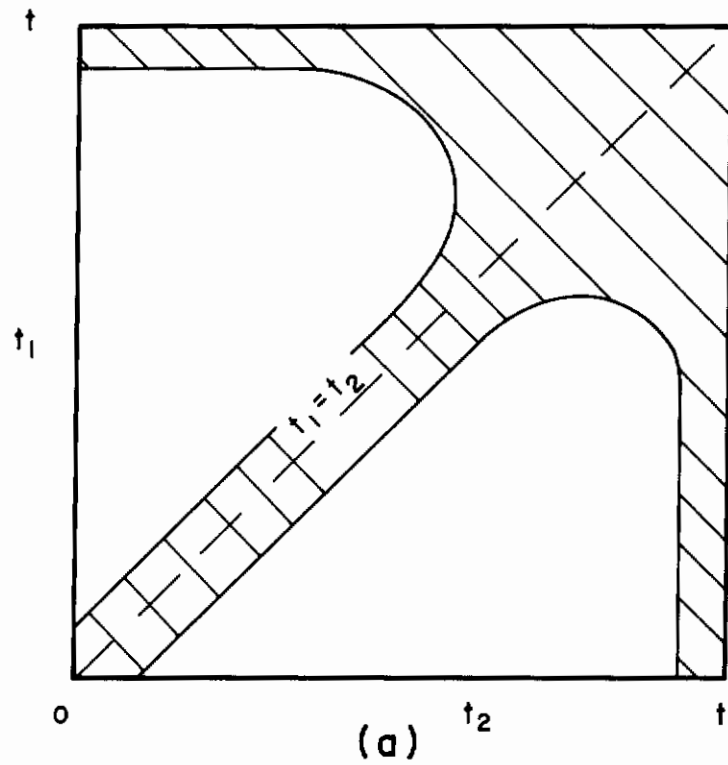
FIGURE 65. DESIRED DISTRIBUTION OF PROBE-PAIR LOCATIONS

230
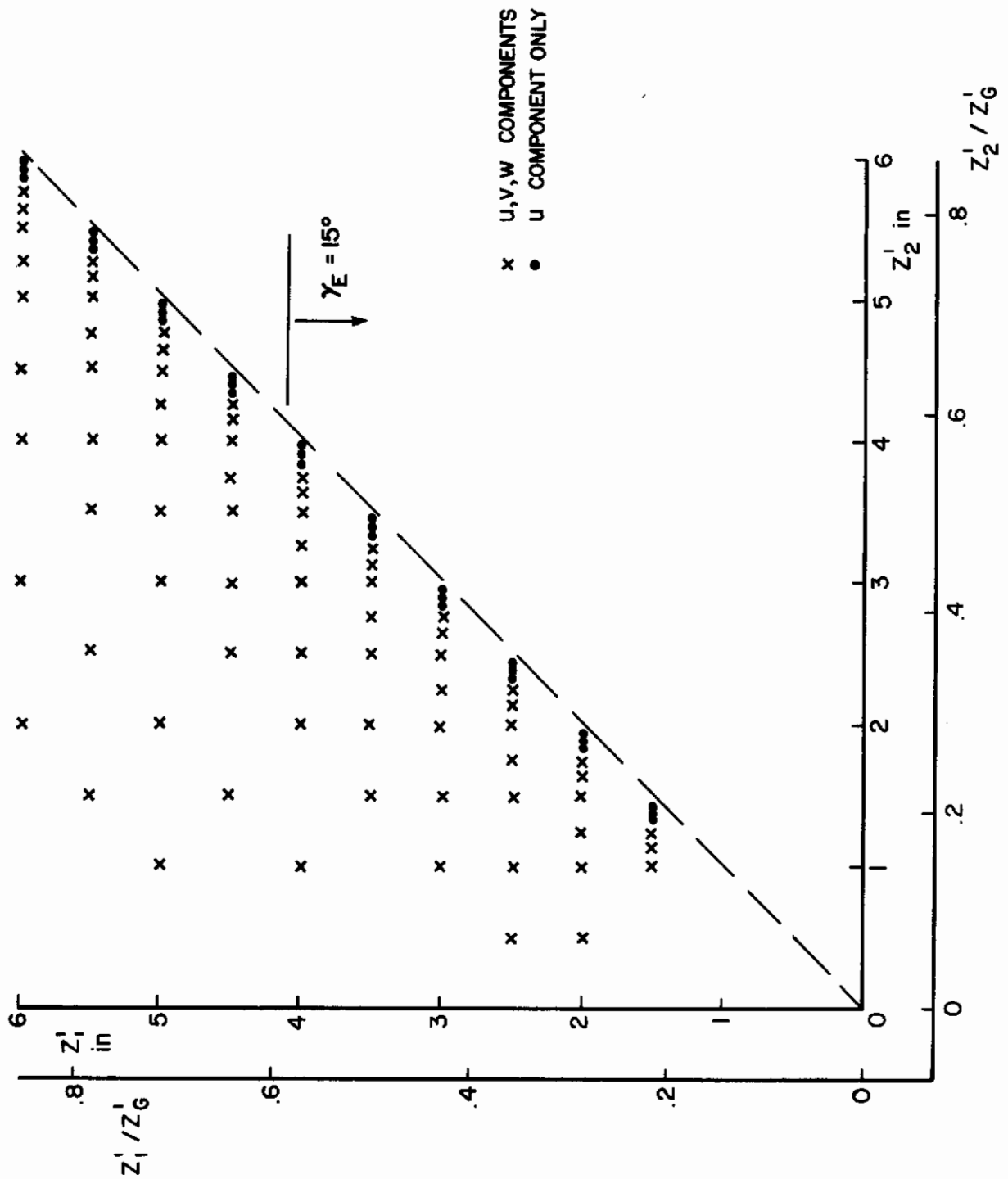
FIGURE 66. DISTRIBUTION OF PROBE-PAIR LOCATIONS, 8" x 8" TUNNEL

231
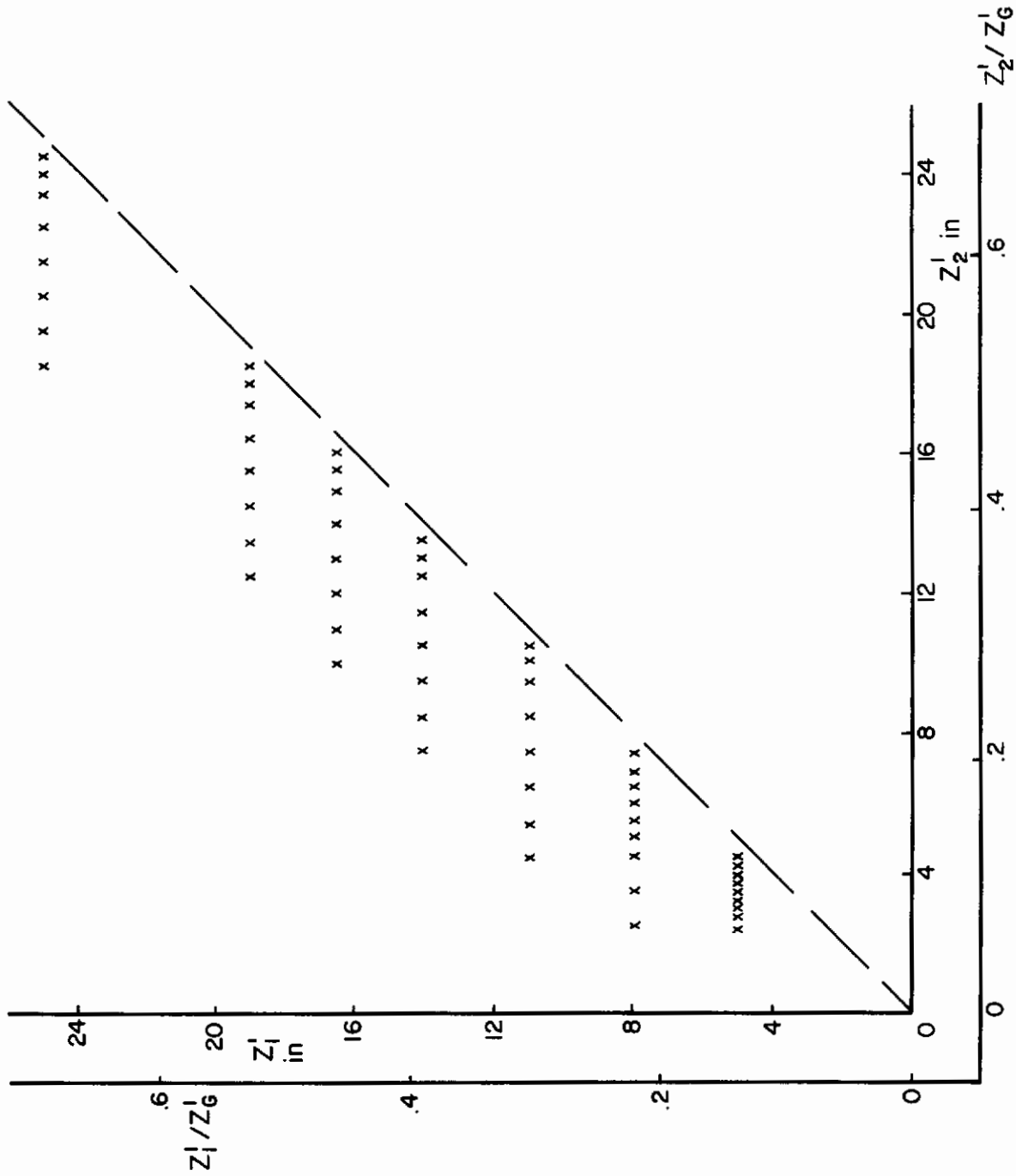
FIGURE 67. DISTRIBUTION OF PROBE-PAIR LOCATIONS, 44" x 66" TUNNEL
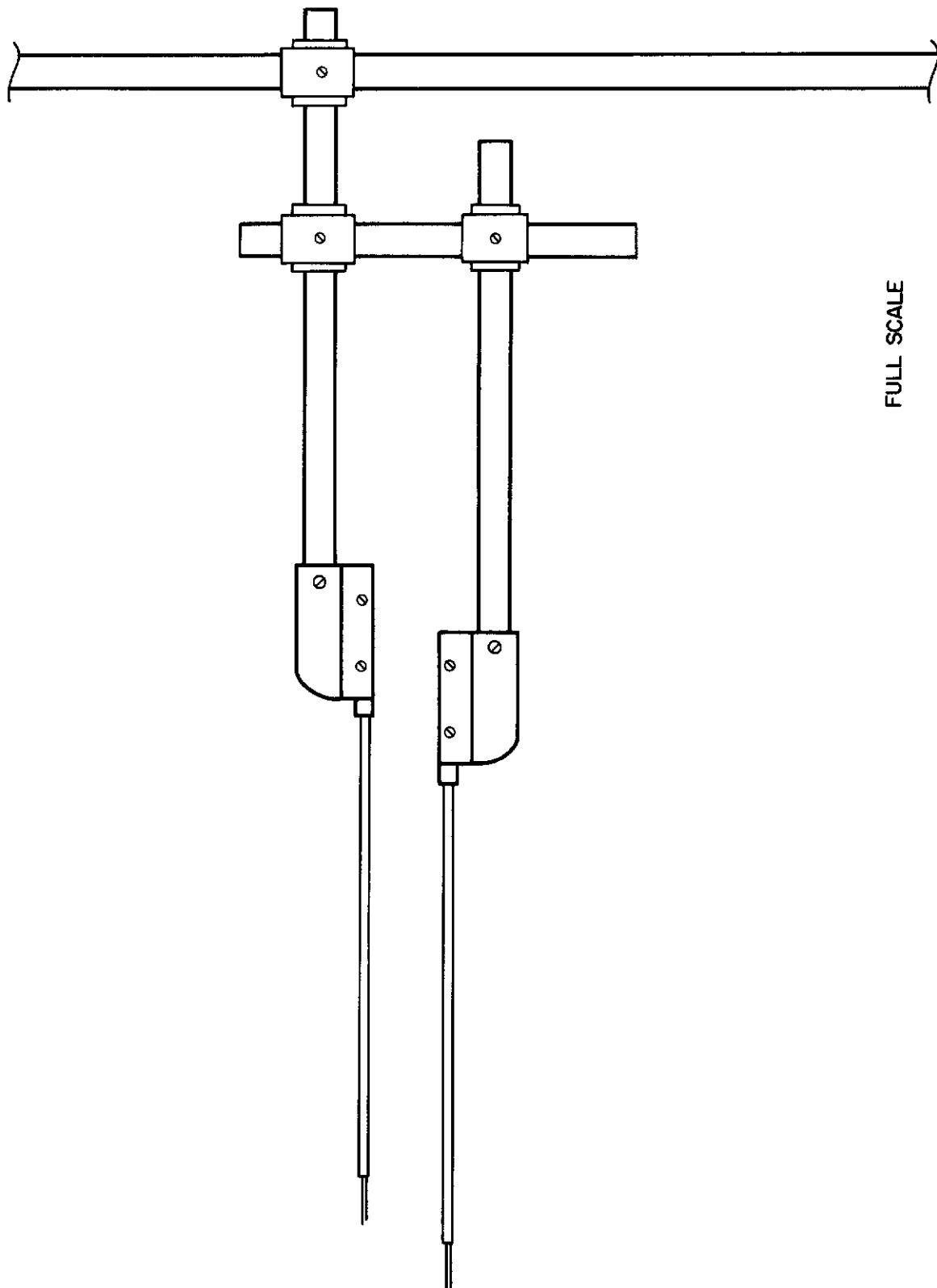
FULL SCALE

FIGURE 68. HOT WIRE PROBE HOLDER, 8" x 8" TUNNEL
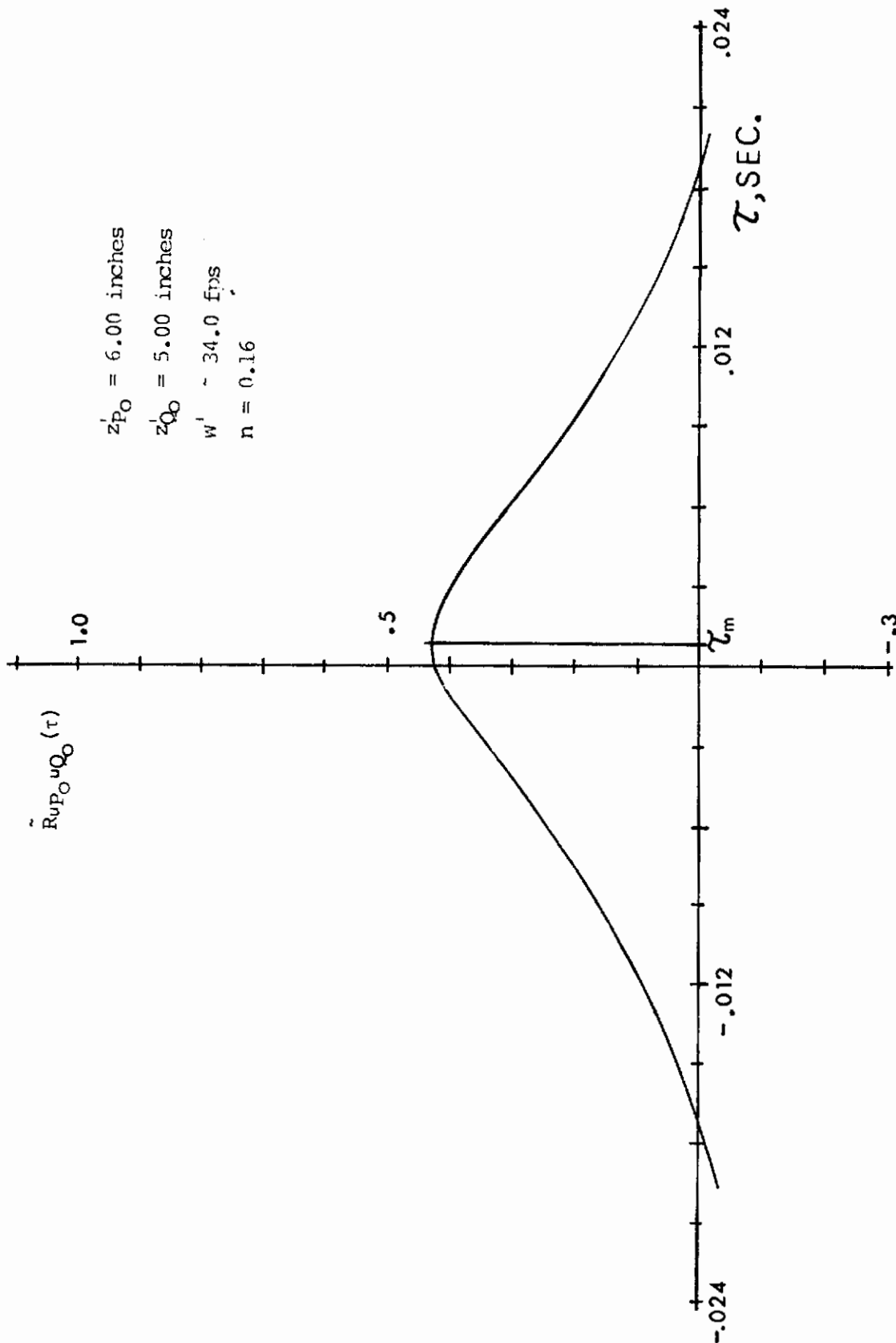
FIGURE 69. TYPICAL TIME-DELAY CROSS-CORRELATION FOR u-COMPONENT
$\gamma_E = 90°$, 8" x 8" TUNNEL
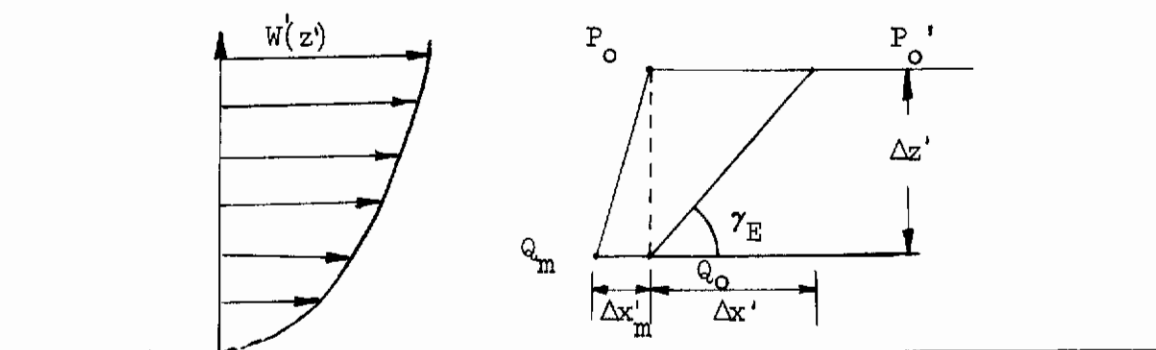
FIGURE 70. TWO-POINT CROSS-CORRELATION GEOMETRY

$\bar{R}_{u_{P_O} u_{Q_O}} (\tau)$

z'_{P_O} = 4.00 inches

z'_{Q_O} = 3.65 inches

W' ~ 31.0 fps

n = 0.16

τ,SEC.
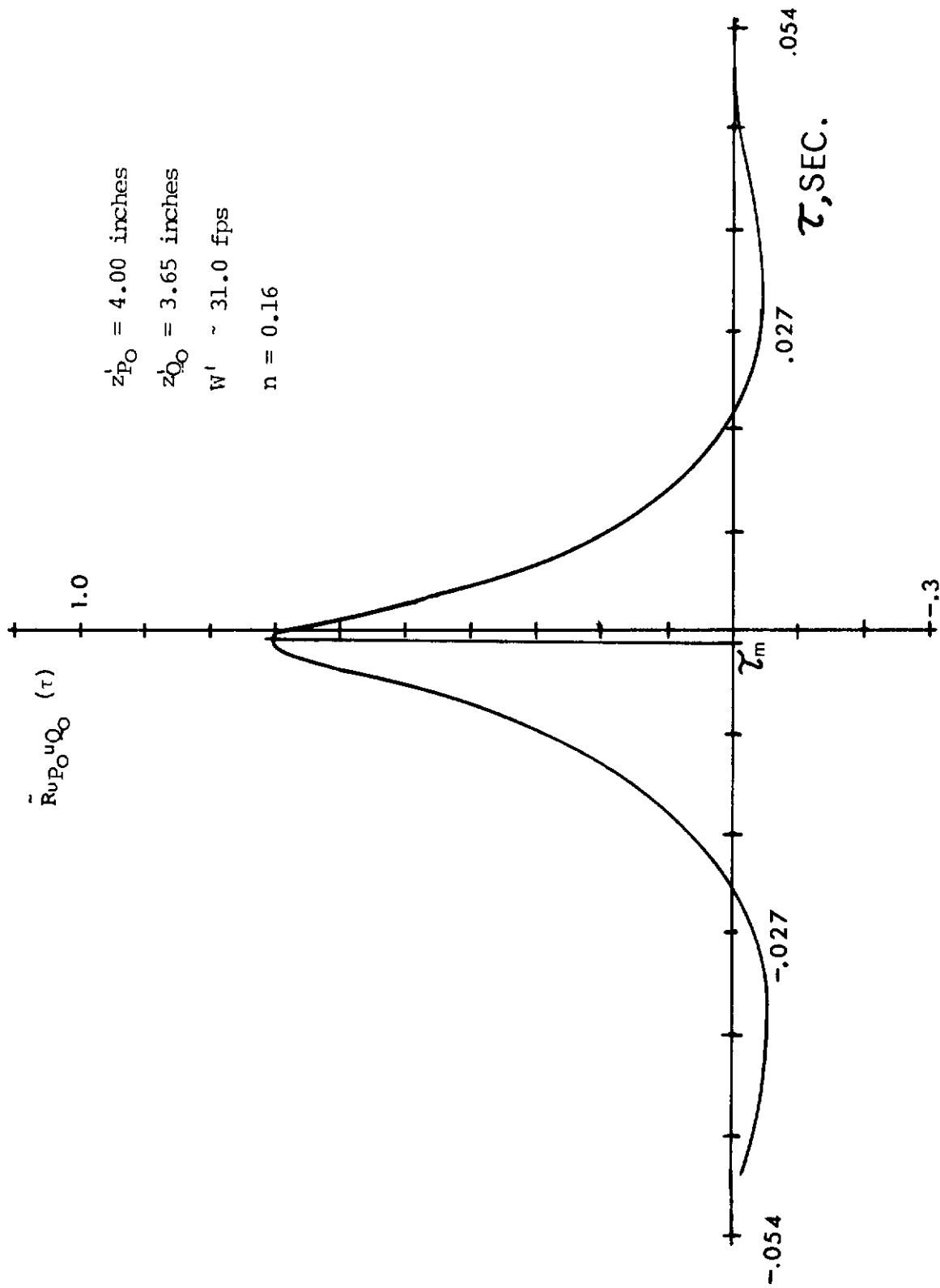
FIGURE 71.   TYPICAL TIME DELAY CROSS-CORRELATION FOR u-COMPONENT, γ_E = 45°, 8" x 8" TUNNEL

236
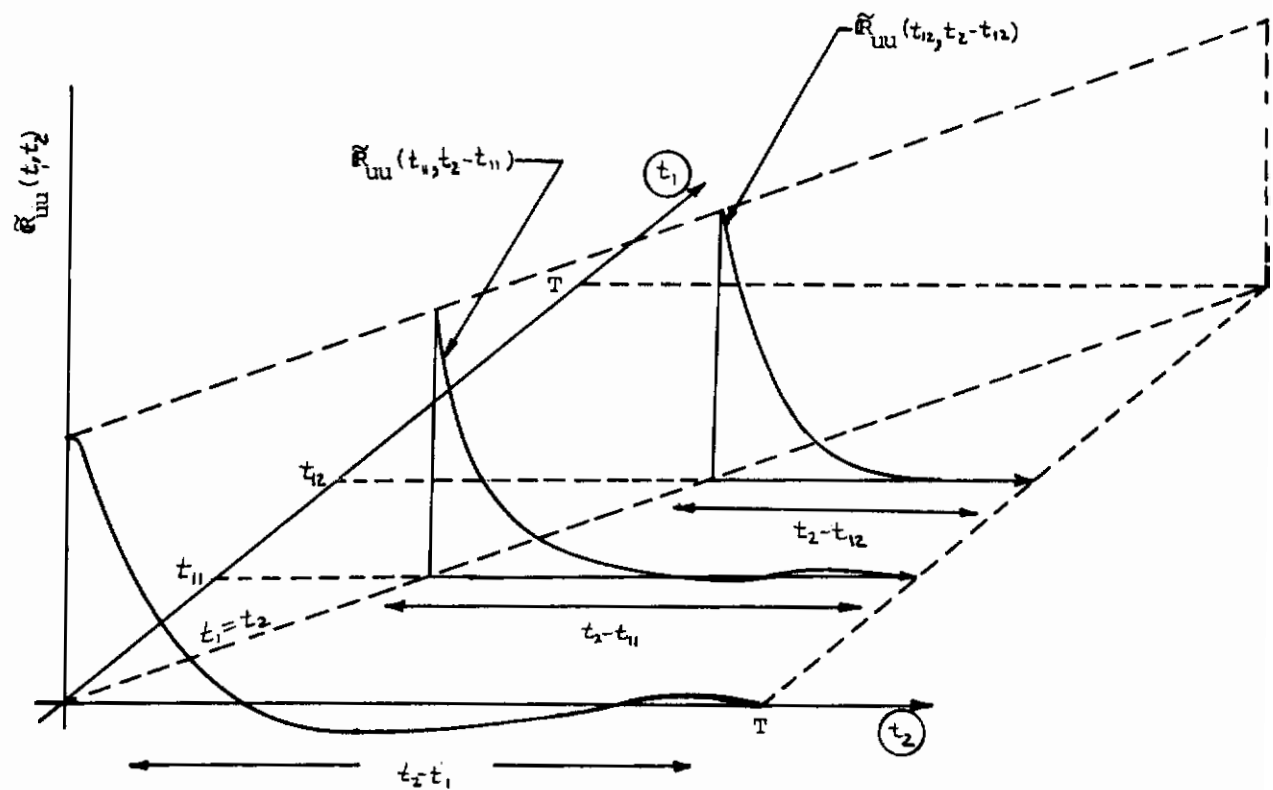
FIGURE 72. DIAGRAM OF TYPICAL $\tilde{R}$ SURFACE

237
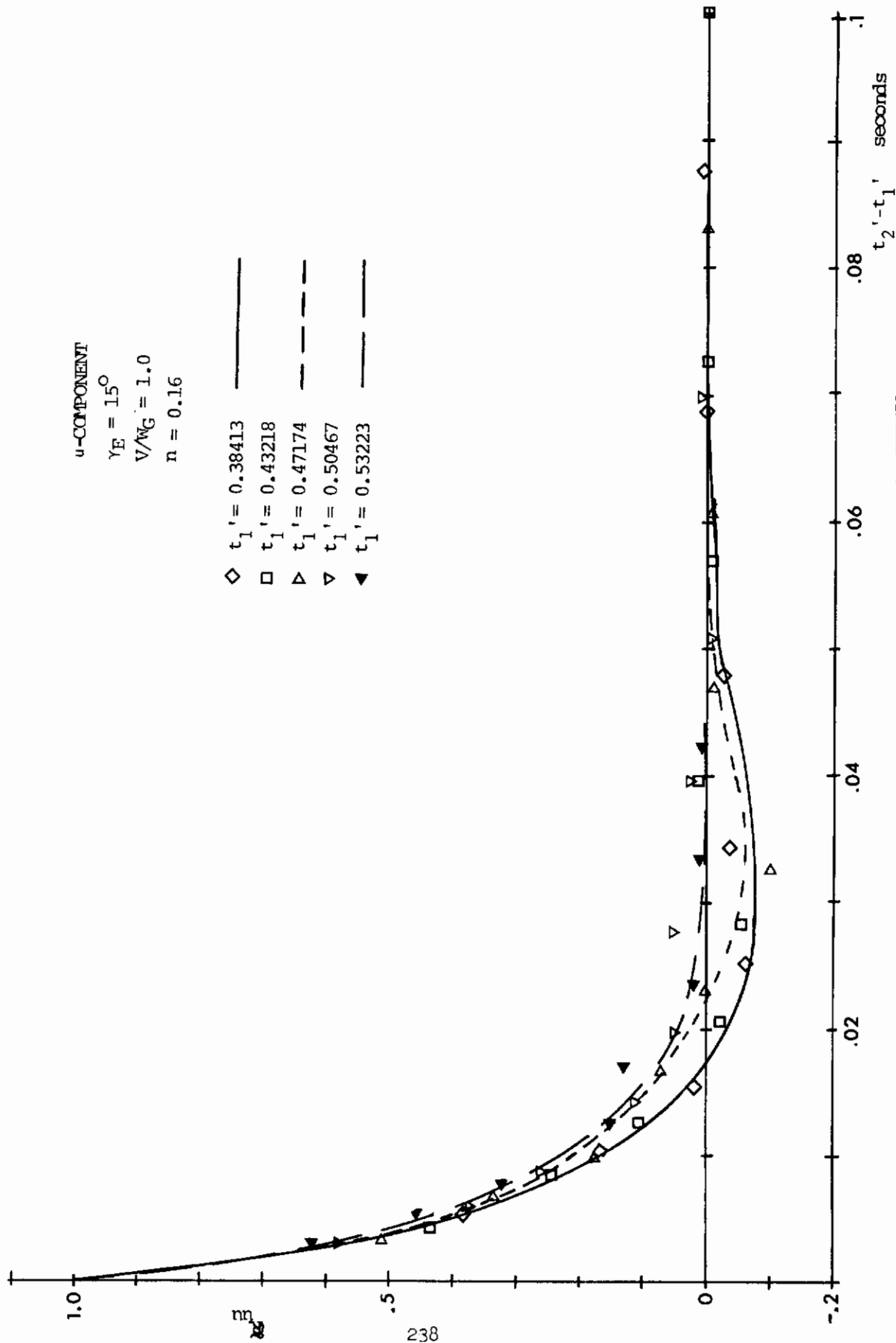
FIGURE 73. FLIGHT PATH TURBULENCE CORRELATION, 8" x 8" TUNNEL

u-COMPONENT

$\gamma_E = 15^{\circ}$

$V/W_G = 1.0$

$n = 0.16$

$\diamondsuit$	$t_1' = 0.38413$
$\square$	$t_1' = 0.43218$
$\triangle$	$t_1' = 0.47174$
$\triangleright$	$t_1' = 0.50467$
$\blacktriangledown$	$t_1' = 0.53223$

$t_2' - t_1'$ seconds

238

u–COMPONENT

$\gamma_E = 15^O$

$V/W_G = 1.2$

$n = 0.16$

$t_1' = 0.07298$
$t_1' = 0.08858$
$t_1' = 0.10318$
$t_1' = 0.11678$
$t_1' = 0.12937$
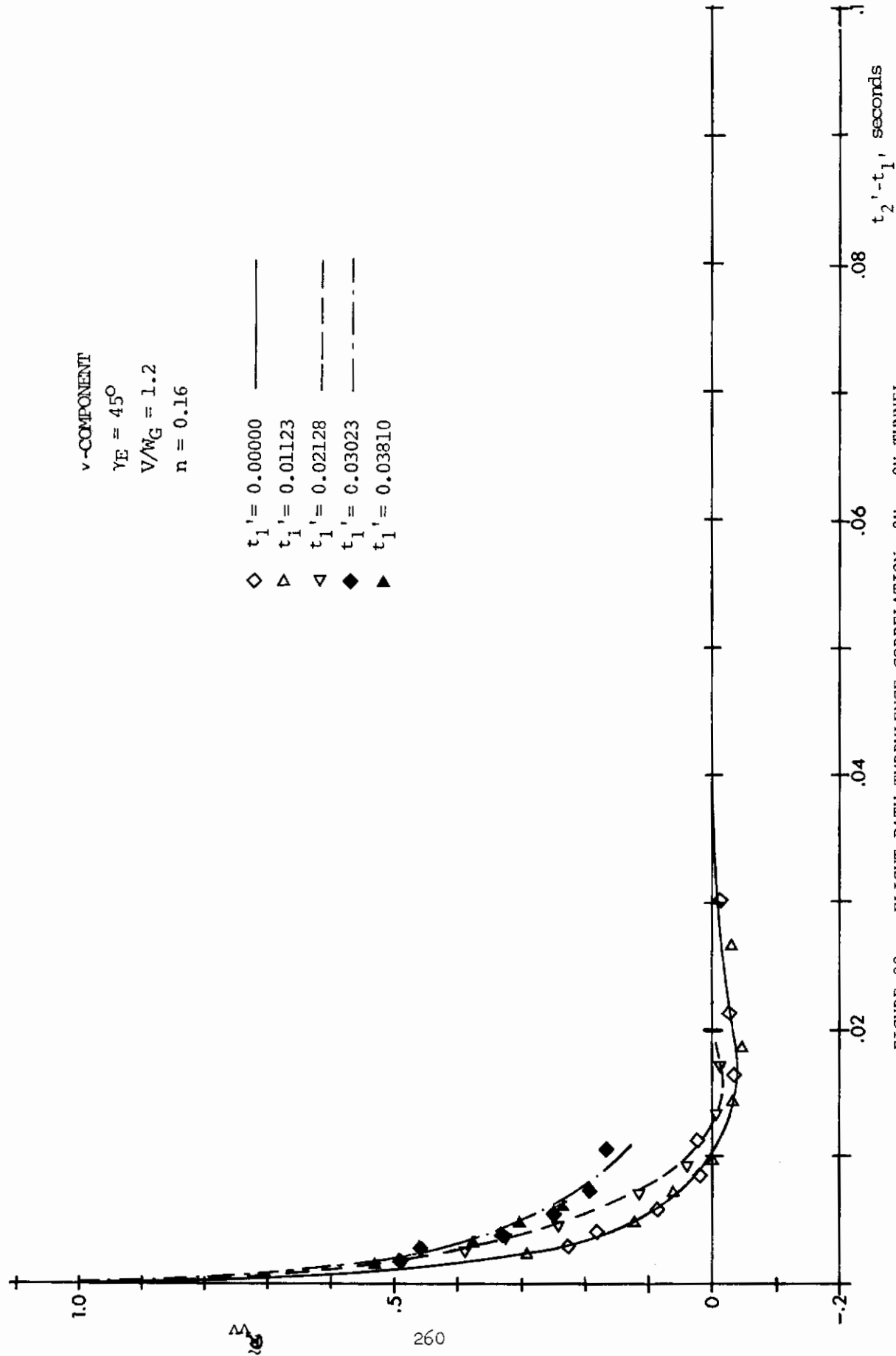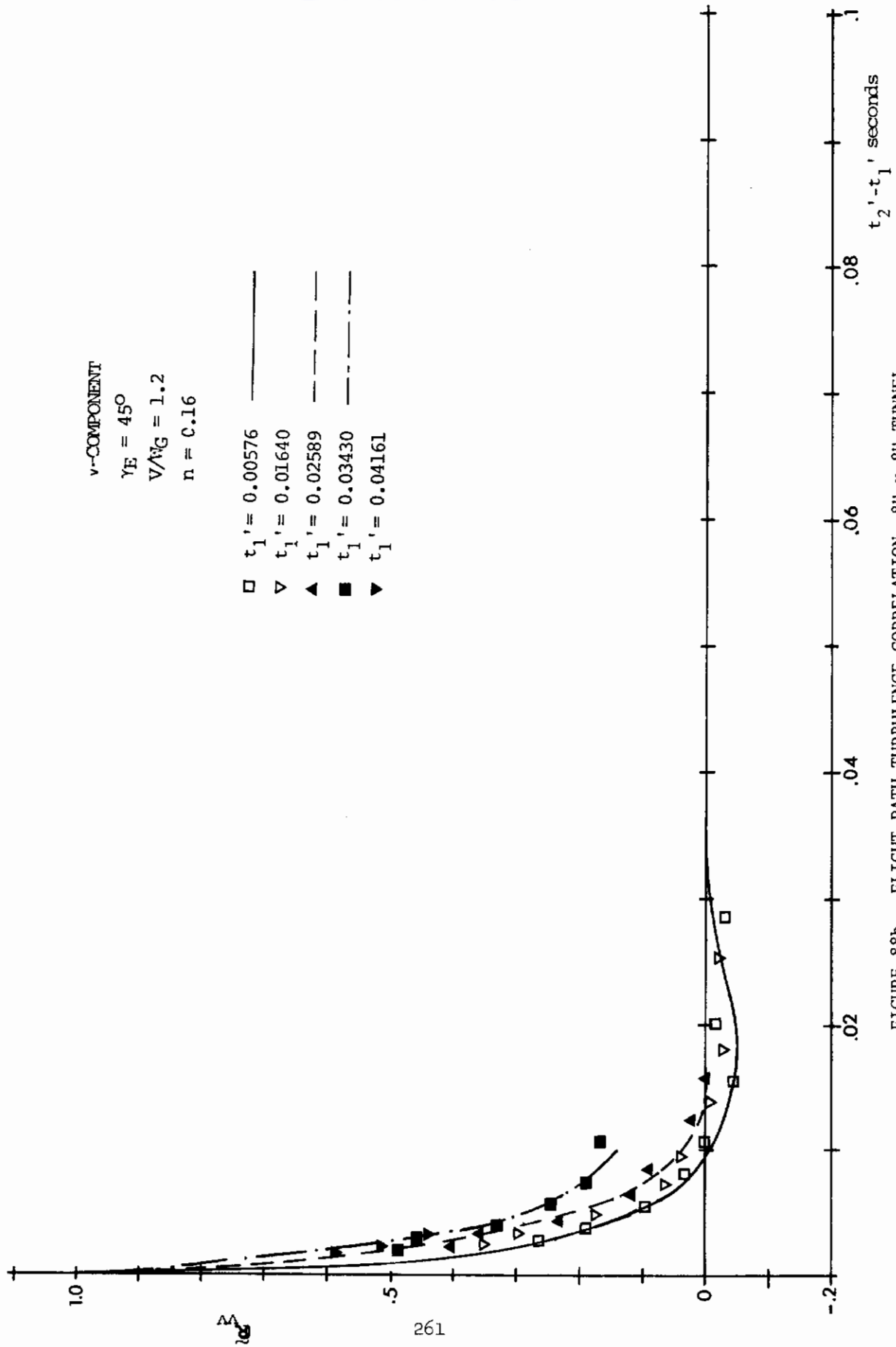
$t_2' - t_1'$ seconds
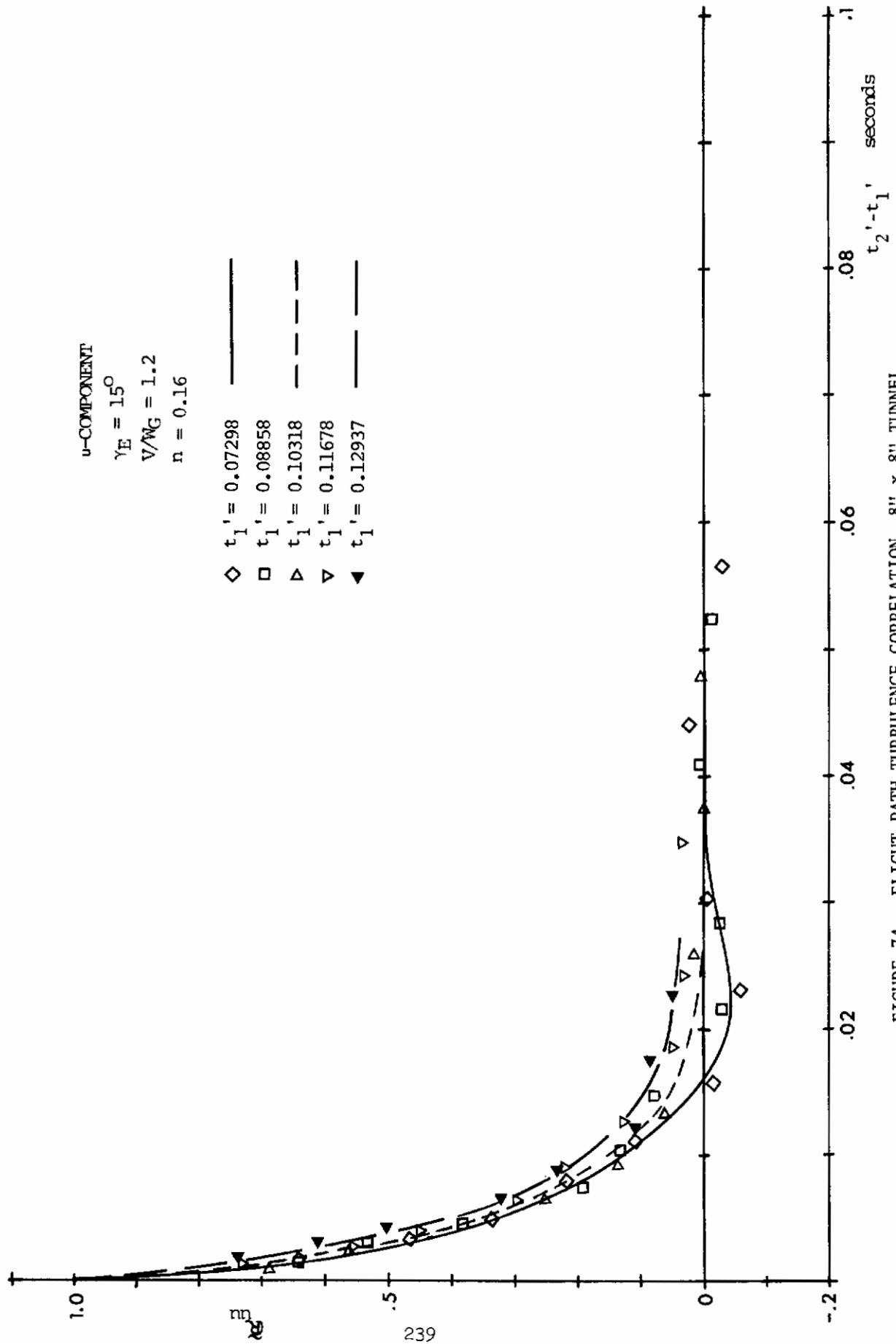
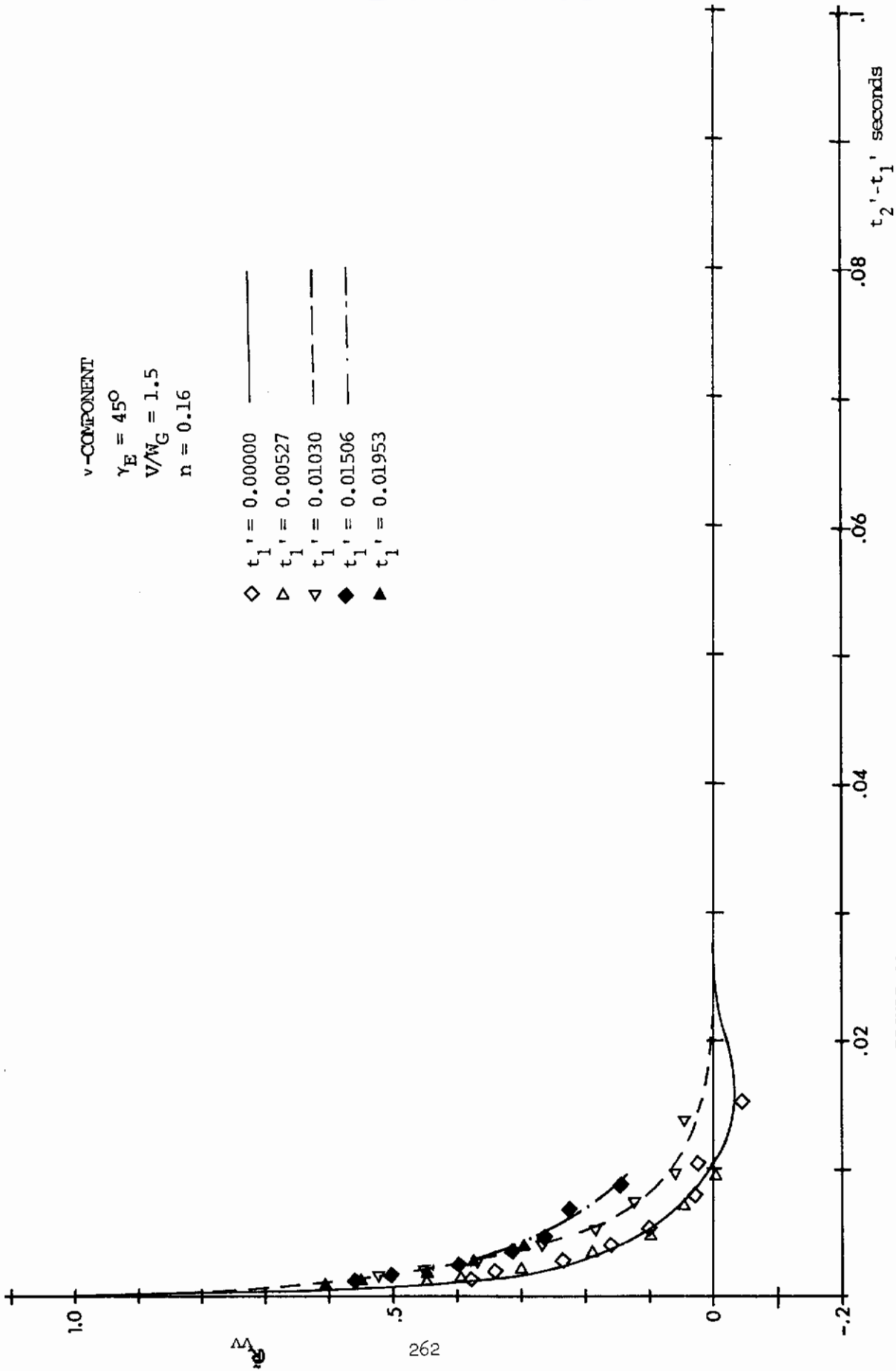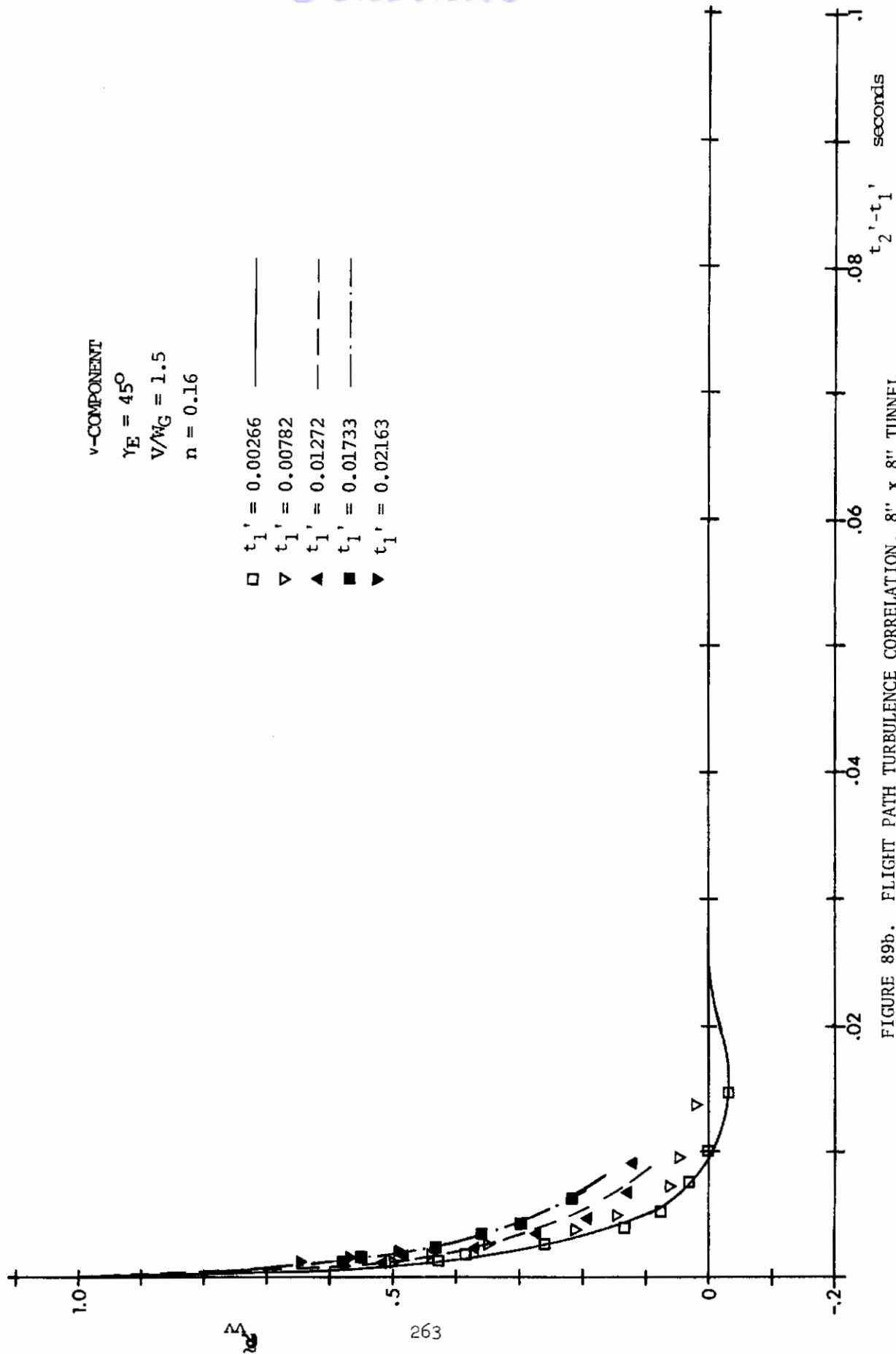FIGURE 74. FLIGHT PATH TURBULENCE CORRELATION, 8" x 8" TUNNEL

239
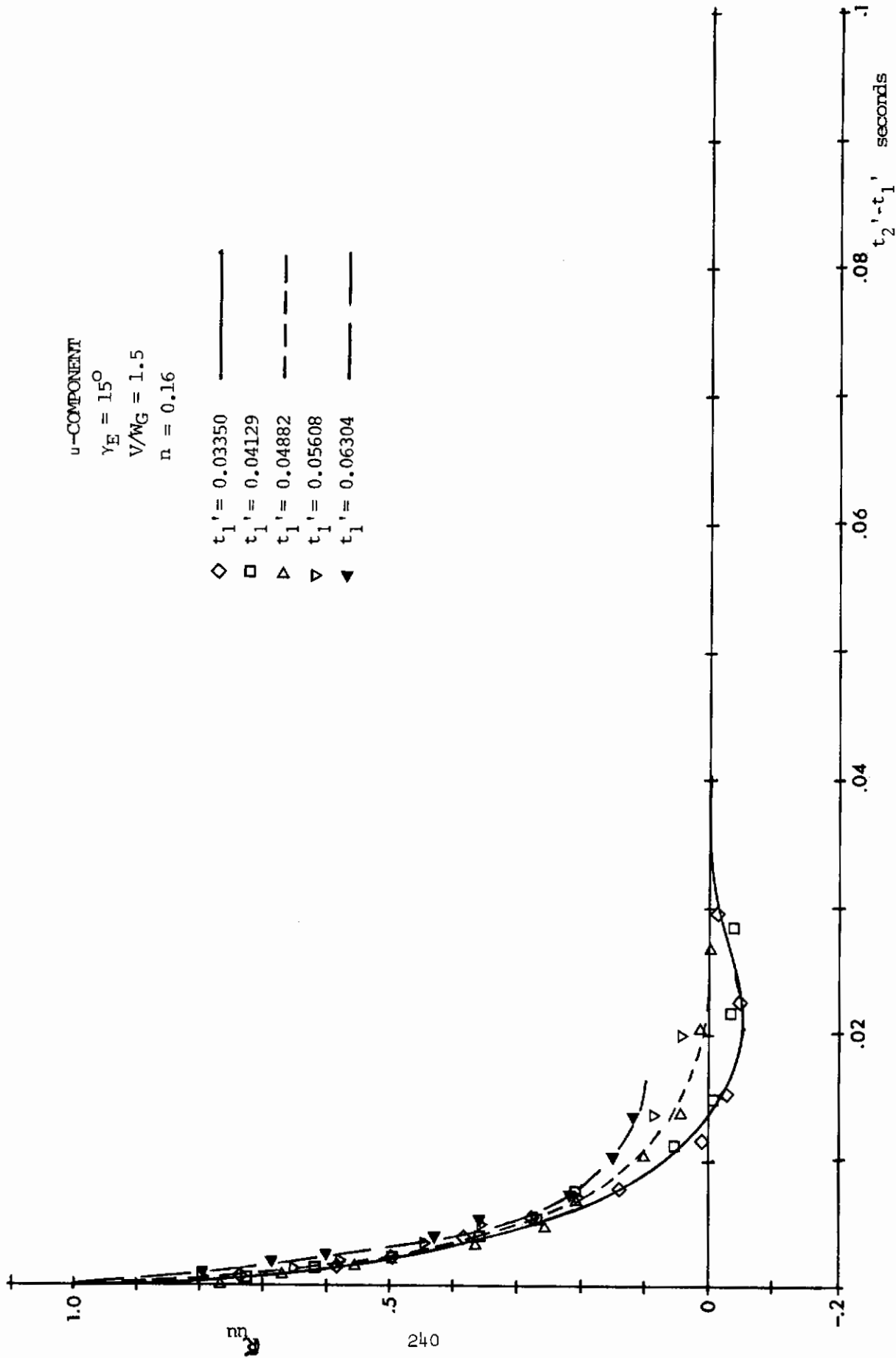
FIGURE 75. FLIGHT PATH TURBULENCE CORRELATION, 8" x 8" TUNNEL.

FIGURE 76. FLIGHT PATH TURBULENCE CORRELATION, 8'' x 8'' TUNNEL

u-COMPONENT

$\gamma_E = 15^O$

$V/W_G = 1.9$

$n = 0.16$

◇	$t_1' = 0.01953$	
□	$t_1' = 0.02421$	
△	$t_1' = 0.02879$	
▷	$t_1' = 0.03328$	
▼	$t_1' = 0.03765$	

$t_2' - t_1'$ seconds

241
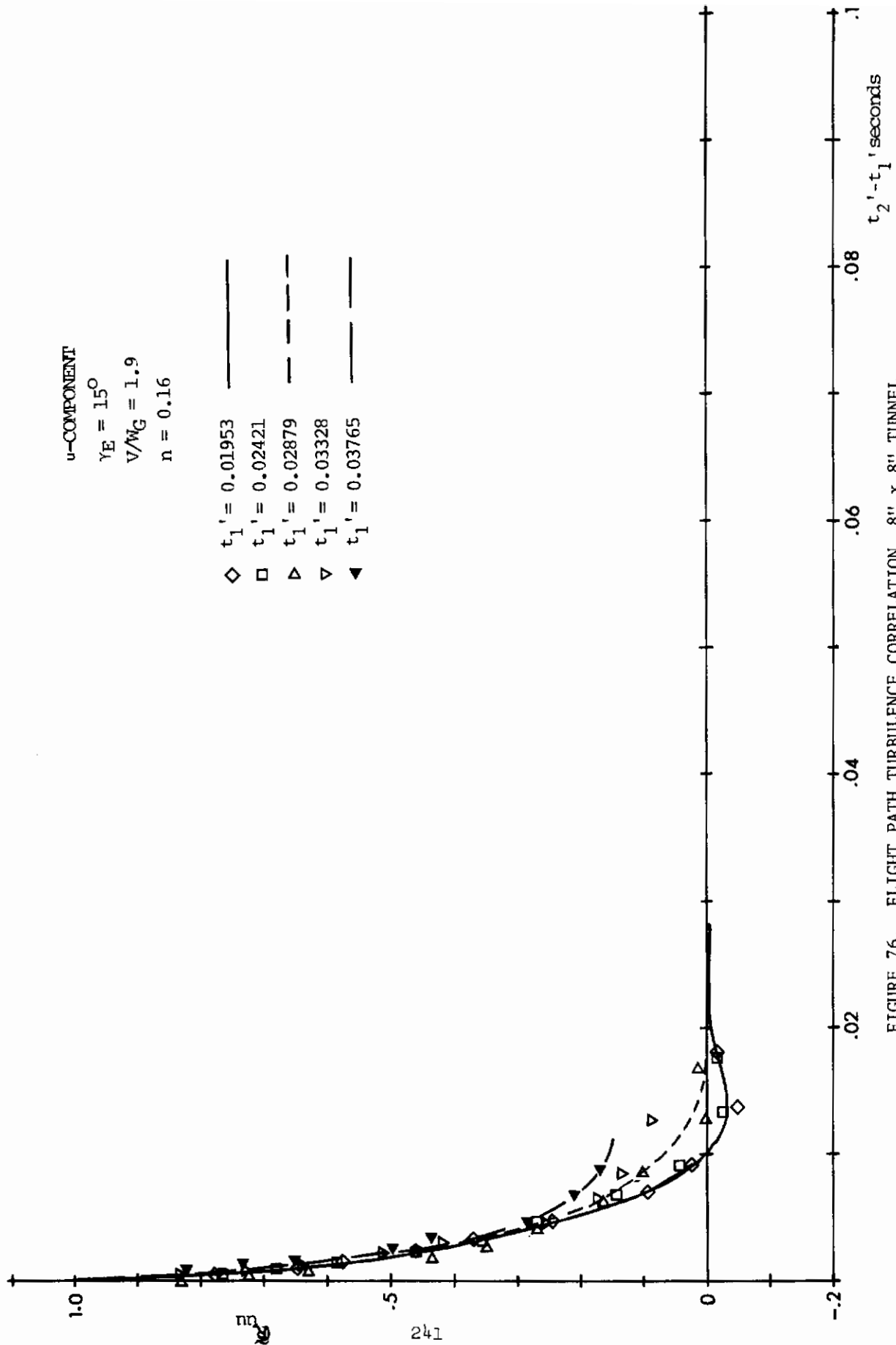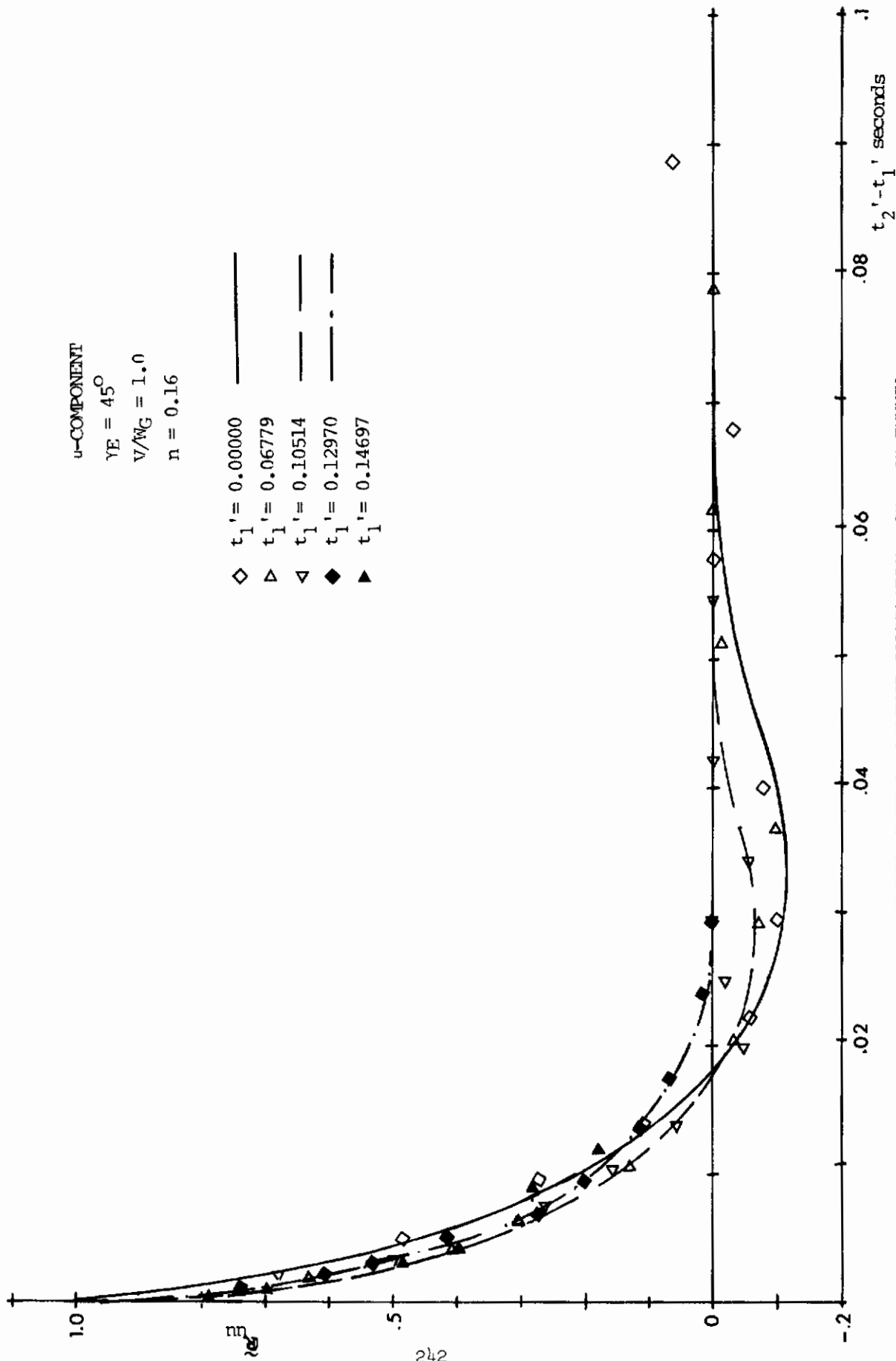
FIGURE 77a.   FLIGHT PATH TURBULENCE CORRELATION, 8" x 8" TUNNEL

242

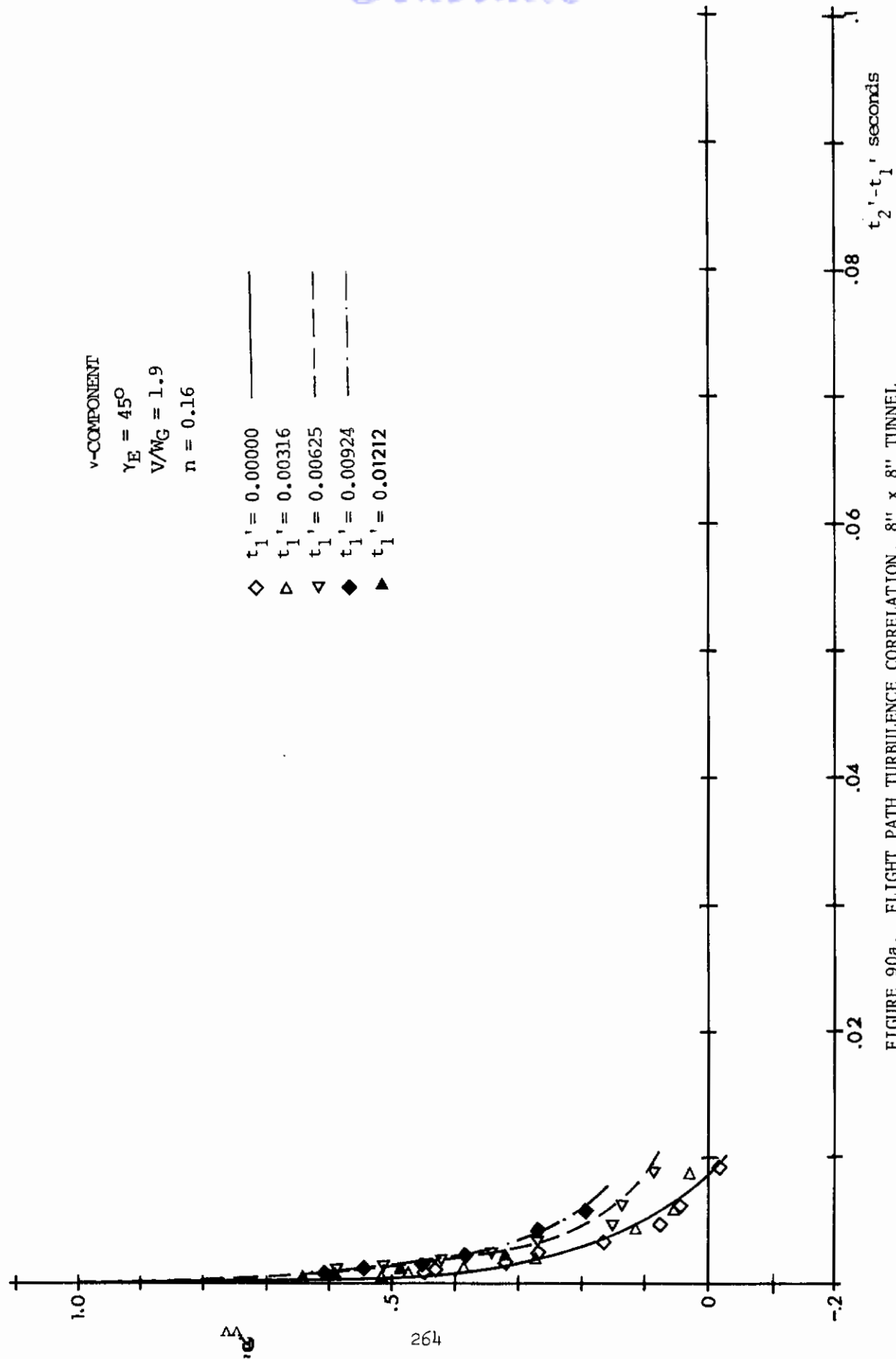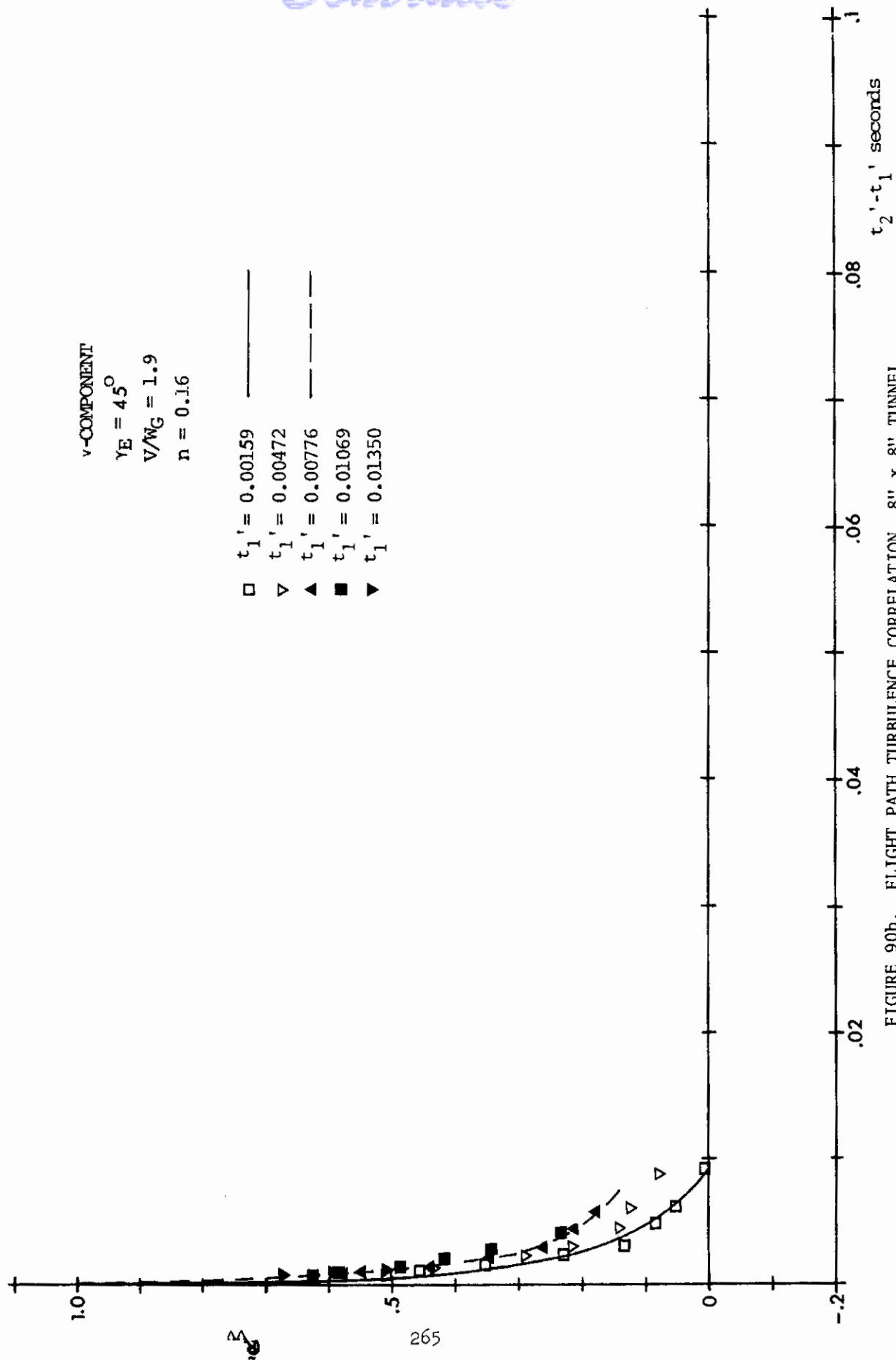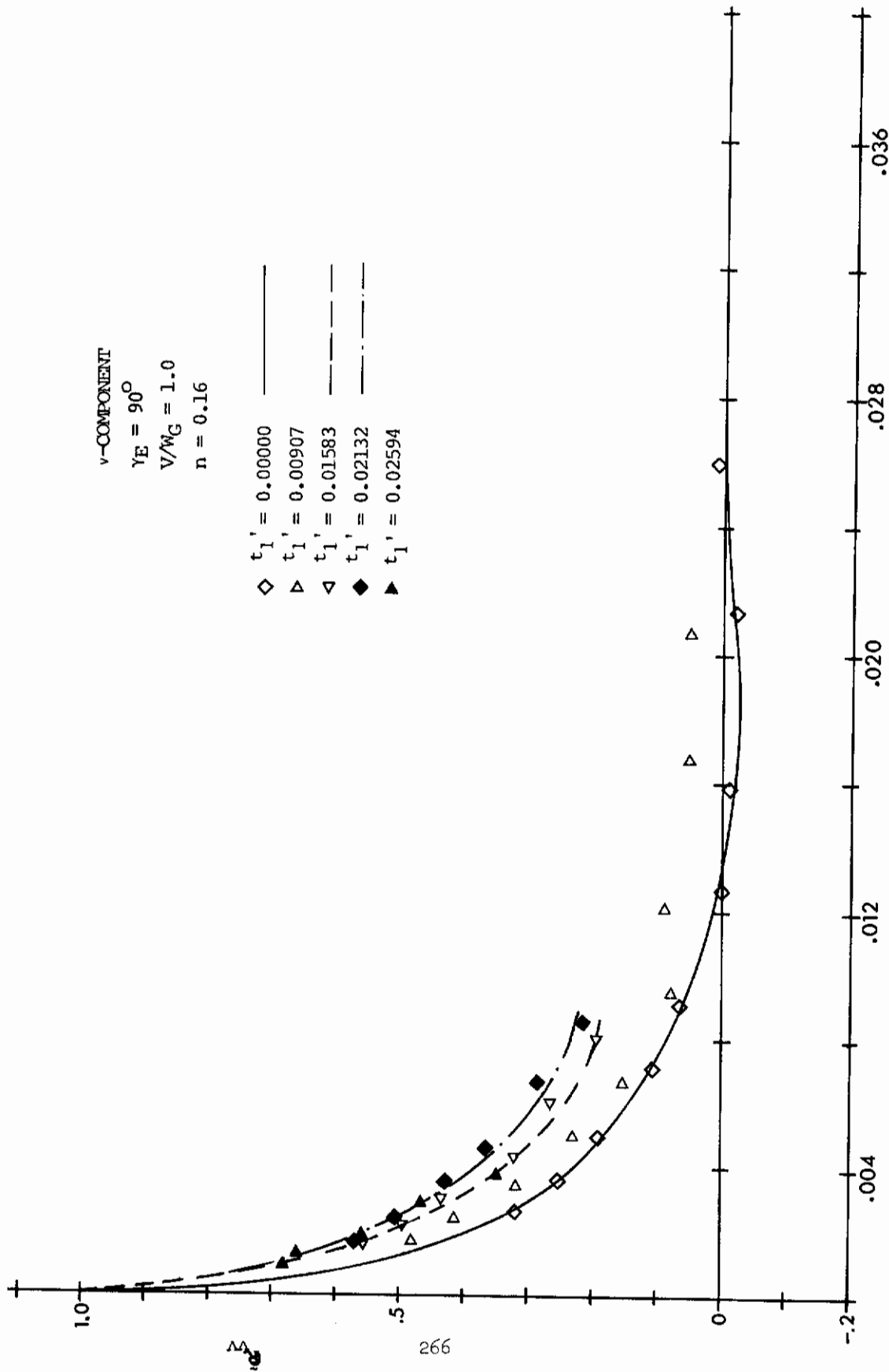FIGURE 77b. FLIGHT PATH TURBULENCE CORRELATION, 8" x 8" TUNNEL

243

FIGURE 78a.   FLIGHT PATH TURBULENCE CORRELATION, 8" x 8" TUNNEL

u-COMPONENT

$Y_E = 45^O$

$V/W_G = 1.2$

$n = 0.16$

◇	$t_1' = 0.00000$
△	$t_1' = 0.01123$
▽	$t_1' = 0.02128$
◆	$t_1' = 0.03023$
▲	$t_1' = 0.03810$

$t_2' - t_1'$, seconds

244

FIGURE 78b. FLIGHT PATH TURBULENCE CORRELATION, 8'' x 8'' TUNNEL

u-COMPONENT

$\gamma_E = 45^O$

$V/W_G = 1.2$

$n = 0.16$

$t_1' = 0.00576$

$t_1' = 0.01640$

$t_1' = 0.02589$

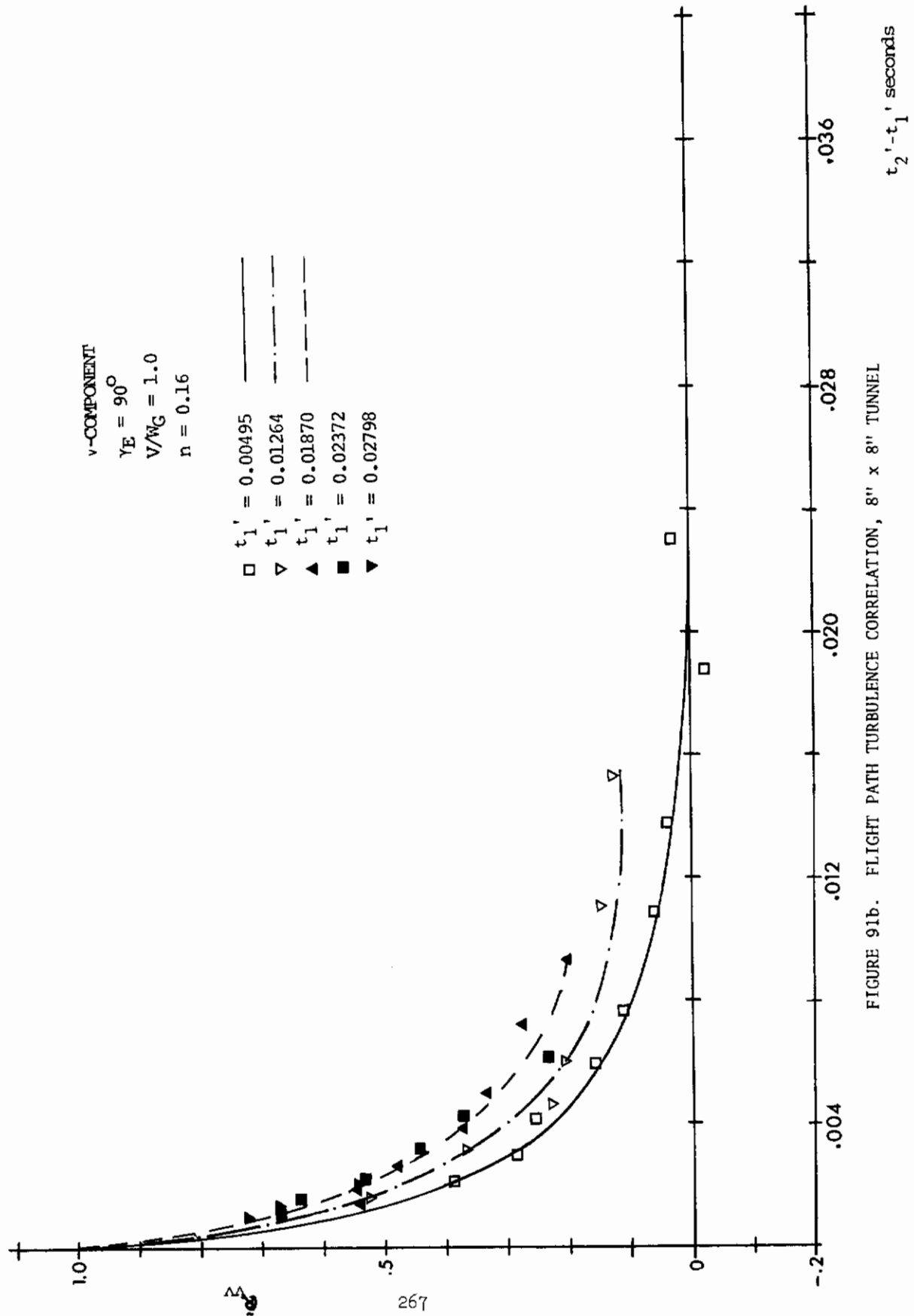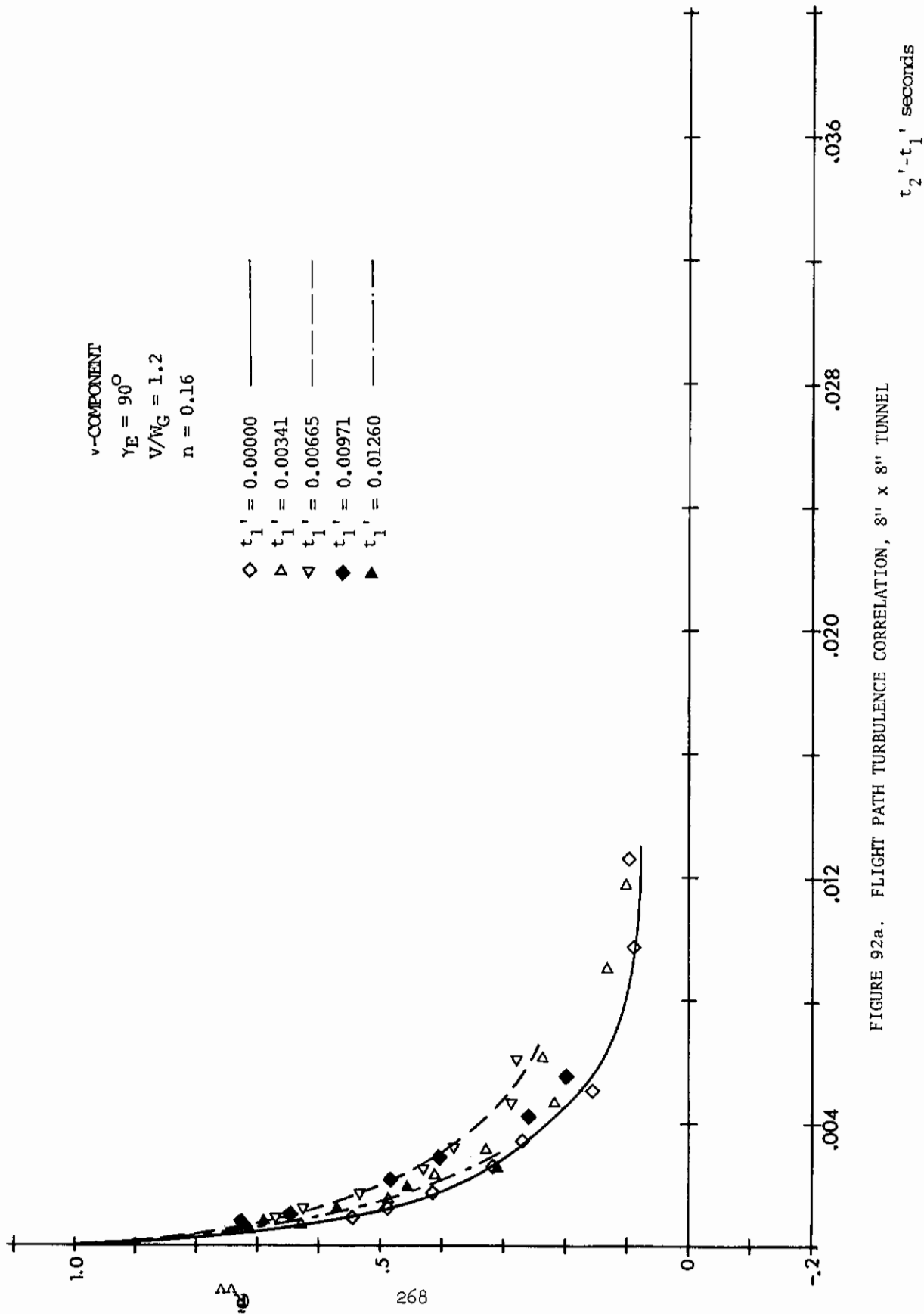$t_1' = 0.03430$

$t_1' = 0.04161$

$t_2' - t_1'$ seconds

245
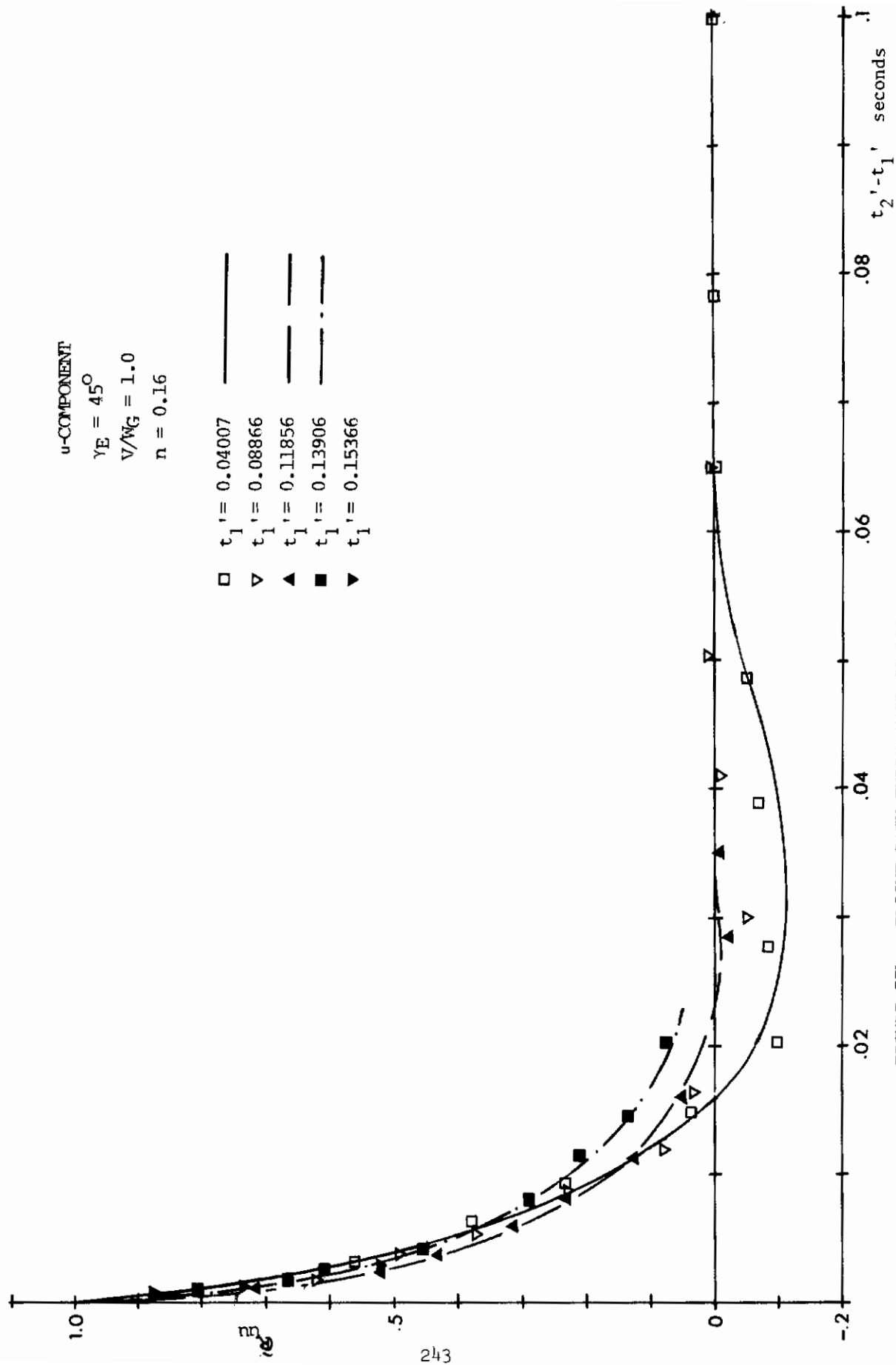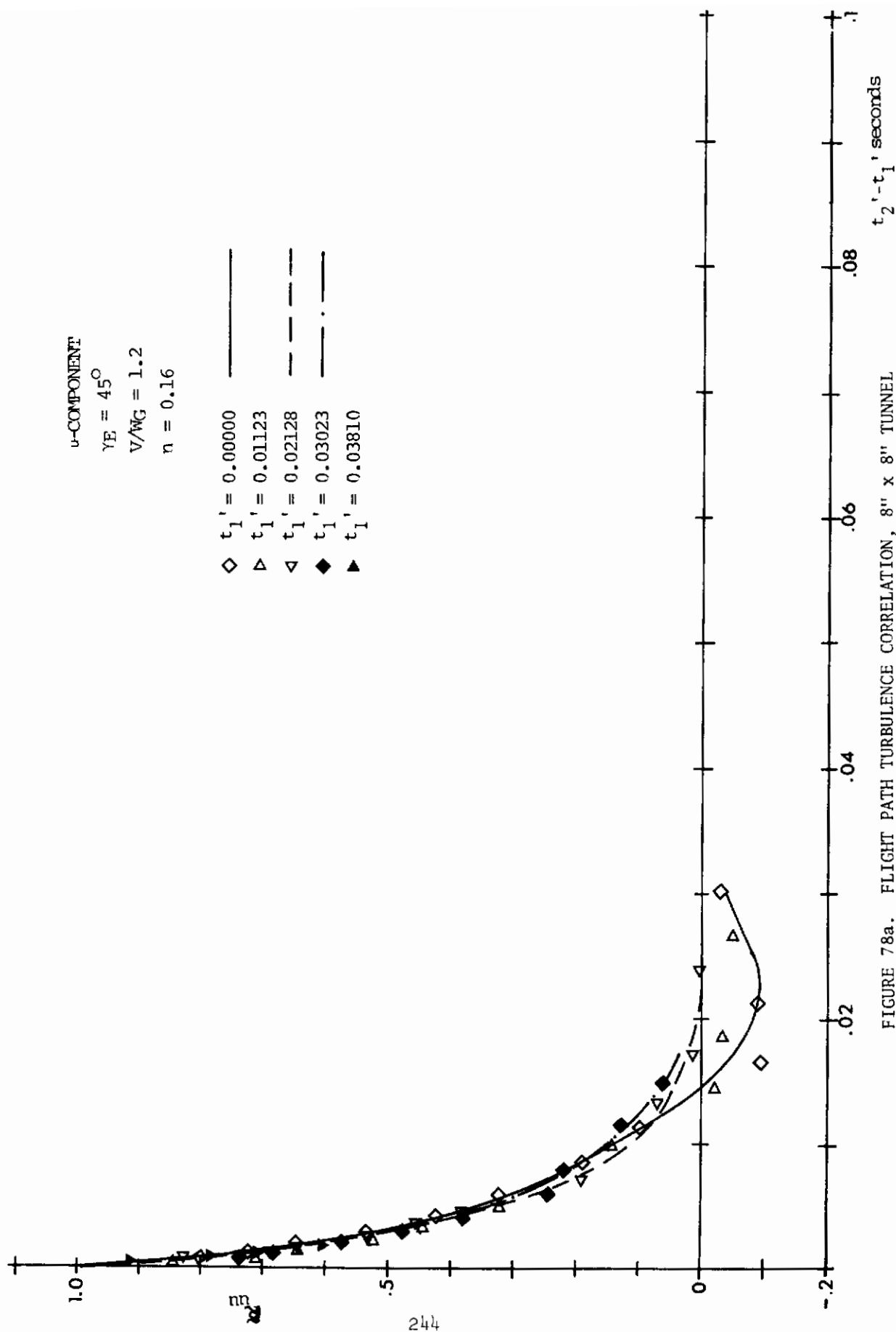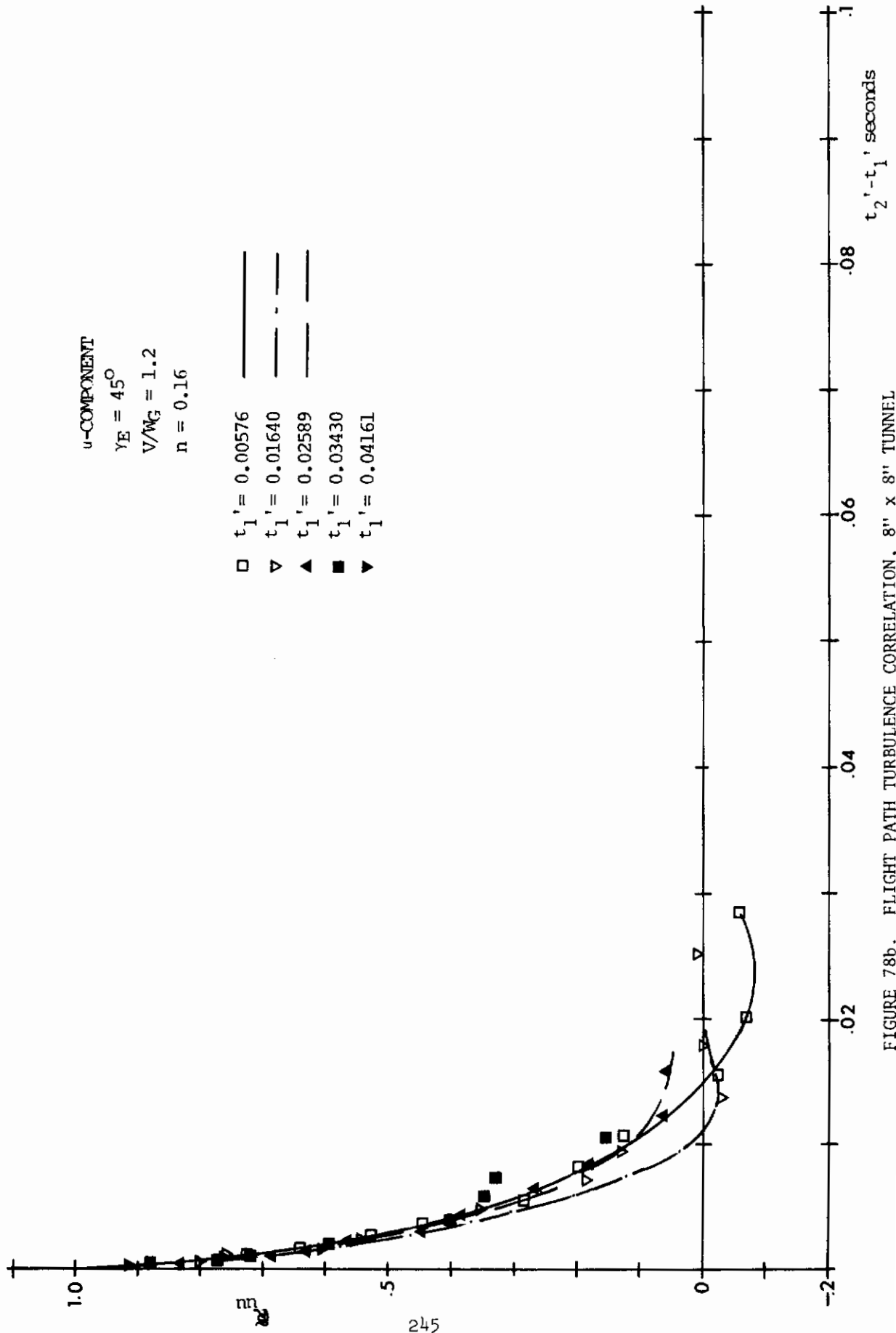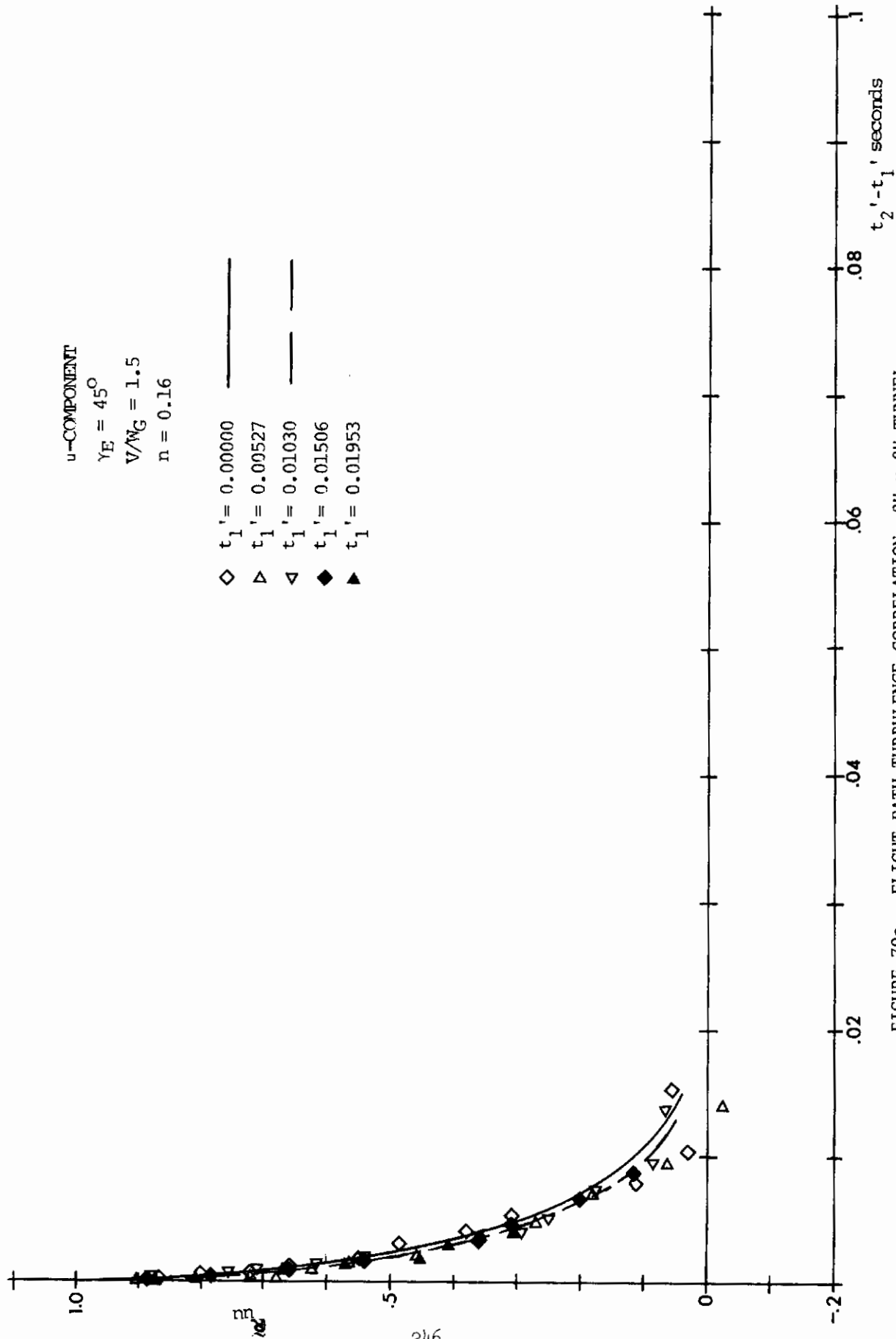
FIGURE 79a.   FLIGHT PATH TURBULENCE CORRELATION, 8" x 8" TUNNEL

u-COMPONENT
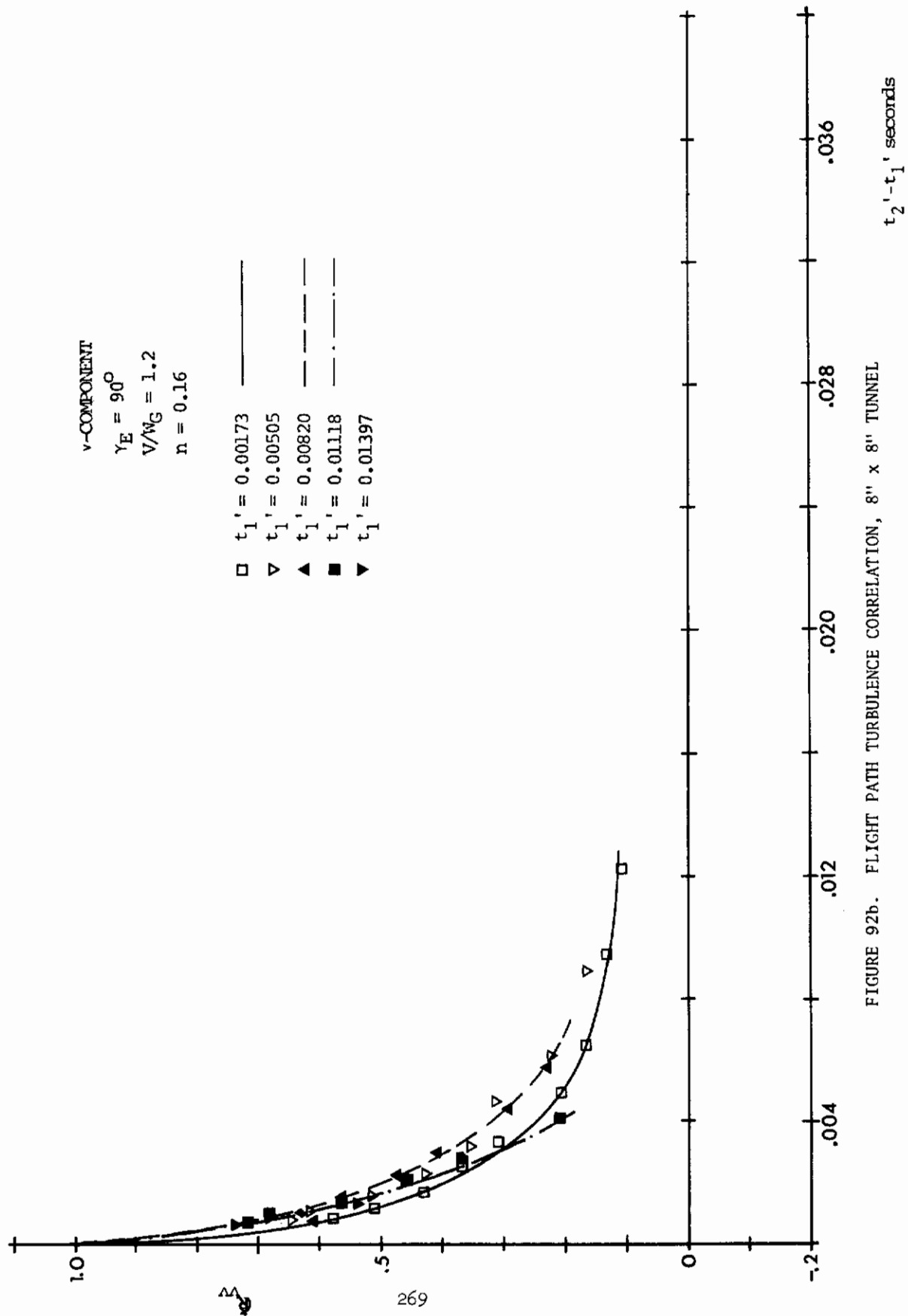
$\gamma_E = 45^o$

$V/w_G = 1.5$

$n = 0.16$

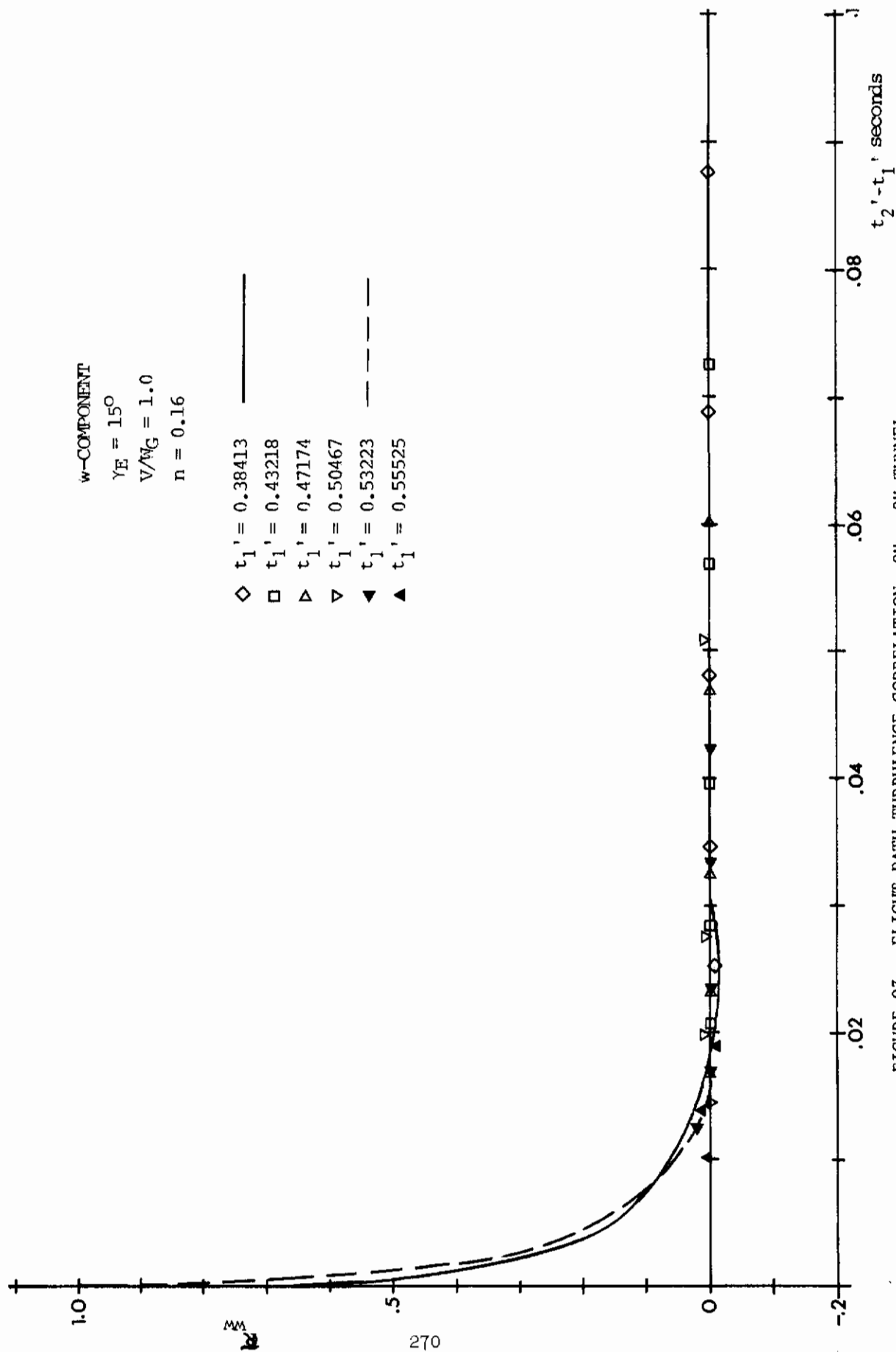|		
◇	$t_1' = 0.00000$	
△	$t_1' = 0.00527$	
▽	$t_1' = 0.01030$	
◆	$t_1' = 0.01506$	
▲	$t_1' = 0.01953$	

$t_2' - t_1'$, seconds

246

FIGURE 79b. FLIGHT PATH TURBULENCE CORRELATION, 8" x 8" TUNNEL

u-COMPONENT

$\gamma_E = 45^O$

$V/W_G = 1.5$

$n = 0.16$

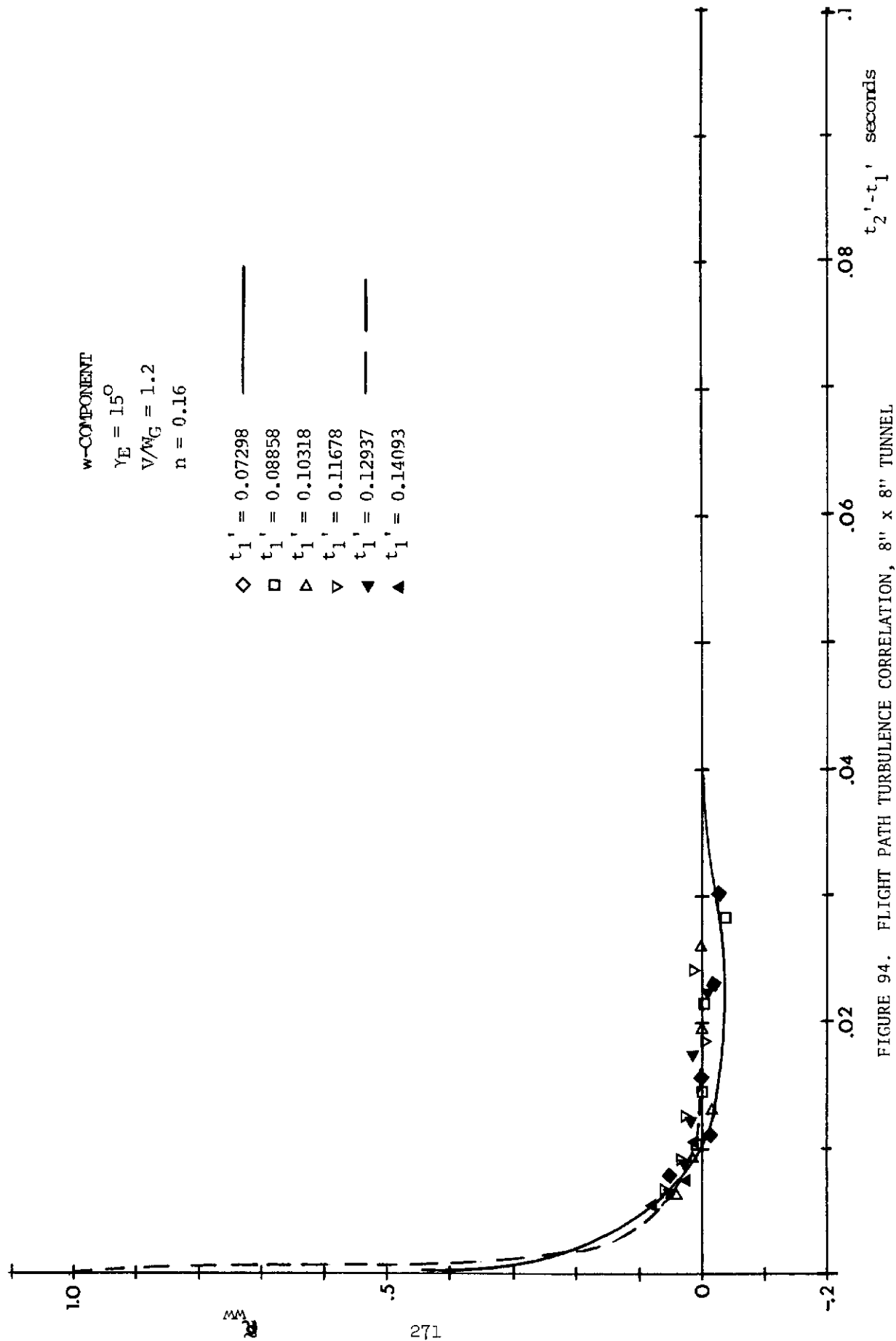|	
□	$t_1' = 0.00266$
▽	$t_1' = 0.00782$
◄	$t_1' = 0.01272$
■	$t_1' = 0.01733$
►	$t_1' = 0.02163$

$t_2' - t_1'$ seconds

R_{nn}

247
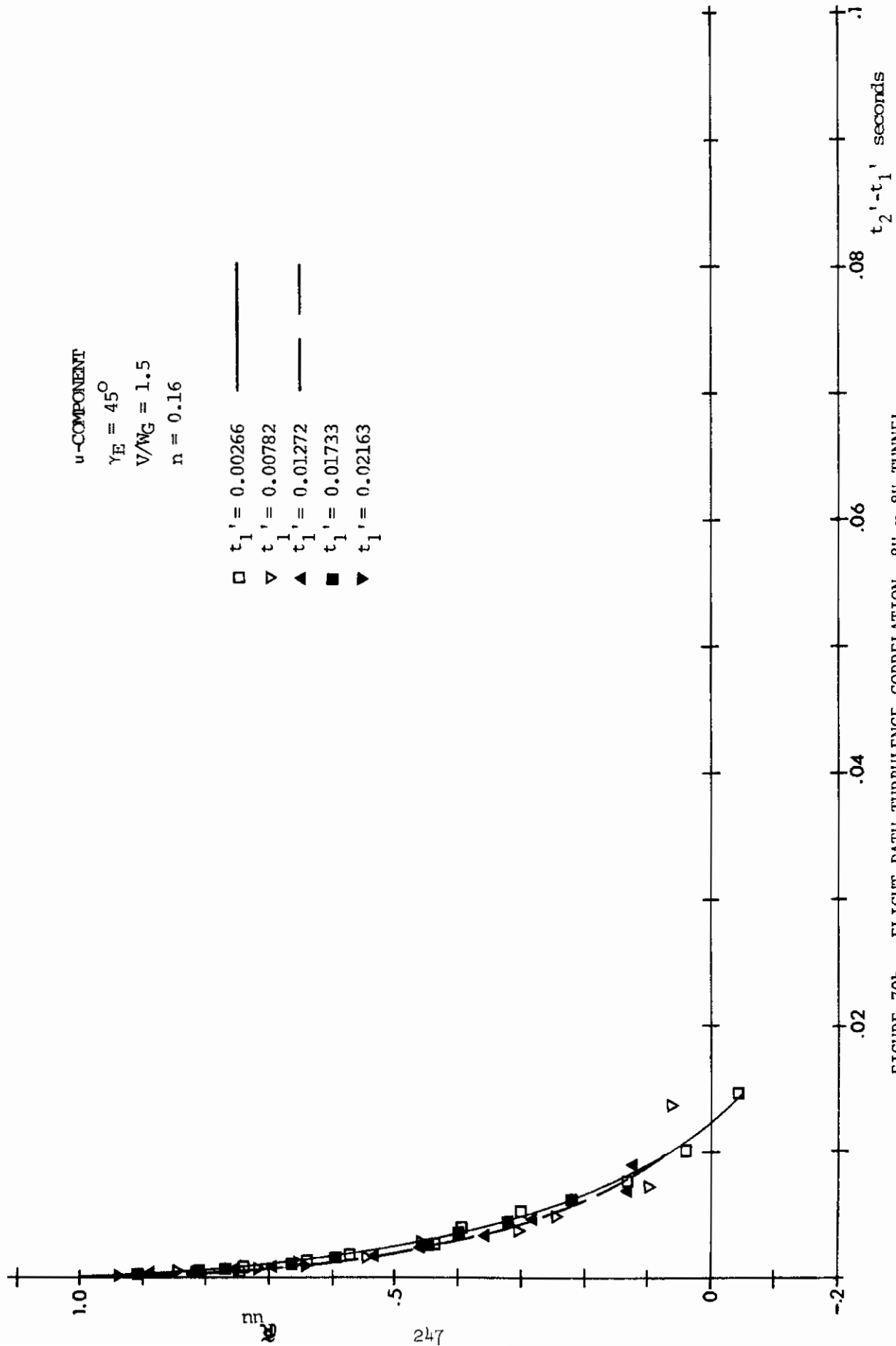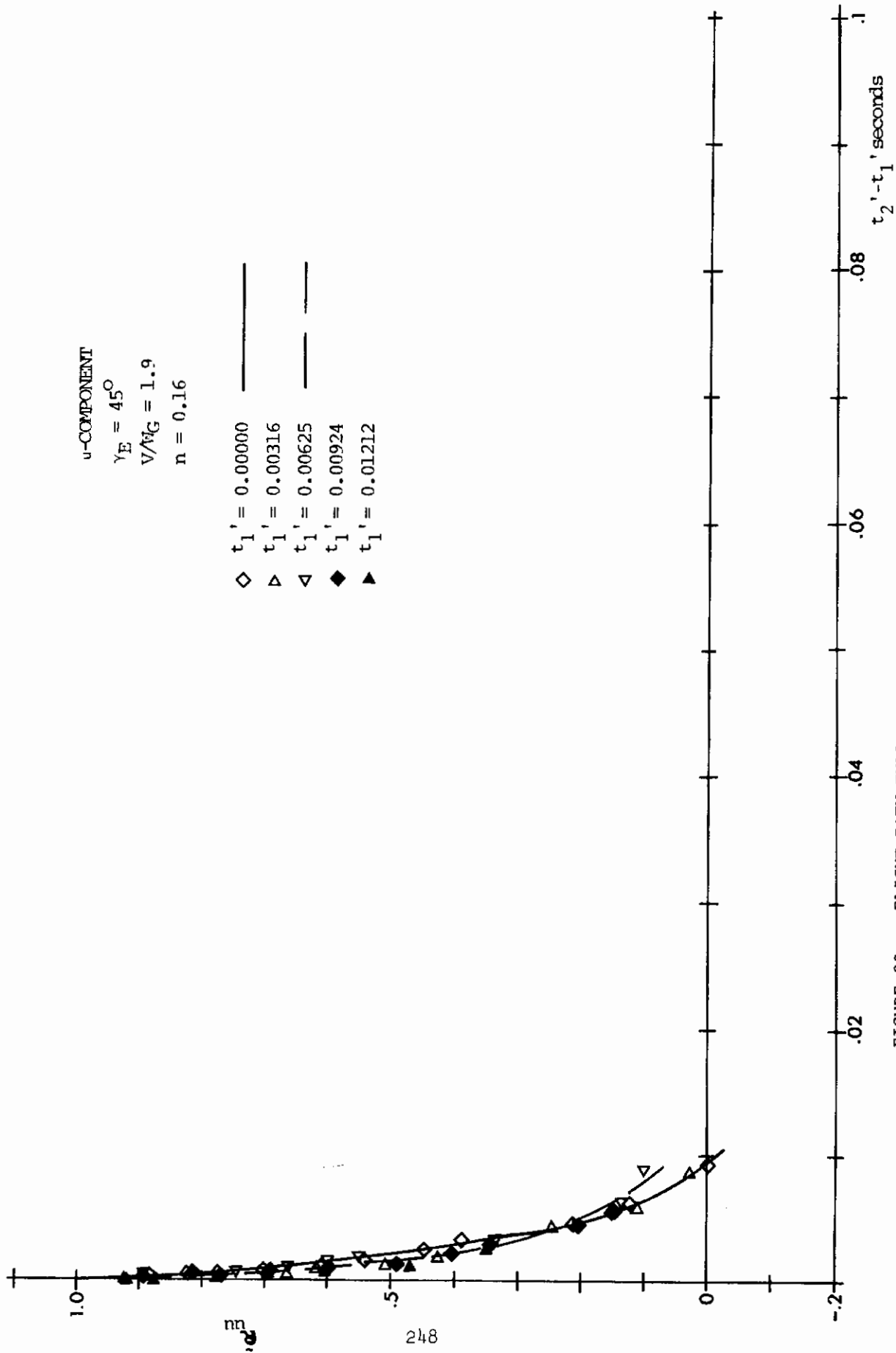
FIGURE 80a.   FLIGHT PATH TURBULENCE CORRELATION, 8" x 8" TUNNEL

u-COMPONENT

$\gamma_E = 45^O$

$V/\mathcal{V}_G = 1.9$

$n = 0.16$

$t_1' = 0.00000$ ◇

$t_1' = 0.00316$ △

$t_1' = 0.00625$ ▽

$t_1' = 0.00924$ ◆

$t_1' = 0.01212$ ▲

R'_{uu}

$t_2' - t_1'$ seconds

248

FIGURE 80b. FLIGHT PATH TURBULENCE CORRELATION, 8'' x 8'' TUNNEL

u-COMPONENT

$\gamma_E = 45^O$

$V/W_G = 1.9$

$n = 0.16$

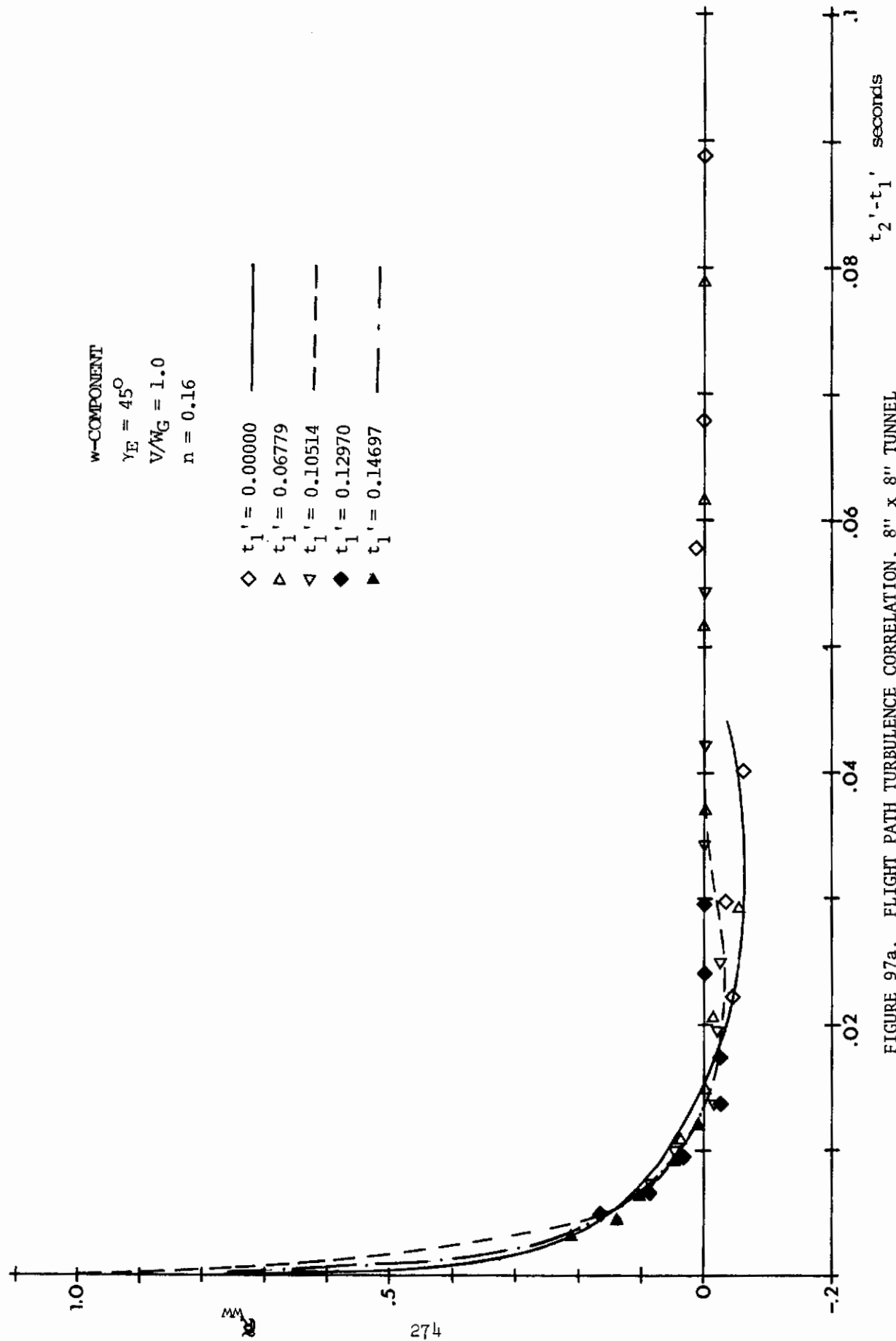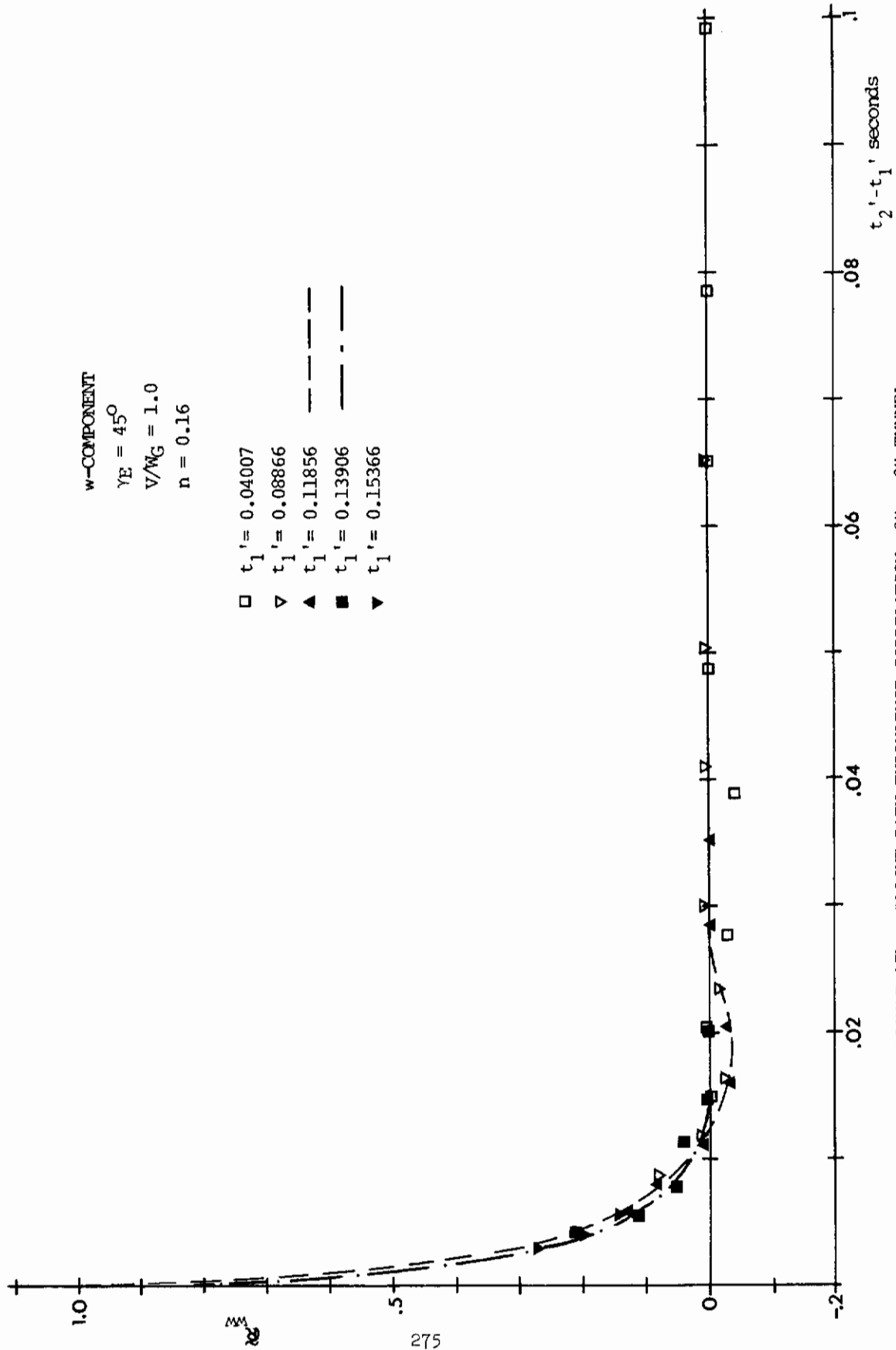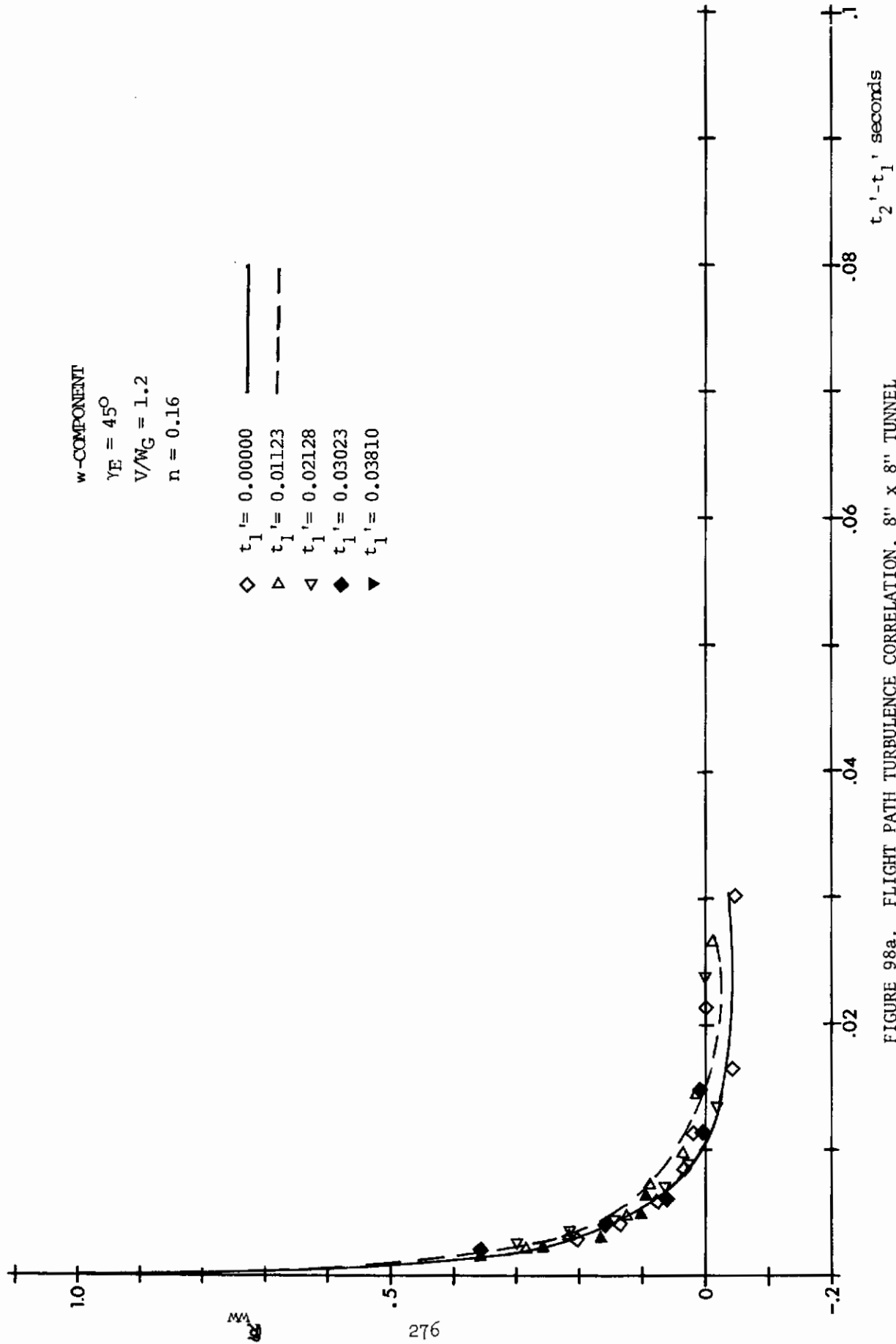|		
□	$t_1' = 0.00159$	
▽	$t_1' = 0.00472$	
◄	$t_1' = 0.00776$	
■	$t_1' = 0.01069$	
►	$t_1' = 0.01350$	

$t_2' - t_1'$, seconds

R'_{uu}

249
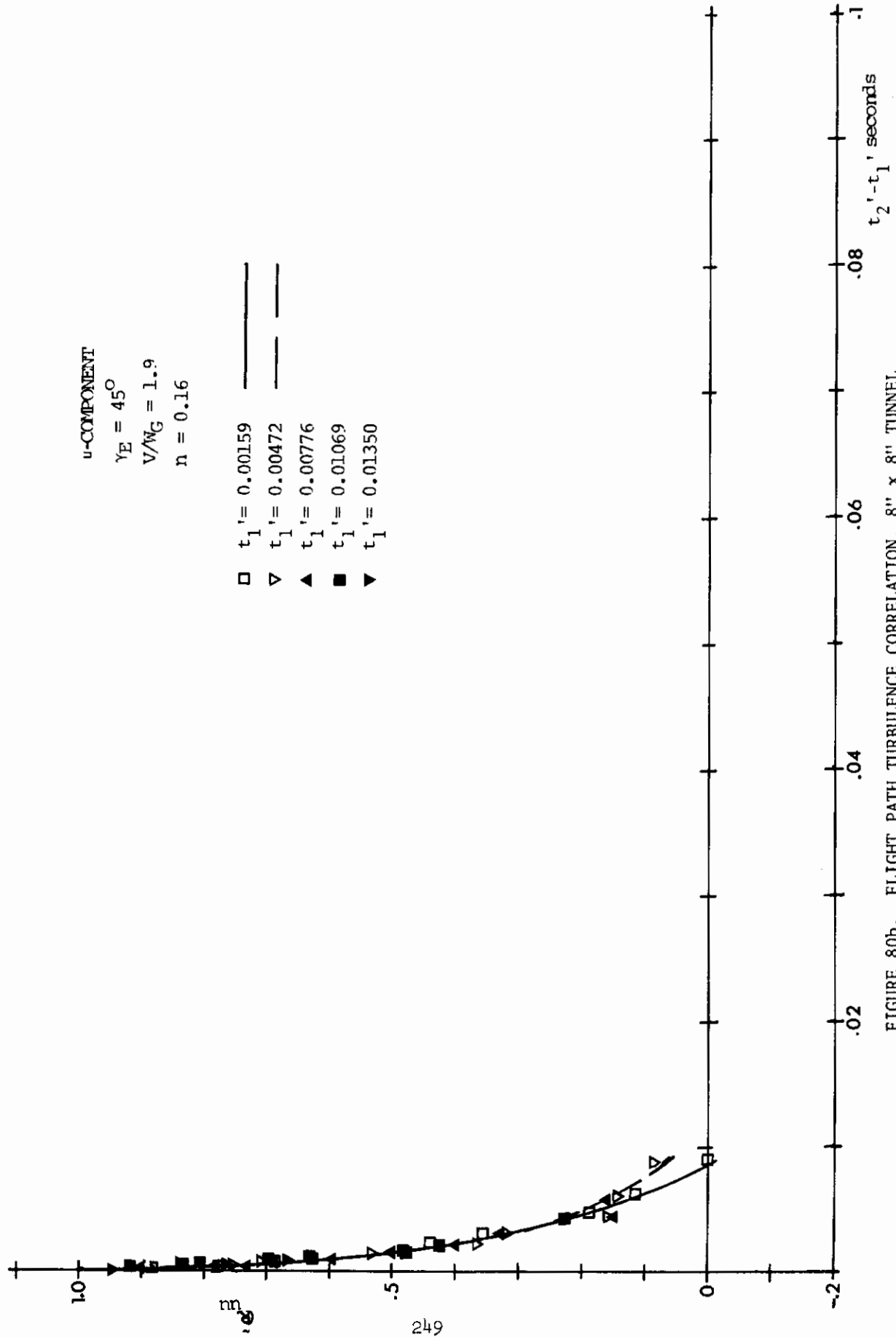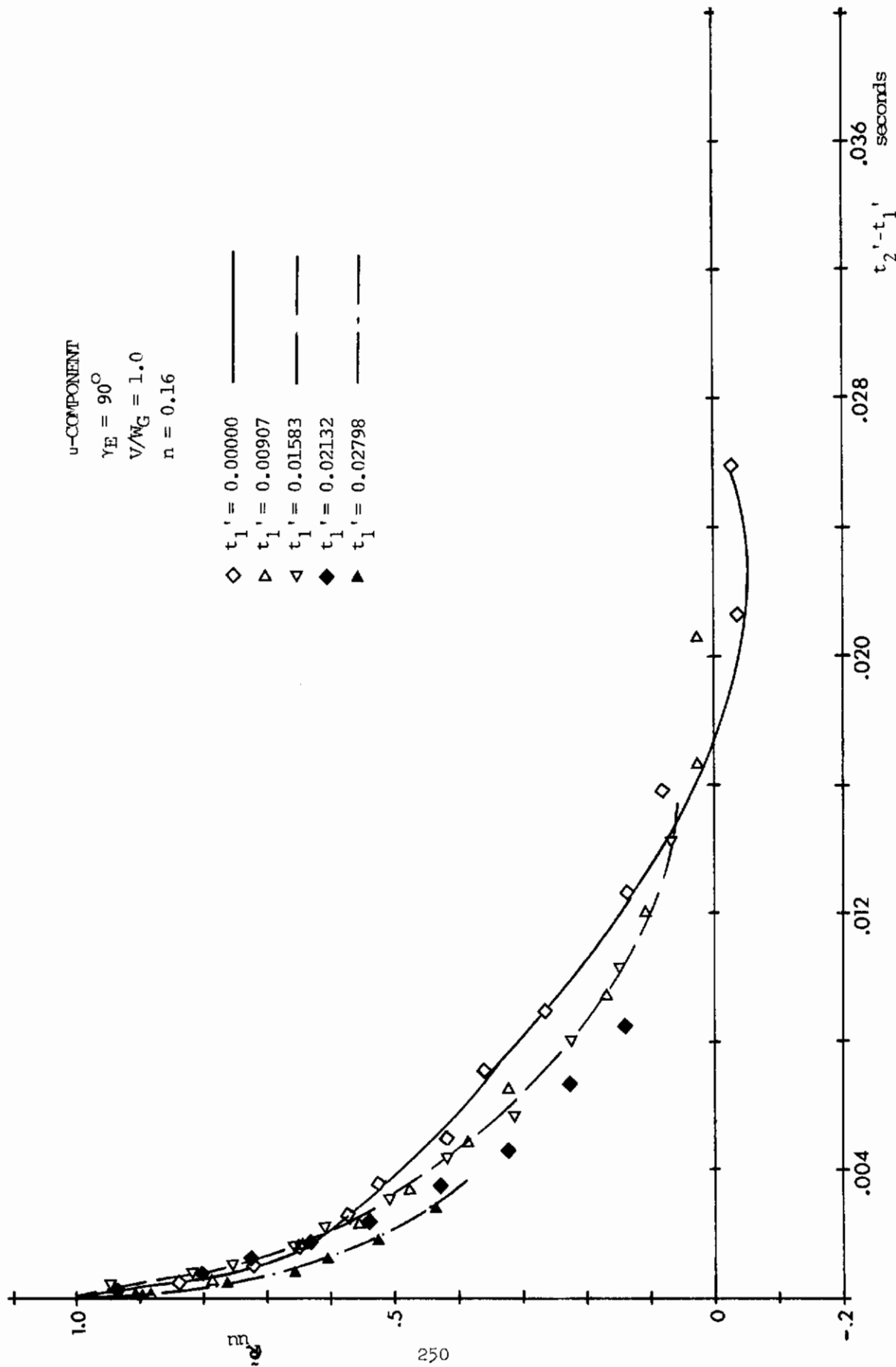
FIGURE 81a. FLIGHT PATH TURBULENCE CORRELATION, 8" x 8" TUNNEL

u-COMPONENT
$\gamma_E = 90^O$
$V/W_G = 1.0$
$n = 0.16$

$\Diamond$	$t_1' = 0.00000$	
$\triangle$	$t_1' = 0.00907$	
$\triangledown$	$t_1' = 0.01583$	
$\blacklozenge$	$t_1' = 0.02132$	
$\blacktriangle$	$t_1' = 0.02798$	

250

u-COMPONENT

$\gamma_E = 90^O$

$V/W_G = 1.0$

$n = 0.16$

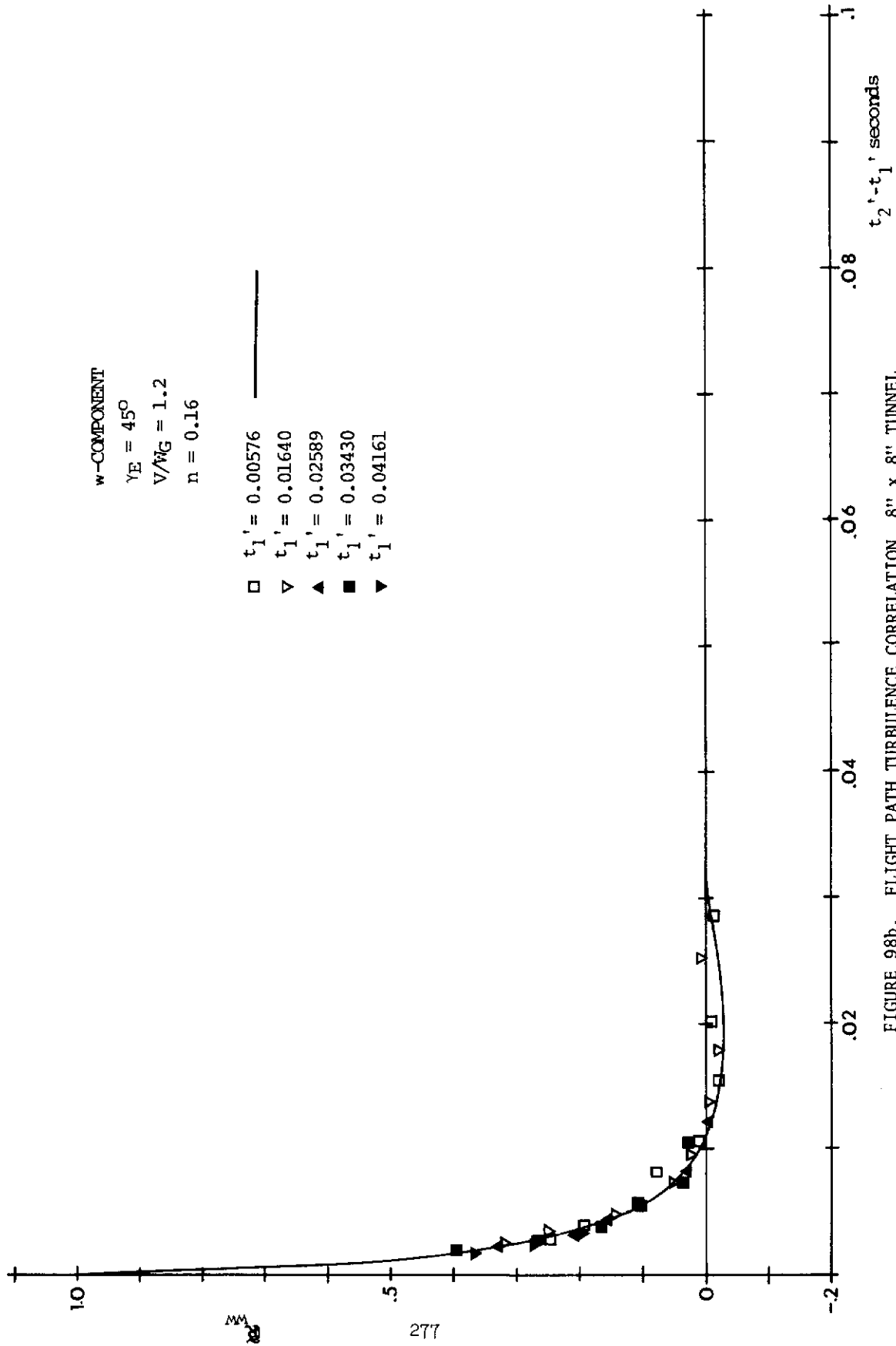|	
□	$t_1' = 0.00495$
▷	$t_1' = 0.01264$
◀	$t_1' = 0.01870$
■	$t_1' = 0.02372$
▶	$t_1' = 0.02594$

$t_2' - t_1'$, seconds

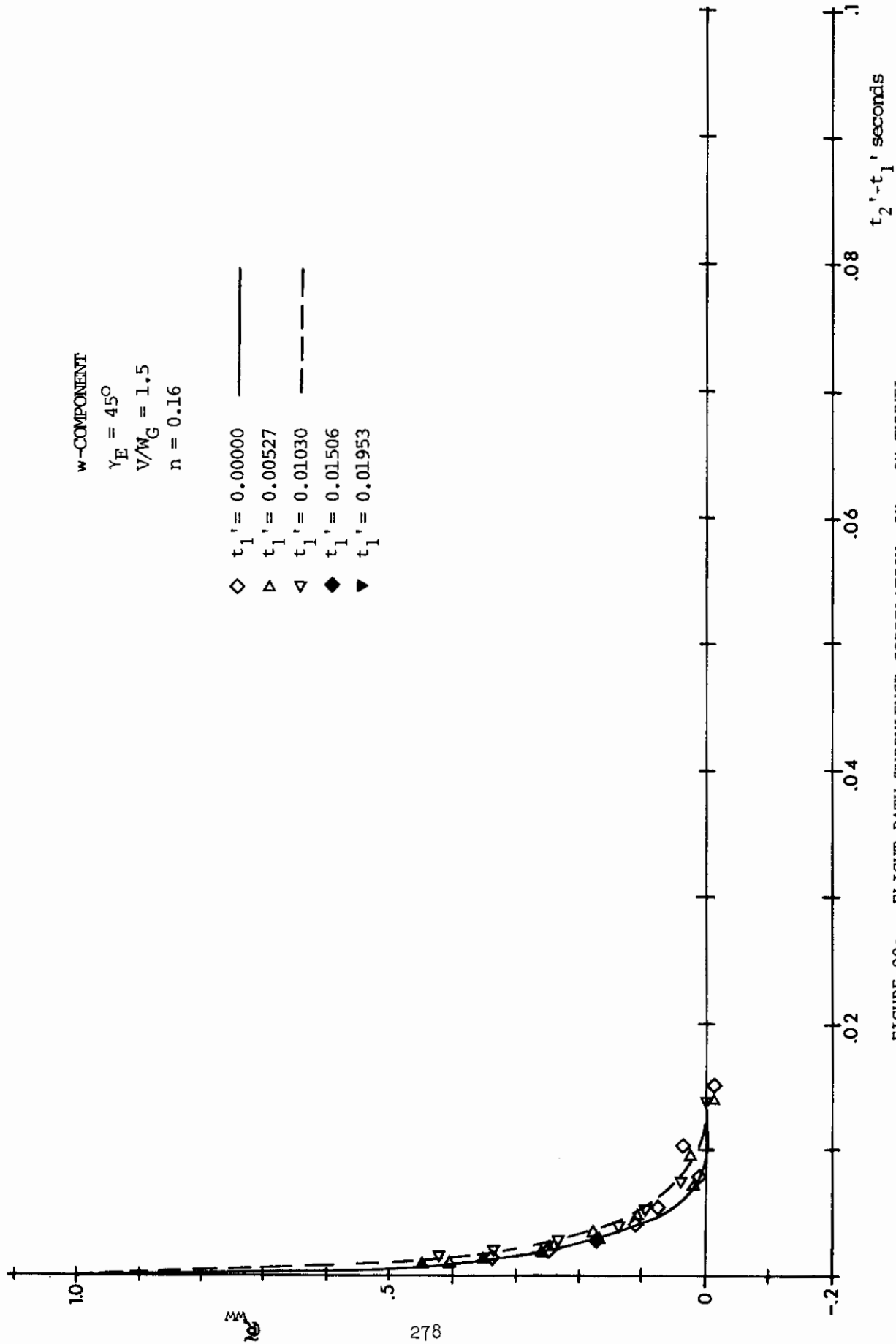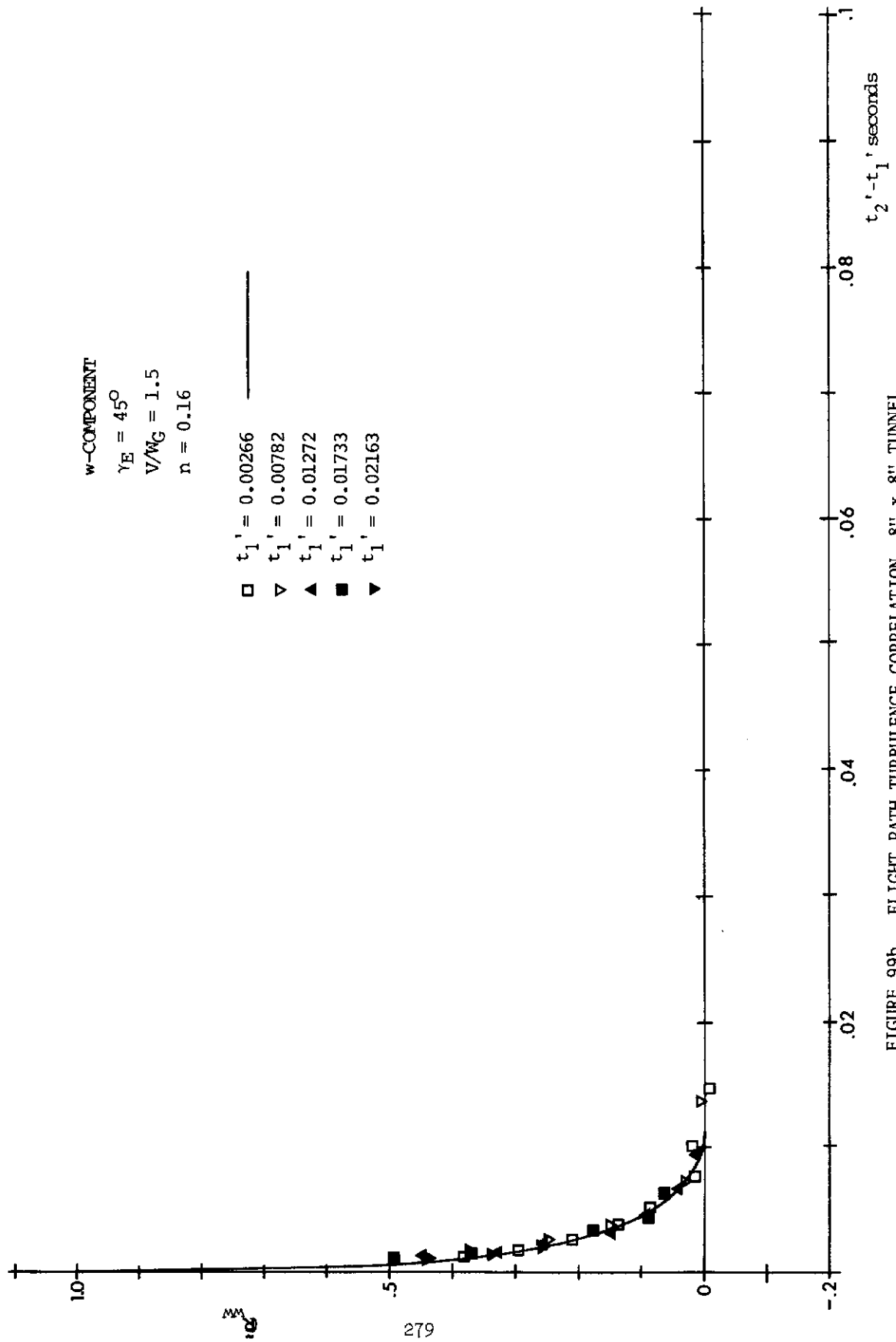FIGURE 81b. FLIGHT PATH TURBULENCE CORRELATION, 8" x 8" TUNNEL

251

FIGURE 82a. FLIGHT PATH TURBULENCE CORRELATION, 8" x 8" TUNNEL

252

u-COMPONENT

$\gamma_E = 90^\circ$

$W/W_G = 1.2$

$n = 0.16$

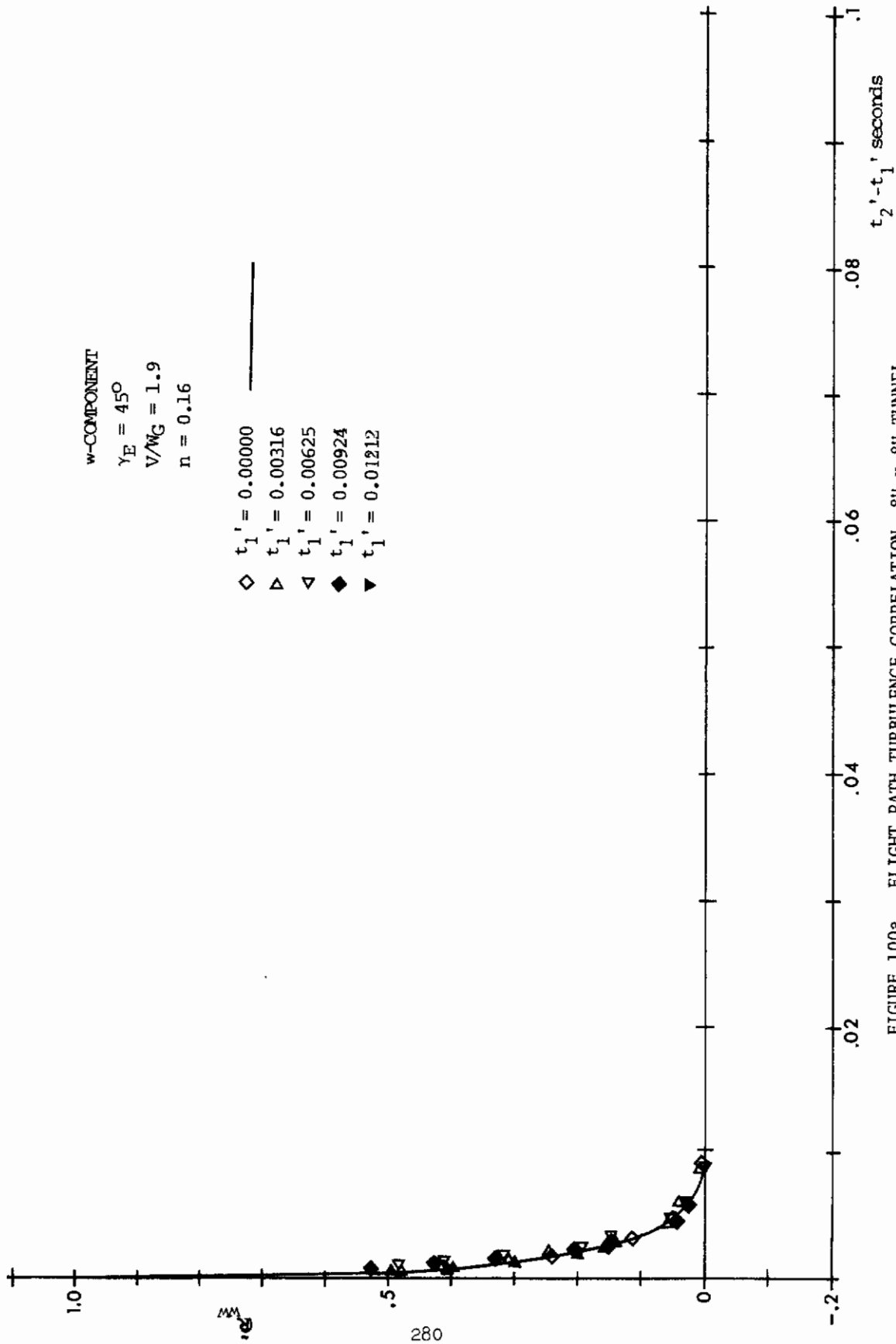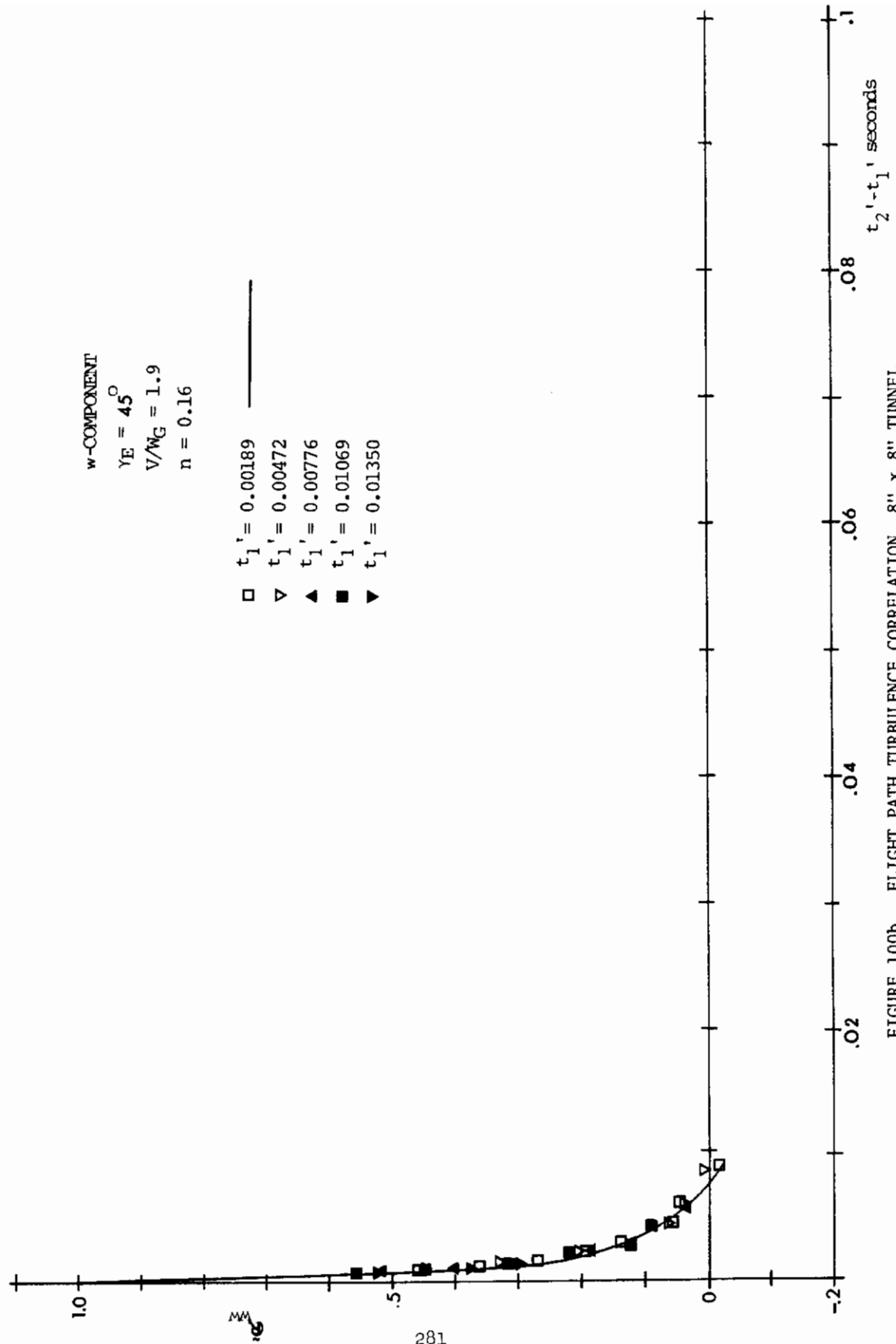|		
□	$t_1' = 0.00173$	——
▷	$t_1' = 0.00505$	— —
◀	$t_1' = 0.00820$	
■	$t_1' = 0.01118$	
▶	$t_1' = 0.01397$	—·—·—

$t_2' - t_1'$ seconds

FIGURE 82b.   FLIGHT PATH TURBULENCE CORRELATION, 8" x 8" TUNNEL

253

FIGURE 83. FLIGHT PATH TURBULENCE CORRELATION, 8" x 8" TUNNEL

v-COMPONENT

$\gamma_E = 15^O$

$V/v_G = 1.0$

$n = 0.16$

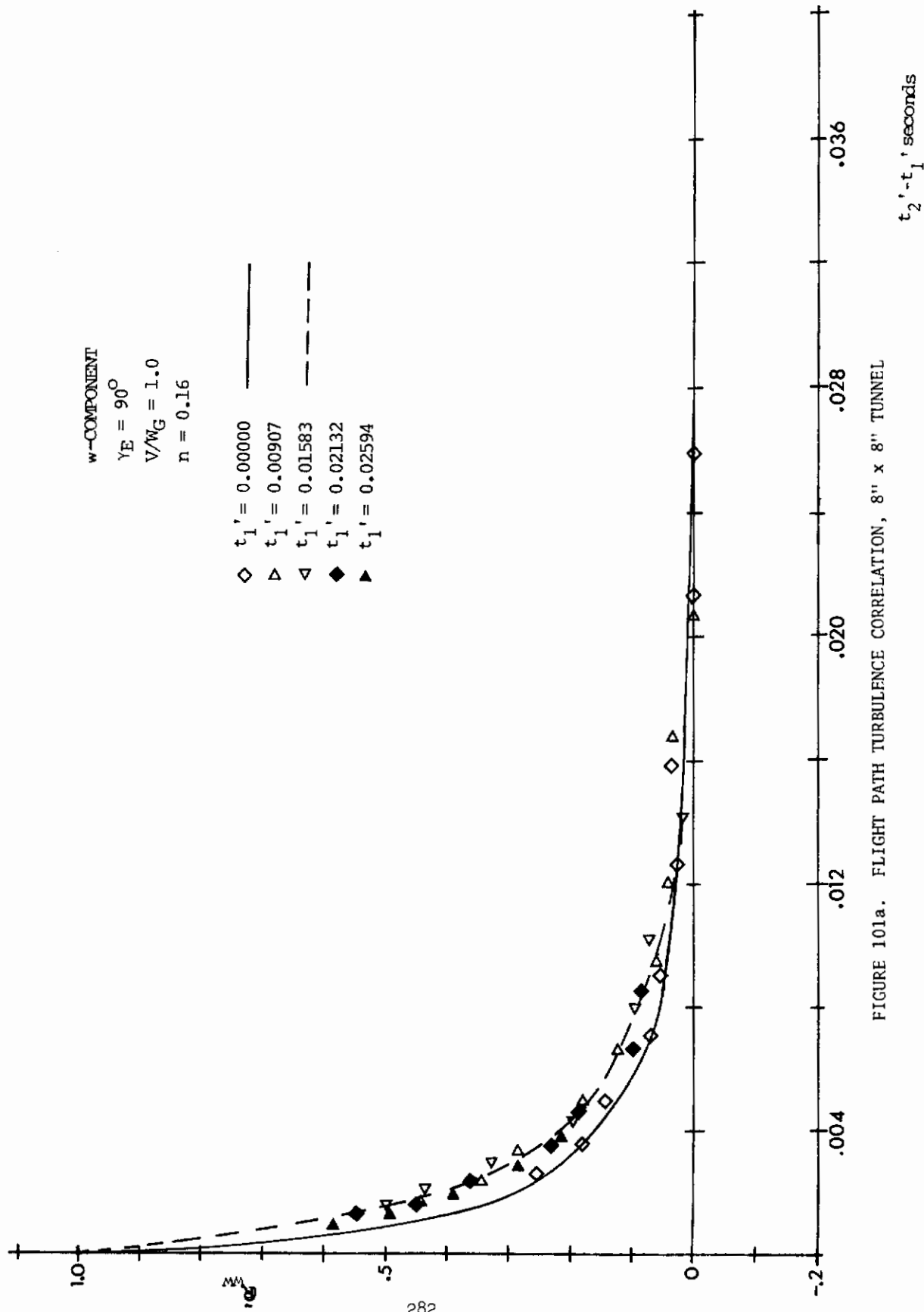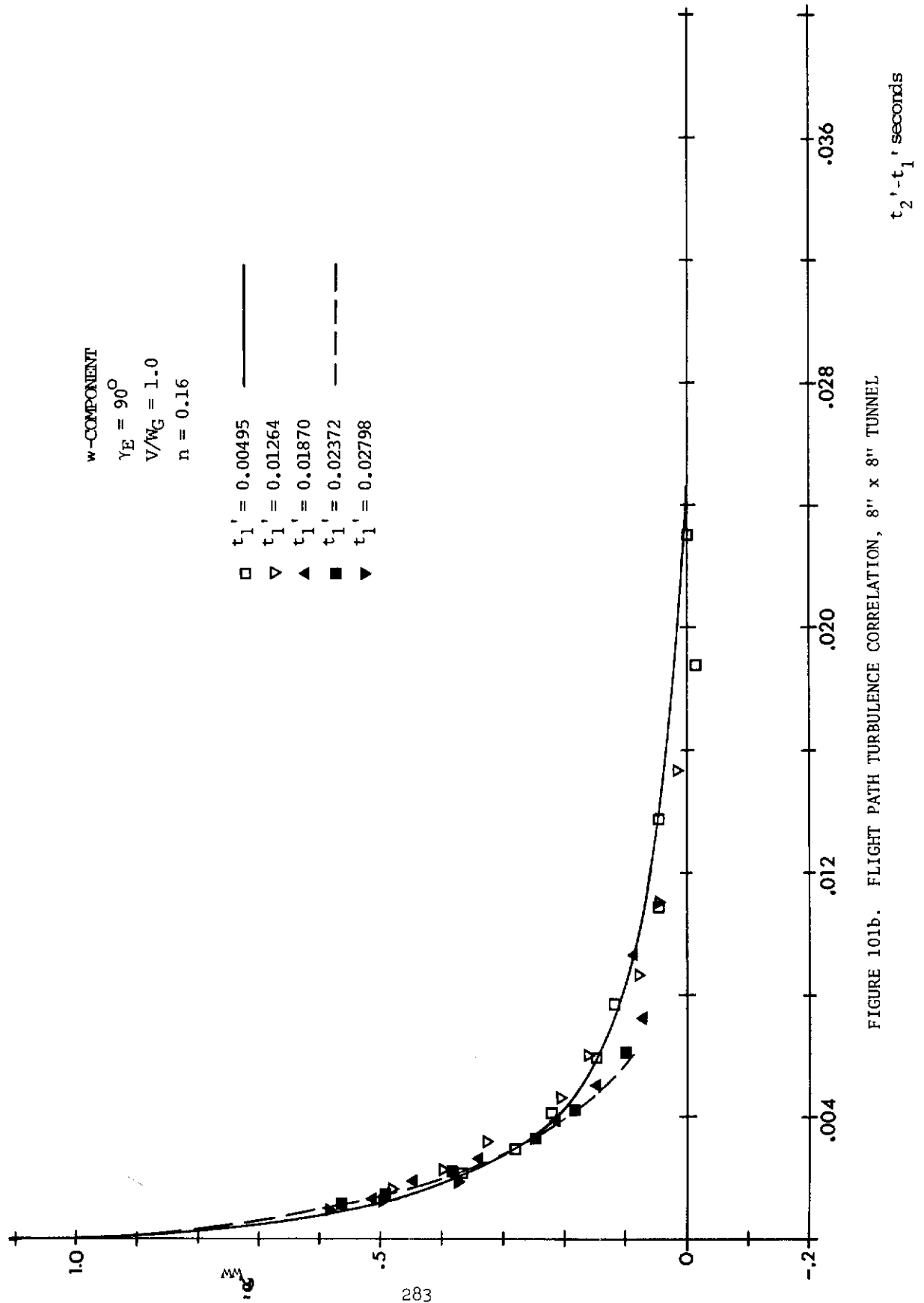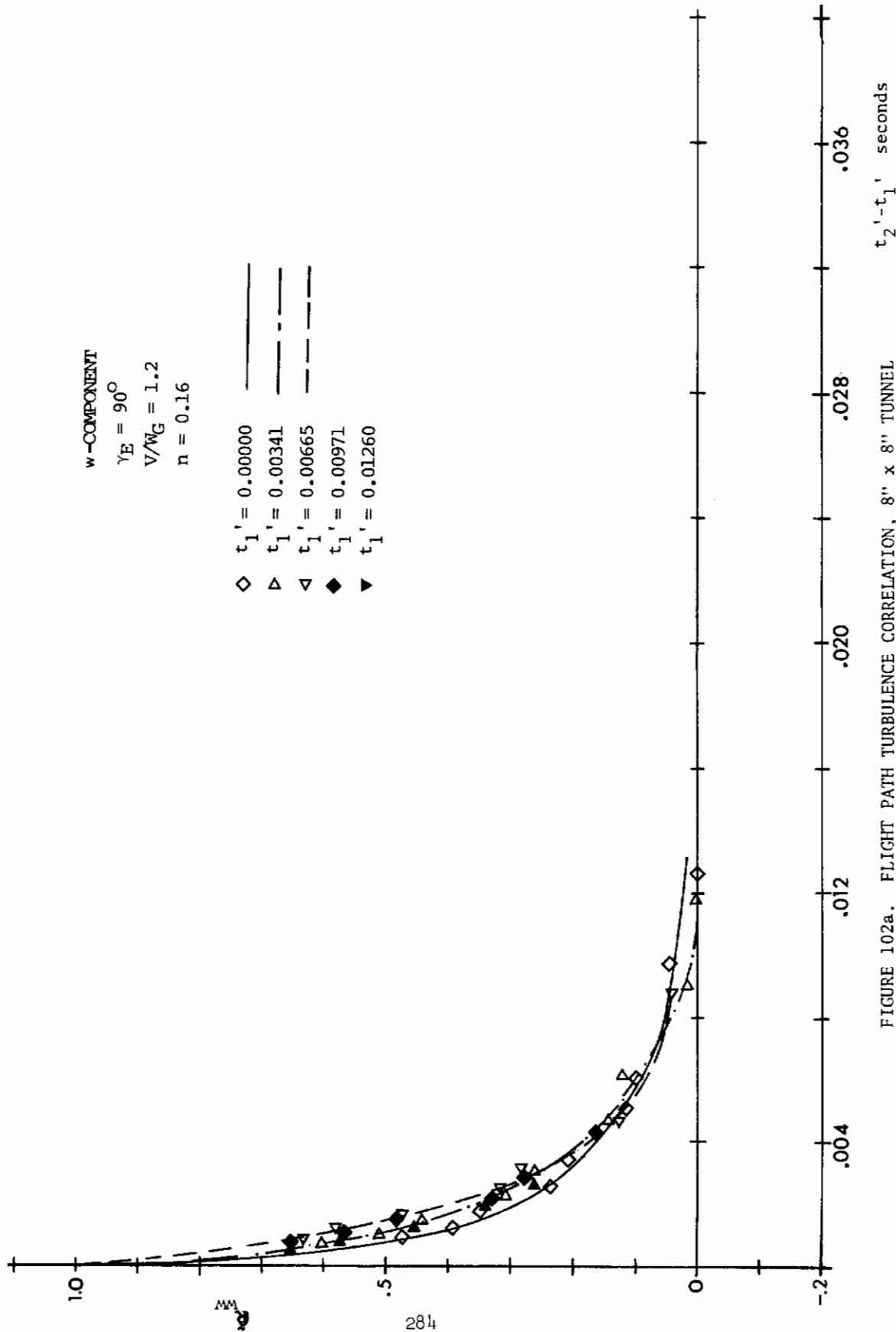|	
◇	$t_1' = 0.38413$
□	$t_1' = 0.43218$
△	$t_1' = 0.47174$
▽	$t_1' = 0.50467$
▼	$t_1' = 0.53223$
◀	$t_1' = 0.55525$

$t_2' - t_1'$, seconds

254
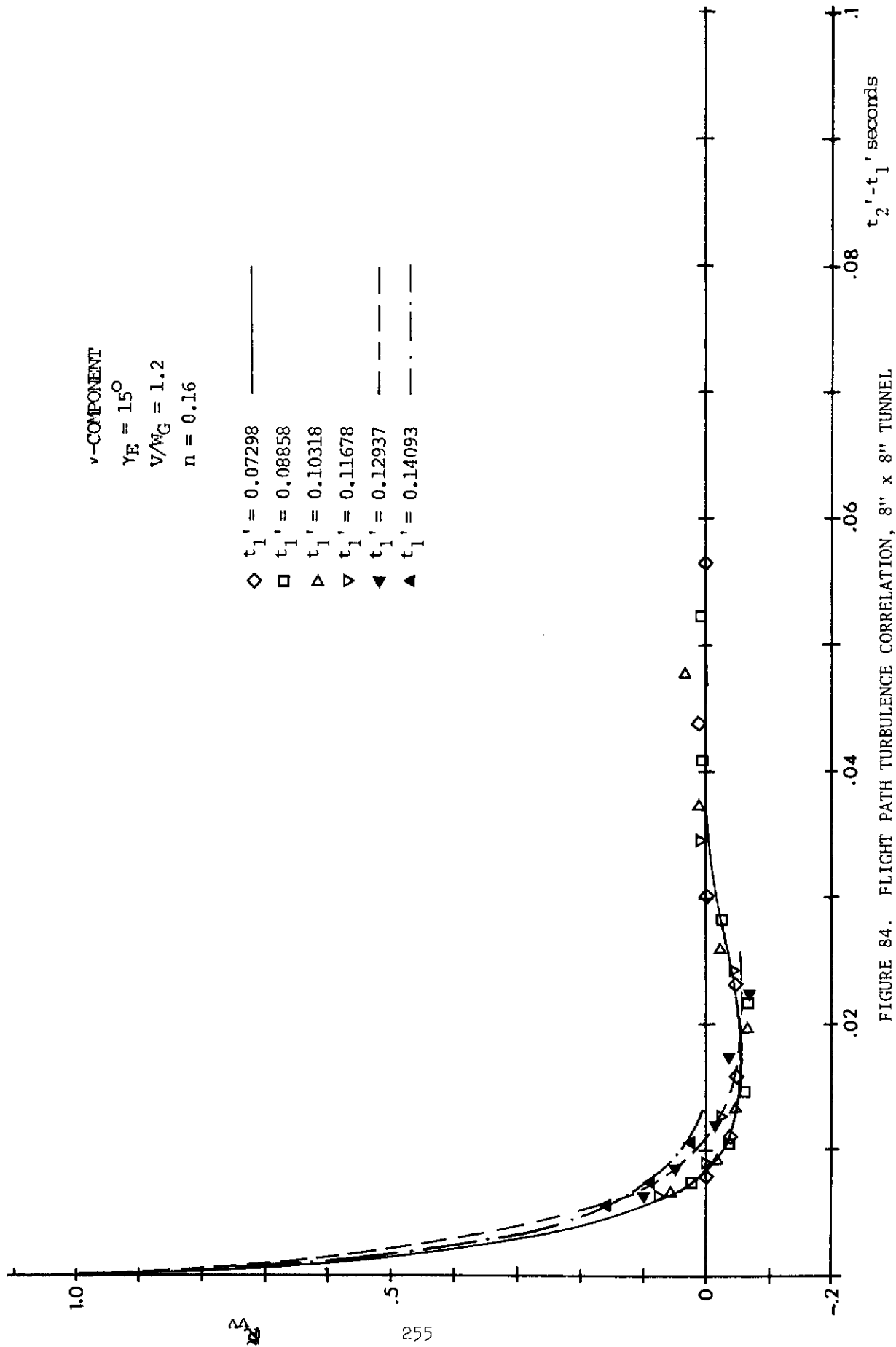
FIGURE 84. FLIGHT PATH TURBULENCE CORRELATION, 8" x 8" TUNNEL

v-COMPONENT

$Y_E = 15^O$

$V/W_G = 1.2$

$n = 0.16$

◇	$t_1' = 0.07298$
□	$t_1' = 0.08858$
△	$t_1' = 0.10318$
▷	$t_1' = 0.11678$
▼	$t_1' = 0.12937$
◀	$t_1' = 0.14093$

$t_2' - t_1'$, seconds

255
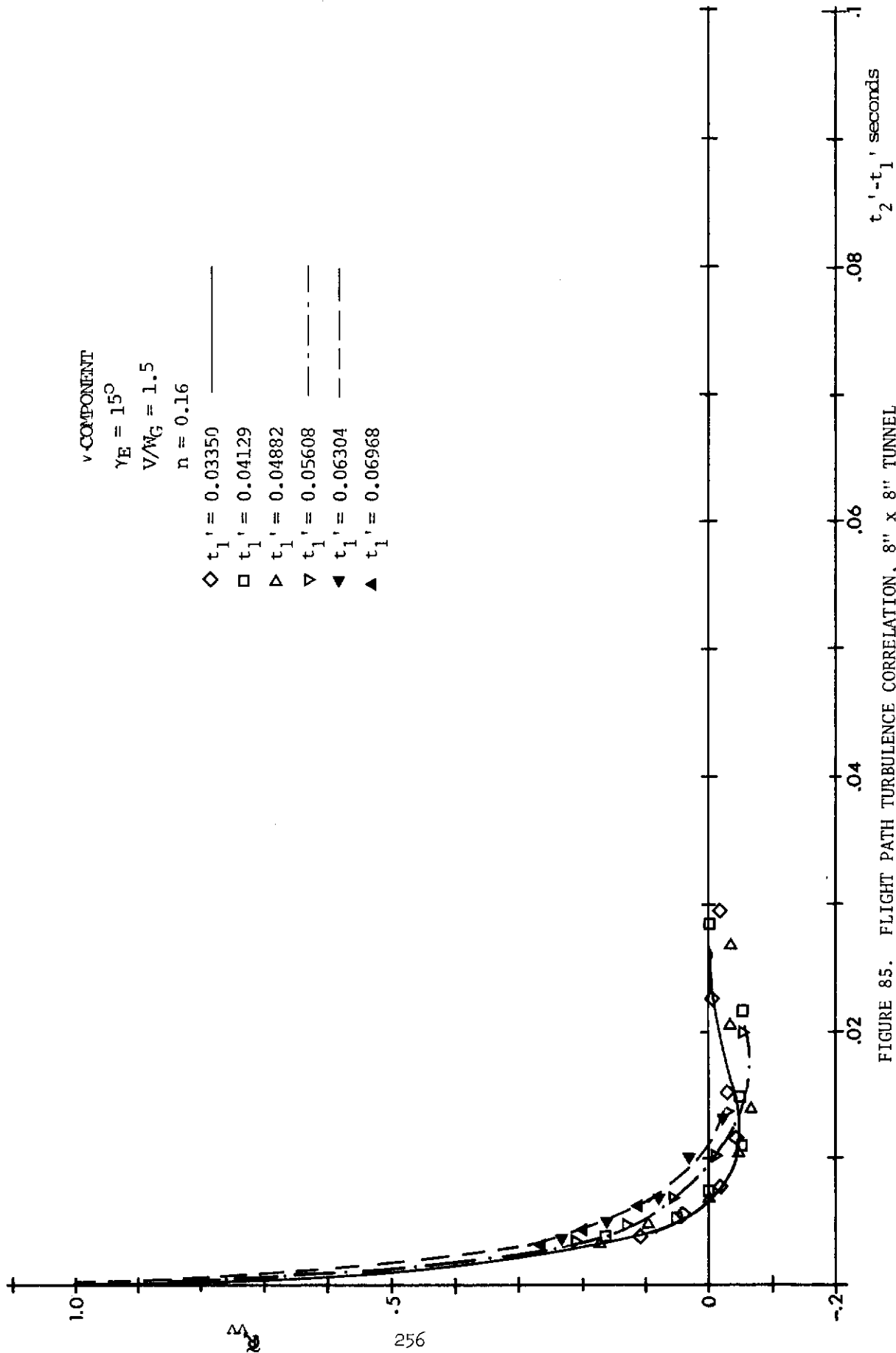
FIGURE 85. FLIGHT PATH TURBULENCE CORRELATION, 8" x 8" TUNNEL

v COMPONENT
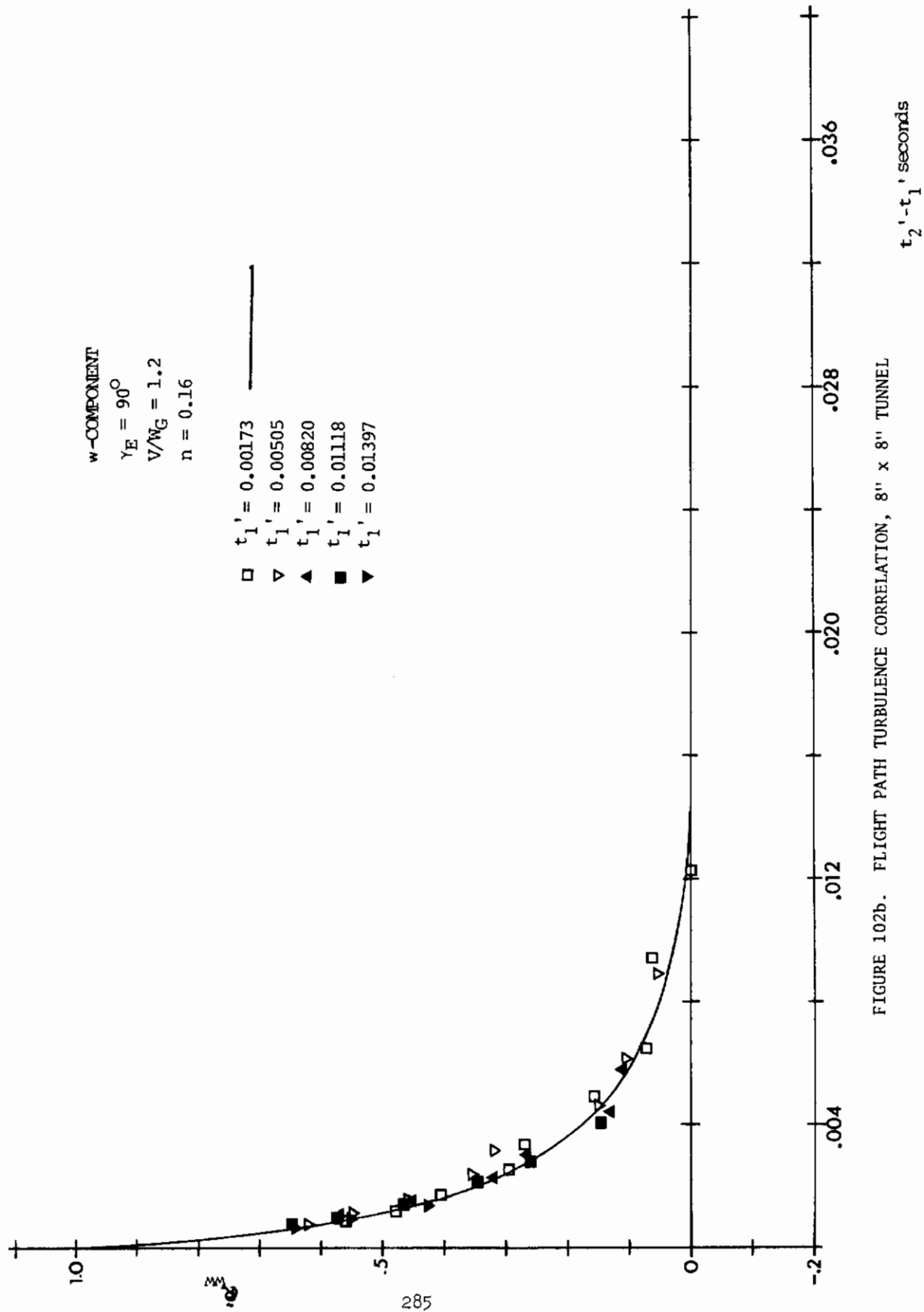$\gamma_E = 15^O$
$V/W_G = 1.5$
$n = 0.16$

◇	$t_1' = 0.03350$	
□	$t_1' = 0.04129$	
△	$t_1' = 0.04882$	
▷	$t_1' = 0.05608$	
▼	$t_1' = 0.06304$	
◀	$t_1' = 0.06968$	

$t_2' - t_1'$, seconds

256
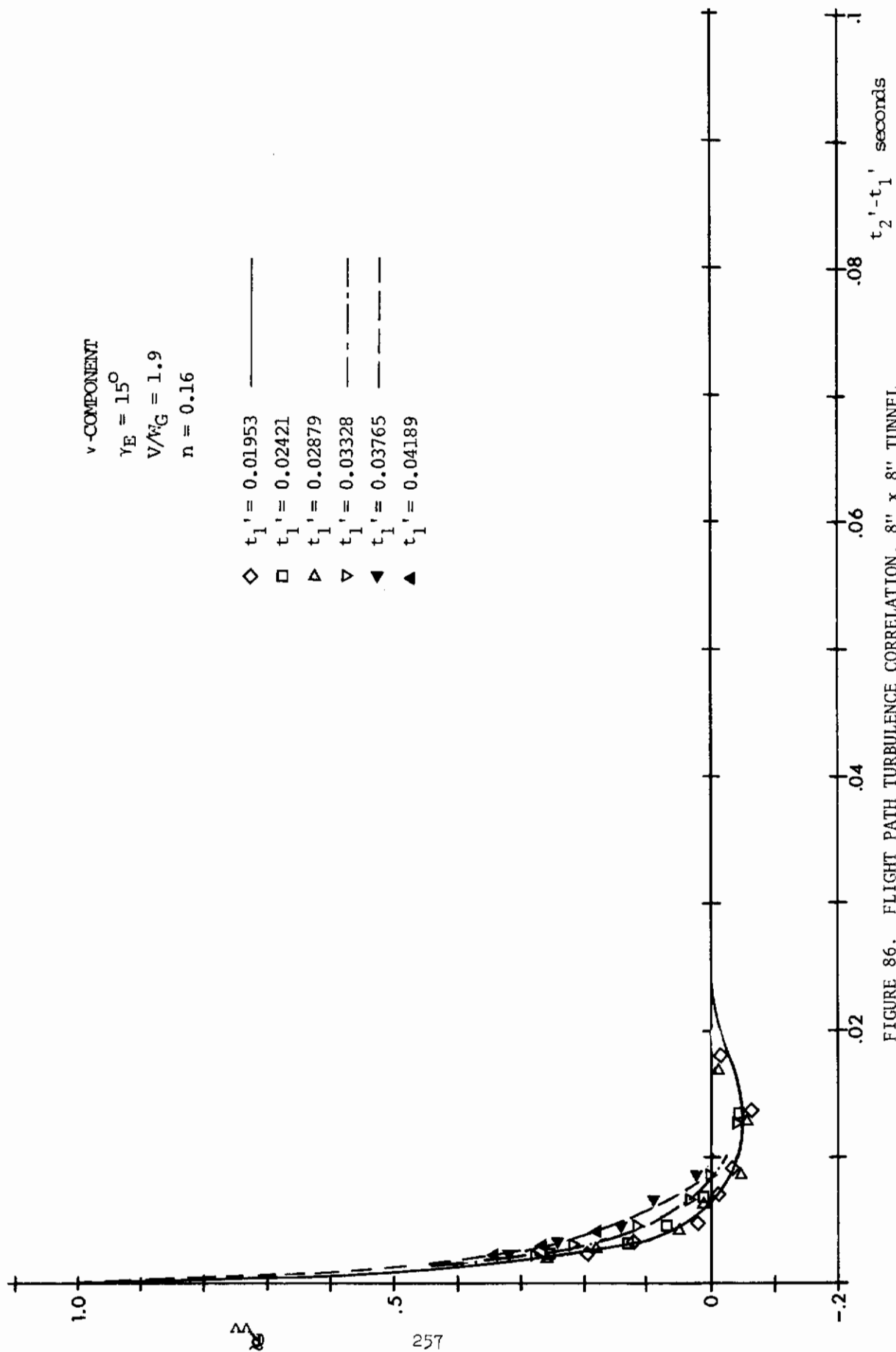
FIGURE 86.   FLIGHT PATH TURBULENCE CORRELATION, 8" x 8" TUNNEL

v-COMPONENT

$\gamma_E = 15^\circ$

$V/V_G = 1.9$

$n = 0.16$

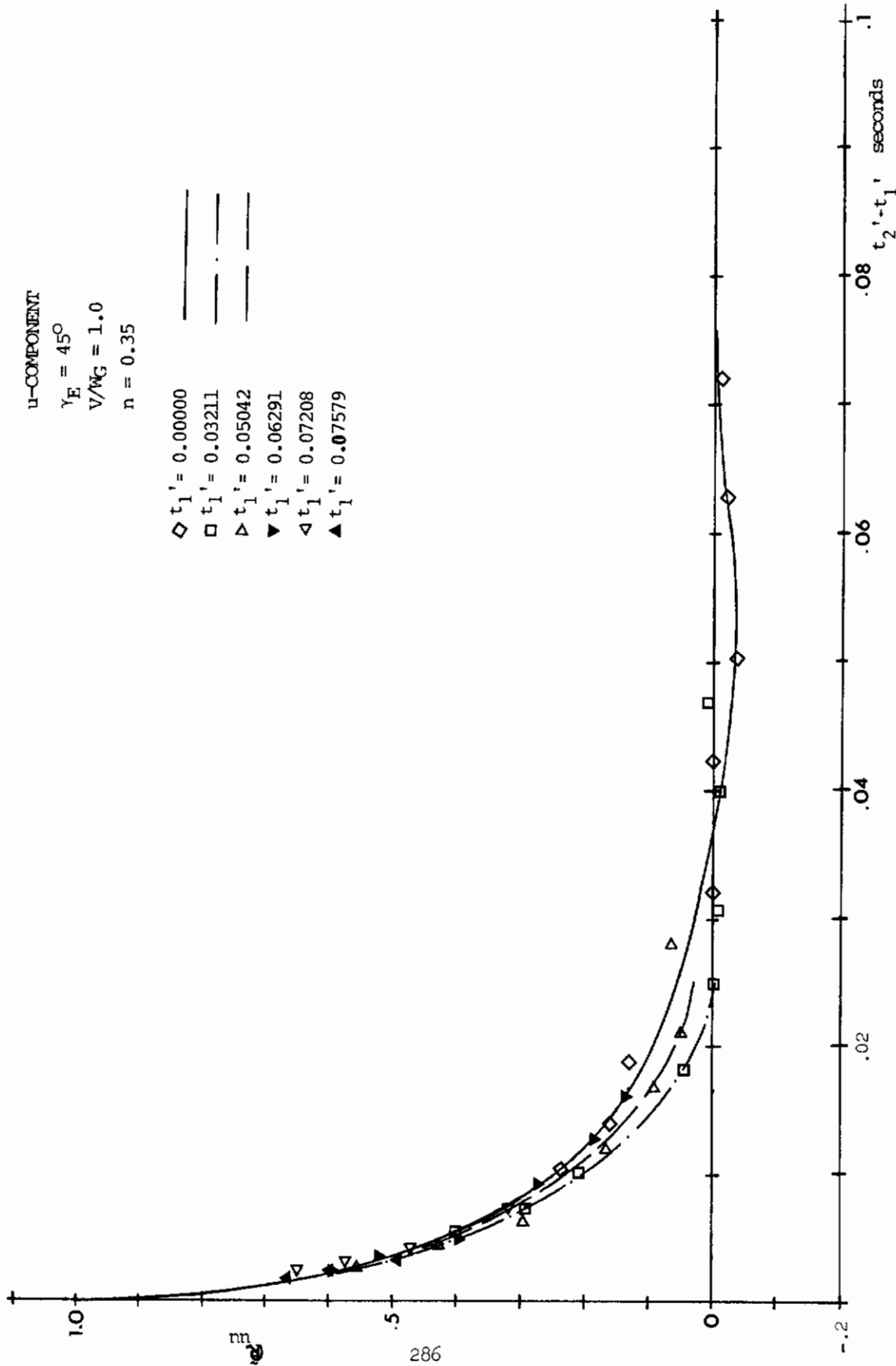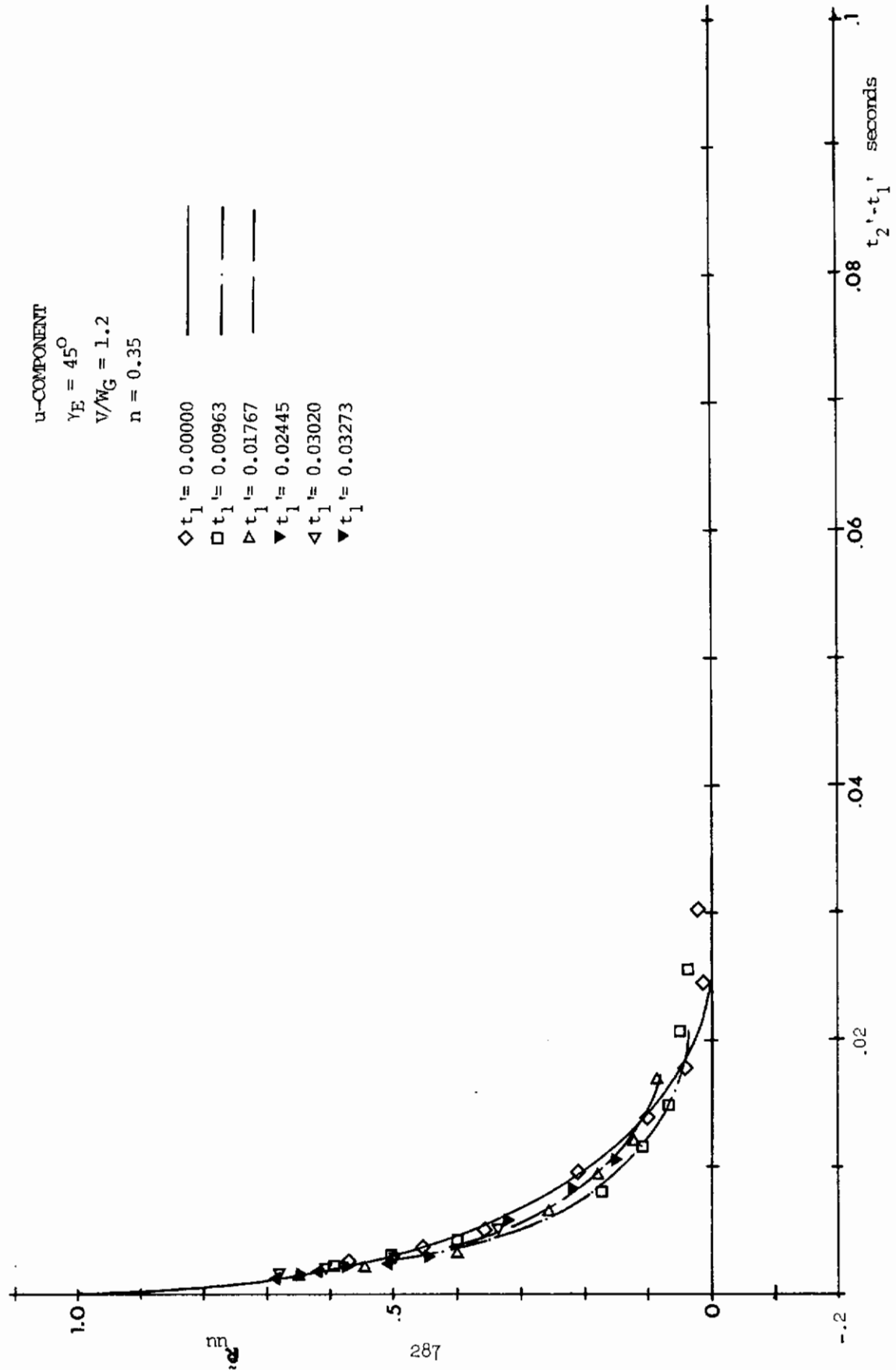|		
◇	$t_1' = 0.01953$	———
□	$t_1' = 0.02421$	
△	$t_1' = 0.02879$	
▷	$t_1' = 0.03328$	—··—
▼	$t_1' = 0.03765$	—·—
◀	$t_1' = 0.04189$	

$t_2' - t_1'$, seconds

257

FIGURE 87a.   FLIGHT PATH TURBULENCE CORRELATION, 8" x 8" TUNNEL

258

FIGURE 87b. FLIGHT PATH TURBULENCE CORRELATION, 8" x 8" TUNNEL

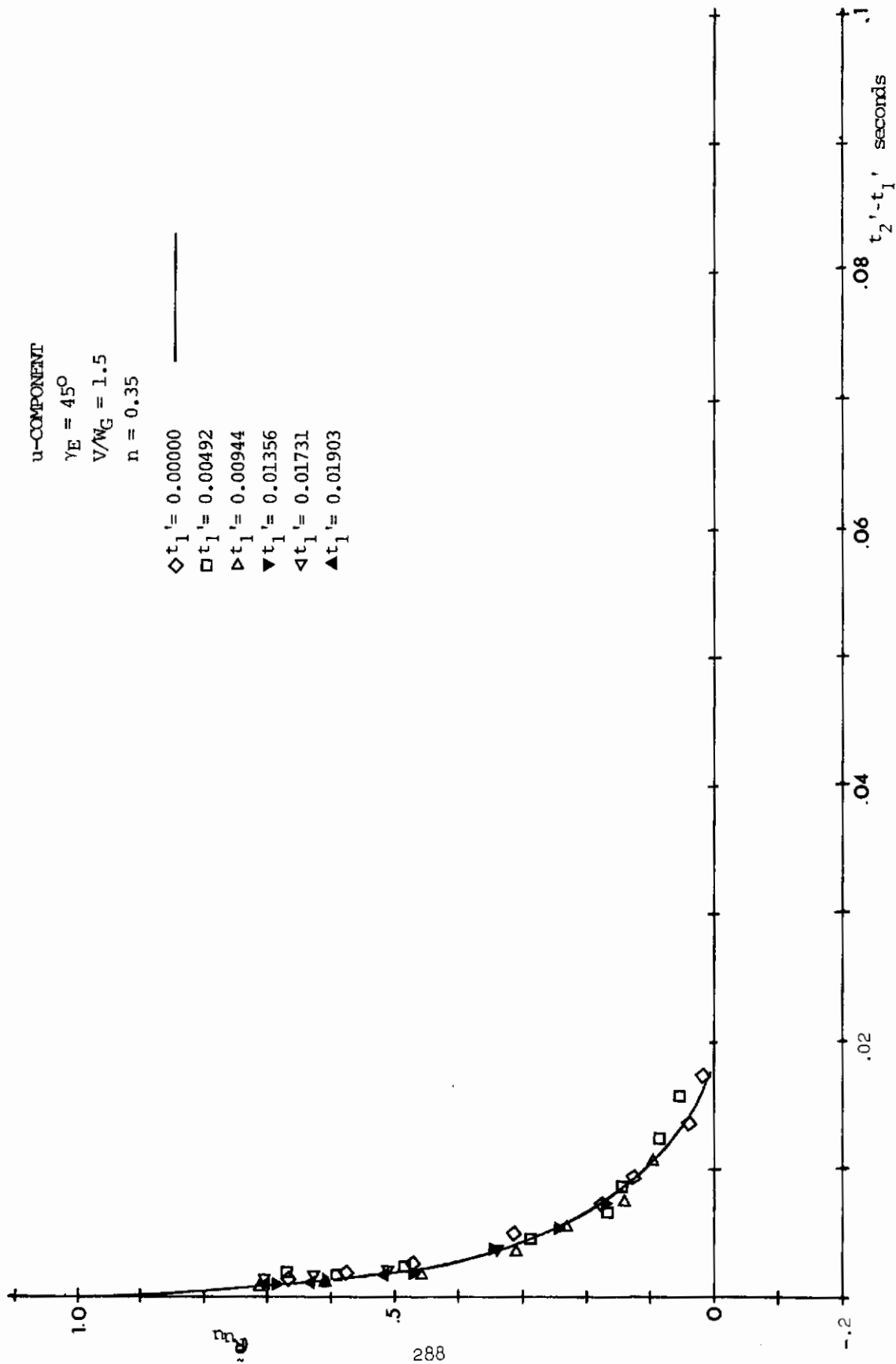v-COMPONENT
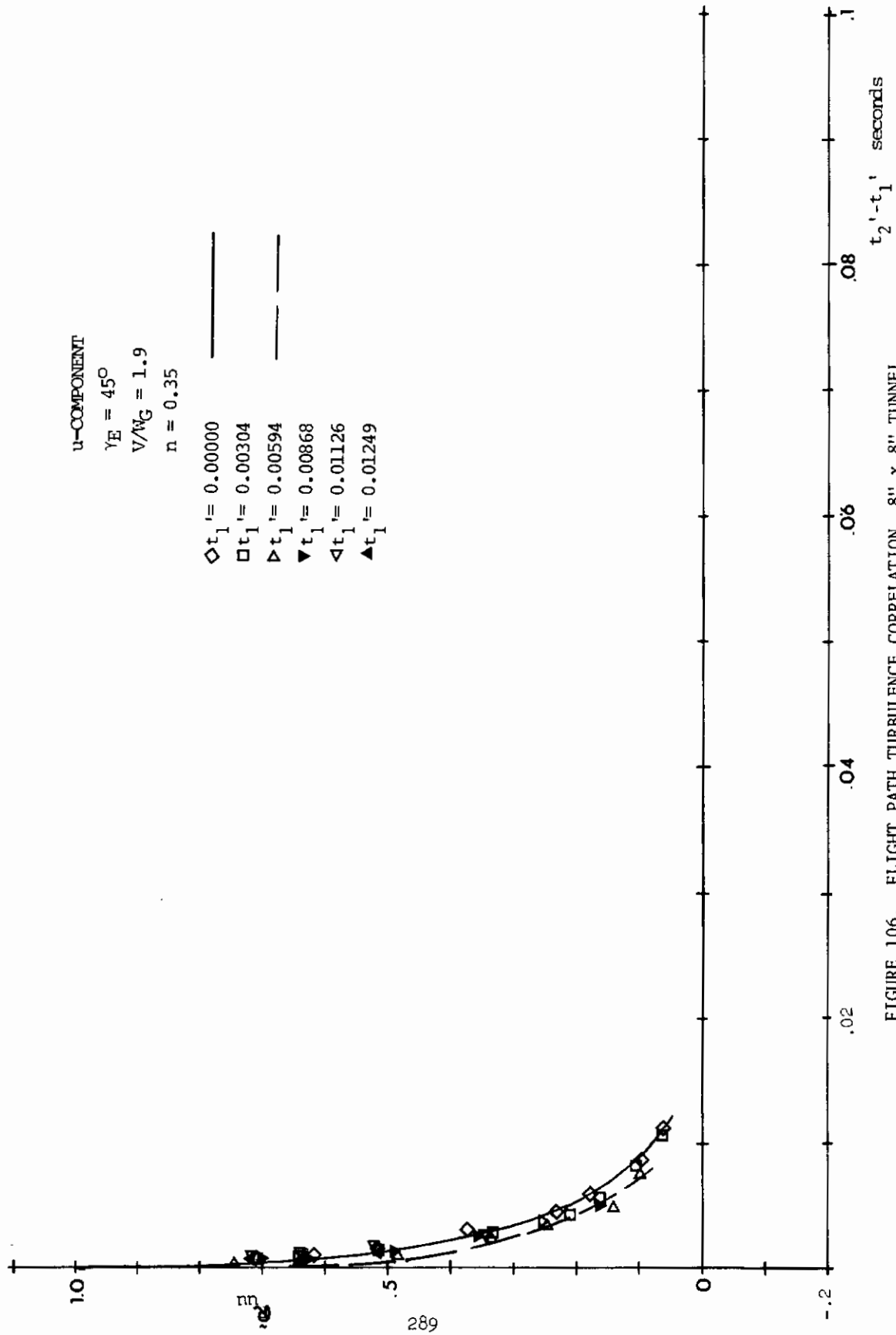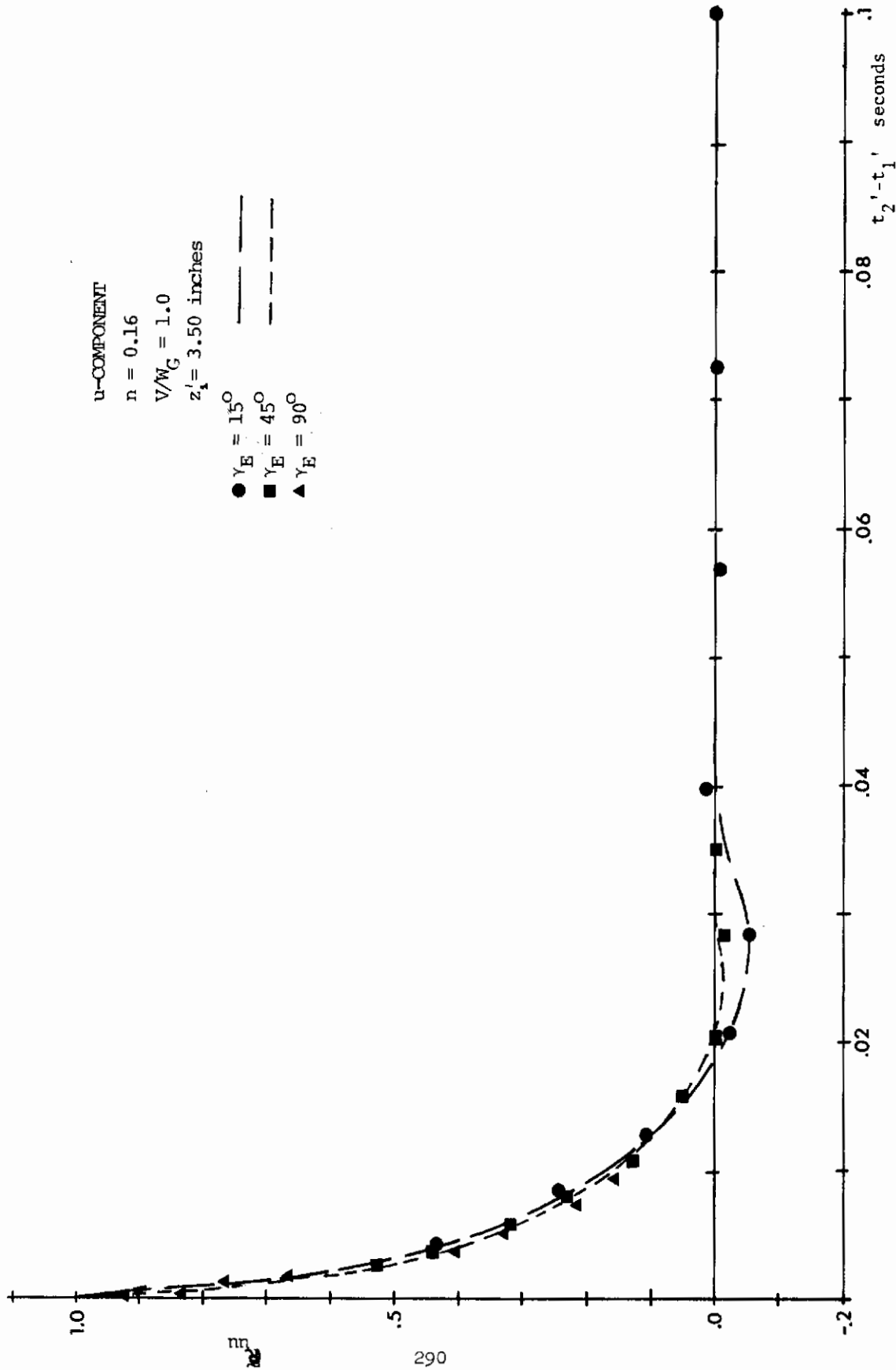
$\gamma_E = 45^O$

$V/W_G = 1.0$

$n = 0.16$

□	$t_1' = 0.04007$	
▷	$t_1' = 0.08866$	
◀	$t_1' = 0.11856$	
■	$t_1' = 0.13906$	
▶	$t_1' = 0.15366$	

$t_2' - t_1'$ seconds

259

FIGURE 88a. FLIGHT PATH TURBULENCE CORRELATION, 8" x 8" TUNNEL

v-COMPONENT

$\gamma_E = 45^O$

$V/W_G = 1.2$

$n = 0.16$

$t_1' = 0.00000$		$\diamond$
$t_1' = 0.01123$		$\triangle$
$t_1' = 0.02128$		$\triangledown$
$t_1' = 0.03023$		$\blacklozenge$
$t_1' = 0.03810$		$\blacktriangle$

$t_2' - t_1$, seconds

260

FIGURE 88b. FLIGHT PATH TURBULENCE CORRELATION, 8" x 8" TUNNEL

v-COMPONENT

$\gamma_E = 45^o$

$V/v_G = 1.2$

$n = 0.16$

□	$t_1' = 0.00576$	———
▽	$t_1' = 0.01640$	— — —
◄	$t_1' = 0.02589$	
■	$t_1' = 0.03430$	—·—·—
▶	$t_1' = 0.04161$	

$t_2' - t_1'$, seconds

R_{vv}

261

FIGURE 89a.   FLIGHT PATH TURBULENCE CORRELATION, 8" x 8" TUNNEL

v-COMPONENT

$\gamma_E = 45^O$

$V/W_G = 1.5$

$n = 0.16$

◇ $t_1' = 0.00000$

△ $t_1' = 0.00527$

▽ $t_1' = 0.01030$

◆ $t_1' = 0.01506$

▲ $t_1' = 0.01953$

$t_2' - t_1'$, seconds

262

FIGURE 89b. FLIGHT PATH TURBULENCE CORRELATION, 8" x 8" TUNNEL

FIGURE 90a.   FLIGHT PATH TURBULENCE CORRELATION, 8" x 8" TUNNEL

v-COMPONENT

$\gamma_E = 45^O$
$V/W_G = 1.9$
$n = 0.16$

$\diamond$	$t_1' = 0.00000$
$\triangle$	$t_1' = 0.00316$
$\triangledown$	$t_1' = 0.00625$
$\blacklozenge$	$t_1' = 0.00924$
$\blacktriangle$	$t_1' = 0.01212$

$t_2' - t_1'$, seconds

264

FIGURE 90b. FLIGHT PATH TURBULENCE CORRELATION, 8" x 8" TUNNEL

v-COMPONENT

$\gamma_E = 45^O$

$V/w_G = 1.9$

$n = 0.16$

□	$t_1' = 0.00159$	
▽	$t_1' = 0.00472$	
◀	$t_1' = 0.00776$	
■	$t_1' = 0.01069$	
▶	$t_1' = 0.01350$	

$t_2' - t_1'$ seconds

265

FIGURE 91a. FLIGHT PATH TURBULENCE CORRELATION, 8" x 8" TUNNEL

$t_2' - t_1'$ seconds

v–COMPONENT
$\gamma_E = 90^\circ$
$V/W_G = 1.0$
$n = 0.16$

◇	$t_1' = 0.00000$
△	$t_1' = 0.00907$
▽	$t_1' = 0.01583$
◆	$t_1' = 0.02132$
▲	$t_1' = 0.02594$

266

v-COMPONENT

$\gamma_E = 90°$

$V/W_G = 1.0$

$n = 0.16$

□	$t_1' = 0.00495$
▽	$t_1' = 0.01264$
◀	$t_1' = 0.01870$
■	$t_1' = 0.02372$
▶	$t_1' = 0.02798$

$t_2' - t_1'$ seconds

FIGURE 91b. FLIGHT PATH TURBULENCE CORRELATION, 8" x 8" TUNNEL

267

FIGURE 92a.   FLIGHT PATH TURBULENCE CORRELATION, 8" x 8" TUNNEL

268

FIGURE 92b.   FLIGHT PATH TURBULENCE CORRELATION, 8" x 8" TUNNEL

ν-COMPONENT

$\gamma_E = 90^0$

$V/W_G = 1.2$

$n = 0.16$

$\square$ $t_1' = 0.00173$

$\triangleright$ $t_1' = 0.00505$

$\blacktriangleleft$ $t_1' = 0.00820$

$\blacksquare$ $t_1' = 0.01118$

$\blacktriangleright$ $t_1' = 0.01397$

$t_2' - t_1'$, seconds

269

w-COMPONENT

$\gamma_E = 15^O$

$V/w_G = 1.0$

$n = 0.16$

◇ $t_1' = 0.38413$
□ $t_1' = 0.43218$
△ $t_1' = 0.47174$
▷ $t_1' = 0.50467$
▼ $t_1' = 0.53223$
◀ $t_1' = 0.55525$

$t_2' - t_1'$, seconds

FIGURE 93.   FLIGHT PATH TURBULENCE CORRELATION, 8" x 8" TUNNEL

270

FIGURE 94. FLIGHT PATH TURBULENCE CORRELATION, 8" x 8" TUNNEL

w-COMPONENT

$Y_E = 15^O$

$V/W_G = 1.2$

$n = 0.16$

◇	$t_1' = 0.07298$	
□	$t_1' = 0.08858$	
△	$t_1' = 0.10318$	
▷	$t_1' = 0.11678$	
▼	$t_1' = 0.12937$	
◀	$t_1' = 0.14093$	

R_{ww}

$t_2' - t_1'$, seconds

271

w-COMPONENT

$\gamma_E = 15^O$

$V/\hbar v_G = 1.5$

$n = 0.16$

◇	$t_1' = 0.03350$
□	$t_1' = 0.04129$
△	$t_1' = 0.04882$
▷	$t_1' = 0.05608$
▼	$t_1' = 0.06304$
◀	$t_1' = 0.06968$

$t_2' - t_1'$, seconds

FIGURE 95. FLIGHT PATH TURBULENCE CORRELATION, 8" x 8" TUNNEL

272

FIGURE 96. FLIGHT PATH TURBULENCE CORRELATION, 8" x 8" TUNNEL

w-COMPONENT

$\gamma_E = 15^O$

$V/w_G = 1.9$

$n = 0.16$

◇	$t_1' = 0.01953$	
□	$t_1' = 0.02421$	
△	$t_1' = 0.02879$	
▷	$t_1' = 0.03328$	
▼	$t_1' = 0.03765$	
◀	$t_1' = 0.04189$	

$t_2' - t_1'$ seconds

R_{ww}

273

FIGURE 97a.   FLIGHT PATH TURBULENCE CORRELATION, 8" x 8" TUNNEL

274

w-COMPONENT

$\gamma_E = 45^O$

$V/W_G = 1.0$

$n = 0.16$

□	$t_1' = 0.04007$
▽	$t_1' = 0.08866$
◄	$t_1' = 0.11856$
■	$t_1' = 0.13906$
►	$t_1' = 0.15366$

$t_2' - t_1'$, seconds

FIGURE 97b. FLIGHT PATH TURBULENCE CORRELATION, 8" x 8" TUNNEL

275

FIGURE 98a. FLIGHT PATH TURBULENCE CORRELATION, 8" x 8" TUNNEL

w-COMPONENT

$\gamma_E = 45^o$

$V/W_G = 1.2$

$n = 0.16$

$t_1' = 0.00000$
$t_1' = 0.01123$
$t_1' = 0.02128$
$t_1' = 0.03023$
$t_1' = 0.03810$

$t_2' - t_1'$ seconds

R_{ww}

276

FIGURE 98b. FLIGHT PATH TURBULENCE CORRELATION, 8" x 8" TUNNEL

w-COMPONENT

$\gamma_E = 45^O$

$V/w_G = 1.2$

n = 0.16

□	$t_1' = 0.00576$
▽	$t_1' = 0.01640$
◀	$t_1' = 0.02589$
■	$t_1' = 0.03430$
▶	$t_1' = 0.04161$

277

w-COMPONENT

$\gamma_E = 45^O$
$V/W_G = 1.5$
$n = 0.16$

———	$t_1' = 0.00000$	$\diamond$
– – –	$t_1' = 0.00527$	$\triangle$
	$t_1' = 0.01030$	$\triangledown$
	$t_1' = 0.01506$	$\blacklozenge$
	$t_1' = 0.01953$	$\blacktriangleright$

FIGURE 99a. FLIGHT PATH TURBULENCE CORRELATION, 8" x 8" TUNNEL

278

FIGURE 99b. FLIGHT PATH TURBULENCE CORRELATION, 8" x 8" TUNNEL

w–COMPONENT

$\gamma_E = 45^O$

$V/W_G = 1.5$

$n = 0.16$

□	$t_1' = 0.00266$
▽	$t_1' = 0.00782$
◀	$t_1' = 0.01272$
■	$t_1' = 0.01733$
▶	$t_1' = 0.02163$

$t_2' - t_1'$ seconds

279

w-COMPONENT

$\gamma_E = 45^0$

$V/w_G = 1.9$

n = 0.16

◇	$t_1' = 0.00000$
△	$t_1' = 0.00316$
▽	$t_1' = 0.00625$
◆	$t_1' = 0.00924$
▶	$t_1' = 0.01212$

$t_2' - t_1'$ seconds

FIGURE 100a.   FLIGHT PATH TURBULENCE CORRELATION, 8" x 8" TUNNEL

280

w-COMPONENT

$\gamma_E = 45^{\circ}$

$V/w_G = 1.9$

$n = 0.16$

□ $t_1' = 0.00189$
▽ $t_1' = 0.00472$
◀ $t_1' = 0.00776$
■ $t_1' = 0.01069$
▶ $t_1' = 0.01350$

FIGURE 100b.   FLIGHT PATH TURBULENCE CORRELATION, 8" x 8" TUNNEL

$t_2' - t_1'$ seconds

281

w-COMPONENT

$Y_E = 90^O$

$V/w_G = 1.0$

$n = 0.16$

	$t_1' = 0.00000$
$\diamond$	$t_1' = 0.00907$
$\triangle$	$t_1' = 0.01583$
$\triangledown$	$t_1' = 0.02132$
$\blacklozenge$	$t_1' = 0.02594$
$\blacktriangle$	

$t_2' - t_1'$ seconds
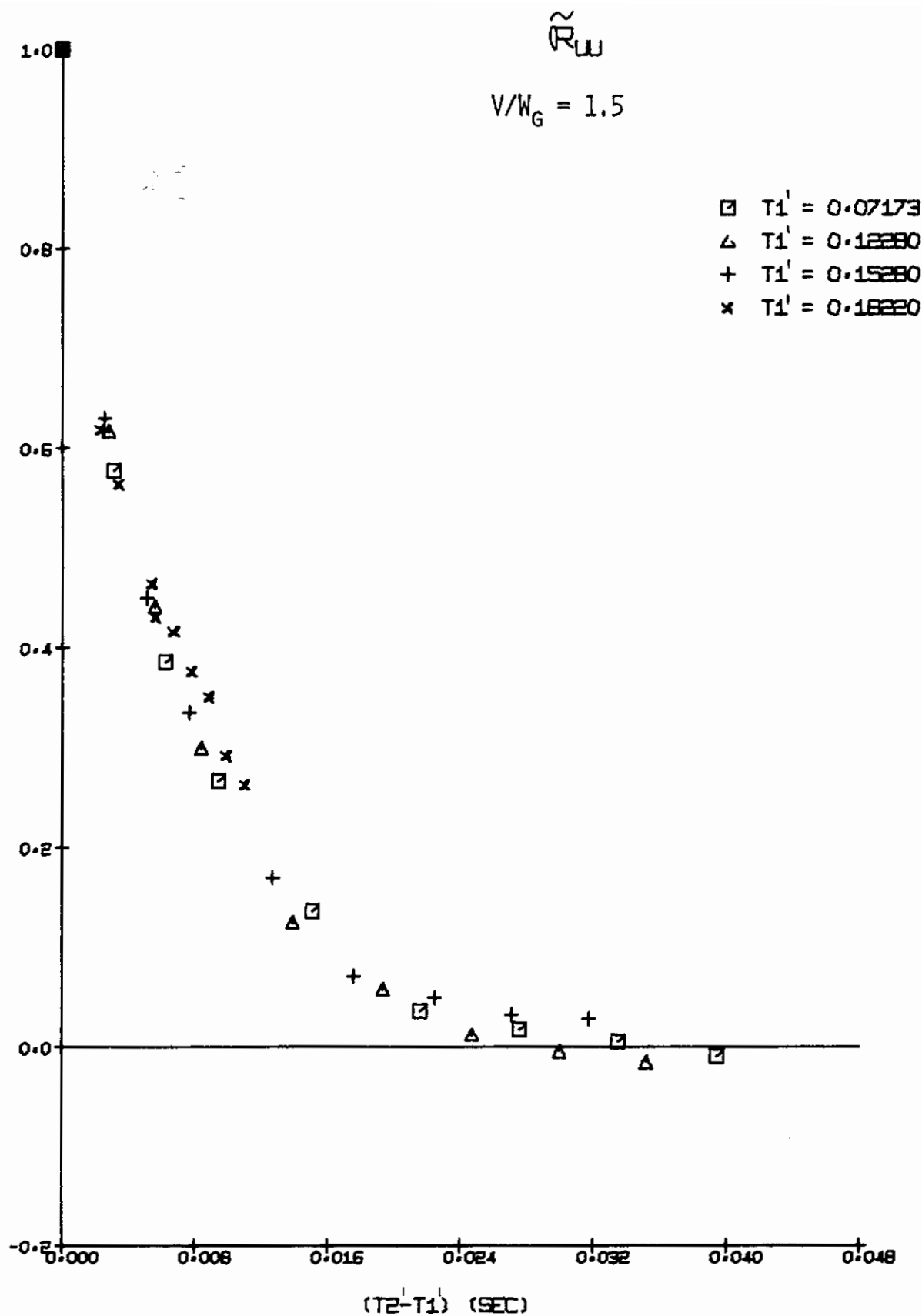
FIGURE 101a. FLIGHT PATH TURBULENCE CORRELATION, 8" x 8" TUNNEL

282

FIGURE 101b. FLIGHT PATH TURBULENCE CORRELATION, 8" x 8" TUNNEL.

w-COMPONENT

$\gamma_E = 90^O$

$V/W_G = 1.0$

$n = 0.16$

□	$t_1' = 0.00495$
▷	$t_1' = 0.01264$
◄	$t_1' = 0.01870$
■	$t_1' = 0.02372$
▶	$t_1' = 0.02798$

$t_2' - t_1'$ seconds

283

FIGURE 102a. FLIGHT PATH TURBULENCE CORRELATION, 8" x 8" TUNNEL

w–COMPONENT
$\gamma_E = 90^\circ$
$V/W_G = 1.2$
$n = 0.16$

◇	$t_1' = 0.00000$
△	$t_1' = 0.00341$
▽	$t_1' = 0.00665$
◆	$t_1' = 0.00971$
▶	$t_1' = 0.01260$

$t_2' - t_1'$ seconds

284

FIGURE 102b. FLIGHT PATH TURBULENCE CORRELATION, 8" x 8" TUNNEL

w—COMPONENT

$\gamma_E = 90^O$

$V/W_G = 1.2$

$n = 0.16$

□	$t_1' = 0.00173$
▷	$t_1' = 0.00505$
◀	$t_1' = 0.00820$
■	$t_1' = 0.01118$
▶	$t_1' = 0.01397$

$t_2' - t_1'$ seconds

285

FIGURE 103. FLIGHT PATH TURBULENCE CORRELATION, 8" x 8" TUNNEL

u-COMPONENT

$\gamma_E = 45^\circ$
$V/w_G = 1.0$
$n = 0.35$

◇ $t_1' = 0.00000$
□ $t_1' = 0.03211$
△ $t_1' = 0.05042$
▶ $t_1' = 0.06291$
▽ $t_1' = 0.07208$
◀ $t_1' = 0.07579$

$t_2' - t_1'$, seconds

286

FIGURE 104. FLIGHT PATH TURBULENCE CORRELATION, 8" x 8" TUNNEL

u-COMPONENT

$\gamma_E = 45^O$

$V/W_G = 1.2$

$n = 0.35$

$\diamond t_1' = 0.00000$
$\square t_1' = 0.00963$
$\triangle t_1' = 0.01767$
$\blacktriangleright t_1' = 0.02445$
$\triangledown t_1' = 0.03020$
$\blacktriangleright t_1' = 0.03273$

$t_2' - t_1'$, seconds

R_{uu}

287

FIGURE 105. FLIGHT PATH TURBULENCE CORRELATION, 8" x 8" TUNNEL

u-COMPONENT

$\gamma_E = 45^o$

$V/W_G = 1.5$

$n = 0.35$

$\diamond\, t_1' = 0.00000$
$\square\, t_1' = 0.00492$
$\triangle\, t_1' = 0.00944$
$\blacktriangledown\, t_1' = 0.01356$
$\triangledown\, t_1' = 0.01731$
$\blacktriangle\, t_1' = 0.01903$

288

FIGURE 106. FLIGHT PATH TURBULENCE CORRELATION, 8" × 8" TUNNEL

u—COMPONENT

$\gamma_E = 45^O$

$V/W_G = 1.9$

$n = 0.35$

$\diamond\, t_1' = 0.00000$
$\square\, t_1' = 0.00304$
$\triangle\, t_1' = 0.00594$
$\blacktriangleright\, t_1' = 0.00868$
$\triangledown\, t_1' = 0.01126$
$\blacktriangle\, t_1' = 0.01249$

$t_2' - t_1'$ seconds

FIGURE 107. EFFECT OF GLIDE PATH ANGLE γ_E ON FLIGHT PATH CORRELATIONS,
8" x 8" TUNNEL

u-COMPONENT

n = 0.16

$V/W_G = 1.0$

$z'_1 = 3.50$ inches

● $\gamma_E = 15^O$

■ $\gamma_E = 45^O$

▲ $\gamma_E = 90^O$

$t'_2 - t'_1$, seconds

290
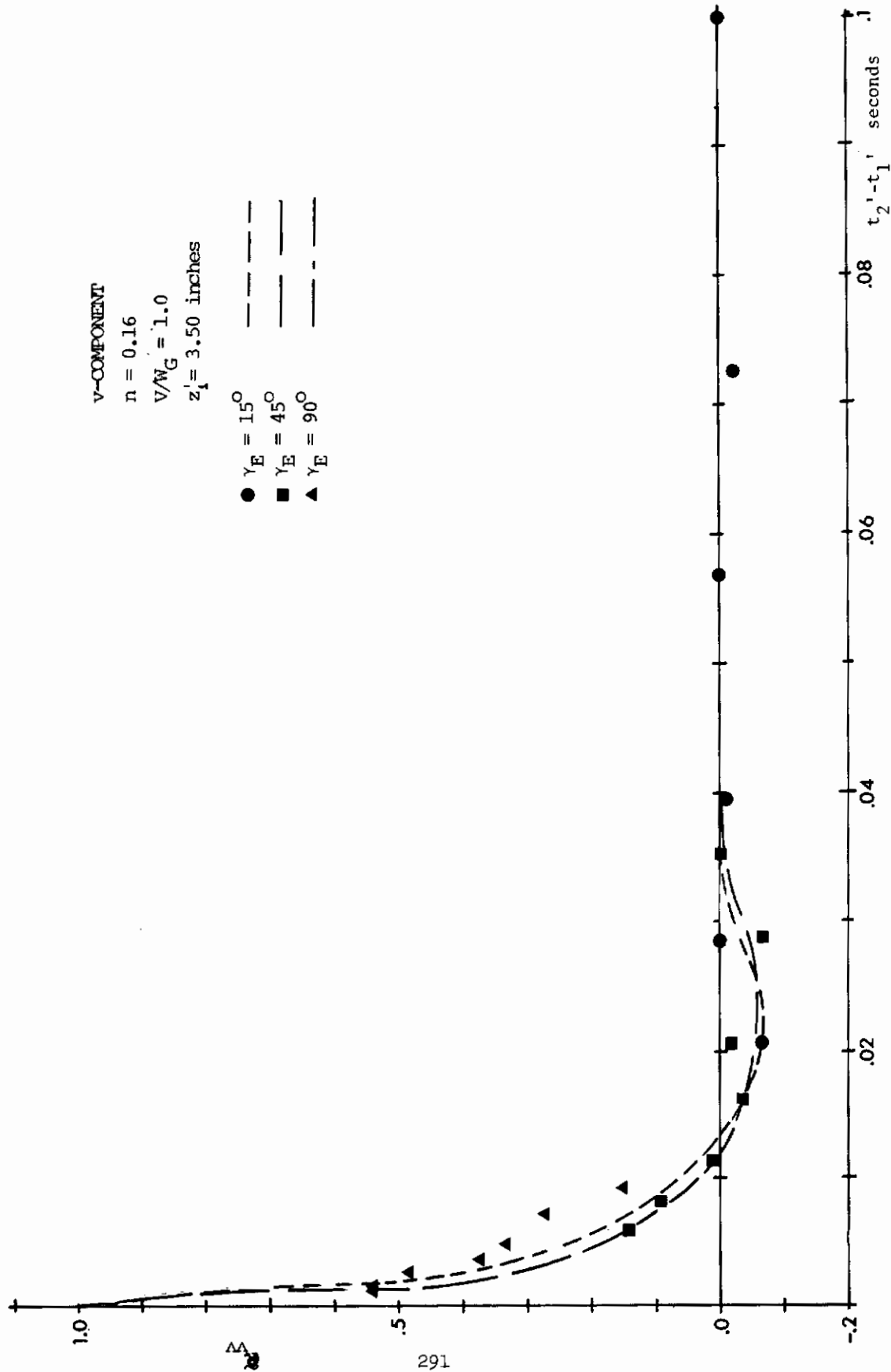
FIGURE 108. EFFECT OF GLIDE PATH ANGLE γ_E ON FLIGHT PATH CORRELATIONS, 8" x 8" TUNNEL

v-COMPONENT

$n = 0.16$
$V/W_G = 1.0$
$z_i' = 3.50$ inches

$\gamma_E = 15^O$
$\gamma_E = 45^O$
$\gamma_E = 90^O$

$t_2' - t_1'$, seconds

291
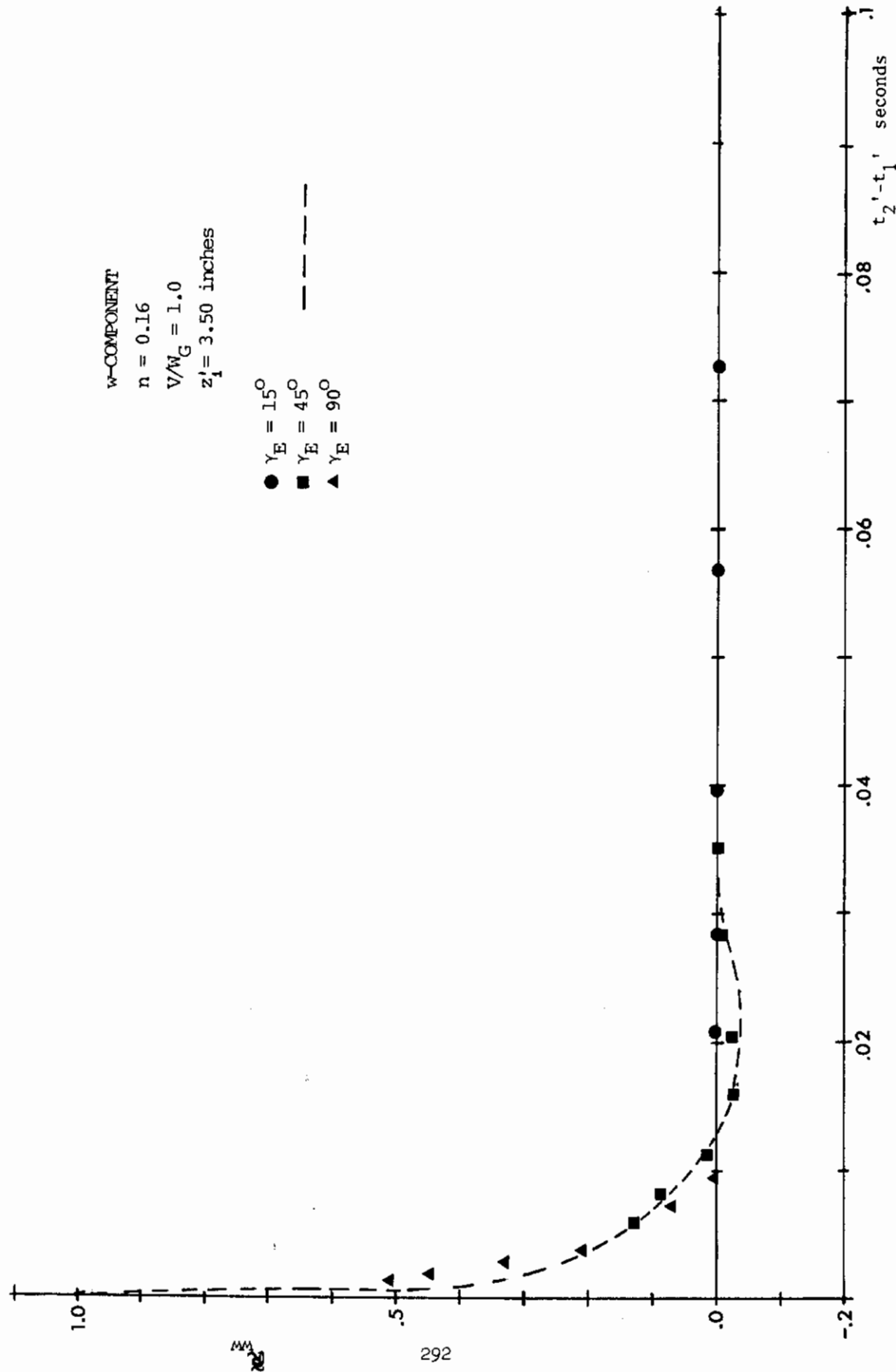
FIGURE 109. EFFECT OF GLIDE PATH ANGLE γ_E ON FLIGHT PATH CORRELATIONS, 8" x 8" TUNNEL

w-COMPONENT
n = 0.16
$V/W_G = 1.0$
$z_1' = 3.50$ inches

- ● $\gamma_E = 15^\circ$
- ■ $\gamma_E = 45^\circ$
- ▲ $\gamma_E = 90^\circ$

292

FIGURE 110. EFFECT OF AIRSPEED ON FLIGHT PATH CORRELATIONS,
8" x 8" TUNNEL

u-COMPONENT

$n = 0.16$

$\gamma_E = 45^O$

$z_1' = 5.50$ inches

□ $V/W_G = 1.0$
■ $V/W_G = 1.2$
△ $V/W_G = 1.5$
▲ $V/W_G = 1.9$

$t_2' - t_1'$, seconds

293
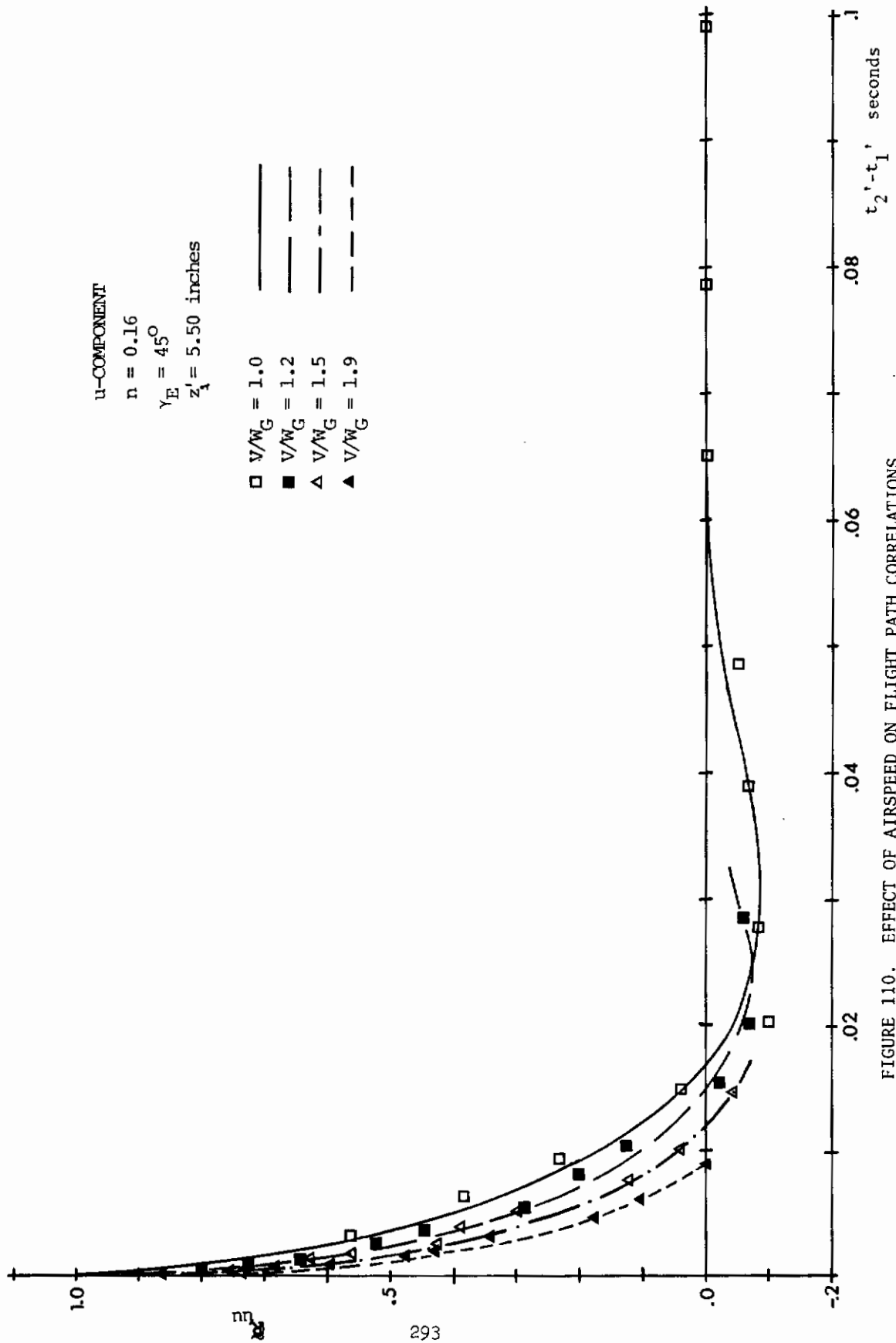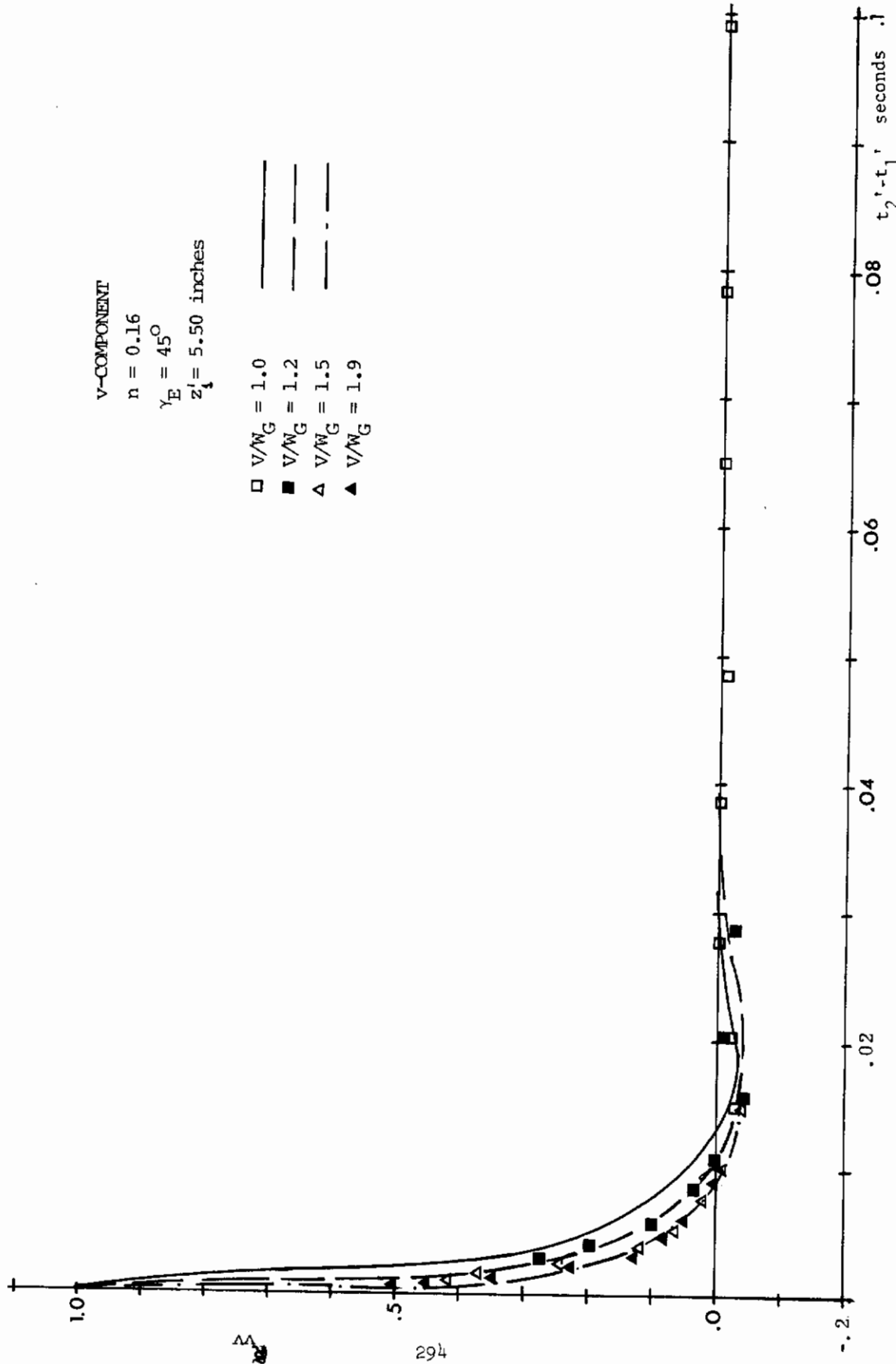
FIGURE 111. EFFECT OF AIRSPEED ON FLIGHT PATH CORRELATIONS,
8" x 8" TUNNEL

v-COMPONENT

$n = 0.16$

$\gamma_E = 45°$

$z_i' = 5.50$ inches

$\square$ $V/W_G = 1.0$

$\blacksquare$ $V/W_G = 1.2$

$\triangle$ $V/W_G = 1.5$

$\blacktriangle$ $V/W_G = 1.9$

$t_2' - t_1'$ seconds

294

FIGURE 112. EFFECT OF AIRSPEED ON FLIGHT PATH CORRELATIONS, 8" x 8" TUNNEL

w-COMPONENT

$n = 0.16$

$\gamma_E = 45^\circ$

$z_i' = 5.50$ inches

□ $V/W_G = 1.0$
■ $V/W_G = 1.2$
△ $V/W_G = 1.5$
▲ $V/W_G = 1.9$

$t_2' - t_1'$, seconds

295
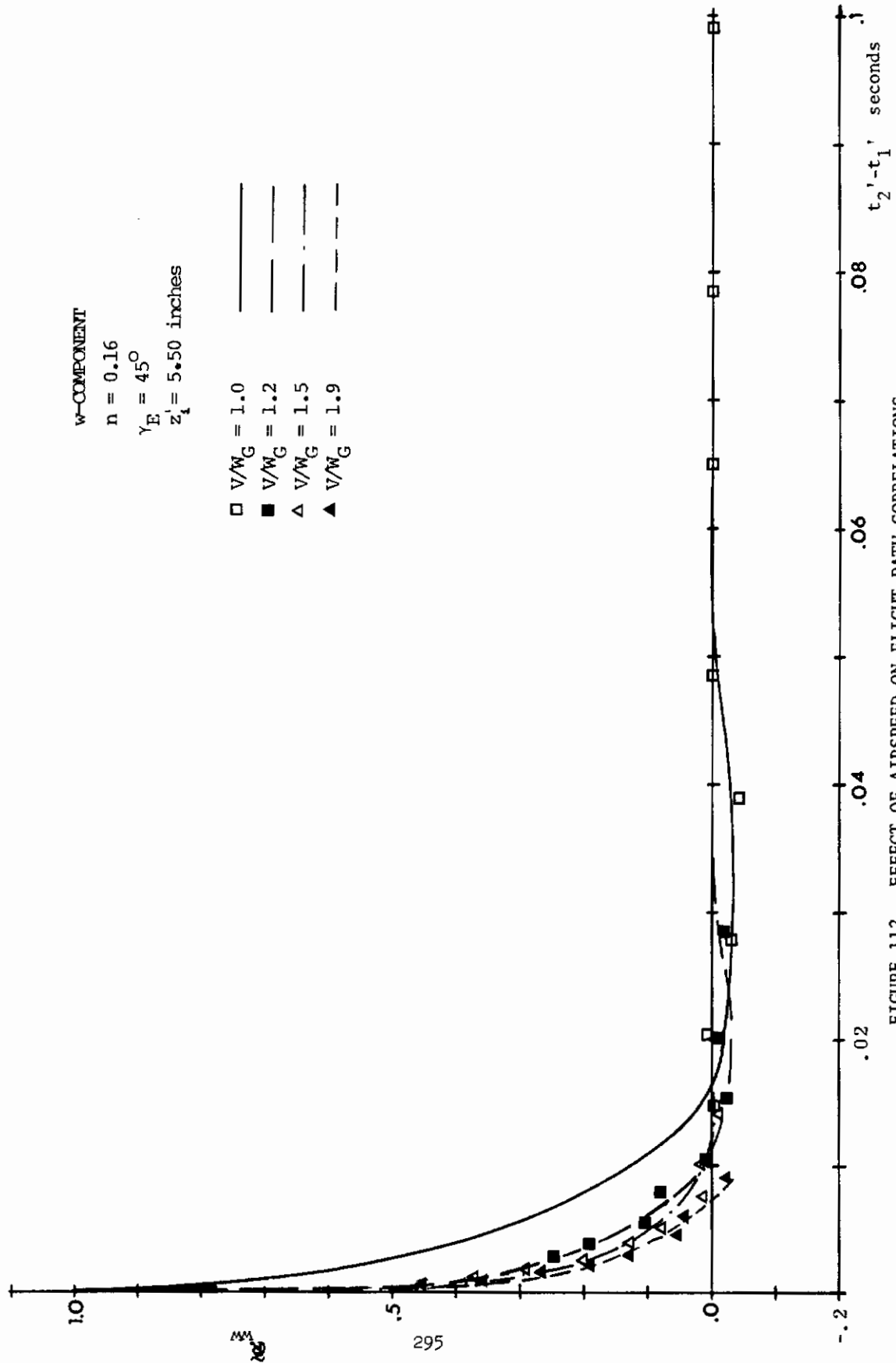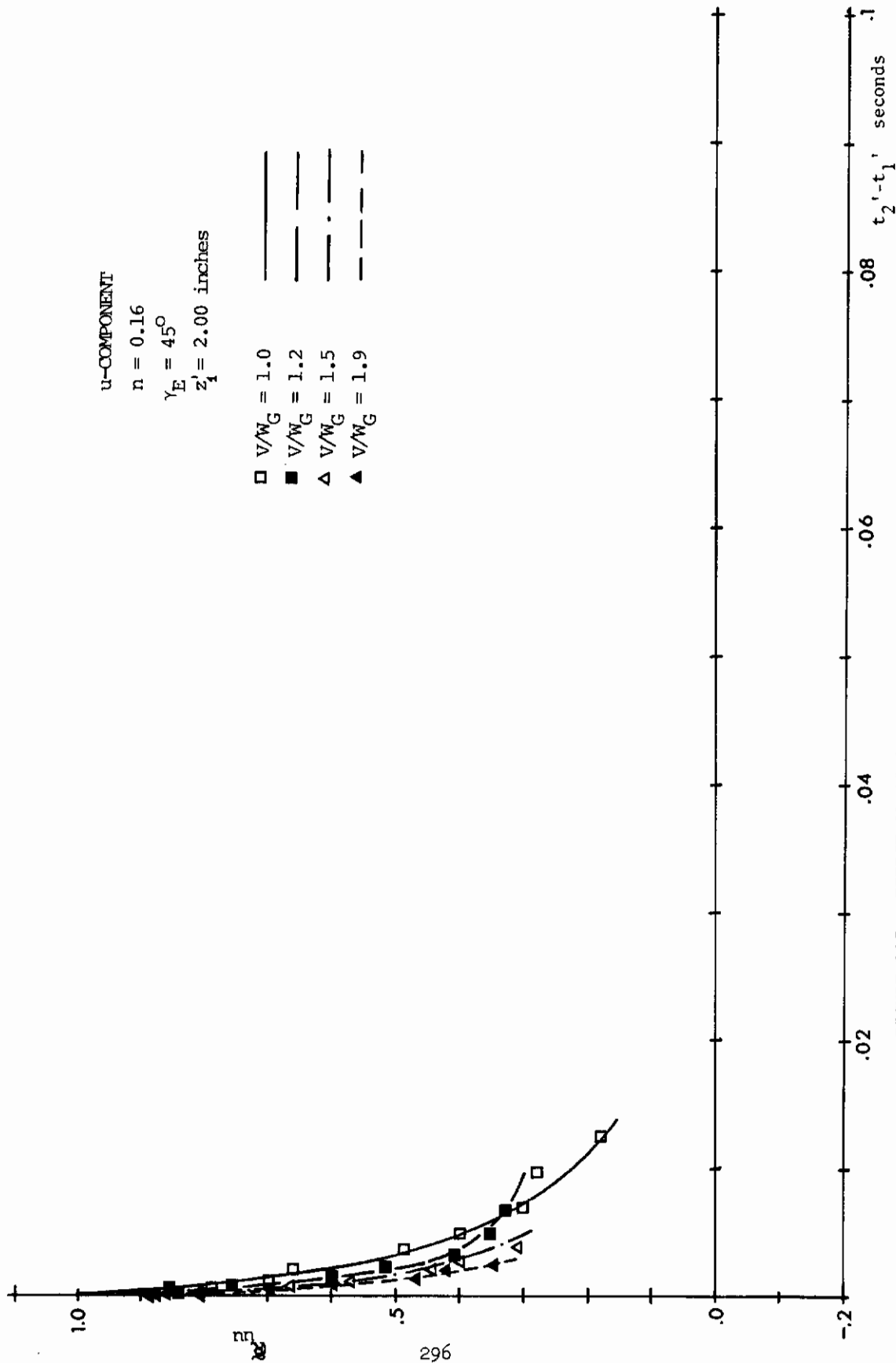
FIGURE 113. EFFECT OF AIRSPEED ON FLIGHT PATH CORRELATIONS,
8" x 8" TUNNEL

u-COMPONENT

$n = 0.16$

$\gamma_E = 45^o$

$z_1' = 2.00$ inches

□ $V/W_G = 1.0$
■ $V/W_G = 1.2$
△ $V/W_G = 1.5$
▲ $V/W_G = 1.9$

$t_2' - t_1'$ seconds

296

v-COMPONENT

n = 0.16

$\gamma_E = 45^O$

$z_1' = 2.00$

□ $V/W_G = 1.0$
■ $V/W_G = 1.2$
△ $V/W_G = 1.5$
▲ $V/W_G = 1.9$

$t_2' - t_1'$, seconds

FIGURE 114. EFFECT OF AIRSPEED ON FLIGHT PATH CORRELATIONS,
8" x 8" TUNNEL

297
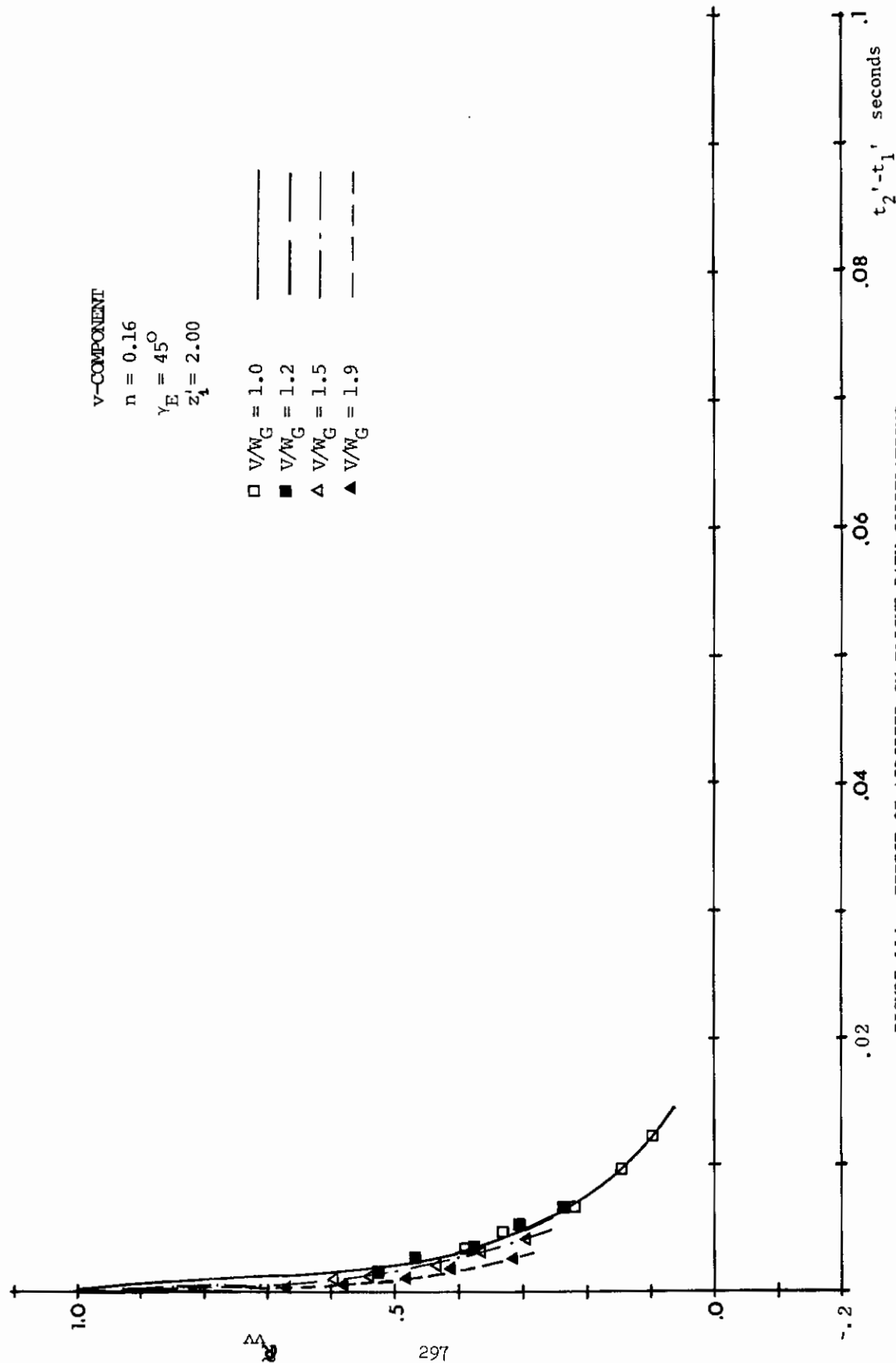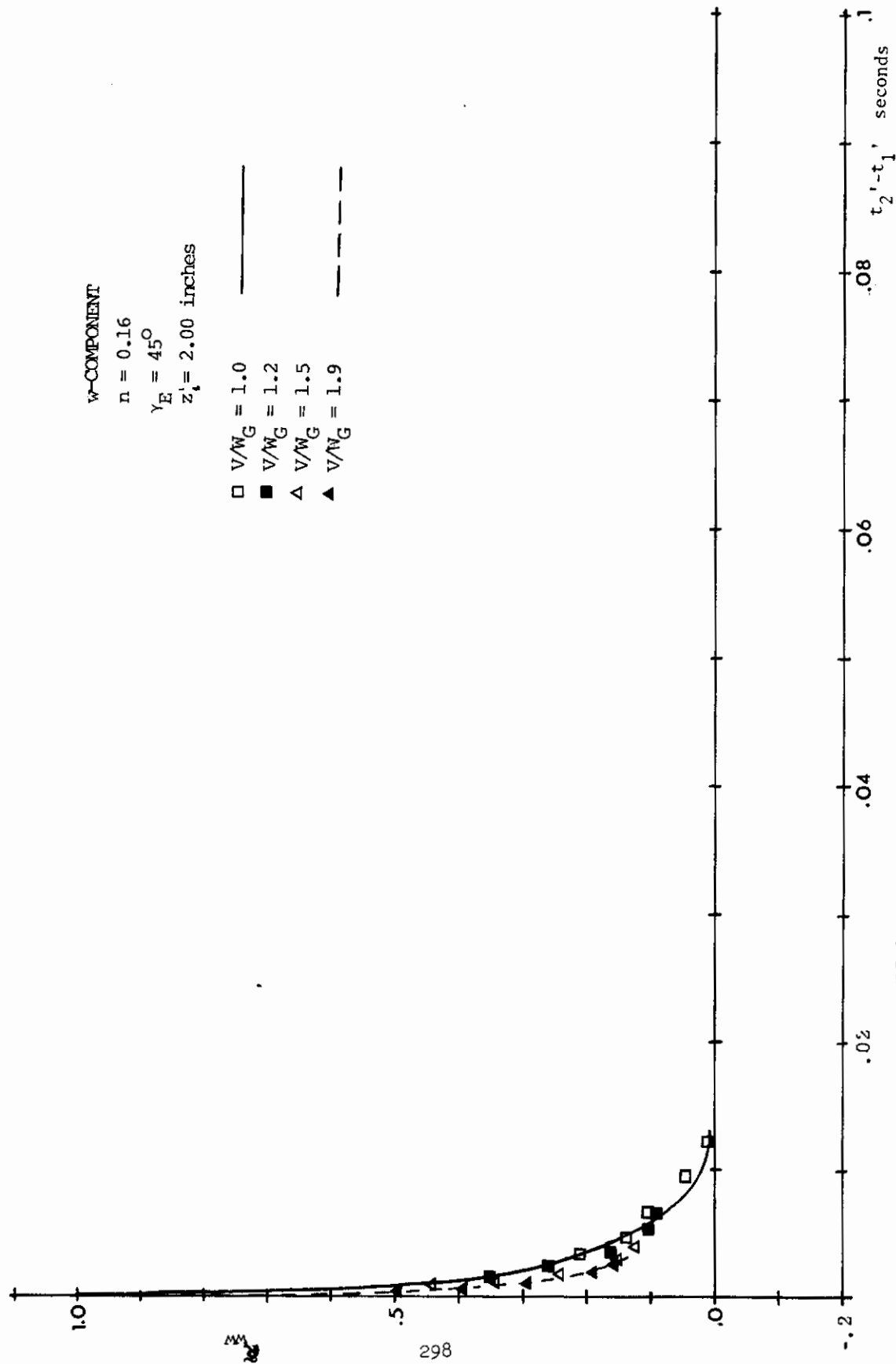
FIGURE 115. EFFECT OF AIRSPEED ON FLIGHT PATH CORRELATIONS, 8" x 8" TUNNEL

w-COMPONENT

$n = 0.16$

$\gamma_E = 45^\circ$

$z_i' = 2.00$ inches

□ $V/W_G = 1.0$
■ $V/W_G = 1.2$
△ $V/W_G = 1.5$
▲ $V/W_G = 1.9$

$t_2' - t_1'$, seconds

298
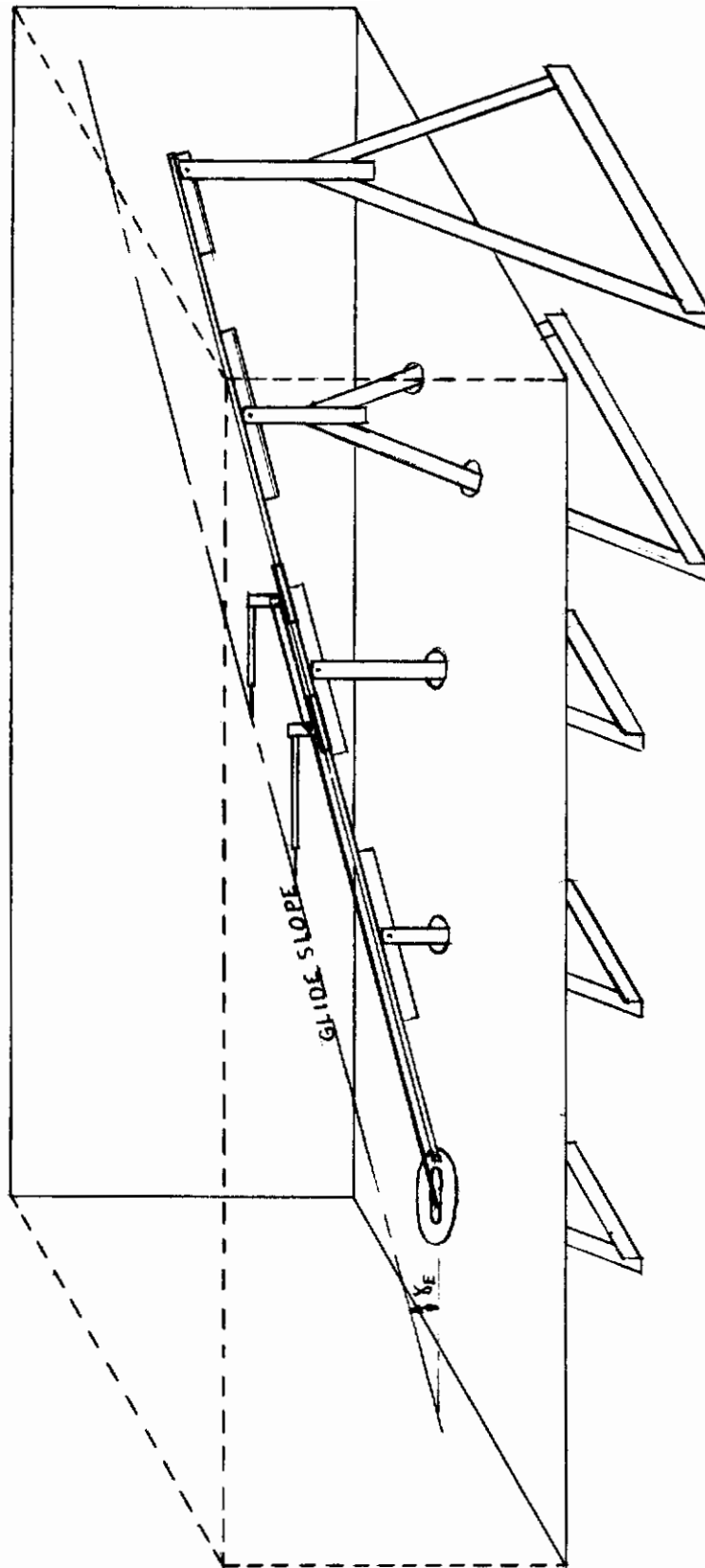
FIGURE 116. GLIDE SLOPE RAIL, 44" x 66" TUNNEL
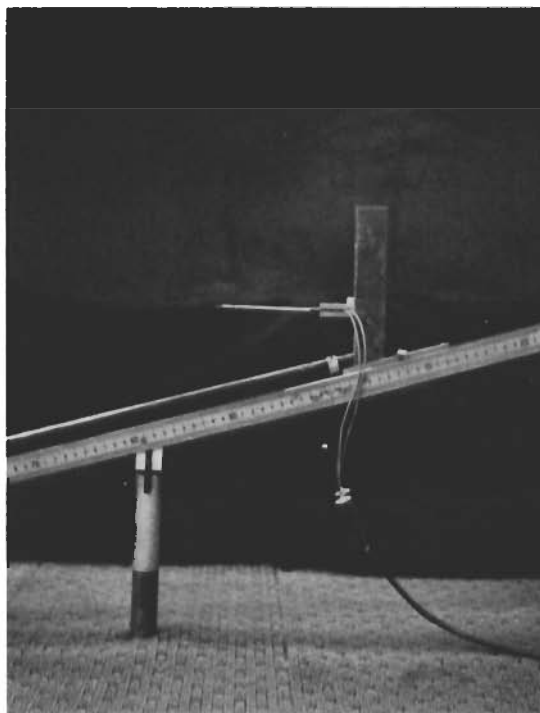
FIGURE 117.   PROBE HOLDER, 44" x 66" TUNNEL
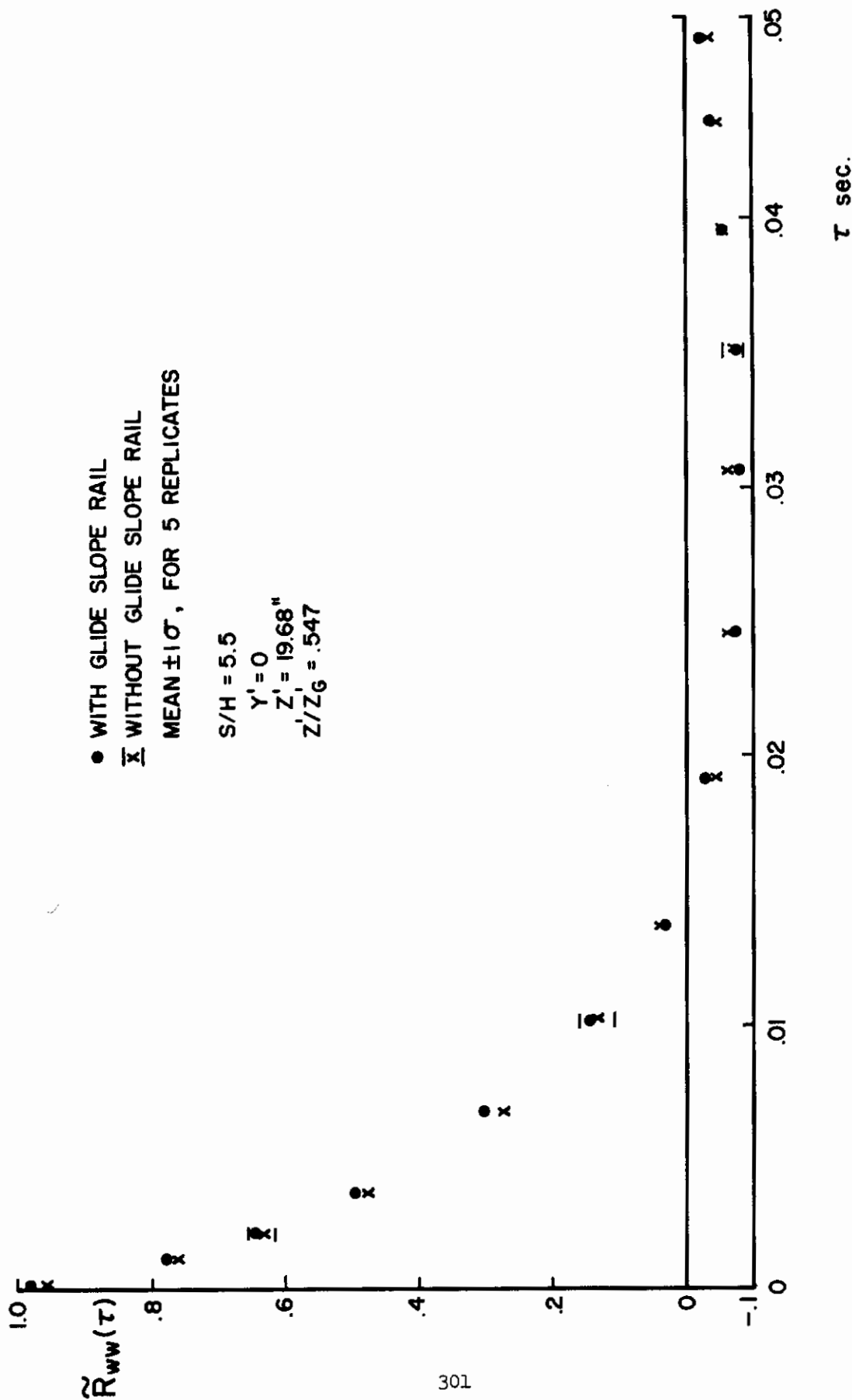
FIGURE 118.   CORRELATION DATA COMPARISON, WITH AND WITHOUT GLIDE
SLOPE RAIL, 44" x 66" TUNNEL
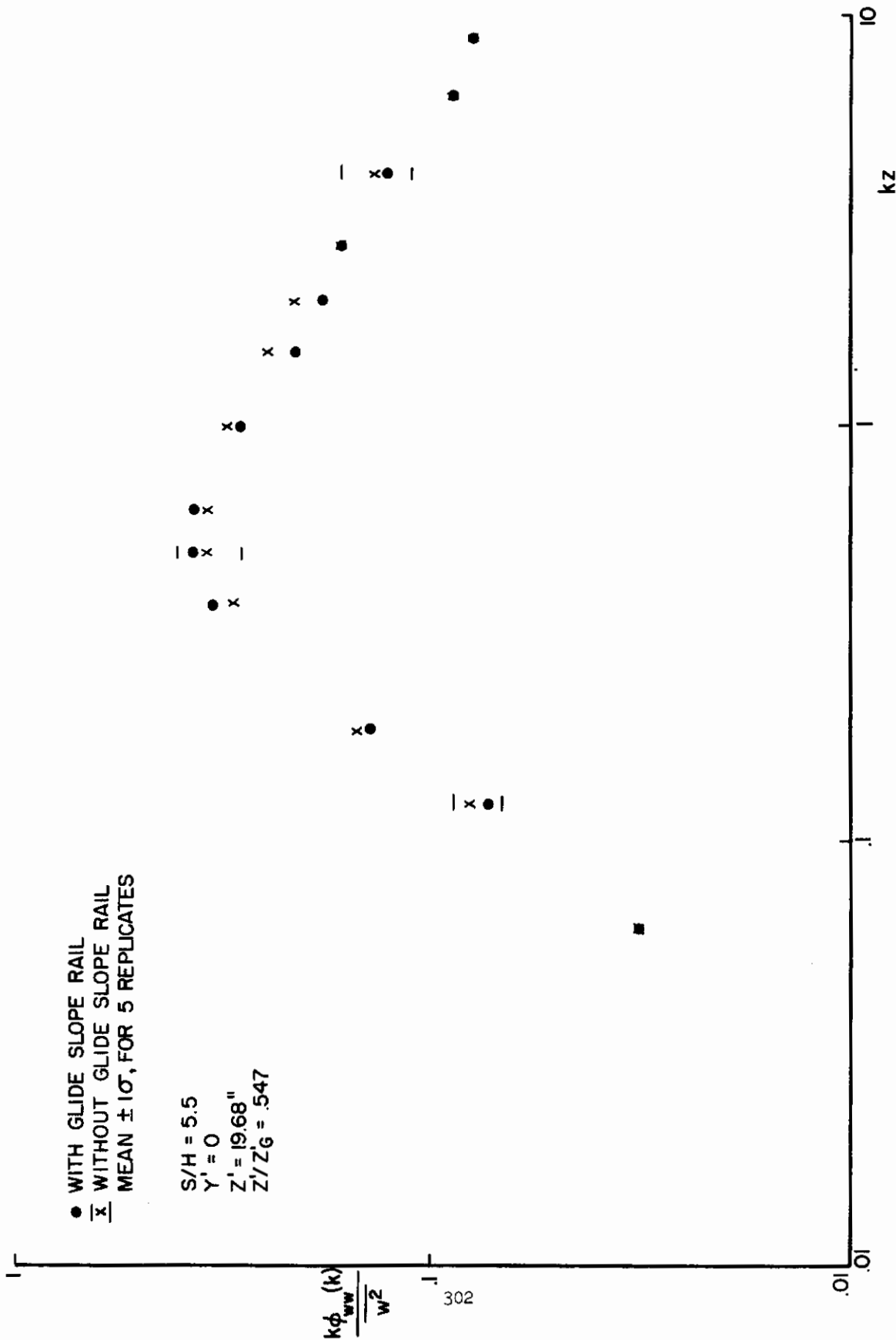
FIGURE 119. POWER SPECTRAL DENSITY COMPARISON, WITH AND WITHOUT
GLIDE SLOPE RAIL, 44" x 66" TUNNEL

● WITH GLIDE SLOPE RAIL
$\overline{x}$ WITHOUT GLIDE SLOPE RAIL
| MEAN ±1σ, FOR 5 REPLICATES

S/H = 5.5
Y' = 0
Z' = 19.68"
$Z'/Z'_G = .547$

$\frac{k\phi_{ww}(k)}{\overline{w^2}}$

302

kz
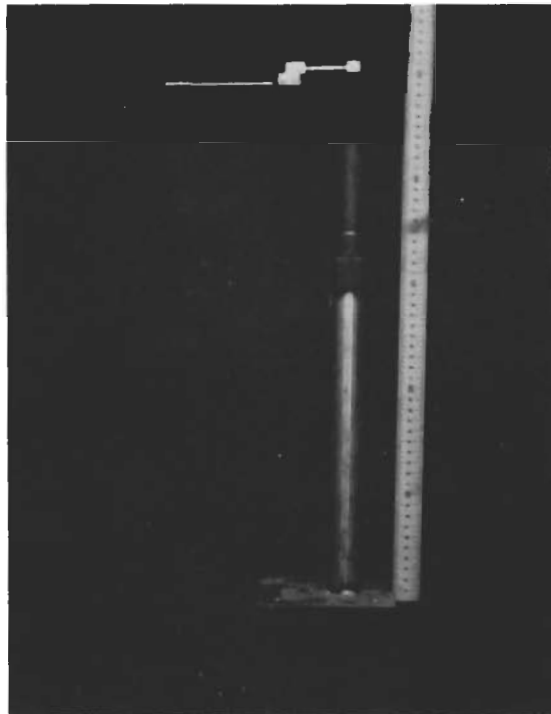
FIGURE 120. PROBE HOLDER FOR COMPARISON TESTS, 44" x 66" TUNNEL

DATA TAKEN ALONG 15° GLIDE SLOPE
$Z_1' = 25''$
$Z_2' = 24.5''$
$Y' = 0$
$Z_G' = 36''$
$W_G' = 90$ fps
ϕ — MEAN $\pm 1\sigma$, 26 REPLICATES

$\tilde{R}_{uu}(\tau)$
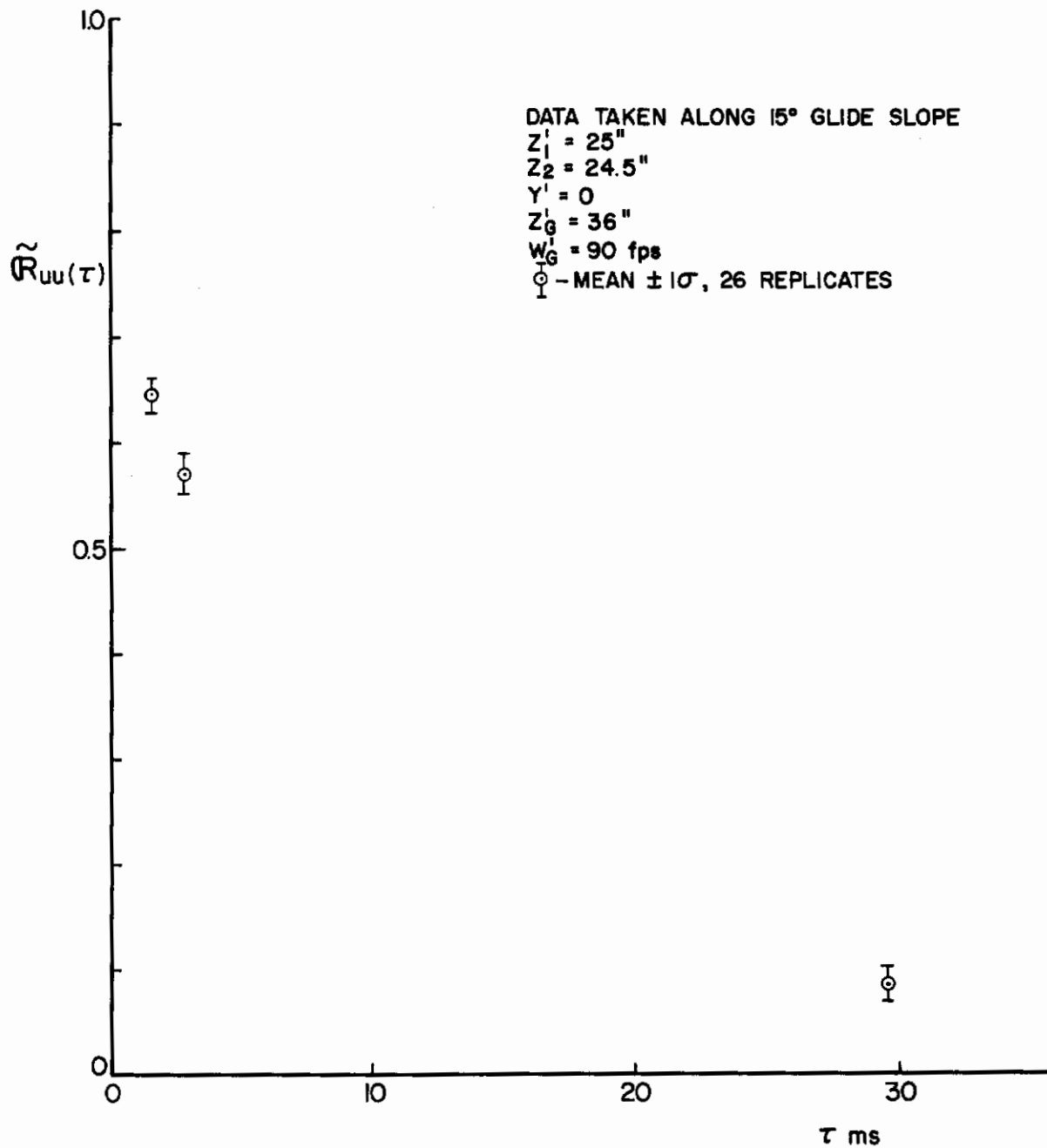
FIGURE 121.   ESTIMATE OF STANDARD DEVIATION FOR $\tilde{R}$ DATA, 44'' x 66'' TUNNEL

304
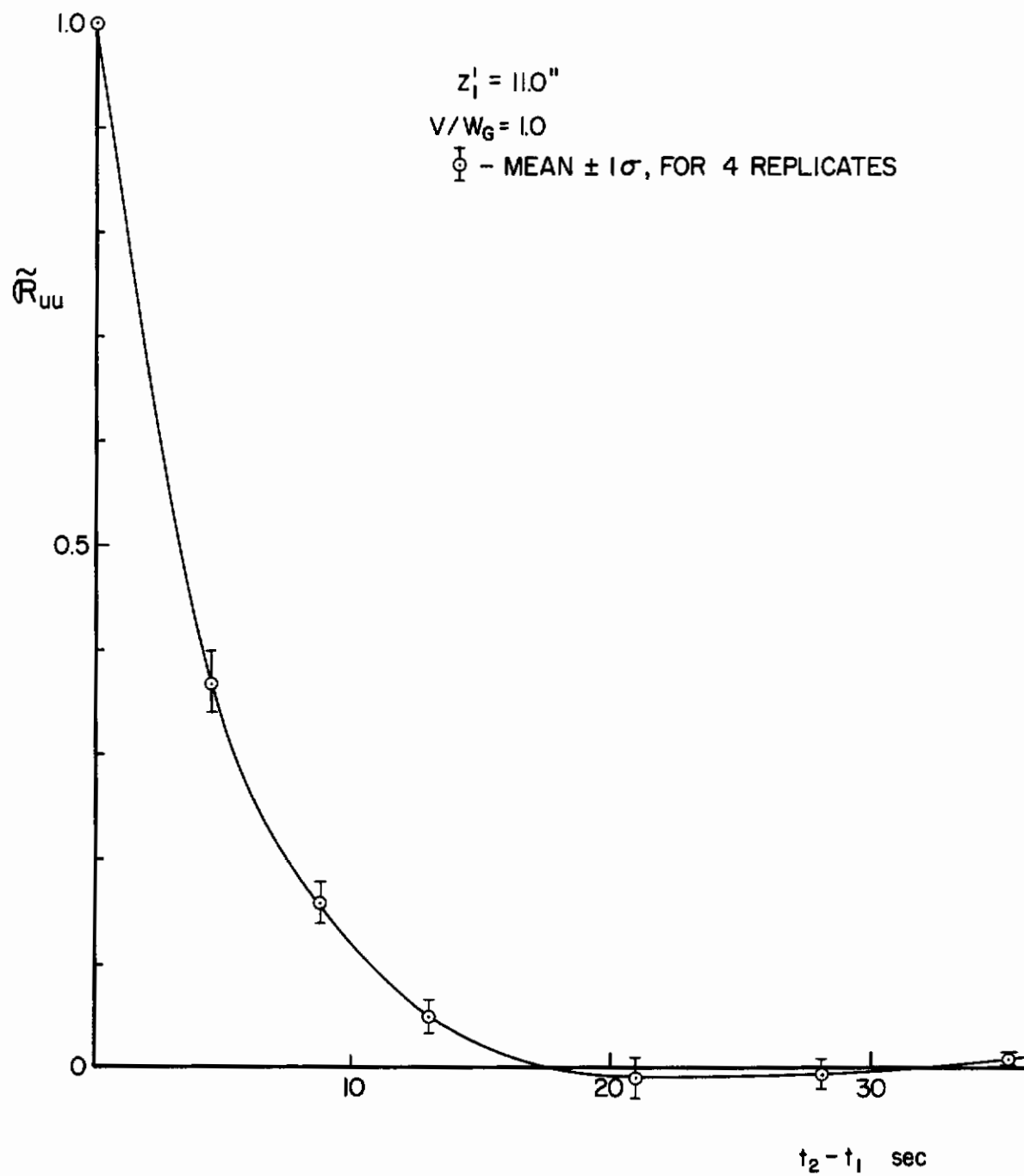
FIGURE 122.   ESTIMATE OF STANDARD DEVIATION FOR $\tilde{R}$ DATA, 44" x 66" TUNNEL

305
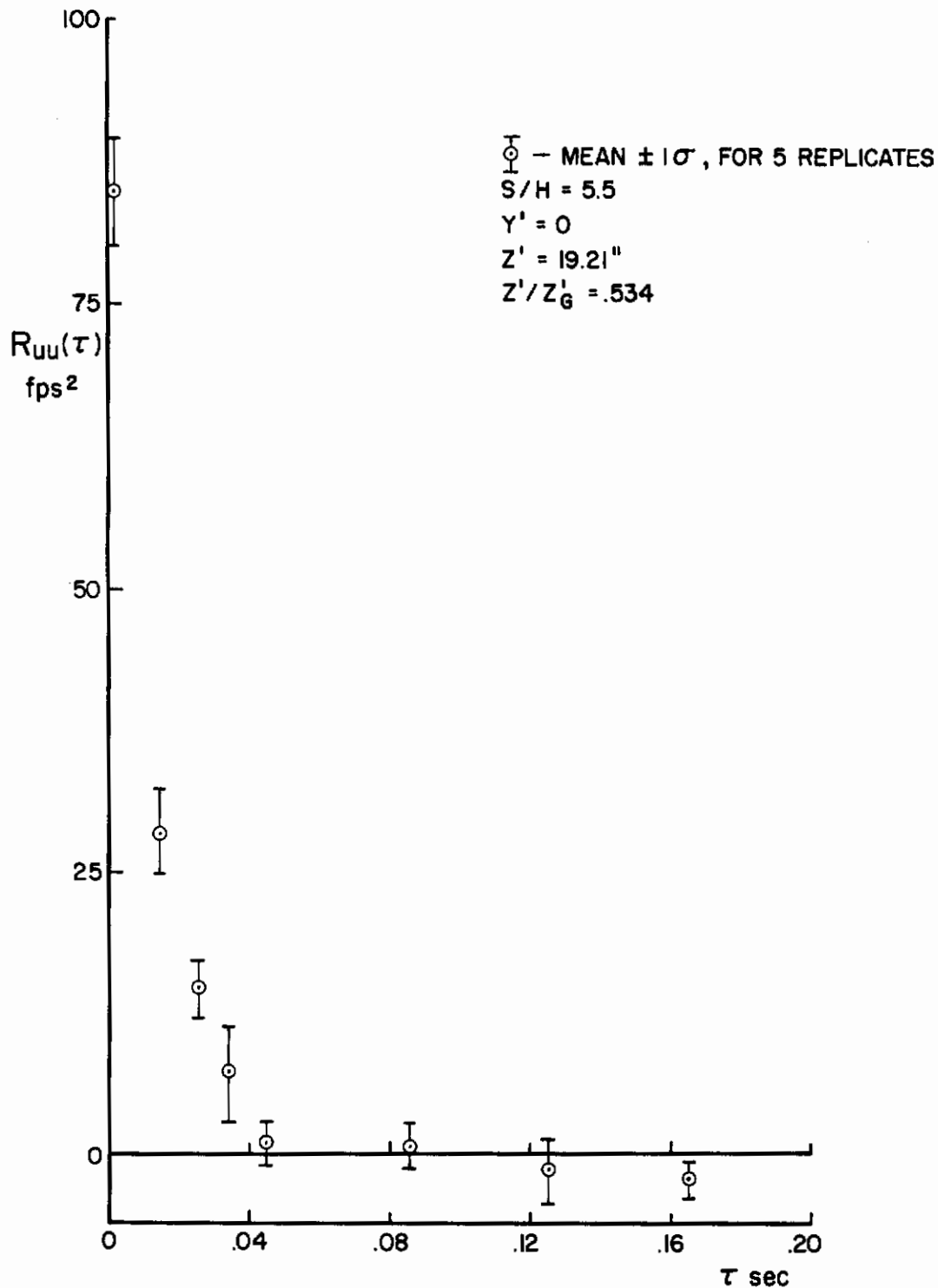
FIGURE 123. ESTIMATE OF STANDARD DEVIATION FOR R DATA, 44" x 66" TUNNEL   306
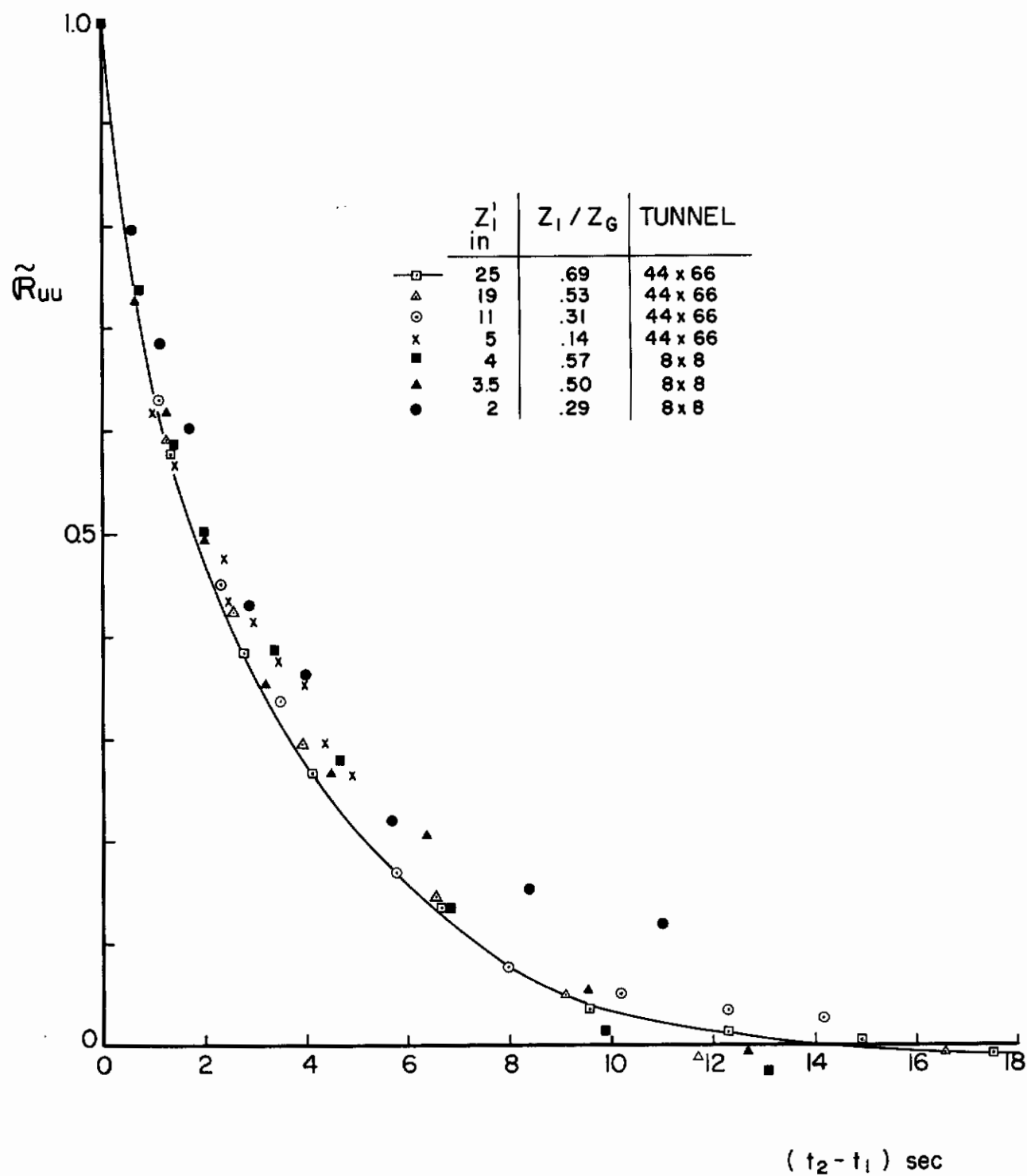
FIGURE 124.   COMPARISON BETWEEN $\tilde{\mathcal{R}}_{uu}$ DATA FROM THE 44" x 66" TUNNEL
AND THE 8" x 8" TUNNEL

307
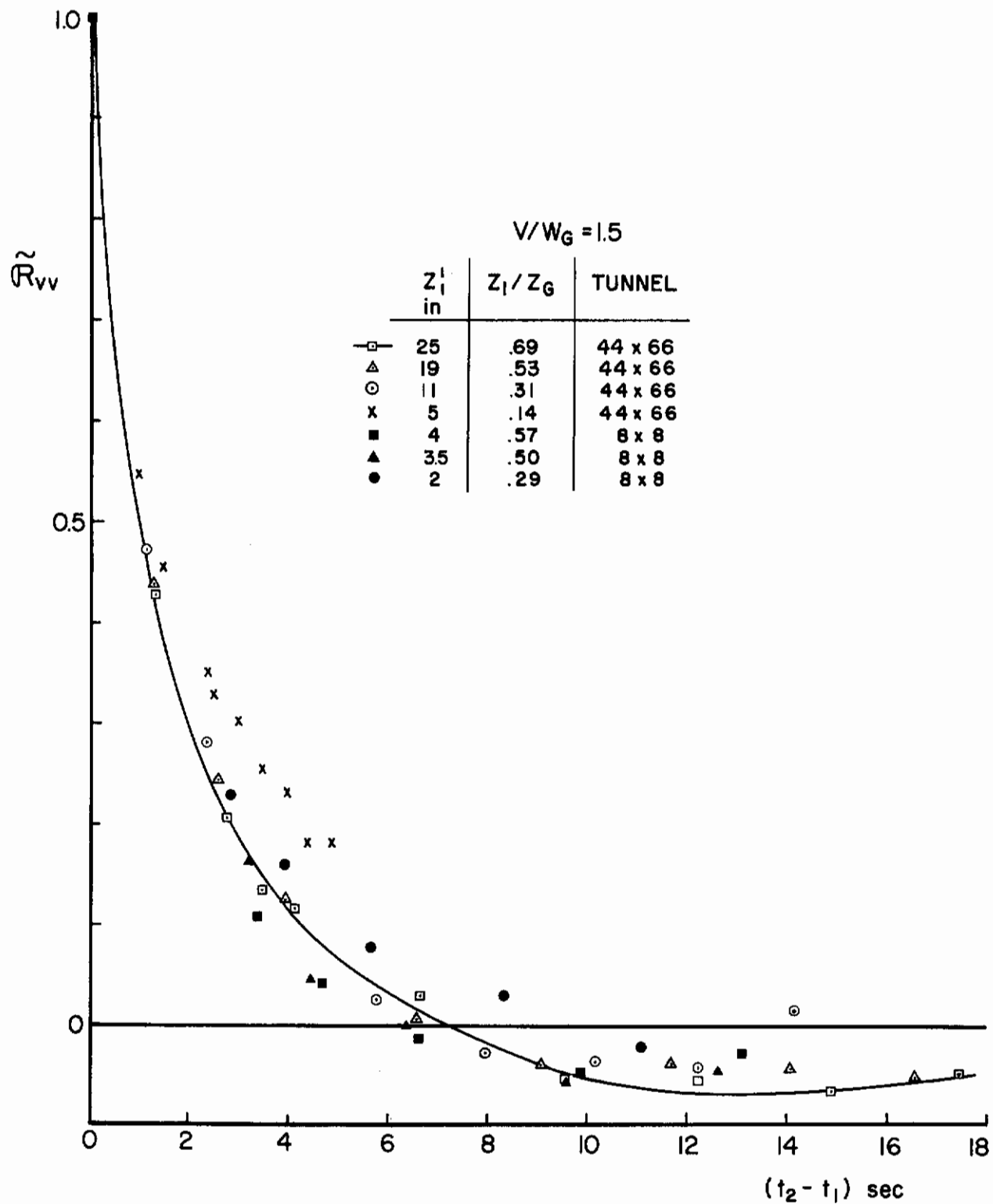
FIGURE 125. COMPARISON BETWEEN $\tilde{R}_{VV}$ DATA FROM THE 44" x 66" TUNNEL AND THE 8" x 8" TUNNEL

308
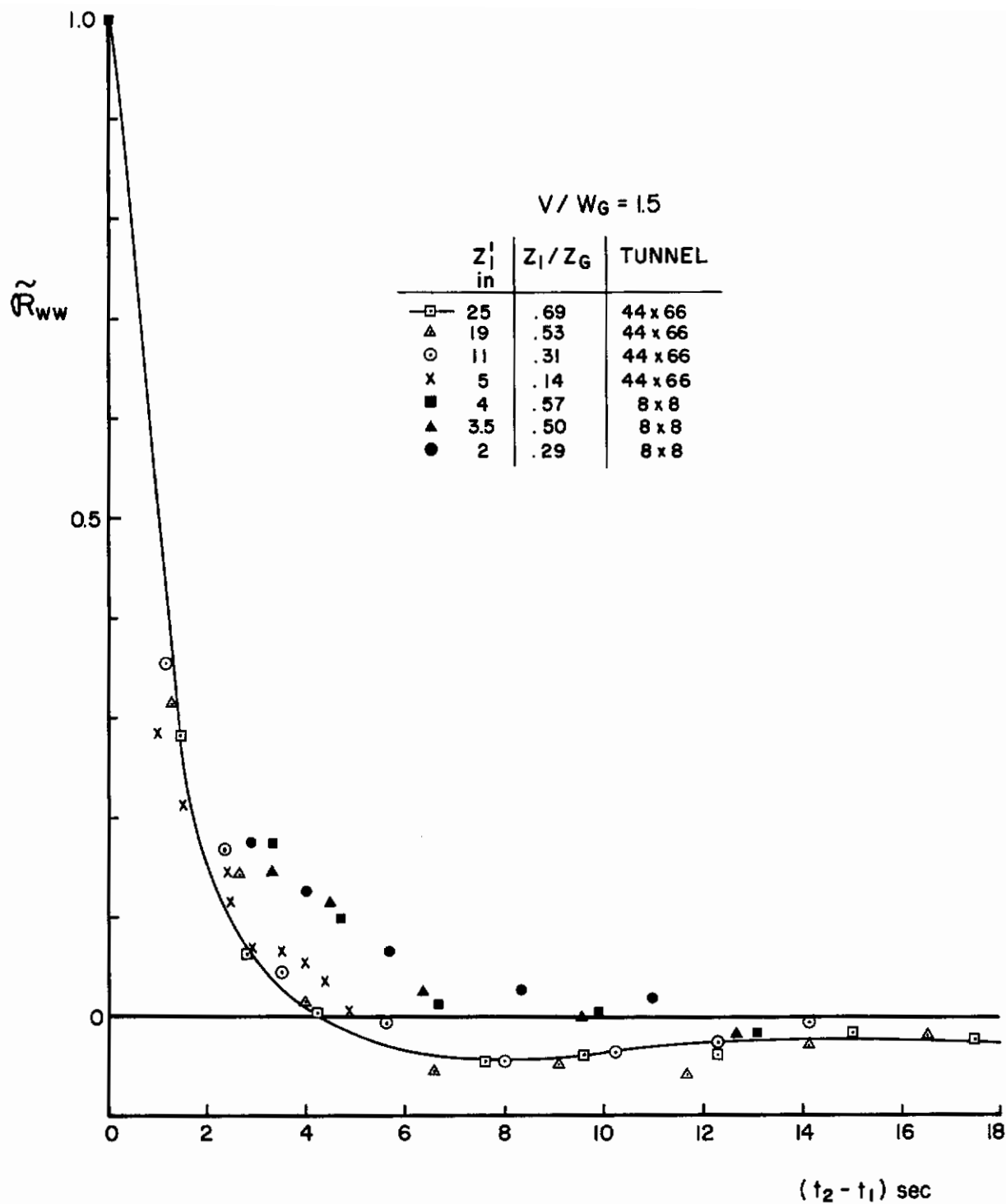
FIGURE 126.   COMPARISON BETWEEN $\tilde{R}_{ww}$ DATA FROM THE 44" x 66" TUNNEL
AND THE 8" x 8" TUNNEL

309
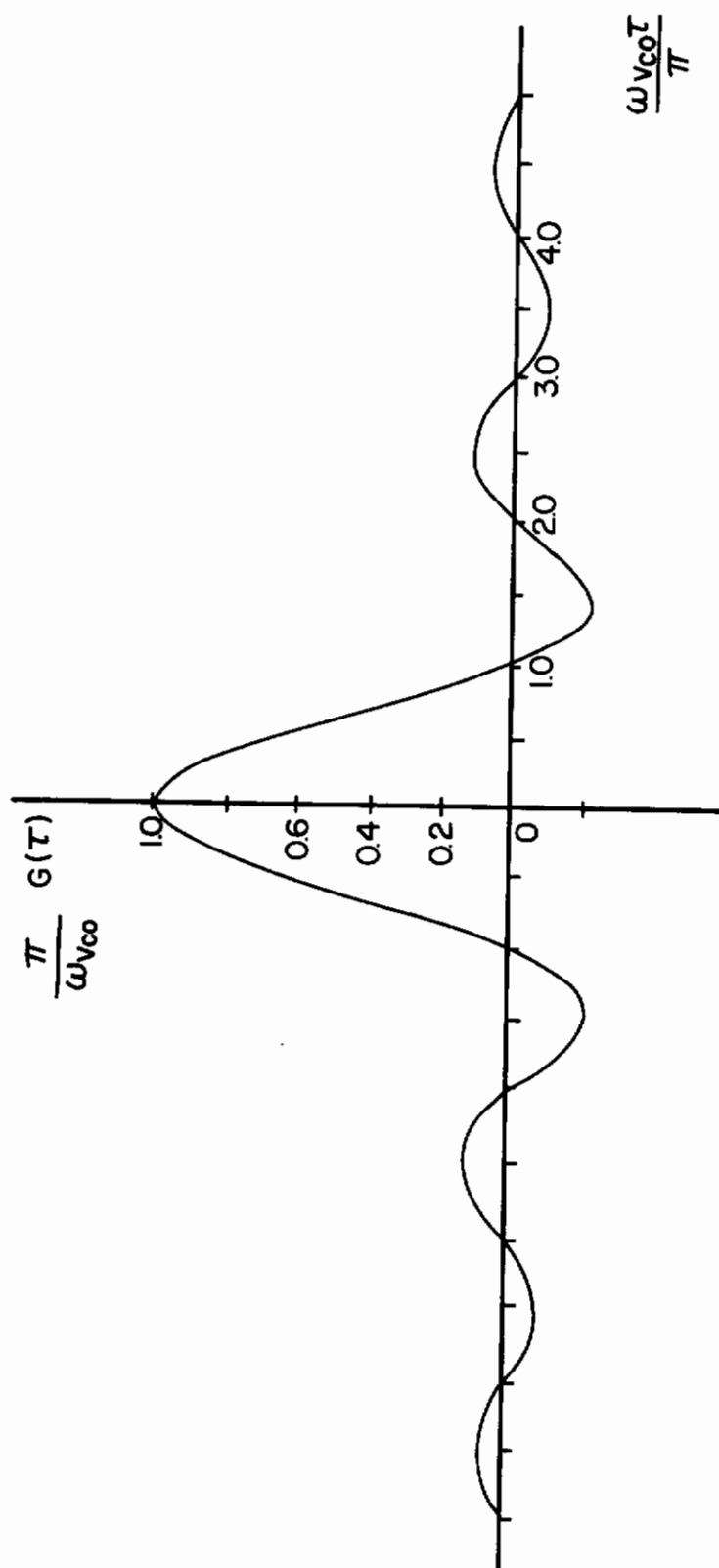
FIGURE 127. WINDOW FUNCTION $G(\tau)$
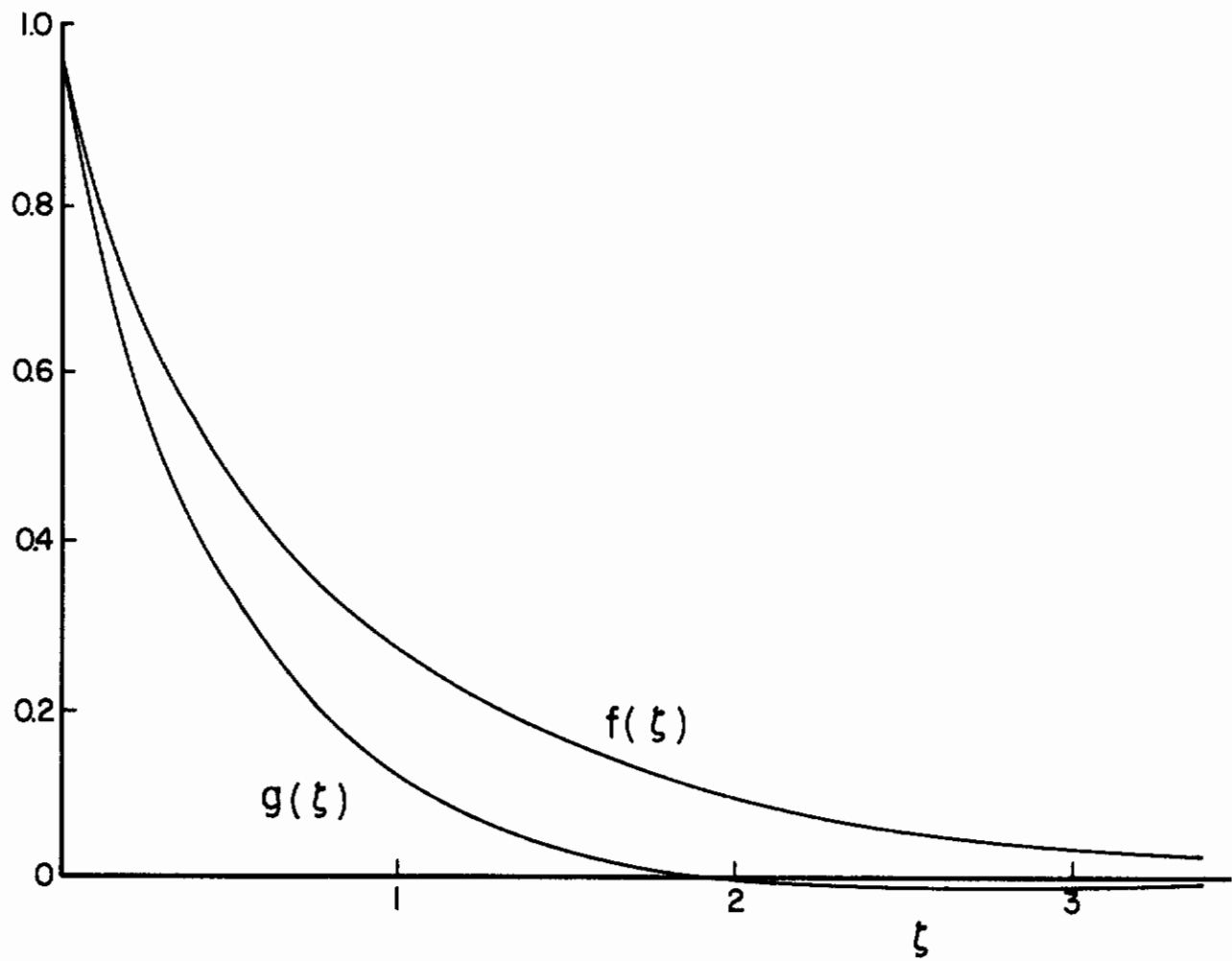
FIGURE 128.   LONGITUDINAL AND LATERAL CORRELATION FUNCTIONS $f(\zeta)$ and $g(\zeta)$
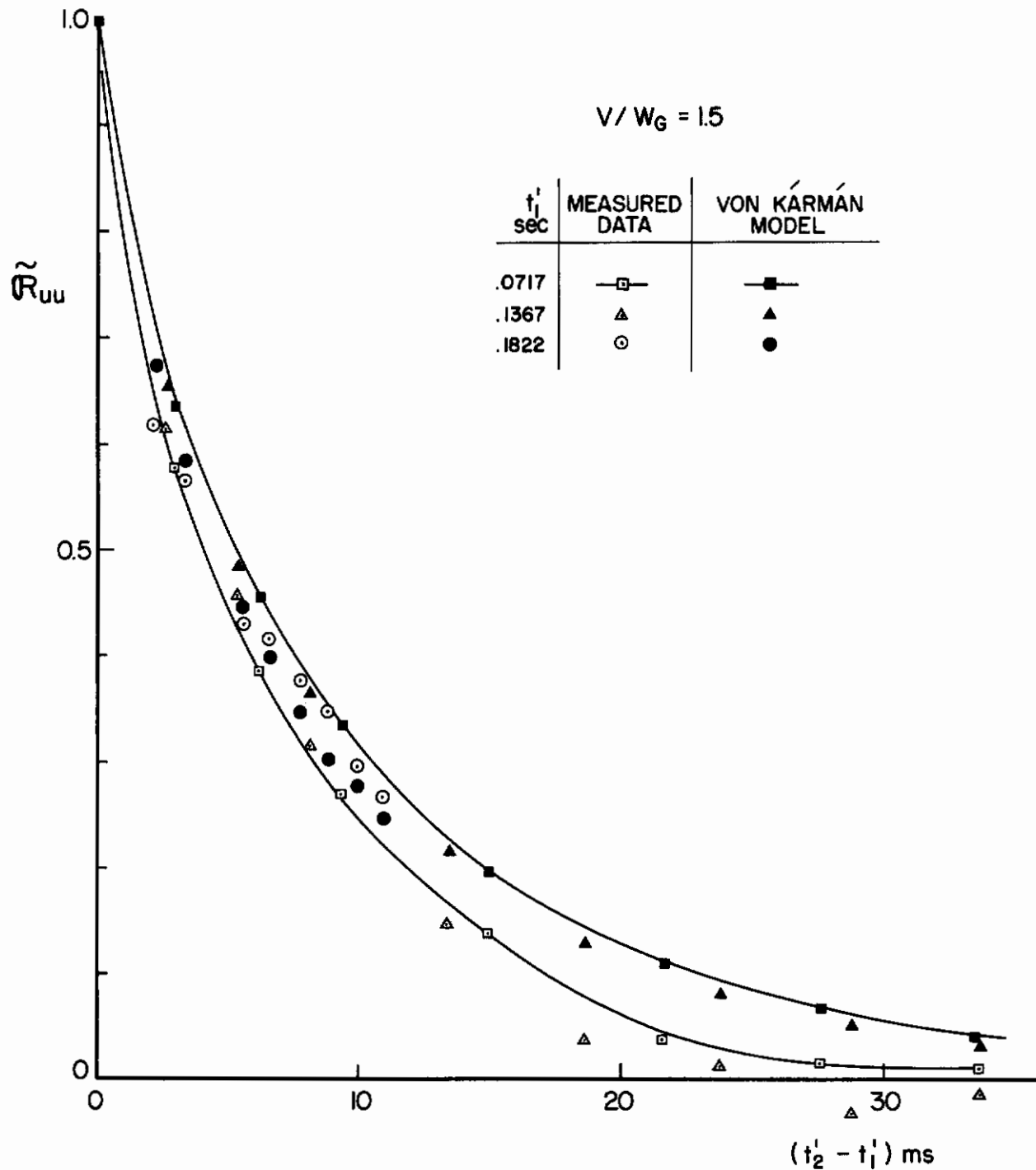
FIGURE 129.   COMPARISON BETWEEN $\tilde{\mathcal{R}}_{uu}$ DATA FROM THE 44" x 66" TUNNEL
AND THE VON KÁRMÁN MODEL

312
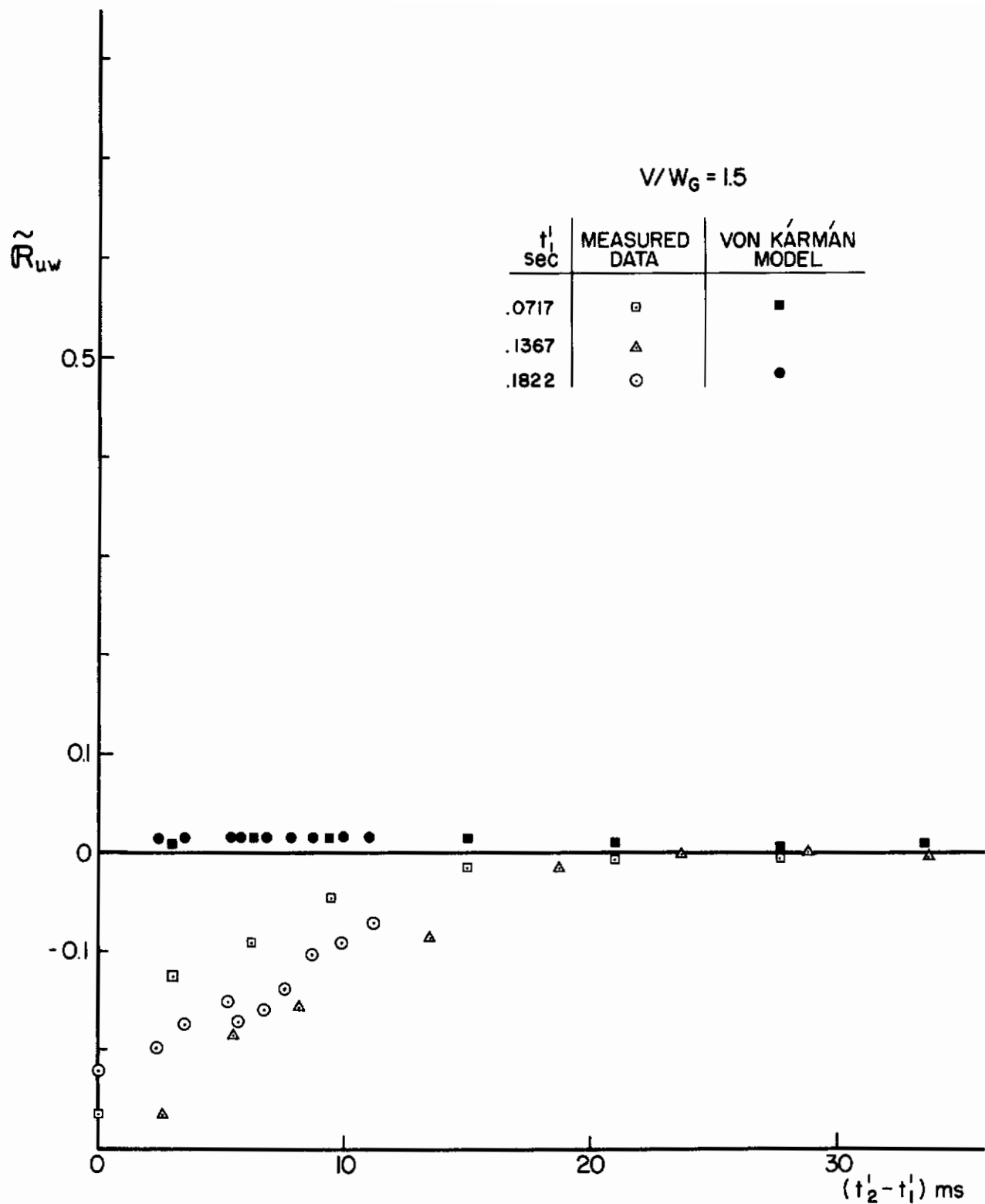
FIGURE 130. COMPARISON BETWEEN $\tilde{R}_{uw}$ DATA FROM THE 44" x 66" TUNNEL
AND THE VON KÁRMÁN MODEL

313
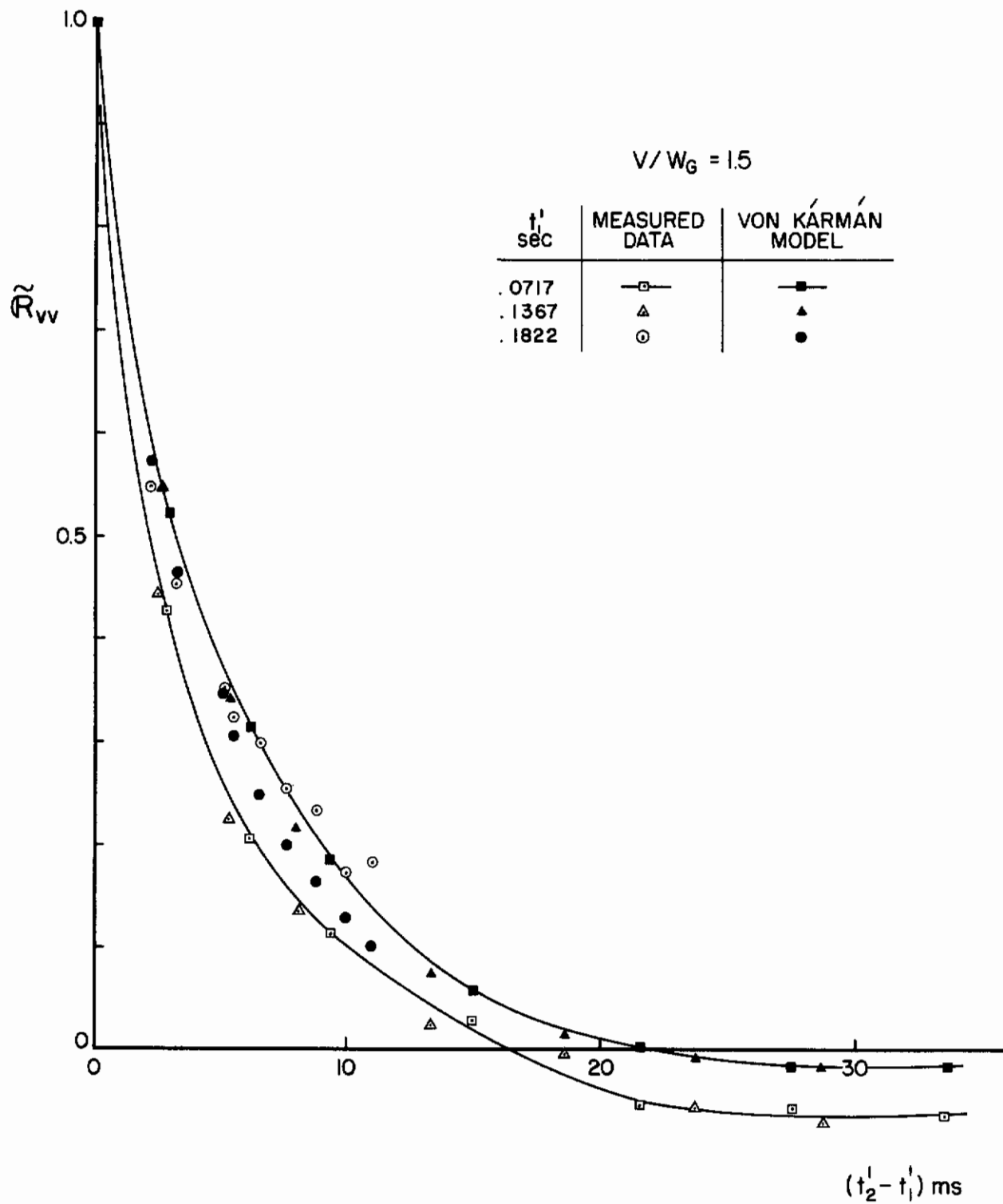
FIGURE 131.   COMPARISON BETWEEN $\tilde{R}_{VV}$ DATA FROM THE 44" x 66" TUNNEL
AND THE VON KÁRMÁN MODEL

314

$$\widetilde{R}_{\omega\omega}$$

$V/W_G = 1.0$

☐ T1$'$ = 3·09700
△ T1$'$ = 3·45800
+ T1$'$ = 3·59300
✶ T1$'$ = 3·69100
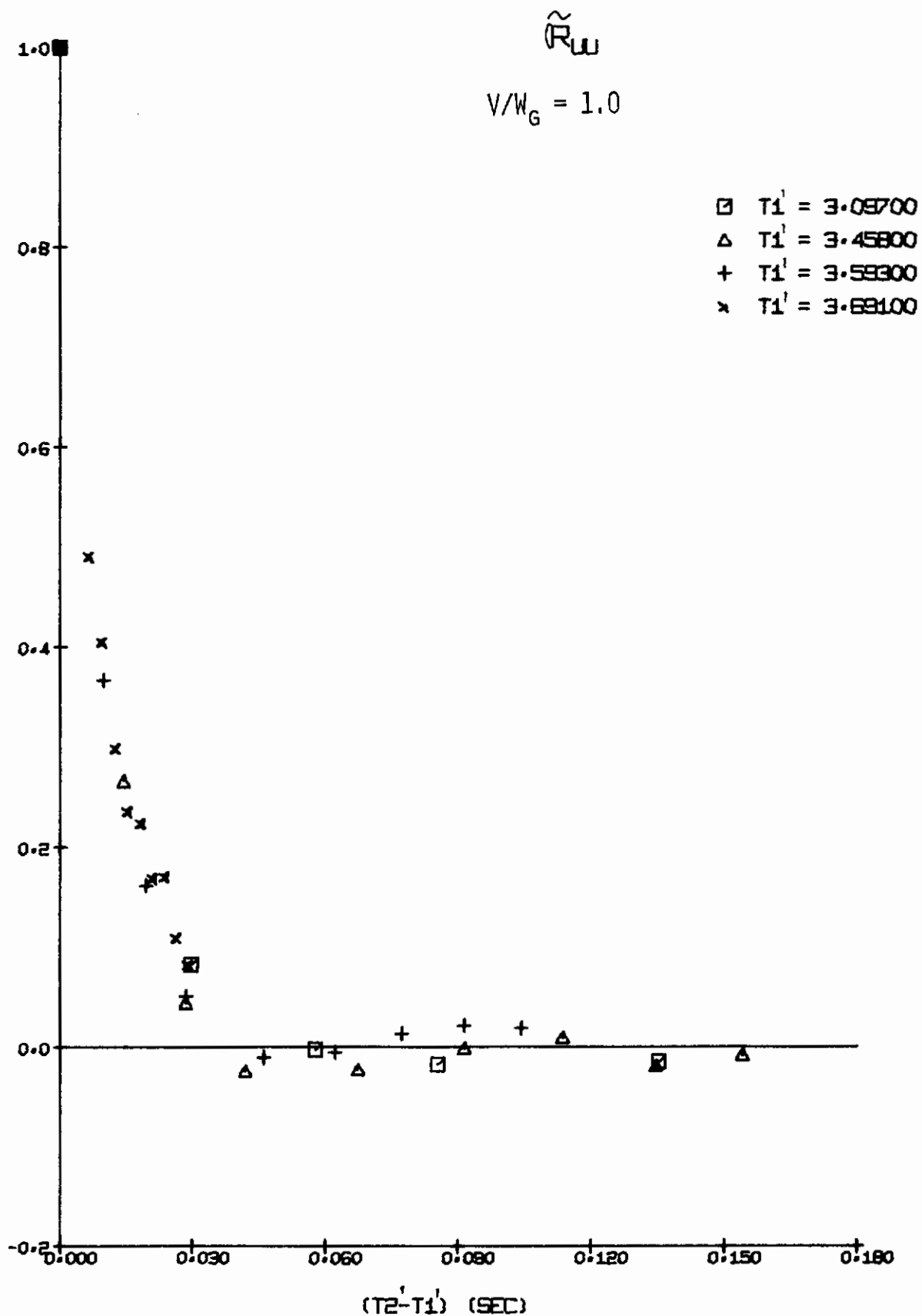
FIGURE 132a.   FLIGHT PATH TURBULENCE CORRELATION, 44" x 66" TUNNEL

315

$$\widetilde{R}_{uu}$$

$$V/W_G = 1.0$$

☑ T1' = 3·37700
△ ⊤1' = 3·52500
+ T1' = 3·64800
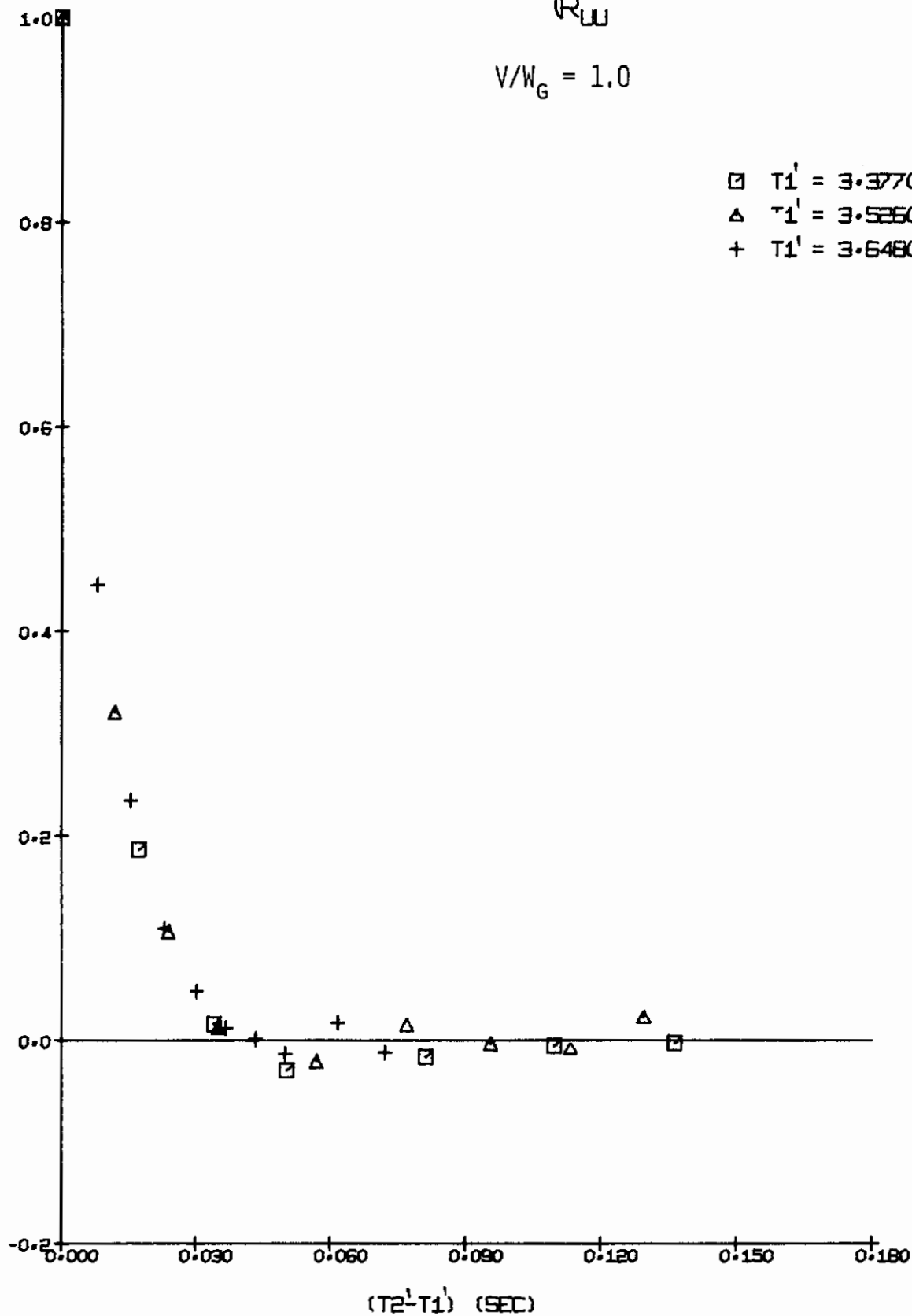
FIGURE 132b.   FLIGHT PATH TURBULENCE CORRELATION, 44" x 66" TUNNEL

316

$$\widetilde{R}_{uu}$$

$$V/W_G = 1.5$$

☐ T1' = 0·07173
△ T1' = 0·12280
+ T1' = 0·15280
✕ T1' = 0·18220

(T2'-T1') (SEC)

FIGURE 133a. FLIGHT PATH TURBULENCE CORRELATION, 44" x 66" TUNNEL

317

$$\tilde{R}_{uu}$$

$$V/W_G = 1.5$$

□ T1' = 0.10830
△ T1' = 0.13670
+ T1' = 0.16800
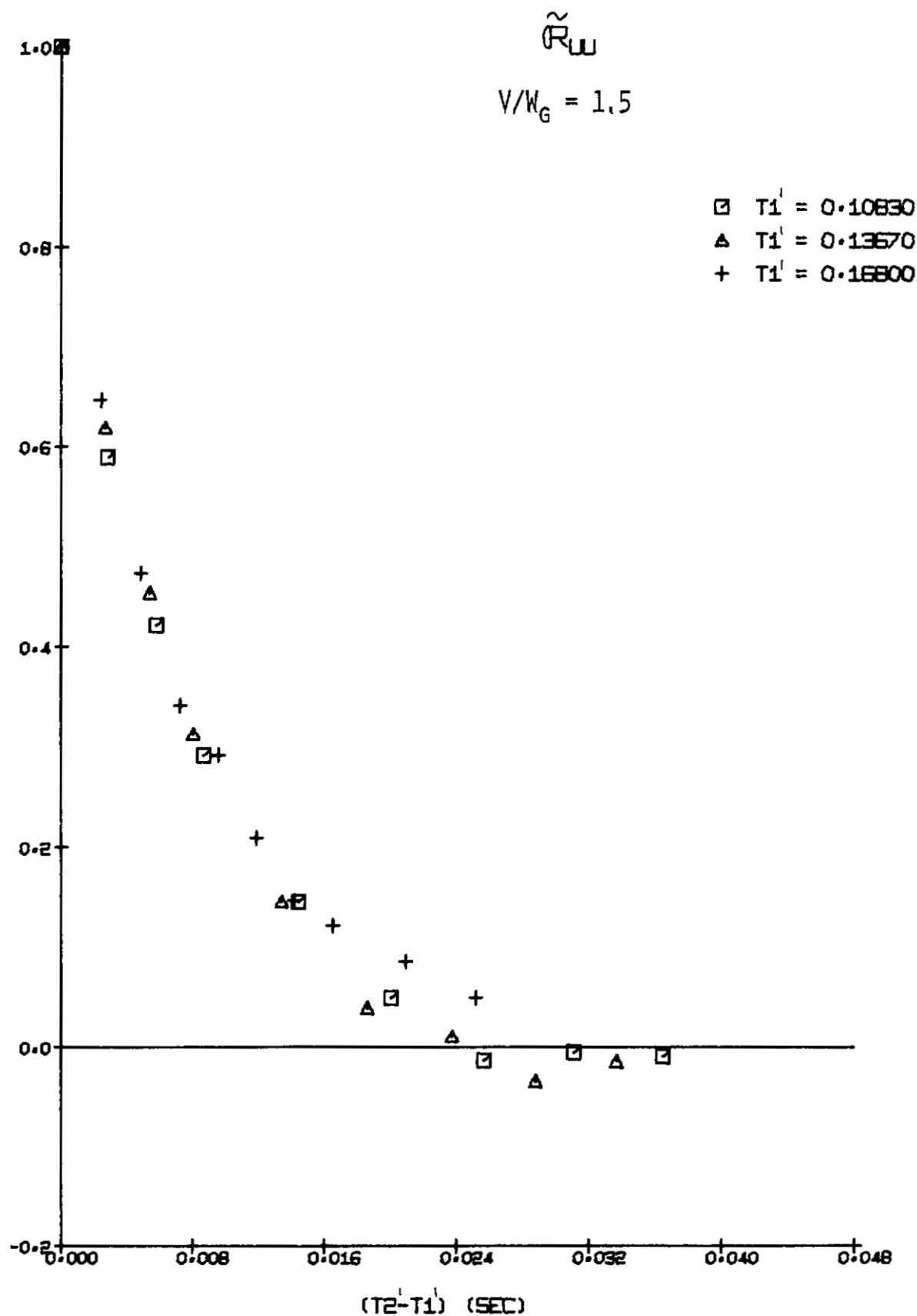
FIGURE 133b.   FLIGHT PATH TURBULENCE CORRELATION, 44" x 66" TUNNEL

318
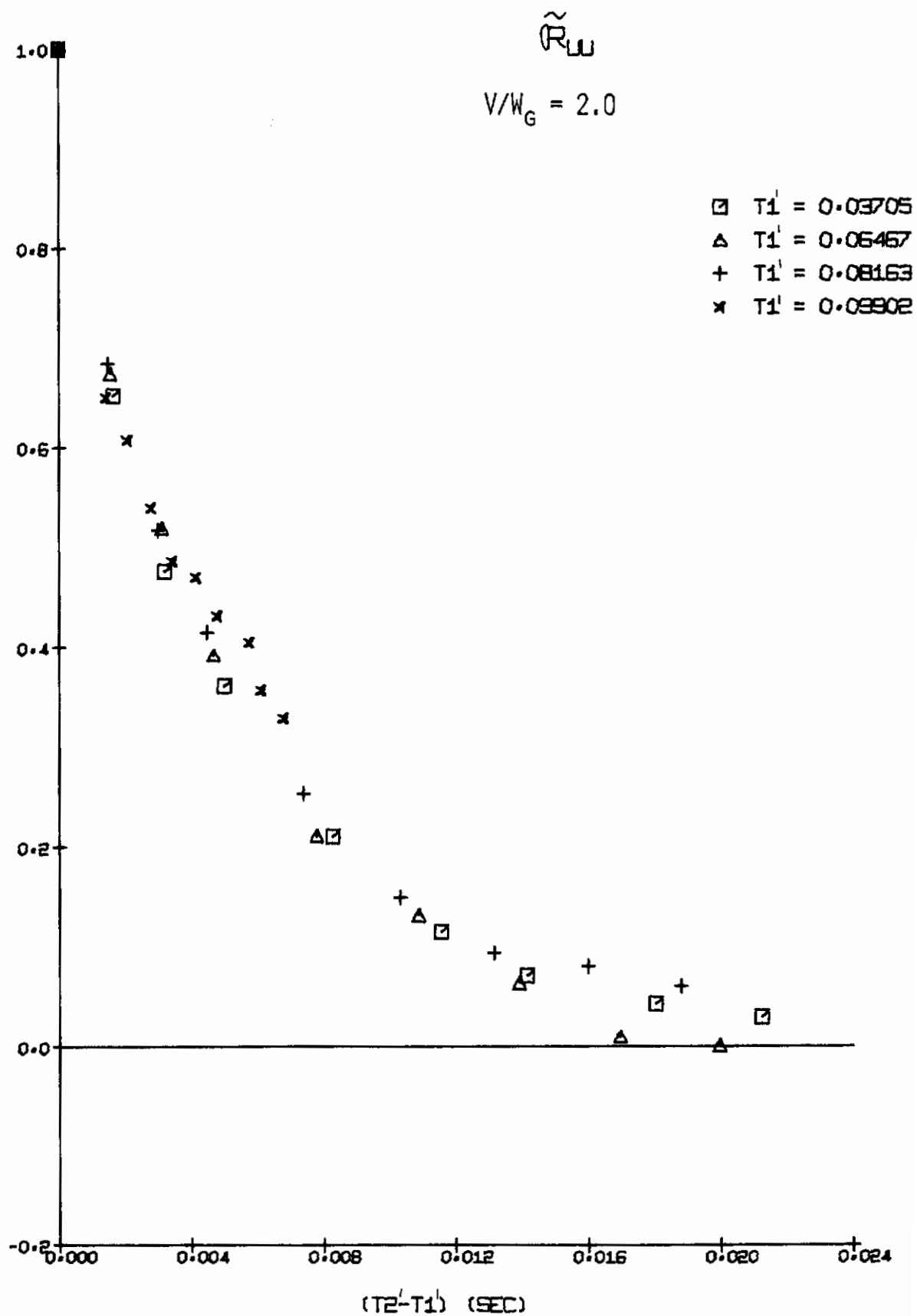
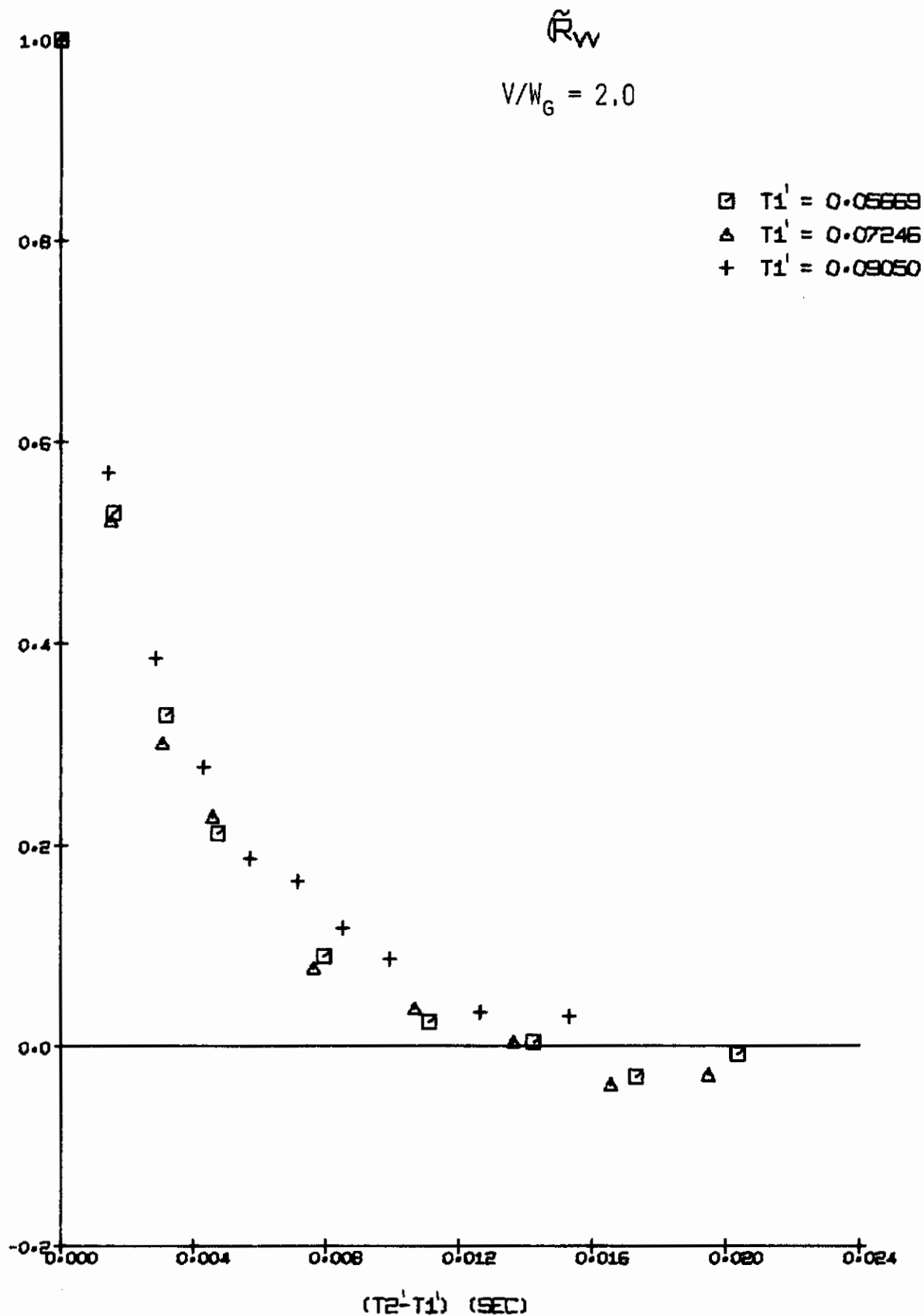FIGURE 134a. FLIGHT PATH TURBULENCE CORRELATION, 44" x 66" TUNNEL

319
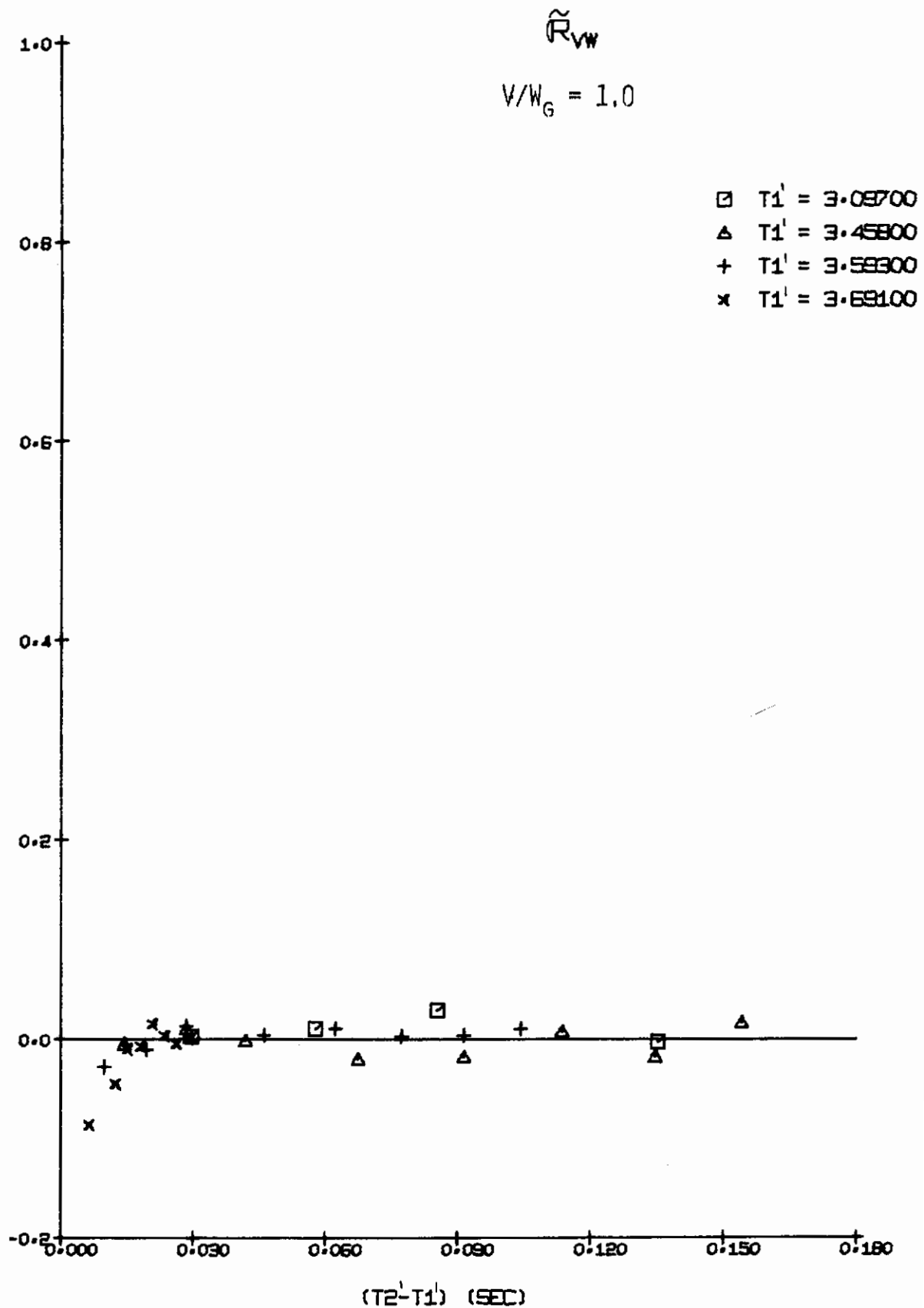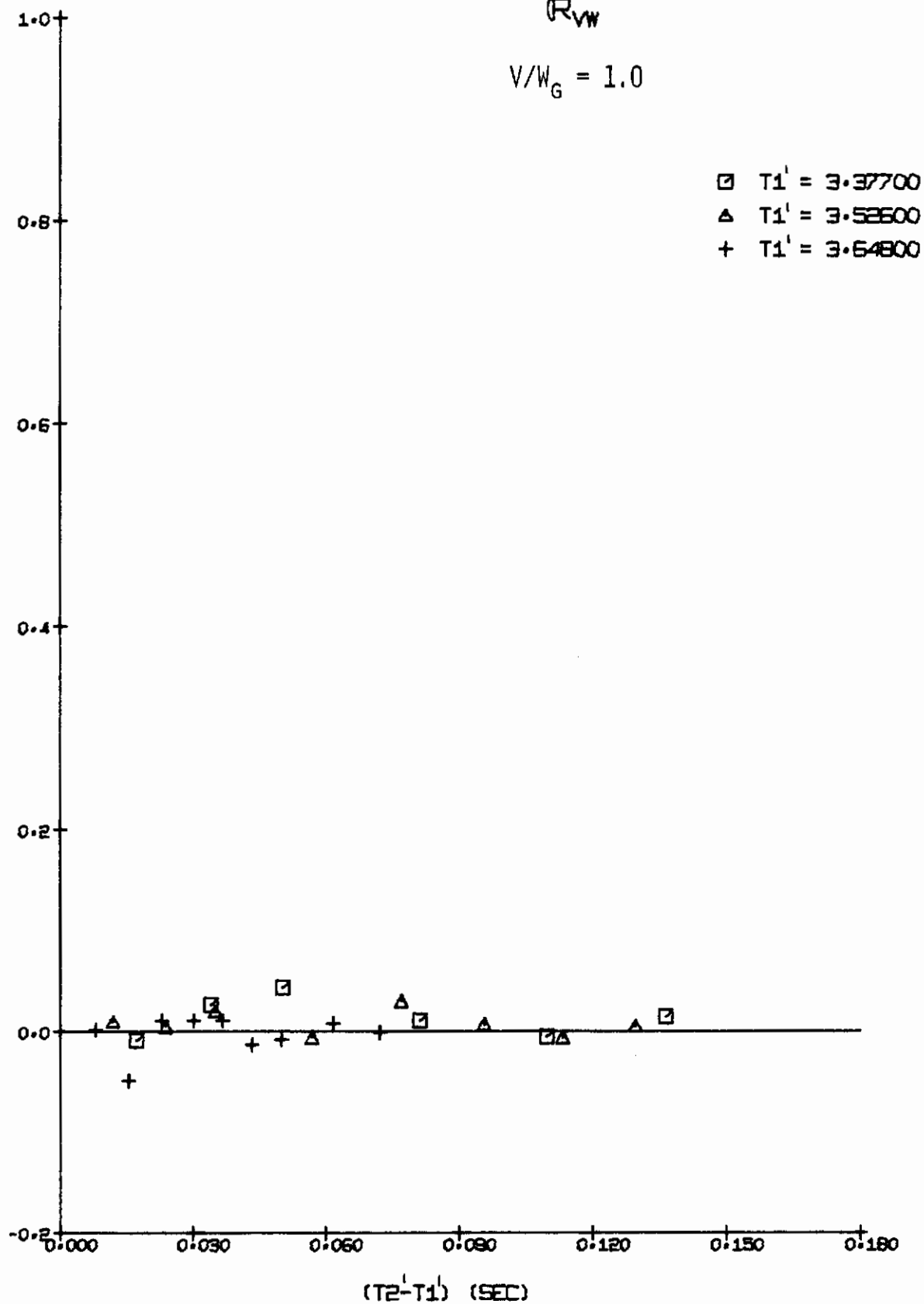
$\widetilde{R}_{\sqcup\sqcup}$

$V/W_G = 2.0$
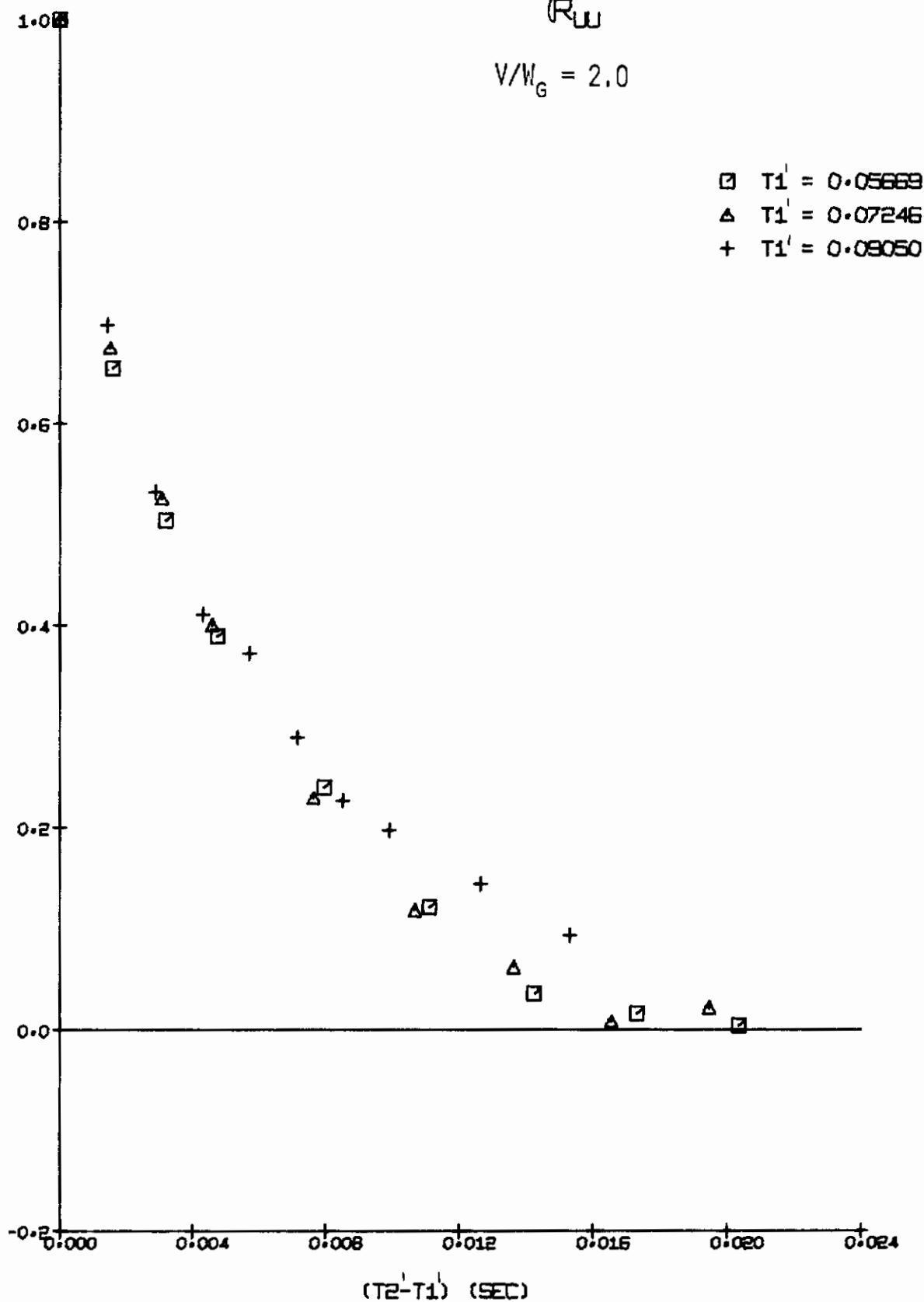
FIGURE 134b.   FLIGHT PATH TURBULENCE CORRELATION, 44" x 66" TUNNEL

320

$\tilde{\mathbb{R}}_{LV}$

$V/W_G = 1.0$

☐ $T_1' = 3.09700$
△ $T_1' = 3.45800$
+ $T_1' = 3.59300$
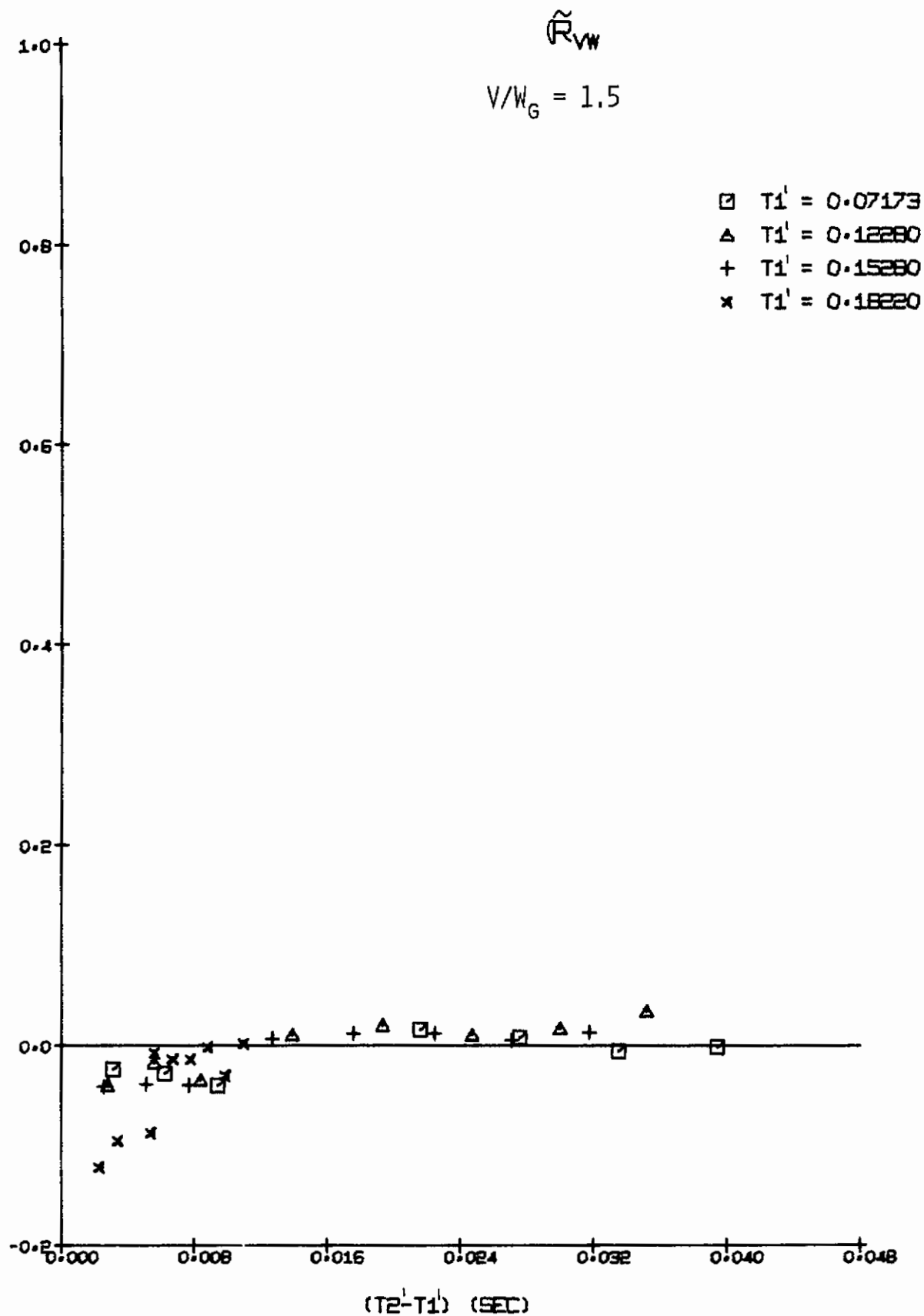✕ $T_1' = 3.69100$
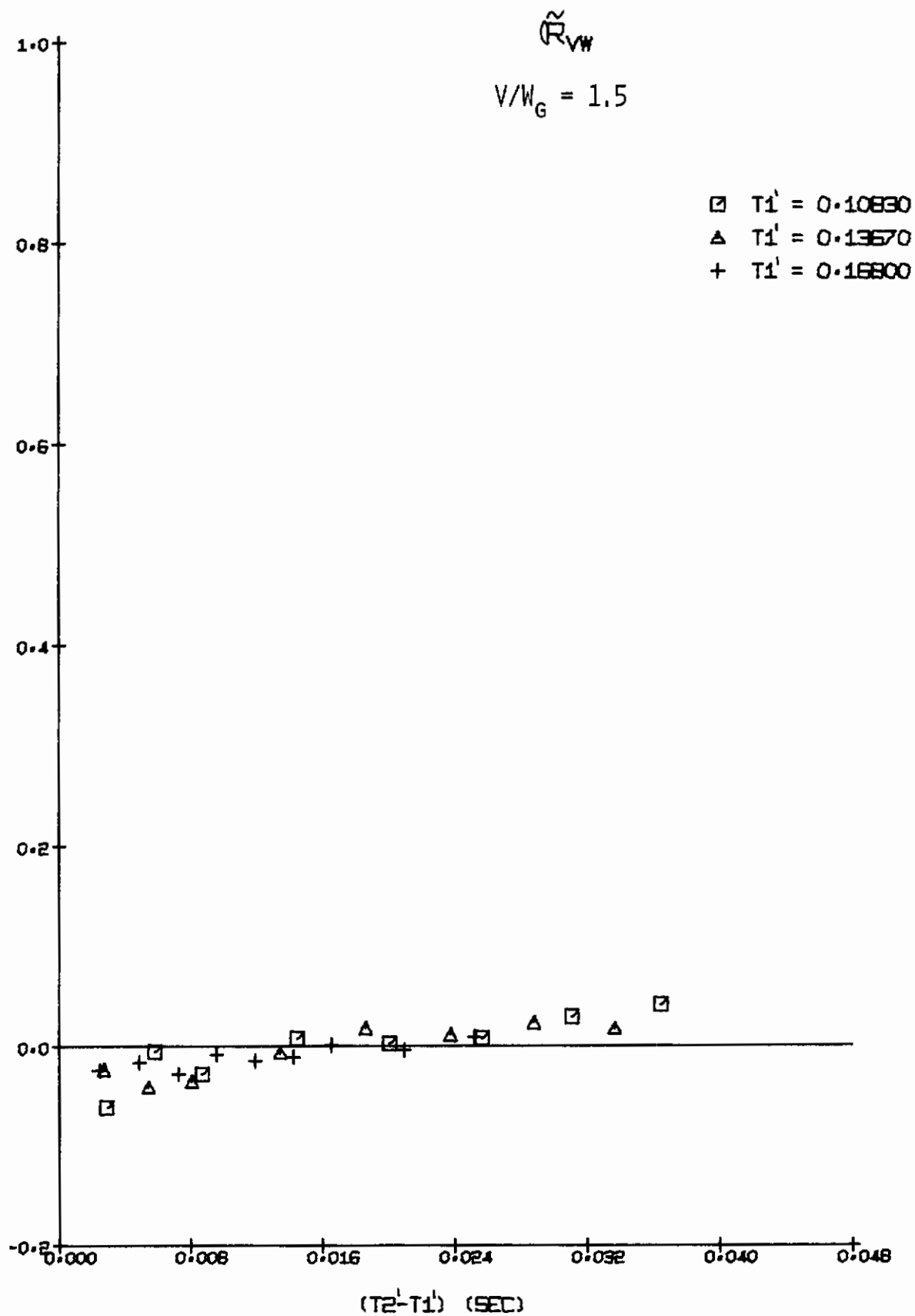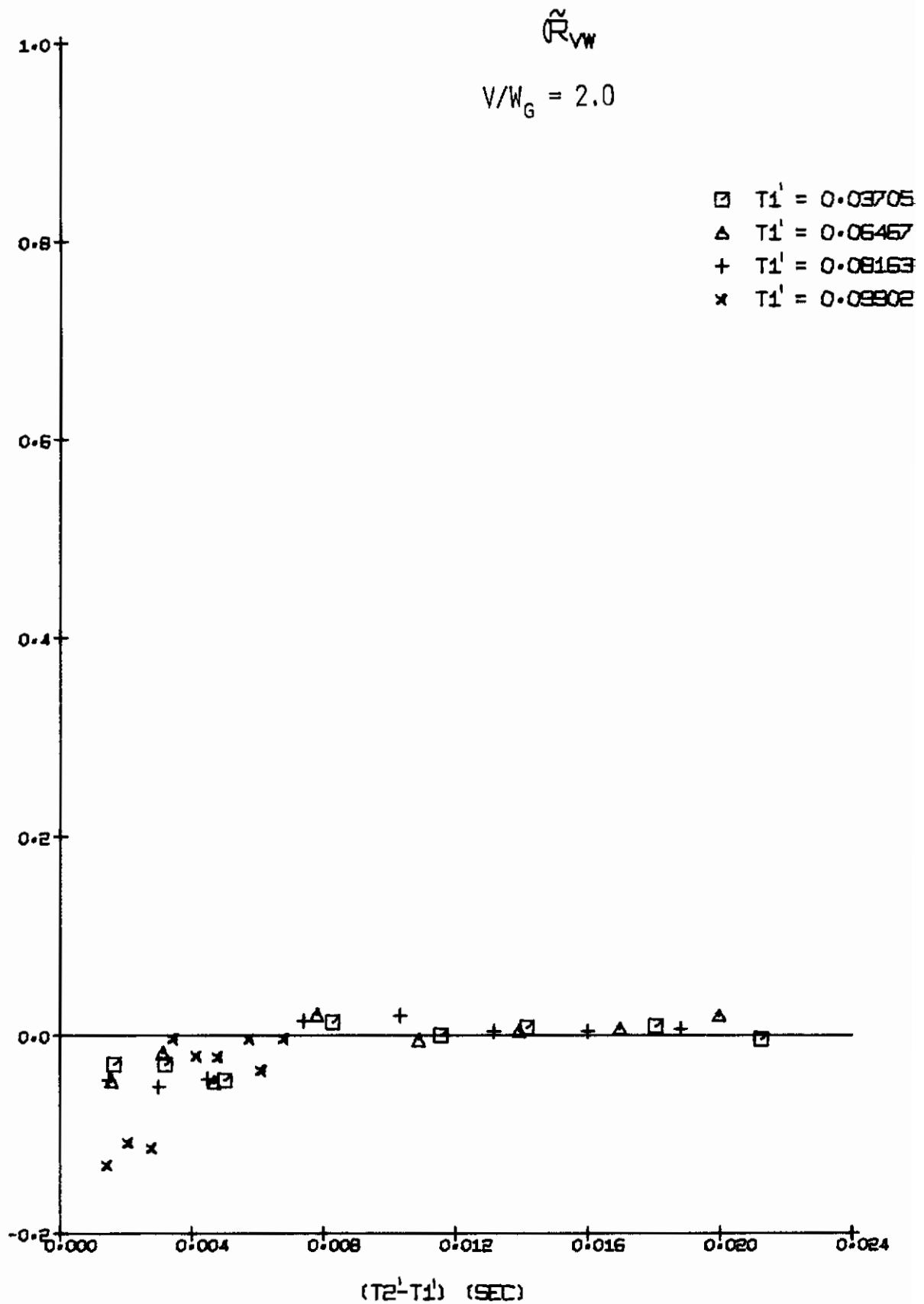
$(T_2' - T_1')$ (SEC)
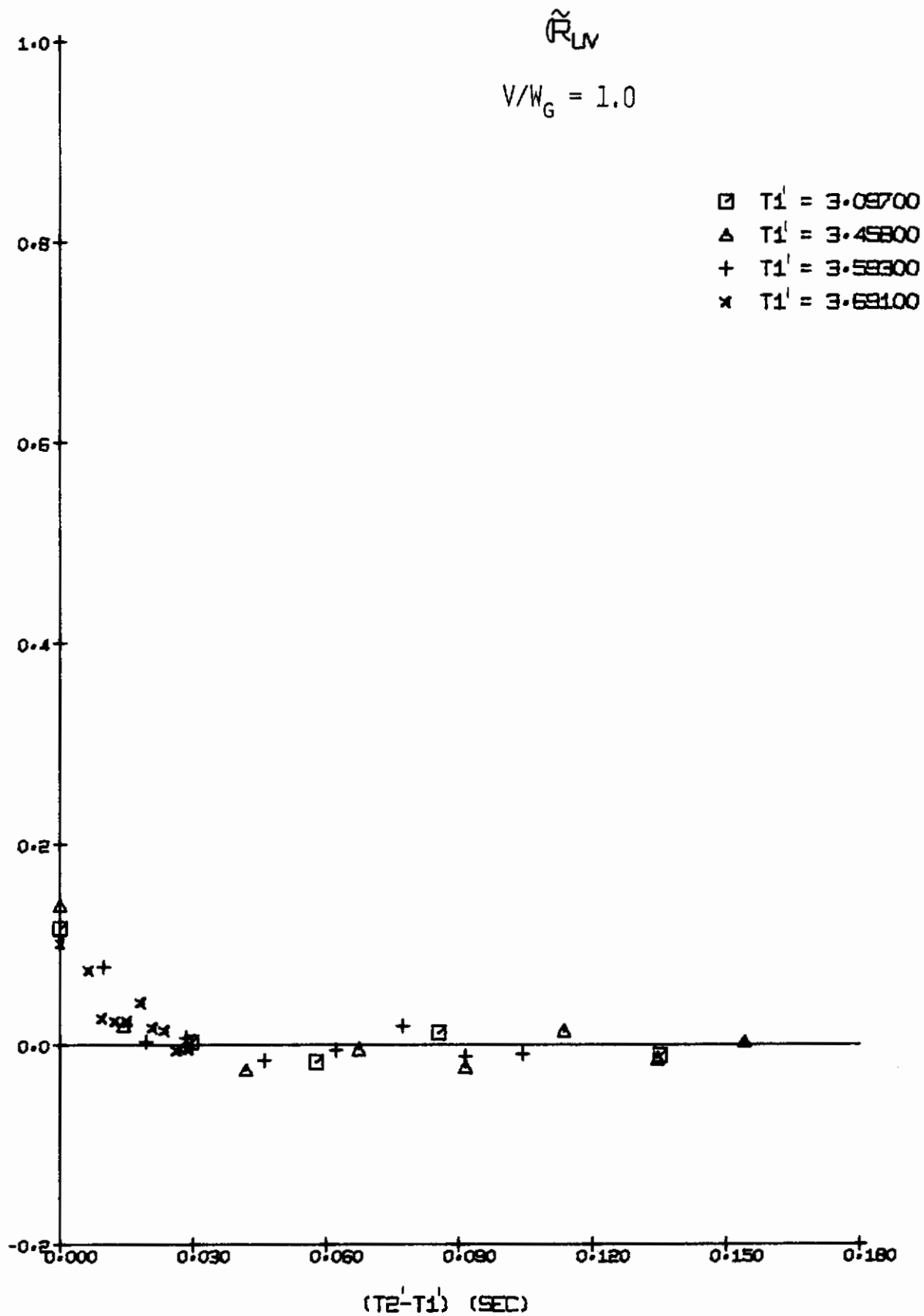
FIGURE 135a.   FLIGHT PATH TURBULENCE CORRELATION, 44" x 66" TUNNEL
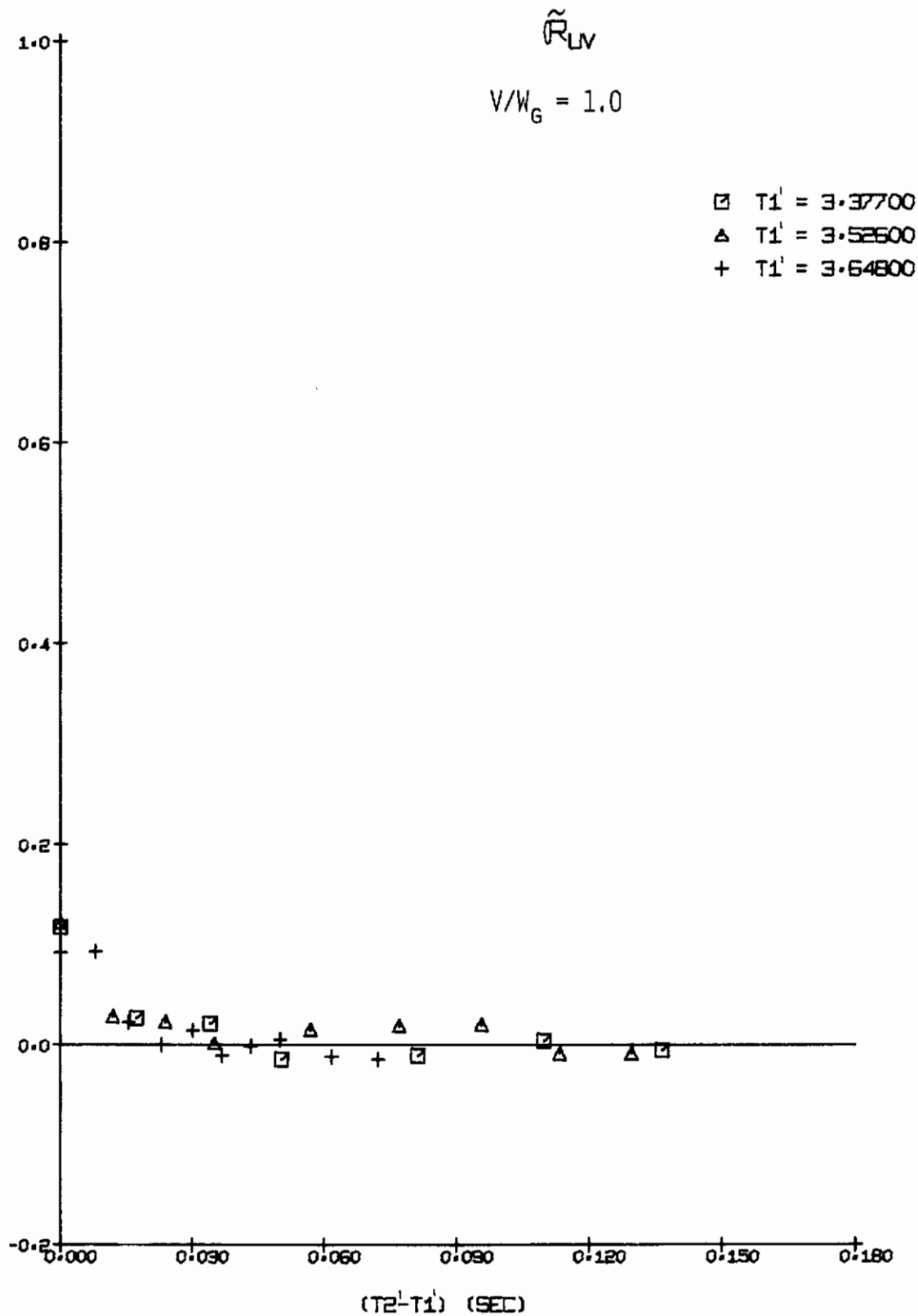
FIGURE 135b.   FLIGHT PATH TURBULENCE CORRELATION, 44" x 66" TUNNEL
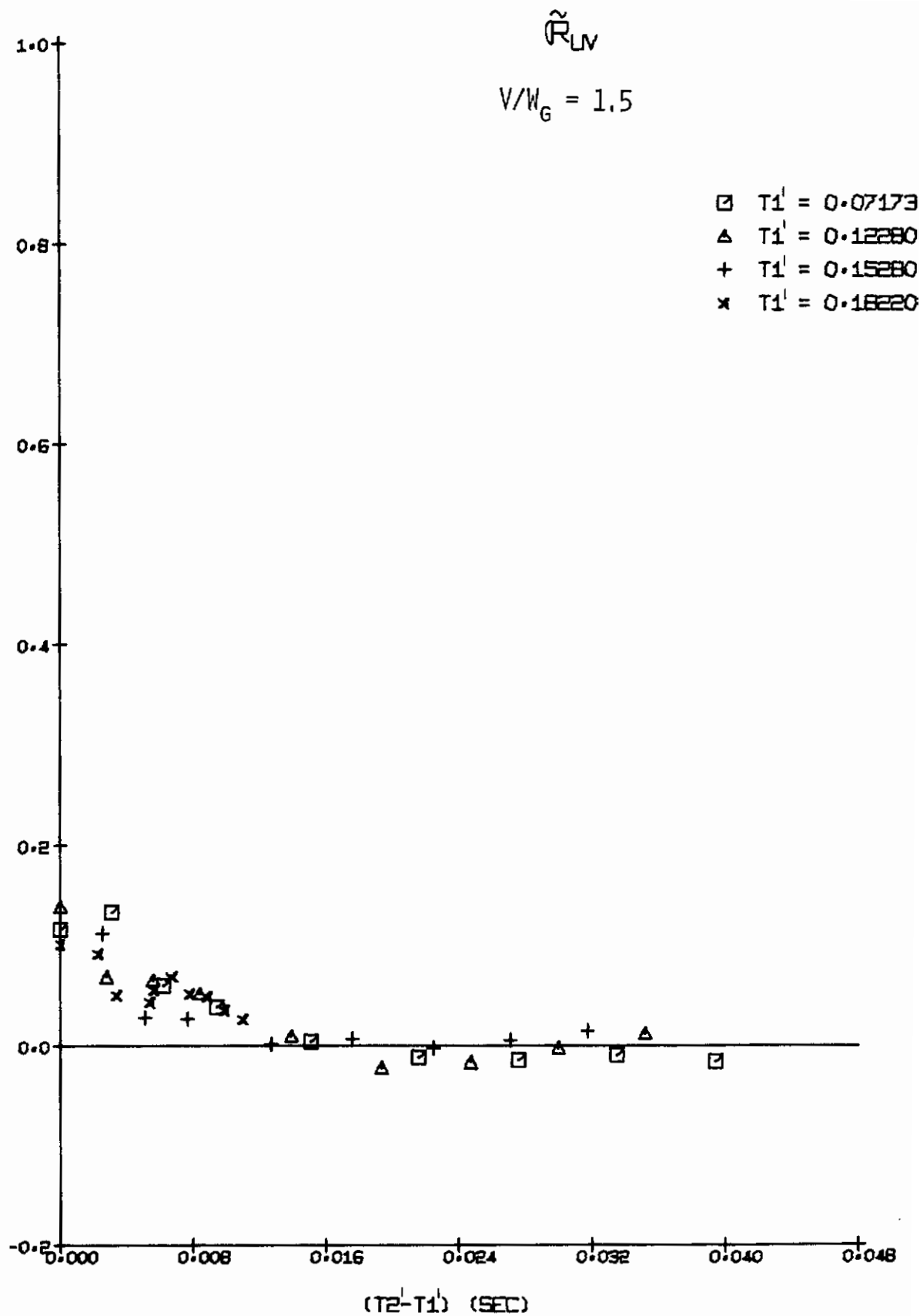
FIGURE 136a.   FLIGHT PATH TURBULENCE CORRELATION, 44" x 66" TUNNEL

323

$$\tilde{R}_{UV}$$

$$V/W_G = 1.5$$

Legend:
- ☑ $T1' = 0.10830$
- △ $T1' = 0.13670$
- + $T1' = 0.15800$

(T2'-T1') (SEC)
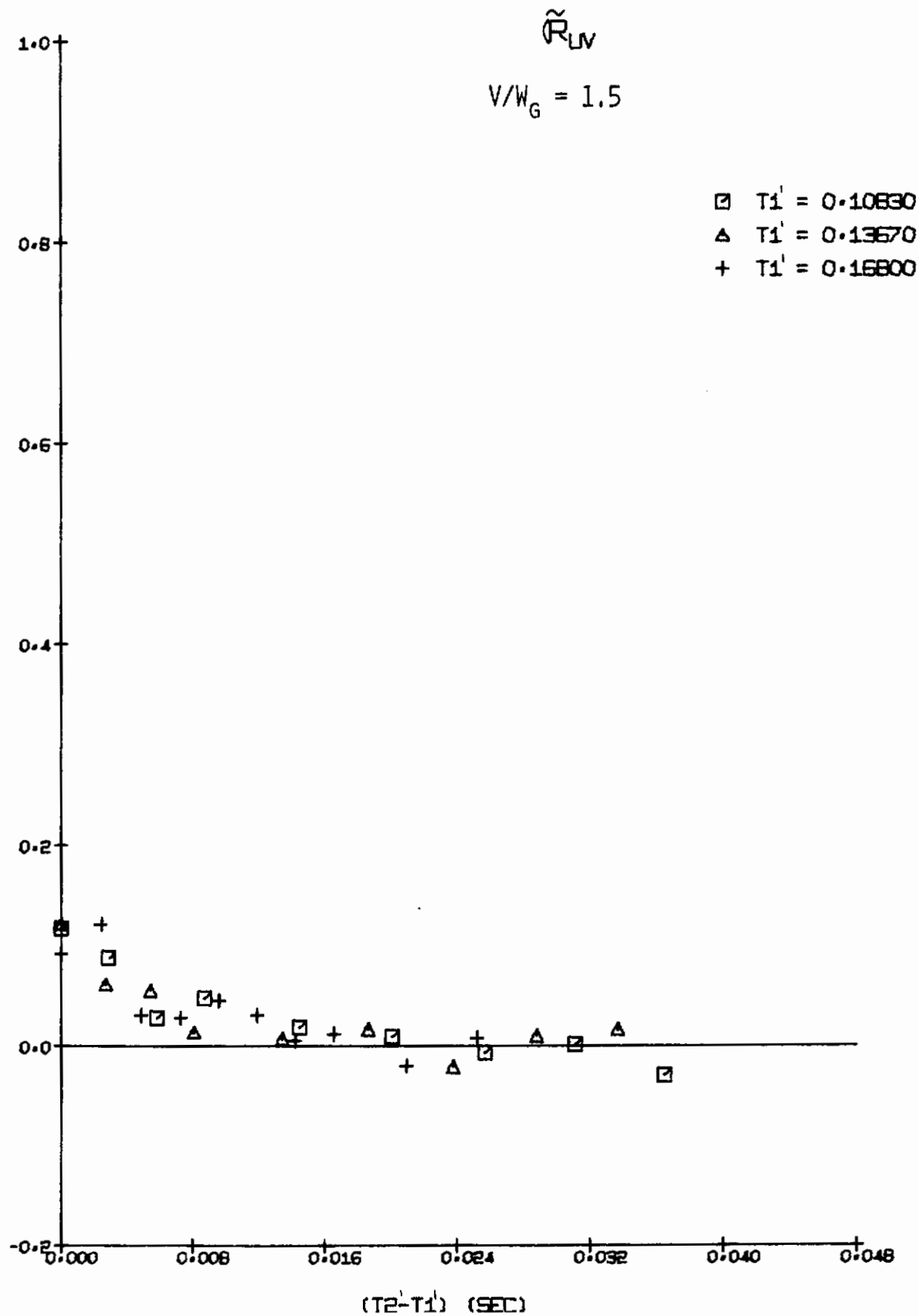
FIGURE 136b.   FLIGHT PATH TURBULENCE CORRELATION, 44" x 66" TUNNEL

324

$\tilde{R}_{UV}$

$V/W_G = 2.0$
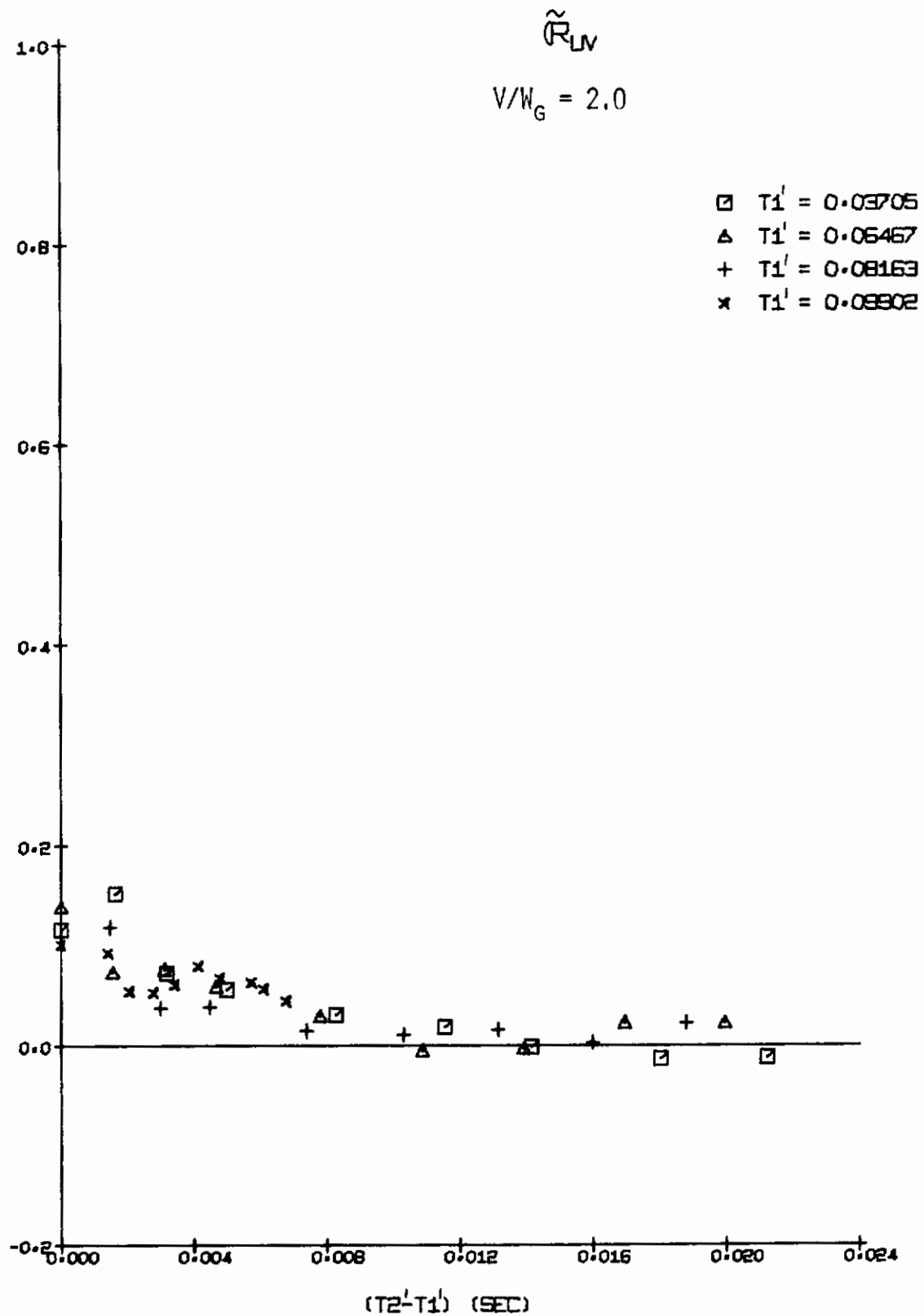
FIGURE 137a.   FLIGHT PATH TURBULENCE CORRELATION, 44" x 66" TUNNEL

325

$\widetilde{R}_{LIV}$

$V/W_G = 2.0$

□ $T1' = 0.05669$
△ $T1' = 0.07246$
+ $T1' = 0.09050$

$(T2'-T1')$ (SEC)
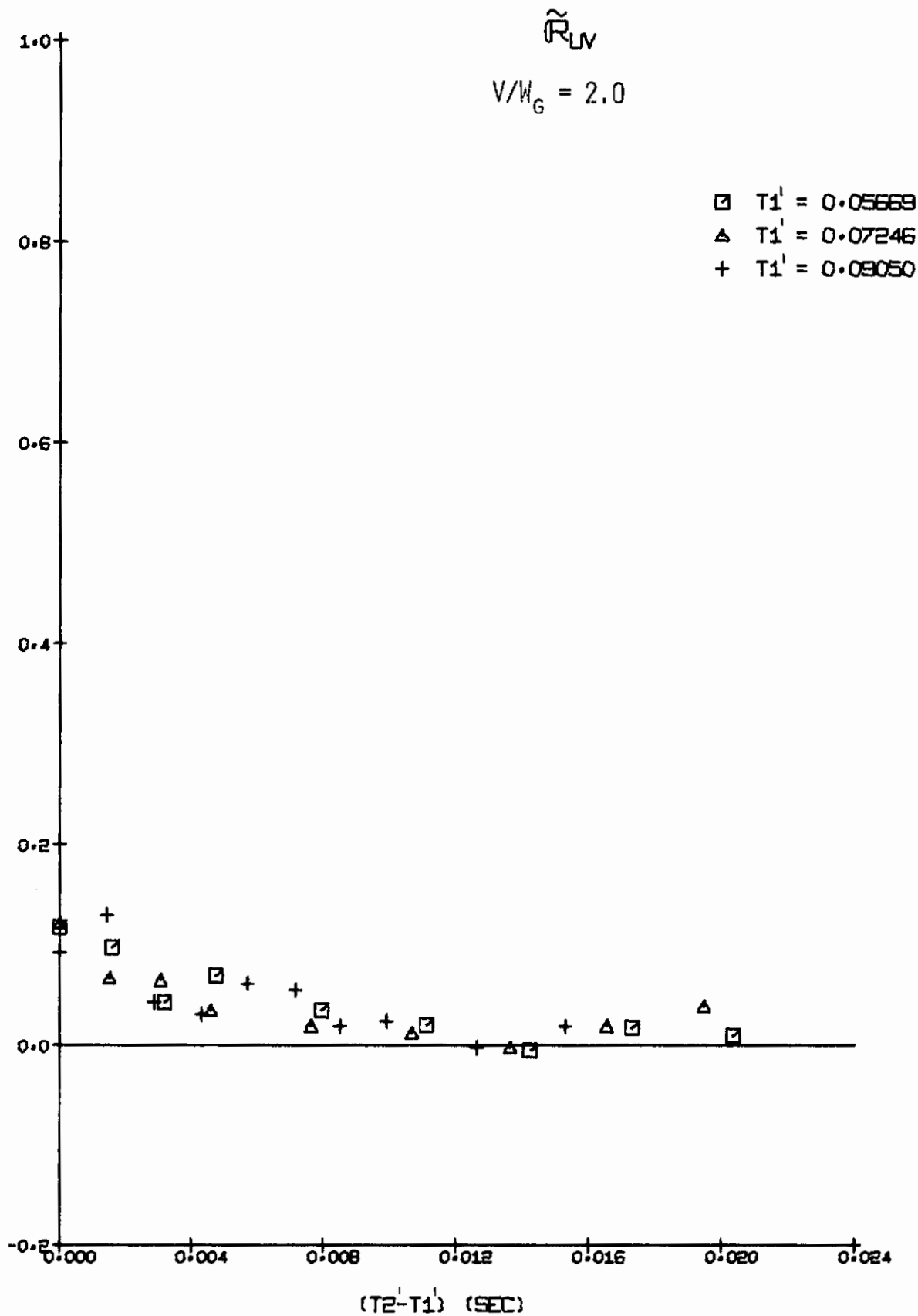
FIGURE 137b.   FLIGHT PATH TURBULENCE CORRELATION, 44" x 66" TUNNEL

326

$$\tilde{R}_{LW}$$

$$V/W_G = 1.0$$

⊠	$T1' = 3 \cdot 09700$
△	$T1' = 3 \cdot 45800$
+	$T1' = 3 \cdot 59300$
✗	$T1' = 3 \cdot 69100$

$(T2' - T1')$ (SEC)
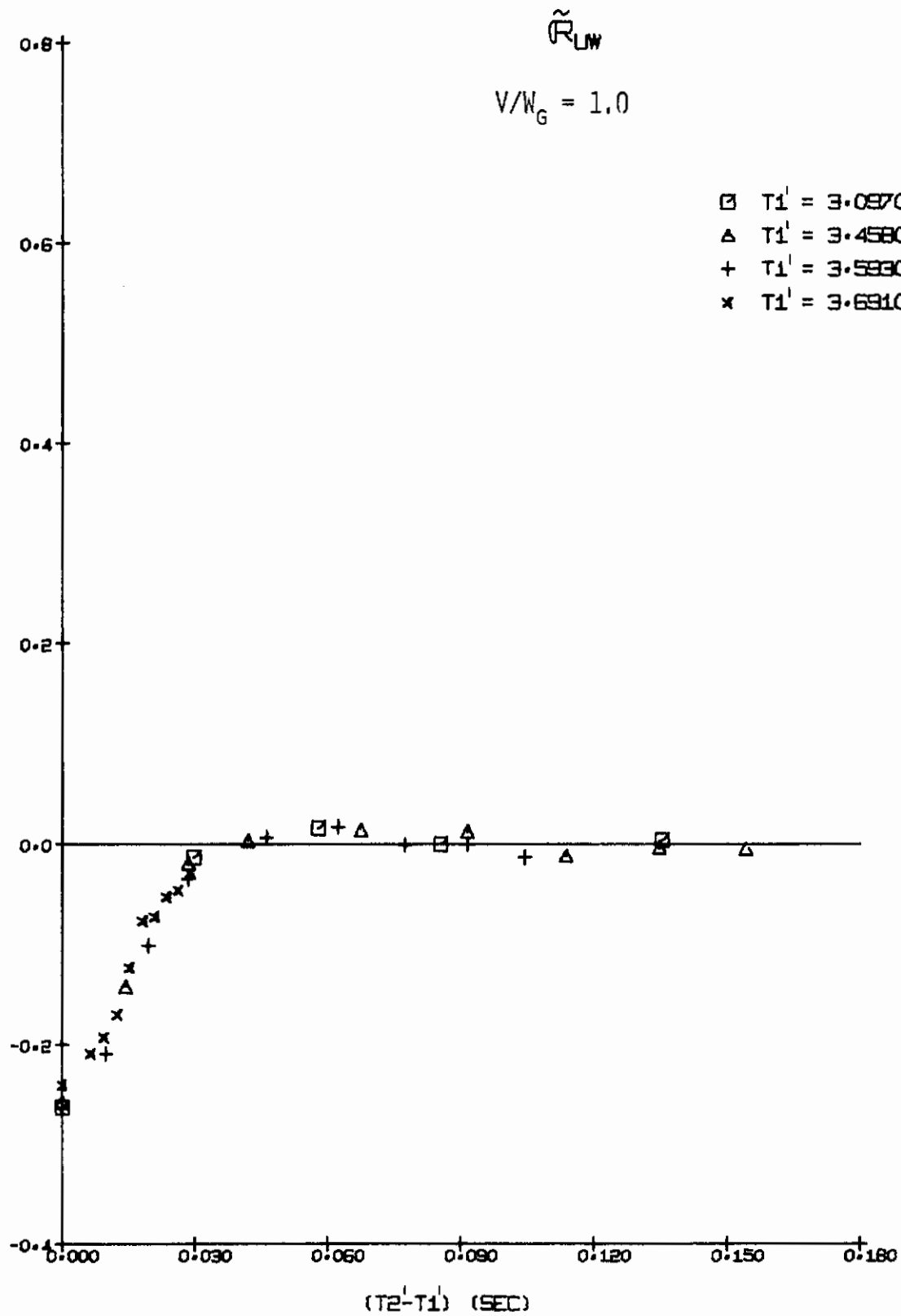
FIGURE 138a.   FLIGHT PATH TURBULENCE CORRELATION, 44" x 66" TUNNEL

327

$$\tilde{R}_{LW}$$

$$V/W_G = 1.0$$
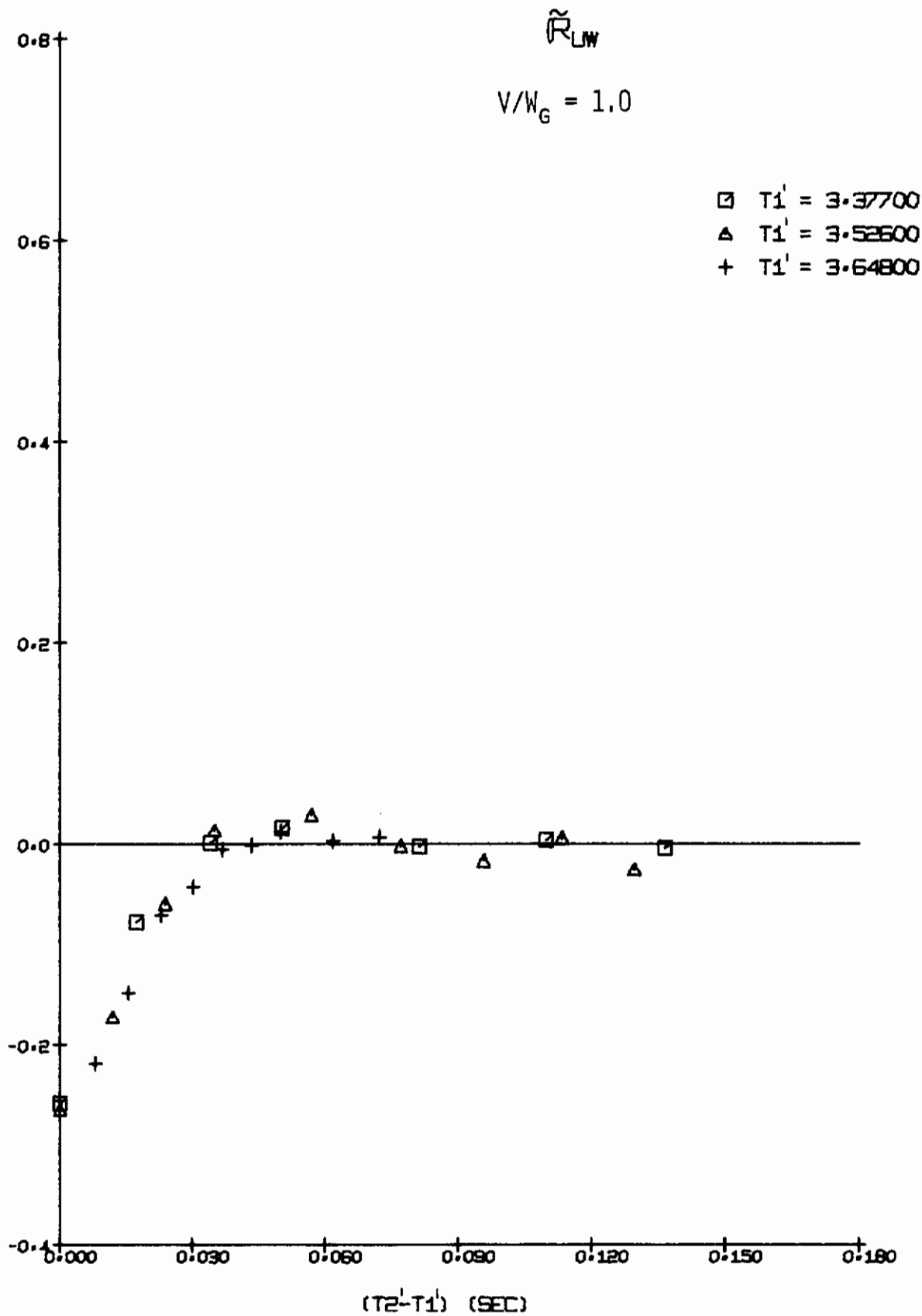
FIGURE 138b.   FLIGHT PATH TURBULENCE CORRELATION, 44" x 66" TUNNEL

$$\tilde{R}_{uw}$$

$$V/W_G = 1.5$$
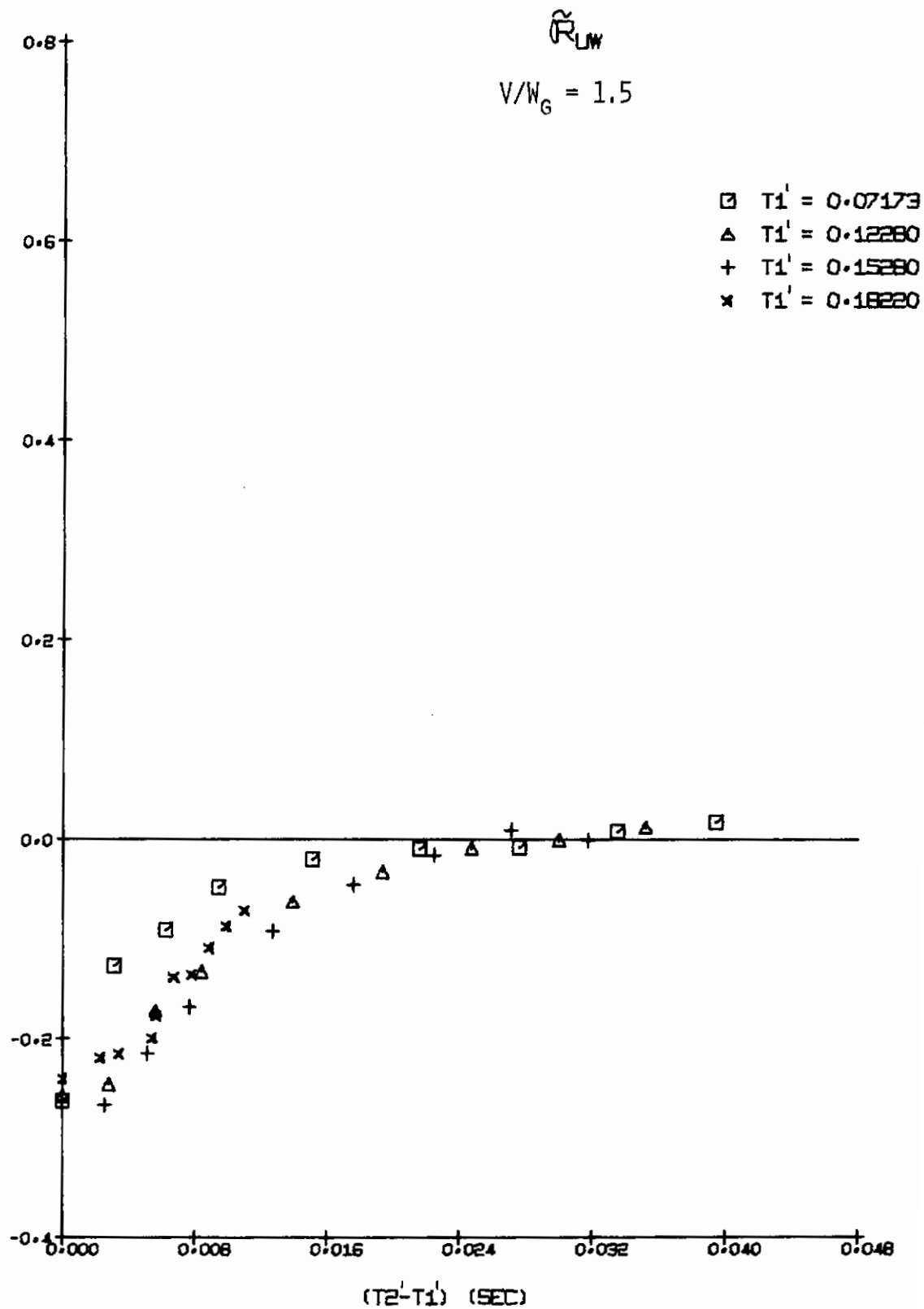
FIGURE 139a.   FLIGHT PATH TURBULENCE CORRELATION, 44" x 66" TUNNEL

$$\tilde{R}_{LW}$$

$$V/W_G = 1.5$$

Legend:
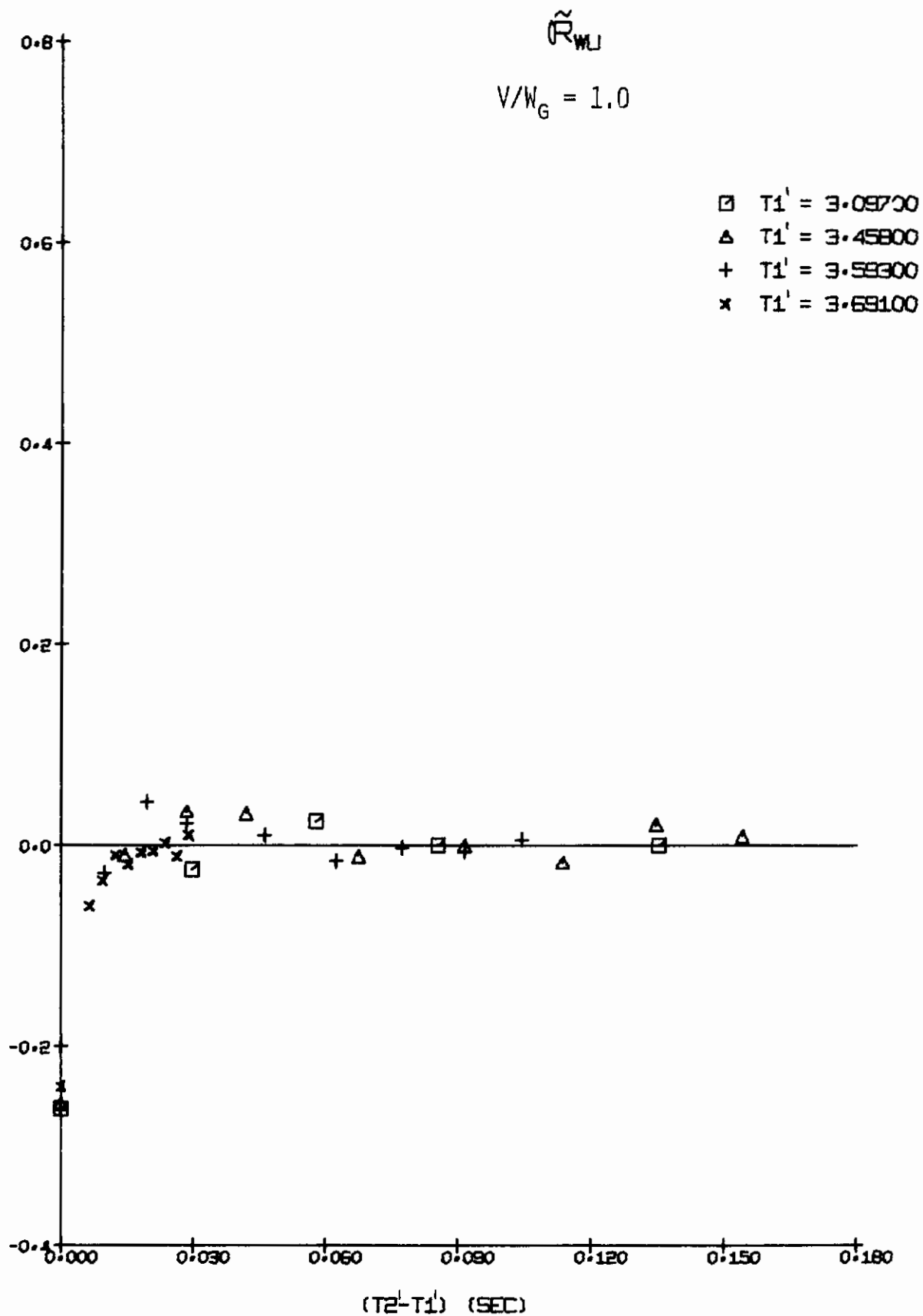- ▣ $T1' = 0.10830$
- △ $T1' = 0.13570$
- + $T1' = 0.16800$
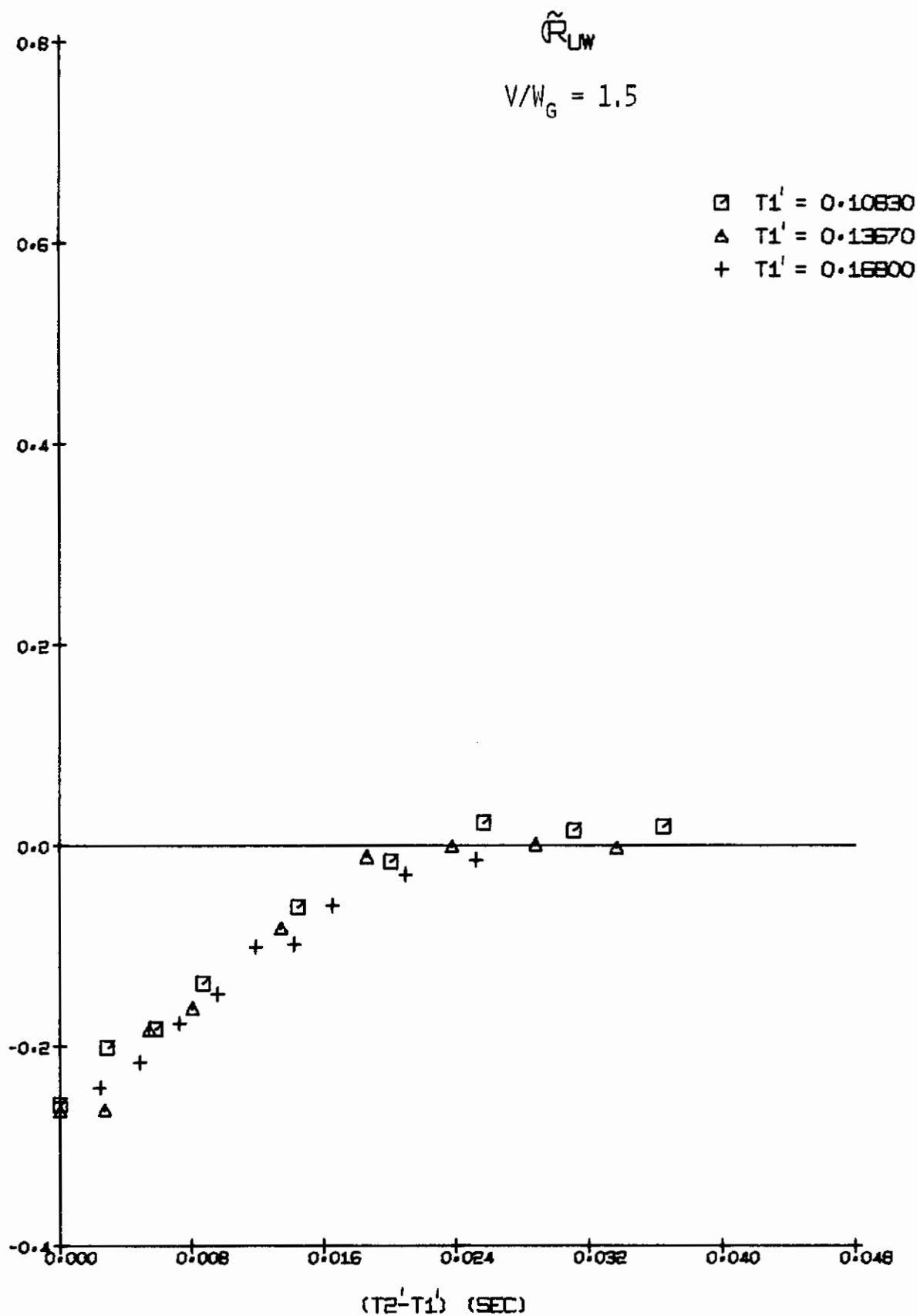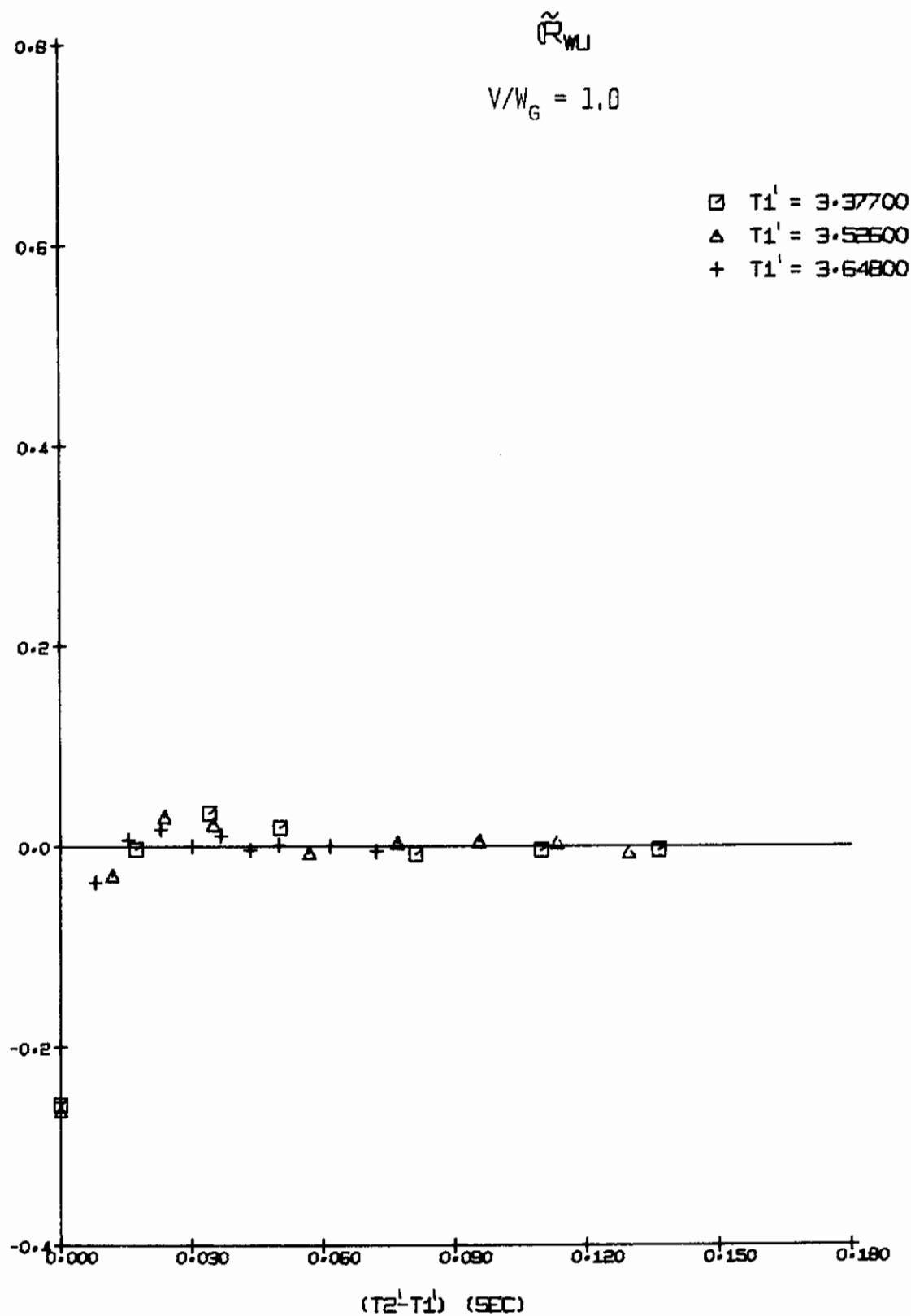
FIGURE 139b.   FLIGHT PATH TURBULENCE CORRELATION, 44" x 66" TUNNEL

330
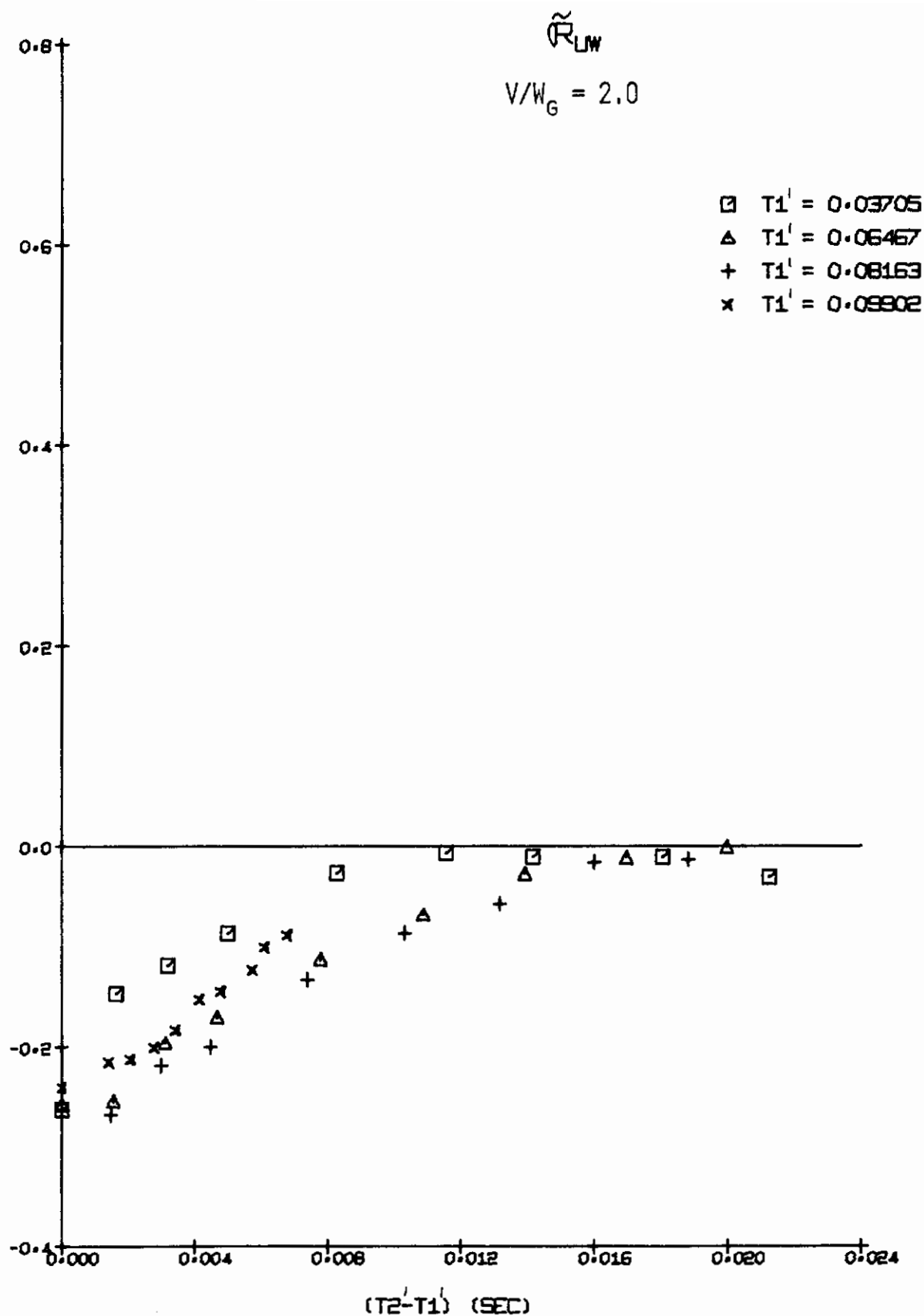
FIGURE 140a. FLIGHT PATH TURBULENCE CORRELATION, 44" x 66" TUNNEL
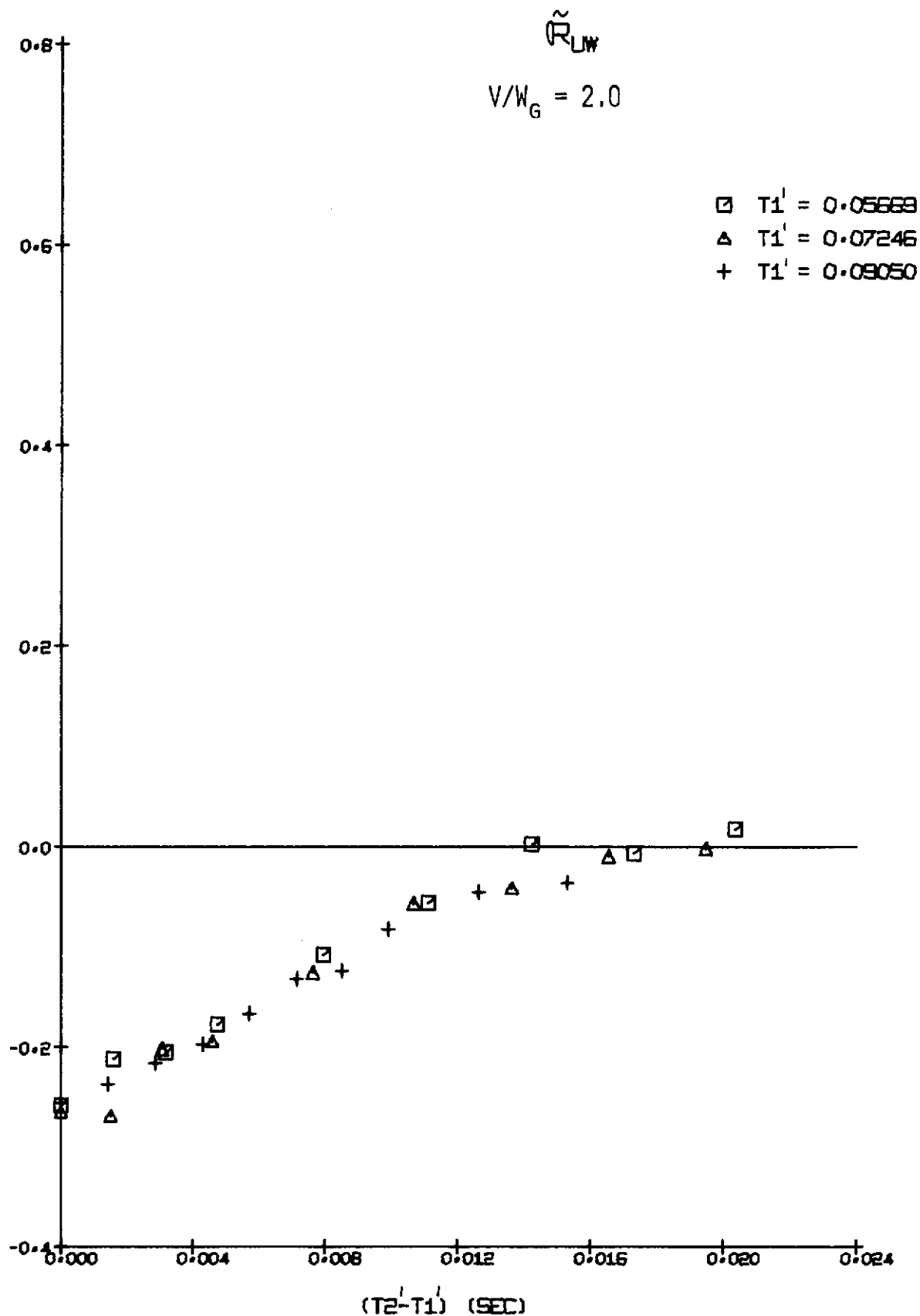
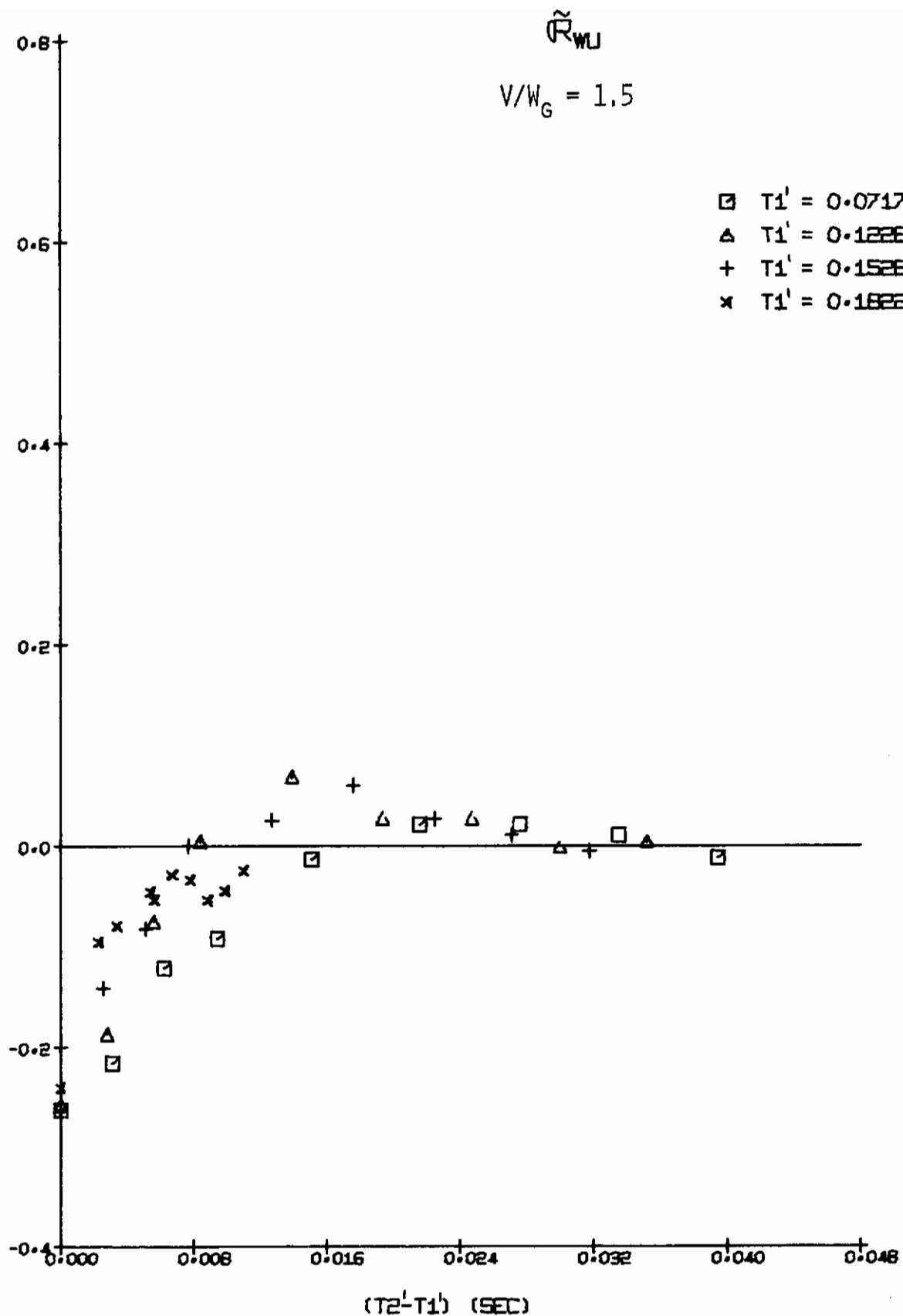FIGURE 140b.   FLIGHT PATH TURBULENCE CORRELATION, 44" x 66" TUNNEL

332
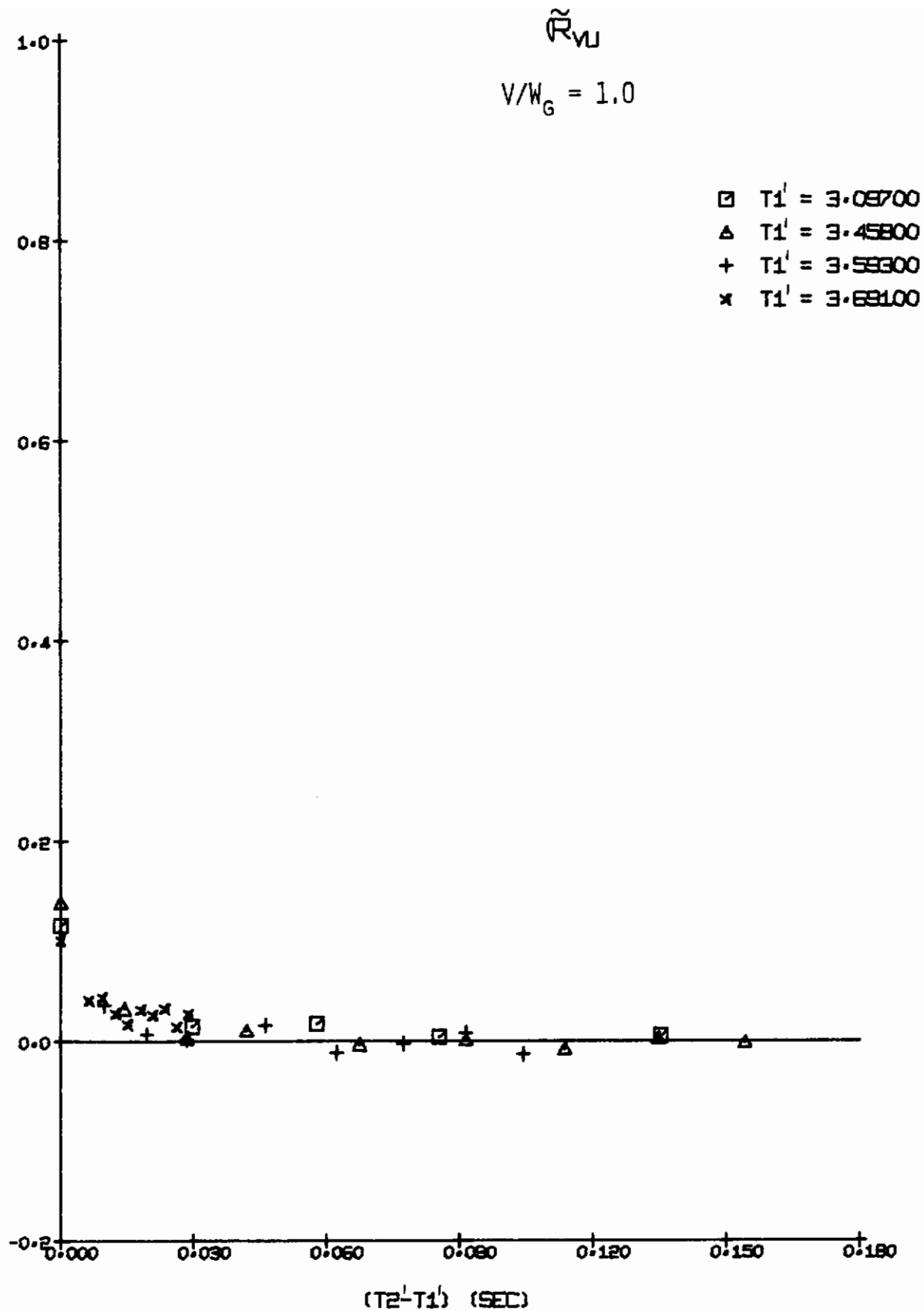
FIGURE 141a. FLIGHT PATH TURBULENCE CORRELATION, 44" x 66" TUNNEL

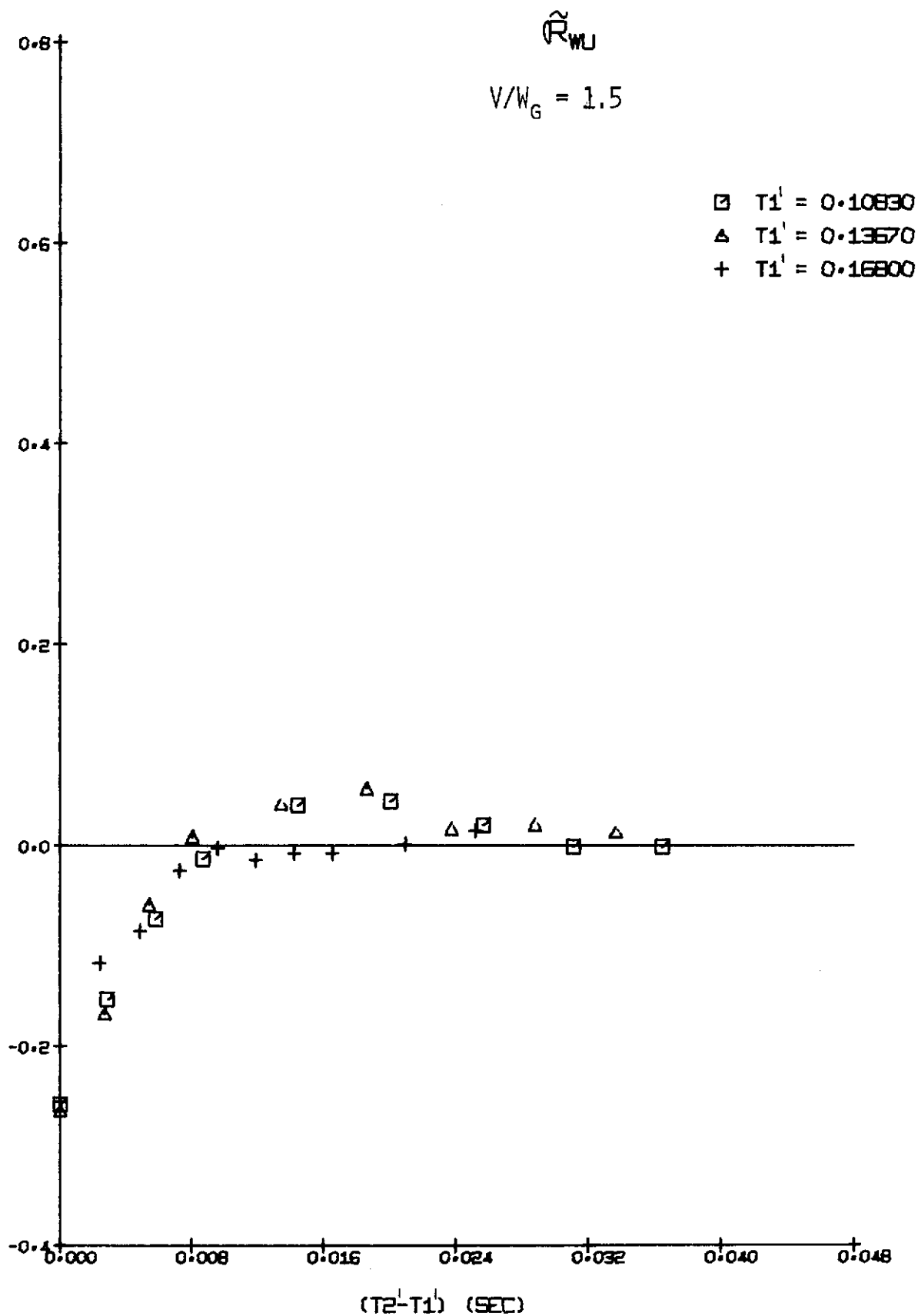$$\tilde{R}_{VU}$$

$$V/W_G = 1.0$$
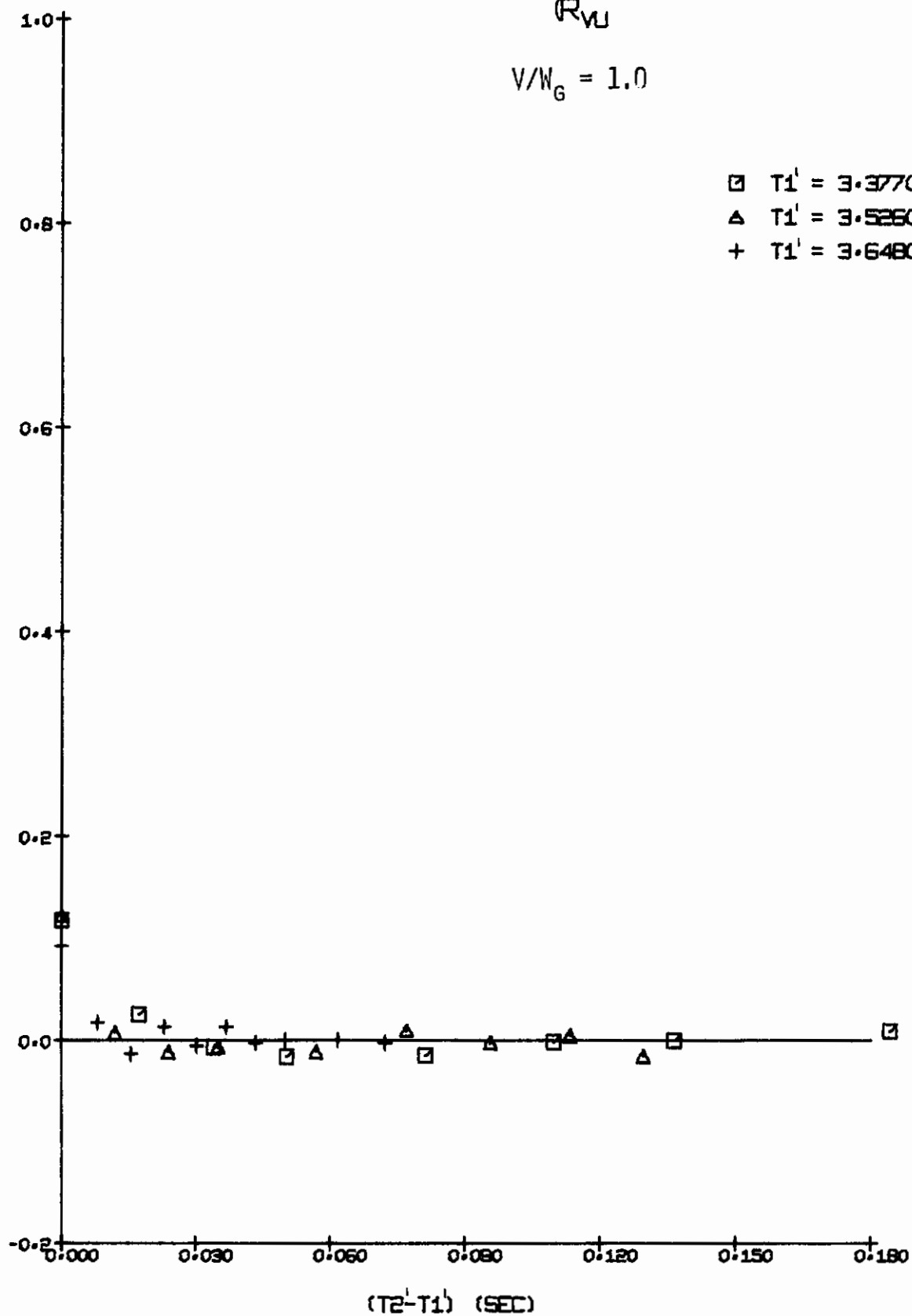
FIGURE 141b.   FLIGHT PATH TURBULENCE CORRELATION, 44" x 66" TUNNEL
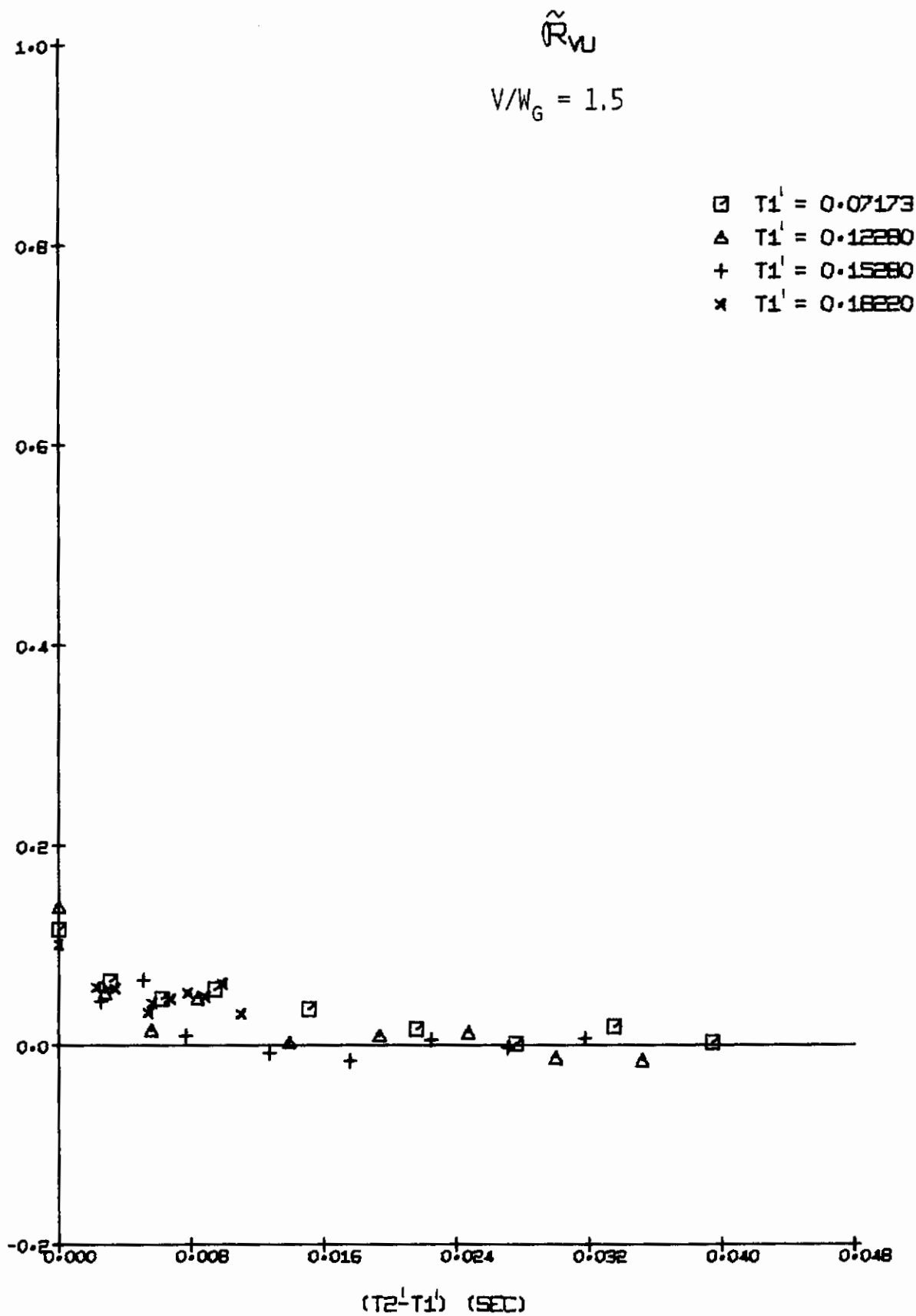
FIGURE 142a.   FLIGHT PATH TURBULENCE CORRELATION, 44" x 66" TUNNEL

335

$$\tilde{\tilde{R}}_{VU}$$

$$V/W_G = 1.5$$

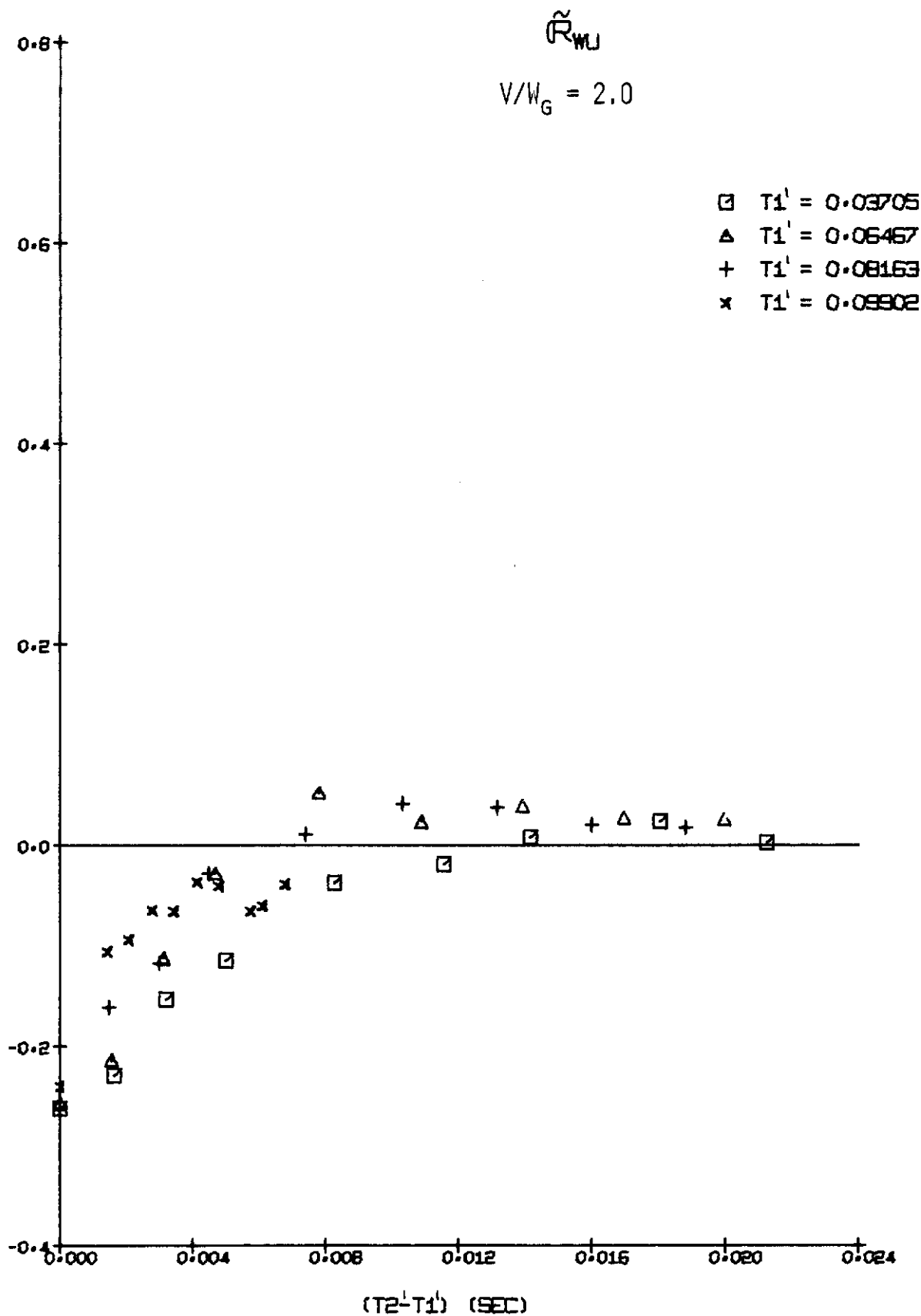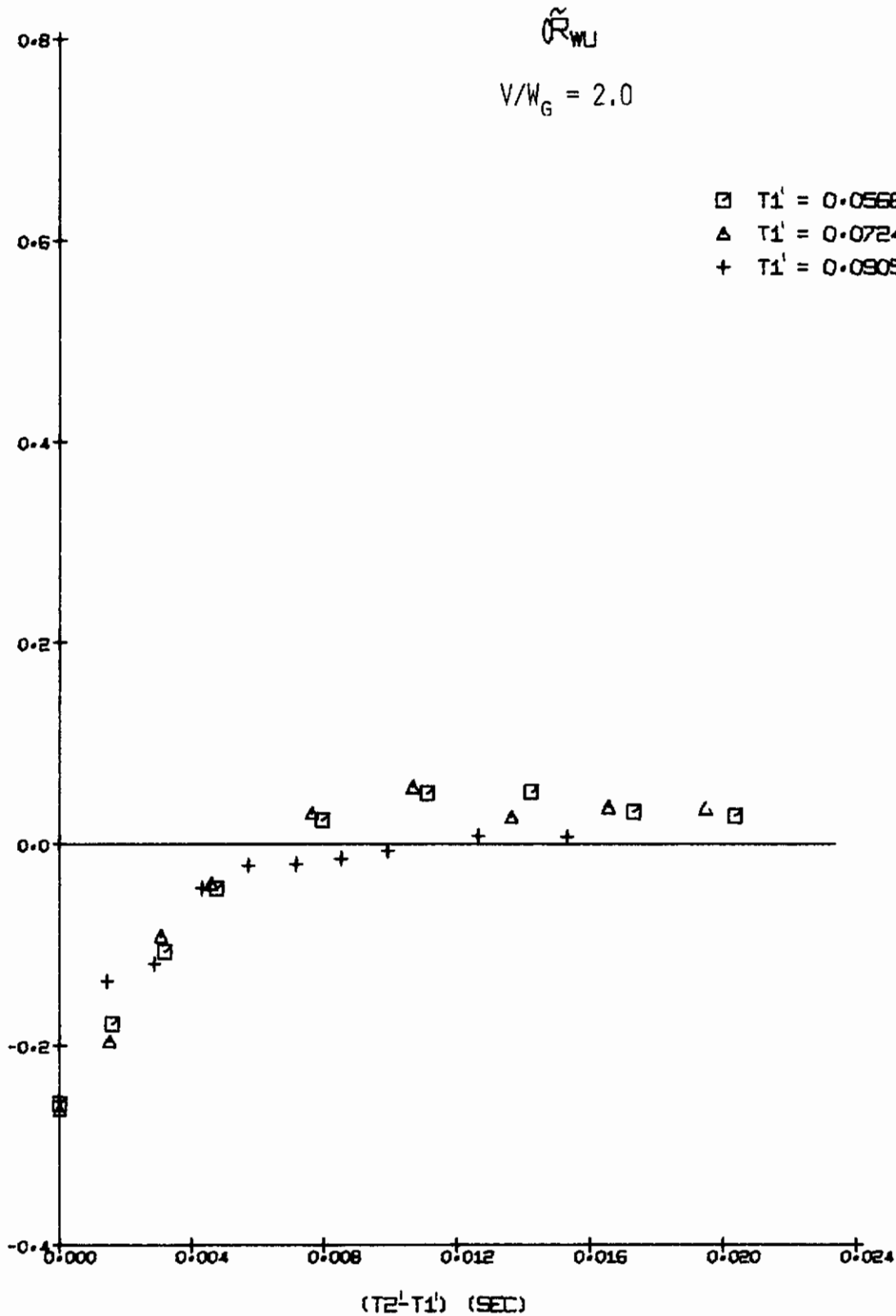Legend:

☑ T1' = 0·10830
△ T1' = 0·13570
+ T1' = 0·16800
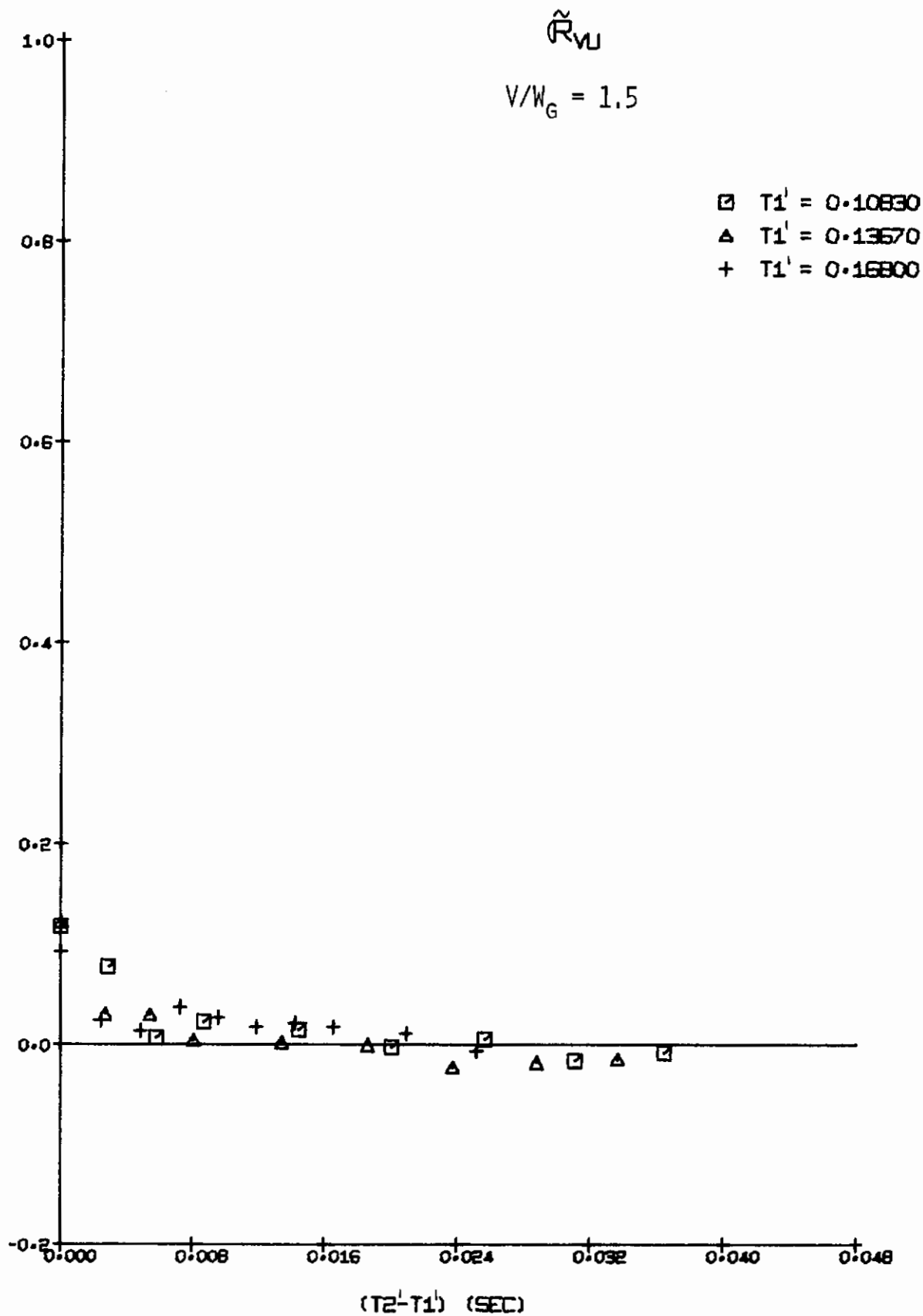
FIGURE 142b.   FLIGHT PATH TURBULENCE CORRELATION, 44" x 66" TUNNEL

336
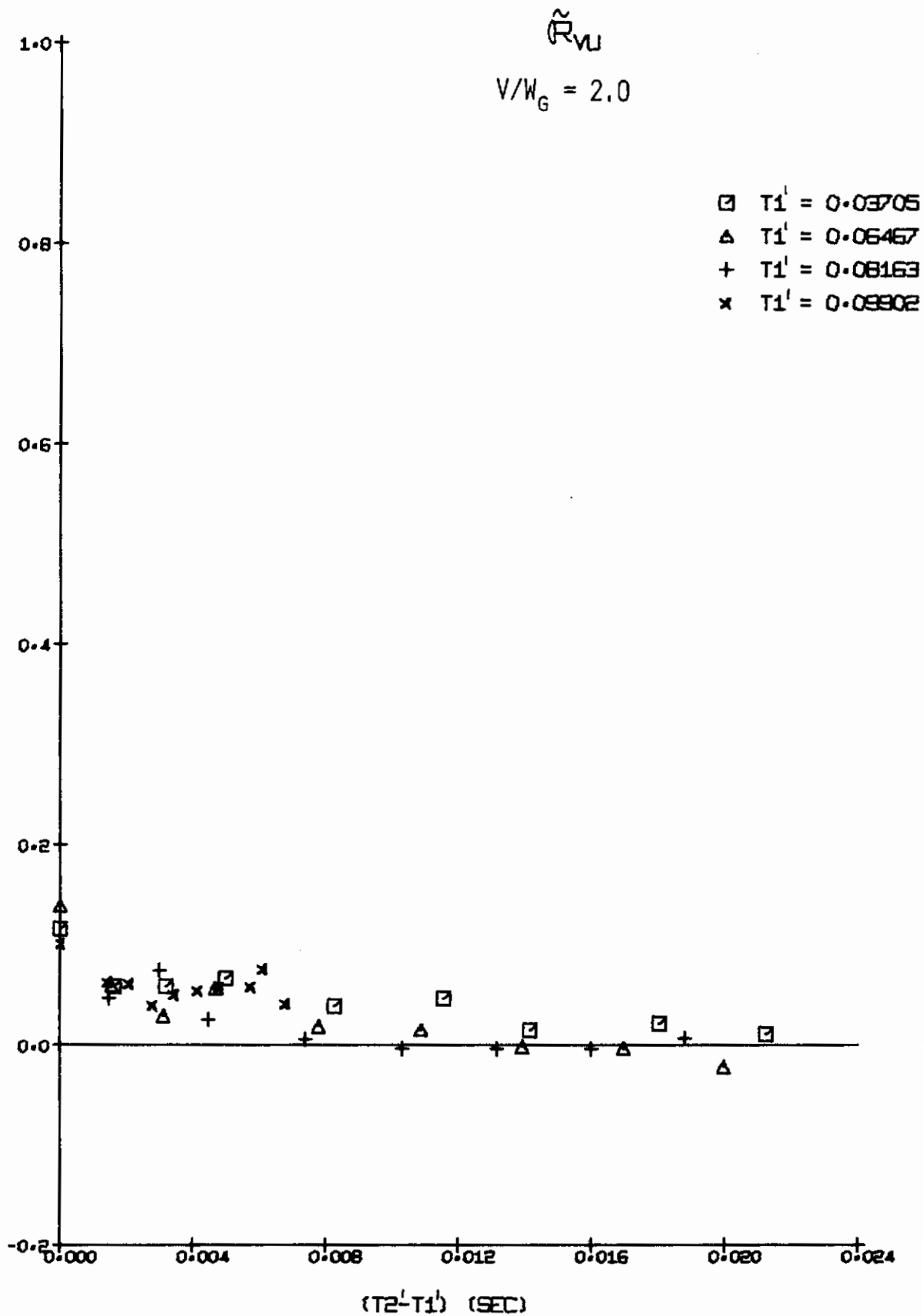
FIGURE 143a.   FLIGHT PATH TURBULENCE CORRELATION, 44" x 66" TUNNEL

$\tilde{R}_{VU}$

$V/W_G = 2.0$

Legend:
- ☑ $T1' = 0.05669$
- △ $T1' = 0.07246$
- + $T1' = 0.09050$

x-axis: $(T2' - T1')$ (SEC)
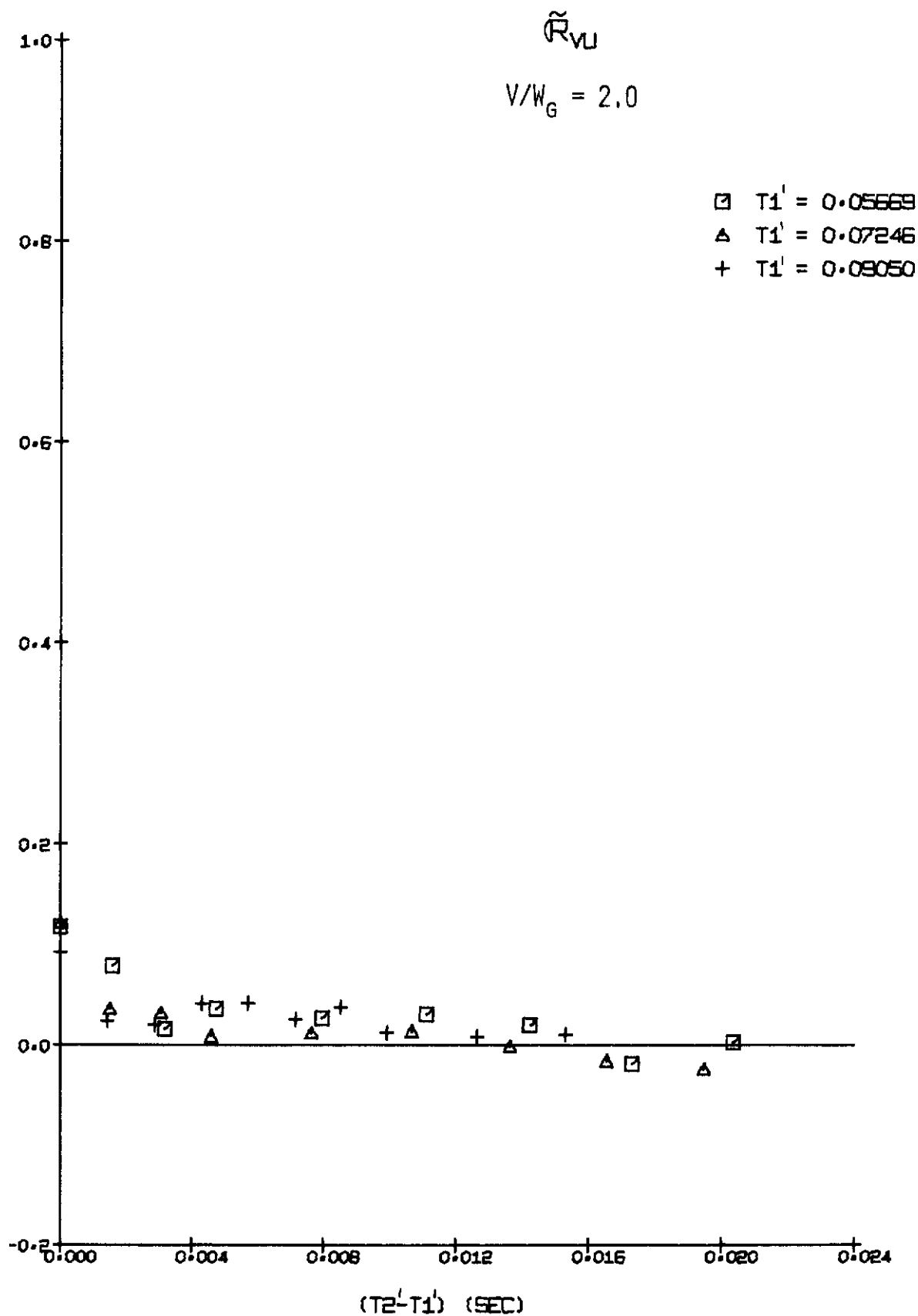
FIGURE 143b. FLIGHT PATH TURBULENCE CORRELATION, 44" x 66" TUNNEL

338
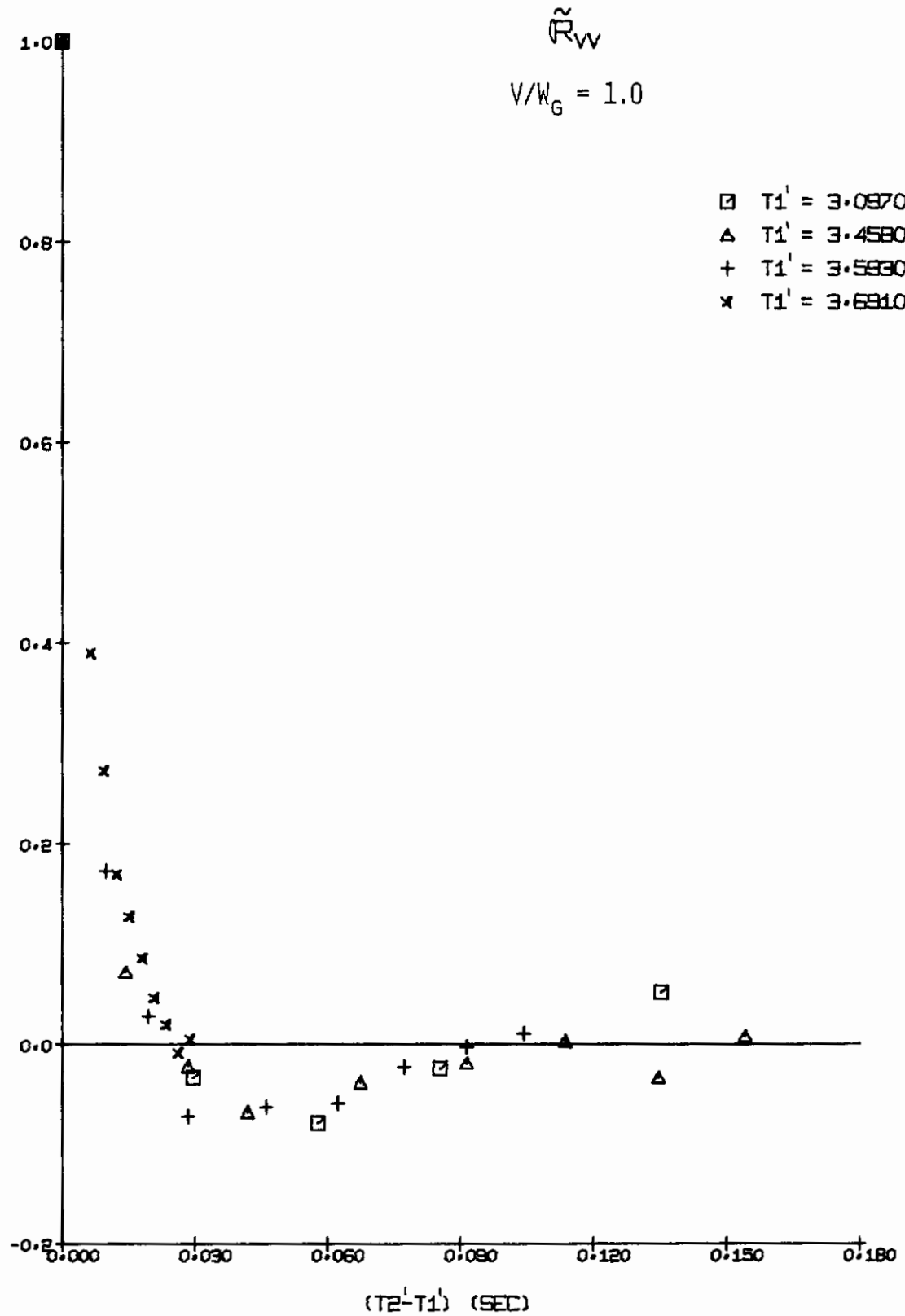
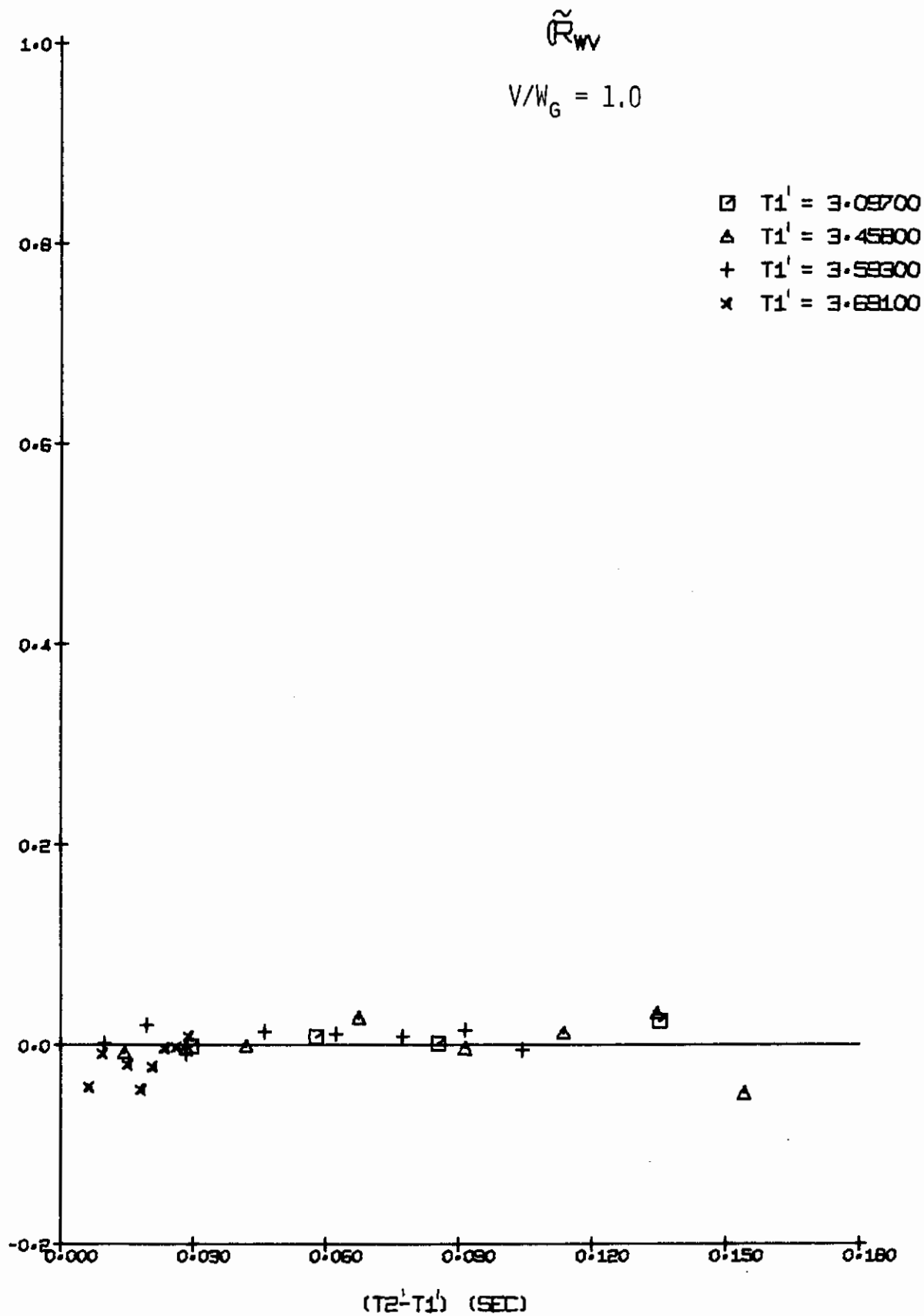FIGURE 144a.   FLIGHT PATH TURBULENCE CORRELATION, 44" x 66" TUNNEL

$\tilde{R}_{VV}$

$V/W_G = 1.0$

Legend:
- ☑ $T1' = 3.37700$
- △ $T1' = 3.52600$
- + $T1' = 3.64800$
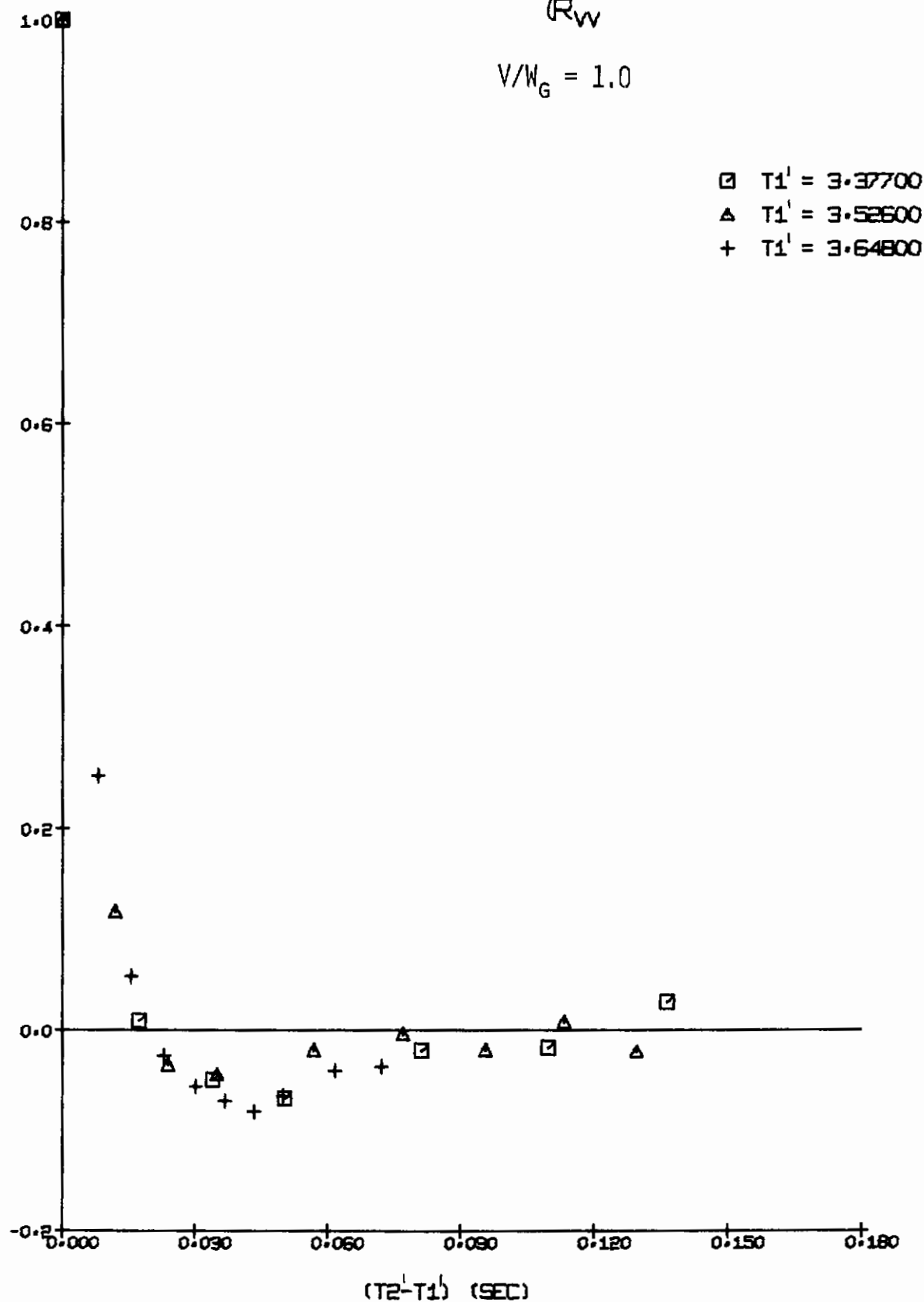
FIGURE 144b.   FLIGHT PATH TURBULENCE CORRELATION, 44" x 66" TUNNEL
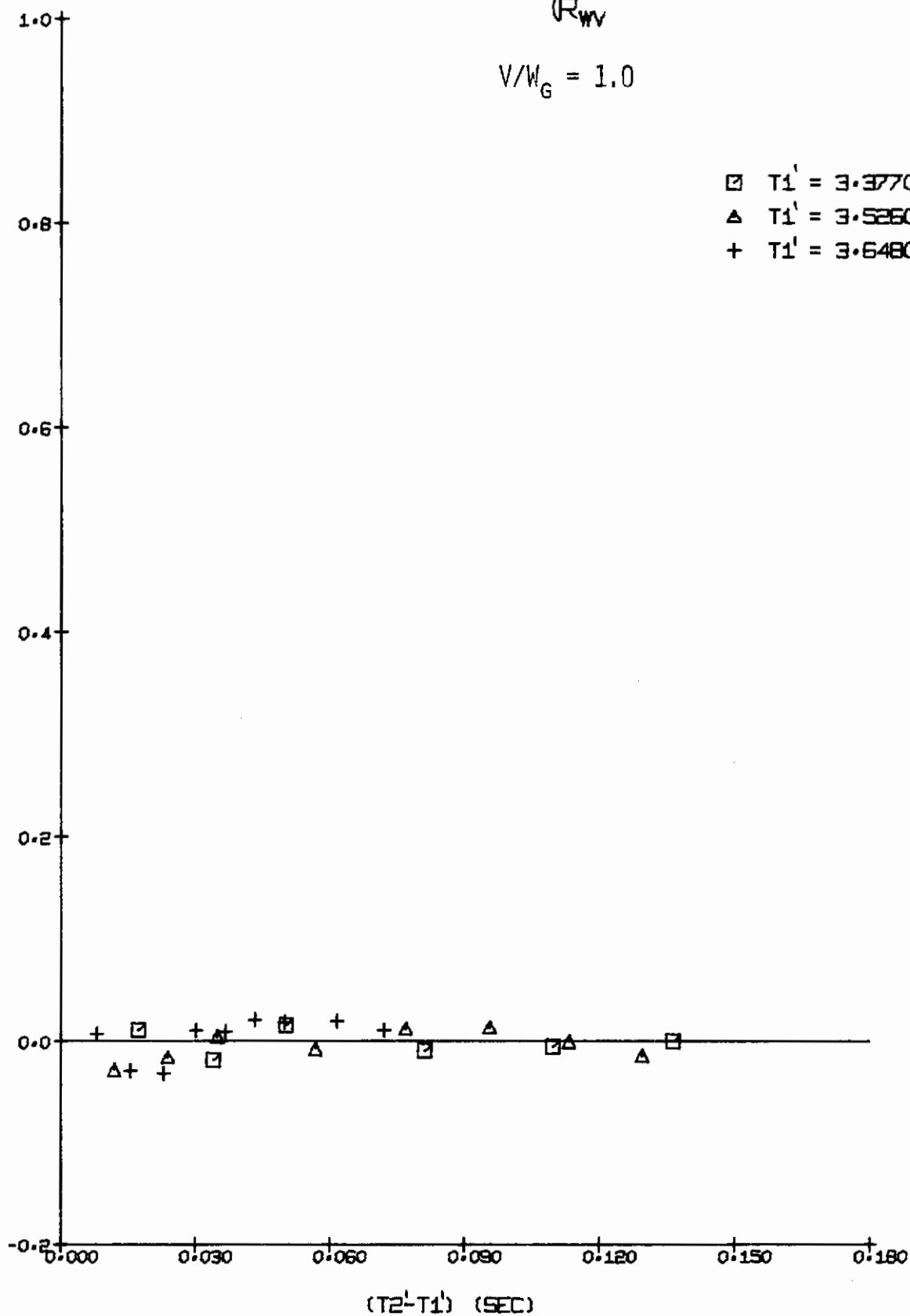
340
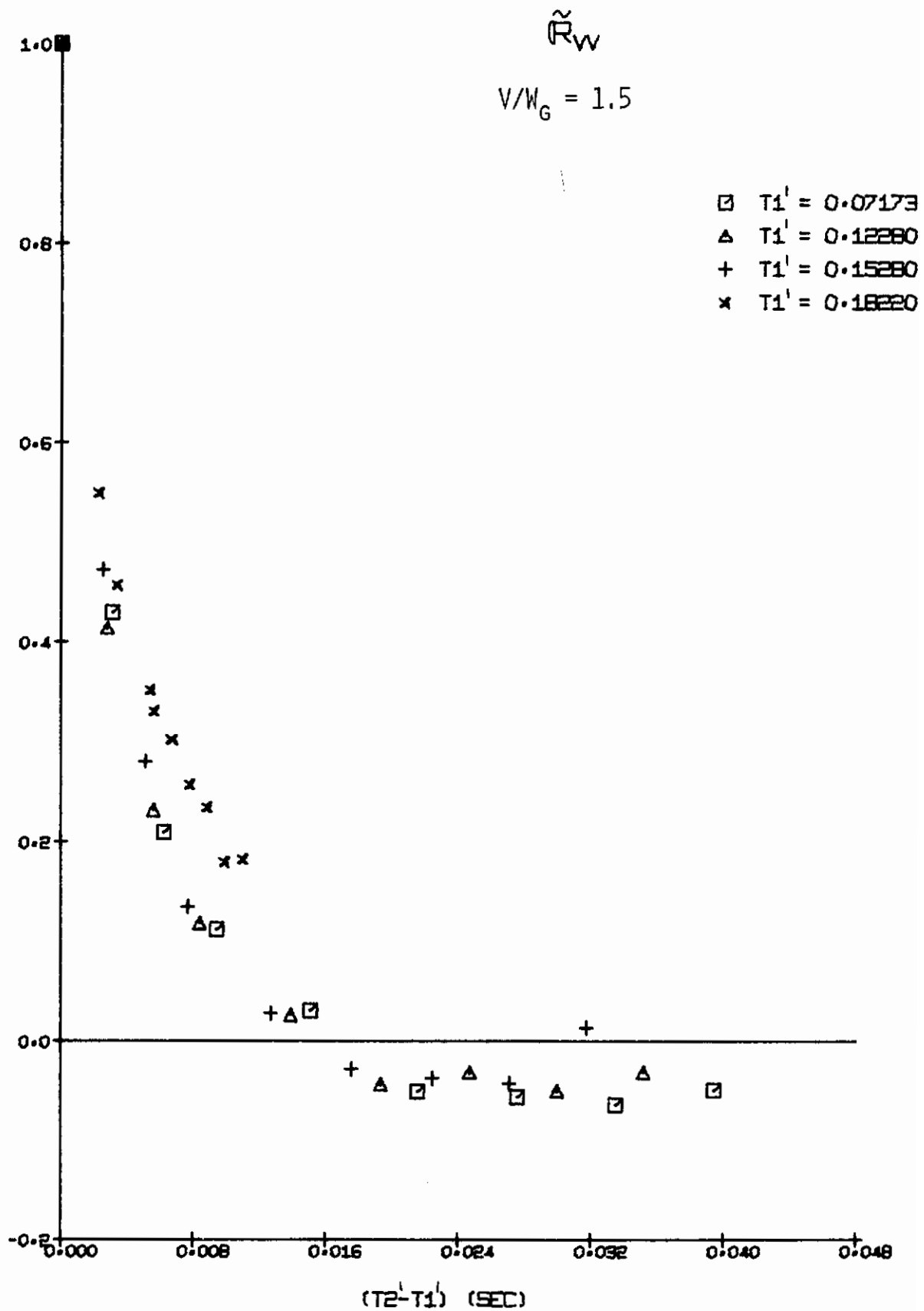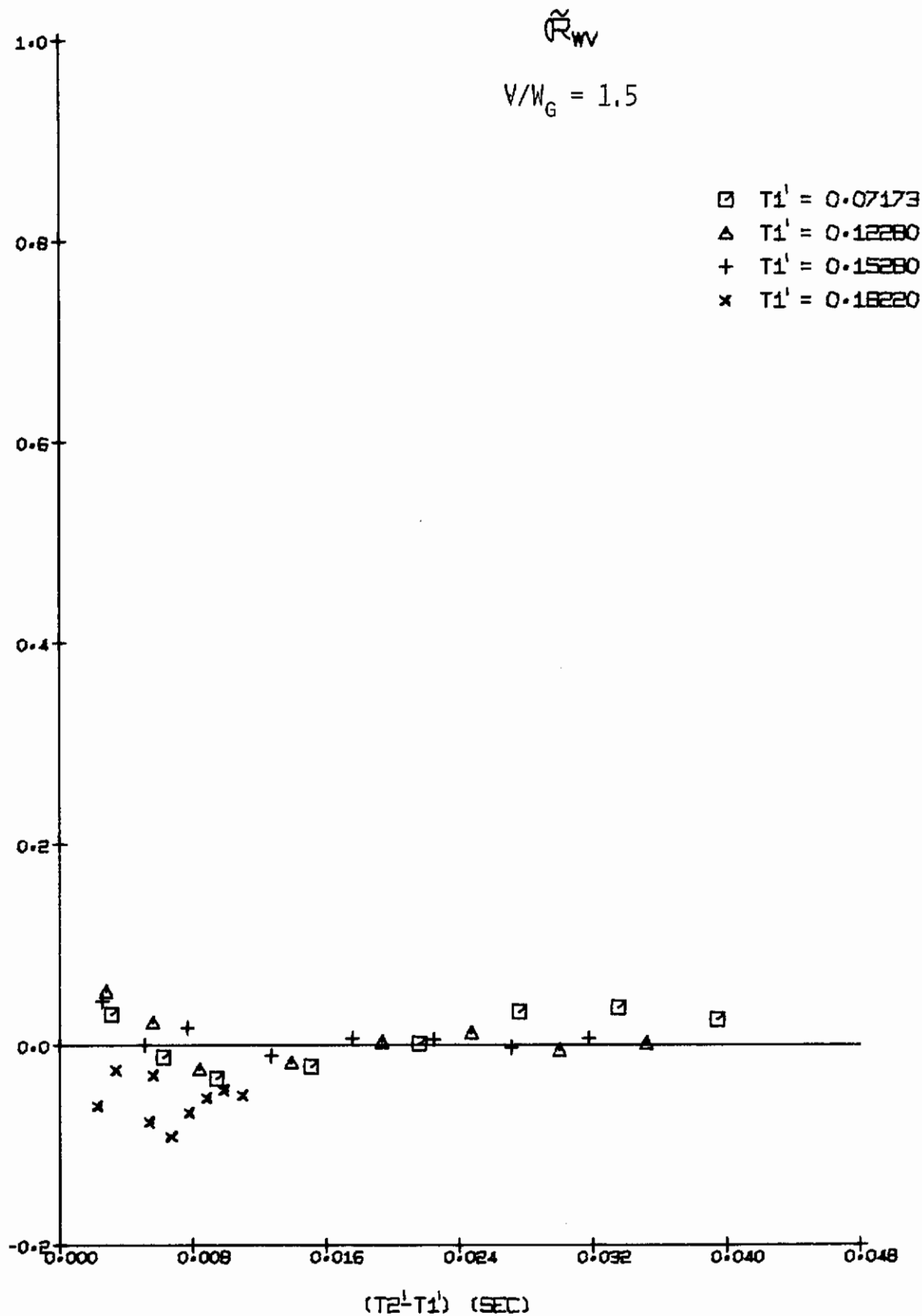
FIGURE 145a.   FLIGHT PATH TURBULENCE CORRELATION, 44" x 66" TUNNEL

341
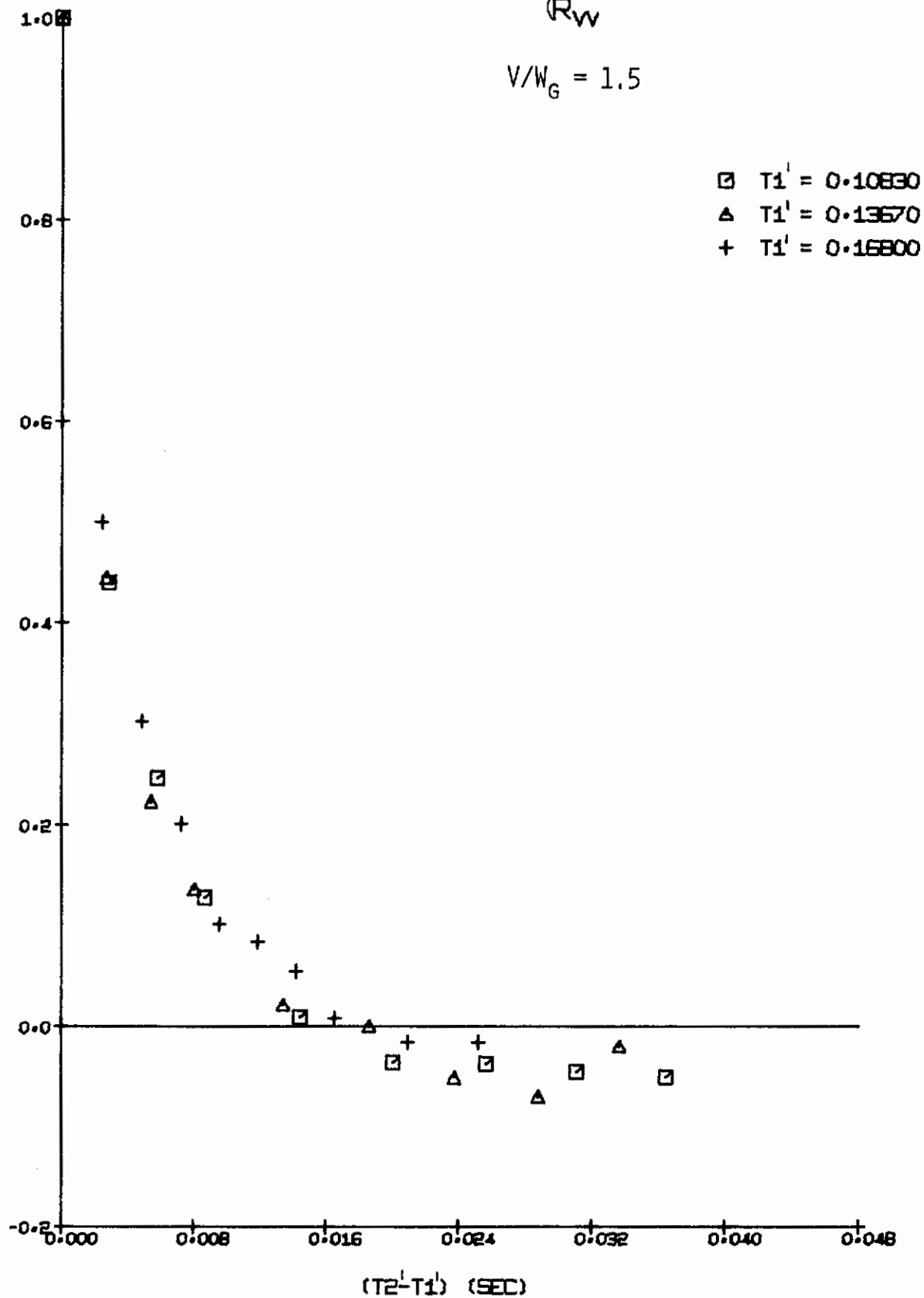
FIGURE 145b.   FLIGHT PATH TURBULENCE CORRELATION, 44" x 66" TUNNEL

342

$$\tilde{R}_{vv}$$

$$V/W_G = 2.0$$

☑ $T_1' = 0.03705$
△ $T_1' = 0.06467$
+ $T_1' = 0.08153$
✕ $T_1' = 0.09302$

$(T_2' - T_1')$ (SEC)
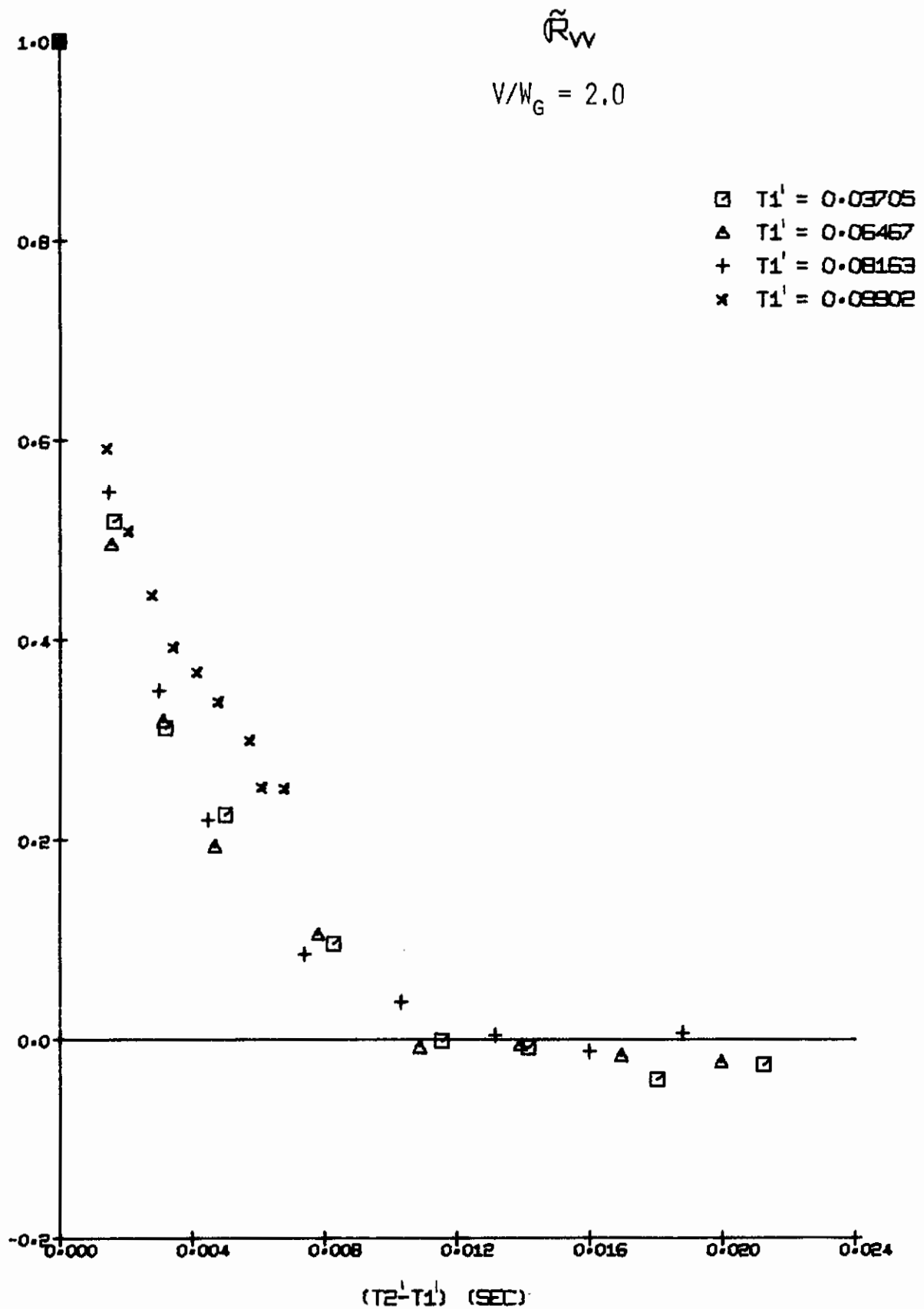
FIGURE 146a. FLIGHT PATH TURBULENCE CORRELATION, 44" x 66" TUNNEL

343

$$\tilde{R}_{VV}$$

$$V/W_G = 2.0$$

Legend:
☐ $T1' = 0.05669$
△ $T1' = 0.07246$
+ $T1' = 0.09050$

$(T2' - T1')$ (SEC)

FIGURE 146b.   FLIGHT PATH TURBULENCE CORRELATION, 44" x 66" TUNNEL

344

$\tilde{R}_{VW}$

$V/W_G = 1.0$

☑	$T_1' = 3.09700$
△	$T_1' = 3.45800$
+	$T_1' = 3.59300$
✕	$T_1' = 3.69100$

$(T_2' - T_1')$ (SEC)

FIGURE 147a. FLIGHT PATH TURBULENCE CORRELATION, 44" x 66" TUNNEL

345

$$\tilde{R}_{VW}$$

$$V/W_G = 1.0$$

FIGURE 147b.   FLIGHT PATH TURBULENCE CORRELATION, 44" x 66" TUNNEL

346

FIGURE 148a.   FLIGHT PATH TURBULENCE CORRELATION, 44" x 66" TUNNEL

347

$$\tilde{R}_{VW}$$

$$V/W_G = 1.5$$
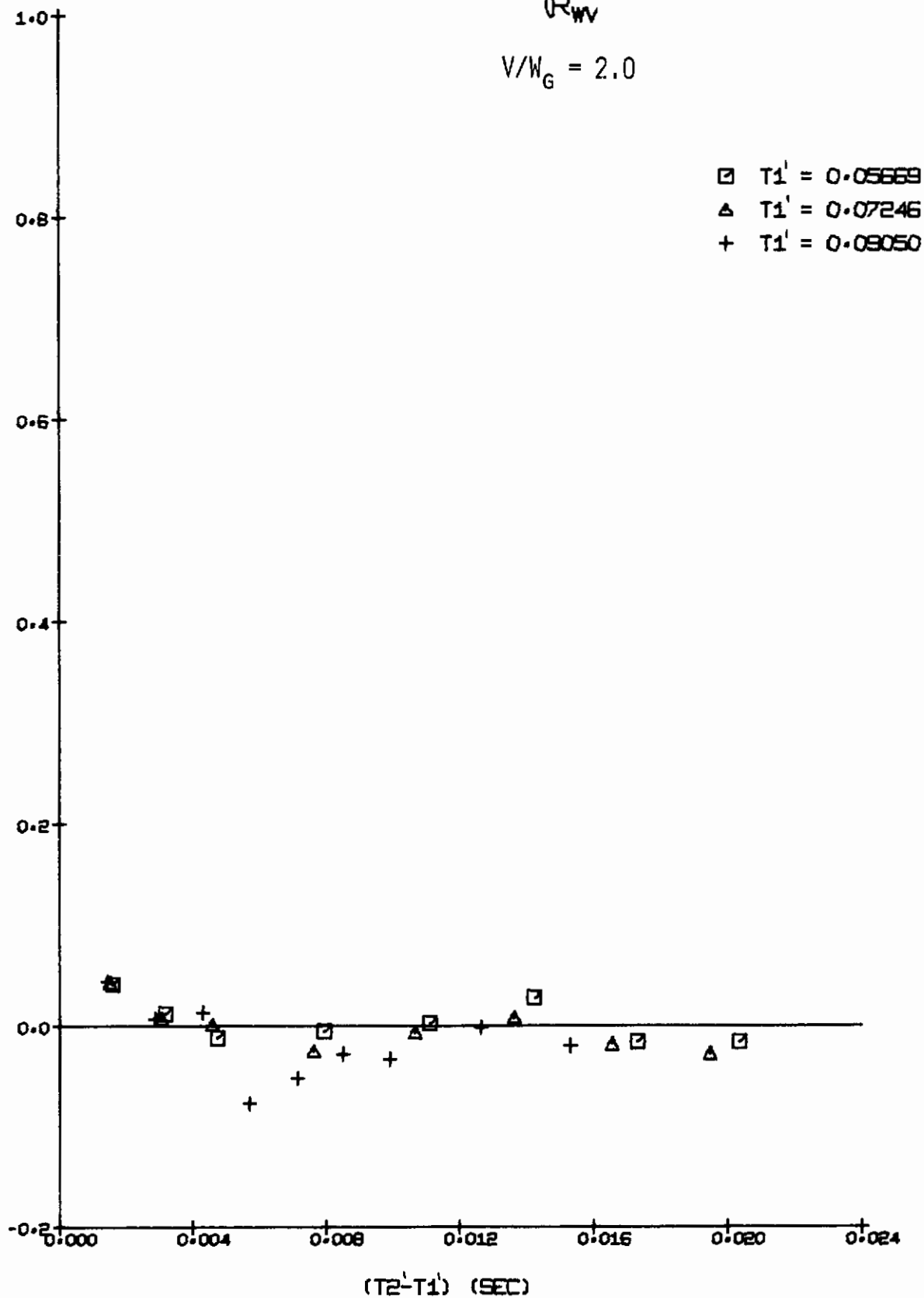
☑ T1' = 0·10830
△ T1' = 0·13670
+ T1' = 0·16800

FIGURE 148b.   FLIGHT PATH TURBULENCE CORRELATION, 44" x 66" TUNNEL

348

FIGURE 149a.   FLIGHT PATH TURBULENCE CORRELATION, 44" x 66" TUNNEL

349
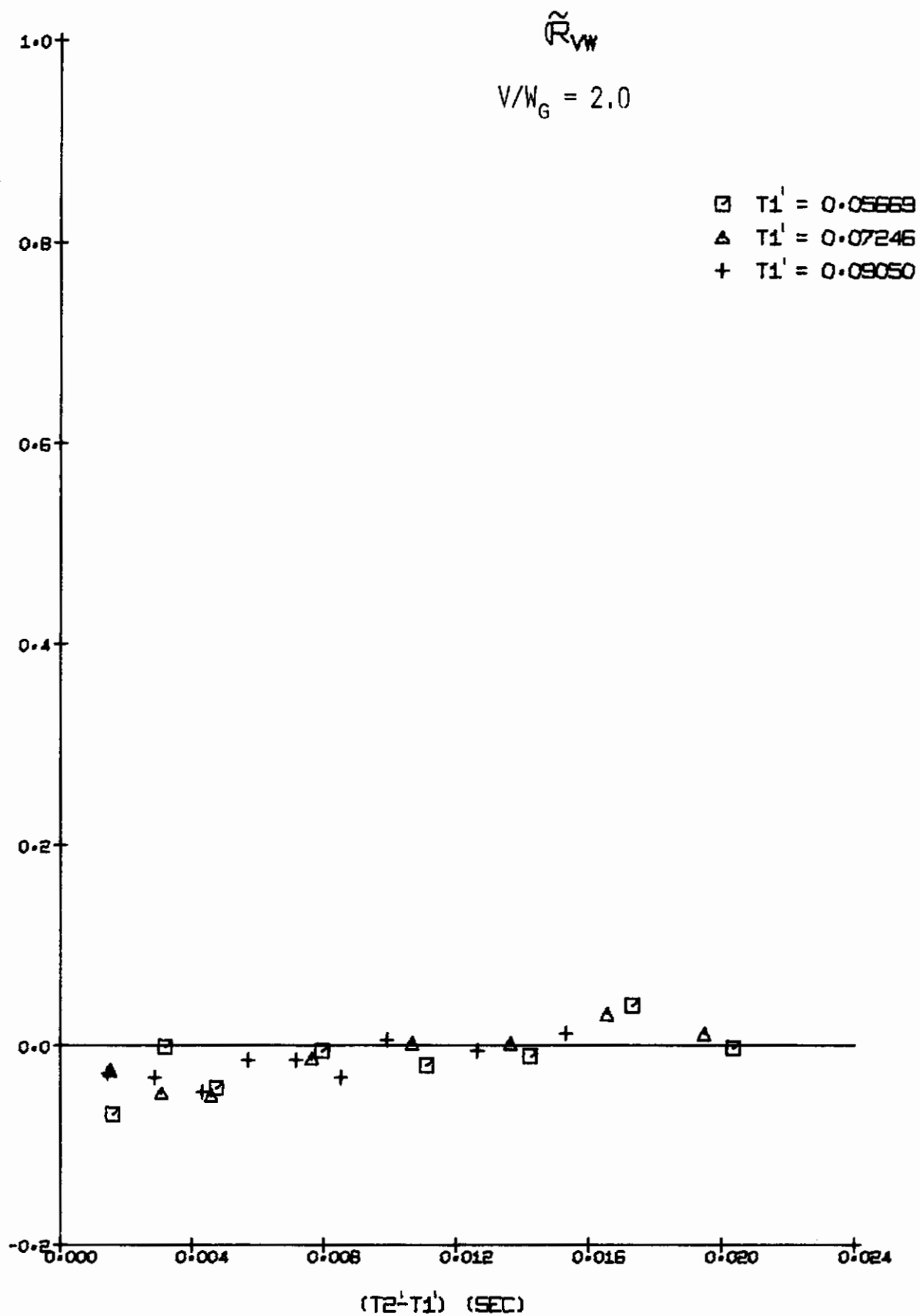
FIGURE 149b.   FLIGHT PATH TURBULENCE CORRELATION, 44" x 66" TUNNEL

350

$$\tilde{R}_{WU}$$

$$V/W_G = 1.0$$

- ☑ T1' = 3·09700
- △ T1' = 3·45800
- + T1' = 3·59300
- ✕ T1' = 3·69100

FIGURE 150a.   FLIGHT PATH TURBULENCE CORRELATION, 44" x 66" TUNNEL

351

$$\tilde{R}_{WU}$$

$$V/W_G = 1.0$$

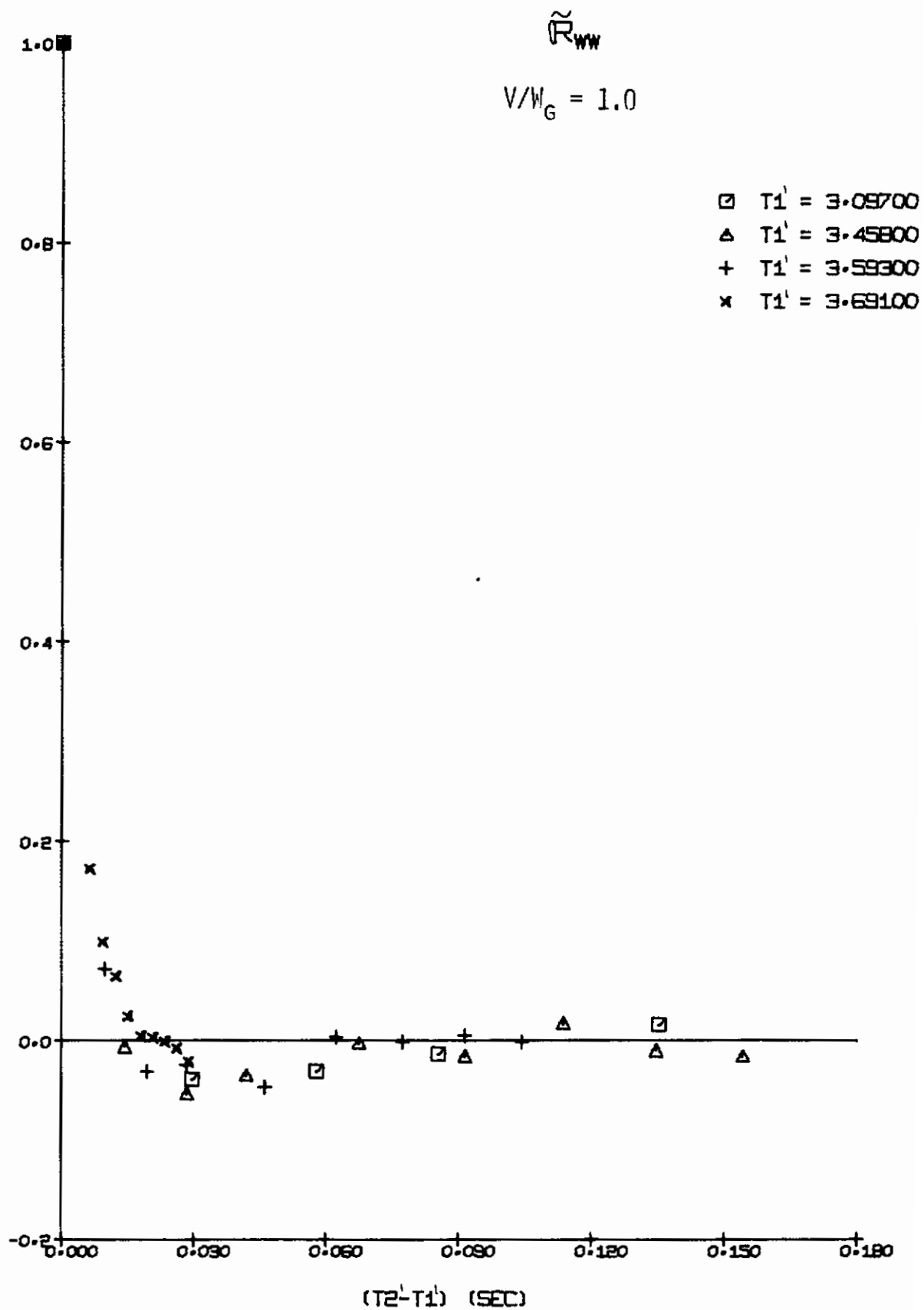□ T1' = 3.37700
△ T1' = 3.52500
+ T1' = 3.64800

FIGURE 150b.   FLIGHT PATH TURBULENCE CORRELATION, 44" x 66" TUNNEL

352

FIGURE 151a.   FLIGHT PATH TURBULENCE CORRELATION, 44" x 66" TUNNEL

353

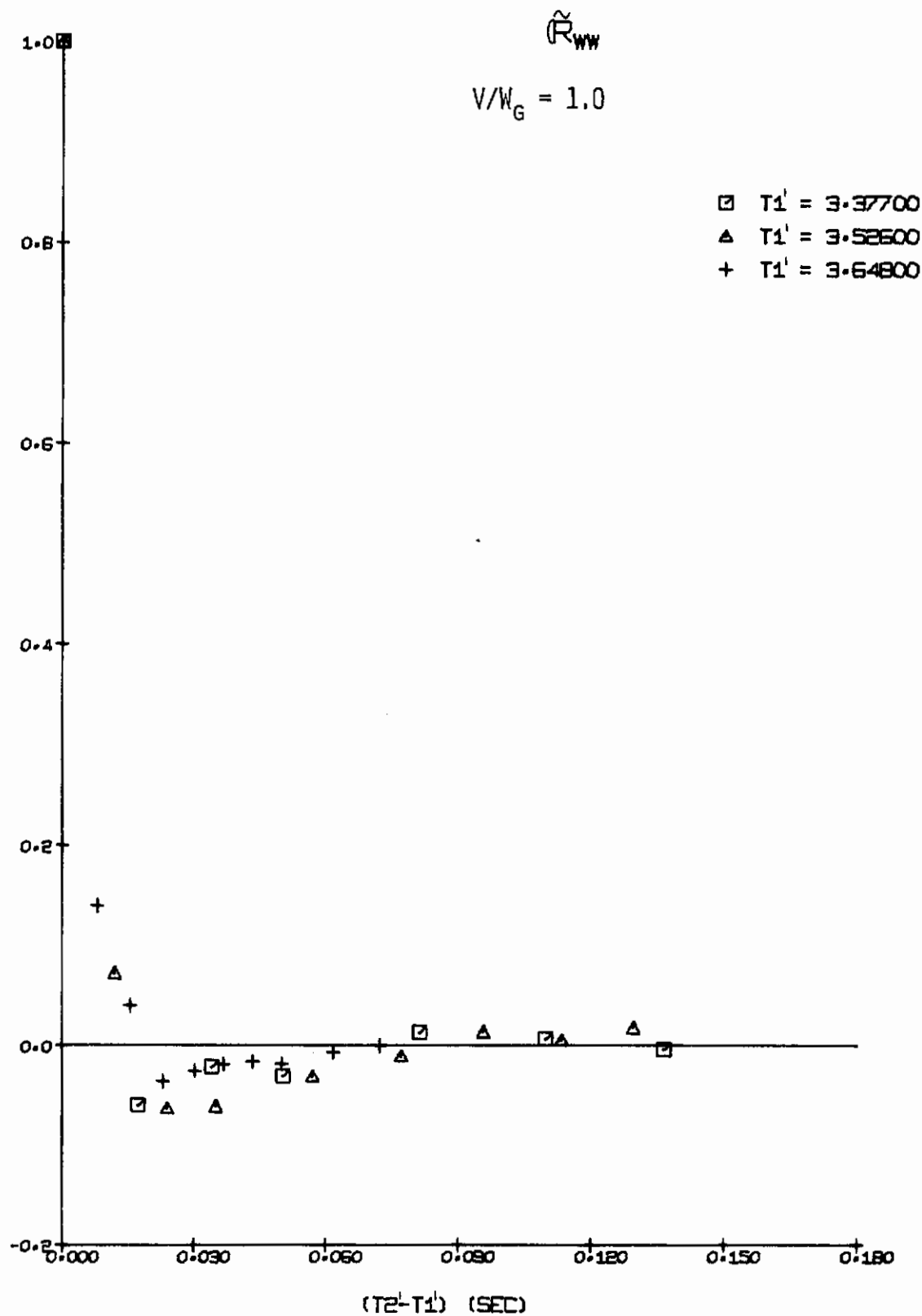FIGURE 151b.   FLIGHT PATH TURBULENCE CORRELATION, 44" x 66" TUNNEL

354

$$\tilde{R}_{WU}$$

$$V/W_G = 2.0$$

Legend:
☑ $T1' = 0.03705$
△ $T1' = 0.06467$
+ $T1' = 0.08163$
✕ $T1' = 0.09902$

FIGURE 152a.   FLIGHT PATH TURBULENCE CORRELATION, 44" x 66" TUNNEL

355

FIGURE 152b.   FLIGHT PATH TURBULENCE CORRELATION, 44" x 66" TUNNEL

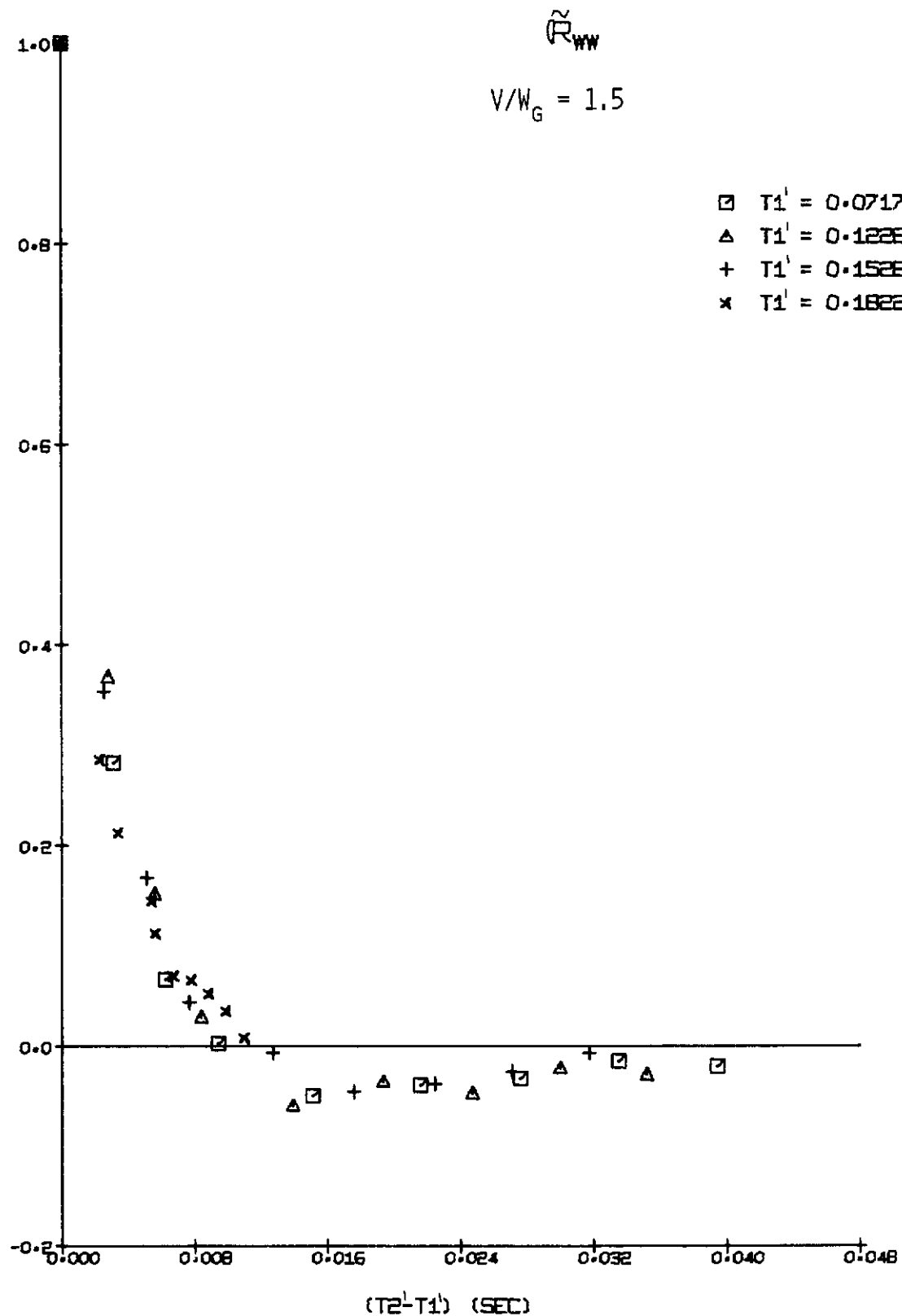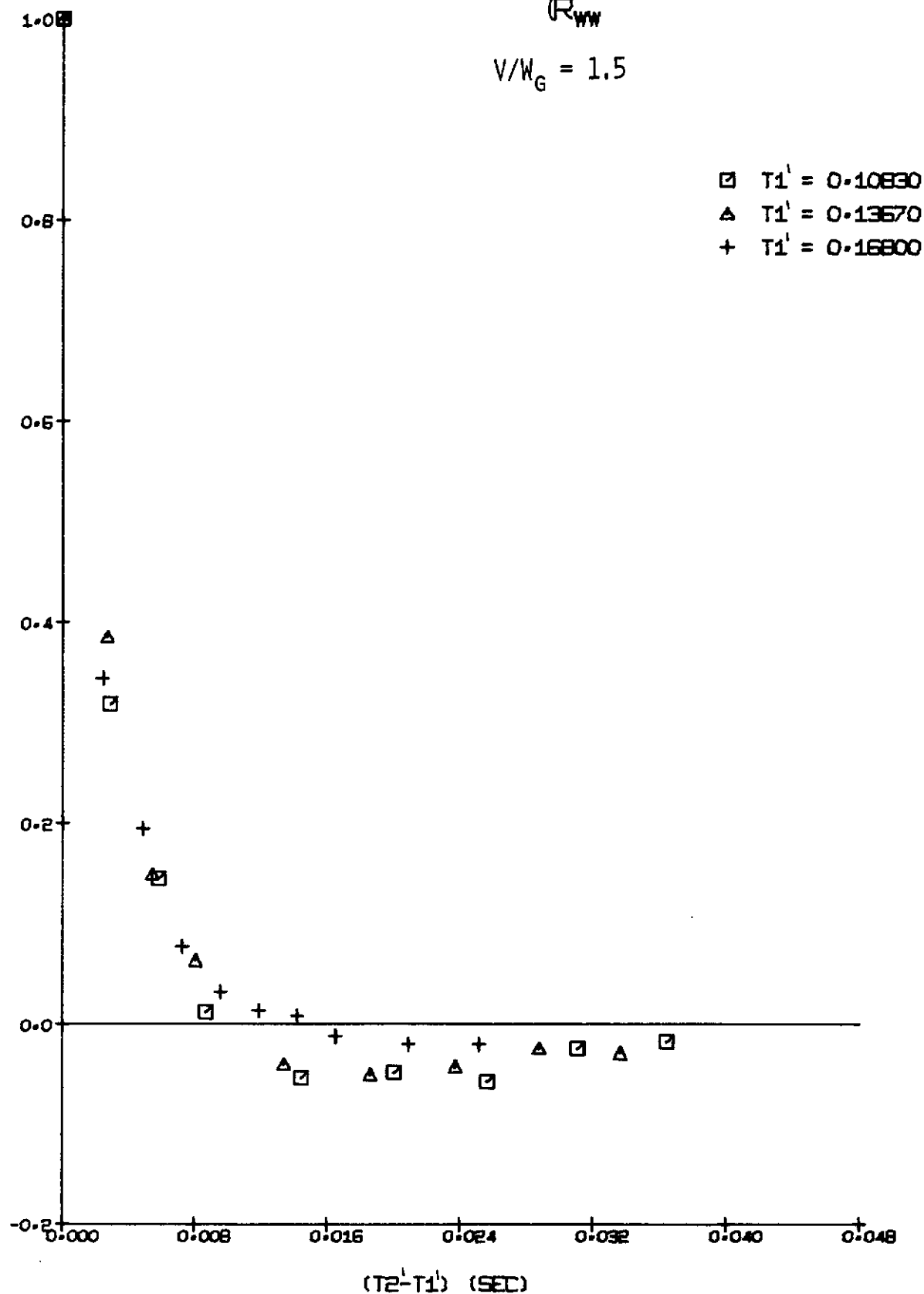$$\tilde{R}_{WV}$$

$$V/W_G = 1.0$$

Legend:
- ☑ $T1' = 3.09700$
- △ $T1' = 3.45800$
- + $T1' = 3.59300$
- ✕ $T1' = 3.69100$

FIGURE 153a.   FLIGHT PATH TURBULENCE CORRELATION, 44" x 66" TUNNEL

357

$\tilde{R}_{wv}$

$V/W_G = 1.0$

☑ T1' = 3·37700
△ T1' = 3·52500
+ T1' = 3·64800

FIGURE 153b.   FLIGHT PATH TURBULENCE CORRELATION, 44" x 66" TUNNEL

FIGURE 154a. FLIGHT PATH TURBULENCE CORRELATION, 44" x 66" TUNNEL

$$\tilde{R}_{wv}$$

$$V/W_G = 1.5$$
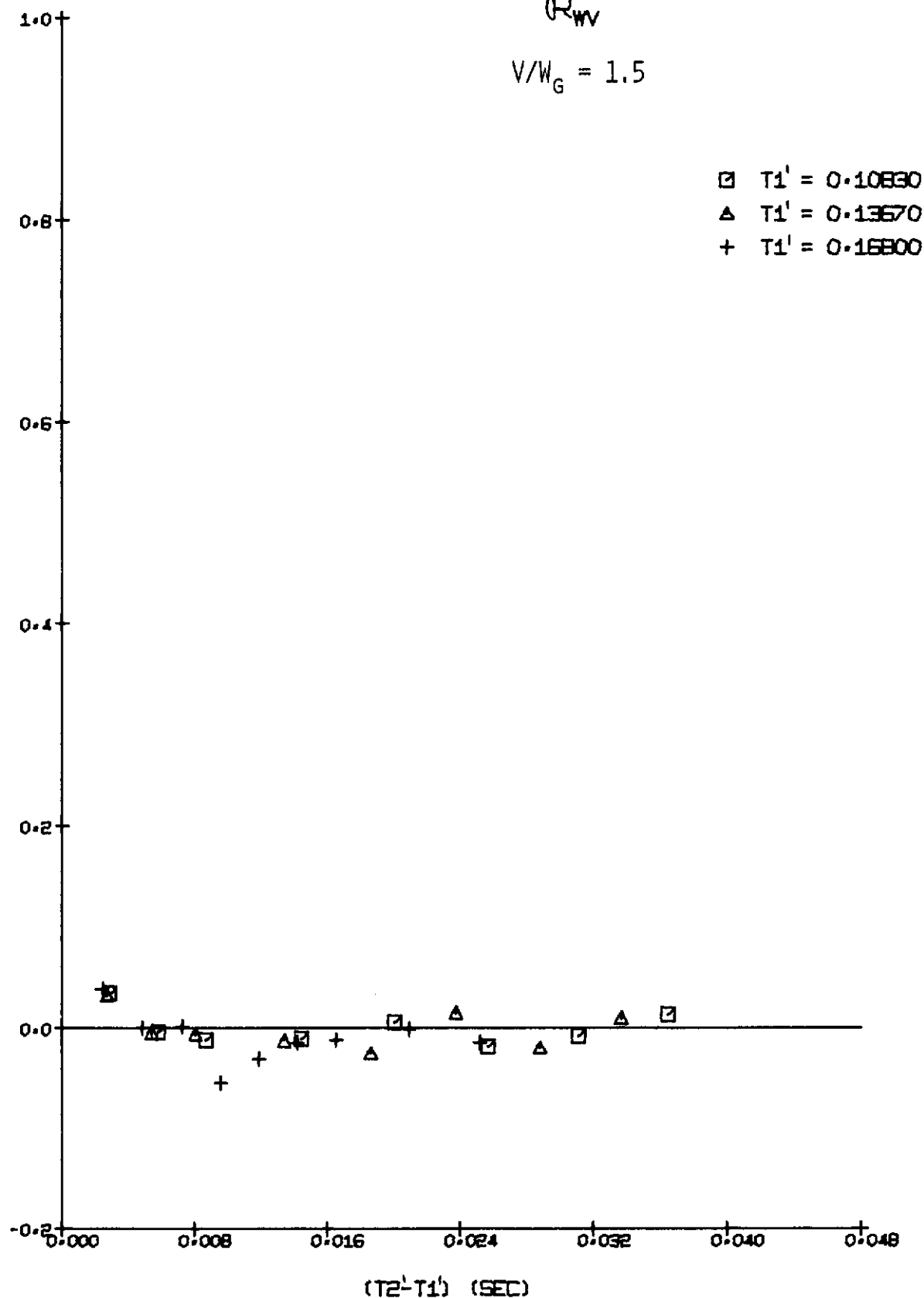
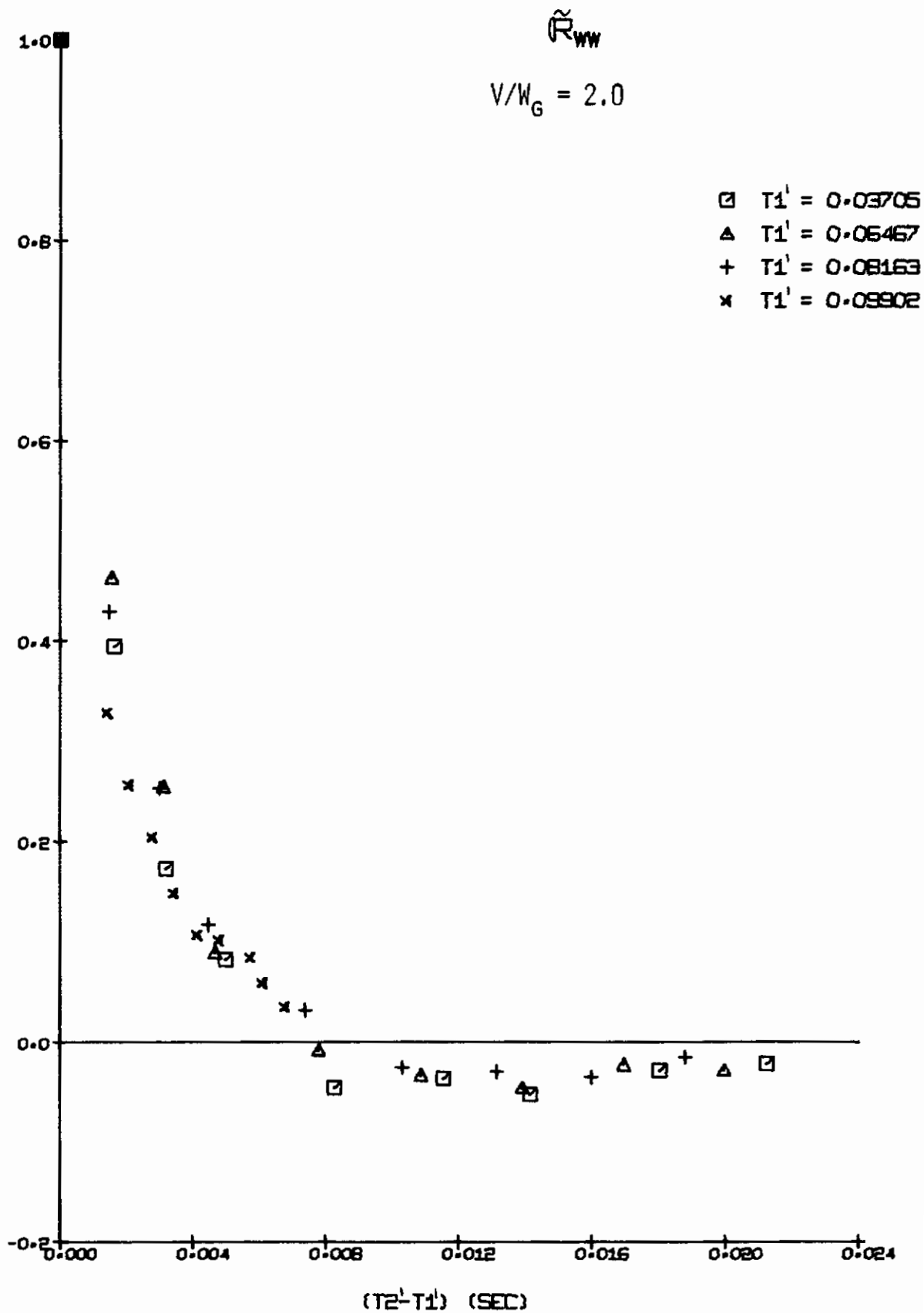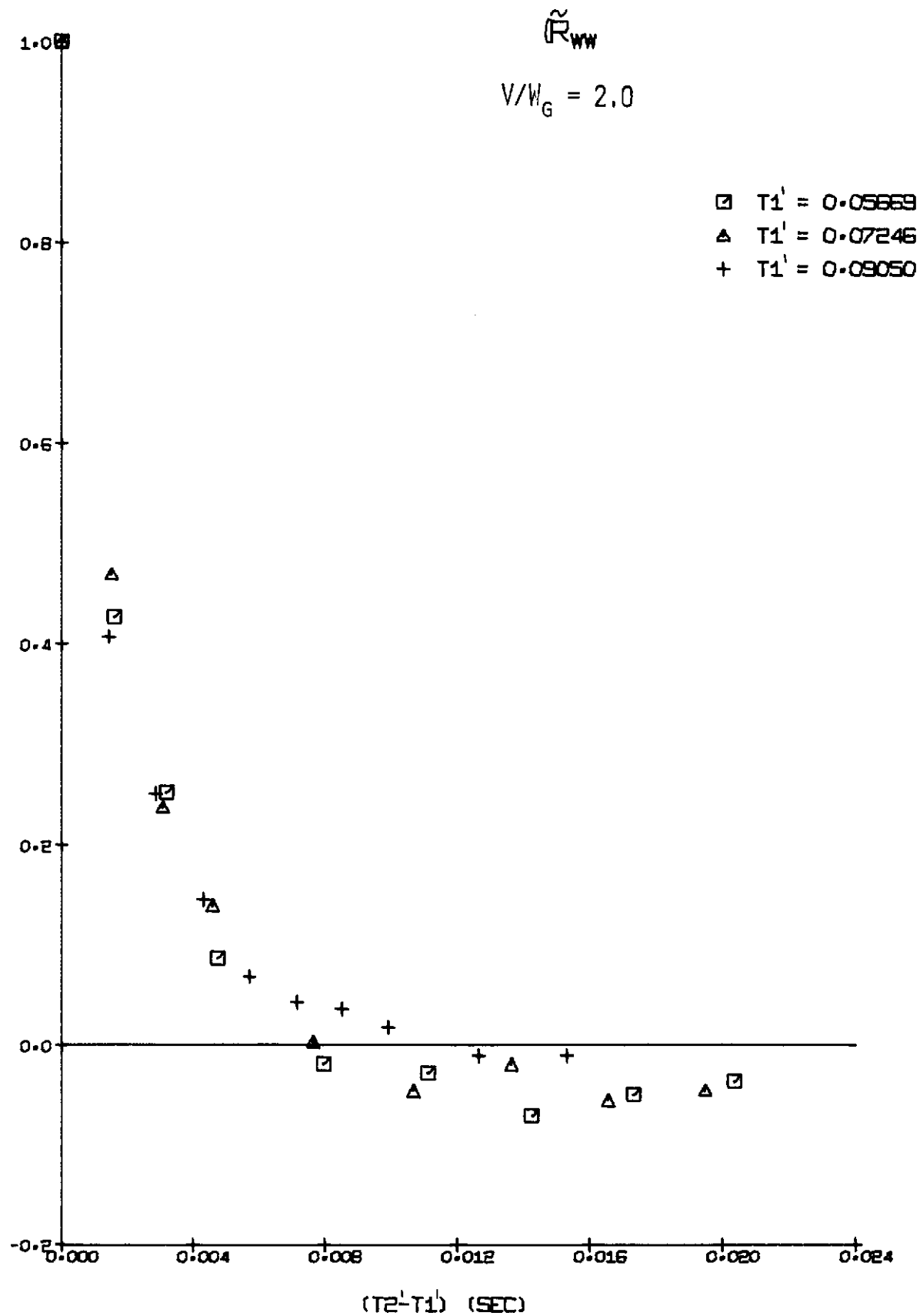FIGURE 154b. FLIGHT PATH TURBULENCE CORRELATION, 44" x 66" TUNNEL

$\tilde{\tilde{R}}_{WV}$

$V/W_G = 2.0$

☑ T1' = 0.03705
△ T1' = 0.06467
+ T1' = 0.08163
✗ T1' = 0.09902

0.0

(T2'-T1') (SEC)
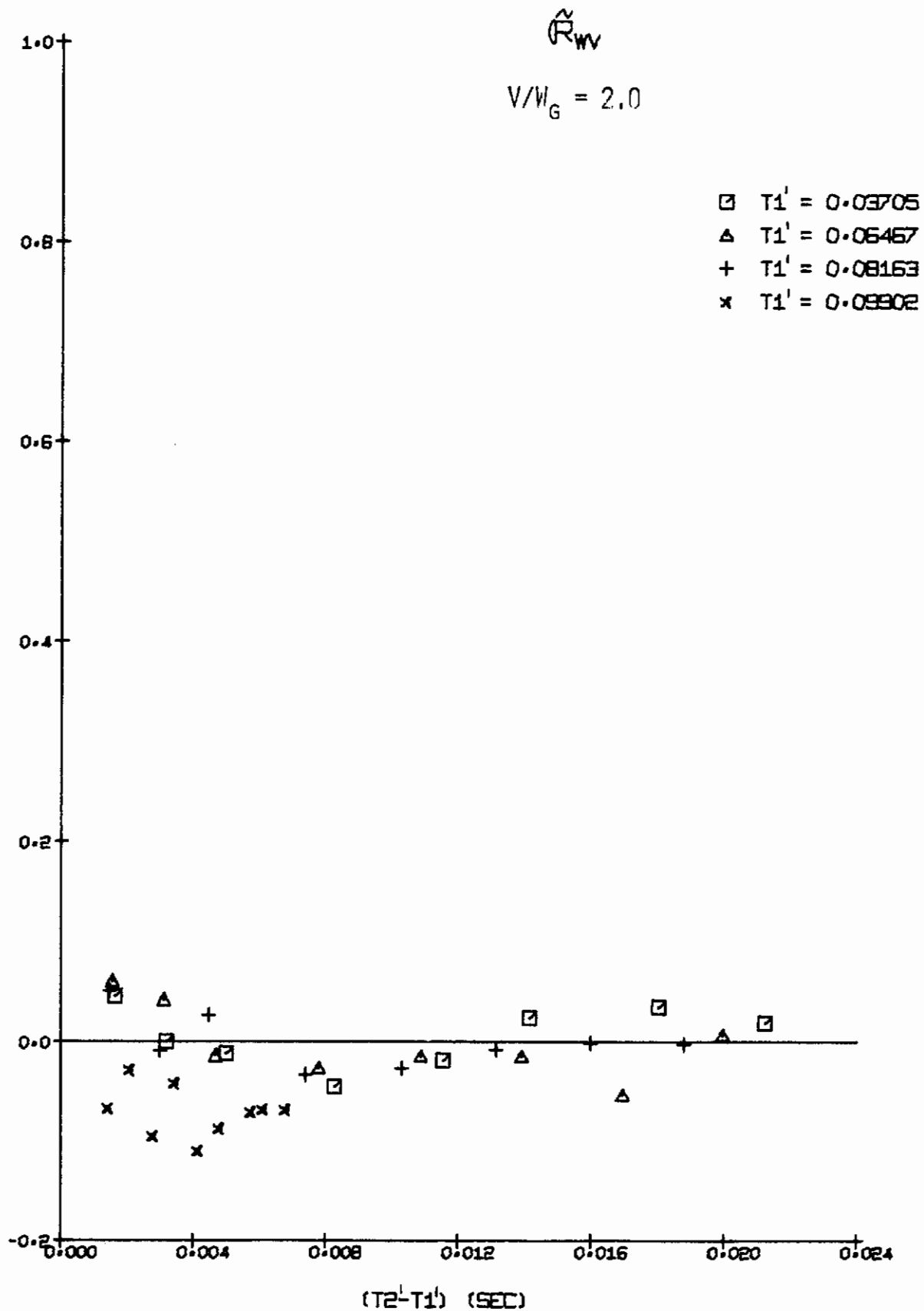
FIGURE 155a. FLIGHT PATH TURBULENCE CORRELATION, 44" x 66" TUNNEL

361

$$\tilde{R}_{wv}$$

$$V/W_G = 2.0$$

FIGURE 155b.   FLIGHT PATH TURBULENCE CORRELATION, 44" x 66" TUNNEL

FIGURE 156a. FLIGHT PATH TURBULENCE CORRELATION, 44" x 66" TUNNEL

363

$$\tilde{R}_{ww}$$

$$V/W_G = 1.0$$

☑ T1' = 3·37700
▲ T1' = 3·52500
+ T1' = 3·64800

FIGURE 156b.   FLIGHT PATH TURBULENCE CORRELATION, 44" x 66" TUNNEL

364

FIGURE 157a. FLIGHT PATH TURBULENCE CORRELATION, 44" x 66" TUNNEL

365

$$\tilde{R}_{ww}$$

$$V/W_G = 1.5$$

Legend:
- ☒ $T1' = 0.10830$
- △ $T1' = 0.13570$
- + $T1' = 0.16800$

$(T2'-T1')$ (SEC)

FIGURE 157b.   FLIGHT PATH TURBULENCE CORRELATION, 44" x 66" TUNNEL

366

FIGURE 158a. FLIGHT PATH TURBULENCE CORRELATION, 44" x 66" TUNNEL

367

$\tilde{R}_{ww}$

$V/W_G = 2.0$

□ T1' = 0·05669
△ T1' = 0·07246
+ T1' = 0·09050

(T2'-T1') (SEC)

FIGURE 158b.   FLIGHT PATH TURBULENCE CORRELATION, 44" x 66" TUNNEL

368
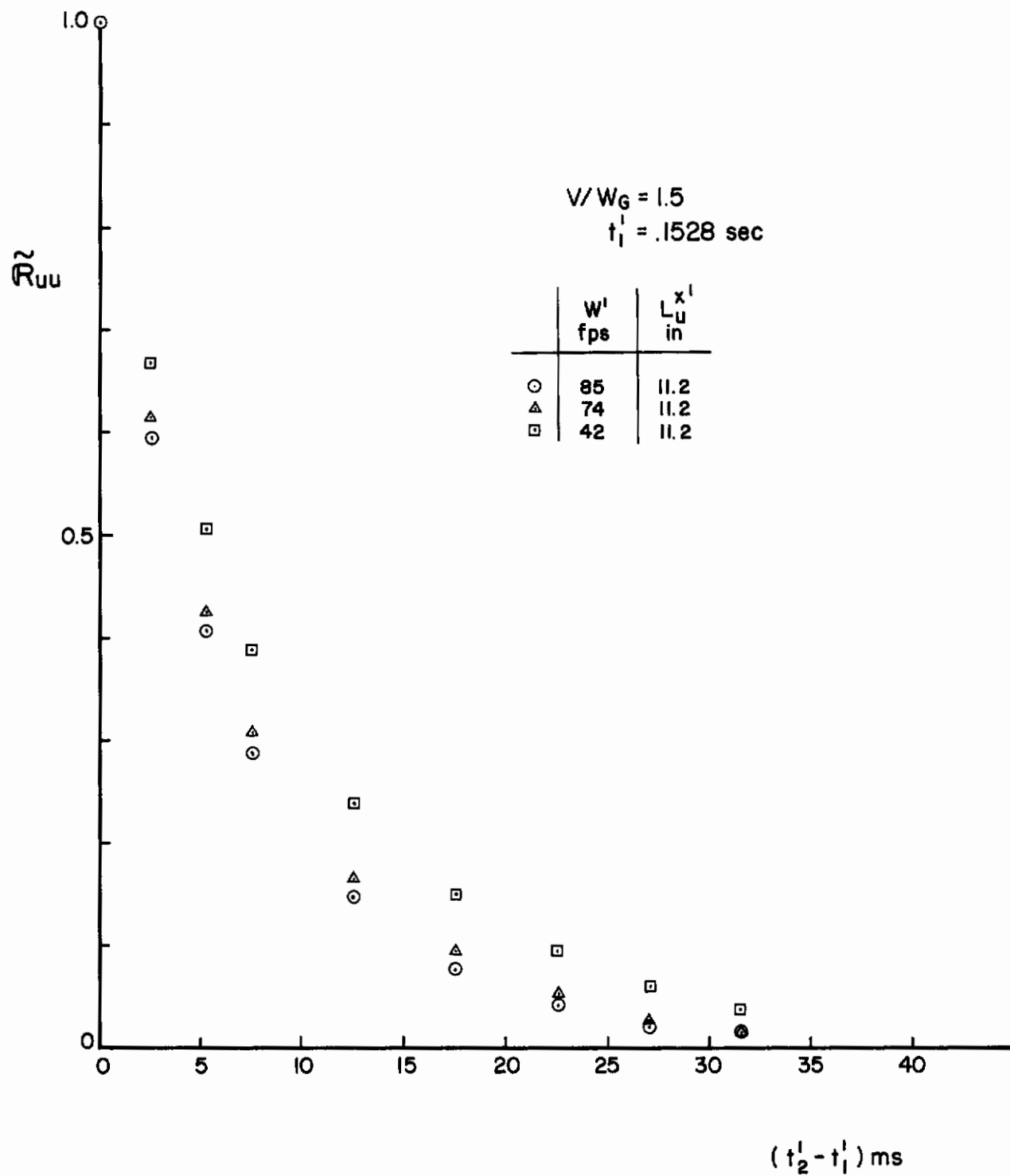
FIGURE 159. THE INFLUENCE OF W' ON THE MODIFIED VON KÁRMÁN MODEL

369
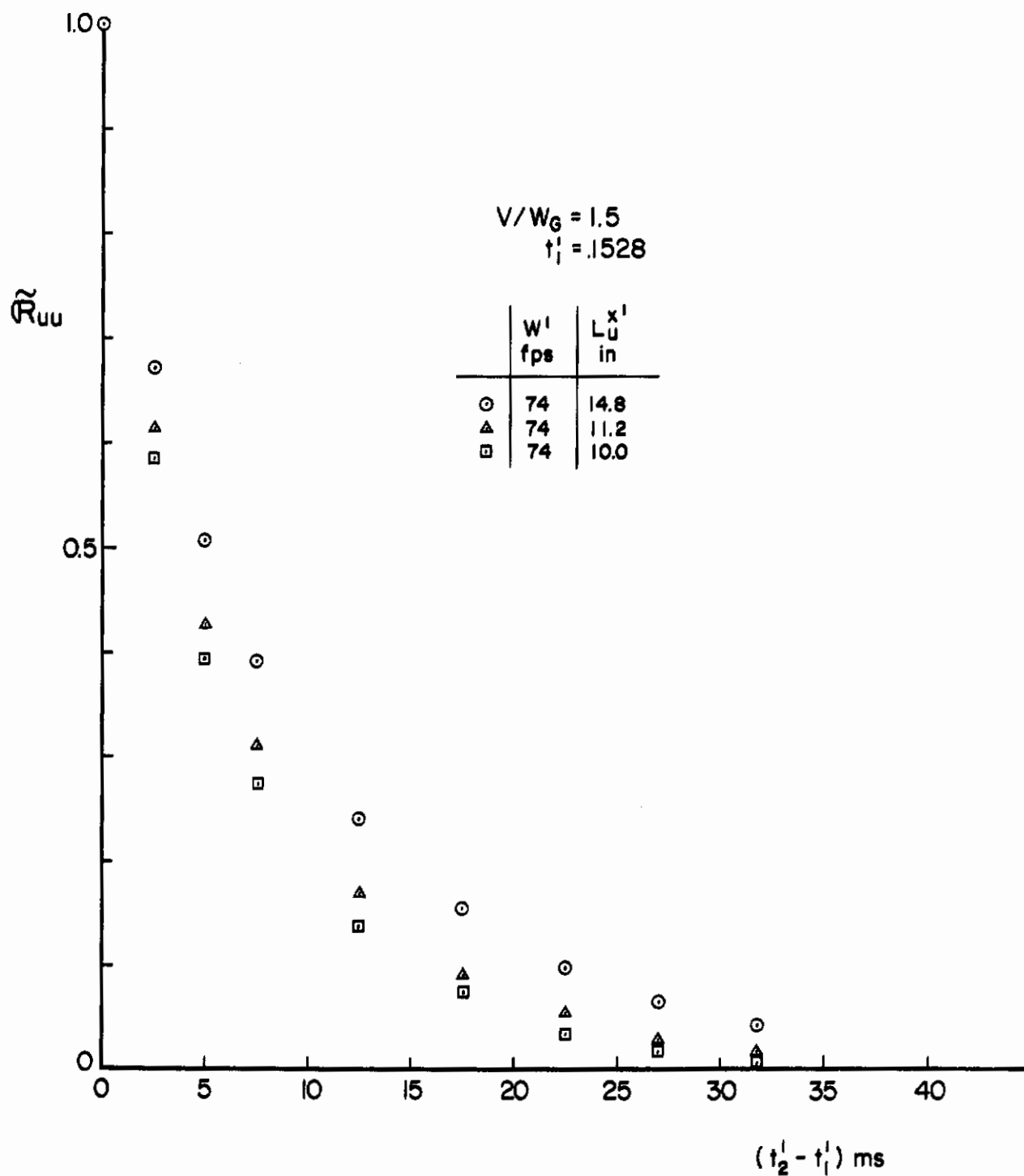
FIGURE 160. THE INFLUENCE OF $L_u^{x'}$ ON THE MODIFIED VON KÁRMÁN MODEL

370
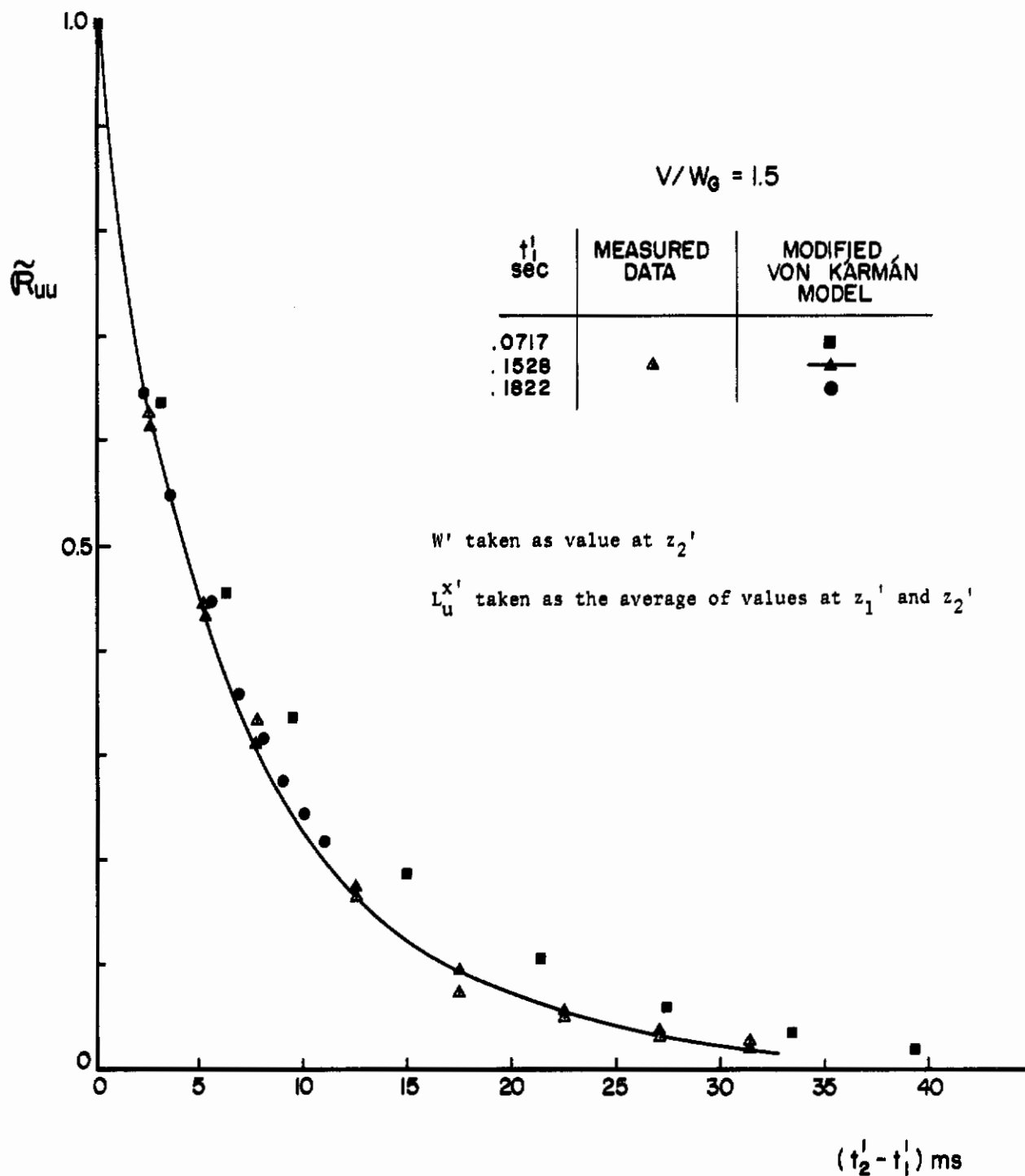
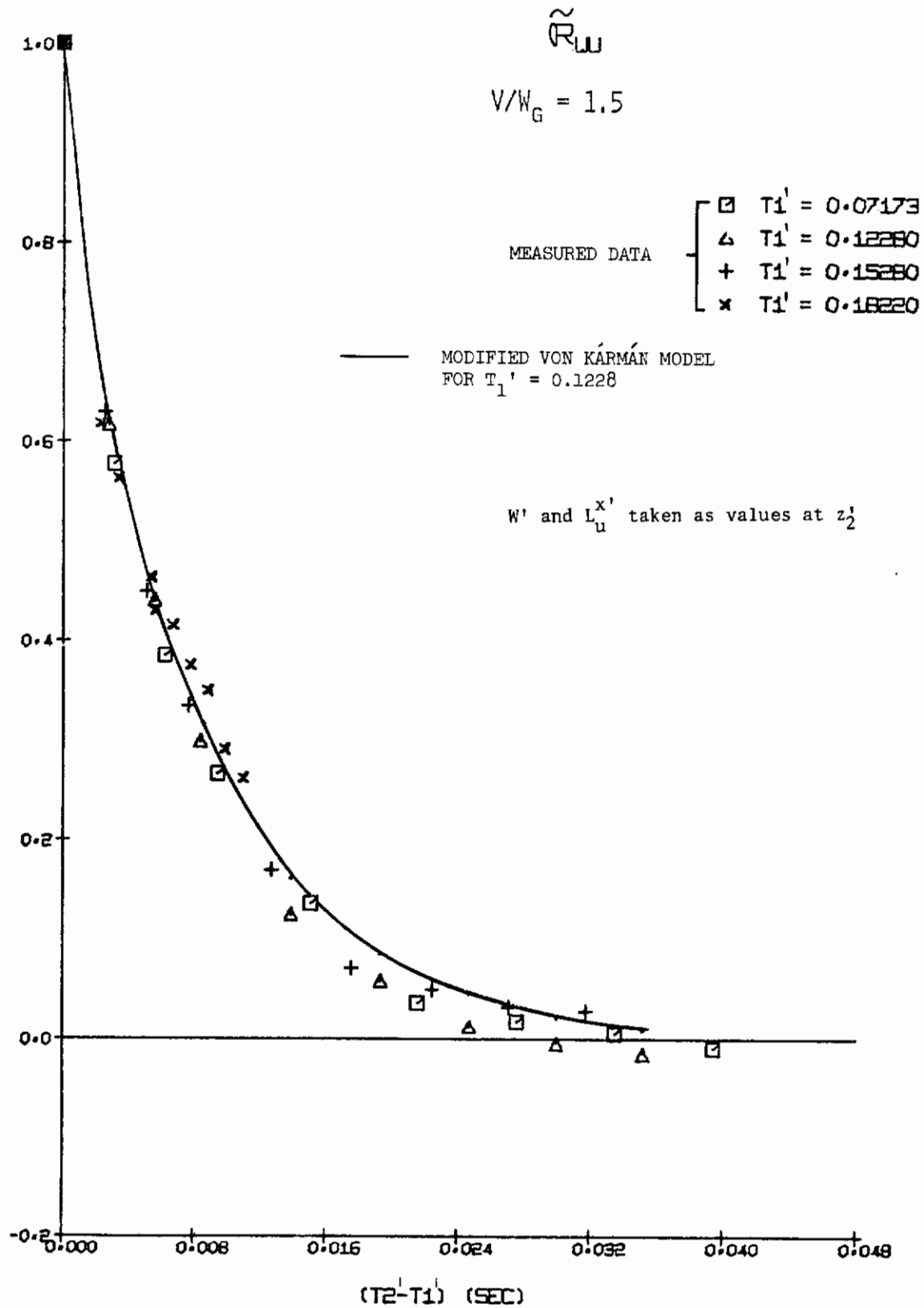FIGURE 161. $\tilde{R}_{uu}$ PREDICTED BY MODIFIED VON KÁRMÁN MODEL FOR THE 44" x 66" TUNNEL

371

FIGURE 162. $\widetilde{R}_{uu}$ PREDICTED BY MODIFIED VON KÁRMÁN MODEL FOR THE 44" x 66" TUNNEL

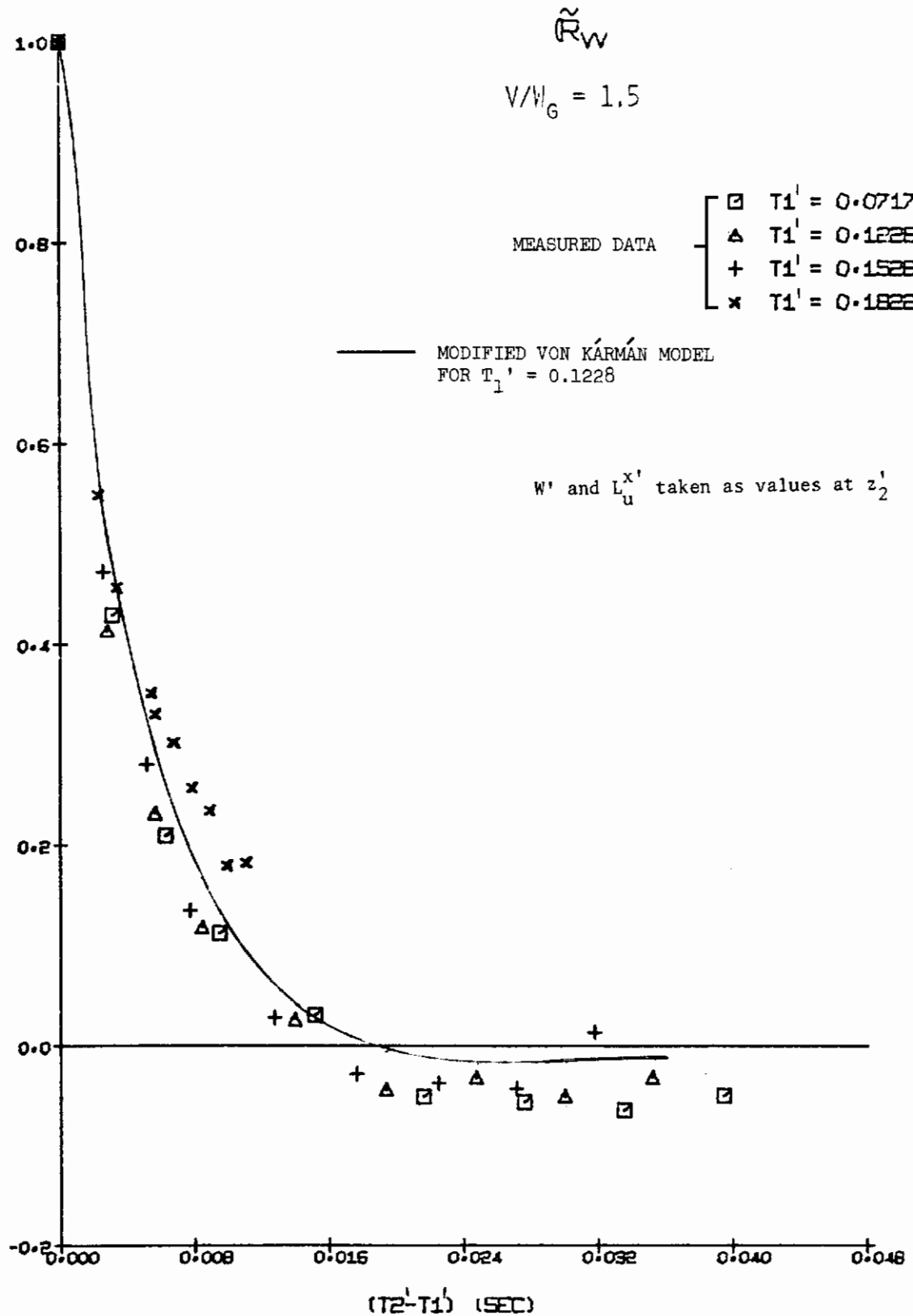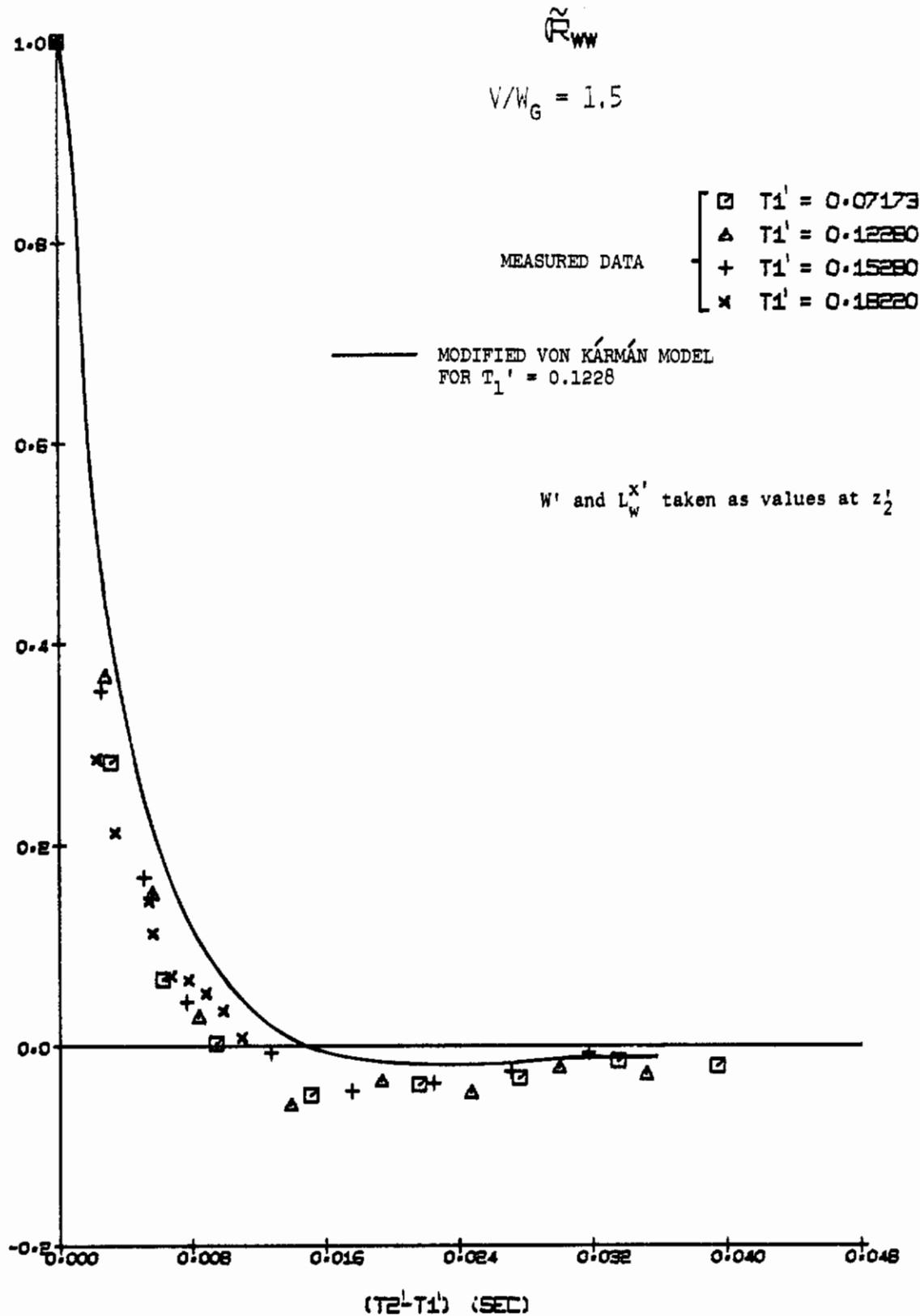FIGURE 163. $\tilde{R}_{vv}$ PREDICTED BY MODIFIED VON KÁRMÁN MODEL FOR THE 44" x 66" TUNNEL
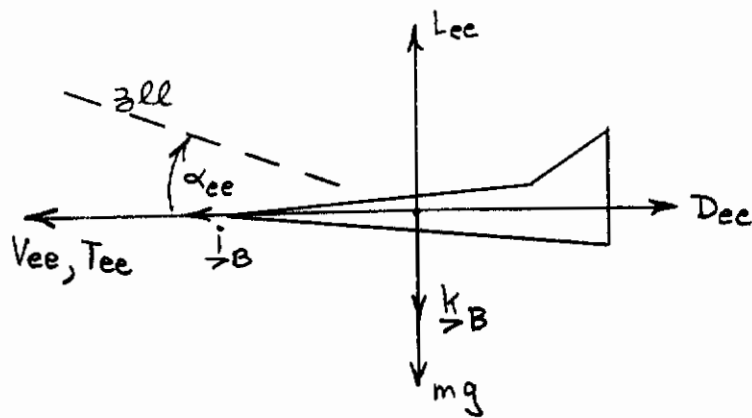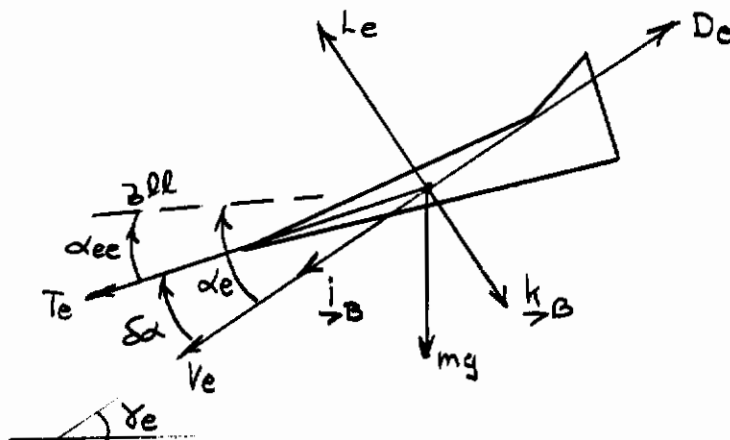
373

$$\tilde{\mathbb{R}}_{ww}$$

$$V/W_G = 1.5$$

▣	$T1' = 0.07173$	
▲	$T1' = 0.12280$	
+	$T1' = 0.15280$	
✖	$T1' = 0.18220$	

MEASURED DATA

———— MODIFIED VON KÁRMÁN MODEL
FOR $T_1' = 0.1228$

W' and $L_w^{x'}$ taken as values at z_2'

$(T2' - T1')$ (SEC)

FIGURE 164. $\tilde{\mathbb{R}}_{ww}$ PREDICTED BY MODIFIED VON KÁRMÁN MODEL FOR THE 44" x 66" TUNNEL

(a)   REFERENCE EQUILIBRIUM FOR REF. 24 ($\mathcal{F}_B$ ALIGNED WITH $\underset{\rightarrow}{V}_{ee}$)

(b)   PRESENT REFERENCE EQUILIBRIUM ($\mathcal{F}_B$ ALIGNED WITH $\underset{\rightarrow}{V}_e$)

FIGURE 165

375
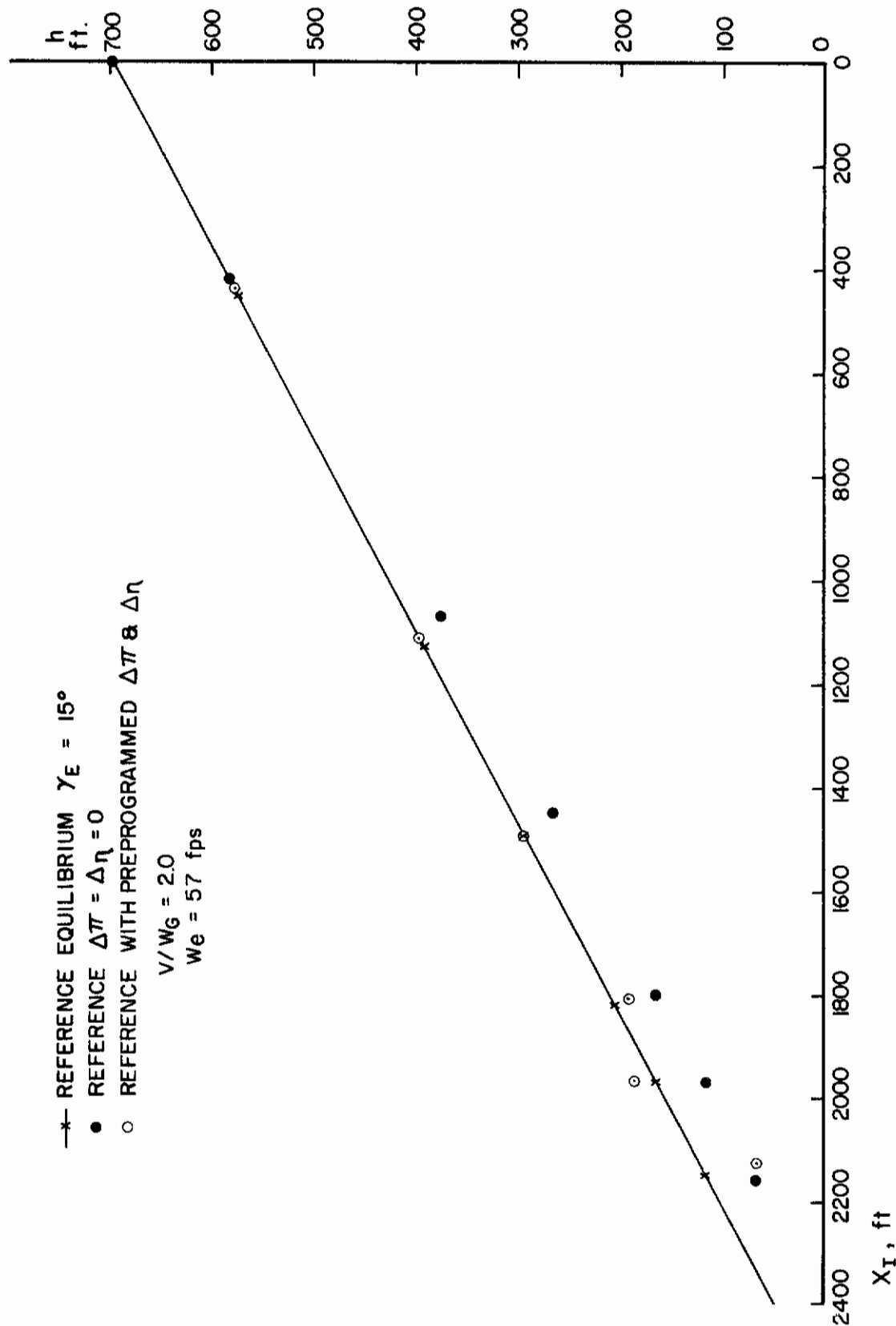
FIGURE 166.   GLIDE SLOPE TRACKING PERFORMANCE

REFERENCE EQUILIBRIUM $\gamma_E = 15°$
REFERENCE $\Delta \pi = \Delta \eta = 0$
REFERENCE WITH PREPROGRAMMED $\Delta \pi$ & $\Delta \eta$
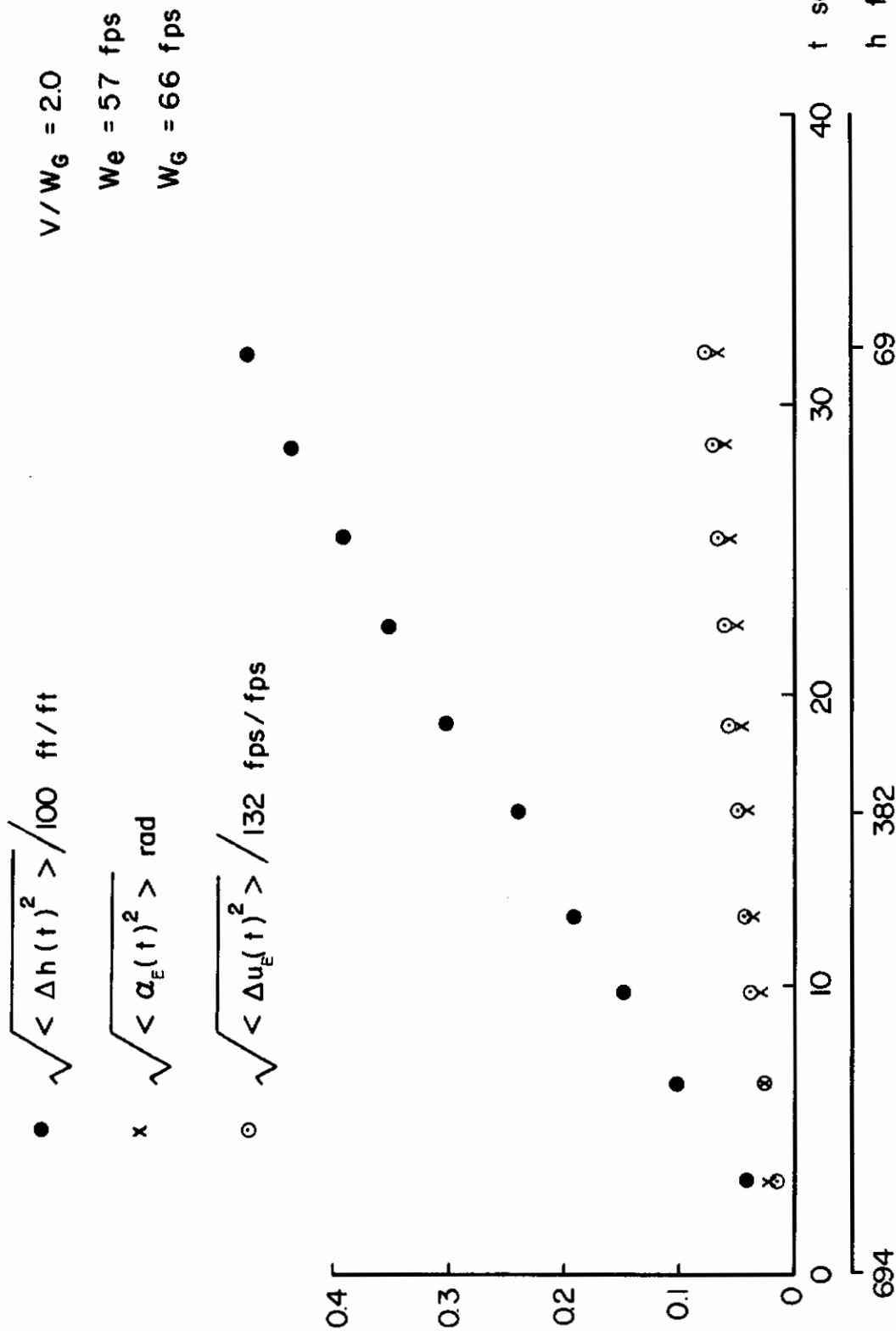
$V/W_G = 2.0$
$W_e = 57$ fps

FIGURE 167. TIME DEPENDENCE OF THE DISPERSION MATRIX $\underline{\Sigma}(t)$

377

REFERENCES

1. Wolkovitch, J., LaMont, C. W. and Lochtie, D. W., "Fundamental Limitations on V/STOL Terminal Guidance Due to Aircraft Characteristics." NASA CR-1901, Dec. 1971

2. Hiscocks, R. D., "STOL Aircraft - A Perspective." AIAA Journal, Vol. 72, No. 685, pp. 11-33, Jan. 1968.

3. Hoffman, L. G. et al, "Investigation of Measuring System Requirements for Low-Visibility Landing." USAF, AFFDL-TR-71-151, Dec. 1971.

4. Johnston, W. A. and McRuer, D. T., "Development of a Category II Approach System Model." NASA CR-2022, May 1972.

5. Etkin, B., "Dynamics of Atmospheric Flight." Wiley, N.Y., 1972.

6. Luers, J. K. and Reeves, J. B., "Effect of Shear on Aircraft Landing." NASA CR-2287, July 1973.

7. Timothy, L. K., and Bona, B. E., "State Space Analysis: An Introduction." McGraw-Hill, New York, 1968.

8. Etkin, B., "Theory of Flight of Airplanes in Isotropic Turbulence - Review and Extension." AGARD Report 372, 1961.

9. Davenport, A. G., "The Dependence of Wind Loads on Meteorological Parameters." Paper 2, Proc. Int. Conf. on Wind Effects on Buildings and Structures, London, H.M.S.O., 1965.

10. Teunissen, H. W., "Characteristics of the Mean Wind and Turbulence in the Planetary Boundary Layer." UTIAS Review No. 32, University of Toronto, Oct. 1970.

11. Teunissen, H. W., "Simulation of the Planetary Boundary Layer in a Multiple-Jet Wind Tunnel." UTIAS Report No. 182, June 1972.

12. Favre, A. J., "Review on Space-Time Correlations in Turbulent Fluids," Trans. ASME, J. Appl. Mech., 1965.

13. Skelton, G. B., "Investigation of the Effects of Gusts on V/STOL Craft in Transition and Hover." USAF, AFFDL-TR-68-85, 1968.

14. Bendat, J. S. and Piersol, A. G., "Measurement and Analysis of Random Data." Wiley, N.Y., 1971.

15. Teunissen, H. W., "Simulation of the Planetary Boundary Layer in a Multiple-Jet Wind Tunnel." Atmospheric Environment 9, No. 2, 1975, pp. 145-174.

16. Reid, L. D., Schuyler, G. D., and Teunissen, H. W., "Design, Construction and Calibration of the UTIAS Planetary Boundary Layer Simulation Wind Tunnel." UTIAS Tech. Note No. 186, University of Toronto, Dec. 1974.

17. Teunissen, H. W., "An Ejector-Driven Wind Tunnel for the Generation of Turbulent Flows with Arbitrary Mean Velocity Profile." UTIAS TN 133, University of Toronto, Feb. 1969.

18. Tsien, Hsue-Shen, "On the Design of the Contraction Cone for a Wind Tunnel." Journal of the Aeronautical Sciences, Feb. 1943.

19. Frost, W., "Review of Data and Prediction Techniques for Wind Profiles Around Man Made Surface Obstructions." AGARD Conf. Proceedings No. 140 on Flight Turbulence, May 1973.

20. Templin, R. J., "Interim Progress Note on Simulation of Earth's Surface Winds by Artificially Thickened Wind Tunnel Boundary Layers." National Research Council of Canada, NAE Report LTR-LA-22, February 1969.

21. Harris, R. I., "Measurements of Wind Structure at Heights up to 598 ft. Above Ground Level." ERA Tech. Rep. 5258, 1968.

22. Davenport, A. G. and Isyumov, N., "The Application of the Boundary Layer Wind Tunnel to the Prediction of Wind Loading." Paper 7, Wind Effects on Buildings and Structures, University of Toronto Press, 1967.

23. Etkin, B., "Dynamics of Flight-Stability and Control," Wiley, New York, 1959.

24. Reeves, P. M., Campbell, G. S., Ganzer, V. M., Joppa, R. G., "Development and Application of a Non-Gaussian Atmospheric Turbulence Model for Use in Flight Simulators," NASA CR-2451, Sept. 1974.

25. Hinze, J. O., "Turbulence - An Introduction to Its Mechanism and Theory." McGraw-Hill, New York, 1959.

26. Etkin, B., Johnston, G. W. and Teunissen, H. W., "Measurements of Turbulence Inputs for V/STOL Approach Paths in a Simulated Planetary Boundary Layer." UTIAS Report No. 189, University of Toronto, July 1973.

27. Etkin, B. and Teunissen, H. W., "A Method for the Estimation of Flight Path Perturbation During Steep Descents of V/STOL Aircraft." CASI Transactions, Vol. 7, No. 2, September 1974.